UNIVERSIDADE ESTADUAL DE CAMPINAS

FACULDADE DE ENGENHARIA MECÂNICA

E INSTITUTO DE GEOCIÊNCIAS

RONALDO HERLINGER JÚNIOR

A Study on Residual Oil in Carbonate Reservoirs of the Barra Velha Formation, Santos Basin

Um Estudo Sobre Óleo Residual em Reservatórios Carbonáticos da Formação Barra Velha, Bacia de Santos

CAMPINAS

2025

RONALDO HERLINGER JÚNIOR

A Study on Residual Oil in Carbonate Reservoirs of the Barra Velha Formation, Santos Basin

Um Estudo Sobre Óleo Residual em Reservatórios Carbonáticos da Formação Barra Velha, Bacia de Santos

Thesis presented to the School of Mechanical Engineering and Institute of Geosciences of the University of Campinas in partial fulfillment of the requirements for the degree of Doctor in Sciences and Petroleum Engineering, in the area of Reservoirs and Management.

Tese apresentada à Faculdade de Engenharia Mecânica e Instituto de Geociências da Universidade Estadual de Campinas como parte dos requisitos exigidos para obtenção do título de Doutor em Ciências e Engenharia de Petróleo, na área de Reservatórios e Gestão.

Orientador: Prof. Dr. Alexandre Campane Vidal

ESTE TRABALHO CORRESPONDE À VERSÃO FINAL DA TESE DEFENDIDA PELO ALUNO RONALDO HERLINGER JUNIOR, E ORIENTADO PELO PROF. DR ALEXANDRE CAMPANE VIDAL.

CAMPINAS

2025

Informações complementares

Título em outro idioma: Um estudo sobre óleo residual em reservatórios carbonáticos
da formação Barra Velha, Bacia de Santos
Palavras-chave em inglês:
Reservoirs (Carbonates)
Pre-salt
Santos basin
Área de concentração: Reservatórios e Gestão
Titulação: Doutor em Ciências e Engenharia de Petróleo
Banca examinadora:
Alexandre Campane Vidal [Orientador]
André Luiz Martins Compan
João Paulo Borges Gomes
José Sérgio de Araújo Cavalcante Filho
Monica Marques da Fonseca
Data de defesa: 17-02-2025
Programa de Pós-Graduação: Ciências e Engenharia de Petróleo

Objetivos de Desenvolvimento Sustentável (ODS)
Não se aplica

Identificação e informações acadêmicas do(a) aluno(a)
- ORCID do autor: https://orcid.org/0000-0003-3553-7230
- Currículo Lattes do autor: http://lattes.cnpq.br/7908834868292138

Prof. Dr. Alexandre Campane Vidal, Presidente
Instituto de Geociências/Unicamp

Dr. André Luiz Martins Compan
Petrobras S.A.

Dr. João Paulo Borges Gomes
Petrobras S.A.

Dr. José Sérgio de Araújo Cavalcante Filho
Petrobras S.A.

Dr. Monica Marques da Fonseca
Petrobras S.A.

A Ata de Defesa com as respectivas assinaturas dos membros encontra-se no SIGA/Sistema de Fluxo de Dissertação/Tese e na Secretaria do Programa da Unidade.

Dedication

I dedicate this work to my wife Alice and my son Ivan.

Acknowledgments

Resumo

O estudo do óleo residual em reservatório é de grande importância para a indústria do petróleo, visto que embasa modelos de simulação de reservatórios, de onde são obtidas curvas de produção, denotando grande relevância econômica, além de fornecer informação relevante para estudos de recuperação melhorada. Desta forma, esta tese tem como objetivo principal investigar o aprisionamento de óleo em rochas carbonáticas da Formação Barra Velha, localizada na Bacia de Santos. De forma secundária, busca-se caracterizar e quantificar o aprisionamento em diversas escalas, além de realizar o *upscaling* dos dados obtidos. Para alcançar esses objetivos, foi utilizado um extenso banco de dados, que incluiu resultados de laboratório de petrofísica básica e especial, perfilagem de poços, técnicas de aprendizado de máquina, modelagem e simulação em escala de poros, além de imageamento em raios-X. A análise dos dados de saturação de óleo residual (Sor) obtidos a partir dos ensaios de permeabilidade relativa em conjunto com petrografia revelou um forte controle textural no aprisionamento de óleo. As rochas mais heterogêneas, com poros maiores e maior permeabilidade, tendem a apresentar maior Sor, tais como rudstones e shrubstones. Por outro lado, grainstones mais finos e mudstones tendem a reter menos óleo, fato observado em resultados laboratoriais e corroborados por *upscale* em poço. O imageamento em escala de poros com resolução média (em torno de 40 micrômetros), realizado após os ensaios sob condições de reservatório, indicou que o aprisionamento de óleo ocorre em uma condição de molhabilidade mista. Já, os ensaios realizados em centrífuga e imageados em resolução mais alta (~4 micrometros), utilizando óleo sintético sob condições de laboratório, demonstraram maior afinidade pelo óleo na primeira amostra estudada e mista na segunda. Ainda, a análise das imagens em alta resolução indicou um alto impacto da textura no aprisionamento de óleo, corroborando com observações feitas em outras escalas. Por fim, uma vez que as variações mineralógicas não impliquem em mudanças significativas em termos de molhabilidade, é provável que o predomínio de calcita deva ditar a tendência geral de molhabilidade das amostras.

Palavras Chave: Óleo residual, Pré-sal, Formação Barra Velha

Abstract

The study of residual oil in reservoirs holds significant importance for the petroleum industry, as it underpins reservoir simulation models, from which production curves are derived, highlighting its considerable economic relevance. Moreover, it provides crucial information for enhanced recovery studies. Hence, this thesis aims primarily to investigate the mechanisms of oil trapping in carbonate rocks of the Barra Velha Formation, located in the Santos Basin. Additionally, it seeks to characterize and quantify this phenomenon across multiple scales and to upscale the data obtained. To achieve these objectives, a comprehensive dataset was employed, encompassing results from routine and special core analyses, well logging, machine learning techniques, pore-scale modeling and simulation, as well as X-ray imaging. The integrated analysis of residual oil saturation (Sor) data obtained from relative permeability tests, combined with petrographic characterization, revealed a strong textural control on oil trapping. Heterogeneous rocks with larger pores and higher permeability, such as rudstones and shrubstones, tend to exhibit higher Sor values. Conversely, finer grainstones and mudstones demonstrated lower oil retention, as evidenced by laboratory results and validated by well-scale upscaling. Pore-scale imaging at medium resolution (~40 micrometers), conducted after tests under reservoir conditions, indicated that oil trapping predominantly occurs under mixed-wettability conditions. Furthermore, centrifuge experiments imaged at higher resolution (~4 micrometers), using synthetic oil under laboratory conditions, revealed greater oil affinity in the first sample analyzed and mixed wettability in the second. Moreover, high-resolution image analysis highlighted the significant impact of texture on oil trapping, corroborating observations made at other scales. Finally, since mineralogical variations do not lead to significant changes in terms of wettability, the predominance of calcite is likely to dictate the overall wettability trend of the samples.

Key Word: Residual oil, Pre-salt, Barra Velha Formation

Illustration List

Table List

Summary

.

.

1. Introduction

Residual Oil Saturation (Sor) corresponds to the trapped oil within the reservoir pores after the displacement of the oil by an immiscible fluid (Donaldson, 1989; Valenti, Valenti, and Koederitz, 2002). Upon the initiation of water flooding the oleic phase, once disrupted, remains entrapped due to capillary forces (Blunt, 2017). The residual phase will be largely inaccessible to conventional flooding methods except enhanced oil recovery (EOR) approaches are applied. Among these techniques, the introduction of surfactants is particularly noteworthy, as it modifies the interfacial properties and the physicochemical characteristics of the fluids, thereby altering their configuration and facilitating a more efficient mobilization of the residual oil (Anto and Bhui, 2022; Massarweh and Abushaikha, 2020).

The fluid flow within pores is shaped via viscous, gravitational, and capillary forces. Within reservoirs, fluid flow typically occurs at low velocities. These flows are referred to as low capillary number flows, where capillary forces are predominant (Bashiri and Kasiri, 2011; Guo, Song and Hilfer, 2020; Speight, 2017). Under these conditions, it is said that Sor is primarily controlled by the factors that influence capillary forces (Blunt, 2017), which include the liquid/solid contact angle, interfacial tension, and the porous morphology, classically related by the Young-Laplace equation:

$$r = \frac{2\sigma cos\theta}{Pc} \qquad (1.1)$$

Where r corresponds to the throat radius, σ the interfacial tension, θ the contact angle, and Pc the capillary pressure. Thus, capillary forces will result from fluids characteristics, environmental conditions, the mineral composition, and the geometry of the porous system. According to Blunt (2017), interfacial tension approximately corresponds to the difference in surface tension between the fluids. Therefore, the controls of the involved fluids' surface tensions will control the interfacial tension. Considering an aqueous phase, the balances of forces acting on the molecules within the bulk tends to zero, as the interactions with neighboring molecules effectively cancel each other out. However, for a molecule located at the liquid surface, a resultant inward force arises due to the absence of attractive interactions from above. This inward force causes the surface molecules to resist deformation. This phenomenon is

referred to as surface tension (Berry, 1971). Among the factors that control the surface tension of water, which are higher than those of hydrocarbons due to hydrogen bonds, are composition, salinity, pressure, temperature, and pH (Liu, Wickramasinghe and Qian, 2017; Slowinski, Gates and Waring, 1957; Wen *et al.*, 2018). Oil, on the other hand, has lower tensions due to the weak polarity of the molecules, typically bonded by Van der Waals forces. Therefore, factors such as oil composition, dissolved gas, pressure, and temperature are highly influential in the surface tensions that determine the degree of cohesion of hydrocarbons (Klein *et al.*, 2019; Liu, Wickramasinghe and Qian, 2017).

The wettability of the rocks is directly related to the contact angle, which has a significant influence on Sor, implying different oil retention configurations. Wettability is associated with a competition between cohesive and adhesive forces. Minerals with a higher amount of surface charges can break the cohesive force of water, causing the rock to be water-wet. Thus, siliciclastic rocks tend to be water-wet (Anderson, 1985, 1986, 1987). On the other hand, carbonate minerals tend to have a lower content of surface charges. Therefore, these minerals often cannot break the water tension and end up being oil-wet, whose cohesion is lower. Although this trend concerning mineral composition is reported in the literature, several factors can lead to different wettability patterns, such as the presence of solid organic compounds adhered to minerals, water composition, and the presence of clay minerals, among others (Alqam *et al.*, 2021; Ballah *et al.*, 2016; Benner and Bartel, 1941; Jia *et al.*, 2022).

Under water-wet conditions, irreducible water, which exhibits a stronger affinity for the minerals, tends to accumulate in the corners of the pores or within pores connected by narrow throats. During imbibition, where the non-wetting phase is replaced by a wetting phase, the oil is often disconnected within the throat region through a mechanism called snap-off (Roof, 1970; Singh *et al.*, 2017). Once disconnected, the capillary forces induce the non-wetting phase entrapment in the center of the pores. Snap-off typically occurs when there is a pronounced size disparity between the pore and the throat linking it to the broader porous structure (Blunt, 2017; Chatzis, Morrow, and Lim, 1983; Wardlaw, 1982).

In oil-wet conditions, the solid medium preferentially attracts the oil phase. During waterflood, large amounts of oil are displaced until the oil phase collapses, leading to entrapment as films or within pore corners (Alhammadi *et al.*, 2017; Iglauer *et al.*, 2012).

Water sweeping is generally more effective in homogeneous media, considering its frontal advance independently of their wettability nature. However, heterogeneous media tends

to promote irregular oil displacement, increasing the potential formation of undrained oil regions within the reservoir (Blunt, 2017; Chatzis, Morrow, and Lim, 1983; Lenormand, Zarcone, and Sarr, 1983).

Residual oil saturation is usually determined using well logging, laboratory-based assays, or numerical models. Microresistivity logs are often utilized in well logging with water-based fluids, and the Archie relation is applied to calculate the water saturation. In this process, the filtrate displaces the moveable oil, leaving the remaining trapped oil portion; this fraction is typically called Sor (Donaldson, 1989; Valenti, Valenti, and Koederitz, 2002). Alternative *in-situ* methods for determining Sor include dielectric, pulsed neutrons, and carbon/oxygen logging (Chang *et al.*, 1988a; Pathak *et al.*, 2012; Wolff, Al-Jalahma, and Hook, 1993). Despite the variety of techniques, the efficiency of mud fluid filtration tends to be limited, potentially leading to inaccuracies in Sor estimation. These estimates can be impacted by some features, such as the depth of investigation of the logging tools, the quality of the hydrocarbons, the duration of exposure, and the petrophysical properties (porosity and permeability). To mitigate these uncertainties and enhance the precision of the results, it is crucial to calibrate the measurements with experimental results (Mohamed *et al.*, 2011).

The water/oil relative permeability experiment is a widely used method for determining Sor in the laboratory (McPhee, Reed, and Zubizarreta, 2015). In this procedure, cleaned rock samples are water saturated, then the oil is injected to reach the irreducible water saturation (Sw_{irr}) state. As soon as the sample is aged to restore the wettability, water injection is performed to produce oil. Once oil production ends, the trapped oil volume is considered Sor. These tests can be conducted under either unsteady-state or steady-state conditions. In the steady-state approach, both water and oil are injected simultaneously, with water flow gradually increasing to facilitate oil displacement. In contrast, in the unsteady-state technique only water is injected with constant volume or pressure.

1.1 Geological Context

The Santos Basin is situated on the south-east continental coast of Brazil. It is bordered to the north by the Cabo Frio High, separating it from the Campos Basin, while Florianópolis High serves as a boundary to the south, separating it from the Pelotas Basin. The Barra Velha Formation rocks were accumulated during sag or post-rift stage of the Santos Basin (Moreira

et al., 2007). These sediments overlay thick packages of bioclastic carbonates, as well as shales, Mg-clay ooidal sandstones, hybrid rocks, volcanic rocks, sandstones, and siltstones (Chinelatto *et al.*, 2020b; Leite, Silva and De Ros, 2020; Thompson, Stilwell and Hall, 2015), deposited during the rift stage and are overlain by evaporite accumulations from the Ariri Formation. This Formation marks the beginning of marine sedimentation that culminates in the drift phase, giving rise to the South Atlantic Ocean formation (Davison, 2007; Nürnberg and Müller, 1991; Rabinowitz and LaBrecque, 1979). The Barra Velha Formation sediments consist of intercalations of chemical precipitations of non-magnesian calcite crusts with fascicular-optic texture ("stromatolites" or "shrubstones") and Mg-clays, commonly found as laminations or particles (peloids and ooids) (Carvalho *et al.*, 2022; Gomes *et al.*, 2020b; Herlinger *et al.*, 2023; Netto, Pozo, Manuel, *et al.*, 2022; Netto, Pozo, M., *et al.*, 2022; Silva, da *et al.*, 2021). Experimental and petrographic evidence indicates that these clays are highly reactive, frequently undergoing dissolution or replacement during eodiagenesis (Tosca and Wright, 2015; Wright and Barnett, 2020). Dolomite and calcite spherulites are referred to as important diagenetic constituents that replace clay deposits. In addition to *in-situ* deposits, particulate rocks formed from the fragmentation of precipitated deposits are common reservoir facies in the Santos Basin (Barnett *et al.*, 2021).

1.2   Motivation

The estimation and comprehension of Sor and oil trapping are crucial for the petroleum industry. This information is used in reservoir flow simulations that form the basis for production forecasts. Consequently, accurately determining Sor has substantial economic implications, influencing both the project profitability and the reserves calculation. Furthermore, it plays a key role in reservoir management studies, providing essential insights for enhanced oil recovery (EOR) research (Masalmeh, 2013; Pathak *et al.*, 2012), vital employments for improving the oilfield's recovery factor.

Besides the direct economic implications of Sor, it is noteworthy that the understanding of Sor controls is still limited, particularly from a geological and petrographic perspective. There is virtually no published literature on the subject, as the study is usually relegated to the engineering fields. Consequently, the link between geological processes that may influence oil entrapment, geological modeling, and reservoir simulation is nonexistent.

1.3 Objectives

This thesis aims to investigate residual oil in reservoirs of the Barra Velha Formation, Campos Basin. To achieve this, various techniques were employed to characterize residual oil, estimate its properties, upscale results, and understand how rock characteristics govern oil entrapment. This study explores residual oil from multiple perspectives to address critical knowledge gaps, particularly regarding the link between fluid saturation and geology. The specific objectives are outlined as follows:

- Identify lithological controls (depositional and diagenetic) on Sor.
- Employ machine learning algorithms to predict and multiply Sor data from existing datasets.
- Integrate RCAL, SCAL, and well-log data to upscale laboratory results to the well scale.
- Model sedimentary facies at the pore scale to simulate fluid flow to understand oil entrapment mechanisms.
- Pore-scale multi-phase X-ray imaging to identify lithological controls on fluid saturation and oil trapping.
- Combine pore-scale X-ray imaging with numerical simulations to improve the interpretation of laboratory results.

By addressing these objectives, this work seeks to bridge the gap between fluid saturation studies and geological characterization, contributing to a more comprehensive understanding of residual oil behavior in complex carbonate reservoirs.

1.4 Structure of the thesis

This thesis is structured into six articles that present various methodologies to investigate residual oil in the rocks of the Barra Velha Formation, and a short communication that describes a methodology for extracting relative permeability curves from X-ray microtomography (μCTs). This section provides a summary of each article. In addition to the articles, the thesis includes the following appendices: Appendix A, which presents the statistical analyses used in

the machine learning model discussed in article 1; Appendices B, C, D, and E, which contain a summary of the petrographic descriptions and laboratory data utilized in article 2; Appendix F, which compiles the simulation results from article 4; and Appendices G, H, I, that shows µCTs slices of all experimental stages developed in Articles 5, 6, and in the short communication, respectively.

1.4.1   Article 1 - HERLINGER, R.; VIDAL, A. C. X-ray µCt extracted pore attributes to predict and understand Sor using ensemble learning techniques in the Barra Velha Pre-salt carbonates, Santos Basin, Offshore Brazil. **Journal of Petroleum Science and Engineering**, v. 212, 2022.

In recent years, the oil industry and society at large have experienced significant technological advancements with the incorporation of artificial intelligence and machine learning in all kinds of tasks, accelerating technical and scientific processes. Given that oil companies have built substantial databases of petrophysical properties, there is a growing demand to streamline workflows and reduce financial costs by training algorithms to predict petrophysical properties. In this context, this study aims to predict Sor derived from relative permeability experiments.

To construct the database for algorithm training, Sor data were combined with RCAL data and X-ray µCT scans. The µCT images were processed and segmented, pores were isolated and labeled, and morphological attributes were calculated to build the training dataset. Additionally, samples were grouped according to their primary lithological types. For the prediction of Sor, ensemble learning algorithms such as AdaBoost, Gradient Boosting, and XGBoost were tested.

The results revealed a lithological control, with more heterogeneous rocks containing larger pores and high permeability showing higher Sor values. These findings provided initial insights for future thesis work while demonstrating the utility and reliability of this technique in predicting petrophysical properties. Furthermore, the used method is emphasized as having potential applicability for predicting various properties and being adaptable to other reservoirs and geological contexts.

1.4.2   Article 2 - HERLINGER, R.; ROS, L. F. DE; SURMAS, R.; VIDAL, A. Residual oil saturation investigation in Barra Velha Formation reservoirs from the Santos Basin, Offshore Brazil: A sedimentological approach. **Sedimentary Geology**, v. 448, 2023.

The link between multiphase fluid flow, whether at macro or micro scales, and lithological characteristics is rarely addressed. Relative permeability data is typically the domain of simulation engineers, while geologists tend to work with static models. Consequently, the impact of lithology on residual oil saturation (Sor) or other flow properties, the focus of this thesis, is scarcely discussed in depth in the literature. This work seeks to establish how the lithological features of rocks from the Barra Velha Formation influence oil retention in reservoirs.

A set of samples was analyzed to determine the petrographic relationship with residual oil saturation. A total of 300 points per thin section were counted to quantify depositional and diagenetic processes, as well as the mineralogical composition of the samples, to identify lithological features influencing oil retention. Additionally, µCT scans were analyzed to locate and characterize the morphology of trapped oil and its relationship with rock textures.

The rocks were classified into two groups: *in-situ* and intraclastic rocks. In the *in-situ* group, rocks dominated by calcite shrubs exhibited highly heterogeneous frameworks with large pores and higher Sor values. Conversely, when dominated by muddy material, these rocks contained a significant amount of dolomite, leading to a more homogeneous pore system and lower oil retention. In the intraclastic group, oil entrapment was closely linked to particle size, with larger particle rocks retaining less oil. This relationship suggests a connection between Sor and depositional energy, offering valuable input for conceptual reservoir models.

X-ray imaging revealed mixed wettability behavior, with regions wet by water and others by oil. These analyses were conducted at a relatively low resolution of approximately 38 microns. This preliminary imaging provides a foundation for the higher-resolution X-ray imaging studies detailed in Papers 5 and 6 of this thesis, which further refine the understanding of lithological controls on fluid behavior.

1.4.3   Article 3 - HERLINGER, R.; BONZANINI, L. A. F.; VIDAL, A.   Residual Oil Saturation in Pre-salt Brazilian Carbonates: A Multi-approach Core-to-log Case Study. **Journal of South American Earth Sciences**, v. 140, 2024.

This study conducted an integrated examination of Sor, addressing challenges related to the upscaling of laboratory data to log scale while drawing parallels with issues observed and discussed in previous works, incorporating conventional well interpretation techniques.

A well with comprehensive logging, including dielectric logs which are rarely employed, was selected for this investigation. In addition to logging data, the well featured core samples and sidewall sampling were supported by an extensive petrophysical database encompassing RCAL and SCAL data. In this study petrography, conventional formation evaluation methods, and machine learning techniques were applied.

The results corroborate the previous studies, confirming that Sor distribution is primarily controlled by the lithology. Sor typically is higher in *in-situ* rocks when compared to reworked facies, considering their more complex texture and pore structure. Both laboratory assays and well-logging data reveal a relation between petrophysical properties (porosity, permeability, and irreducible water saturation) with Sor, supporting the upscaling of laboratory information to field-scale applications.

The dielectric logging provided the most reliable Sor estimates, thanks to its shallower investigation depth when compared to other techniques, high sampling rate, and the Archie equation unknowns' uncertainties elimination. Moreover, nuclear magnetic resonance (NMR) effectively identifies areas containing high remaining oil amounts, correlating these regions with elevated Sor. However, NMR alone is not able to quantitatively assess Sor using traditional cutoff methods. On the other hand, machine learning models suggest that NMR T2 relaxation times are proper to estimate Sor from dielectric logging.

1.4.4   Article 4 - HERLINGER, R.; ROS, L. F. DE; VIDAL, A. Assessing the Role of Dolomite in Oil Trapping in *In-situ* Brazilian Pre-salt Carbonate Reservoirs by Pore-Scale Modelling and Simulation. **Petroleum Geoscience**, v. 31, 2025.

In this study, the main *in-situ* facies of the Pre-salt were modeled in 3D at pore scale to evaluate the impact of textures and attempt to draw parallels and validate observations from previous studies. To this end, we developed various models incorporating the main components of these rocks, including shrubs, spherulites, and their relationship with dolomite.

The methodology included assessing the impact of textures on the topology of the pore system and the distribution of pore and throat sizes. Additionally, simulations were employed to estimate Sor through simulation. The results indicated that dolomite significantly influences the pore system, resulting in a more uniform medium, a reduction in the pore-to-throat size ratio, and an increase in surface area. The simulation indicated that the increase in dolomite reduces Sor under water-wet conditions. Conversely, in oil-wet simulations, increasing dolomite leads to greater oil entrapment.

Previous studies indicated that *in-situ* facies with high dolomite content tend to exhibit low Sor. Thus, it is likely that much of the oil trapped in these rocks results from snap-off effects under mixed- to water-wet conditions.

1.4.5 Article 5 - HERLINGER, R.; KNACKSTEDT, M.; YOUNG, Y.; VIDAL, A. C. Coupling X-ray µCTs, BSE, and QEMSCAN Imaging to Unravel Details of Water Saturation and Oil Trapping in a Brazilian Pre-salt Carbonate Under Oil-wet Conditions. **Tomography of Materials and Structures**, submitted, 2025.

To complement observations at other scales, we conducted drainage and imbibition cycles using a centrifuge to understand oil saturation and trapping at the pore scale. During the experiment, X-ray µCT images were acquired and subsequently integrated with QEMSCAN data and Back-Scattering Electron (BSE) images to evaluate and understand fluid configuration.

After the drainage and aging cycles, oil almost completely displaced the brine within the interparticle macropores, relegating the brine to small, isolated droplets formed through snap-off processes. Additionally, a significant proportion of intraparticle micro- and macropores was filled with oil after drainage, with further saturation occurring during aging, demonstrating the rock's affinity for oil. Images obtained after forced imbibition revealed that nearly all the oil initially present in the interparticle macropores had been replaced by water, with only minimal traces of oil remaining as thin films on mineral surfaces. Conversely, the intraparticle macro

and micropores, which are typically less connected, retained most of the oil, highlighting the porous medium's tendency to trap fluids in poorly connected regions.

Finally, our experiments did not reveal any substantial effect of mineralogical variations on fluid saturation during any phase of the cycles, suggesting that the observed oil-wet condition is independent of relative mineralogical proportions, particularly given the predominance of calcite and dolomite in the sample. In other words, it seems that the predominance of calcite in the sample is controlling wettability.

This paper illustrates a typical core flooding under oil-wet conditions, providing insights into drainage and imbibition processes as well as oil trapping under these conditions.

1.4.6   Article 6 – HERLINGER, R.; KNACKSTEDT, M.; YOUNG, Y.; VIDAL, A. C. Pore Scale Fluid Saturation and Oil Trapping in Heterogeneous Carbonates Under Mixed-Wet Conditions: Insights from Brazilian Pre-salt Reservoirs. **SPE Journal**, submitted, 2025.

This article complements the interpretation presented in the previous paper, where we showcased drainage and imbibition results using a methodology similar to that of the previous study. In this case study, the chosen sample represents an *in-situ* facies with high textural and mineralogical variability resulting from depositional and diagenetic processes. This study emphasizes a strong interpretation of rock characteristics in terms of genesis and processes, aiming to engage the geosciences community in the discussion.

The sample exhibited mixed-wettability behavior in macropores and water-wet behavior in micropores. Rock texture played a critical role in fluid distribution during primary drainage and forced imbibition. Irreducible water and residual oil were primarily trapped in intracrystalline pores, where narrow pore throats limited connectivity and accessibility.

During primary drainage, oil initially acted as a non-wetting phase but transitioned to a wetting phase in macropores under higher pressures, though its entry into smaller pores remained restricted. Aging and spontaneous imbibition caused fluid redistribution, with water returning to tighter regions, particularly in dolomite- and quartz-rich areas. Oil entrapment was primarily controlled by rock texture, with minimal influence from local mineral species. This behavior is likely attributed to the dominance of calcite, which exhibited a greater affinity for oil during aging and spontaneous imbibition.

Secondary drainage imaging revealed complex wettability patterns: smaller pores retained their water-wet behavior, while macropores exhibited oil- to mixed-wet conditions. Processes such as recrystallization, mineral precipitation, and dissolution increased surface roughness, promoting local water-wet conditions and leading to highly complex saturation patterns.

These findings enhance our understanding of fluid behavior in complex carbonate systems, highlighting the interplay between rock texture, wettability, and fluid distribution, with significant implications for carbonate reservoir characterization and enhanced oil recovery.

1.4.7   Article 7 - HERLINGER, R.; KNACKSTEDT, M.; YOUNG, Y.; VIDAL, A. C. Integrating X-ray µCT and Pore-Scale Simulation for Relative Permeability Prediction. **Geoenergy Science and Engineering**, submitted, 2025.

Finally, the last article of this thesis, submitted as a short communication, presents a straightforward methodology for obtaining relative permeability curves based on multiphase X-ray imaging and pore-scale simulations. Post-drainage and spontaneous imbibition images were acquired and processed to segment the liquid and solid phases. Subsequently, pore-scale permeability simulations were performed in different regions of the sample to represent a range of fluid saturations. The resulting data enabled the construction of relative permeability curves for water and oil. This methodology provides valuable insights into the processes and even operational challenges encountered during laboratory-based relative permeability measurements, as it offers enhanced control by providing direct visual access to the phenomena occurring within the porous medium.

2. Article 1 - HERLINGER, R.; VIDAL, A. C. X-ray µCt extracted pore attributes to predict and understand Sor using ensemble learning techniques in the Barra Velha Pre-salt carbonates, Santos Basin, Offshore Brazil. Journal of Petroleum Science and Engineering, v. 212, 2022.

2.1 Abstract

The residual oil saturation (Sor) evaluation is relevant for developing oil fields, standing out as an input to flow simulation models for production forecasting. Also, Sor's understanding is crucial to guide enhanced oil recovery techniques. Moreover, Sor laboratory measurement tends to be time-consuming and expensive. This work aims to understand and predict Sor from X-ray µCt and RCAL data employing Ensemble Learning techniques (AdaBoost, Gradient Boost, and XGBoost) in Pre-Salt carbonates of the Barra Velha Formation, Santos Basin. Morphological attributes related to pore size, shape, and orientation were extracted from X-ray µCt scans. Hence, these attributes, together with routine core analysis (RCAL) data, were used to build machine learning (ML) models for the prediction of Sor. The results indicated strong faciological control in Sor, where the genesis of the rock implies different characteristics of the porous framework, impacting Sor and other petrophysical features. Rocks with larger pores usually lead to larger heterogeneity, which tends to trap more oil. Furthermore, the shape and orientation of the pores have substantial faciological control, given the textural organization of the different rock facies. These attributes showed weak control over Sor, impacting each type of facies differently, depending on the rock fabric. Even though the ML algorithms have similar results, the Gradient Boosting showed the best results. Furthermore, the inclusion of RCAL data does not increase the accuracy of the models. So, it is possible to predict the Sor only with morphological pore attributes reasonably. The most important features are mainly related to pore size and subordinately to orientation, confirming their impact on Sor. Finally, this methodology, in addition to predicting and bringing understanding to Sor in Pre-Salt rocks, can be adapted for use in other reservoirs.

2.2   Introduction

Residual oil saturation (Sor) corresponds to the fraction of pore volume occupied by undrained oil after displacement (Donaldson, 1989). This information is paramount for the characterization of reservoirs, as its quantification and understanding are fundamental for reservoir simulation and guidance for enhanced hydrocarbon recovery (EOR) techniques (Guo *et al.*, 2017; Humphry *et al.*, 2014a; Pham and Al-Shahri, 2001). Sor measurements are accurately obtained in the laboratory through imbibition experiments (McPhee, Reed and Zubizarreta, 2015; Murphy and Owens, 1973), but these are time-consuming and expensive. For this reason, Sor core information tends to be scarce, which generates high uncertainty, mainly in heterogeneous carbonates (Al-Housani *et al.*, 2012), as in the case of Brazilian Pre-Salt reservoirs, whose deposition, diagenetic, and hydrothermal processes tend to generate a very complex porous framework (Herlinger, Zambonato and De Ros, 2017; Lima *et al.*, 2020).

The flow of fluids in the reservoirs is governed by the capillary, gravitational, and viscous forces, which control residual oil trapping (Blunt, 1998; Perkins, 1957). The main oil trapping controls are the rock's interfacial tension, wettability, and texture, including pore and throat geometry (Anderson, 1986, 1987; Wardlaw, 1982). Interfacial tension is controlled by the nature of the fluids and reservoir conditions as pressure and temperature. Meanwhile, wettability is influenced by the interfacial tension (Blunt, 2017), the characteristics of the fluids involved, and the mineralogy of the rock (Arshadi *et al.*, 2020). The morphology of the pores has great relevance since the porosity and its configuration, in terms of pores and throats, impact the initial distribution of fluids, as does its flow and oil trapping (Chatzis, Morrow and Lim, 1983; Spiteri *et al.*, 2008; Wardlaw, 1982; Yuan, 1981).

Greater computational capabilities and data availability have driven the development of powerful tools for predicting different data types in all areas of knowledge. In reservoir characterization and petrophysics, machine learning (ML) has traditionally been applied to the prediction of rock properties (RCAL), such as porosity, permeability, or even facies using logging data (Serra and Abbott, 1982; Shokir, Alsughayer and Al-Ateeq, 2005; Wong and Shibli, 1998). RCAL data are plentiful and tend to generate reliable results on ML predictions.

On the other hand, special core analysis (SCAL) data are less abundant, making the prediction of these properties less common. However, the popularization and improvement of ML techniques have significantly increased the number of published works predicting well and core petrophysical, sedimentological, dynamical, and other data (Cuddy, 2021; Gao *et al.*, 2011; Huang and Chen, 2021; Oliveira and Carneiro, 2021; Safaei-Farouji and Kadkhodaie, 2022).

Digital rock physics (DRP) is a discipline that has gained prominence in recent years with the possibility of imaging samples at high resolution in X-ray micro-computed tomography (μCt). From μCts, samples can be segmented to extract porous models. Therefore, it is possible to simulate various physical processes, including multiphase fluid flow, which allows the Sor to be estimated (Andrä *et al.*, 2013; Blunt, 1998; Valvatne and Blunt, 2004). However, subsamples are often used, and this can return low representative results, thus limiting these techniques, although they show high potential and will possibly gain space concerning conventional approaches in the future. On the other hand, tomographic images are common and relatively cheap while also having much textural information about the porous framework, which has encouraged several authors in recent years to train ML algorithms for the prediction of petrophysical properties (Alqahtani *et al.*, 2020; Sudakov, Burnaev and Koroteev, 2019; Tembely, AlSumaiti and Alameri, 2021).

Ensemble learning methods are robust algorithms that learn by clustering, combining several simpler prediction models, called weak learners. This training generates a more complex clustered model, or strong learners, usually with sequential predictors correcting the predecessors. These techniques result in quick and efficient regression on structured data, having been used in a wide range of applications. Examples of commonly used methods are Gradient Boosting (Friedman, 2001), AdaBoost (Freund and Schapire, 1997; Zhu *et al.*, 2009), and XBoost algorithms (Chen and Guestrin, 2016). The AdaBoost algorithm (short for Adaptive Boosting) uses sequential predictors to adjust the previous prediction. With each new cycle, the relative weight of the default training information is adjusted. The weaker learner's predictions are then combined to produce the final prediction. The Gradient Boosting algorithm works similarly to AdaBoost, adding the predictors in sequence (usually a decision tree) to a set, each correcting its predecessor. However, when adjusting the weights, this method adjusts the new predictor to the residual error of the previous one. Finally, XGBoost operates similarly to Gradient Boosting but implements differences regarding the loss function, using second-order derivatives, aside from having L1 and L2 regularization and higher training speed.

Using different ensemble learning algorithms, this work applies a pore attribute-based method for Sor prediction in carbonate samples from the Brazilian Pre-salt from Santos Basin. The interpretation of the statistical results of pore morphology and the feature importance will also provide an essential basis for interpreting Sor pore controls in different types of Pre-salt facies.

2.3 Geological Setting

The Santos Basin is located in the south-eastern Brazilian margin (Figure 2-1), and it is limited to the north by the Cabo Frio High, which separates it from the Campos Basin, and to the south by the Florianópolis High, which separates it from the Pelotas Basin. It was formed under an extensional tectonic regime during the break-up of the Gondwana continent during the early Cretaceous/late Jurassic, an event that preceded the separation of South America and Africa and culminated in the formation of the Atlantic Ocean (Austin and Uchupi, 1982; Nürnberg and Müller, 1991; Rabinowitz and LaBrecque, 1979). The formation of the Atlantic Ocean occurred from a crustal thinning and rupture of the São Francisco-Congo-Rio de la Plata-Kalahari cratons and the Proterozoic folding belt, with the later formation of the seafloor. The rupture of the South Atlantic began with a rift to the south, in the region of Argentina, during the Jurassic period and across the equatorial margin (Meisling, Cobbold and Mount, 2001; Mohriak, Nemcok and Enciso, 2008; Szatmari, 2000). The central portion had a late onset of rupture in the Hauveterivian, controlled by a resistant craton nucleus (San Francisco - Congo craton), resulting in the development of a narrow rift basin in this region (Clemson, Cartwright and Booth, 1997; Karner and Driscoll, 1999; Rosendahl *et al.*, 2005).

The Santos Basin stratigraphy is divided into three Super-sequences: Rift, Post-rift, and Drift (Moreira *et al.*, 2007) (Figure 2-2). The Pre-Cambrian basement was covered by the tholeiitic volcanism of the Camboriú Formation during the early stages of Lower Cretaceous rifting (Mizusaki *et al.*, 1992). Overlying the volcanic rocks are sediments from the Piçarras and Itapema Formation, composed of siliciclastic rocks in the proximal portions, and sandstones, volcanoclastics, siltstones, shales, bioclastic rudstones and grainstones, and stevensitic rocks (Chinelatto *et al.*, 2020a; Leite, Silva and De Ros, 2020; Moreira *et al.*, 2007). Unconformable covering the Rift Super-sequence is seen the post-rift sediments of the Barra-Velha Formation, formed by the intercalation of precipitated calcite shrub crusts (stromatolites),

Mg-claystones, laminites, and intraclastic grainstones and rudstones (Gomes *et al.*, 2020a; Herlinger Jr *et al.*, 2020; Wright and Barnett, 2015), like the Macabu Formation of the adjacent Campos Basin (Herlinger, Zambonato and De Ros, 2017; Lima and De Ros, 2019). Finally, the basin evolved into a passive margin, and the continental deposits are covered by evaporites, followed by shallow and deep marine sedimentation from the Drift Super-Sequence.
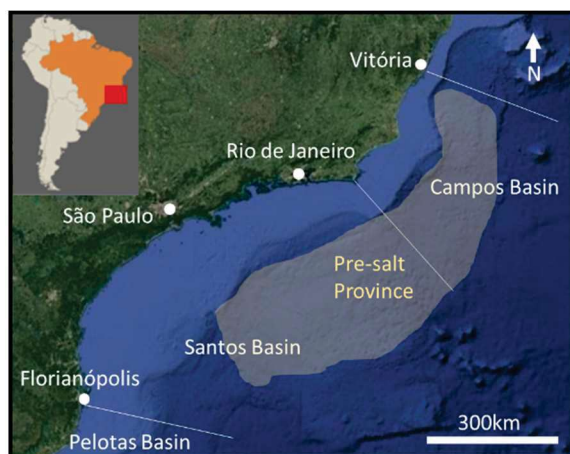
Figure 2-1 - Map illustrating the Localization of the Santos Basin and the Pre-Salt Province.

2.4 Materials and Methods

2.4.1 Lithological Characteristics

A total of 111 Pre-salt carbonate plugs from the Barra Velha Formation were used in this study. The samples represent the main reservoir facies, including fascicular-optic calcite shrub crusts (CSC), laminites (LMN), and intraclastic grainstones and rudstones (IGR). The CSC facies are *in-situ* calcite precipitates that grow vertically and divergently with a characteristic fascicular-optic habit. Shrubs have millimeter dimensions and tend to coalesce laterally and vertically to form crusts. They typically have well-connected large growth-framework porosity, commonly reduced by dolomite cementation, although calcite and silica are common. The LMN facies has a laminated aspect and is mainly composed of Mg-clays, dolomite, silica, and calcite. It has secondary porosity generated by the dissolution of clay minerals matrix or diagenetic phases. Their pore system tends to be controlled by original lamination, and usually, the pores are small, even though fenestral aligned vugs can occur. IGR are composed of fragments of CSC, LMN, and other calcite particles. Their interparticle porosity is reduced mainly by

compaction and dolomite cement, while porosity increase by particle dissolution is frequent. Figure 2-3 illustrates the common petrographic aspects of these rocks.

My	Geochronology			Stratigraphy		Tectonic
	Epoch	Stage	Local Stage	Group	Formation	Stage
					Ariri	Drift
120	Lower Cretaceous	Aptian	Alagoas	Guaratiba	Barra Velha	Pos-Rift
125		Barremian	Jiquiá		Itapema	Rift
			Buracica		Piçarras	
130		Hauterivian	Aratu		Camboriú	

Figure 2-2 Stratigraphy of Santos Basin (Moreira et al., 2007).

2.4.2 Laboratory Data

This study was based on routine (RCAL) and special core analysis (SCAL), including porosity, permeability, density, Sor, and X-ray micro-computed tomography (µCT). RCAL and SCAL were performed according to the recommended techniques of the American Petroleum Institute (API, 1998). The residual oil saturation was obtained from waterflood by low capillary number unsteady state water-oil relative permeability tests. The employed fluids were formation and injection brines, and dead oil. Irreducible water saturation (Sw_{irr}) was achieved by centrifugation (CORELAB ACES-200), and the samples were then aged to restore the reservoir wettability conditions before the imbibition experiment. µCTs were obtained on GE Phoenix VTomex 300 Kv|L tomograph with the following acquisition parameters: voltage 160kV, current 240µA, exposure time 1000ms, average equal to 3, skip 1, 1cm quartz filter, and total acquisition time of 120 minutes. The sample resolutions ranged from 30 to 55µm, typically composed of 1800 images.
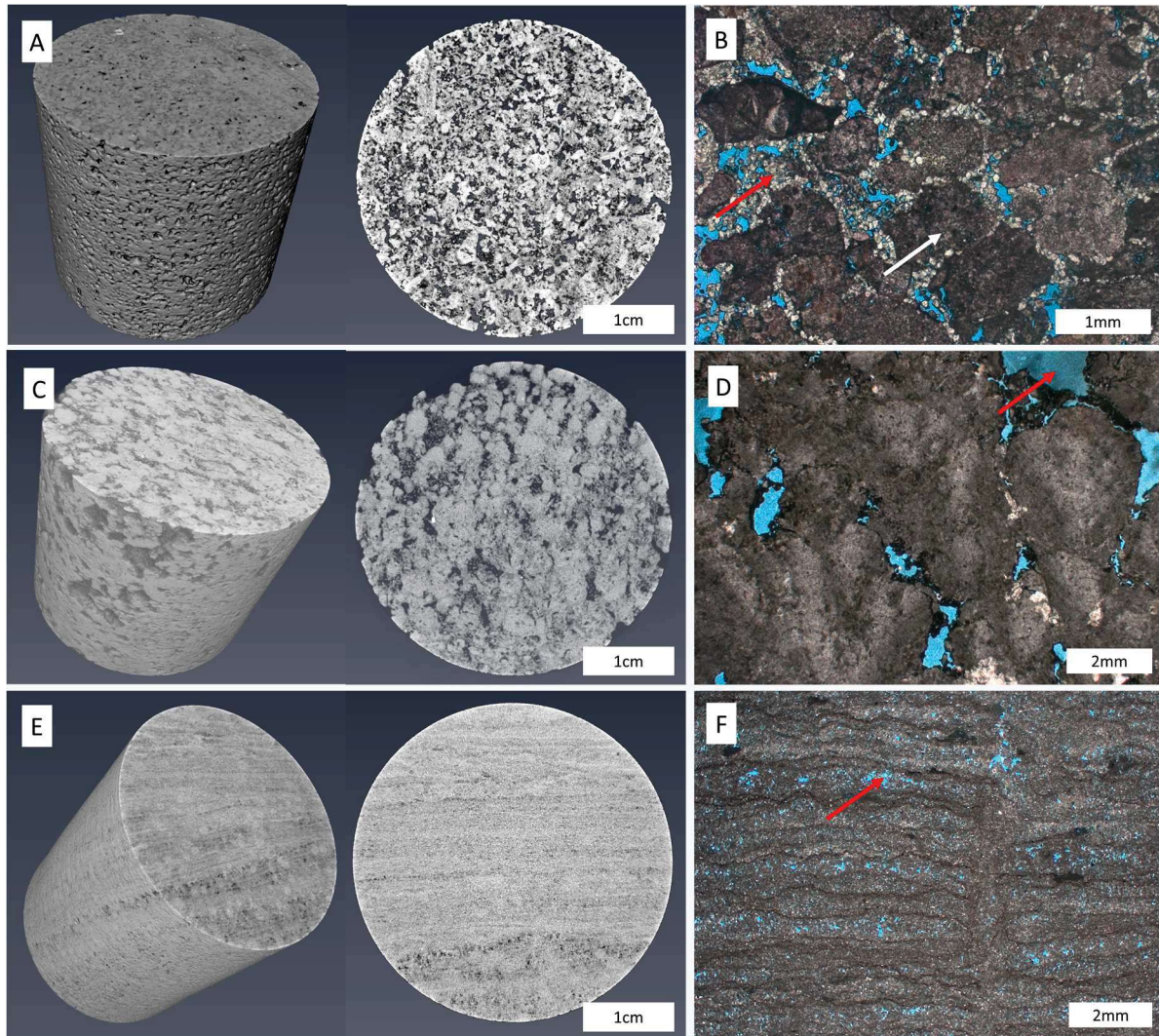
Figure 2-3 - X-ray µCT and photomicrographs showing petrographic aspects of the studied facies (porosity impregnated by blue epoxy resin): A and B) grainstone composed of calcite intraclasts (white arrow) with interparticle porosity reduced by cementation of dolomite (red arrow) (plane-polarized light - PL); C and D) CSC formed by calcite shrubs with growth-framework porosity (red arrow) (PL); E and F) LMN composed of microcrystalline calcite, dolomite, and Mg-clays with matrix dissolution porosity (red arrow) (PL).

2.4.3 µCT Processing and Pore Attribute Extraction

The µCTs were processed in the Avizo™ software, with noise removal, when necessary, using a median or non-local means filter. The µCTs were rescaled to 50µm to keep the same pore size cutoff. Subsequently, the images were segmented to separate the pores and matrix. A watershed-type algorithm (Beucher, 1992) was then used to separate the pores in regions with constrictions. Once the pores were individualized, these were labeled to extract the morphological attributes. Figure 2-4 illustrates the processing workflow of µCTs.
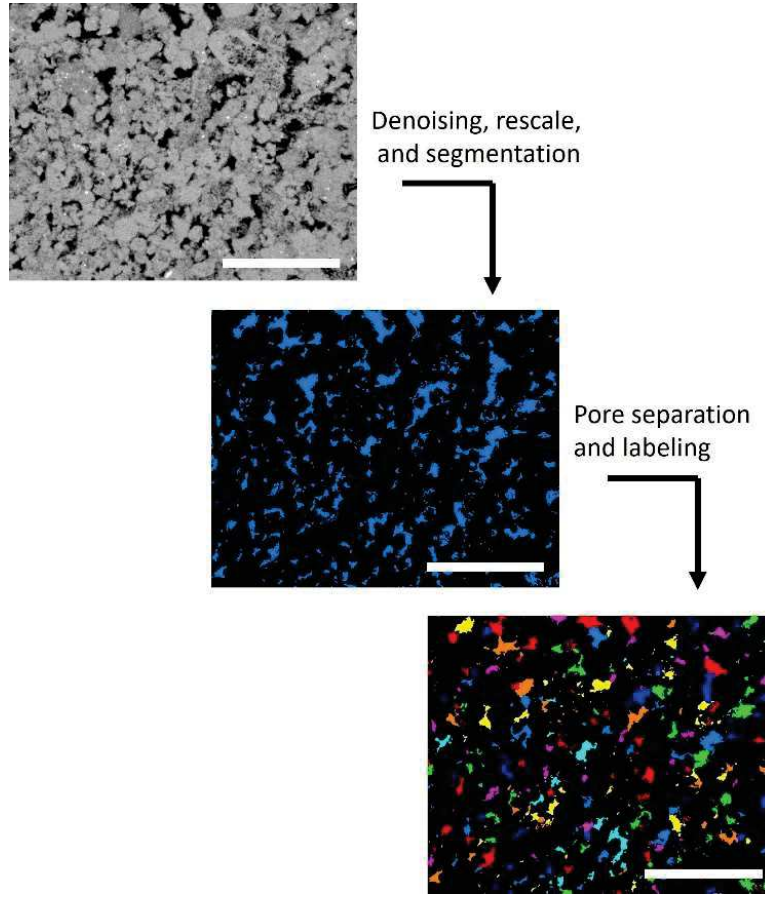
Figure 2-4 - μCT processing includes pre-processing, segmentation, and pore labeling (bar scale = 2mm).

After pore labeling, the pore morphological attributes were extracted to characterize the samples' size, orientation, and shape (Table 2-1). Attributes related to pore size correspond to Area3d, CroftonPerimeter, Volume, EqDiameter, Perimeter, and VoxelFaceArea. The Area3d is the area of the adjacent object, where each voxel can contribute with 1 to 3 faces, depending on the pore configuration. In the continuum, Area3d is calculated with the following equation:

$$Area3d = \int \sqrt{x'^2 + y'^2 + z'^2} \, dt \qquad (2.1)$$

CroftonPerimeter is the average perimeter calculated by Crofton's Equation (Carmo, Do, 2016; Crofton, 1868). The Volume attribute corresponds to the number of voxels in the pore. The equivalent diameter is the diameter of the sphere with the same pore volume, according to the equation below:

$$EqDiameter = \sqrt[3]{\frac{6\,Volume}{\pi}} \qquad (2.2)$$

Table 2-1 - Description of pore morphological attributes extracted from µCT calculated in the Avizo™ software.

Category	Attribute	Description
Pore Size	Area3d	The pore boundary area accounts for the exposed surface of the external voxels. Each voxel can contribute with 1 to 3 depending on the configuration of the surrounding voxels.
	CroftonPerimeter	The average pore perimeter is calculated by Crofton's Formula (Carmo, Do, 2016; Crofton, 1868).
	EqDiameter	Equivalent diameter represents the diameter of the sphere of the same volume.
	Perimeter	Average perimeter considering a pixel boundary count.
	VoxelFaceArea	Sum of the voxel surfaces outside of each pore.
	Volume	Voxel number of the pore.
Pore Orientation	OrientationPhi	Phi orientation of the pore in degrees [0,+90°], computed with the inertia moments. It defines with OrientationTheta the eigenvector of the largest eigenvalue of the covariance matrix.
	Orientation2Phi	Phi minor orientation of the pore in degrees [0,+90°], computed with the inertia moments. It defines with Orientation2Theta the eigenvector of the smallest eigenvalue of the covariance matrix.
	OrientationTheta	Theta orientation of the pore in degrees [-180,180°[, computed with the inertia moments. It defines with OrientationPhi the eigenvector of the largest eigenvalue of the covariance matrix.
	Orientation2Theta	Theta minor orientation of the particle in degrees [-180,180°[, computed with the inertia moments. It defines with Orientation2Phi the eigenvector of the smallest eigenvalue of the covariance matrix.
Pore Shape	ShapeVA3d	The shape factor 3d is defined as sphericity^{-3}.
	Elongation	The ratio of the average to the largest eigenvalue of the covariance matrix. Elongated objects will have small values close to 0.
	Flatness	The ratio of the smallest to the average eigenvalue of the covariance matrix. Flat objects have small values close to 0.

The Perimeter is the average length of the object's boundary and can be obtained as a boundary curve in the continuum, as follows:

$$Perimeter = \int \sqrt{x'^2 + y'^2} \, dt \qquad (2.3)$$

In the case of the digital image, the Perimeter is the number of voxels that surround the object. The VoxelFaceArea attribute is the sum of the areas of the voxels that are outside each connected component. The orientation-related attributes OrientationPhi, Orientation2Phi, OrientationTheta, and Orientation2Theta, were computed with the moments of inertia of the pores. OrientationPhi is the pore's orientation in degrees [0,+90°] to the z-axis, calculated with the inertia moments. It defines with OrientationTheta the eigenvector of the largest eigenvalue of the covariance matrix. OrientationPhi is the polar angle regarding the z-axis, while OrientationTheta is the polar angle concerning the x-axis. Orientation2Phi and Orientation2Theta attributes are defined with the smallest eigenvalue of the covariance matrix. Figure 2-5 shows an example of how polar orientation measurements are made.
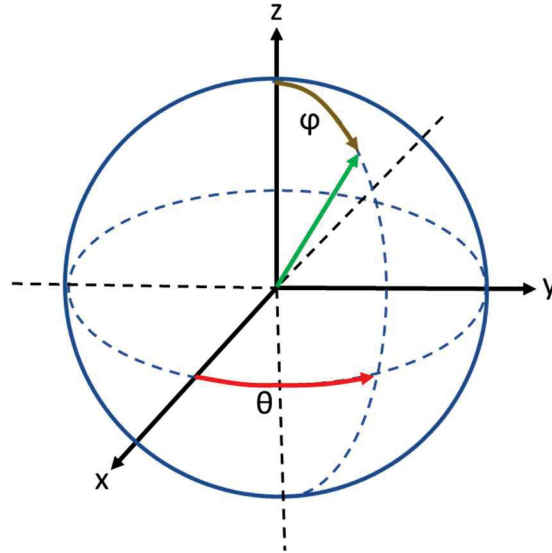
Figure 2-5 - Schematic showing the relationship between the theta (ϑ) and phi (φ) polar coordinates to the x, y, and z-axes.

2.4.4 Statistical Analysis

Statistics were calculated with the attributes extracted for each pore to compose a structured database with features to train the ML algorithms. Pores with orientation 0 or 90° were excluded from the pore shape and orientation attributes category statistics to avoid bias generated by the resolution limitation. In other words, pores with 1 or 2 voxels tend to generate anomalous results of shape and orientation since the resolution is insufficient for morphological characterization. The pore size features were extracted from average, volume-weighted average, median, maximum, and standard deviation of attribute and log(attribute) distributions. The features average, volume-weighted average, median, and standard deviation were extracted from the orientation and shape categories. In the end, 88 features were created, 60 were calculated with pore size category, with 28 features derived from the pore shape and orientation categories.

2.4.5 Sor Prediction ML Model

Three ensemble learning algorithms for Sor prediction were tested, including Gradient Boosting, AdaBoost, and XGBoost with and without the RCAL data according to the workflow

shown in Figure 2-6. The dataset with the 88 features extracted from the μCTs plus the RCAL from the 111 plugs was first divided into testing (20%) and training (80%). Since the three lithological types (IGR, LMN, CSC) have very distinct lithological characteristics, the test and training data were randomly stratified split to contemplate the proportion of this facies. Due to high dimensionality of the dataset, it was necessary to reduce it to avoid overfitting and increase the model's accuracy. The Recursive Feature Elimination (RFE) (Guyon, Weston and Barnhill, 2002) technique was used, employing an external estimator to assign weights to features to recursively eliminate those with smaller weights, therefore creating smaller sets with the most important features. In this work, the RFE was used with the Random Forest estimator (Ho, 1995), a robust regressor with a low computational cost. The training was carried out iteratively with 2 to 20 features to find the features that returned the best model.
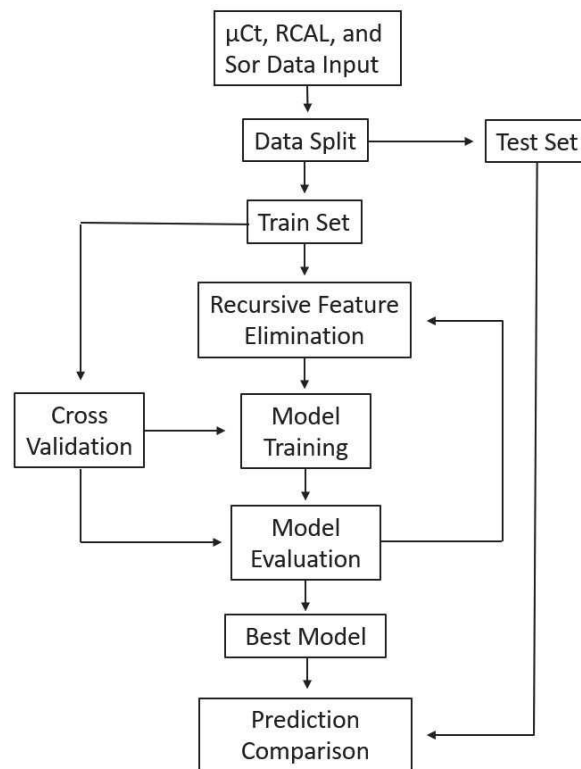
Figure 2-6 - Workflow used in the construction of the Sor prediction models.

Each training was performed with k-fold cross-validation, where the set was divided into five folds. In each step, four folds were used as a training set and one-fold as a validation set, repeating this process five times. The result of R^2 was stored to choose the hyperparameters that best fit the data. Cross-validation is relevant given the small dataset, thus reducing

overfitting and increasing the robustness of the model. Finally, the best models were tested with the data split in the first step, totaling two models for each algorithm, one with RCAL and the other without this data. In addition to the Sor prediction, the ML models provided the ranking with the importance of each feature, which is essential for interpreting the results.

2.5   Results and Discussion

2.5.1   RCAL and Sor

The RCAL and Sor results showed distinct petrophysical characteristics between the different facies (Figure 2-7 and Figure 2-8). Porosity values were similar between facies with an average range of around 15 to 17%, with greater variability in the CSC. At the same time, the LMN presented more homogeneous values than the other facies. The permeability of the LMN was significantly lower than IGR and CSC, denoting different characteristics of the porous systems, typically below 100mD. CSC and IGR have greater variability, with minimum values close to 1mD and higher values above 1,000mD. LMN density tended to be higher than the other facies, reflecting a higher proportion of dolomite in its mineralogy. In contrast, the density of CSC is lower since the composition is dominated by calcite in this facies. Finally, there are significant differences in Sor distributions, indicating that the depositional fabric has an important weight in Sor, given its distinct porous characteristics, as discussed in the following items. LMN has a narrow Sor distribution with values between 15 and 30%. But in the case of CSC, in addition to a higher Sor average, around 30%, showed high variability, which reflects the heterogeneous framework of these rocks. Finally, the results indicate that IGR has intermediate average Sor and lower variability than observed for CSC, although there are two outliers with Sor above 50%.

Sor = 17%
k = 3.15mD
φ = 13.6%
Density = 2.73g/cm³

Sor = 22.4%
k = 62.4mD
φ = 19.1%
Density = 2.71g/cm³

Sor = 27.5%
k = 23.4mD
φ = 16.2%
Density = 2.75g/cm³

Sor = 19.6%
k = 14.7mD
φ = 12.9%
Density = 2.72g/cm³

Sor = 26.2%
k = 104mD
φ = 15.3%
Density = 2.71g/cm³

Sor = 44%
k = 12.7mD
φ = 14%
Density = 2.71g/cm³

Sor = 14.28%
k = 51mD
φ = 19.57%
Density = 2.73g/cm³

Sor = 23.5%
k = 254mD
φ = 15.6%
Density = 2.68g/cm³

Sor = 57.2%
k = 2293mD
φ = 25.7%
Density = 2.73g/cm³
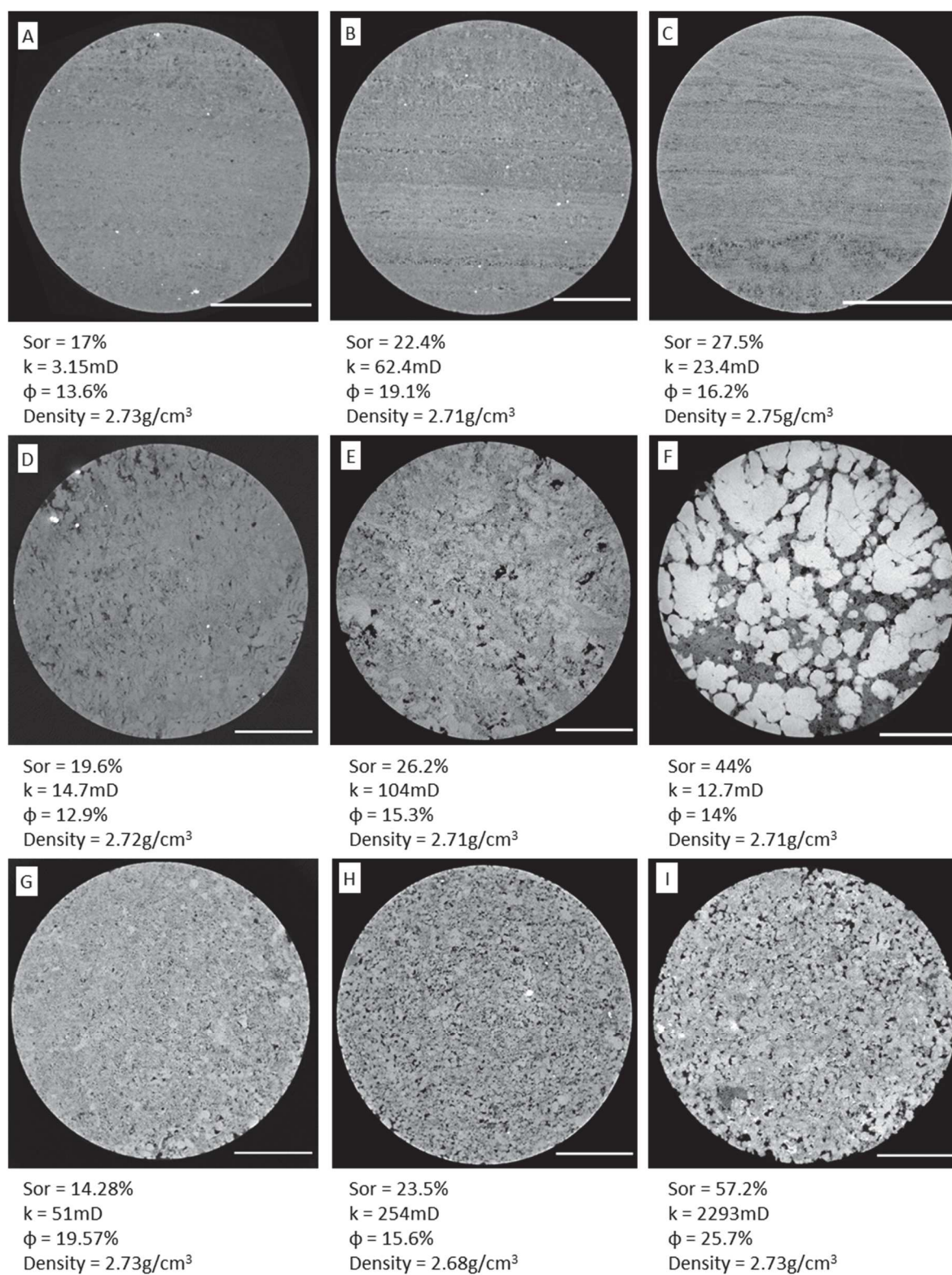
Figure 2-7 - Template with examples of LMN (A to C), IGR (D to F), and CSC (G to I) µCTs, illustrating the textural differences and their influence on Sor and RCAL.
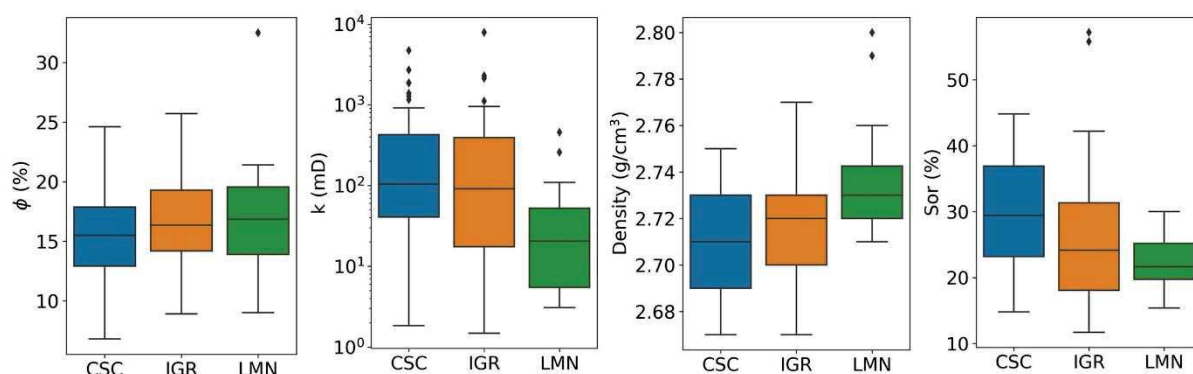
Figure 2-8 - Boxplots exhibiting porosity, permeability, density, and Sor distributions in the studied facies.

In general, one can observe that the greater homogeneity of the LMN reflects in less variability of RCAL and Sor, as opposed to IGR and CSC, which have significant heterogeneity between samples. The correlation between porosity and Sor is low when considering all facies (Figure 2-9). When evaluated separately, we observe that the CSC facies has a Pearson correlation coefficient (r) equal to 0.53 (Table 2-2), which indicates that, though low, there is a relationship between porosity and Sor for this facies. Porosity has been cited as an important controlling factor of Sor since the greater it is, the greater the percolation probability. This means that more available paths for oil displacement are available (Yuan, 1981). However, a clear relationship was not observed, indicating that this premise cannot be generalized since porosity in carbonates is not necessarily related to connectivity, since intraparticle, vugs or moldic pores, common in these rocks, are frequently poorly connected. Permeability is related to Sor with r equal to 0.5 (Table 2-2), with a clear relationship when the cross plot is observed. This value is higher in the IGR facies, indicating that the porous organization of particulate rocks tends to affect both petrophysical properties. Finally, we note that although a trend of decreasing Sor with increasing density is observed (Figure 2-9), the relationship is fragile. The increase in density in these samples is probably caused by dolomite, which would change wettability, altering the efficiency of the sweep (Anderson, 1987). However, a systematic experimental and petrographic characterization would be needed to understand the real impact of mineralogy on Sor in these samples.
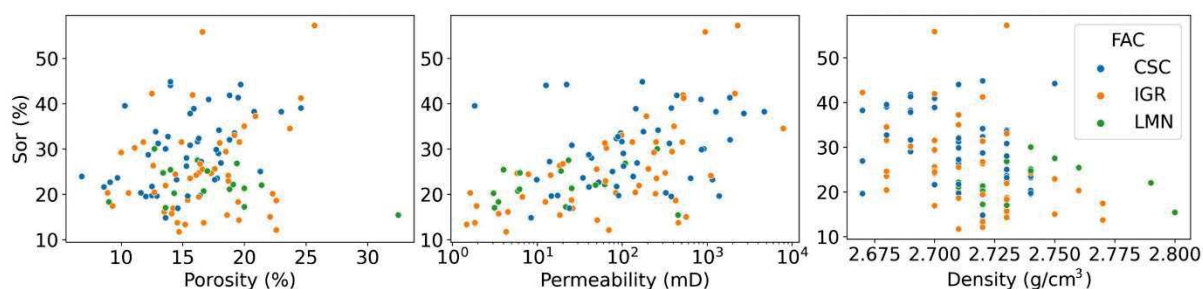
Figure 2-9 - Relationship between RCAL and Sor.

Table 2-2 - Pearson correlation coefficients between Sor and Features, including statistics from pore attributes and RCAL.

Feature	CSC	IGR	LMN	All Data
Avg Area3d	0.70573	0.703615	0.610012	0.708235
Avg VoxelFaceArea	0.703887	0.699744	0.61606	0.707131
Avg CroftonPerimeter	0.698364	0.69338	0.628368	0.702783
Std EqDiameter	0.684283	0.718927	0.562778	0.701561
Avg Perimeter	0.695482	0.69231	0.618707	0.700307
Avg Weighted Log EqDiameter	0.493029	0.541258	0.651684	0.575631
Std Perimeter	0.575326	0.514402	0.566057	0.558605
Std Area3d	0.58077	0.51417	0.568819	0.558603
Avg Weighted Log Perimeter	0.469771	0.519521	0.637147	0.555685
Std VoxelFaceArea	0.570049	0.510049	0.566627	0.553964
Avg Weighted Log Area3d	0.466069	0.513419	0.635382	0.551349
Std CroftonPerimeter	0.563112	0.503379	0.562985	0.548499
Avg Weighted Log VoxelFaceArea	0.455405	0.508231	0.633697	0.546053
Avg Weighted Log CroftonPerimeter	0.451707	0.504805	0.630416	0.543613
Avg Weighted EqDiameter	0.445501	0.490794	0.586028	0.528336
Avg Volume	0.617014	0.438585	0.744024	0.52566
Std Log VoxelFaceArea	0.595904	0.482768	0.267565	0.521566
Std Log CroftonPerimeter	0.584027	0.476345	0.282788	0.5171
Std Log Area3d	0.591727	0.479972	0.259827	0.515973
Std Log EqDiameter	0.593601	0.478439	0.237674	0.509519
Permeability	0.316782	0.586696	0.509944	0.504398
Std Log Volume	0.591414	0.472848	0.193279	0.502387
Std Log Perimeter	0.589173	0.464249	0.241359	0.500827
Avg Shape_VA3d	0.442388	0.47641	0.580302	0.495574
Avg EqDiameter	0.62404	0.469666	0.134348	0.482617
Avg Weighted Log Volume	0.320913	0.423685	0.710363	0.482406
Std Flatness	0.606169	0.459939	0.26166	0.453192
Avg Weighted Perimeter	0.341529	0.40724	0.497226	0.44428
Avg Weighted Area3d	0.338611	0.405428	0.496212	0.441431
Avg Weighted VoxelFaceArea	0.326099	0.40206	0.494505	0.437267
Avg Weighted CroftonPerimeter	0.317784	0.397018	0.490886	0.432866
Std Volume	0.320529	0.37115	0.654432	0.43153
Max EqDiameter	0.345734	0.417785	0.439202	0.429618
Std Shape_VA3d	0.256595	0.366538	0.474628	0.390059
Median Log Area3d	0.51734	0.377867	0.181676	0.387583
Median Log EqDiameter	0.540083	0.391804	0.122626	0.386714
Median EqDiameter	0.540608	0.393773	0.108335	0.386416
Std Orientation2Phi	0.559801	0.284297	0.111407	0.384493
Median Log VoxelFaceArea	0.521751	0.375550	0.180462	0.383136
Median Area3d	0.514759	0.380991	0.136905	0.382757
Median VoxelFaceArea	0.518617	0.384558	0.13777	0.380947
Avg Log EqDiameter	0.599185	0.358735	0.060898	0.37349

Feature	CSC	IGR	LMN	All Data
Avg Log VoxelFaceArea	0.610133	0.357043	0.065853	0.37316
Max Perimeter	0.218816	0.3823	0.376974	0.372157
Median Log Perimeter	0.532921	0.345907	0.126203	0.370644
Avg Log Area3d	0.596826	0.350533	0.06247	0.370493
Median Perimeter	0.529407	0.347597	0.085843	0.367376
Avg Log CroftonPerimeter	0.59269	0.337708	0.069541	0.366539
Max Area3d	0.205193	0.379109	0.372615	0.364643
Max VoxelFaceArea	0.187928	0.375328	0.370114	0.359014
Avg Weighted Volume	0.098635	0.315281	0.561152	0.357065
Avg Log Perimeter	0.596172	0.319281	0.060856	0.356856
Max CroftonPerimeter	0.1712	0.36857	0.366487	0.352311
Median Log CroftonPerimeter	0.405491	0.322658	0.247468	0.335353
Std Elongation	0.630537	0.2817	-0.04133	0.335239
Median CroftonPerimeter	0.411096	0.327986	0.209278	0.333301
Median OrientationPhi	0.567592	0.259772	0.076199	0.323506
Avg Weighted Shape_VA3d	0.099675	0.304316	0.413146	0.315689
Avg OrientationPhi	0.563653	0.256231	0.055186	0.314527
Avg Weighted Elongation	0.413846	0.191248	0.382615	0.31231
Median Shape_VA3d	0.290822	0.253714	0.277283	0.294238
Max Volume	-0.02167	0.261968	0.436473	0.265912
Avg Weighted Flatness	0.337347	0.158251	0.286434	0.24309
Porosity	0.529017	0.10275	-0.02398	0.196654
Avg Weighted OrientationPhi	0.121082	0.153468	0.209311	0.158956
Avg Weighted Orientation2Theta	0.034652	0.117529	0.186985	0.08953
Avg Weighted Avg Orientation	0.170523	-0.07495	0.171274	0.088676
Median Orientation2Theta	0.150532	-0.01905	0.193642	0.087137
Avg Elongation	0.482343	-0.0067	-0.09628	0.074806
Median Elongation	0.458592	-0.01925	-0.09154	0.050384
Avg OrientationTheta	-0.00107	0.199288	-0.20947	0.015678
Std OrientationTheta	-0.07267	-0.06915	0.09281	-0.01992
Avg Weighted OrientationTheta	-0.00089	0.068121	-0.2515	-0.02091
Std Orientation2Theta	-0.17239	0.081546	-0.01174	-0.03105
Median OrientationTheta	-0.02164	0.018662	-0.12347	-0.04173
Avg Log Volume	-0.12116	-0.01899	-0.09089	-0.08241
Median Log Volume	-0.30179	-0.06866	-0.07889	-0.15279
Avg Weighted Orientation2Phi	-0.11945	-0.24372	-0.12581	-0.17788
Median Flatness	-0.28964	-0.21026	-0.13547	-0.24936
Std OrientationPhi	-0.53243	-0.21647	-0.01744	-0.25913
Median Volume	-0.33384	-0.20244	-0.13035	-0.26298
Avg Flatness	-0.36283	-0.24668	-0.14249	-0.28777
Avg Orientation2Phi	-0.57917	-0.28034	-0.02621	-0.32337
Median Orientation2Phi	-0.5816	-0.28045	-0.02692	-0.32817
Density	-0.26968	-0.45399	-0.44038	-0.39533

2.5.2 Pore Attributes

2.5.2.1   Pore Size

Attributes related to average pore size generally presented the largest r concerning Sor (excluding Volume and EqDiameter), indicating that, among the parameters analyzed, these more significantly impact the Sor, especially in the CSC facies and IGR (Table 2-2, Figure 2-10A). We also observed that they tend to be highly correlated, given their relationship with pore dimensions. We also noted that facies show critical differences in the distribution of these attributes (Figure 2-11A). The average Area3d shows that LMN has the smaller pores among the studied facies, reflecting on the permeability of the samples, which are usually low. On the other hand, the CSC tends to have the largest average Area3d, while the IGR has intermediate values but with more significant variability in the average distribution. In general, this attribute is like permeability in terms of distributions. Although the cross plots between these two properties present significant dispersion (Figure 2-10B), there is an evident relationship between the two properties, indicating that, at least for some samples, the average pore size is related to the pore throats dimensions. The logarithmic average of Area3d shows a low correlation with Sor (Table 2-2), probably reflecting the greater weight attributed to the smaller pores. Hence, this feature is a worse estimator than the non-logarithmized one. This observation indicates that larger pores have great relevance in oil trapping, a fact observed in microchip experiments (Chatzis, Morrow and Lim, 1983). Finally, we noticed that these observations justify the low Sor of the LMN, given the small average size of the pores and their homogeneity, which also reflects a lower Pearson correlation of the average Area3d to Sor for LMN facies (Table 2-2).

The features calculated with the weighted average did not return good correlations in relation to Sor (Table 2-2). Although a trend of increasing Sor with the weighted average is observed, there is high dispersion in the correlation (Figure 2-10C). This behavior is mainly because the larger pores receive very high weight, which reduces the variability of the data when large pores are present. This characteristic is more clearly observed in the CSC, which tend to have larger pores than the other facies (Figure 2-11B). When the weighted average is calculated with the attribute log, we observed that the weight between the small and large pores becomes balanced, which increases the r concerning the Sor (Table 2-2), especially in the LMN whose pores are smaller. Finally, the logarithmic weighted average Area3d distributions of the

LMN have their variability increased (Figure 2-11C), which allows for a better correlation with Sor.

The features related to the median pore size showed poor correlations with Sor, except for the CSC, which led r above 0.5 (Table 2-2). However, the median Area3d vs. Sor cross plot does not establish a good relationship (Figure 2-10). The medians are significantly affected by the smaller pores, which tend to be very abundant but generally less representative in terms of volume. The logarithmic median showed the same trend observed by the median, which indicates that both features are not good estimators for Sor.

The features related to the maximum value showed poor correlation with Sor (Table 2-2), which means that it is not a piece of helpful information. In general, it should be expected to see correlations between pore size statistical features, such as maximum and median. But due to heterogeneity, some correlations are very poor. In the average versus maximum Area3d scatter plot (Figure 2-10E), we observed a relationship mainly in rocks with small pores. From an average size of around 10^{11}nm^2, this correlation ceases to exist.

The standard deviation of the attributes related to pore size stands out as having the highest r, after the average, considering all facies. The standard deviation of the EqDiameter showed r around 0.7 (Table 2-2, Figure 2-10F) correlated with Sor. The standard deviation tends to be highly correlated with the average (Figure 2-10G), since in general, the larger the rock pores, the greater their variability. This tendency is seen in their similar distributions (Figure 2-11A and 11D). Therefore, the standard deviation manages to follow the trend observed in the average. When the standard deviation of the attribute logarithm is calculated, some differences are observed (Figure 2-11E), the correlations tend to be worse (Table 2-2), except for the CSC. Log tends to decrease the weight of larger pores, reducing the variability, which diminishes the correlation with Sor.

Finally, considering the resolution of the μCT images used in this study (50μm), part of the porosity cannot be resolved. This effect is quite significant in LMN, whose great part of pores are under the resolution, unlike other facies with larger pores. This limitation has an impact on pore attribute statistics. In other words, LMN's actual pore size is smaller than the calculated ones. Conversely, despite their obvious influence on pore size statistics, we expected that the trends and correlations should not be seriously affected.
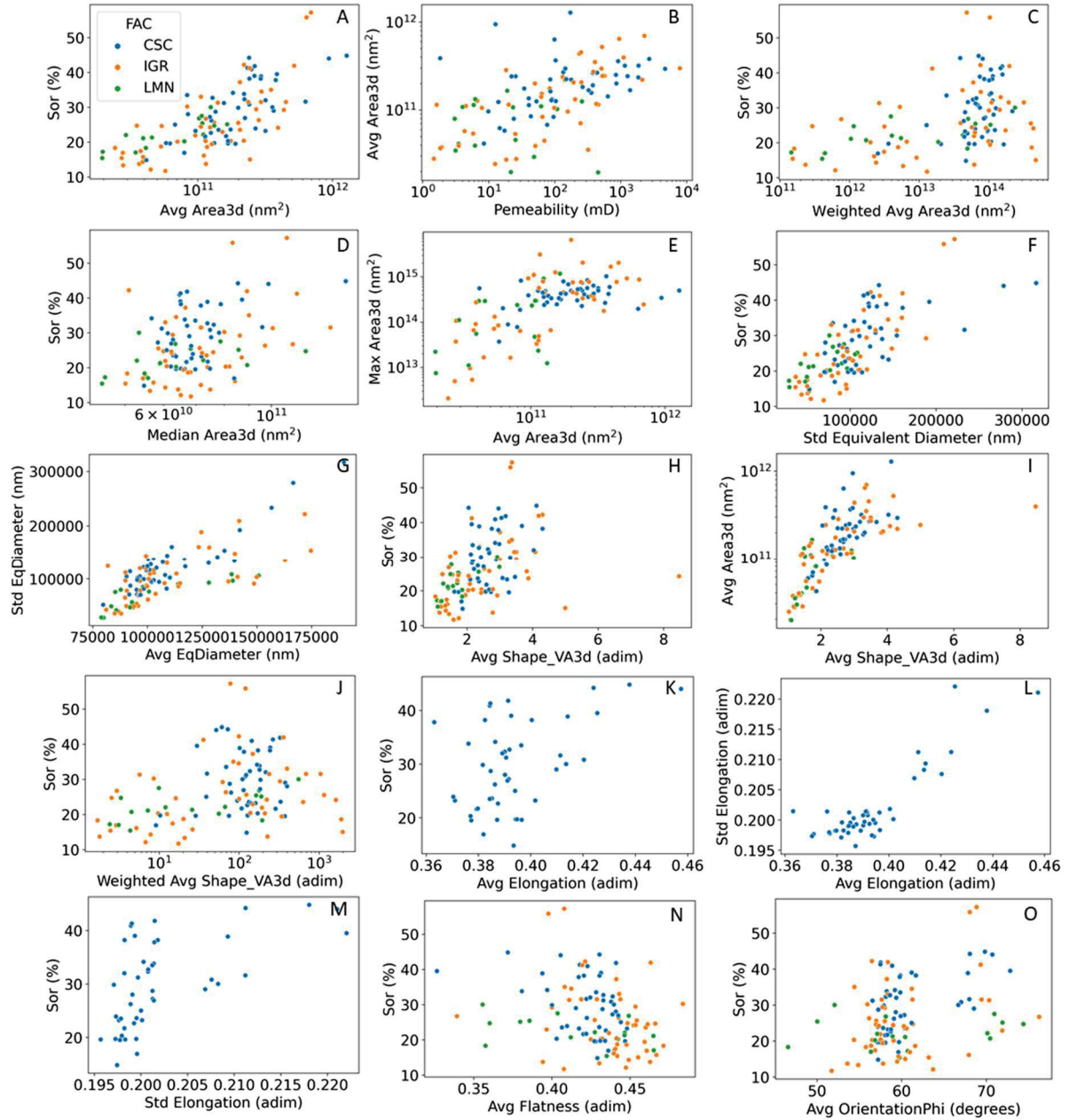
Figure 2-10 - Scatter plots illustrating relationships between Sor and statistical features calculated from the pore attributes.

2.5.2.2   Pore Shape

Features related to pore shape (ShapeVA3d, Elongation, and Flatness) are closely linked to facies. Figure 2-11F illustrates the distributions of the average ShapeVA3d in the different facies. CSC has the highest average, which means that this facies has the lowest sphericity tendency (sphere is close to 1). This characteristic is related to the genesis of their growth-

framework porosity, in which the voids are conditioned to the vertical growth of calcite shrubs. The IGR facies has lower averages, as its interparticle pores tend to be equidimensional, depending on the configuration of the particles, diagenetic processes, and selection of grainstones and rudstones. As a consequence, the distribution presents significant heterogeneity. Finally, the LMN distribution showed a greater tendency to sphericity, probably because the pores are small, mainly inferior to the sample resolution. Hence, pores whose size is close to the resolution limit will have a more equidimensional shape. Although the Person correlation coefficients are low (Table 2-2), except for LMN (r=0.58), there is an evident relationship between ShapeVA3d and Sor (Figure 2-10H). This may be related to the fact that the ShapeVA3d is calculated with the Volume and Area3d attributes. Therefore, there is a good correlation between ShapeVA3d and Area3d, especially in samples with a small pore size (Figure 2-10I). When the weighted average of the ShapeVA3d is calculated, the weight of the small pores is lost, increasing the variability of the average distributions (Figure 2-11G), particularly of the LMN and IGR, since large pores predominate in the CSC, unlike the other facies. Hence, the correlation with Sor decreases, although a relationship still can be observed (Figure 2-10J). ShapeVA3d median and standard deviation have a poor correlation with Sor (Table 2-2), as we can see the same tendency observed in previous features, where CSC has higher values than other facies. In contrast, the LMN distributions have the lowest average standard deviation and median.

The Elongation-related features have similar behavior to ShapeVA3d ones, with strong faciological control (Figure 2-11H). Once again, the nature of the CSC genesis makes pore Elongation more pronounced in this facies than in others, while LMN pores have the lowest Elongation. Considering all samples, there is no reasonable relationship between Elongation and Sor (Table 2-2). However, when looking only at CSC, the Elongation-related features appear to have some relationship to it. The pores tend to be less elongated in the other facies, given their genesis. Although weak, the relationship between average Elongation and Sor in CSC facies is observed. The greater the average Elongation (elongated pores have Elongation close to zero), the greater the Sor (Figure 2-10K). In addition, the standard deviation with r equal to 0.63 stands out, indicating that the heterogeneity of the Elongation somehow affects the Sor. There is a good correlation between the average and standard deviation of the Elongation (Figure 2-10L), which implies that the greater the average Elongation, the greater its variability. Considering that the pores of CSC generally have large dimensions, small pores

may increase the mean Elongation (less elongated pores), thus increasing the standard deviation. In other words, pore elongation seems to be directly related to CSC Sor (Figure 2-10M). On the other hand, the other facies do not show a good relationship between Sor and the Elongation feature.
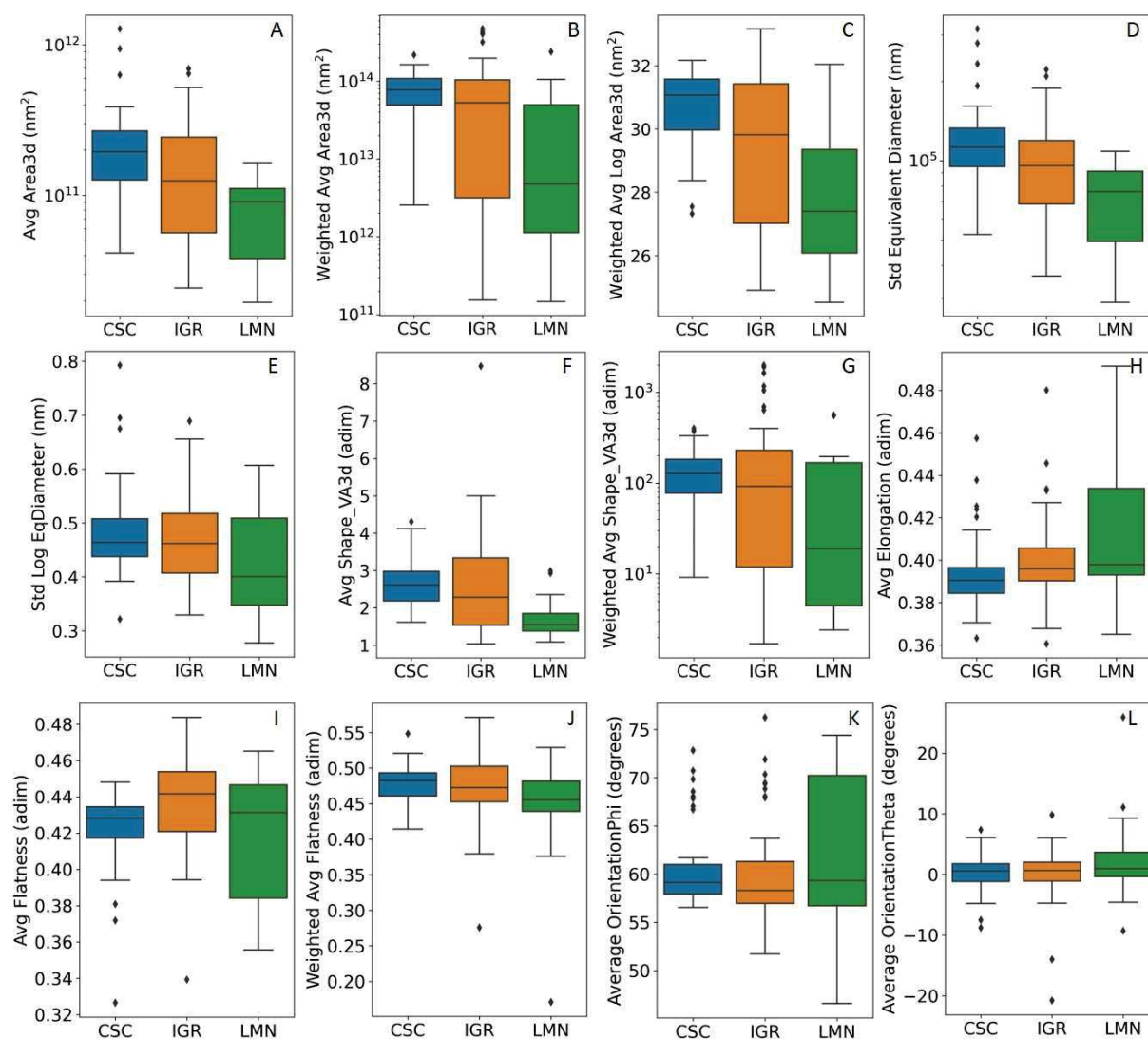
Figure 2-11 - Boxplots exhibit statistical features' distributions calculated from the pore attributes.

Finally, the features related to the flattening of the pores have their distributions controlled by the facies (Figure 2-11I), as occurs with the previous features. The IGR show higher values of average Flatness, which indicates low flatness of the pores since the organization of particles tends to generate predominantly equidimensional pores. Considering the laminated nature of the LMN, we should expect that this facies had greater flattening of the

pores. However, there is significant heterogeneity in the distribution of average Flatness. The statistics are possibly influenced by small pores close to the image resolution. This bias is solved with the weighted average, which will attribute more weight to the larger pores, consequently generating distributions that are more in line with expectations (Figure 2-11J). Although the correlations of Sor with features related to Flatness are low (Table 2-2), Figure 2-10N shows that there is a clear trend between the average Flatness and Sor, indicating that pore flatness may have some control on Sor as observed in the elongation correlations.

2.5.2.3   Pore Orientation

The pore orientation has similar average values between the facies, around 60° about the z-axis, given by the OrientationPhi attribute (Figure 2-11K). LMN has a high orientation dispersion, while the other facies have a narrower distribution but with outliers at higher angles. According to Pearson's correlation coefficient, the orientation of the pores only impacts the Sor in the CSC facies, since in the other facies, no correlation is observed (Table 2-2). Hence, this is probably because the pores of the other facies have a greater tendency to equidimensionality. However, when analyzing the scatter plot average OrientationPhi vs. Sor (Figure 2-10O), we observe a high dispersion, with a very weak tendency to increase Sor to angle ϕ for the CSC facies. During the waterflooding test, the flow occurred along the z-axis, so the greater the angle between the pores and the z-axis, the greater the Sor. However, several other factors also affect the Sor, which could mask the effect as the samples are very distinct. Adebayo *et al.* (2017) investigated the influence of anisotropy on residual oil, showing that the vertical test has a more significant amount of residual oil, which corroborates our evidence. Finally, we observed that the mean angle with the x-axis (θ), given by the OrientationTheta attribute, has similar distributions between the different facies (Figure 2-11L), while also not showing any relationship with Sor (Table 2-2).

2.5.3   ML Model

2.5.3.1   Cross-Validation and Test Results

According to the R^2 obtained in the cross-validation, the best models for each algorithm presented similar results (Table 2-3). When using RCAL and µCT data, the R^2 ranged between 0.51 ± 0.07 for XGBoost and 0.54 ± 0.12 for Gradient Boosting. Although Gradient Boosting has the highest R^2, we noticed a higher standard deviation, indicating that its model is more unstable compared to other techniques, which showed a standard deviation equal to 0.07. We also observed that Gradient Boosting showed the best result with a smaller number of features (6), while AdaBoost and XGBoost used 12 and 19 features, respectively. Among the features of RCAL, porosity was the only one included among the features used by the best models. When using only the features calculated with µCTs, the AdaBoost algorithm showed worse results in cross-validation, with low R^2 (0.44) and high standard deviation (0.11). On the other hand, Gradient Boosting and XGBoost had similar results, with a coefficient of determination of 0.55 ± 0.08 and 0.54 ± 0.10, indicating that the latter two should be preferred when considering only the result of the cross-validation.

The test result, considering the models with RCAL, showed a coefficient of determination within the range defined by the standard deviation of the cross-validation, which suggests that the models are predicting the Sor as projected in the selection of hyperparameters, with R^2 similar for the three algorithms tested. The root mean squared error (RMSE) of Gradient Boost and AdaBoost was similar, 4.55 and 4.62%, respectively. XGBoost showed the worst RMSE, equal to 5.19, indicating lower model accuracy (Figure 2-12). Regarding the distribution of residuals, the Gradient Boosting model showed the best result, with an average of $0.06 \pm 4.65\%$, while AdaBoost showed intermediate values ($0.66 \pm 4.68\%$) and XGBoost the worst result ($0.29 \pm 5.31\%$) (Figure 2-13). Regarding the normality of the residuals, there is a good correlation between the theoretical and the ordered quantiles (Figure 2-14), indicating that their behavior is close to normal, with no significant differences among the three models. This fact is confirmed by the Shapiro-Wilk normality test, which suggests that the null hypothesis of normality cannot be rejected in any of the three models considering a 90% confidence level (Table 2-4). Assuming a 90% confidence interval, only the predicted vs. measured regression obtained with the XGBoost algorithm intercepts zero with a slope equal to 1; hence, this model has a lower bias than the other models obtained with the different algorithms, which only intercept zero with 95% confidence (Table 2-4). In conclusion, although the RMSE of the

AdaBoost and Gradient Boosting models is superior, we observed that the regression between measured and predicted Sor has a higher bias than XGBoost, which indicates that this algorithm will have a greater capacity to predict extreme values.

Table 2-3 Cross-validation best model results, including features, hyperparameters, average and std R^2.

	Algorithm	Features	Hyperparameters	Avg R^2	Std R^2
µCT and RCAL	AdaBoost	Average Area3d, Average Log CroftonPerimeter, Median Log CroftonPerimeter, Average CroftonPerimeter, Weighted Average Log EqDiameter, Average EqDiameter, Std EqDiameter, Median Orientation2Phi, Median Orientation2Theta, Std Orientation2Theta, Weighted Avg OrientationTheta, Porosity	base_estimator = decision tree, learning_rate = 4, loss = exponential, n_estimators = 50	0.52	0.07
	Gradient Boosting	Average Area3d, Std EqDiameter, Median Orientation2Phi, Std Orientation2Theta, Porosity	alpha = 0.9, learning_rate = 0.05, max_depth = 2, min_samples_split = 2, min_samples_leaf = 1, n_estimators = 50, subsample = 0.2	0.54	0.12
	XGBoost	Average Area3d, Average Log CroftonPerimeter, Max Log CroftonPerimeter, Median Log CroftonPerimeter, Average CroftonPerimeter, Average Log EqDiameter, Weighted Average EqDiameter, Average EqDiameter, Std EqDiameter, Max Volume, Median Orientation2Phi, Std Orientation2Phi, Median Orientation2Theta, Std Orientation2Theta, Median OrientationPhi, Weighted Average OrientationTheta, Std OrientationTheta, Porosity	base_score = 0.5, booster = 'gbtree', colsample_bylevel = 1, colsample_bynode = 1, colsample_bytree = 0.2, gamma = 0, importance_type = 'gain', learning_rate = 0.5, max_delta_step = 0, max_depth = 1, min_child_weight = 1, n_estimators = 30, n_jobs = 32, num_parallel_tree = 1, reg_alpha = 0.5, reg_lambda = 0.3, scale_pos_weight = 1, subsample = 1, tree_method = 'exact'	0.51	0.07

	Algorithm	Features	Hyperparameters	Avg R²	Std R²
	AdaBoost	Average Log CroftonPerimeter, Median Log CroftonPerimeter, Weighted Average CroftonPerimeter, Average EqDiameter, Std EqDiameter, Average VoxelFaceArea, Max Volume, Median Orientation2Theta, Std Orientation2Theta, Avg OrientationTheta, Median OrientationTheta, Std OrientationTheta	base_estimator = decision tree, learning_rate = 4, loss = exponential, n_estimators = 100	0.44	0.11
	Gradient Boosting	Weighted Average CroftonPerimeter, Average EqDiameter, Std EqDiameter, Average VoxelFaceArea, Median Orientation2Theta, Std Orientation2Theta, Average OrientationTheta, Median OrientationTheta	alpha = 0.9, learning_rate = 0.05, max_depth = 2, min_samples_split = 2, min_samples_leaf = 1, n_estimators = 60, subsample = 0.5	0.55	0.08
μCT	XGBoost	Average Log CroftonPerimeter, Weighted Average CroftonPerimeter, Weighted Log EqDiameter, Median Log EqDiameter, Std Log EqDiameter, Average EqDiameter, Std EqDiameter, Avg Perimeter, Max Log VoxelFaceArea, Avg VoxelFaceArea, Std Volume, Std Orientation2Phi, Average Orientation2Theta, Median Orientation2Theta, Std Orientation2Theta, Average OrientationTheta, Weighted OrientationTheta, Median OrientationTheta	base_score = 0.5, booster = 'gbtree', colsample_bylevel = 1, colsample_bynode = 1, colsample_bytree = 0.1, gamma=0, importance_type = 'gain', learning_rate = 0.5, max_delta_step = 0, max_depth = 2, min_child_weight = 1, n_estimators = 40, n_jobs = 32, num_parallel_tree = 1, reg_alpha = 0, reg_lambda = 0.5, scale_pos_weight = 1, subsample = 1, tree_method = 'exact'	0.54	0.10

Excluding RCAL, the model created with Gradient Boosting showed the highest R^2 (0.63), which is within the range obtained in the cross-validation, in addition to the lowest RMSE (4.38%) among the tested models. Consequently, their mean residuals were close to zero (Figure 2-13), and their dispersion was low (0.02 ± 4.49%). The null hypothesis of normality of the Shapiro-Wilk test (Table 2-4) is not rejected in either model for a 90% confidence level,

as illustrated in the QQ Plots (Figure 2-14D to F). Furthermore, the predicted vs. measured regression analysis showed that the models built with the XGBoost and Gradient Boosting algorithms have slope one and cross zero at a 90% confidence interval, demonstrating a good ability to predict extreme values.
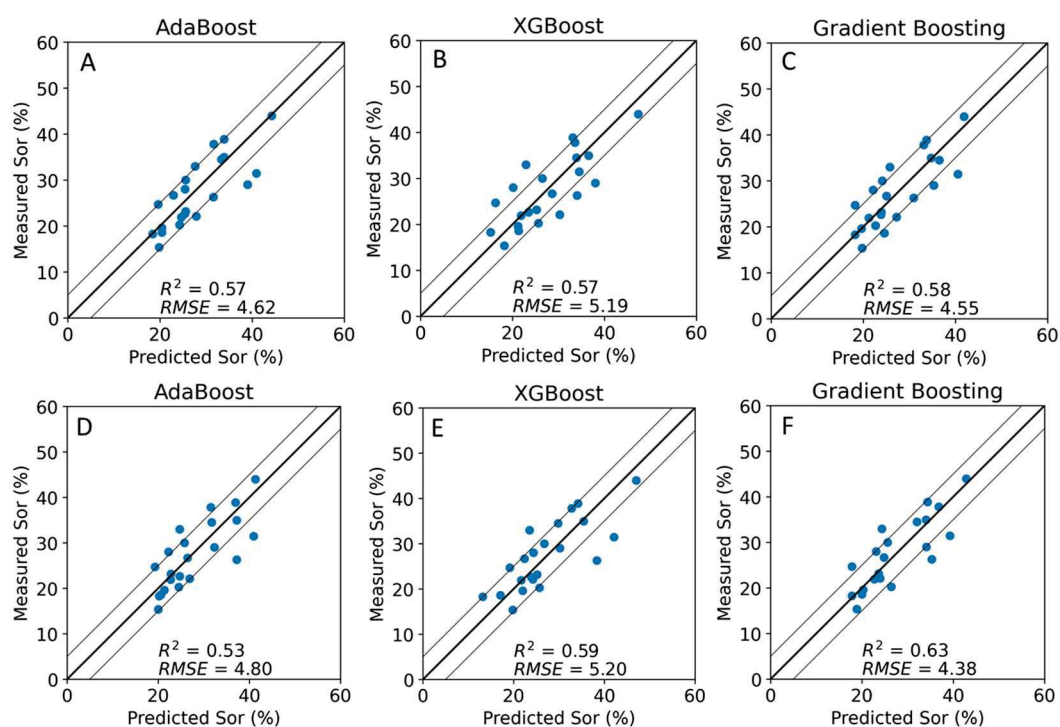
Figure 2-12 - Scatter plots exhibiting predict vs. measured Sor for the best models. A to C represents the models built with RCAL *and µCT, while D to F used only µCT data.*
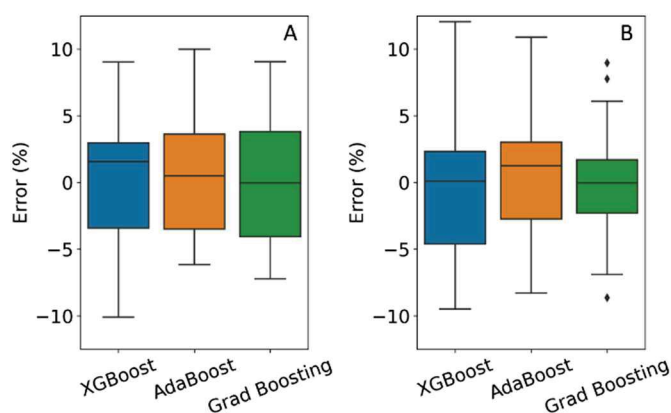
Figure 2-13 - Box plots show Sor residual distributions considering models built with RCAL (A) and without it (B).
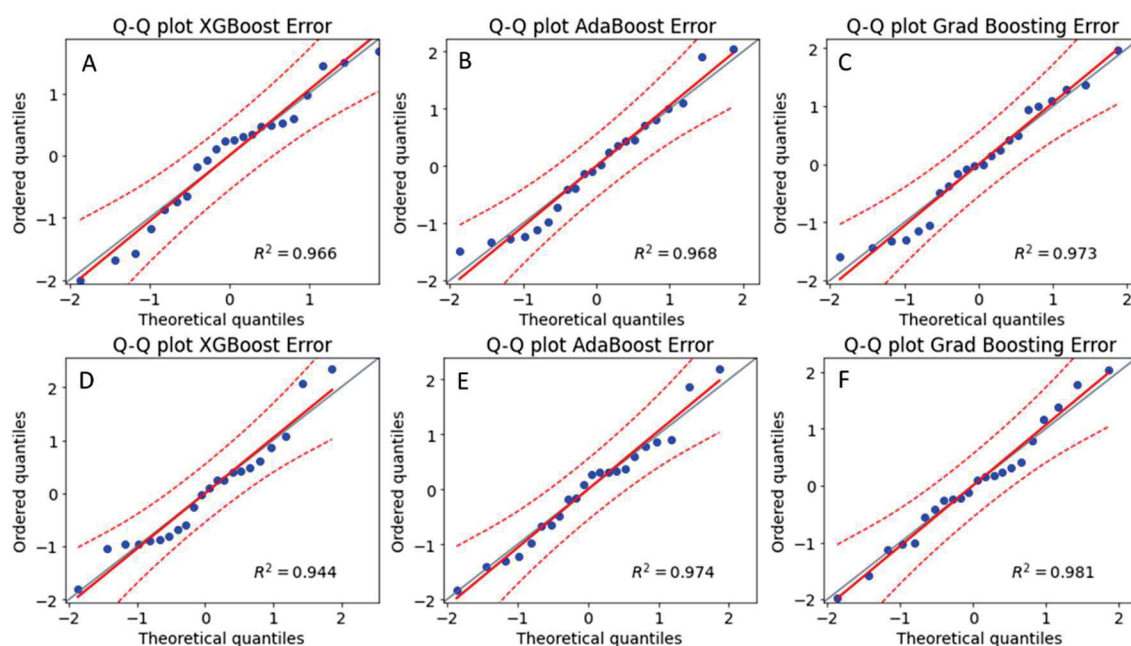
Figure 2-14 - Q-Q plots presenting the relationship between ordered and theoretical quantile errors of the models built with RCAL and μCT (A to C) and only with μCT (D to F). The dashed red line limits the 90% confidence region.

Table 2-4 - Shapiro-Wilk normality and regression analysis tests, considering regressions between predicted and measured Sor.

	Algorithm	Shapiro-Wilk Test	Parameter	Coeff	Std Error	Confidence Interval			
		p-value				<95%	>95%	<90%	>90%
μCT and RCAL	XGBoost	0.440	Intercept	5.094	4.298	-3.870	14.059	-2.318	12.507
			Slope	0.824	0.152	0.508	1.141	0.563	1.086
	AdaBoost	0.414	Intercept	7.080	3.624	-0.478	14.639	0.831	13.330
			Slope	0.765	0.128	0.499	1.032	0.545	0.986
	Gradient Boosting	0.506	Intercept	6.468	3.600	-1.042	13.977	0.259	12.677
			Slope	0.766	0.127	0.501	1.031	0.546	0.985
μCT	XGBoost	0.270	Intercept	3.824	4.355	-5.261	12.909	-3.687	11.336
			Slope	0.855	0.154	0.535	1.176	0.590	1.121
	AdaBoost	0.767	Intercept	7.673	3.735	-0.119	15.465	1.231	14.115
			Slope	0.735	0.132	0.460	1.010	0.508	0.963
	Gradient Boosting	0.904	Intercept	5.397	3.539	-1.985	12.779	-0.707	11.501
			Slope	0.803	0.125	0.543	1.064	0.588	1.019

In general, it is observed that both the models built with RCAL and those without this data presented similar results. RCAL should improve models' prediction considering that they provide petrophysical information. However, the results of the predictions without them were similar. This is probably because the information contained in the RCAL was accessed by the

extracted μCTs attributes, although the resolution did not resolve part of the porosity: density is poorly correlated with Sor and it was not used in any of the models; in addition, albeit it has entered the models with RCAL, porosity has a low correlation with Sor, resulting in a small contribution in the models. Even though permeability has a positive correlation with Sor (r = 0.5), it has a lower correlation than features related to pore size and variability, which may explain why this feature was deprecated. Therefore, apparently, RCAL does not contain additional information for the Sor prediction in relation to the μCTs pore attributes. Given the limited number of samples, both results are satisfactory, which indicates that there is no need to aggregate RCAL data. Hence, it speeds up the prediction process provided that RCAL is only obtained after cleaning the samples, which can take months. Finally, the Gradient Boosting algorithm had the best results given the metrics used to evaluate the models.

2.5.3.2   Feature Importance

Although only porosity has been included in the best models with RCAL, employing them influences the elimination of features by RFE, implying different selections of parameters (Table 2-3). The most important features in the models where RCAL was used correspond to the pore size and orientation categories (Figure *2-15*). Features related to pore size showed good correlations with Sor; conversely, orientation was less evident than pore size. The most frequent features and more weight in the three models were average Area3d and std EqDiameter. As discussed previously, these features showed reasonable correlations with Sor and confirmed the relationship of Sor with pore size and its heterogeneity. Furthermore, orientation parameters with some correlation, such as the median OrientationPhi and Orientation2Phi, were also important, and their load was above 0.05. On the other hand, features like median Orientation2Theta did not show a clear correlation, although important in the models. Finally, among the RCAL data, we note that only porosity was used, although it does not have a reasonable correlation with Sor. While porosity does not correlate with Sor (Figure 2-9), this feature does have a relationship with Sor and average Area3d (Figure 2-16A). We noticed that porosity tends to amplify Sor in samples with smaller pores. Figure 2-16B shows the relationship of the slope regression coefficient between Sor and average Area3d considering incremental moving windows of porosity. Samples included in windows with smaller porosities

show smaller slopes of the linear correlation between Sor and average Area3d. This effect possibly has lithological control, as the CSC facies tend to have greater Sor and pore size, although it has relatively lower porosity. Instead, IGR tend to increase Sor with smaller pores and higher porosities to CSC. As shown in Figure 2-16C, the median Orientation2Phi shows that the samples with larger pores have smaller values, which should help the algorithms to predict samples with larger Sor. Finally, even though the median Orientation2Theta is important in the models, it does not show a clear relationship to Sor and median Area3d (Figure 2-16D).
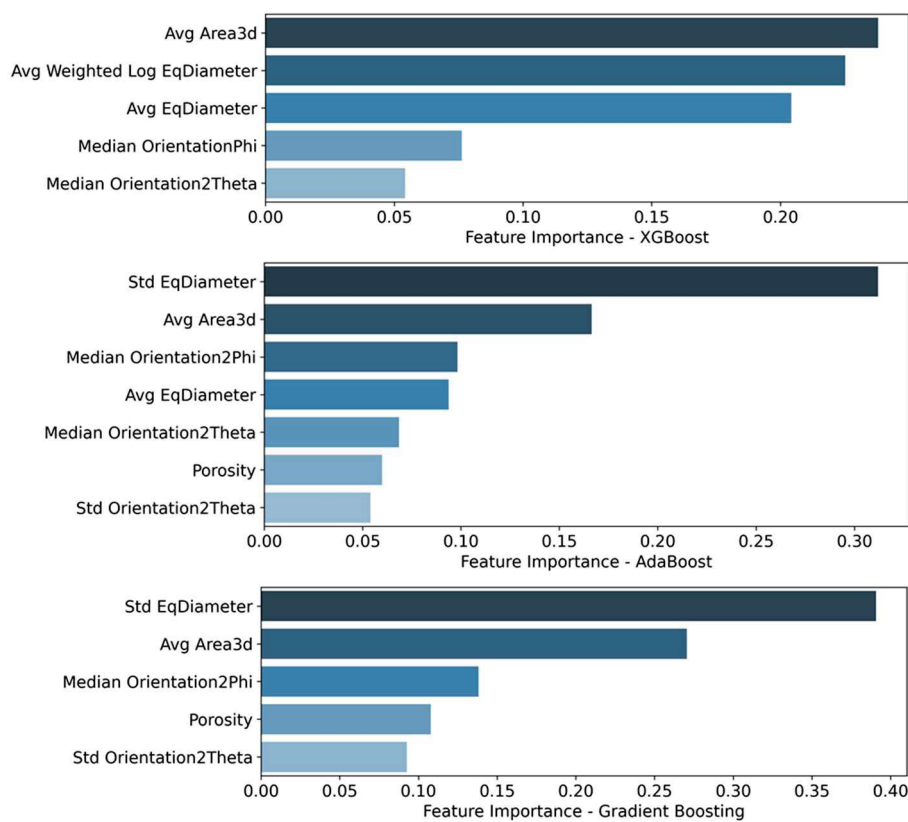
Figure 2-15 - Feature importance (>0.05) of models built with RCAL *and* μCT.

The three best models built without RCAL had the same most important features (std EqDiameter and average VoxelFaceArea) related to the pore size category. Concerning the other features, these models presented differences (Figure 2-17): the model built with XGBoost put more weight on features related to pore size, while AdaBoost balanced it with orientation features. The Gradient Boosting, whose model showed the best results, in addition to the features mentioned above, used the average EqDiameter, the weighted average Crofton Perimeter, and finally, the average OrientationTetha.
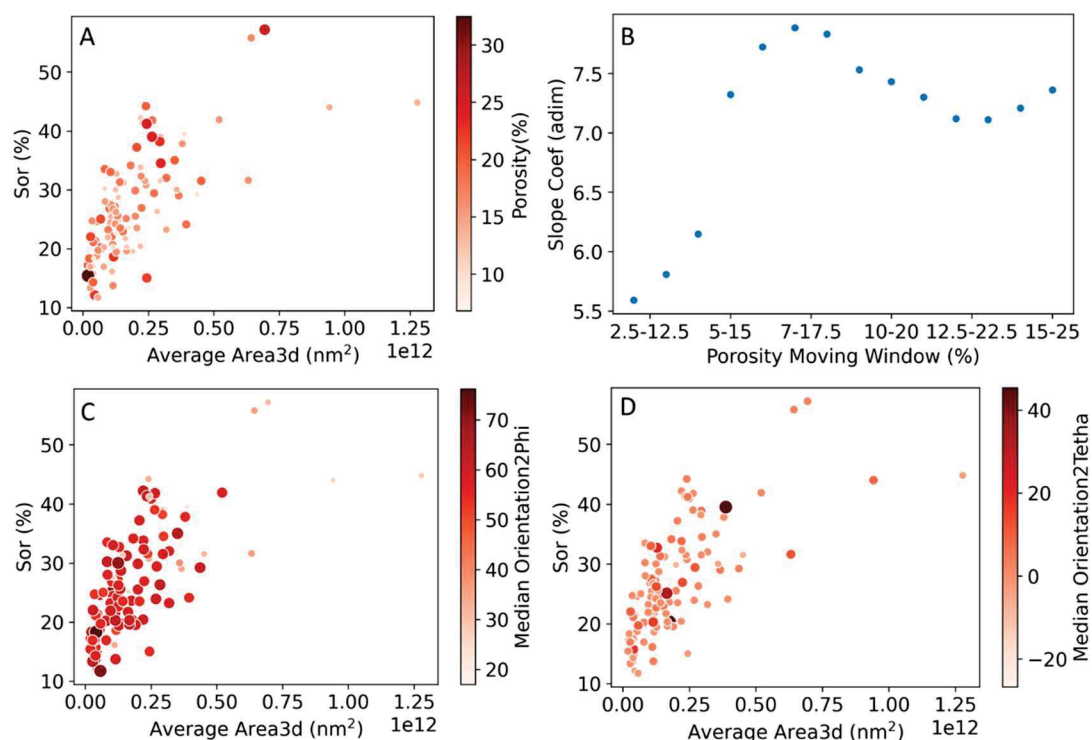
Figure 2-16 - Scatter plot illustrating Sor vs. average Area3d colored by porosity (A), median Orientation2Phi (C), and median Orientation2Theta (D). Figure B shows the relation of the slope coefficient of regression between Sor and average Area3d to porosity moving windows, illustrating the effect of increasing porosity combined to average Area3d on Sor.
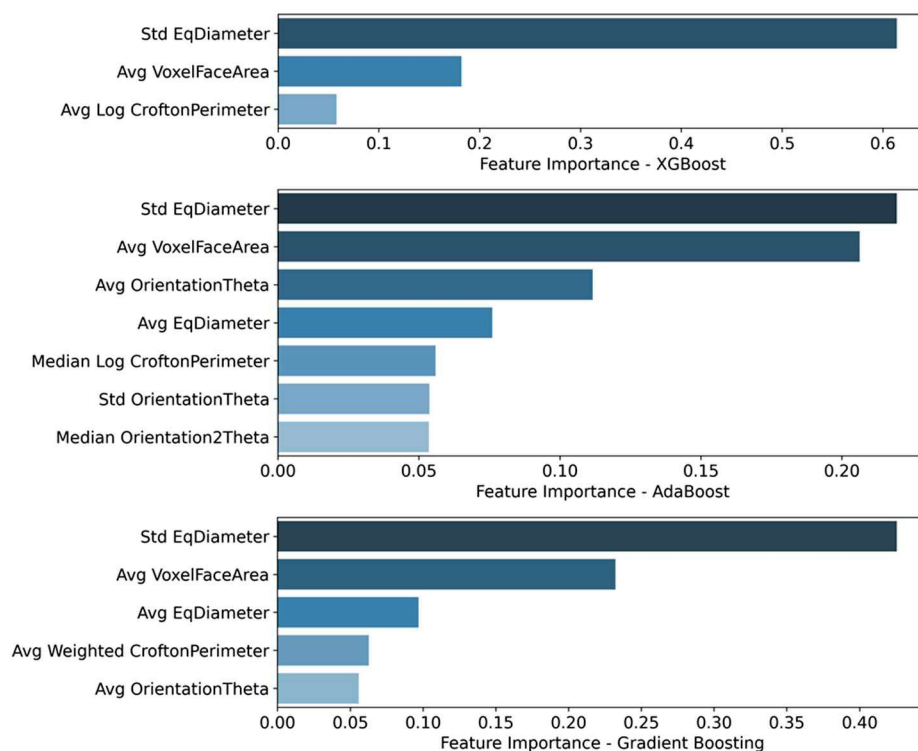
Figure 2-17 - Feature importance (>0.05) of models built with μCT.

Lastly, permeability was not chosen in the best models, although there is a clear relationship with Sor (Figure 2-9). Also, density was not used, which was expected given the low correlation with Sor, which emphasizes the observation that mineralogy should not be crucial for the Sor differences. Although they correlate with Sor, features related to the pore shape did not have a high weight in the best models. Attributes related to the pore size category highly correlate, indicating that the algorithms used have high generalization power even with correlated variables. Still, we observed that even attributes without apparent control over Sor are useful for prediction, showing the robustness of the Ensemble Learning techniques.

2.6   Conclusions

This work sought to use RCAL data and pore attributes extracted from μCt scans to predict Sor in carbonates from the Barra Velha Formation, Santos Basin, Offshore, Brazil. In addition, it aimed to improve the understanding of how pore morphology controls Sor in these rocks. Thus, we emphasize as the main conclusions of this work:

- The three studied facies have a very distinct porous framework, given the genesis of their formation and specific diagenetic alterations. So, these particularities imply distinct petrophysical and Sor characteristics.

- Density values do not show a clear relationship with Sor, denoting those mineralogical changes are not an essential factor in residual oil control of Pre-salt rocks.

- Features related to pore size and its heterogeneities have the best correlations among the studied attributes, indicating that rocks with larger pores tend to have a more heterogeneous framework and, consequently, a more significant amount of trapped oil after the waterflood.

- The orientation and shape of pores are related to facies: particulate rocks such as IGR have equidimensional pores, which tends to generate poor correlations with Sor; conversely, CSC pore shape is controlled by the growth of calcite crystals, and LMN has pore morphology impacted by the laminated nature of the rock. Thus, CSC and LMN tend to show some correlation between orientation and form, in contrast to IGR.

- The ML models showed satisfactory results, given the number of samples. These models can therefore reduce the uncertainty of Sor in reservoirs. Moreover, the methodology based on μCT pore attribute extraction can be adapted in different reservoirs.

- Comparison between the three LM models built with and without RCAL did not show significant differences. Considering that the RCAL data takes time to be obtained, we assume that models made only with μCT are the best option. Still, among the tested algorithms, the best model was built with Gradient Boosting.

- Finally, the models indicated that the features with greater importance are related to pore size and orientation, confirming the impact of these properties on Sor.

2.7 Acknowledgments

3. Article 2 - HERLINGER, R.; ROS, L. F. DE; SURMAS, R.; VIDAL, A. Residual oil saturation investigation in Barra Velha Formation reservoirs from the Santos Basin, Offshore Brazil: A sedimentological approach. Sedimentary Geology, v. 448, 2023.

3.1 Abstract

Residual oil saturation (Sor) is a petrophysical parameter of great relevance, as it is used for flow simulation, production forecast, and reserve estimation. However, oil trapping is rarely investigated from a geological point of view. This work integrates petrography, RCAL, SCAL, and X-ray µCT to understand how lithological characteristics control Sor in the lacustrine carbonate reservoirs of the Pre-salt section of the Santos Basin, offshore eastern Brazil. The *in-situ* facies, composed of calcite shrubs and spherulites, and magnesian clays, have Sor directly related to the diagenetic evolution of the Mg-clays, including processes of replacement by dolomite and dissolution and their relationships to the calcite shrubs and spherulites. The intense replacement of the clay matrix by dolomite, followed by dissolution, developed intercrystalline porosity with a small pore-to-throat ratio, favoring water sweeping. On the other hand, the preservation of primary porosity among shrubs or the development of large matrix dissolution pores favors oil trapping. In intraclastic rocks made by redeposited fragments of shrubs and spherulites, the main control of Sor is depositional texture: rocks with larger grain size tend to have greater porosity heterogeneity and, consequently more oil trapped. On the other hand, fine-grained calcarenites tend to have a more homogeneous porous medium, which enables oil displacement. Finally, the imaging of Sor in reservoir conditions indicates mixed wettability. However, there is no clear relationship between Sor and predominant mineralogy, which should be investigated in future works.

Keywords: Sor, Pre-Salt, Diagenesis, Wettability, X-ray µCt

3.2 Introduction

Understanding residual oil saturation (Sor) in carbonate rocks tends to be challenging since these reservoirs often present mixed- or oil-wettability (Alhammadi *et al.*, 2017; Anderson, 1985; Faramarzi-Palangar *et al.*, 2022; Ferrari *et al.*, 2021; Salathiel, 1973) and present highly heterogeneous porous systems, as in the Brazilian Pre-salt rocks (Herlinger, Zambonato and De Ros, 2017; Lima and De Ros, 2019). Oil trapping in reservoirs after waterflood results from several factors, including rock characteristics, such as mineralogy and texture, the morphology of pores and their throats, the composition of the fluids involved, and the environmental conditions of the reservoirs, such as pressure and temperature. These interactions among mineralogy, texture, fluids, and environmental characteristics impact wettability (Anderson, 1985, 1987), interfacial tension (Hoeiland *et al.*, 2001; Ling and He, 2012; Wardlaw, 1982), and distribution of capillary forces within the fundamental factors for the flow and entrapment of fluids (Blunt, 2017; Chandler *et al.*, 1982; Perkins, 1957).

Initial studies with direct observation of displacement mechanisms and multiphase trapping go back to experiments in glass microtubes by Roof (1970). In his seminal study, Roof directly observed the so-called snap-off mechanism, where the non-wetting phase is disrupted, and the oil remains trapped within the center of the pores. The author theoretically related and visually verified the proportions between the morphologies of pores and throats and their impact on non-wetting phase trapping. Later, several theoretical, simulation, and experimental studies with micromodels and sphere packs showed the influence of textural factors, such as throat/pore ratio, porosity, coordination number (number of throats per pore), and heterogeneity on oil trapping and consequent recovery efficiency (Chandler *et al.*, 1982; Chatzis, Morrow and Lim, 1983; Cieplak and Robbins, 1988, 1990; Larson, Scriven and Davis, 1977; Lenormand and Zarcone, 1984; Lenormand, Zarcone and Sarr, 1983; Mohanty, Davis and Scriven, 1987; Stegemeier, 1977; Wardlaw, 1982; Yuan, 1981).

Fluid trapping is highly dependent on reservoir wettability, which determines their initial configuration, flow, and retention mechanisms (Gharbi and Blunt, 2012; Humphry *et al.*, 2014a; Ryazanov, Sorbie and Dijke, van, 2014; Spiteri *et al.*, 2008; Wolf, Siebert and Surmas, 2020). Typically, under water-wet conditions, oil occupies the center of the pores at the initial irreducible water saturation (Sw$_{irr}$) condition, as aforementioned. In contrast, the water will be confined to the corners and roughness of the constituents' surfaces at high capillary pressures.

As the water pressure increases, the inflow of water generates a displacement of the oil/water/rock interface, leading to the oil phase disconnection observed by Roof (1970). Hence, in heterogeneous porous media, water displaces the oil, initially occupying the smaller regions. This leads to oil trapping by snap-off in larger pores, a process commonly related to a high pore/throat size ratio. This displacement pattern is named percolation with trapping (Blunt, 2017; Chandler *et al.*, 1982) (Figure 3-1).
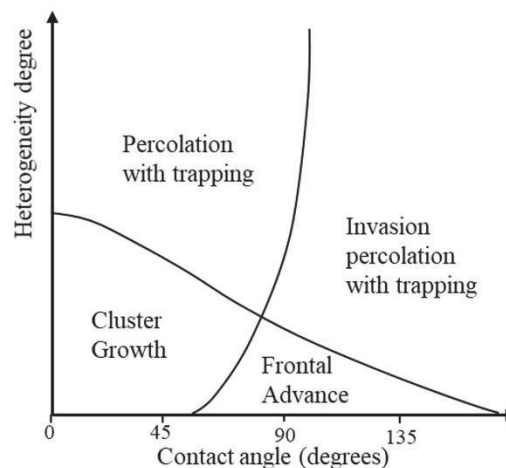
Figure 3-1 - Diagram showing the displacement pattern predominance, considering the contact angle and the degree of heterogeneity of the porous media (modified from BLUNT (2017)).

In very homogeneous media under mid-water- to strong oil-wet conditions (contact angle ~60 to 180°), there is cooperation among the pores and throats (Blunt, 2017; Blunt, King and Scher, 1992; Lenormand and Zarcone, 1984; Lenormand, Zarcone and Sarr, 1983; Valvatne and Blunt, 2004), favoring waterflooding and decreasing Sor. In this type of displacement pattern, referred to as frontal advance (Figure 3-1), variations in pore and throat dimensions are less critical because the differences between threshold pressures are smaller, resulting in a uniform displacement (Blunt, 2017). In homogeneous media, considering strong water-wet conditions, the growth of clusters of the wetting phase may occur instead of frontal advance. When these regions merge, oil is trapped (Blunt, 2017; Chatzis, Morrow and Lim, 1983; Lenormand and Zarcone, 1984). Finally, during waterflood in a heterogenous oil-wet reservoir, water first preferentially displaces oil from large pores. Subsequently, the displacement continues by layers of oil adhered to the minerals in a pattern called invasion percolation with trapping (Dias and Wilkinson, 1986). After the layers collapse and disconnect, the oil is retained adhered to the minerals.

More recently, the advancement of X-ray imaging techniques and the possibility of directly observing fluids in high resolution allowed a significant improvement in understanding pore-scale processes. Several studies accurately show the configuration of fluids and their relationships with pores and minerals. This made it possible to evaluate displacement processes and trapping mechanisms directly, including measurements of contact angles, snap-off dynamics, and oil entrapment by layers (Andrew, Bijeljic and Blunt, 2014a; Singh *et al.*, 2017; Singh, Branko and Blunt, 2016). These advances validated theoretical concepts and observations made in micromodels and calibrated simulation models.

Although undeniable advances have been made to understand multiphase flow and trapping, its connection with reservoir geological features is still treated superficially, especially concerning carbonate rocks. This work, therefore, aims to integrate petrography, routine and special core analysis (RCAL and SCAL), and digital rock (DRP) to assess the impact of diagenetic and depositional processes on oil trapping in the Pre-salt Barra Velha Formation reservoirs of the Santos Basin, Brazil.

3.3   Geological Setting

The Santos Basin is located on the southeastern Brazilian margin (Figure 3-2), limited to the north by the Cabo Frio High and to the south by the Florianópolis platform. It was formed under a tectonic extension regime during the breakup of the Gondwana continent during the early Cretaceous/Later Jurassic, preceding the separation of South American and African continents and culminating in the formation of the Atlantic Ocean (Austin and Uchupi, 1982; Cainelli and Mohriak, 1999; Davison, 2007; Nürnberg and Müller, 1991; Rabinowitz and LaBrecque, 1979). According to Moreira *et al.* (2007), the stratigraphy of the Santos Basin is divided into three Super-sequences: Rift, Post-rift, and Drift (Figure 3-3). During the early rift formation, the Precambrian basement was covered by the Camboriú tholeiitic volcanic rocks during the Lower Cretaceous (Mizusaki *et al.*, 1992). The sedimentary infill of the Santos Basin begins with rocks from the Piçarras Formation in the Barremian, which includes the deposition of siliciclastic rocks and Mg-clays ooids and peloids, accumulated in a high alkalinity environment, as well as hybrid sediments (Leite, Silva and De Ros, 2020). The Itapema Formation, deposited during the Jiquiá Local Stage, is composed of thick accumulations of bioclastic bivalve rocks ("coquinas") (Chinelatto *et al.*, 2020b; Rocha, Favoreto and Borghi,

2021) in addition to peloids and ooids of Mg-clays, which often occur mixed with the bioclastic sediments (Leite, Silva and De Ros, 2020). Dark shales occur interspersed with the bioclastic deposits and represent the main source rocks of the basin. The top of these deposits is recognized as a regional stratigraphic marker, resulting from basin uplift and erosion, which marks a drastic change in environmental conditions (Dias, 2005).

Figure 3-2 - Map illustrating the Santos Basin and the study location (dashed areas).

The Barra Velha Formation occurs unconformably covering the Rift Super-sequence, and is separated into Lower and Upper by the Intra-Alagoas unconformity. Their sediments are formed by the intercalation of precipitated calcite shrub crusts, deposits of Mg-clays with calcite spherulites, laminated Mg-clays replaced by microcrystalline calcite, dolomite and silica, and intraclastic rocks (Basso *et al.*, 2021; Carramal *et al.*, 2022; Carvalho *et al.*, 2022; Gomes *et al.*, 2020b; Netto, Pozo, Manuel, *et al.*, 2022; Netto, Pozo, M., *et al.*, 2022; Silva, da *et al.*, 2021; Wright and Barnett, 2015, 2020). Due to the lack of data, Moreira *et al.* (2007) initially interpreted these accumulations as deposited in a transitional to marine environment. Subsequently, after the giant hydrocarbon accumulation discoveries, the Barra Velha Formation deposits were reinterpreted as deposited in an alkaline lacustrine environment (Wright and Barnett, 2015). Aside from these studies in the Santos Basin, studies of the equivalent deposits in the adjacent Campos and Kwanza (Angola) Basins revealed close depositional, diagenetic,

and mineralogical similarities (Herlinger, Zambonato and De Ros, 2017; Lima and De Ros, 2019; Sabato-Ceraldi and Green, 2017; Saller *et al.*, 2016).

My	Geochronology			Stratigraphy		Unconformities	Tectonic
	Epoch	Stage	Local Stage	Group	Formation		Stage
					Ariri		Drift
						Salt Base	
120	Lower Cretaceous	Aptian	Alagoas	Guaratiba	Barra Velha		Pos-Rift
						Intra-Alagoas	
125			Jiquiá		Itapema	Pre-Alagoas	
		Barremian	Buracica		Piçarras		Rift
130			Aratu			Top Basalt	
		Hauterivian			Camboriú		

Figure 3-3 - Stratigraphy of the Santos Basin (Moreira et al., 2007).

Calcite crusts, also referred to as shrubstones or stromatolites, are constituted by fibrous calcite aggregates crystals ("shrubs") with divergent extinction and fascicular-optic habit (Herlinger, Zambonato and De Ros, 2017; Lima and De Ros, 2019; Rodríguez-Berriguete *et al.*, 2022). The aggregates encrust each other or other materials, growing vertically and coalescing horizontally, resulting in the development of crusts of varying dimensions. The syngenetic precipitation of calcite is closely related to the deposition of Mg-clays, which occurs as laminations, peloids, ooids, and as a coating in particles of different origins (Carramal *et al.*, 2022; Carvalho *et al.*, 2022). These clays often occur interspersed with the calcite crusts, filling the inter-shrubs spaces.

Spherical, fibro-radial calcite aggregates (spherulites) were precipitated during early diagenesis replacing and displacing the Mg-clay laminations. Remnants of Mg-clays included in the calcite shrubs indicate that they also frequently replaced the clays. Mg-clays are highly

reactive, resulting in their dissolution, which generated abundant secondary porosity (Carramal *et al.*, 2022; Tosca and Masterson, 2014; Tosca and Wright, 2015; Wright, 2022). In addition, the Mg-clays were frequently replaced by dolomite crystals and other mineral phases. Where the clay matrix was dissolved, calcite spherulites and dolomite crystals are commonly observed "floating" in the secondary pores. Recently, (De Ros and Oliveira, 2023) proposed a system for the simple classification of the *in-situ* rocks of the Brazilian Pre-Salt, based on the proportion among shrubs, spherulites, and matrix.

In addition to the *in-situ* rocks, re-sedimented particulate deposits constitute important reservoirs in the Barra Velha Formation (Barnett *et al.*, 2021; Rodríguez-Berriguete *et al.*, 2022). These facies are mainly formed by intraclasts of fragmented calcite shrubs and spherulites (Gomes *et al.*, 2020b), associated with intraclasts of the Mg-clay matrix, Mg-clay ooids and peloids, in addition to subordinate phosphate fragments, ostracods, siliciclastic, and volcanoclastic grains (Carramal *et al.*, 2022; Carvalho *et al.*, 2022; Netto, Pozo, M., *et al.*, 2022). Although common, the clay peloids and ooids are often challenging to identify, as they were usually entirely replaced by calcite or dolomite. Dolomite, calcite, and quartz are the main diagenetic constituents, replacing and cementing the particles (Basso *et al.*, 2021; Carvalho *et al.*, 2022).

3.4 Materials and Methods

3.4.1 RCAL and SCAL

This study was carried out with routine and special core analysis (RCAL and SCAL) data from 131 plug samples with 1.5" diameter, cut from 28 wells belonging to several fields located in the Santos Basin. Eleven wells are comprised within the black polygon (Figure 3-2), sampled in the Upper and Lower Barra Velha Formation, both intraclast- and *in-situ*-dominated sections. The red, blue, and yellow areas have 4, 7, and 5 wells, respectively, and were mostly sampled in the Upper Barra Velha Formation, while the white area has only one well and was sampled in the Upper Barra Velha Formation. Wells in the red area were sampled in both *in-situ*- and intraclastic-dominated sections, while wells in the white and yellow areas were sampled exclusively in *in-situ*-dominated sections; finally, wells in the blue area were sampled mostly in *in-situ*-dominated sections. The data include 131 porosity, permeability, Sor and Sw_{irr} results,

and mercury injection capillary pressure (MICP) data from 70 samples. The analyses were performed according to the recommendations of the American Petroleum Institute (API, 1998).

Porosity was measured in a porosimeter, where the plug is placed in a chamber with a known volume. The rock volume is then deduced from the pressure difference between the empty and full chamber, from which the porosity is estimated. Permeability was determined in a permeameter: the sample was inserted into a chamber under confinement. Then the gas is injected into the sample so that there is percolation. The pressure difference between the inlet and the outlet will be related to permeability by Darcy's law:

$$q = \frac{-kA}{\mu L} dP \tag{3.1}$$

where q is the total discharge, k is the permeability, A the cross-sectional area of flow, μ is the fluid viscosity, L is the length of the sample, and dP the pressure drop. In the MICP method, a fragment of about $1cm^3$ is inserted in a holder under vacuum conditions. Then, mercury is injected at incremental pressures. As the pressure increases, the mercury intrudes smaller and smaller throats, from which it is possible to extract pore throats distributions from the pressure and the intruded volume according to the Young-Laplace equation:

$$r^{th} = \frac{2\sigma cos\theta}{Pc} \tag{3.2}$$

where r^{th} is the throat radius, σ the interfacial tension, θ is the contact angle, and Pc is the capillary pressure. Sw_{irr} was reached after centrifugation (CORELAB ACES-200). The samples were then aged to restore the wettability before the waterflood experiment. Sor was obtained after waterflood by low capillary number unsteady state water-oil relative permeability tests, employing formation and injection brines and dead oil. The test starts at Sw_{irr} condition, then water is injected into the sample and the oil starts to be displaced by the water. As time passes, oil production decreases, until it ceases. At this point, the oil is trapped by capillary forces and is considered residual oil. The petrophysical analyses were performed at Petrobras Research Center (CENPES).

3.4.2   Imaging of the residual oil saturation

For qualitative assessment of fluid distribution after water flooding, five 1.5" diameter plug samples were selected for X-ray microtomographic imaging (X-ray μCT). Rocks were imaged in the Sor condition after the waterflood, according to the previously discussed method.

The fluids used correspond to dead oil and injection waters doped with iodine to enhance oil/water contrast. A GE VTomex L300 equipment was used for sample scanning, operating in voltage 160kV, current 240μA, and exposure time of 500ms, totaling 72 minutes of acquisition per plug. To reduce the noise and the beam-hardening effect (Brooks and Chiro, 1976), a 1cm quartz filter was used. Plugs were imaged at a resolution between 38 and 39.2μm. Due to the resolution limitation, rocks with large pores were selected. The images were segmented with a machine learning method called Trainable WEKA Segmentation (Arganda-Carreras *et al.*, 2017) to individualize oil, water, and solid phase and these were processed by Avizo^{TM} software.

3.4.3   Petrography

The samples were cleaned from oil and impregnated with blue epoxy resin to identify the porosity, and dyed with a solution of alizarin and potassium ferrocyanide to distinguish the carbonate phases (Dickson, 1965). Eighty thin sections were point-counted (300 points) (Chayes, 1949; Hutchison, 1974; Plas, Van Der and Tobi, 1965) to characterize and quantify the primary and diagenetic constituents, pore types, textures, structures, and their interrelationships. The thin section is swept in regular steps to regularly cover the area. At each step, the constituent that occurs exactly at the intersection of the reticule is recorded. The descriptions were registered, quantified, and interpreted in the software Petroledge^{TM}. The *in-situ* rocks were classified according to the system proposed by De Ros and Oliveira (2023), while the particulate rocks were classified according to Grabau (1904). In addition, photomicrographs of 123 samples were segmented to quantify pore size, and the particle size was measured in 63 samples. Photomicrographs were analyzed in Fiji software (Schindelin *et al.*, 2012). To implement the segmentation, the images' contrast was adjusted, then they were filtered, when necessary, and finally segmented by cutoff pore/rock.

3.5   Results

3.5.1   Petrography, SCAL, and RCAL

3.5.1.1   In-Situ Rocks

The main primary components of *in-situ* rocks correspond to Mg-clays and calcite shrubs. Even though Mg-clays were mostly dissolved or replaced in the studied samples (Figure 3-4A, B, D, and F), their original content (average 22.6%, maximum 89.7%) was estimated by the dissolution volume and replacement minerals. The clays occur as laminated matrix and peloids, which are replaced and/or encrusted by calcite shrubs, and replaced by calcite (mainly as spherulites, but other habits are common), silica (average 1.0%; maximum 10.7%), and dolomite (average 14.1%; maximum 76.0%). Calcite shrubs are, in general, a few millimeters long. Their vertical and horizontal coalescence formed calcite crusts that constitute, on average, 45.9, and up to 86.3% of the analyzed samples (Figure 3-4C, D, E, and F). Replacement of the shrubs by dolomite (average 2.5%; maximum 19.3%) and silica (average 1.2%; maximum 11.0%) is common, although the average replacement volume is less than 5%.

Interstitial spaces among the calcite shrubs may have been originally empty, as growth-framework pores, or filled with Mg-clays. Primary inter-shrub growth-framework porosity averages 2.1%, reaching 11% in shrubstones. Such primary porosity was reduced mainly by dolomite (average 0.8%; maximum 11.3%), calcite (average 0.2%; maximum 5.3%), and silica (average 0.4%; maximum 11.0%) cementation. Along with Mg-clays and calcite shrubs, spherulites with submillimeter to millimeter diameter constitute the main components of the analyzed *in-situ* rocks (average 27.2; maximum 80%) (Figure 3-4B and F). Spherulites were formed replacing and displacing the clay matrix. Spherulstones, where the clays were mostly dissolved, suffered compaction. In those where the matrix has been replaced mainly by dolomite, the spherulites appear "floating" among dolomite crystals (Figure 3-4B and F).

Asides from inter-aggregate dissolution and growth-framework porosity, the *in-situ* facies contain a fair amount of intra-aggregate porosity inside partially-dissolved calcite shrubs and spherulites (average of 2.5; maximum 10%). The proportion between Mg-clays, shrubs, and calcite spherulites allowed the classification of the *in-situ* samples as shrubstones (29%), shrub-spherulstones (22%), spherulstones (13%), Mg-clay mudstones (5%), muddy shrubstones (14%), and muddy spherulstones (17%) (Figure 3-5).

Sor = 0.172
ø = 0.200
k = 21.7mD

Sor = 0.247
ø = 0.134
k = 6.26mD

Sor = 0.379
ø = 0.130
k = 852mD

Sor = 0.413
ø = 0.195
k = 1853mD

Sor = 0.420
ø = 0.096
k = 2519mD

Sor = 0.465
ø = 0.203
k = 143mD

Pore Throat Radius (micrometer)
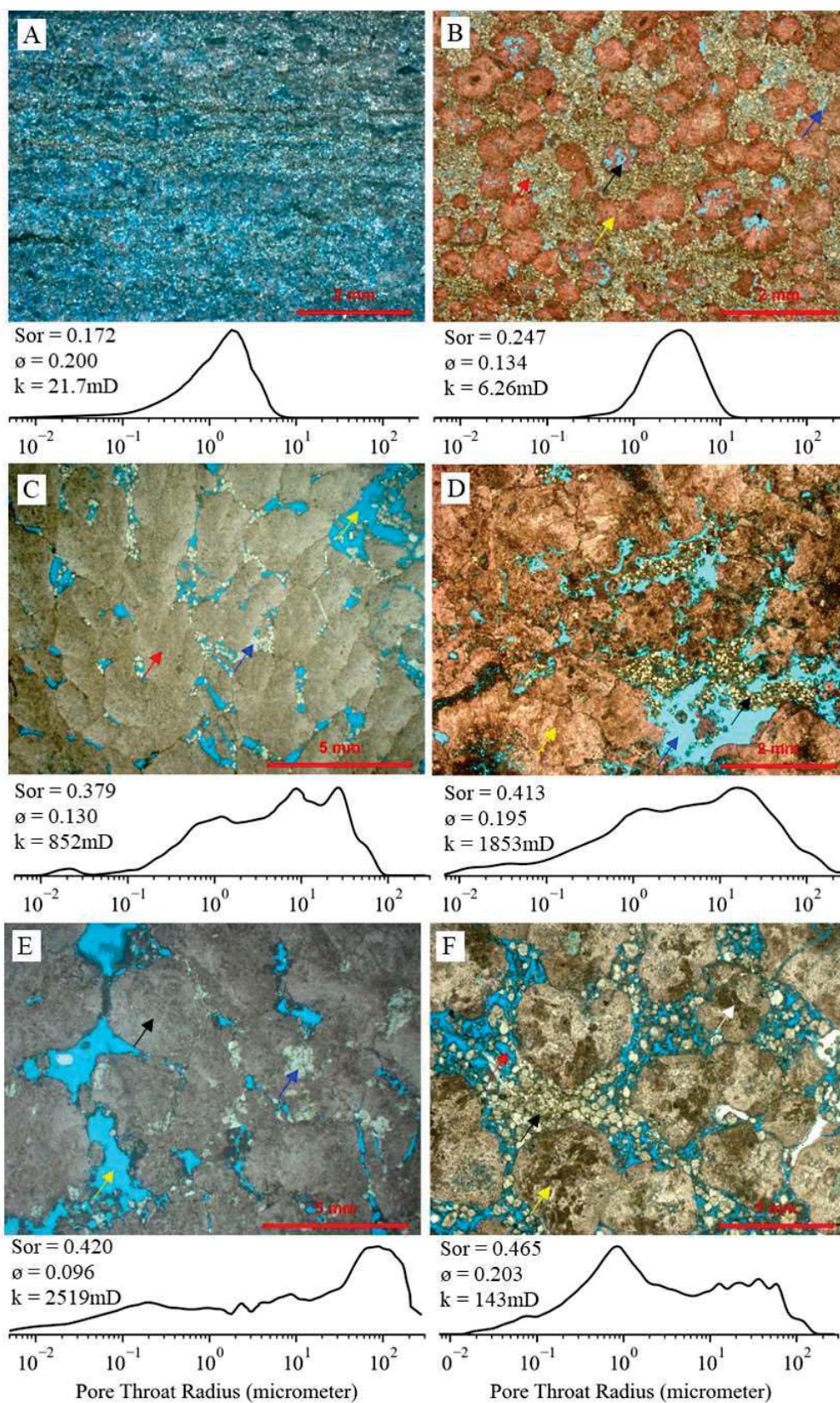
Figure 3-4 - Template with photomicrographs (uncrossed polarizers) showing important petrographic aspects of the in-situ rocks (porosity impregnated by blue epoxy resin), and respective petrophysical properties including Sor, laboratory (helium) porosity (ø), permeability (k), and pore throats radius

distribution. A) Mudstone with original matrix dissolved and replaced by dolomite and calcite small crystals, resulting in a highly homogeneous pore system. B) Muddy spherulstone with calcite spherulites (yellow arrow) partially "floating" in matrix-replacive dolomite (red arrow), with intercrystalline porosity (blue arrow) and intra-aggregate porosity from the partial dissolution of spherulites (black arrow). MICP indicates a homogeneous porous media. C) Shrubstone with well-preserved calcite shrubs (red arrow) and growth-framework porosity (yellow arrow) partially reduced by dolomite cementation (blue arrow). D) Muddy shrubstone composed of calcite shrubs (yellow arrow) and clay matrix partially replaced by dolomite (black arrow) and partially dissolved, with the formation of vugs resulting in a heterogeneous pore throat distribution. E) Shrubstone composed of calcite shrubs (black arrow) locally replaced by silica (blue arrow), with preserved growth-framework porosity (yellow arrow). F) Muddy shrubstone consisting of calcite shrubs (yellow arrow) and spherulites (white arrow) with matrix mostly dissolved (red arrow) and partially replaced by dolomite (black arrow).
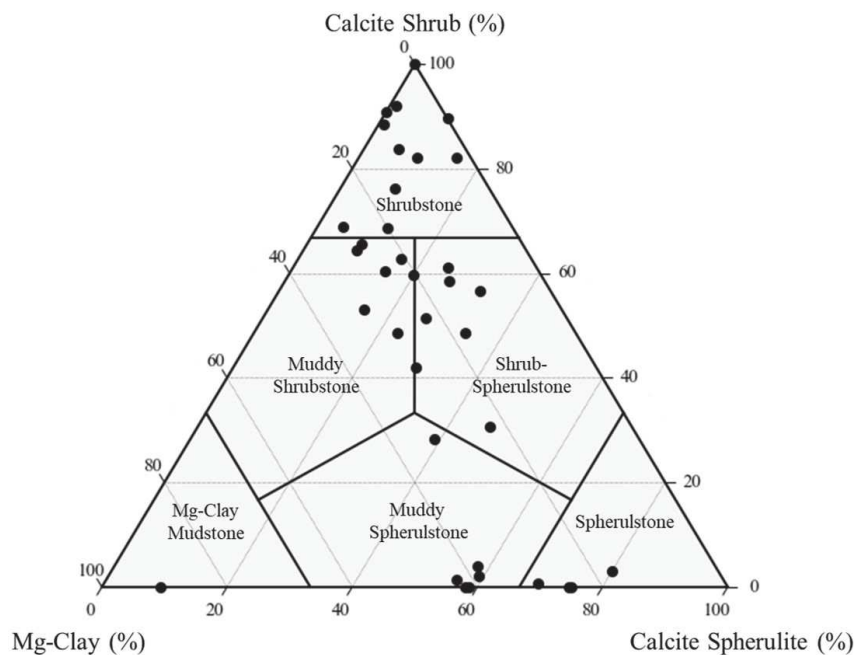
Figure 3-5 - Classification of the in-situ quantified samples based on the original percentage of Mg-clays, calcite spherulites, and shrubs (De Ros and Oliveira, 2023).

The average porosity of the studied samples occurs around 15%, with no significant difference between the facies; shrubstones have the smallest porosity (13.1%), while shrub-spherulstones have the largest (17.1%). Average permeability, in turn, is greater where shrubs are present (shrubstone – 738.6mD; muddy shrubstone – 439.4mD; shrub-spherulstone – 972.9mD). On the other hand, in the facies where there is a predominance of spherulites and Mg-clay, the average permeability tends to have lower values (muddy-spherulstone – 128.0mD; spherulstone – 82.1mD; Mg-clay mudstone – 18.5mD). The average P10 Throat Radius, which represents the larger throats, is higher in samples rich in shrubs (shrubstone – 66.4μm) and lower in the results referring to samples dominated by Mg-clay (Mg-clay mudstone – 1.9μm). On the other hand, excepting Mg-clay mudstones, which have a significantly lower P50 Throat Radius (0.5μm), other facies have similar average values, ranging from 4.7 to 10.6 μm. The

average P10 throat radius varies from 0.1 to 0.4µm. Finally, rocks with shrubs present higher Sor values (shrubstone – 35.2%; muddy shrubstone – 35.0%; shrub-spherulstone – 35.2%mD), in contrast to rocks where there is a predominance of spherulites and Mg-clays (muddy spherulstone – 25.6%; spherulstone – 23.5%; Mg-clay mudstone – 19.1%). Table 3-1 and Table 3-2 summarize the petrographic and petrophysical results.

Table 3-1 - Statistical summary including average, maximum, and standard deviation of constituents of in-situ rocks.

	Constituents (%)	Average	Maximum	Std deviation
Syngenetic	Mg-clay	0.4	8.0	1.5
	Calcite Shrub	40.5	81.0	28.1
Diagenetic	Calcite spherulite	23.3	75.0	22.2
	Silica replacing calcite shrubs	1.2	11.0	2.1
	Silica replacing spherulites	0.5	11.0	1.8
	Silica replacing Mg-clays + filling matrix dissolution porosity	1.0	10.7	2.1
	Silica growth-framework pores filling	0.4	11.0	1.8
	Dolomite replacing calcite shrubs	2.5	19.3	3.9
	Dolomite replacing calcite spherulites	2.2	22.0	4.4
	Dolomite replacing Mg-clays + filling matrix dissolution porosity	14.1	76.0	14.3
	Dolomite growth-framework pores filling	0.8	11.3	2.2
	Dolomite replacing undifferentiated primary constituent	0.1	4.7	0.8
	Calcite replacing Mg-clays + filling matrix dissolution porosity	0.2	5.3	0.9
	Calcite growth-framework pores filling	0.2	5.3	0.9
	Other diagenetic constituents	0.6	10.0	1.7
Porosity	Matrix dissolution porosity	6.6	18.0	4.2
	Intra-aggregate porosity	2.5	10.0	2.5
	Growth-framework porosity	2.1	11.0	2.8
	Other porosity (vugs, fractures, channels, molds, and breccia)	0.6	5.3	1.1

3.5.1.2 Intraclastic Rocks

The intraclastic rocks are predominantly massive, formed by submillimeter to millimeter particles (0.05 – 1.22, average 0.58mm), corresponding to calcarenites. Fine-grained calcarenites tend to be well sorted, while coarse-grained calcarenites are commonly poorly sorted. In order of abundance, most particle types are undifferentiated, spherulitic, and fascicular calcite intraclasts (Figure 3-6). In 36% of the samples (average 4.9%; maximum 54.7%), there are peloids originally composed of Mg-clays (Figure 3-6A), that were extensively

replaced by calcite or dolomite, and/or of Mg-clay ooids with intraclast nuclei, also replaced by calcite (Figure 3-6F). Interparticle Mg-clays matrix thin intercalated levels were observed in 14% of the samples (average 0.9%; maximum 17.3%). Ostracods (Figure 3-6A) and bivalve bioclasts, siliciclastic grains, and phosphate fragments are minor constituents.

Table 3-2 - Summary of petrophysical properties, including helium porosity, permeability, Sor, and pore throat radius (TR) volume statistics (P10, P50, P90, and mode).

	Shrubstones					Muddy Spherulstone			
	n	Avg	Std	Min	Max	n	Avg	Std	Min	Max
Phi (%)	18	13.1	4.2	6.7	20.8	11	15.4	4.0	6.8	21.3
k (mD)	18	738.6	899.8	12.7	2709.0	11	128.0	276.7	4.0	951.0
Sor (%)	18	35.2	9.3	20.3	48.2	11	25.6	10.8	14.8	55.8
P10 TR (µm)	13	66.4	46.1	0.6	133.3	7	22.9	30.4	1.4	82.0
P50 TR (µm)	13	9.7	8.4	0.3	29.8	7	4.7	6.2	0.6	18.3
P90 TR (µm)	13	0.3	0.3	0.0	0.8	7	0.5	0.5	0.1	1.5
Modal TR (µm)	13	35.6	37.7	0.4	125.5	7	7.9	13.1	1.0	37.2

	Spherulstone					Mg-Clay Mudstone			
	n	Avg	Std	Min	Max	n	Avg	Std	Min	Max
Phi (%)	8	14.7	2.6	12.0	19.1	3	14.7	6.3	9.0	21.4
k (mD)	8	82.1	124.9	5.8	379.0	3	18.5	26.2	3.2	48.7
Sor (%)	8	23.5	4.7	19.5	33.6	3	19.1	2.6	17.0	22.0
P10 TR (µm)	2	34.2	44.7	2.6	65.8	2	1.9	0.0	1.9	1.9
P50 TR (µm)	2	10.6	14.1	0.7	20.6	2	0.5	0.2	0.4	0.7
P90 TR (µm)	2	0.1	0.0	0.1	0.1	2	0.1	0.0	0.1	0.1
Modal TR (µm)	2	23.9	32.4	1.0	46.8	2	1.0	0.9	0.4	1.6

	Muddy Shrubstone					Shrub-spherulstone			
	n	Avg	Std	Min	Max	n	Avg	Std	Min	Max
Phi (%)	9	16.3	3.2	13.0	20.7	14	17.1	3.6	9.9	23.7
k (mD)	9	439.4	334.3	98.5	861.0	14	972.9	2036.8	14.0	7893.0
Sor (%)	9	35.0	10.0	21.9	54.0	14	35.2	9.1	16.3	47.7
P10 TR (µm)	3	47.3	16.6	32.7	65.4	10	32.7	23.0	4.5	84.0
P50 TR (µm)	3	7.6	7.0	2.0	15.4	10	6.0	5.4	1.3	18.4
P90 TR (µm)	3	0.3	0.2	0.1	0.5	10	0.4	0.3	0.1	1.1
Modal TR (µm)	3	18.1	22.6	1.0	43.7	10	17.0	16.6	0.8	53.1

	Intraclastic Calcarenite			
	n	Avg	Std	Min	Max
Phi (%)	67	17.7	4.1	9.7	32.5
k (mD)	67	397.1	736.2	1.5	4714.0
Sor (%)	67	26.5	10.6	9.1	57.2
P10 TR (µm)	33	15.1	12.5	2.1	46.4
P50 TR (µm)	33	4.4	4.5	0.7	20.6
P90 TR (µm)	33	0.4	0.2	0.2	0.5
Modal TR (µm)	33	9.7	9.9	0.7	31.0
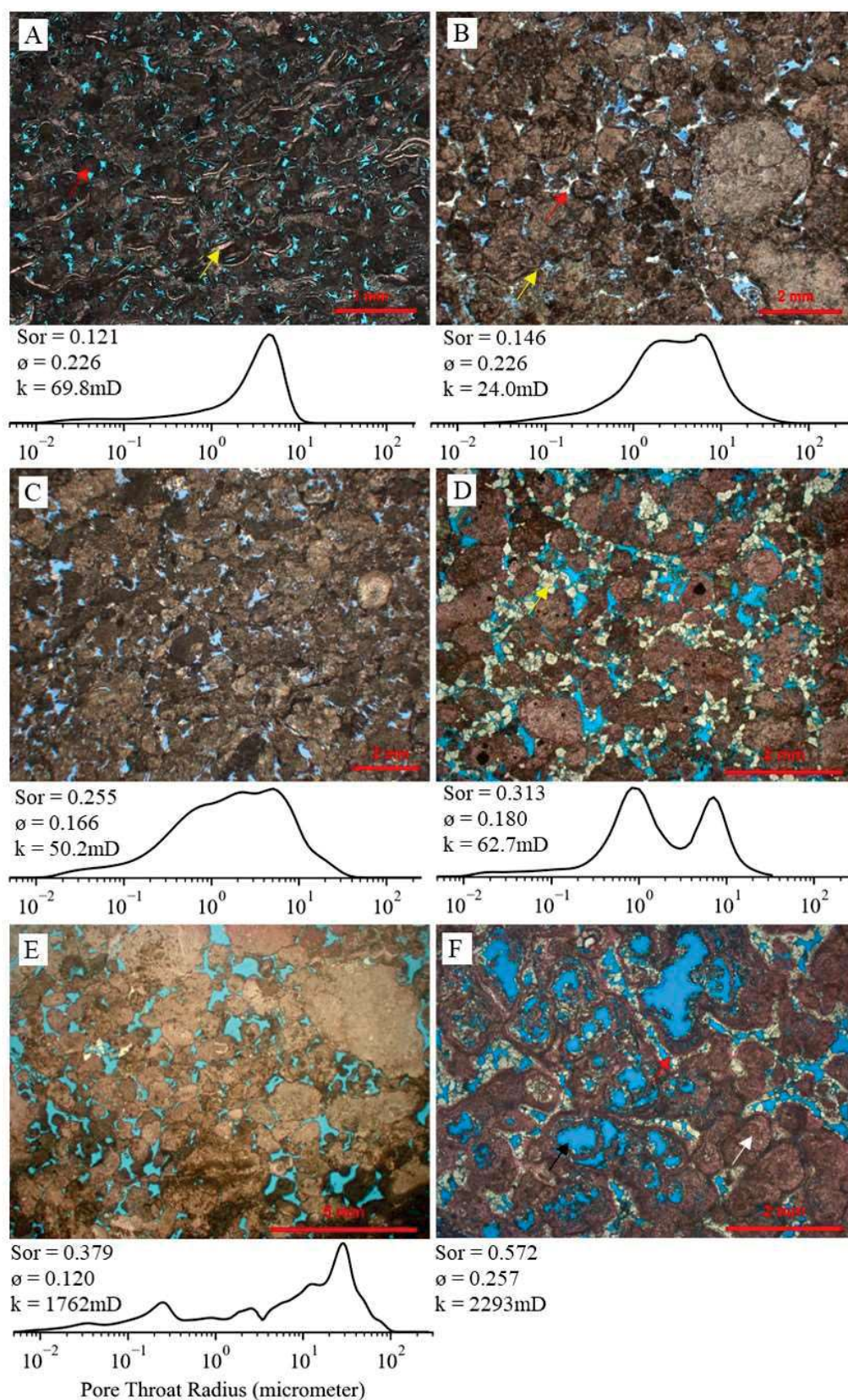
Figure 3-6 - Photomicrographs (uncrossed polarizers) exhibiting aspects of the intraclastic rocks (porosity impregnated by blue epoxy resin), and petrophysical properties, including Sor, laboratory (helium) porosity (ø), permeability (k), and pore throats radius distribution. A) Well-sorted hybrid arenite composed of calcite-

replaced Mg-clay peloids (red arrow), ostracod bioclasts (yellow arrow), and calcite intraclasts. B) Poorly-sorted intraclastic calcarenite, in which the pore system was homogenized by compaction, particle rearrangement, and cementation by dolomite (yellow arrow) and quartz (red arrow), as seen in throat distribution. C) Well-sorted intraclastic calcarenite, where MICP data indicate greater heterogeneity than the previous sample, although for its better selection. D) Well-sorted intraclastic calcarenite cemented by dolomite (yellow arrow) with two populations of pore throats. E) Poorly-sorted intraclastic calcarenite with high variability of pore throats. F) Calcarenite with Mg-clay ooids replaced by calcite (white arrow) or partially dissolved (black arrow), and primary and secondary porosity lined and filled by dolomite (red arrow).

Dolomite is the main diagenetic constituent (Figure 3-6D and F), and commonly occurs as interparticle cement filling pores or lining (average 9.7; maximum 23.7%) and replacing particles (average 8.5; maximum 37.0%). Calcite commonly replaced particles (average 4.0; maximum 44.0%), while calcite interparticle pore-filling cement is scarcer (average 0.9; maximum 7.7%). Silica occurs in minor quantities, replacing particles (around 1.1%; maximum 7%) and cementing interparticle pores in small amounts (average 0.4; maximum 7.7%) (Figure 3-6B). Pyrite, dawsonite, bitumen, barite, and other secondary components are occasionally observed.

Primary interparticle porosity occurs preserved in different degrees (2.7 to 17%; average 9.3%), partially reduced by cementation and compaction. Secondary intraparticle porosity arises, in some cases, in greater volume than primary porosity (average 3.8, maximum 10.7%). Secondary porosity also occurs as vugs, molds, and interparticle matrix dissolution pores. Finally, interparticle packing is highly variable according to the interparticle packing proximity (Kahn, 1956; average 42.1; maximum 83.0%).

The petrophysical properties of intraclastic rocks are highly variable: porosity varies between 9.7 and 32.5%, with an average of 17.7%; the permeability ranges from 1.5 to 4714.0mD (average 397.1mD), and the Sor averages 26.5% (9.1-57.2%). The average P50 throat radius is 4.4µm, ranging from 0.7 to 20.6 µm; the P10 throat radius ranges from 2.1 to 46.4µm (average 15.1 µm). Finally, the average P90 throat radius is 0.4 µm, occurring between 0.2 and 0.5 µm. The summary of petrophysical and quantitative petrography data of the primary and diagenetic constituents of the intraclastic rocks are found in Table 3-2 and 7.

3.5.2 Imaging the residual oil saturation

Macroscopically, the trapped oil clusters are conditioned by the texture and structure of rocks in terms of abundance, morphology, and dimension, as seen in Figure 3-7. Of the five plugs studied, two have a predominance of residual oil in the center of the large pores, indicating

a water-wet behavior, one has oil located dominated in the corners of the pores and as layers covering the solid surfaces, denoting oil-wettable favorability, while the last two have a mixed-wetting behavior (Table 3-4, Figure 3-8). Clusters in the center of the pores exhibit spherical droplets or more complex shapes (Figure 3-9A), frequently extending through large pores without constrictions (*i.e.*, pore throats) surrounding spherulites or shrubs (Figure 3-9B and C). Droplets with prolate or oblate shapes are mainly observed in the shrubstones (Figure 3-9D and E). Oblate forms partially adhered to the walls are observed in flat growth-framework, fractures, and channel pores. Under oil-wet conditions, the morphology of the trapped oil tends to assume more complex flattened shapes than in water-wet rocks, given their tendency to adhere to solid surfaces (Figure 3-9F to H), and typically shows smaller average volume than the non-wetting oil clusters (Table 3-4).
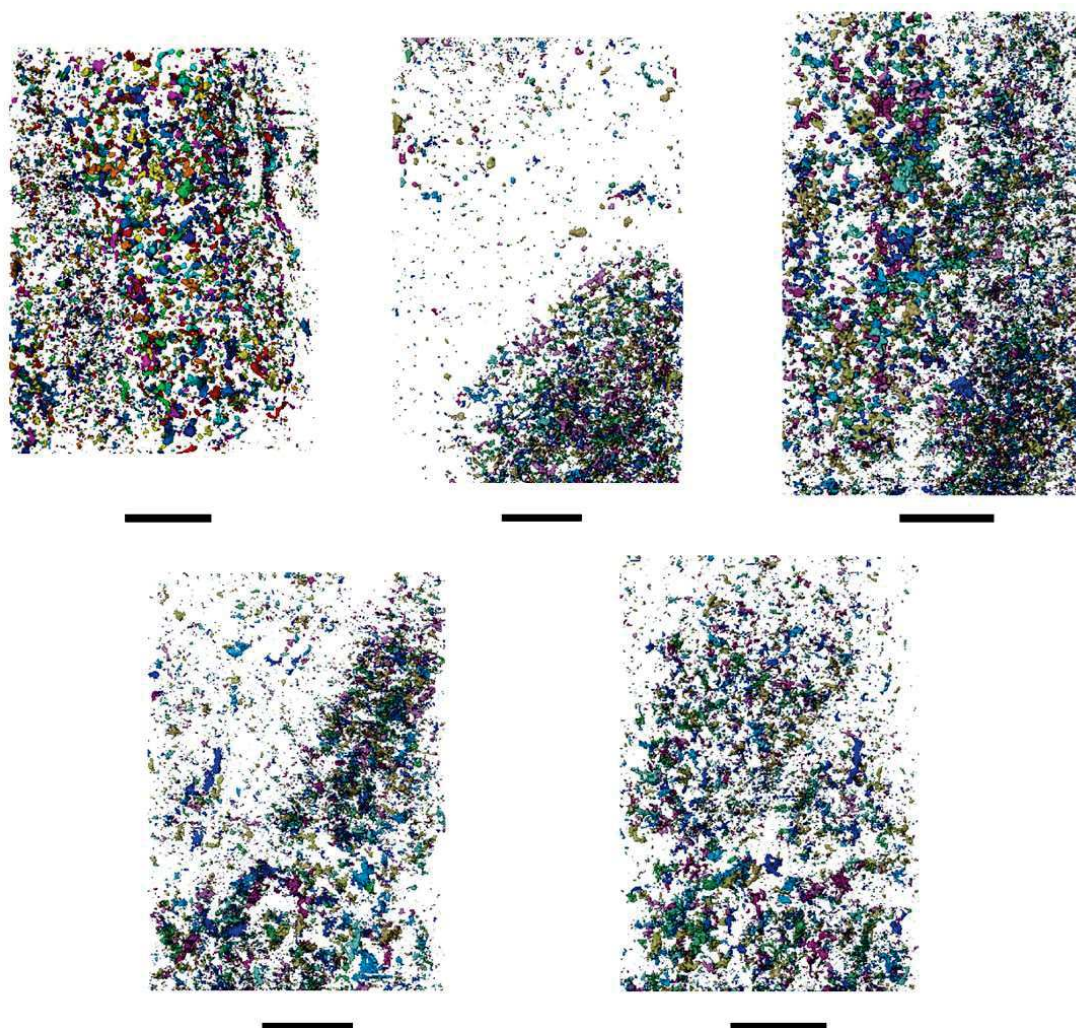
Figure 3-7 – 3D segmented images showing oil clusters, evidencing the macroscopic distribution of residual oil, illustrating the influence of porous media heterogeneities on the distribution of oil clusters. The sample number corresponds to 1 to 5, from left to right (Scale bar = 1cm).

Table 3-3 - Statistical summary including average, maximum, and standard deviation of constituents of intraclastic rocks.

	Constituents (%)	Average	Max	Std deviation
Primary	Calcite intraclasts	53.9	83.0	24.1
	Mg-clay ooids	7.4	75.7	19.6
	Mg-clay peloids	4.9	54.7	14.5
	Mg-clay matrix	0.9	17.3	3.1
Diagenetic	Intraparticle calcite	4.0	44.0	11.7
	Interparticle calcite	0.9	7.7	1.6
	Intraparticle dolomite	8.5	37.0	8.4
	Interparticle dolomite	9.7	23.7	7.7
	Intraparticle silica	1.1	7.0	1.5
	Interparticle silica	0.4	7.7	1.4
	Others	0.1	2.0	0.4
Porosity	Interparticle	9.3	17.0	3.5
	Intraparticle	3.8	10.7	2.4
	Others (vug, channel, mold)	0.3	2.7	0.6
	Total	13.5	22.0	3.4
	Packing	42.1	83.0	18.2

Table 3-4 - Average oil cluster volume and flatness (sphere equals 1), porosity, permeability, density, Sor, facies, and wettability tendency of samples.

Sample	Volume (nm^2)	Flatness (adim)	Porosity (%)	k (mD)	Density (g/cm^3)	Sor (%)	Facies	Wettability
1	2.6E+16	0.43	12.5	86.2	2.71	21.7	Spherulstone	Water
2	3.5E+16	0.45	13.1	677	2.72	23.9	Shrubstone	Water
3	1.9E+16	0.37	18.8	1866	2.71	32.0	Shrubstone	Mixed
4	2.5E+16	0.41	12.6	210	2.72	12.6	Muddy Shrubstone	Mixed
5	1.5E+16	0.35	15.3	104	2.71	26.6	Shrubstone	Oil

3.6 Discussion

3.6.1 Petrography, RCAL, SCAL, and Sor

3.6.1.1 In-situ Facies

The porosity of *in-situ* rocks is dominated by the dissolution of Mg-clays (Table 3-1, Figure 3-10A), a process common in most facies, except in shrubstones, where the growth of

calcite shrubs developed mainly primary growth-framework porosity (Figure 3-4; Table 3-1). Although matrix dissolution contributes significantly to the development of porosity, rocks with large volumes of matrix dissolution porosity tend to have smaller pores and significant amounts of microporosity (Figure 3-10B), defined as the difference between laboratory (helium) and petrographic porosity.
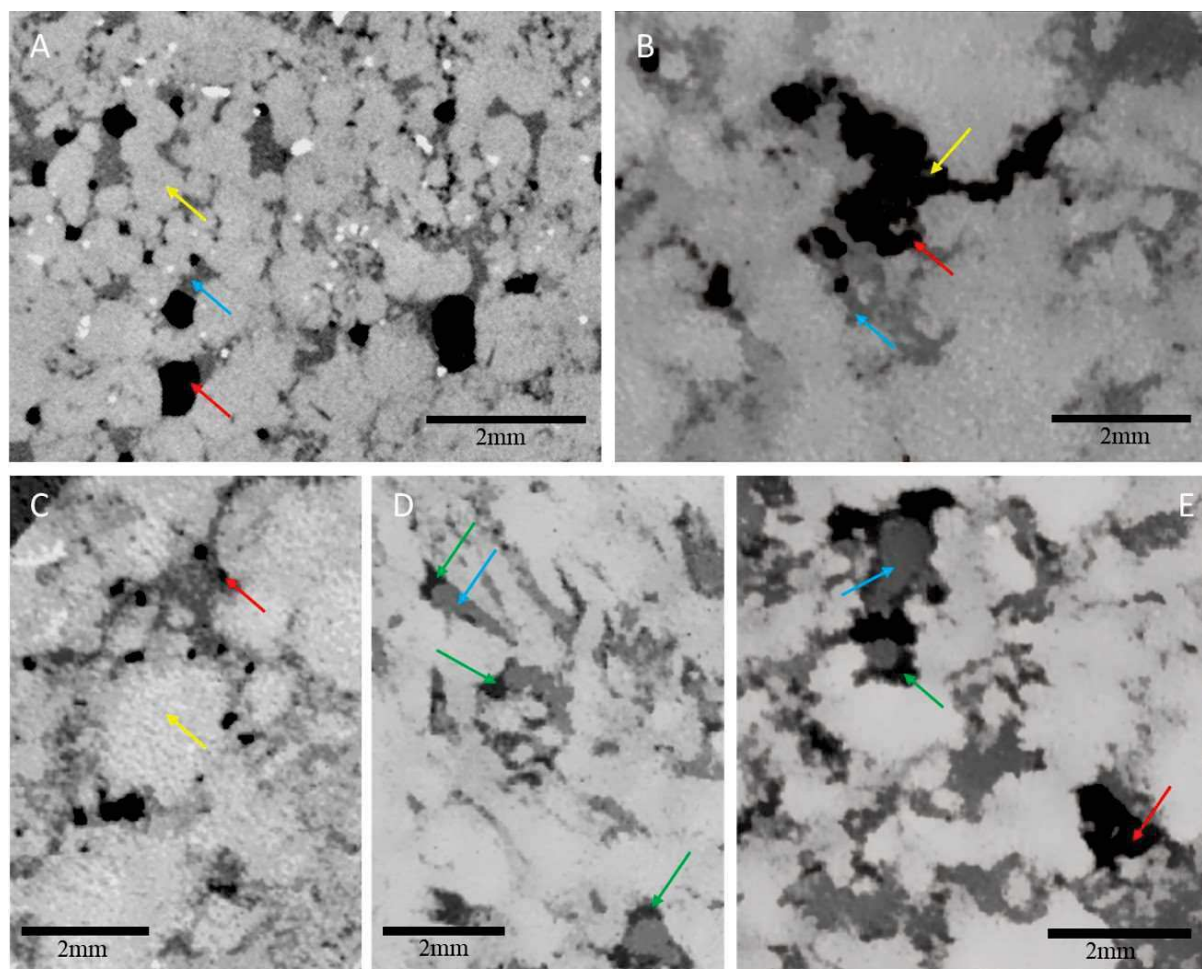
Figure 3-8 – X-ray µCT illustrating the relationship between rock (yellow arrows), water (blue arrows), and oil (red (non-wetting) and green (wetting) arrows). A) Water-wet spherulstone with abundant matrix dissolution porosity, with oil preferentially occupying large pores. B) Oil cluster with complex shape engulfing dolomite crystals (yellow arrow) filling growth-framework pore. C) Oil trapped as droplets among dolomite crystals. D) Oil-wet shrubstone with oil trapped in the corners of the pores. E) Mixed-wet muddy shrubstone composed essentially of calcite.

In rocks where shrubs predominate, the framework is heterogeneous, controlled by the vertical growth of the millimetric aggregates (Figure 3-4C and E). This arrangement makes the rocks less susceptible to compaction and, consequently, large primary or secondary pores are preserved (Figure 3-4C, D, and E). Since dolomite crystals or calcite spherulites often replace the Mg-clay matrix, these diagenetic minerals control the arrangement between pores and

throats. Equidimensional dolomite crystals tend to replace the matrix with nearly regular spacing, resulting in a very distinct peak population in pore throat distribution (Figure 3-4A, B, C, D, and F). Where dolomite precipitation predominates over the generation of secondary porosity, the tendency is to produce a very homogeneous intercrystalline pore system, even with the presence of spherulites (Figure 3-4A and B) or shrubs, a fact that can be observed in the MICP data (Figure 3-10C).
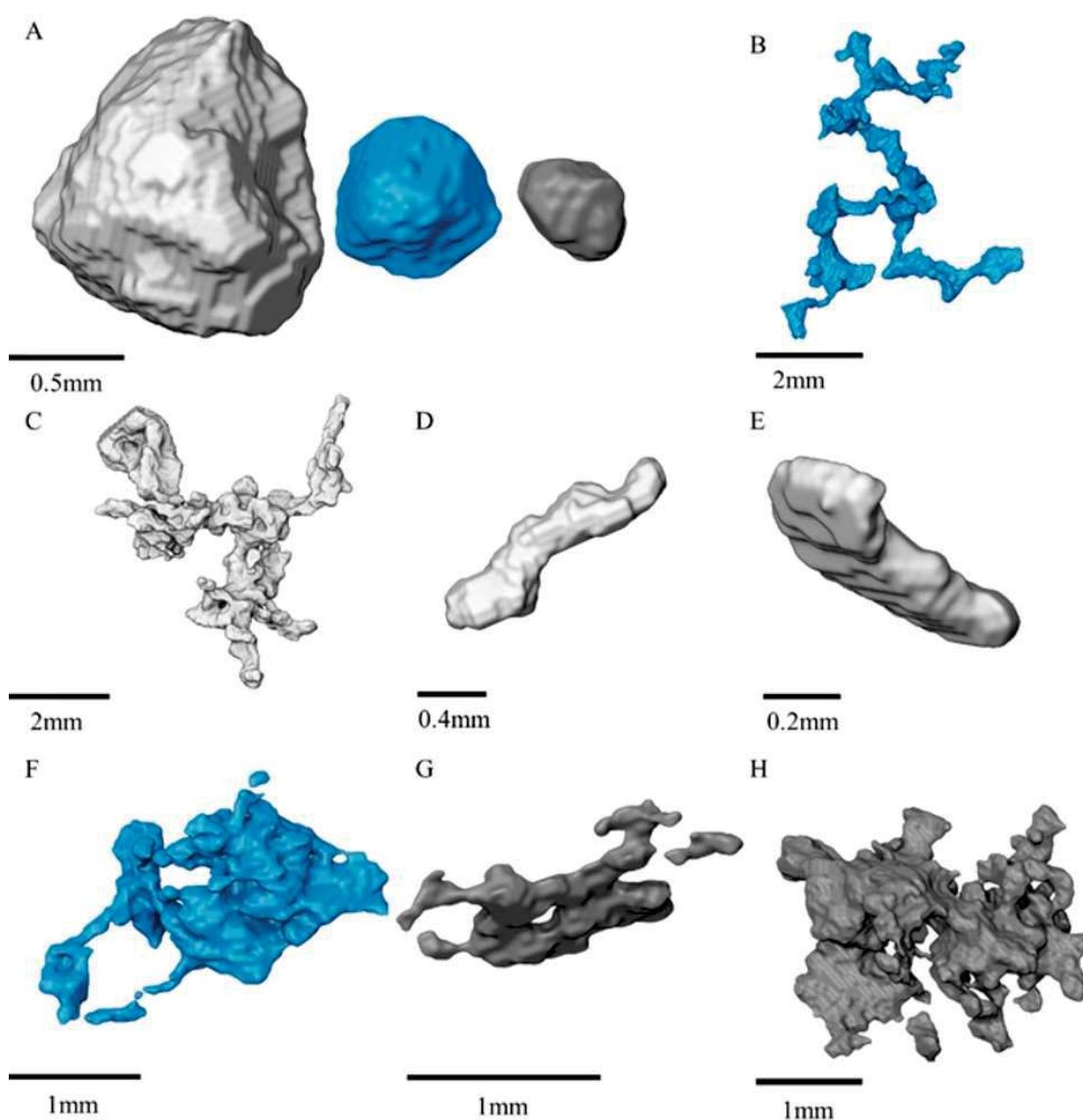
Figure 3-9 – Typical oil cluster shapes under water- (A to E) and oil-wet (F to H) conditions. A) Near spherical oil drops with different dimensions usually located in the center of the pores. Large oil clusters occur in complex pores without constrictions surrounding spherulites (B) and shrubs (C). Oil clusters conditioned to elongated (D) or flattened (E) pore morphology. F to H) Complex clusters in oil-wet rocks, where flattened forms adhere to minerals and in the corners of pores.

In contrast, when there is a large amount of secondary porosity, pores tend to be larger, and their throats will be controlled by the relative location of spherulites and shrubs. Consequently, there will be greater heterogeneity in both the pore size and the distribution of their throats (Figure 3-4F). The predominance of shrubs results in rocks with larger pores and throats compared to spherulstones or Mg-clay mudstones, but with significant heterogeneity (Figure 3-4C and D). Though heterogeneous, shrubstones are much more permeable than rocks dominated by Mg-clays (Table 3-2) given that the volume connected by larger pores essentially controls permeability (Figure 3-10D).
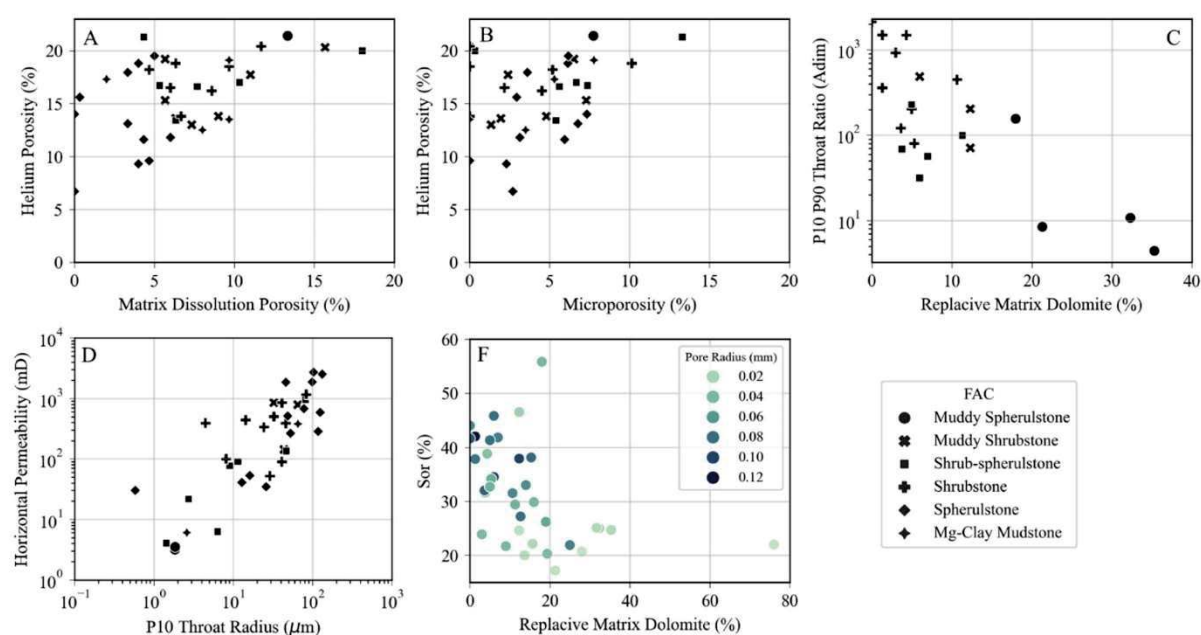
Figure 3-10 – Relationship between laboratory (helium) porosity and matrix dissolution petrographic porosity (A) and microporosity (B). C) P10 P90 throat ratio represents the ratio between throats intruded by 10 (largest throats) and 90% (smallest throats) of mercury volume. This ratio measures how the pore system is heterogeneous, exhibiting the clear effect of matrix-replacive dolomite on the homogenization of porous media. D) Scatter plot illustrating the relationship between horizontal permeability and P10 throat radius and the faciological impact on these properties. F) Diagram indicating the influence of the matrix-replacive dolomite on residual oil saturation and its relationship with pore size.

Since there is a great diversity and complexity of porosity-generating processes, which results in a great variety of pore types and their relations, a direct relationship between total porosity and Sor is not evident. Hence, this contradicts the general assumption that increasing porosity would increase pore connectivity, increasing the coordination number (number of throats per pore) and reducing Sor (Yuan, 1981). Intercrystalline porosity among dolomite crystals tends to show high connectivity, unlike intra-aggregate pores within shrubs and spherulites, which are poorly connected, while growth-framework pores among shrubs are

highly complex. Thus, coordination number cannot be simply related to porosity on Pre-salt *in-situ* facies.

Pore size positively correlates to Sor values, indicating strong textural control on oil trapping. Shrubstones with large primary or secondary pores tend to retain more oil (Table 3-2). This is related to more oil trapped in larger pores by snap-off, a process typical of heterogeneous water-wet media, as aforementioned. Since permeability is higher in facies with large pores and throats (Figure 3-10D), rocks with higher permeability retain more undrained oil.

Matrix-replacive dolomite correlates negatively with Sor (Figure 3-10E), indicating that, as previously discussed, its presence generates a more homogeneous intercrystalline pore system (Figure 3-10C). This favors the homogeneous oil displacement by frontal advance, probably preventing water fingering, which results in low Sor. Thus, in other words, rocks with a predominance of Mg-clays over syngenetic calcite precipitation may develop, upon replacement of the Mg-clays by dolomite, pore systems that favor oil recovery. In this way, a typical stratigraphic succession with variation in the proportions of calcite shrubs and spherulites, and Mg-clay generate typical petrophysical trends: the predominance of clays and calcite spherulites implies a decrease in permeability and Sor and an increase in Swirr, in contrast to the predominance of shrubs, which generates opposite trends (Figure 3-11). However, these trends will only be valid in the case of non-preservation of Mg-clays, that is, in the presence of reservoir rocks.
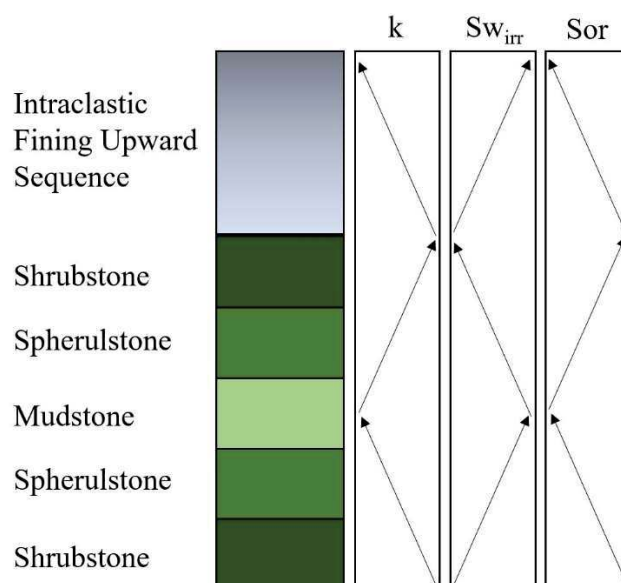
Figure 3-11 - Idealized stratigraphic succession and its impact on petrophysical trends, including Sor, Swirr, and permeability.

Finally, variations in mineralogy do not clearly affect Sor, indicating that the textures, habits, and fabric, *i.e.*, how diagenetic and primary constituents are related, are more critical for oil trapping variations. This is probably because calcite and dolomite, the predominant minerals in these rocks, do not differ significantly in terms of wettability when subjected to the same fluids and reservoir conditions (Alqam *et al.*, 2021; Ferrari *et al.*, 2021; Muñoz, Winter and Trevisan, 2015).

3.6.1.2 Intraclastic Facies

The porosity of intraclastic rocks shows controls typical of particulate rocks, similar to siliciclastic rocks. Interparticle cementation in these rocks is dominated by dolomite, which constitutes around 10% of the rock volume, while the average interparticle porosity is 9.3%. This indicates that most of the primary porosity was reduced by compaction, as shown in (Figure 3-12A), considering an initial porosity of around 40%. Furthermore, the control of cementation over compaction is clearly observed, as pre-compactional cement tends to inhibit compaction (Figure 3-12B), thus preserving interparticle volume. Intraparticle dissolution is abundant and corresponds to important generation of secondary porosity (Figure 3-6F, Table 3-3). Hence, the pore system of the intraclastic rocks was controlled by a combination of depositional and diagenetic factors. Particle size remains a fundamental control of their pore system: coarse-grained calcarenites tend to have larger pores and throats, with greater heterogeneity due to their worse selection (Figure 3-12C), in contrast to fine-grained ones (Figure 3-6).

Although cementation and compaction decrease interparticle porosity, their influence on throat size and throat/pore ratio differs. When porosity reduction is dominated by cementation, a strong impact on the throats is observed concerning pore size (Figure 3-12D), increasing the system's heterogeneity and often resulting in bimodal distributions in MICP (Figure 3-6D). This is because dolomite generates a secondary intercrystalline pore system within the interparticle spaces, mainly impacting the largest pores. On the other hand, where pre-compactional cementation was sparse, and consequently, compaction was stronger, the impact of dolomite on the pore/throat size ratio was smaller (Figure 3-12E). Finally, as discussed

above, permeability was mainly controlled by interparticle porosity, jointly controlled by compaction and cementation, and secondarily by clast size, as indicated in Figure 3-12F.
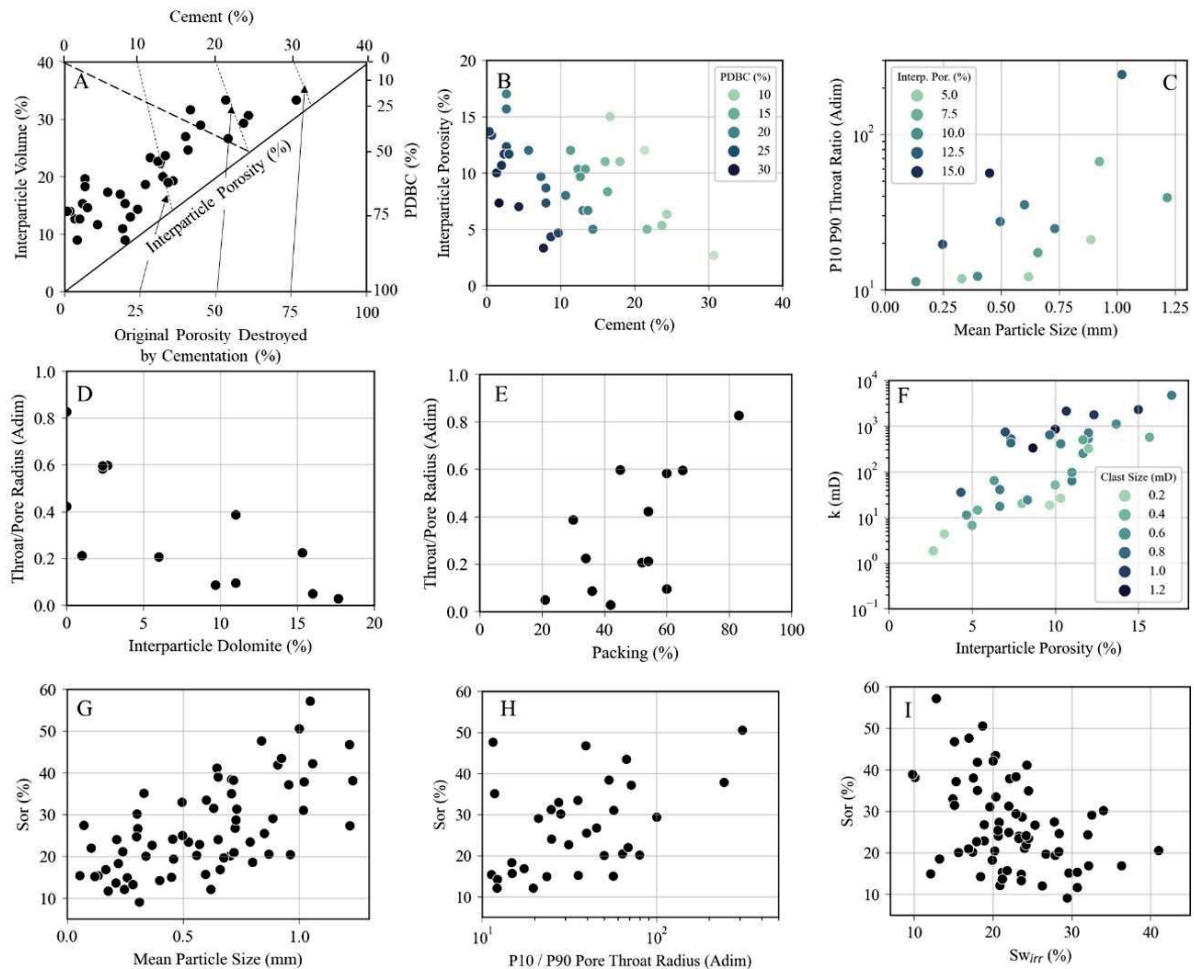
Figure 3-12 – A) Diagram illustrating the role of compaction and cementation on the reduction of interparticle porosity, interparticle volume, original porosity destroyed by cementation, and compaction (PDBC). Most of the primary porosity was destroyed by compaction (Houseknecht (1987) plot modified by Ehrenberg (1989)); B) Scatter plot relating cementation, interparticle porosity, and PDBC. C) Relationship between average particle size and P10 P90 pore throat ratio; colored by the amount of interparticle porosity, showing the impact of grain size and preservation of primary porosity on the heterogeneity of the pore system. Figures D and E relate the impact of interparticle dolomite cement and packing on the pore/throat radius ratio. F) Influence of the amount of interparticle porosity on the permeability, colored by particle size. Figures G, H, and I show the relationship between Sor with mean particle size, P10/P90 pore throat radius ratio, and Sw_{irr}.

Particle size is an important control of Sor in these rocks, as well as on the other petrophysical properties (Figure 3-12G), implying stratigraphic control (Figure 3-11). The larger the particle size, the smaller the sorting and the greater the Sor (Figure 3-13), a correlation described by laboratory studies using siliciclastics and synthetic models (Coskun, Wardlaw and Haverslew, 1993; Taiwo *et al.*, 2016). As particle size conditions the pore systems, coarser

rocks have greater heterogeneity, increasing the complexity of the porous media. A direct relationship between diagenetic processes and products with Sor is not observed, probably because of the limited number of samples and groups with different diagenetic patterns. Intraclastic rocks with low cement content tend to have more homogeneous pore systems, while cementation and partial or total particle dissolution tend to generate heterogeneity. However, these processes are frequently related.
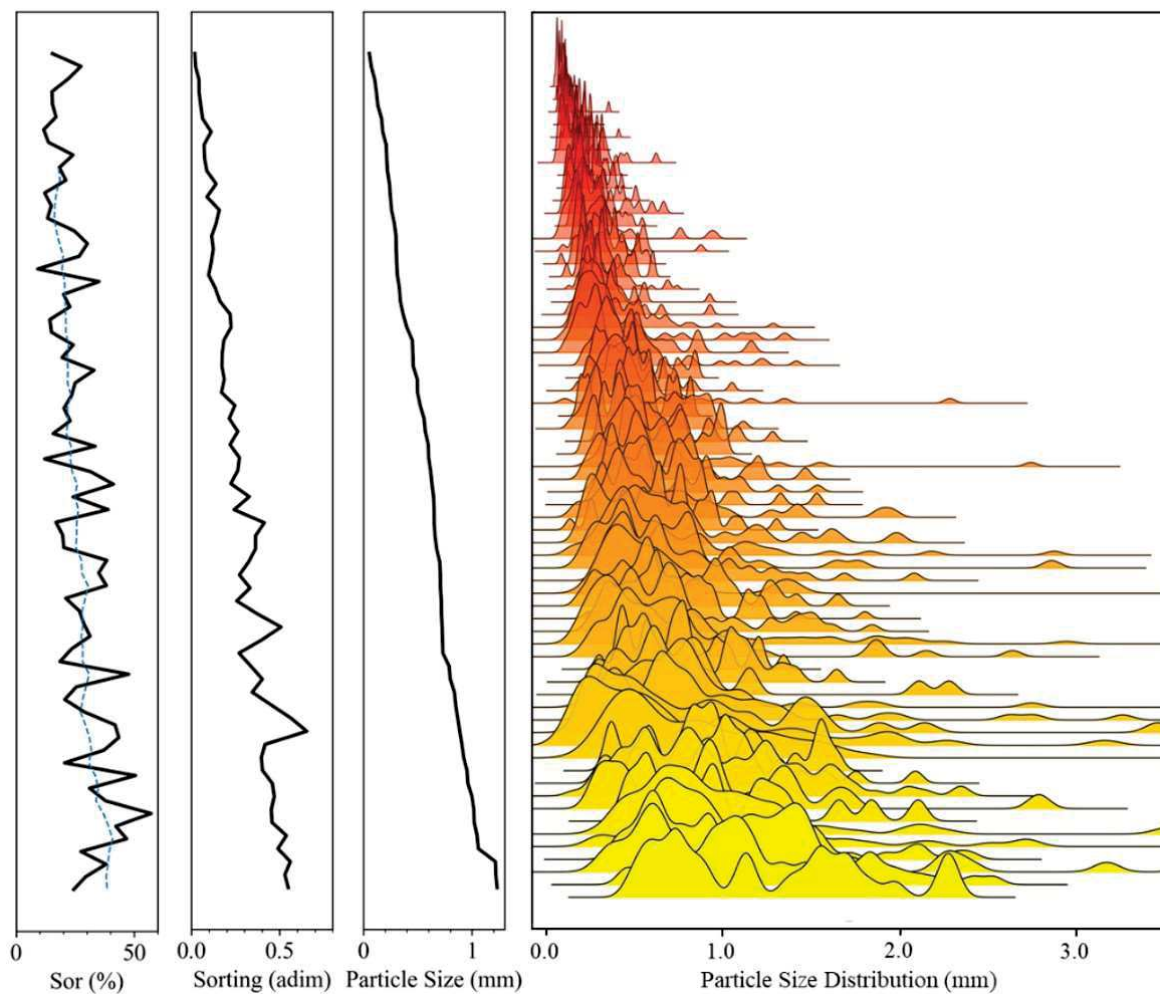
Figure 3-13 – Relation between particle size distribution, mean particle size, particle sorting coefficient (very well selected close to 0 (Folk and Ward, 1957)), and Sor. The dashed blue line is a moving average that shows the tendency of increasing Sor with incremental sorting coefficient and mean particle size.

In some cases, the combination of compaction and cementation can homogenize the pore system (Figure 3-6B). However, this relationship is not observed in all samples given the heterogeneity of the diagenetic processes. Thus, the homogenization of the porous medium

conditioned by depositional and diagenetic processes decreases the Sor, which is observed in the MICP data (Figure 3-12H). As particle size controls pore throat size, Sor positively correlates with permeability and negatively with Sw_{irr} (Figure 3-12I), indicating that depositional energy, apart from controlling reservoir quality, also impacts the potential amount of oil that can be trapped. As for the *in-situ* facies, mineralogical variations, mainly related to the relative proportion of calcite and dolomite, do not impact the observed differences of Sor. In conclusion, like the *in-situ* facies, the homogeneous pore system of the fine-grained calcarenites tends to have lower Sor, probably related to greater sweep efficiency, preventing fingering development, and increasing the effectiveness of the frontal advance.

3.6.2   Sor Imaging

The X-ray μCT imaging of the plugs revealed important details about the shape and location of the oil trapped in the rocks of the Barra Velha Formation. Although the resolution of the images does not allow the entire pore system to be resolved, the imaging clearly shows the location and affinity of the oil to the large pores, especially when the oil is the non-wetting phase. On the other hand, under oil-wetting conditions, oil layers can be below resolution, which hinders their identification. In general, there is a variation in terms of wettability for both inter-sample and intra-sample (Figure 3-8). This variation is not clearly related to the predominant mineralogy of the samples, indicating that, in addition to not having a direct relationship with Sor variations, the mineral composition may act along with other factors for wettability alterations. Since the pressure and temperature conditions, and the fluids used in the experiments are the same, differences in wettability might be associated with undetectable mineral constituents, remains of drilling fluid, or residual organic compounds after sample cleaning.

Small amounts of Mg-clays not detected by petrography could generate differences in surface charges since smectites (saponite and stevensite) typically have a high density of negative surface charges (Nadeau, 1985; Sperry and Peirce, 1999), which could favor water-wetting (Ballah *et al.*, 2016; Jia *et al.*, 2022). The bitumen typically favors oil wettability (Alqam *et al.*, 2021; Sakthivel, 2021) and is often observed in thin sections. On the other hand, basic components present in bitumen, such as quinolines, a basic heterocyclic nitrogenous compound, could be solubilized and favor water-wettability in carbonates (Benner and Bartel, 1941). Aside from the natural constituents of reservoirs, facies with large pores tend to be

invaded by barite particles, a high-density mineral used in the drilling fluid to increase the mud weight and favor the formation of mud cake. Although barite was not detected in the thin sections during petrography, probably removed in the preparation process, they are typically observed in X-ray μCTs as high attenuation spots. Although the impact of mud filtrate invasion in sample cores has been studied in other reservoirs (Amanullah and Allen, 2013; Elkatatny *et al.*, 2019), its influence on the wettability in carbonate rocks is still uncertain. To summarize, even though we have enumerated some hypotheses, the controls of wettability in these rocks are very uncertain and should be appropriately investigated in future works.

The morphology and relationship of the oil blobs in large pores indicate that part of the oil is trapped by snap-off (Figure 3-8A to C, and Figure 3-9A), a disconnection mechanism of the oil phase typical of water-wet reservoirs. This process tends to retain large amounts of oil in pores that extend over large regions, mainly in growth-framework or large dissolution pores among shrubs (Figure 3-9C) or spherulites (Figure 3-9B). The morphology of growth-framework porosity and lack of compaction generate pore systems without clear development of throats. Hence, the average size ratio between pores and their respective throats calculated by MICP data in shrubstones tends to be close to 1. Consequently, a large part of the pore volume is connected without the presence of throats. Thus, a pore network model would be very unrepresentative of this rock type.

Although less abundant in volume, when throats occur, they are much smaller than the pores. Thus, if the snap-off arises, the volume of oil retained is large due to the high relative volume that the pores occupy. This could explain why *in-situ* rocks with larger pores and greater heterogeneity tend to have higher Sor, given the mixed wettability behavior observed in these rocks. Unfortunately, we do not have X-ray μCt Sor images from particulate rocks. Hence, this oil trapping interpretation cannot be extrapolated to those rocks. Lastly, the retained fraction adhered to minerals as a wetting fluid is difficult to evaluate, mainly because the resolution often does not allow its distinction.

Finally, as studied by other authors (Honarpour and Saad, 1994; Iverson, Dunn and Ajdari, 1996), the direction of the test concerning the rock fabric influences the results, given the tensor nature of permeability. Thus, anisotropic laminated rocks with great contrast of porosity and permeability may favor water fingering during waterflood, which can increase the Sor if the plug is not sampled parallel to the rock fabric. This can be seen in samples 2 and 4 (Figure 3-7), where the concentration of oil droplets is clearly controlled by textural contrast.

This factor may show more impact in heterogeneous rocks, possibly increasing Sor in the laboratory, which may generate pessimistic results from the actual reservoir values.

3.7 Conclusions

We performed an integrated study using petrography, RCAL, SCAL, and X-ray μCT imaging to understand how depositional and diagenetic lithological features control Sor in the rocks of the Barra Velha Formation of the Santos Basin Pre-salt section. Our main conclusions are:

- The critical element for understanding petrophysical controls, including Sor *in-situ* rocks, is understanding Mg-clays deposition, dissolution, and replacement processes. Partial replacement of the matrix by dolomite followed by dissolution developed intercrystalline pore systems, in which homogeneity favors water sweeping. On the other hand, the preservation of large primary growth-framework pores among shrubs or the development of large matrix dissolution pores facilitates oil trapping.
- In intraclastic calcarenites, the main control of Sor is depositional: rocks with greater granulometry tend to show greater oil retention. Conversely, fine-grained ones tend to have more homogeneous pore systems, which facilitates oil displacement.
- Oil trapping occurs by snap-off, adherence to minerals, and in pore corners, denoting mixed-wet conditions. Although the carbonate mineralogy should favor oil-wettability, the control of the partial water-wet behavior remains unclear and should be appropriately investigated in future works.

3.8 Acknowledgments

4. Article 3 - HERLINGER, R.; BONZANINI, L. A. F.; VIDAL, A. Residual Oil Saturation in Pre-salt Brazilian Carbonates: A Multi-approach Core-to-log Case Study. Journal of South American Earth Sciences, v. 140, 2024.

4.1 Abstract

Accurate residual oil saturation (Sor) measurement is paramount for successful reservoir management and has significant economic implications. Considerable uncertainty surrounds its estimation due to inaccurate direct measurements and non-representative lab results. This case study combines well logging, petrography, RCAL, and SCAL to estimate and understand Sor in Pre-salt reservoirs in Santos Basin, Brazil. The results indicate that the distribution of Sor is strongly influenced by lithology. *In-situ* facies have higher Sor values than reworked facies due to their greater textural and porous complexity. It has been observed that laboratory experiments and well logging results show a correlation between irreducible water saturation, porosity, and permeability with Sor, thus validating the upscaling of laboratory data. The dielectric tool provides the most accurate results in Sor logging evaluation. This is due to its shallow depth of investigation, high sampling rate, and the elimination of uncertainty associated with electrical parameters and salinity used in the Archie equation. Nuclear magnetic resonance (NMR) logging can qualitatively identify regions with higher remaining oil, which can be correlated with areas of high Sor. Still, it cannot quantitatively directly assess residual saturation by the conventional cutoff approach. Conversely, machine learning results indicate that NMR T2 times can be used to predict Sor values obtained by dielectric logging.

Keywords: Sor, Pre-salt, SCAL, RCAL, dielectric logging

4.2 Introduction

Residual oil saturation (Sor) is a concept used to describe the amount of oil that cannot be removed from the pores after a non-miscible phase displacement (Donaldson, 1989; Valenti, Valenti and Koederitz, 2002). Once a reservoir containing oil is subjected to water sweep, whether from injection or the aquifer, the oil phase, after being disconnected, becomes trapped by capillary forces (Blunt, 2017). This oil can no longer be removed by regular water sweeping unless enhanced oil recovery (EOR) techniques are used, such as the use of surfactants for instance, which will change the physicochemical conditions of the fluids, thus changing their configurations, which can mobilize more oil (Anto and Bhui, 2022; Massarweh and Abushaikha, 2020). The quantification and understanding of Sor is of great importance for the oil industry, as it is information used to simulate flow in reservoirs, from which production forecasts come. Therefore, it is noteworthy that the accurate determination of Sor has a great economic impact, determining the economicity of a project and the calculation of reserves. Additionally, this information is valuable for reservoir management studies and can aid in guiding studies related to EOR studies (Masalmeh, 2013; Pathak *et al.*, 2012), which are fundamental for increasing the recovery factor of oil fields.

Sor estimation can be done directly in the reservoir by well logging evaluation, laboratory experiments, or simulation. In the well, microresistivity log data are typically used in an aqueous fluid logging environment using the Archie relationship, where the filtrate removes the mobile oil. The remaining oil fraction is considered the Sor. In addition to resistive tools, dielectric, pulsed neutron, and carbon/oxygen logging stand out for *in-situ* Sor estimation (Chang *et al.*, 1988a; Pathak *et al.*, 2012; Wolff, Al-Jalahma and Hook, 1993). However, the drilling fluid filtration process is not always efficient, which can interfere with the evaluation, returning pessimistic Sor values depending on the tool's depth of investigation, hydrocarbon quality, exposure time, and reservoir characteristics, such as porosity and permeability. Therefore, to obtain more accurate results, they must be calibrated with laboratory data (Mohamed *et al.*, 2011).

In laboratory settings, the waterflood experiment is the most commonly used technique for obtaining Sor (McPhee, Reed and Zubizarreta, 2015). In this procedure, the previously cleaned samples are soaked in water and drained with oil injection until irreducible water saturation (Sw$_{irr}$) is achieved. After aging to reach the original wettability, water is injected to

displace mobile oil. Hence, Sor is the oil volume trapped in the rock. Oil and water tests can be performed in either a steady or non-steady state. In the steady state method, oil and water are injected together while gradually increasing the water flow rate to remove the oil. On the other hand, the non-steady state method involves injecting only water at a constant pressure or volume. Due to cost and assay complexity, laboratory data is scarce, and the sampling tends to be biased since experiments run better in good porosity and permeability samples.

Fluid flow in porous media is influenced by capillary, viscous, and gravitational forces. In low capillary number flows, which are typically found on the reservoirs (Bashiri and Kasiri, 2011; Blunt, 2017; Guo, Song and Hilfer, 2020; Speight, 2017), where the flow velocity is low, Sor is primarily controlled by capillary forces, which are governed by contact angle, interfacial tension, and porous media geometry (Blunt, 2017). The contact angle is linked to rock wettability, which affects how the oil will be trapped in the rock. On average, siliciclastic rocks tend to be water-wet, while carbonate minerals are often oil-wet due to lower surface charge content (Anderson, 1986, 1987).

In a water-wet condition, oil is disconnected and trapped in the center of pores by capillary forces (Roof, 1970; Singh *et al.*, 2017). Snap-off occurs when there is a significant difference between the size of the pore about the throat that connects it with the rest of the porous medium (Blunt, 2017; Chatzis, Morrow and Lim, 1983; Morrow, 1975; Wardlaw, 1982). In oil-wet conditions, oil is removed in large quantities until the oily phase collapses, generating entrapment in the form of films or in the corners of the pores (Alhammadi *et al.*, 2017; Iglauer *et al.*, 2012). Water sweeping tends to be more efficient in homogeneous media, which occurs as a frontal advance in water- and oil-wet conditions. Hence, heterogeneity increases the probability of water fingering, leaving undrained "islands" (Blunt, 2017; Chatzis, Morrow and Lim, 1983; Lenormand, Zarcone and Sarr, 1983).

On one hand, the availability of laboratory data is limited and biased, while the logging estimates are plagued with inaccuracy and uncertainty. Hence, upscaling laboratory data becomes necessary to check and adjust logging data. With this objective, we integrate rock data with microresistivity, nuclear magnetic resonance (NMR), and dielectric logging to understand the response of these tools better, quantify, and understand Sor in Pre-salt reservoirs of the Santos Basin. For this purpose, we used formation evaluation and sedimentological approaches, mainly focusing on the dielectric tool. Finally, since this tool is rarely used, their results were applied to train machine learning algorithms to predict dielectric Sor using the NMR data.

4.3   Geological Setting

The Santos Basin is located in southeastern Brazil, bordered by Cabo Frio High to the north and Florianópolis platform to the south (Figure 4-1). It was formed during the early Cretaceous/Late Jurassic period due to tectonic extension, preceding the separation of the South American and African continents and resulting in the formation of the Atlantic Ocean (Austin and Uchupi, 1982; Cainelli and Mohriak, 1999; Davison, 1999, 2007; Rabinowitz and LaBrecque, 1979). The Santos Basin's stratigraphy is categorized into three Super-sequences (Moreira *et al.*, 2007): Rift, Post-rift, and Drift (Figure 4-2).

Figure 4-1 Location of the Santos Basin and the Pre-salt Province (reproduced from Herlinger et al. (2020)).

The initial phase of rift formation involved the coverage of the Precambrian basement by the Camboriú tholeiitic volcanic rocks during the Lower Cretaceous (Mizusaki, Thomaz Filho and Cesero, 1998). The deposition of siliciclastic rocks and Mg-clays ooids and peloids began with the Piçarras Formation in the Barremian, marking the start of the Santos Basin sedimentary filling. These sediments were accumulated in a highly alkaline environment, along with hybrid sediments (Leite, Silva and De Ros, 2020). The Itapema Formation, deposited during the Jiquiá Local Stage, is characterized by significant accumulations of bioclastic bivalve rocks known as "coquinas" (Chinelatto *et al.*, 2020b; Rocha, Favoreto and Borghi, 2021). Additionally, peloids and ooids of Mg-clays are present, often mixed with the bioclastic sediments (Leite, Silva and De Ros, 2020). Dark shales are interspersed with bioclastic deposits and are the primary source rocks of the basin. The upper boundary of these deposits is identified as a regional stratigraphic

marker, resulting from basin uplift and erosion, resulting in a significant change in environmental conditions (Dias, 2005).

My	Geochronology			Stratigraphy		Unconformities	Tectonic Stage
	Epoch	Stage	Local Stage	Group	Formation		
					Ariri		Drift
						Salt Base	
120	Lower Cretaceous	Aptian	Alagoas	Guaratiba	Barra Velha		Pos-Rift
						Intra-Alagoas	
125			Jiquiá		Itapema	Pre-Alagoas	
		Barremian	Buracica		Piçarras		Rift
130			Aratu			Top Basalt	
		Hauterivian			Camboriú		

Figure 4-2 - Stratigraphy of the Santos Basin (Moreira et al., 2007).

The Barra Velha Formation covers the Rift Super-sequence unconformably and is further classified into Lower and Upper sections due to the Intra-Alagoas unconformity. The sediments comprising this formation consist of calcite shrub crusts, Mg-clay deposits with calcite spherulites, laminated carbonates, dolomite and silica, and intraclastic rocks (Basso *et al.*, 2021; Carramal *et al.*, 2022; Carvalho *et al.*, 2022; Gomes *et al.*, 2020b; Netto, Pozo, Manuel, *et al.*, 2022; Netto, Pozo, M., *et al.*, 2022; Silva, da *et al.*, 2021; Wright and Barnett, 2015). The Barra Velha Formation deposits were initially thought to have been accumulated in a transitional to marine environment due to the lack of data. However, after discovering giant hydrocarbon accumulations, the deposits were reinterpreted as forming in an alkaline lacustrine environment (Wright and Barnett, 2015). Close similarities exist in depositional, diagenetic, and mineralogical aspects between the equivalent deposits in the Santos, Campos, and Kwanza Basins (Herlinger, Zambonato and De Ros, 2017; Sabato-Ceraldi and Green, 2017; Saller *et al.*, 2016).

During the early stages of diagenesis, calcite spherulites, which are spherical, fibro-radial calcite aggregates, were formed and replaced the Mg-clay accumulations. These spherulites displaced the Mg-clay laminations. The Mg-clays are highly reactive and can dissolve, which

creates a significant amount of secondary porosity (Carramal *et al.*, 2022; Tosca and Masterson, 2014; Tosca and Wright, 2015; Wright, 2022). Furthermore, the Mg-clays were frequently replaced by dolomite crystals and other mineral phases. Calcite spherulites and dolomite crystals are commonly observed "floating" in the secondary pores where the clay matrix was dissolved. Recently, De Ros and Oliveira (2023) proposed a simple system for classifying the *in-situ* rocks of the Brazilian Pre-salt based on the proportions of shrubs, spherulites, and matrix. This classification system is based on the idea that the proportion of these components can provide insights into the depositional environment, diagenesis, and rock reservoir quality.

Calcite crusts, also known as shrubstones or stromatolites, are formed by the fibrous calcite aggregate crystals (shrubs). These crystals have divergent extinction and fascicular-optic habit (Herlinger, Zambonato and De Ros, 2017; Rodríguez-Berriguete *et al.*, 2022). The shrubs encrust each other or other materials, growing vertically and merging horizontally, forming crusts of varying dimensions. Calcite precipitation is closely linked to the deposition of Mg-clays, which occur as laminations, peloids, ooids, and coatings on particles of various origins (Carramal *et al.*, 2022; Carvalho *et al.*, 2022). These clays are often interspersed with calcite crusts, occasionally filling the spaces between the shrubs.

Apart from the *in-situ* rocks, reworked rocks are significant reservoirs in the Barra Velha Formation (Barnett *et al.*, 2021; Rodríguez-Berriguete *et al.*, 2022). These sedimentary facies comprise calcite shrubs and spherulite fragments associated with Mg-clay matrix intraclasts, Mg-clay ooids and peloids. Additionally, these facies contain subordinate phosphate fragments, ostracods, siliciclastic, and volcanoclastic grains. Identifying clay peloids and ooids can be challenging as they are often wholly replaced by calcite or dolomite. Dolomite, calcite, and quartz are the main diagenetic constituents that replace and cement the particles (Basso *et al.*, 2021; Carvalho *et al.*, 2022).

4.4 Materials and Methods

4.4.1 Well Data

This study is based on a well situated in Tupi field in the Barra Velha Formation. The well was drilled with a diameter of 12.25", and the logging data includes spectral gamma ray, resistivity, focused microresistivity, density, neutron, sonic, nuclear magnetic resonance

(NMR), dielectric logging, and elemental spectroscopy (Figure 4-3 and Figure 4-4). Water-based drilling fluid with a salinity equivalent to 210,035 ppm was used for logging the well. The resistivity of mud, mud filtrate and cake were 0.0653, 0.035, and 0.1182 ohm.m at 73.5, 72.5, and 73.5° F, respectively. In addition to the logging, a 38-meter core was collected from the top of the reservoir. The temperature ranged from 131 to 137° F from the top to the bottom of the well. Furthermore, 142 lateral samples were collected throughout the well. The data gathered from these samples were analyzed to provide a detailed view of the well, including the rock formation properties, density, porosity, and permeability.

4.4.2 Rock Data

Routine core analysis (RCAL) and special core analysis (SCAL) were done in plugs and sidewall core samples from the studied well and other field wells. The samples from analogous wells have similar lithological and petrophysical features, in addition to sharing comparable pressure and temperature conditions, as well as oil and water formation characteristics. The data include porosity, permeability, Sor, Sw_{irr}, m and n electric parameters, centrifuge and mercury injection capillary pressure (CentCP and MICP) sampled according to Table 4-1. In order to perform the waterflood procedure, the samples were first brought to the Sw_{irr} condition through centrifugation. Afterward, the samples were aged to restore their wettability before the waterflood experiment. The Sor value was obtained through low capillary number unsteady state water-oil relative permeability tests using formation and injection brines and dead oil. The analyses complied with the guidelines provided by the American Petroleum Institute (API, 1998).

After thoroughly cleaning, the samples were impregnated with blue epoxy resin to identify the porosity. Characterization of 35 thin sections was conducted to identify the primary and diagenetic constituents, pore types, textures, structures, and their interrelationships. The rocks were classified using the De Ros and Oliveira (2023) and Grabau (1904) methods.

Table 4-1 – Samples used in this study, including the ones collected in other wells (field samples) and those collected in the studied well (well samples).

		Porosity	Permeability	MICP	Sor	Sw_{irr}	CentCP	m and n
Well Samples	plug	136	136	26	5	5	10	-
	sidewall cores	114	114	-	-	-	-	-
Field Samples	plug	-	-	-	46	46	-	105
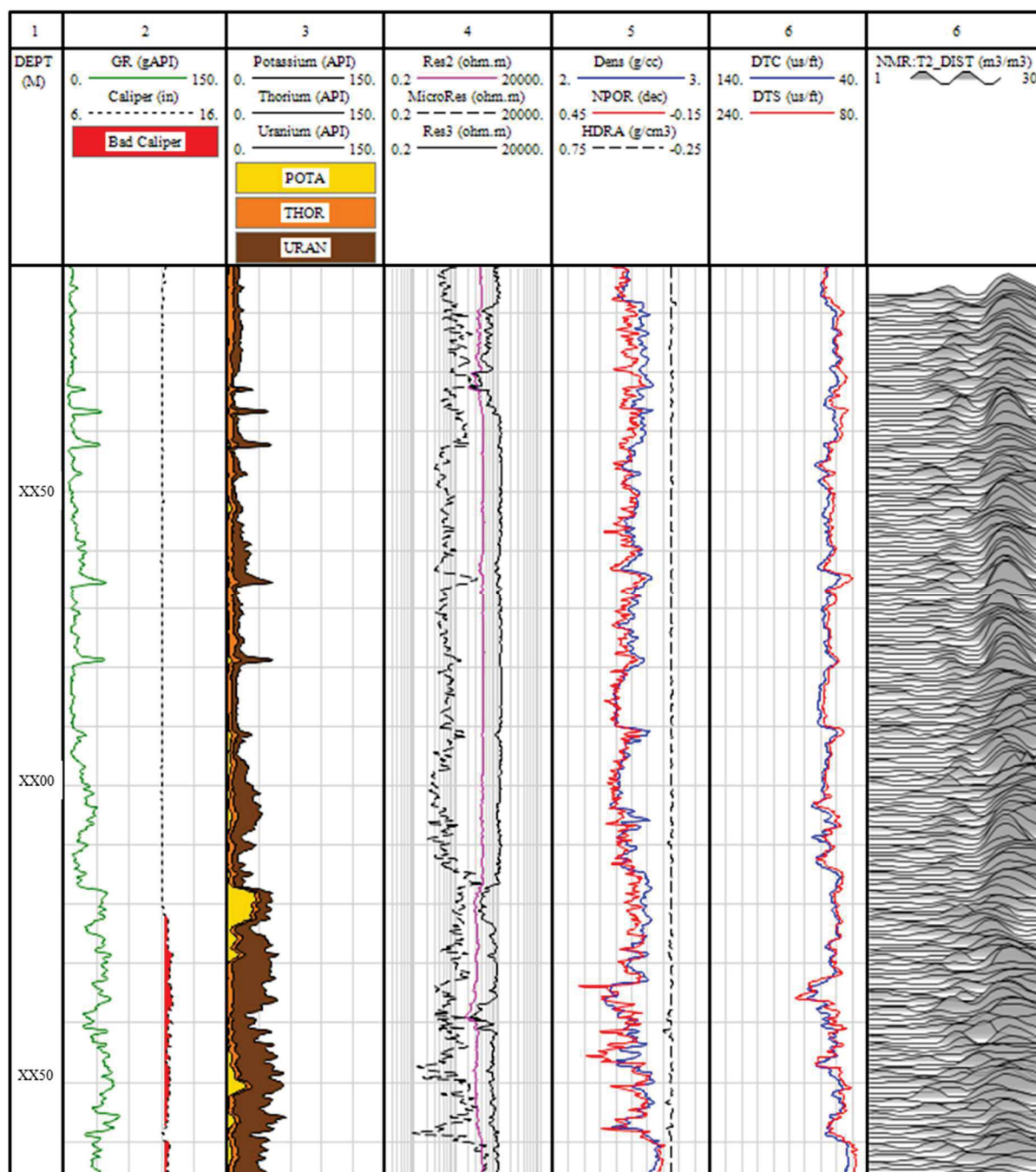
Figure 4-3 - Plot showing the main curves from the studied well: total and spectral gamma ray (tracks 2 and 3), resistivity (track 4), density and neutrons (track 5), compressional and shear sonic logs (track 6), and transverse relaxation time (T2) (track 7).
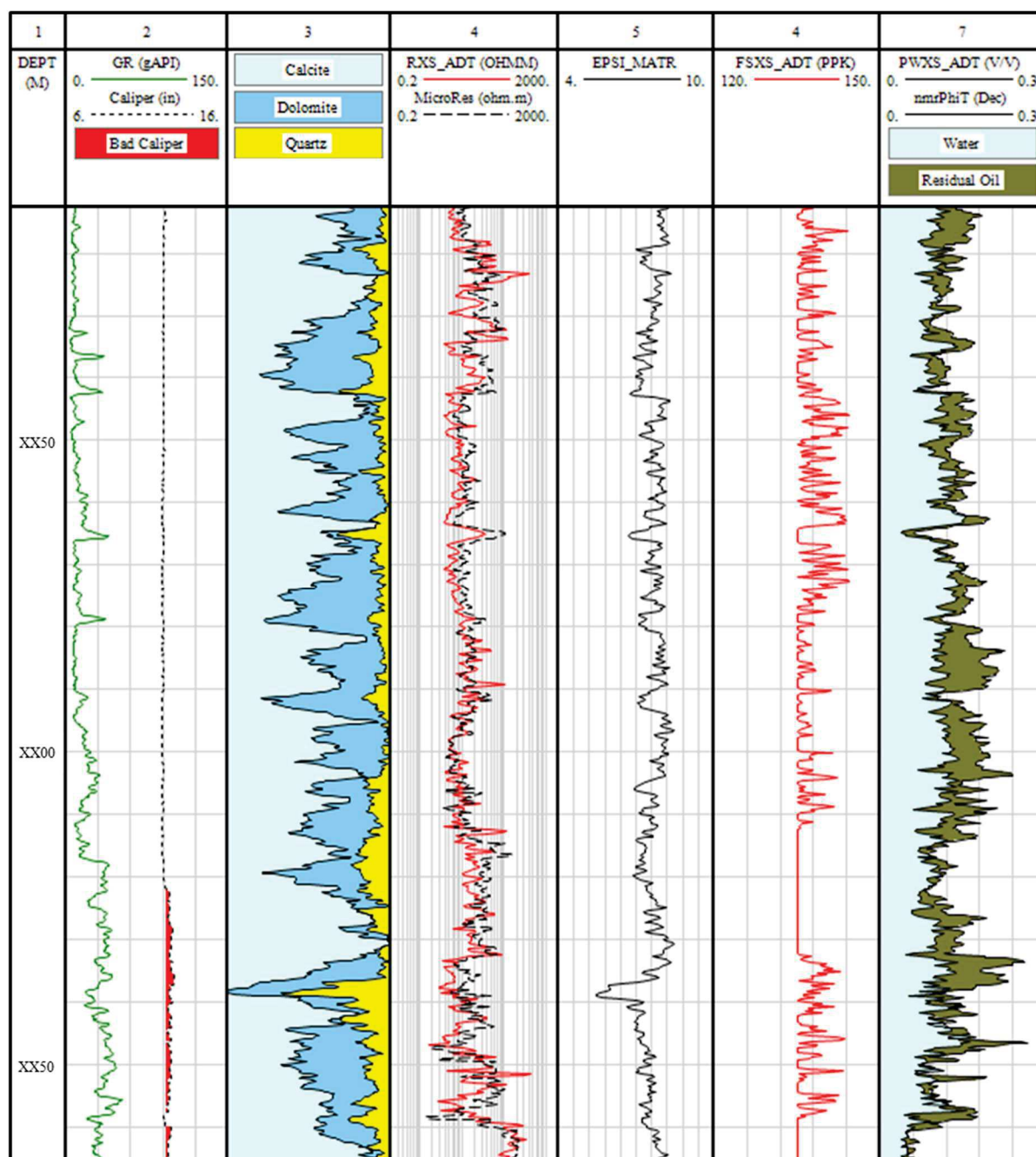
Figure 4-4 – Well logging exhibiting interpretation of elemental spectroscopy and dielectric logging: mineral model (track 3), dielectric and focused microresistivity, matrix permittivity, dielectric-derived salinity, and water-filled porosity (PWX_ADT) (tracks 4, 5, 6, and 7, respectively).

4.4.3 Formation Evaluation

The well interpretation included multimineral modeling based on linear inversion of elemental spectroscopy data. The most abundant constituents observed in thin sections of these wells were the minerals quartz, calcite, and dolomite, which were considered for the modeling. The porosity used in this study corresponds to the total porosity (PhiT) obtained with the NMR

logging. The Free (FF) and Bound Fluids (BF) were calculated with a cutoff of 100ms. Since resistivity curves typically show anomalously high values (*e.g.*, 8,000 ohm.m), they were considered inappropriate for estimating Sw. Therefore, water saturation (Sw) was calculated by upscaling centrifuge capillary pressure curves by the saturation height method (Ahmed, 2010; Leverett, 1941; Skelt and Harrison, 1995). It was used the following adjustment equation:

$$Sw = \frac{(\, a + bLog(Pc) + cLog(Pc)^2 + dLog(Pc)^3\,)}{\emptyset^f} \tag{4.1}$$

where Sw is the water saturation, Pc the capillary pressure, $\emptyset$ the porosity and a, b, c, d and f fit parameters. The permeability curve was calculated with an adapted Timur-Coates equation (Coates, Xiao and Prammer, 1999):

$$k = a\left(\frac{FF}{BF}\right)^b \emptyset^c \tag{4.2}$$

where k is the permeability, and a, b and c are fit parameters. The curve was calibrated with RCAL permeability data to adjust the fit parameters by optimization using least squares to reach the least error.

4.4.4 Sor Evaluation

Sor was estimated with four different techniques, which include focused and dielectric microresistivity, dielectric water-filled porosity method, and core multilinear regression upscale.

4.4.4.1 Regression Analysis

Using laboratory data, a regression analysis was carried out with ordinary least squares to evaluate the Sor regressions with porosity, permeability, and Sw_{irr} to upscale the rock trends to logging data. Once we have the porosity, permeability, and Sw_{irr} calculated by well logging, the resulting equation can be applied to the well to have a continuous estimative of Sor based on laboratory results.

4.4.4.2 Focused microresistivity

The water saturation in the flushed zone (Sxo) was calculated with the focused microresistivity using m and n lab average, which corresponds to 2.12 and 3.07, NMR total porosity (PhiT), and the resistivity of the filtrate in the reservoir condition with Archie's Law (Archie, 1942):

$$Sxo = \sqrt[n]{\frac{aRw}{\emptyset^m Rxo}}$$

(4.3)

where n and m are the saturation and cementation coefficients, Rxo the water resistivity in the washed zone, Rw the water resistivity, and a an empirical regression constant that in this study was considered 1. Thus, with the relationship below, the Sor:

$$Sor = 1 - Sxo$$

(4.4)

4.4.4.3 Dielectric Logging

The dielectric logging tool estimates the volume of water in a reservoir by using a property called permittivity (Calvert and Wells, 1977; Meador and Cox, 1975). When logging, an electric field is applied to the formation. The level of polarization affects the relative permittivity. Relative permittivity is a complex number that comprises an imaginary part proportional to conductivity and a real part representing the energy stored in polarization. This energy is known as permittivity. The dielectric dispersion, or mixing law, enables the computation of petrophysical parameters such as water-filled porosity ($\emptyset_w$), conductivity, and water salinity. Several factors influence complex permittivity (Donadille, Faivre and Leech, 2016; Psarras, 2018):

$$\varepsilon^*(\omega) = f_{mix}(\emptyset_w, C_w, \tau, \omega, \emptyset_T, \varepsilon_m, \varepsilon_o, T, p)$$

(4.5)

where ε^* is the complex permittivity, ω the angular frequency, C_w the water conductivity, τ the rock texture, $\emptyset_T$ the total porosity, ε_m the matrix permittivity, ε_o the oil permittivity, T the temperature, and p the pressure. The total permittivity is given by the CRIM equations (complex refractive inclusion model), according to the equation below (Meador and Cox, 1975; Penney, Calcraft and Pietsch, 1996; Pirrone *et al.*, 2011):

$$\sqrt{\varepsilon}_{crim} = (1 - \emptyset_T)\sqrt{\varepsilon}_m + S_w\emptyset_T\sqrt{\varepsilon}_w + (1 - S_w)\emptyset_T\sqrt{\varepsilon}_{HC} \qquad (4.6)$$

where $\emptyset_T$ is the total porosity, and ε_{crim}, ε_{HC}, ε_m, and ε_w are the permittivities of the medium, hydrocarbon, matrix, and water, respectively. Furthermore, the minerals' and fluids' permittivity will be necessary, and the multimineral model gives the proportion of them. The CRIM model does not consider the textural effect of the rock, taking only the components into account. The textural model considers the CRIM model and the textural effect to minimize the non-accounting of the incremental polarization generated by the interfacial mechanism in the CRIM equation (Seleznev *et al.*, 2006). The model considers the permittivity of ellipsoidal grains and pores dispersed in a medium with CRIM as a background. The model introduces a depolarization factor, which ranges from 1 to 3 and can be used to adjust numerical data. As discussed previously, this model can help determine water saturation at lower frequencies. Mathematically, the model can be described as follows:

$$\varepsilon_{eff} = \varepsilon_{crim} + \frac{\frac{1}{3}\sum_{j=1}^{n} f_j(\varepsilon_j - \varepsilon_{crim})\sum_{i=1}^{3}\frac{\varepsilon_{crim}}{\varepsilon_{crim} + N_j^i(\varepsilon_j - \varepsilon_{crim})}}{1 - \frac{1}{3}\sum_{j=1}^{n} f_j(\varepsilon_j - \varepsilon_{crim})\sum_{i=1}^{3}\frac{N_j^i}{\varepsilon_{crim} + N_j^i(\varepsilon_j - \varepsilon_{crim})}} \qquad (4.7)$$

where ε_{eff} is the effective permittivity, ε_j the complex permittivity of the j-th spheroidal inclusion of each phase, N the depolarization factor that is given by the pore geometry or inclusion considering spheroid proportions, and volumetric fractions: f matrix = (1-$\emptyset$), f water = ($\emptyset$Sw), and f oil = $\emptyset$ (1-Sw). The volume of residual oil, then, is calculated by the equation below:

$$Sor = \frac{\emptyset_T - \emptyset_W}{\emptyset_T} \qquad (4.8)$$

4.4.4.4 Dielectric microresistivity

The dielectric derived microresistivity Archie method used the salinity information obtained from the mathematical inversion of polarization data and the textural parameter MN (which replaces m and n) to calculate Sxo. This calculation was based on the relationship derived from Archie's law:

$$MN = \frac{log\ ^{Rw}/_{Rxo}}{log\ \emptyset_w} \qquad (4.9)$$

4.4.4.5   Machine Learning

Clustering and curve prediction techniques were employed to analyze NMR data, assessing its capability to detect the residual oil. The algorithms used for curve prediction were Random Forest (Ho, 1995), Gradient Boosting (Friedman, 2001), and K-nearest neighbors (Fix and Hodges, 1989). The dataset included 978 data composed of 30 relaxation time bins, separated into training (80%) and testing (20%) used to predict the Sor of the dielectric logging. Bins whose correlation coefficient was greater than 0.95 were excluded, resulting in 27 bins. The unsupervised clustering was performed with k-means (Lloyd, 1982) to identify similar groups of rocks based on relaxing times higher than 100 ms to identify zones with high remnant oil content.

4.5   Results

4.5.1   Petrography

The analysis of the core and description of the petrographic thin sections indicated a section dominated by intraclastic particulate rocks (Figure 4-5). Shrub-dominated rocks are the most relevant *in-situ* facies up to 2m thick. In contrast, the mud-dominated facies are subordinated in the sampled section with a few layers no more than 60cm thick. Intercalation of mud- and shrub-dominated *in-situ* rocks with calcarenites at the base of the cored section is observed, grading to calcirudites at the top of the reservoir. Figure 4-6 illustrates the macroscopic aspect of the main facies described on the core.

4.5.1.1   In-situ Rocks

The main primary components of *in-situ* rocks correspond to Mg-clays and calcite shrubs. The clays occur as laminated matrix and peloids, replaced and/or encrusted by calcite shrubs, and replaced mainly by calcite spherulites, and dolomite. The precipitation of calcite shrubs causes the formation of interstices, which Mg-clays may have filled during the formation of the crusts. Primary inter-shrub growth-framework porosity was not observed in thin sections. The

porosity is essentially secondary by matrix or intracrystalline dissolution. Along with Mg-clays and calcite shrubs, spherulites with submillimeter to millimeter diameter constitute the main components of the analyzed *in-situ* rocks (Figure 4-7). Spherulites were formed replacing and displacing the clay matrix. Dolomite is the main matrix replacer, while calcite and quartz are secondary. Pyrite, dawsonite, bitumen, barite, and other diagenetic components are occasionally observed. The proportion between Mg-clays, shrubs, and calcite spherulites allowed the classification of the *in-situ* samples, as shown in Figure 4-8, and the main components of these rocks are summarized in Figure 4-9.
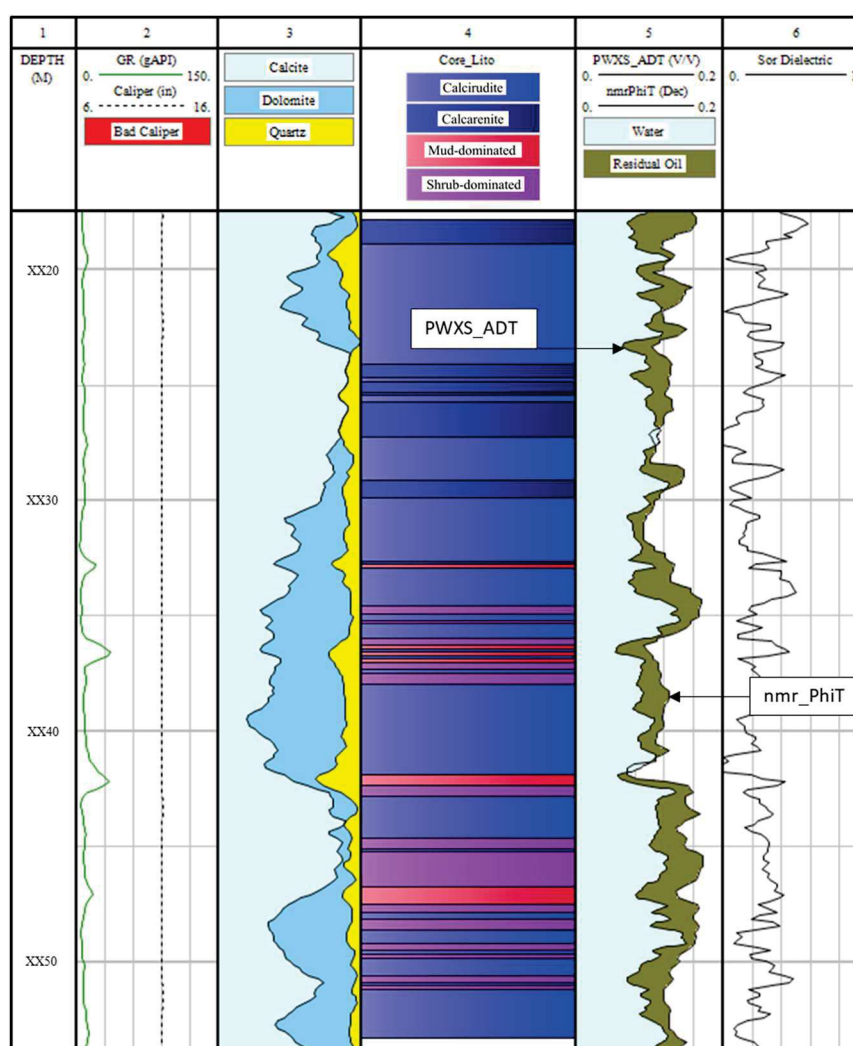
Figure 4-5 – Well plot showing the core succession (track 4) and its relationship with GR (track 2), interpreted mineralogy (track 3), water-filled and total porosity (track 5), and dielectric Sor (track 6).
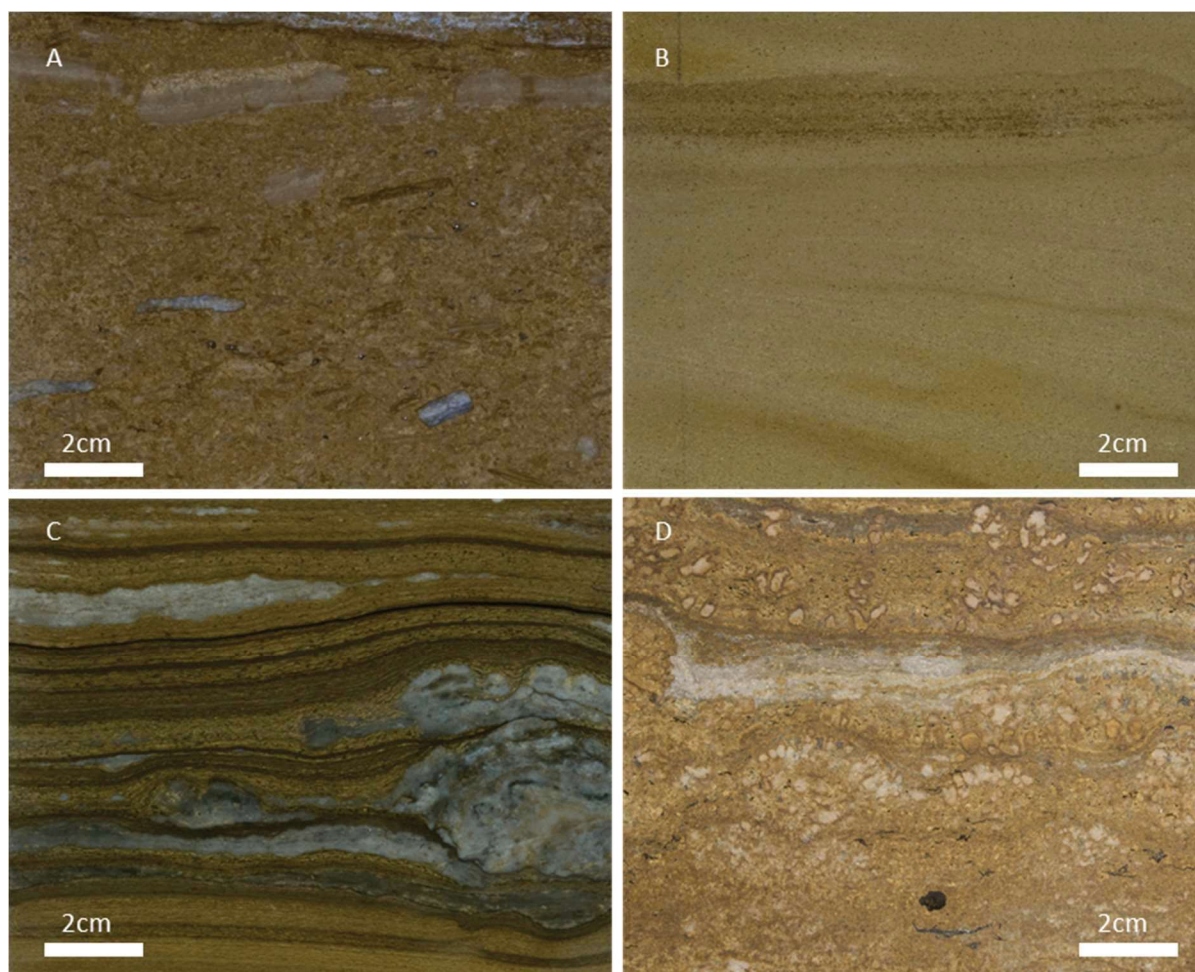
Figure 4-6 – Macroscopic aspect of the studied rocks: A) Poorly-sorted calcirudite composed of floating millimetric to centimetric calcite and mudstone intraclasts supported by sand-sized particles; B) Well-sorted intraclastic grainstone with incipient cross-bedding; C) Partially silicified mudstone; D) Shrub-dominated facies composed mainly of calcite shrubs and interstitial dolomite.

4.5.1.2   Intraclastic Rocks

The intraclastic rocks are predominantly massive at thin sections, even though incipient cross-bedding can be observed in macroscopic cores. They are formed by submillimeter to millimeter particles, corresponding to calcarenites and calcirudites. At the core scale, poorly sorted calcirudite with centimetric floating intraclasts supported by sand-sized particles are observed. Fine-grained calcarenites tend to be well sorted, while coarse-grained calcarenites are commonly poorly sorted. In order of abundance, most particle types are undifferentiated, spherulitic, and fascicular calcite intraclasts (Figure 4-7). Mg-clay peloids and ooids replaced

by calcite are common, while volcanoclastics, siliciclastic grains, and phosphate fragments are minor constituents.
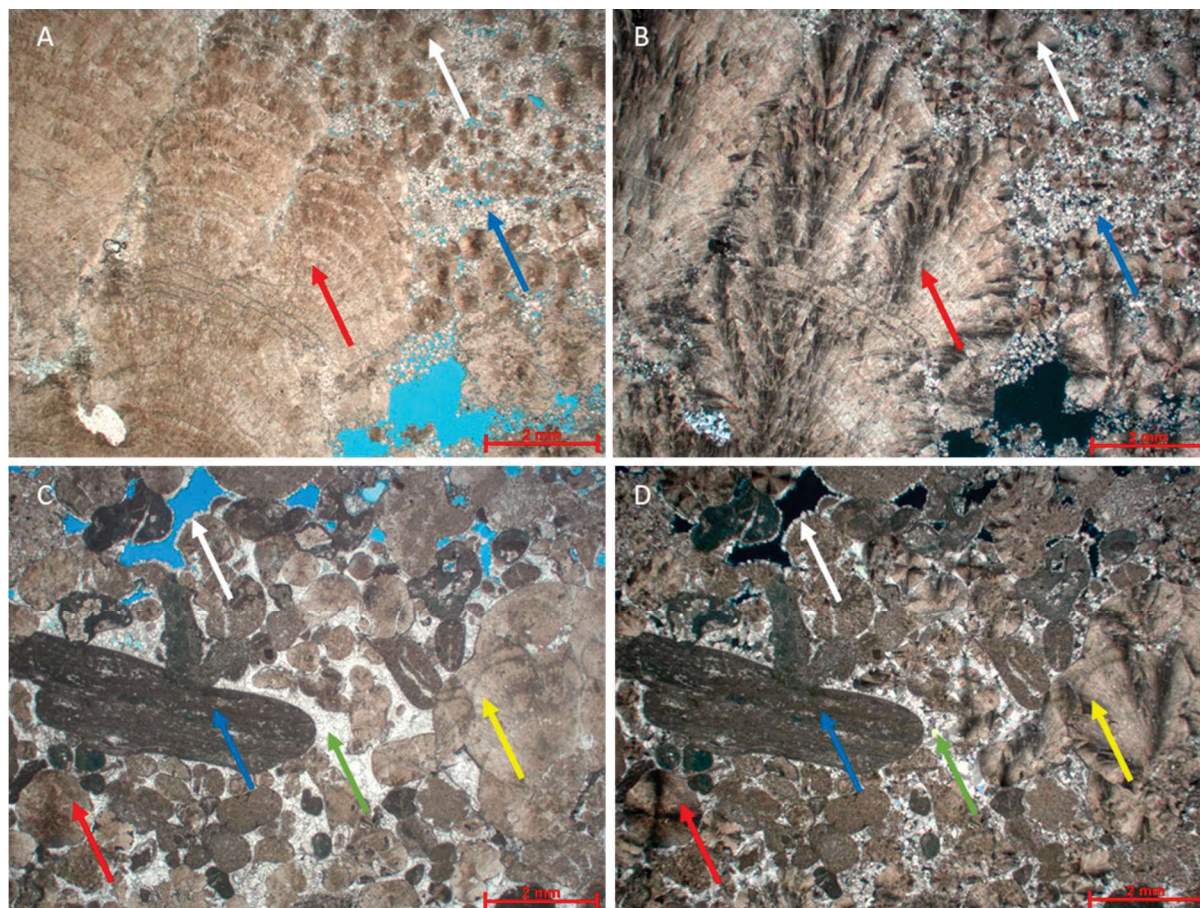
Figure 4-7 - Photomicrographs (uncrossed (A and C) and crossed (B and D) polarizers) exhibiting aspects of the rocks: A and B) Rock composed of large shrubs (red arrow), covered by spherulites (white arrow), and matrix replacive dolomite (blue arrow); C and D: Intraclastic rock formed by spherulites (red arrow), fragments of mudstones (blue arrow), and shrubs (yellow arrow), cemented by pore filling and lining dolomite (green and white arrows).

Dolomite is the main diagenetic constituent, commonly occurring as interparticle cement filling pores or lining and replacing particles (Figure 4-7). Calcite interparticle pore-filling cement is a secondary cement, while silica, pyrite, dawsonite, bitumen, barite, and other secondary components are occasionally observed. Primary interparticle porosity is poorly preserved and typically reduced by cementation and compaction. In most cases, secondary intraparticle porosity is in greater volume than primary porosity. Secondary porosity also occurs as vugs and molds. The main components are summarized in Figure 4-9.

4.5.2 RCAL and SCAL

Table 4-2 presents the results of the RCAL and Sor. In the *in-situ* facies, the porosity ranges from 0.068 to 0.268, with an average of 0.155. The permeability ranges from 3.5 to 7893.0 mD, with an average of approximately 771 mD. The Sw_{irr} varies between 0.080 and 0.410 (average 0.257), whereas the Sor value averages 0.279 (0.126 to 0.540).
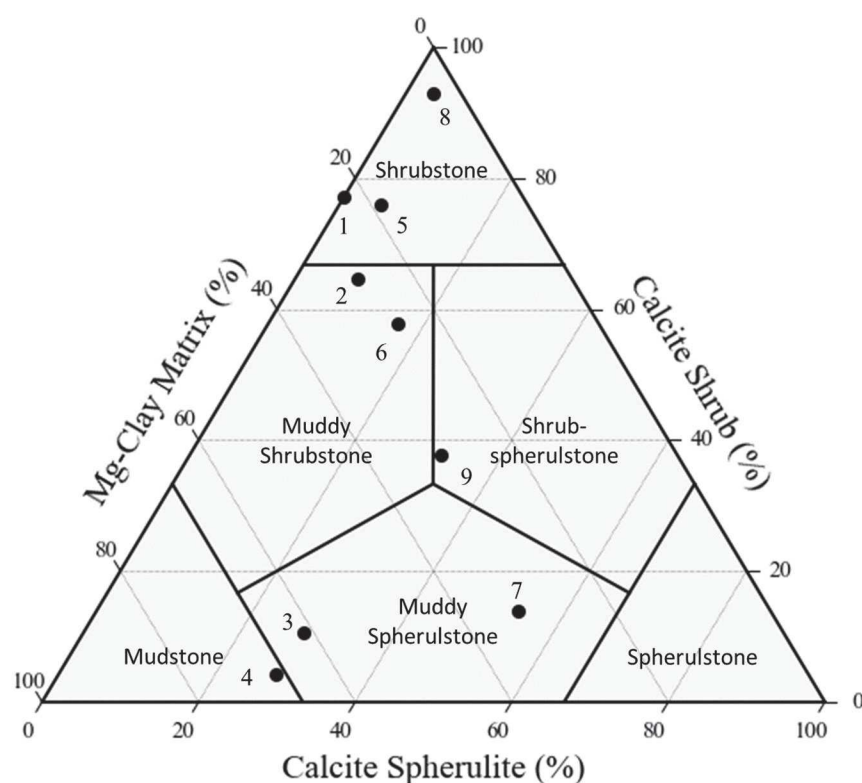
Figure 4-8 - In-situ classification according to the original percentage of Mg-clays, calcite spherulites, and shrubs (De Ros and Oliveira, 2023). The samples' main constituents are found in Figure 4-9.

Table 4-2 – Statistical summary of RCAL, Sw_{irr}, and Sor laboratory results.

	In-situ Rocks				Intraclastic Rocks			
	Permeability (mD)	Phi (dec)	Sw_{irr} (dec)	Sor (dec)	Permeability (mD)	Phi (dec)	Sw_{irr} (dec)	Sor (dec)
n	30	30	30	30	19	19	19	19
Average	771.2	0.155	0.257	0.279	404.1	0.149	0.240	0.228
Standard Deviation	1531.5	0.047	0.082	0.102	1066.1	0.042	0.077	0.107
Minimun	3.5	0.068	0.080	0.126	1.5	0.089	0.098	0.070
Maximum	7893.0	0.268	0.410	0.540	4714.0	0.246	0.363	0.477

In the intraclastic rocks, the porosity ranged from 0.089 to 0.246, with an average of 0.149. The average permeability was approximately 404 mD, ranging from 1.5 to 4714.0 mD.

The Sw$_{irr}$ values were between 0.098 to 0.363, with an average of 0.240. The Sor values averaged at 0.228, ranging from 0.070 to 0.477. Finally, the MICP and CentCP data used in this study are exhibited in Figure 4-10. The CentCP shows Sw$_{irr}$ ranging from 15.5 to 36.1% (average 24.5%).
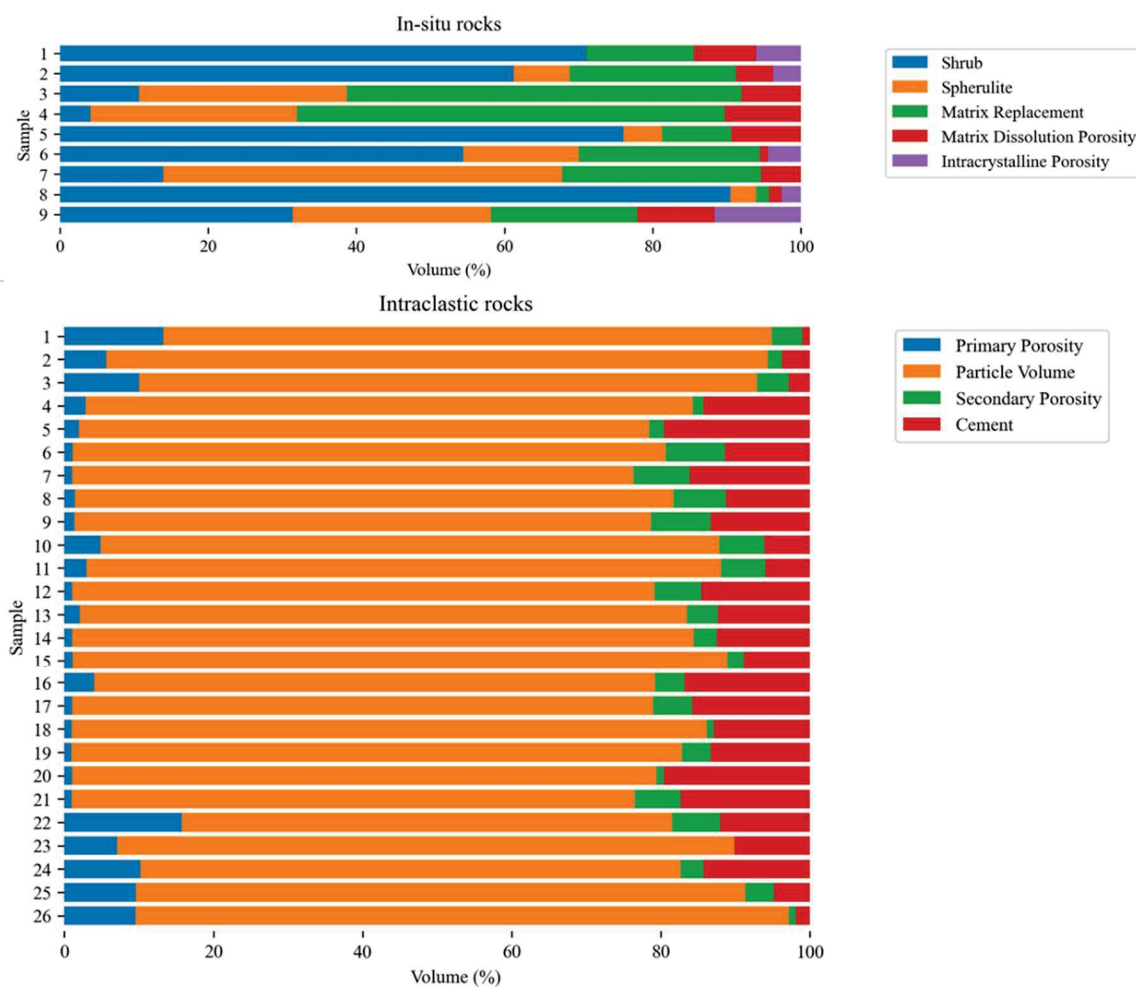
Figure 4-9 – Proportions of main constituents of studied rocks.
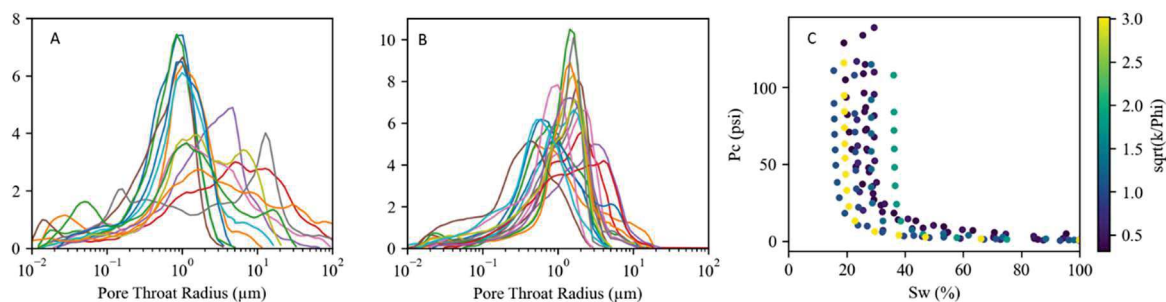
Figure 4-10 – MICP data from in-situ (A) and intraclastic (B) rocks, and CentCP data (C).

4.5.3 Regression Analysis

Laboratory Sor exhibits a positive correlation with porosity and permeability, and a negative correlation with Sw_{irr}, as shown in Figure 4-11. The Pearson's correlation coefficients between Sor and Sw_{irr}, porosity, and permeability were -0.67, 0.62, and 0.43, respectively. The regression analysis indicated that the best model is built with porosity and Sw_{irr}. The regression p-values were 0.0021, 0.0023, and 0.0537 for the constant, Sw_{irr}, and porosity, respectively. Hence, the null hypothesis that the coefficients are zero was rejected, considering a confidence level of 90%. This correlation satisfactorily predicts Sor (root mean squared error equals 0.073), as shown in Figure 4-11. This generates a multilinear regression equation for Sor upscaling from rock data as follows:

$$Sor = -0.64\ Sw_{irr} + 0.69\ Phi + 31.0509 \qquad (4.10)$$
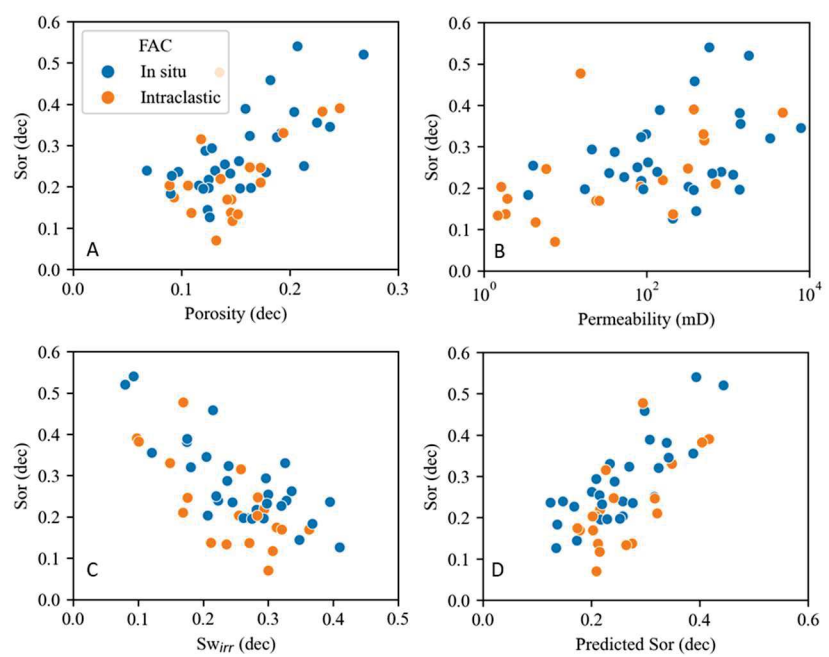
Figure 4-11 - Correlation between Sor and porosity, permeability, and Sw_{irr} (A, B, and C), and predicted versus actual Sor (D).

4.5.4 Formation Evaluation

The well's porosity averaged around 14%, while the Sw average is nearly 27%. The average permeability is approximately 11mD. The mineralogical modeling showed that the mineralogy is dominated by calcite (60%), followed by dolomite (29%), and finally quartz (8%). The dielectric porosity indicated an average water-filled porosity of about 10% and

salinity of 135,000 ppm in the area investigated by the tool. The Sor calculated using data from the dielectric tool is roughly 26%, whereas the Sor obtained with conventional microresistivity is significantly higher (55%). The result obtained by upscale laboratory data was around 26%, consistent with the dielectric logging data. Figure 4-12 shows the calculated curves.
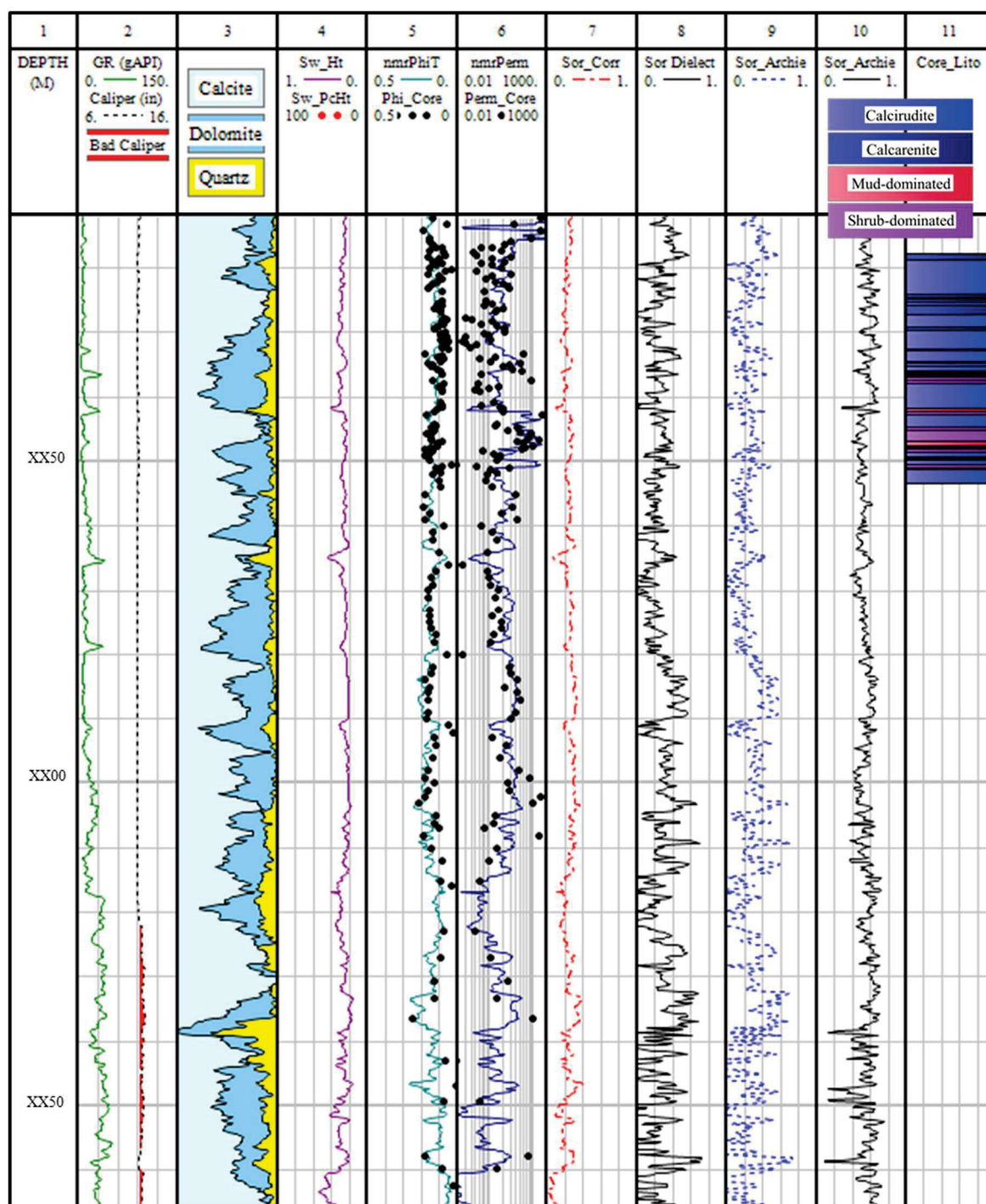
Figure 4-12 – Well plot exhibiting resulting curves: saturation height water saturation (track 4), porosity (track 5), permeability (track 6), Sor from multilinear correlation, dielectric, Archie result from dielectric microresistivy and conventional microresistivity (tracks 7, 8, 9, and 10), and core location in track 11.

Considering the core interval, the average porosity of the intraclastic facies is approximately 13%, which is quite close to the *in-situ* facies at 14%. Similarly, the Sw_{irr} showed 25.5% and 27% averages for the intraclastic and *in-situ* facies, respectively. However, the average permeabilities between the *in-situ* and intraclastic facies differed significantly, with the *in-situ* facies boasting a much higher 12mD compared to the 2mD of the intraclastic facies. Additionally, the Sor was consistent between the dielectric tool and multilinear model for the intraclastic facies, hovering around 23%. Meanwhile, the Sor for the dielectric logging and multilinear correlation averaged 25% and 28% for *in-situ* facies (Figure 4-13). Finally, Archie's relationship with the conventional microresivity tool showed 56% and 51% Sor for the intraclastic and *in-situ* facies, respectively, while Sor calculated with dielectric microresistivity was very similar to the dielectric water-filled porosity approach.
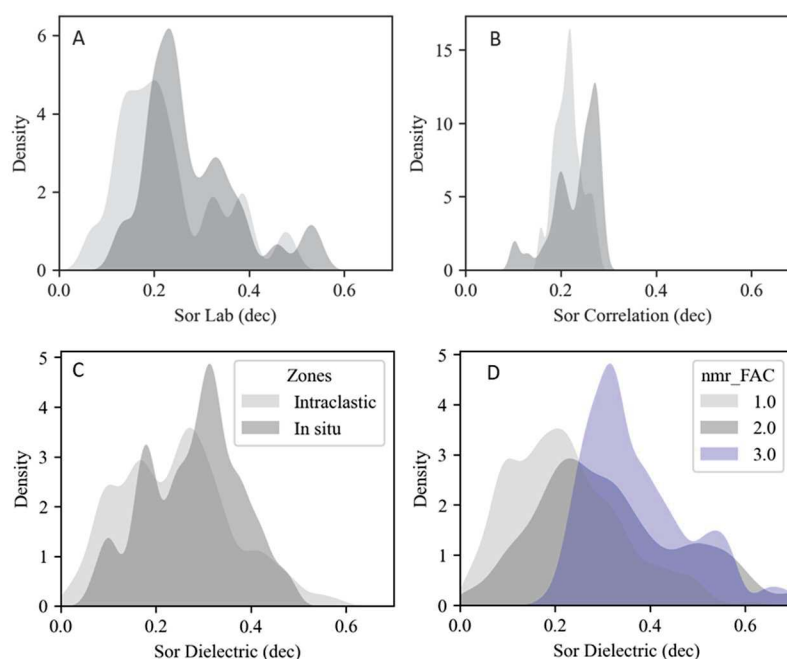
Figure 4-13 – Histograms illustrating the Sor distributions of lab (A), upscaled multilinear correlation (B), and dielectric logging classified by facies (C), and dielectric Sor classified by NMR electrofacies (D).

The NMR clustering data yielded three electrofacies based on NMR relaxation times. The average Sor values of the dielectric logging are approximately 19.5%, 31%, and 37%, respectively, for the three electrofacies (Figure 4-13D Figure 4-14), showing significant differences according to T2 relaxation times. The prediction models achieved similar results (Figure 4-15), with a reasonable prediction of water-filled porosity. The Random Forest

Regressor was the best model to reproduce the actual data. Its R^2 value was 0.56, and the rooted mean squared error was 0.016, considering the predicted and the actual Sor from the test set.
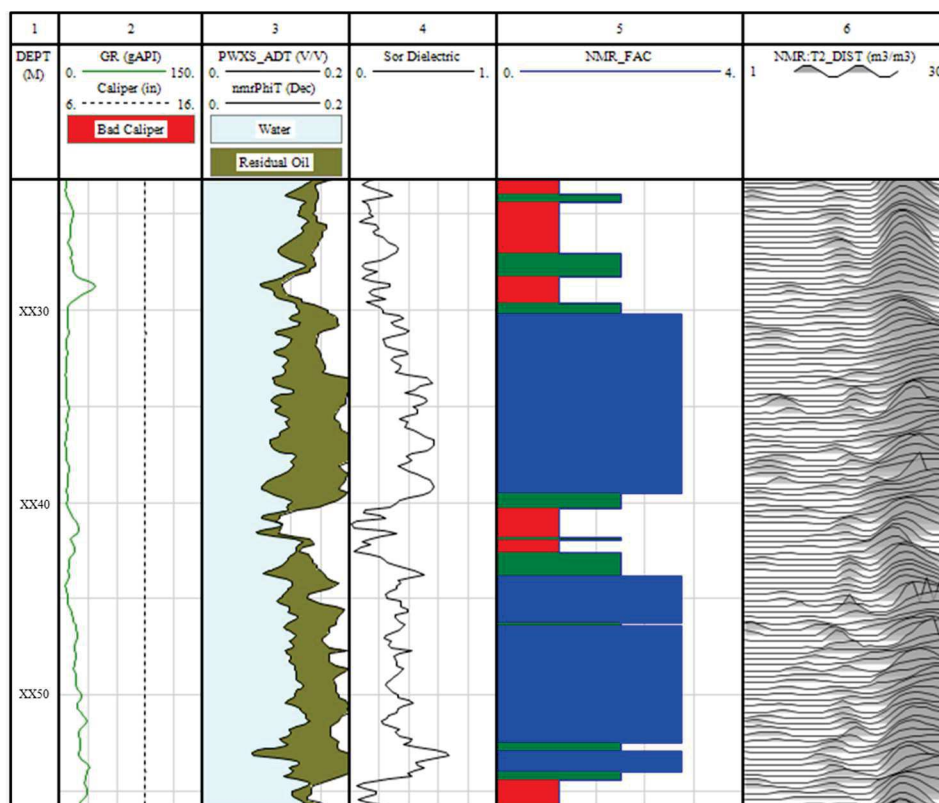
Figure 4-14 – Clustering results showing the relationship between clusters (track 5), NMR t2 (track 6), and dielectric Sor (tracks 3 and 4).

4.6 Discussion

4.6.1 RCAL, SCAL, and Sor and upscale

According to the laboratory data, Sor has a good correlation with Sw_{irr} (r = -0.67) and Phi (r = 0.62) and a fair correlation with logPerm (r = 0.43) (Figure 4-11). Typically, Sw_{irr} has a negative correlation with Sor since, in general, the greater the amount of initial oil, the less likely this oil is to be mobilized, as observed by several authors (Blunt, 2017; Jerauld, 1997; Mansoori, Al *et al.*, 2010). The positive correlation between porosity and Sor contradicts the assumption that porosity destruction during diagenesis would increase Sor (Blunt, 2017; Prodanović, Bryant and Davis, 2013; Yuan, 1981). These rocks' highly complex cementation patterns can profoundly alter the relationship between pores and throats since dolomite cement can compartmentalize primary pores, creating a new pore framework inside them.

Additionally, Sw$_{irr}$ tends to increase with decreasing porosity and permeability, a commonly observed fact opposing the over-simplistic statement of these authors. Therefore, the decrease in porosity implies narrowing of throats, reducing permeability, and preventing oil access during drainage, which increases Sw$_{irr}$.
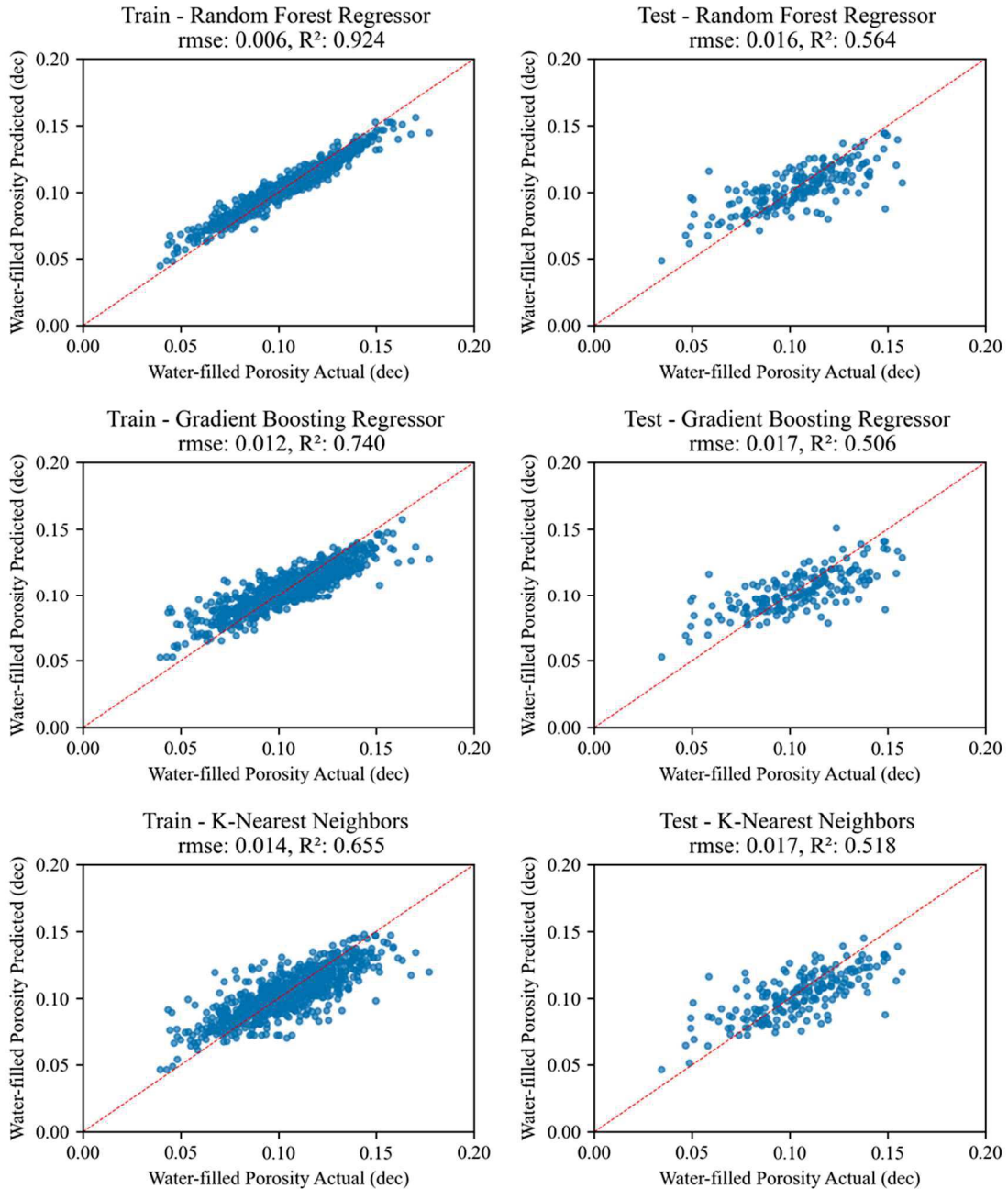
Figure 4-15 – Scatter plots showing the actual vs the predicted water-filled porosity, considering the sets train and test for the methods Random Forest Regressor, Gradient Boosting Regressor, and K-Nearest Neighbors.

Furthermore, it is observed that in intraclastic rocks, the decrease in porosity is related to greater homogenization of the porous medium, as shown by MICP (Figure 4-10), which leads to higher sweeping efficiency (Al-Shalabi and Ghosh, 2016; Blunt, 2017; Pandey *et al.*, 2023). It seems that the destruction of porosity causes the aspect ratio to approach 1; that is, the difference between the size of pores and throats becomes small, hindering the oil trapping by capillary forces. Also, it is observed that there is a faciological control in the Sor, where the *in-situ* facies that have a more heterogeneous porous media, as observed in the MICP data, tend to have greater Sor, in contrast to the reworked (Figure 4-10), which tend to have greater homogeneity. These observations indicate that the correlations are not casual and are supported by lithological relationships. This way, the correlations obtained in the laboratory can be used robustly, where the regression model with porosity and Sw_{irr} propagates the Sor directly to the well logging.

4.6.2   Sor logging interpretation

The logging interpretation indicated that laterolog microresistivity has a greater depth of investigation than dielectric logging. Consequently, the Sor values estimated by the conventional Sxo Archie approach are pessimistic (Figure 4-12), indicating that the laterolog microresivity does not provide adequate values for these reservoirs. On the other hand, the results obtained with dielectric log (water-filled porosity) present values close to laboratory data (Figure 4-13), demonstrating that, at the logged depth, the reservoir is in a condition close to Sor. Estimating Sor with resistivity, MN, and salinity data from the dielectric tool resulted in similar values to the method calculated with the water-filled porosity. In this way, it provides redundant information and cannot be used as an alternative scenario.

A positive correlation between Sor and porosity and permeability, and a negative correlation between Sw_{irr} is observed in the log data (Figure 4-16). These relationships are also observed in laboratory data, as discussed previously (Figure 4-11), indicating that the Sor of the dielectric log is consistent with the experimental data. Furthermore, facies control is still observed, with *in-situ* facies showing higher values than the intraclastic ones (Figure 4-13), results observed both in laboratory data, in the result obtained by dielectric log, and in the curve obtained with multilinear regression. Although there is a correlation between the dielectric Sor curve and the multilinear regression curve, there is less variability in the regression results since the curve from the dielectric logging has a larger resolution than the curves used in the

construction of the saturation height model, thus impacting the upscale of rock data. As a result, the dielectric log shows more significant variability, even though the averages are close, indicating the validity of both methods, even with differences in sampling support.

4.6.3 Lithology versus Logging

It was observed that the grain size measured in thin sections corresponds well with the dielectric Sor (Figure 4-17), indicating that rocks with larger grain sizes present greater Sor. On the other hand, no significant difference is observed between the calcirudite and calcarenite zones in the cored region. This probably occurs because these calcirudites have pebble-sized or larger particles floating on the sand-sized particles. Therefore, what will matter for the flow of fluids will be the size of the clasts that support the pebbles. Moreover, there was no clear relationship between the amount of cement and compaction quantified by petrography and dielectric Sor values.
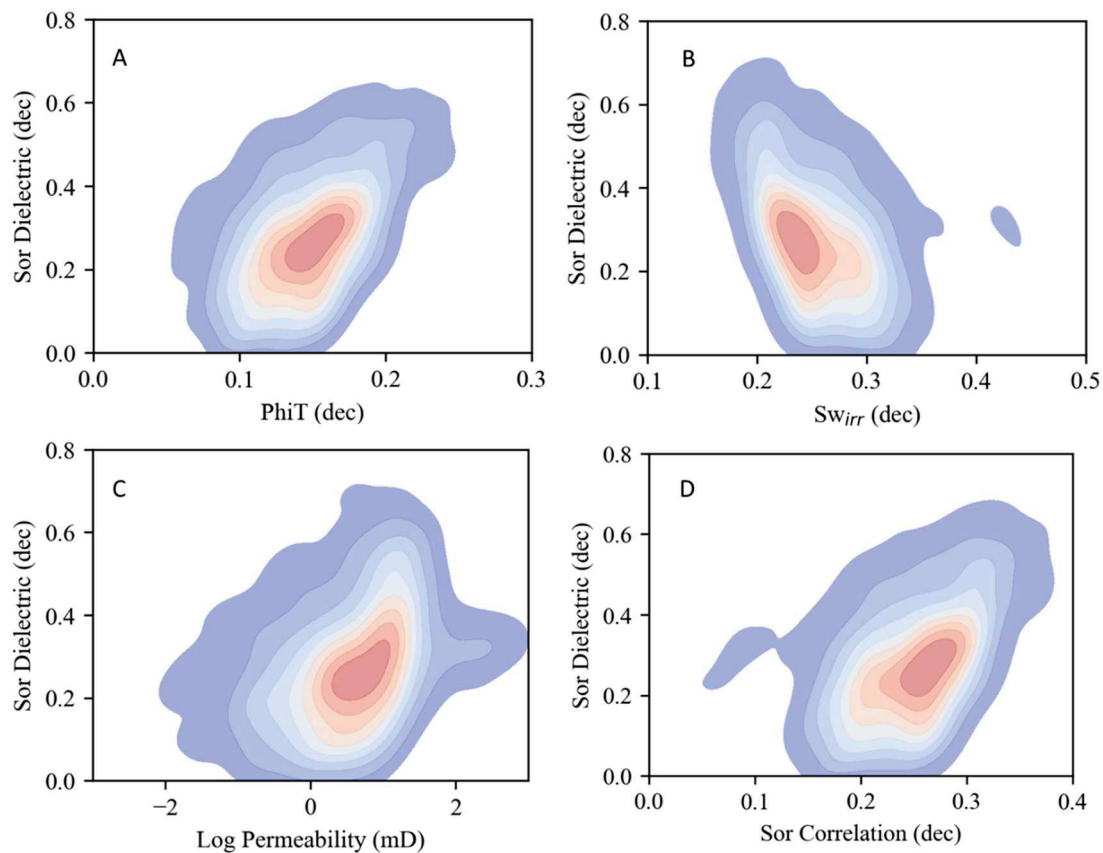
Figure 4-16 – Scatter plots illustrating the correlation of dielectric Sor with PhiT (A), Sw$_{irr}$ (B), permeability (C), and Sor calculated with multilinear regression correlation (D).

Because these rocks' cement is typically pre-compactional, it directly controls compaction. However, the heterogeneity of diagenetic processes probably makes it difficult to match petrographic data with curves, the accuracy of which is hampered by the resolution and amount of noise. Clast size patterns tend to be less heterogeneous than diagenesis, which may explain the good correspondence. This relationship has been observed in other studies (Coskun, Wardlaw and Haverslew, 1993; Herlinger *et al.*, 2023; Taiwo *et al.*, 2016), indicating that the homogeneity of finer rocks facilitates oil recovery. Given the low sampling of *in-situ* rocks, no relationship was observed between petrography and logging data for these facies.

The mineralogical content from mineral modeling does not show an apparent relationship with porosity or permeability. Although the main cement of these rocks is dolomite, this mineral also occurs by replacing particles or components of the *in-situ* rocks. So, although useful for petrophysical calculations, mineralogical curves do not help study porosity destruction processes by cementation in these rocks. Furthermore, it is observed that silica is a crucial porosity reducer. In this well, silica is mainly related to mudstones, so where this facies exists, silica peaks are typically observed, resulting in loss of porosity (Figure 4-5). Important silica cement is not abundant in thin sections as it is concentrated in thin layers. Highly silica-cemented regions are typically not sampled due to their low porosity and permeability.
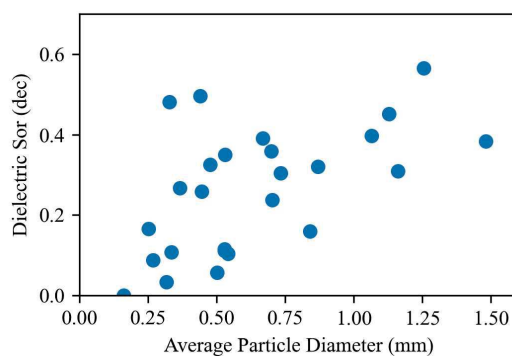
Figure 4-17 – Correlation between average particle size measured in thin section and dielectric Sor at corresponding depth.

Moreover, there is no clear relationship between Sor and the dolomite/calcite ratio; similarly, calcite and dolomite content do not correlate to porosity, permeability, or Sw_{irr}. On the other hand, the destruction of porosity by silica leads to a decrease in porosity, as aforementioned. Consequently, it hinders the oil entrance, which increases Sw_{irr} and, consequently, reduces Sor.

4.6.4   NMR versus dielectric curves

The Pearson's correlations between the water- and oil-filled porosity and the T2 bins indicate that the highest relaxation times are related to the residual oil (Figure 4-18). In contrast, water has shorter times, which is probably influenced by surface relaxation mechanisms. Furthermore, the oil-filled porosity correlates with T2 times about 1 ms, a relaxation time typically attributed to clay-bound water (Coates, Xiao and Prammer, 1999). However, water-filled porosity does not correlate with these times, indicating that this porosity should be related to oil.

Although it is interpreted that there were originally Mg-clays in these rocks, all of the original content was dissolved or replaced, as no traces of these minerals were observed in the investigated thin sections. On the other hand, bitumen is often observed in thin sections and is related in many Pre-salt fields in Santos, Campos, and Kwanza Basins (Guzzo *et al.*, 2018; Lima *et al.*, 2020; Liu *et al.*, 2022) (Figure 4-19). Although it has been frequently recognized in Pre-salt, the sample cleaning process can partially or entirely remove this component (Schleifer, Kesse and Lawrence, 2018). Furthermore, several studies indicate bitumen relaxation times of around 1 ms (Li *et al.*, 2020; Wen, Bryan and Kantzas, 2003; Yang and Hirasaki, 2008), consistent with the time observed in the correlations. Therefore, it is highly likely that the short relaxation times are related to bitumen.
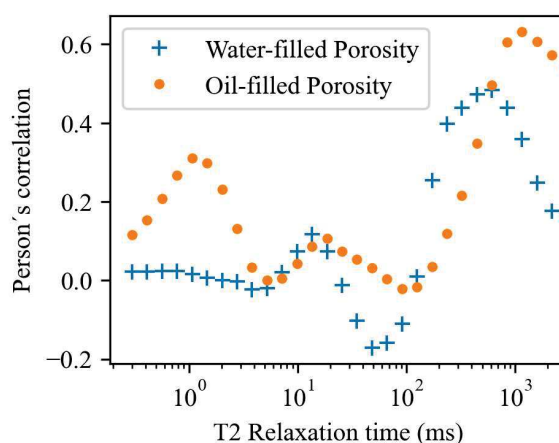
Figure 4-18 – Chart illustrating the Pearson's correlation coefficient between the water- and oil-filled porosity and the porosity bins considering each T2 relaxation time interval. This graph shows the contribution of each time to each curve, indicating relevant correlation peaks at 1 and 1000 ms for oil, while water has an important peak at around 600 ms.
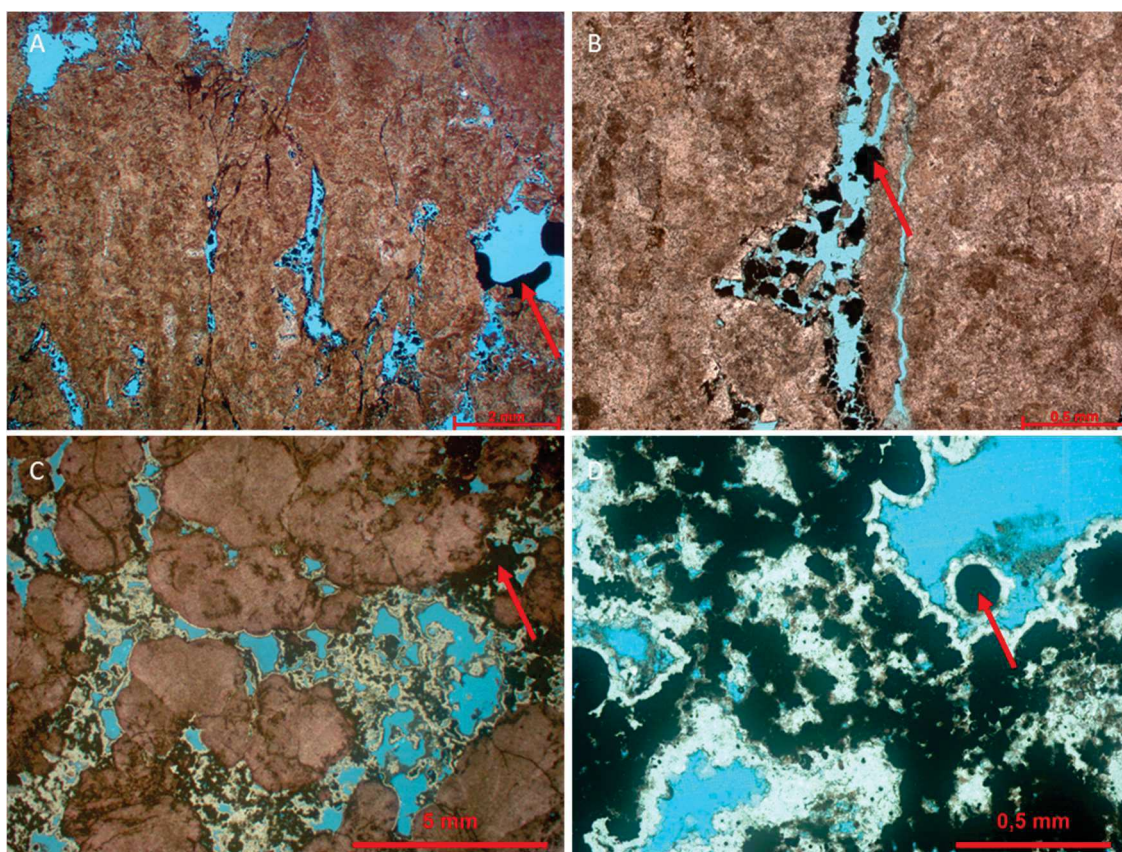
Figure 4-19 – Examples of bitumen-rich shrubstones from analogous wells (red arrows): A) Bitumen lining and filling growth-framework pores; B) Cracked bitumen in growth-framework pore; C and D) Bitumen peloids filling growth-framework pores, covered by quartz cement.

4.6.5   Clustering and Curve Prediction

Since there is a good relationship between dielectric Sor and relaxation times, clustering methods are expected to identify areas with higher residual oil content. Thus, the cluster analysis showed good results, indicating three zones with significant differences in oil saturation calculated by the dielectric log (Figure 4-13 and Figure 4-14). The cluster with the highest oil saturation has higher NMR times, often with high values close to 3000 ms, coherent with Pearson's correlation. Moreover, the curve prediction methods can satisfactorily predict the water-filled porosity from which Sor is obtained, indicating that dielectric logging and NMR have similar depths of investigation. In addition, although cutoffs cannot accurately define fluid saturation, the time distributions appear to be influenced by different fluids, resulting in distinct signatures. Finally, it is highlighted that the model trained with dielectric data can propagate Sor in wells where this tool was not used.

4.7 Conclusions

In this study, we integrated logging data, RCAL, SCAL, and petrography to understand and quantify Sor in a Pre-salt reservoir in the Santos Basin, Brazil, and concluded that:

• Sor exhibits strong facies control, where *in-situ* facies have higher values than intraclastic ones, owing to their greater textural and mineralogical complexity.

• There is a good correlation between Sor and Sw_{irr}, Phi, and permeability. This relationship can be observed in both laboratory and logging data, enabling us to upscale laboratory data.

• Dielectric tool yielded accurate results for Sor logging evaluation due to its shallow depth of investigation and properly matched laboratory data trends.

• NMR logging cannot directly measure Sor, but it can identify areas with more remaining oil, indicating regions with high residual oil. In addition, machine learning techniques can use NMR data to predict dielectric Sor.

• According to the data interpretation, bitumen might be related to short relaxation times in NMR. It could be wrongly quantified as residual oil by the dielectric tool interpretation. Therefore, it is crucial to investigate the effect of bitumen on the logging tools' response in more depth in future studies.

4.8 Acknowledgements

5. Article 4 - HERLINGER, R.; ROS, L. F. DE; VIDAL, A. Assessing the Role of Dolomite in Oil Trapping in In-situ Brazilian Pre-salt Carbonate Reservoirs by Pore-Scale Modelling and Simulation. Petroleum Geoscience, v. 31, 2025.

5.1 Abstract

The main Aptian Pre-salt *in-situ* facies were modeled in 3D pore-scale to evaluate the impact of diagenetic textures; specifically, the influence of matrix-replacive dolomite on pore system development. Our objective is to evaluate how these textures affect residual oil saturation (Sor) under water- and oil-wet conditions through pore-scale simulations. We developed 12 models with varying proportions of dolomite and calcite spherulites, three models with calcite shrubs, 21 models with shrubs and regularly-spaced dolomite, and 9 models with shrubs and heterogeneously arranged dolomites. The methodology involved evaluating the tortuosity, surface area, and size distribution of pores and throats. Additionally, the Quasi-Static Morphology method was used to estimate the Sor. The results indicated dolomite significantly affects the pore system, leading to a more uniform medium, a decrease in the throat-to-pore size ratio, and an increase in surface area. The increase of dolomite decreases Sor in water-wet conditions. Conversely, in oil-wet simulations, increasing dolomite leads to an increase in oil entrapment. Previous research on waterflood experiments concluded that *in-situ* facies with high content of replacive dolomite tend to show low Sor. Hence, it is probable that much of the oil trapped in these rocks is a result of the snap-off under water- or mixed-wet conditions.

Keywords: dolomite, simulation, pore-scale modeling, oil trapping, Pre-salt.

5.2 Introduction

The Brazilian Pre-salt reservoirs from the sag stage (post-rift) of the Campos and Santos Basins host world-class hydrocarbon reserves. Exploration in Angola conjugate Kwanza-Benguela and Namibe Basins also discovered reservoirs with the same genesis and characteristics. Nevertheless, while the origin of these unique deposits is the subject of controversial debate, their depositional and diagenetic evolution generated highly heterogeneous pore systems (Carvalho *et al.*, 2022; Herlinger *et al.*, 2020; Herlinger, Zambonato and De Ros, 2017; Saller *et al.*, 2016). These rocks, deposited in an alkaline lacustrine environment, were predominantly formed by the in-situ precipitation of Mg-clays and calcite shrubs. During eodiagenesis, these clay minerals were replaced by calcite and dolomite spherulites. Subsequently, due to their high instability, the clay-rich sediment tends to undergo dissolution, resulting in complex porosity patterns (Herlinger *et al.* 2017; Carramal *et al.* 2022; Carvalho *et al.* 2022).

The concept of residual oil saturation (Sor) refers to the portion of pore volume that remains filled with oil after displacement, trapped by capillary forces. This information is crucial for reservoir understanding and characterization, as it plays a significant role in reservoir simulation and in determining effective techniques for enhanced hydrocarbon recovery. Various studies, such as those by Rathmell *et al.* (1973), Chang *et al.* (1988), and Teklu *et al.* (2013), have emphasized the importance of quantifying and understanding Sor. Several factors contribute to the trapping of oil in reservoirs after waterflood. These factors include the mineralogy and texture of the rock, the morphology of the pores and their throats, the composition of the fluids involved, and the environmental conditions of the reservoirs, such as pressure and temperature. The interactions among these factors impact wettability, interfacial tension, and the distribution of capillary forces, which are fundamental to the flow and entrapment of fluids. Studies by Perkins (1957), Anderson (1987, 1985), Chandler *et al.* (1982), Wardlaw (1982), Hoeiland *et al.* (2001), Ling and He (2012), and Blunt (2017) have shed light on the complex nature of these interactions.

Understanding of pore-scale petrophysical characteristics, especially multiphase flow, has dramatically improved with recent technological advances in pore-scale 3D imaging (Blunt, 2017). Since Flannery *et al.* (1987) first imaged rocks both in synchrotron and with radioactive source equipment, the quality of the images, the capacity and the speed of processing have

evolved significantly. Although fundamental for understanding pore scale, tomographic imaging is expensive. In addition, the X-ray image has limited resolution, making it impossible to image and simulate textures with small dimensions. Furthermore, sampling often represents only a few facies, and rock characteristics may be affected during sampling, particularly of clay-rich rocks. On the other hand, pore-scale modeling can drastically save the number of experiments needed to establish the necessary link between rock types and sedimentological classifications (Mehmani, Verma and Prodanović, 2020). Furthermore, pore-scale modeling can be helpful for sensitivity studies. In other words, textural parameters can be systematically varied in order to assess the impact of textural modifications, such as progressive cementation or dissolution.

The first process-based pore-scale models were built with spheres to model the compaction and cementation of granular rocks for permeability prediction (Bryant, Cade and Mellor, 1993). Since then, several studies have used sedimentological concepts, processes, and products for modeling and simulating petrophysical properties (Bakke and Øren, 1997; Hosa and Wood, 2020; van der Land *et al.*, 2013; Øren and Bakke, 2002; Torskaya *et al.*, 2014). Hosa *et al.* (2020) modeled Pre-salt shrubs to assess the impact of depositional and diagenetic processes on reservoir properties. However, the fundamental relationship between calcite shrubs, spherulites, and dolomite has not yet been evaluated.

Dolomite is a common constituent of carbonate reservoirs, cementing pores, replacing primary or secondary constituents, or even wholly modifying their primary fabric (Machel, 2004; Warren, 2000). It plays a significant role in petrophysical properties, and its impact on permeability and porosity has been debated for decades (Ehrenberg *et al.*, 2006; Lucia, 2004; Mountjoy and Marquez, 1997). Luo and Machel (1995) studied aspects of dolomitization and its impact on capillary pressure mercury injection curves. Based on these data, they related the recovery efficiency from dolostones to the dispersion of pore throats. However, little has been done since then to understand the impact of dolomite on multiphase flow and oil retention in porous media. Therefore, we propose to model pore-scale textures of Brazilian Pre-salt *in-situ* post-rift (sag) reservoirs in order to perform numerical simulations to evaluate the impact of dolomite on oil trapping after waterflooding.

5.3   Geological Context

The Campos and Santos basins are located on the southeastern Brazilian margin (Figure 5-1). According to Moreira *et al.* (2007) and Winter *et al.* (2007), their stratigraphy is divided into three Super-sequences: rift, post-rift (sag), and drift. The continental deposits of the rift and post-rift (sag) stages were formed during the breakup of Gondwana, an event that precedes the drift deposits and the formation of the Atlantic Ocean (Austin and Uchupi, 1982; Nürnberg and Müller, 1991; Rabinowitz and LaBrecque, 1979). The Aptian post-rift (sag) deposits, focus of this study, cover the rift stage bivalve bioclastic limestones, shales, Mg-clay ooids arenites, hybrid rocks, volcanic rocks, sandstones, and siltstones (Armelenti *et al.*, 2016; Carvalho and De Ros, 2015; Chinelatto *et al.*, 2020b; Leite, Silva e De Ros, 2020; Mizusaki, Thomaz Filho e Cesero, 1998; Rehim *et al.*, 1986; Thompson, Stilwell e Hall, 2015).
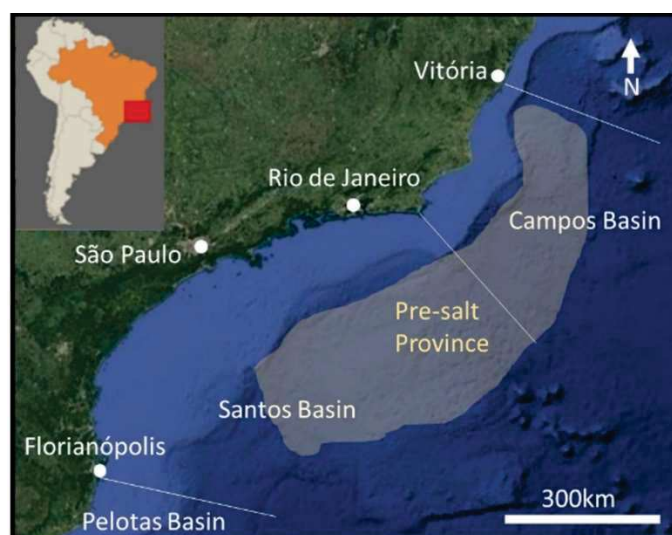
Figure 5-1 - Map illustrating the location of the Brazilian Pre-salt Province and the Campos and Santos basins (reproduced from Herlinger et al. 2020).

The sag deposits were formed in an alkaline lacustrine environment, which favored the syngenetic precipitation of Mg-clays in close relationship with calcite shrubs and spherulites (Carvalho *et al.*, 2022; Gomes *et al.*, 2020; Herlinger, Zambonato and De Ros, 2017; Netto *et al.*, 2022; da Silva *et al.*, 2021). In addition, intraclastic rocks formed by fragments from *in-situ* accumulations represent important reservoirs (Barnett *et al.*, 2021). These sag deposits are covered by evaporites that mark the beginning of the marine sedimentation of the Brazilian marginal basins.

Magnesian clays, represented mostly by stevensite, saponite, and kerolite, constituted the background of the sag lacustrine sedimentation. These clays are commonly associated with all facies as laminated matrix, ooids, or peloids and are present in both the *in-situ* and reworked

rocks (Carramal *et al.*, 2022; Carvalho *et al.*, 2022; Herlinger, Zambonato and De Ros, 2017). Rocks originally constituted by abundant Mg-clays are called mudstones (De Ros e Oliveira, 2023) or laminites and are not normally considered reservoirs. In these rocks, the Mg-clays were commonly replaced by microcrystalline calcite, dolomite, and/or silica The association between Mg-clays and calcite spherulites represents the most recurrent *in-situ* facies. These rocks are classified as spherulstones or muddy-spherulstones, according to the original proportion between spherulites and Mg-clays (De Ros e Oliveira, 2023). Spherulites are calcite fibro-radial aggregates precipitated during early diagenesis within the Mg-clays, displacing and replacing them. Since the Mg-clays are unstable, abundant secondary porosity is generated by their dissolution (Tosca and Masterson, 2014; Tosca and Wright, 2014; Wright and Barnett, 2015, 2020). In addition, the replacement of the Mg-clays by dolomite is common. The dissolution of the Mg-clays after their partial replacement by calcite spherulites and dolomite crystals left these carbonates apparently "floating" in the secondary pores. Figure 5-2 illustrates common aspects of the spherulites and their relationships with the Mg-clays and with dolomite crystals.

The calcite shrubs are fibrous aggregates with predominantly vertical orientation and increasingly divergent extinction, in a feathery habit also known as fascicular-optic (Kendall, 1977). Typically, such shrubstones (*sensu* De Ros e Oliveira, 2023) were formed by calcite shrubs that coalesced vertically and horizontally, forming crusts (Carvalho *et al.*, 2022; Gomes *et al.*, 2020b; Herlinger, Zambonato and De Ros, 2017). In some cases, as with the spherulites, the shrubs were formed displacing and replacing the Mg-clays matrix. Hence, clay peloids or laminations are frequently included inside the shrubs, as well as fill the spaces among the shrubs.

Dolomite is the most important component in the interstitial spaces of the shrubstones, filling the primary porosity or replacing Mg-clays, as in the spherulstones. Spherulites and shrubs are commonly associated in shrub-spherulstones (De Ros and Oliveira, 2023). Figure 5-3 shows the relevant relationships between shrubs, matrix, and dolomite. Crusts essentially made of shrub framework usually contain primary porosity. Shrubs that were formed within the Mg-clay matrix may be separated by larger spaces. As in the spherulstones, the Mg-clay matrix among the shrubs was commonly partially replaced by dolomite crystals. After the dissolution of the clay matrix, a floating pattern can be seen in the interstitial dolomite. Furthermore, dolomites may also have lined primary pores among shrubs of the crusts, covering the surface

of the shrubs, as seen in Figure 5-3c. Figure 5-4 exhibits a schematic evolution for the *in-situ* Pre-salt rocks, including the interrelationships of Mg-clays, calcite shrubs and spherulites, and dolomite.
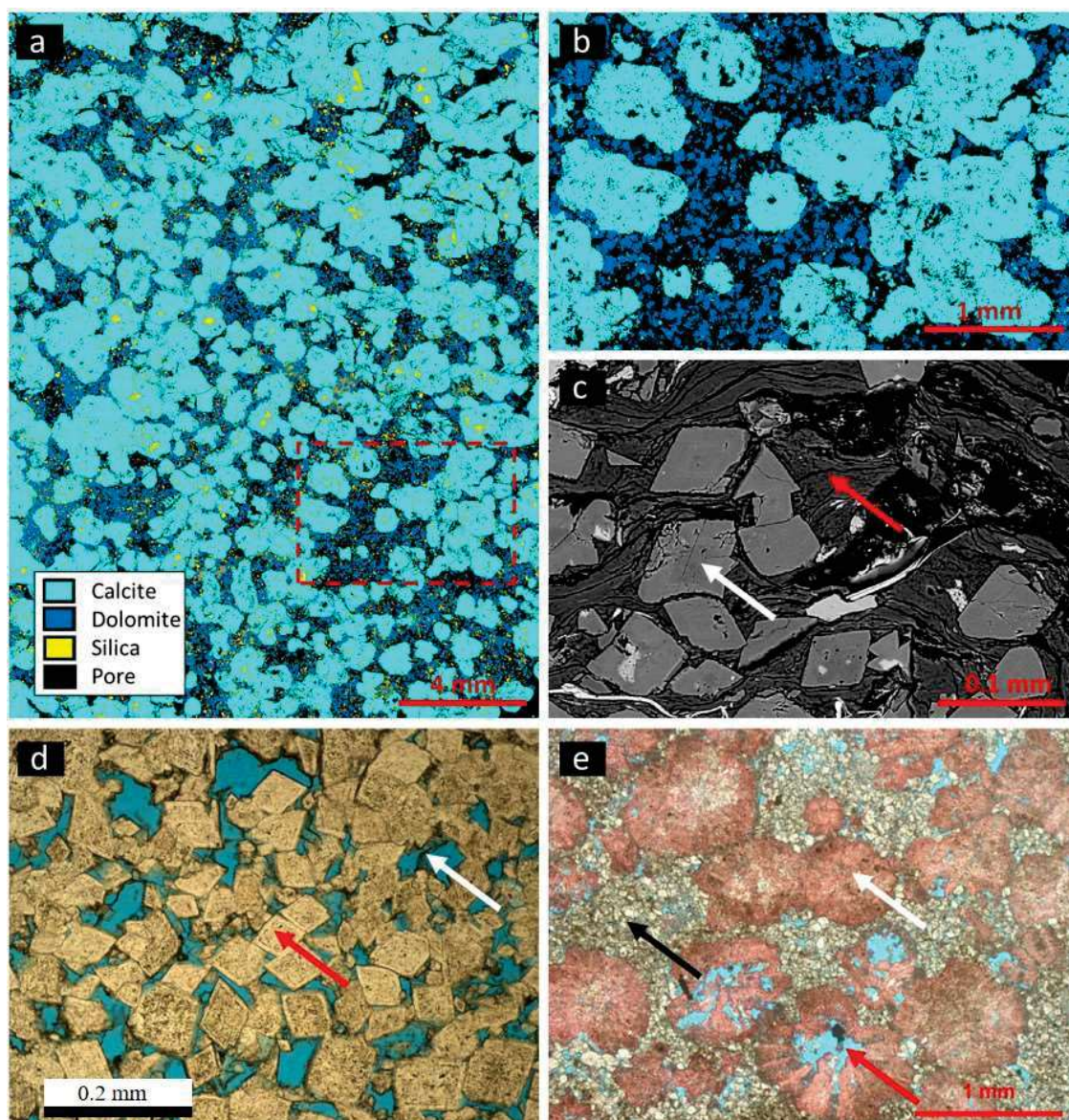
Figure 5-2 – a) QEMSCAN image illustrating a spherulstone composed of calcite spherulites locally replaced by silica. The porosity was generated by the dissolution of the Mg-clays matrix within which calcite and dolomite were formed, resulting in the "floating" pattern of spherulites and dolomite. The dashed rectangle is seen in detail in figure b. Silica and other minor phases have been omitted for a better understanding of the relationship between porosity, calcite, and dolomites. c) Backscattered electrons image of dolomite crystals (white arrow) that replaced partially Mg-clay laminated matrix (red arrow). d) Photomicrograph showing matrix-replacive dolomite crystals (red arrow), residual material from the dissolution of Mg-clay matrix (white arrow), and abundant intercrystalline porosity impregnated by blue-epoxy resin (uncrossed polarizers, //P). e) Photomicrograph exhibiting spherulites (stained pink; white arrow) and matrix-replacive dolomite (black arrow). The red arrow indicates intracrystalline porosity generated by the dissolution of the spherulites. (//P).
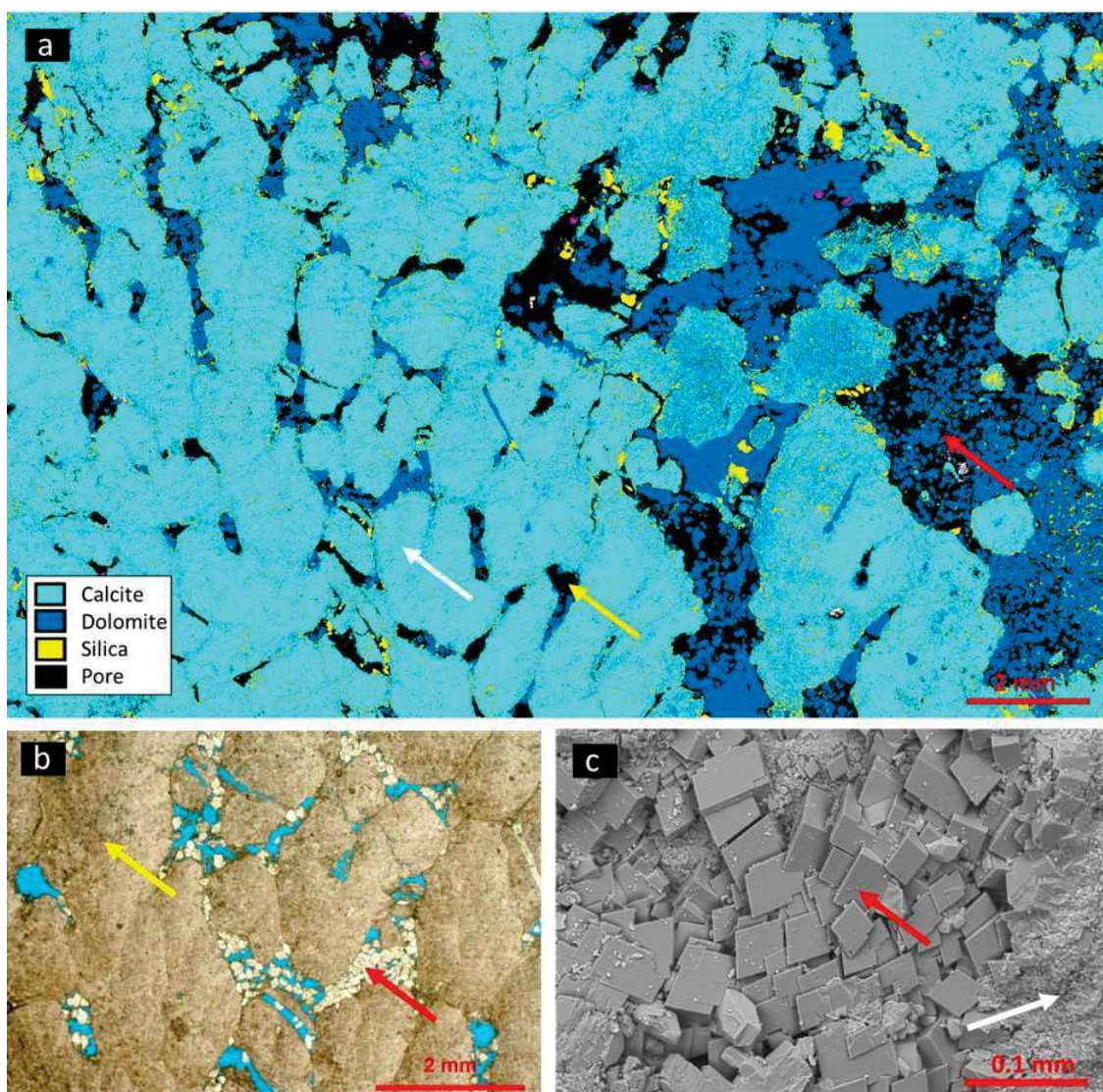
Figure 5-3 – a) QEMSCAN image showing a shrubstone formed by heterogeneously distributed calcite shrubs (white arrow). In the area with denser shrub development to the left, primary inter-shrub porosity was partially cemented by dolomite (yellow arrow). In the area with shrubs and spherulites growing within the original Mg-clays matrix to the right, intense dolomite replacement was followed by dissolution of the remaining Mg-clay matrix, forming a heterogeneous pattern of denser and floating dolomite (red arrow). b) Photomicrograph of calcite shrubs (yellow arrow) with growth-framework porosity partially filled by dolomite (red arrow) (//P). c) Secondary electrons image (SEI) of dolomite rhombohedral crystals (red arrow) partially covering the shrub surface (white arrow).

In addition to the rhombohedral matrix-replacive type, dolomite exhibits various timings and occurrences as indicated by numerous petrographic studies published in recent years (Herlinger et. al., 2017; Carramal *et al.* 2022; Carvalho *et al.* 2022) further corroborated by isotopic analyses (Godeau, 2021; Brito, 2024; Lima *et al.*, 2020). Nevertheless, the matrix-replacive type is the most commonly associated form of dolomite in reservoir contexts, both in the Santos and Campos Basins (Herlinger et. al., 2017; Carramal *et al.*, 2022; Carvalho *et al.*, 2022). Other dolomite forms, such as microcrystalline or bridge-like varieties (Rochelle-Bates,

2022; Brito, 2024), are typically unrelated to reservoirs facies. Furthermore, saddle dolomites tend to occur in localized settings, as do other forms associated with hydrothermalism or late-stage precipitation (Herlinger et. al., 2017; Lima *et al.*, 2020). Consequently, our study focuses on rhombohedral matrix-replacive dolomite, which is more commonly linked to reservoir occurrences.
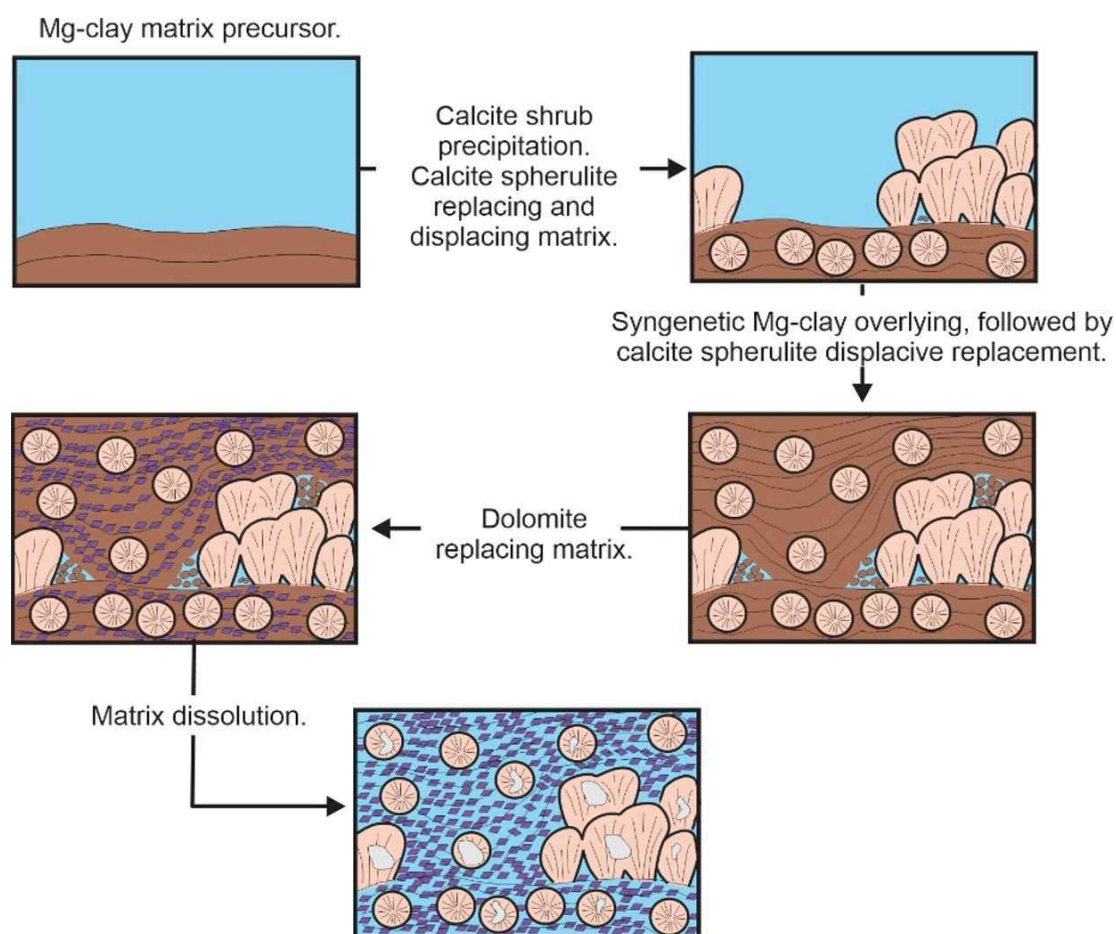
Figure 5-4 – Schematic evolution of Pre-salt in-situ facies (modified from Herlinger et al. (2017)).

5.4 Petrophysical Properties

The *in-situ* rocks, as described above, were essentially formed by the syngenetic precipitation of different proportions of Mg-clays and calcite shrubs, followed by the eogenetic formation of spherulites and/or shrubs and dolomite. As Mg-clays are highly reactive, they were extensively replaced by the carbonates and later dissolved, generating the floating aspect of dolomite crystals and calcite spherulites. This evolution generated significant petrophysical differences, conditioning the pore systems of these rocks.

The mudstones or laminites, originally constituted by abundant Mg-clays, are normally not considered reservoirs. However, according to SCAL and RCAL data compiled from Santos Basin rocks (Herlinger *et al.*, 2023; Herlinger and Vidal, 2022), some Mg-clay mudstones suffered extensive dissolution, with porosity around 20 %, although with relatively low permeability, rarely exceeding 100 mD due to their small pores and narrow throats. These rocks tend to have highly homogeneous MICP data and Sor around 20 %.

The muddy-spherulstones and spherulstones tend to have porosity values similar to the porous mudstones. Conversely, their average permeability and Sor are around 100 mD and 25 %, respectively, with little variability observed in MICP data. Finally, the shrubs-rich facies often have lower porosity, but with permeability typically exceeding 100 mD, displaying a highly heterogeneous pore system, and Sor averaging around 30 %.

5.5 Methodology

5.5.1 3D Pore-scale Models

We have developed 48 3D pore-scale models using 1000^3 voxels to represent the characteristic Pre-salt *in-situ* facies. Our approach for rocks dominated by Mg-clays and spherulites was based on the conceptual model that considers that dolomites and spherulites were precipitated in the Mg-clays matrix, which dissolution left the carbonates with a distinctive "floating" appearance. The components' dimensions were chosen according to observations in thin sections and SEM images shown in several studies (Herlinger *et al.*, 2017, 2023; Lima and De Ros, 2019; Carramal *et al.*, 2022; Carvalho *et al.*, 2022). Although their dimensions may vary, matrix-replacement dolomites typically have an average side length of less than 100 micrometers. On the other hand, spherulites and, especially, shrubs can exhibit greater variability, ranging from tens of micrometers to millimeters. However, given the limitations of the models size due to computational costs, dimensions were chosen that would fit within the model without compromising the geometric representation of the pore space. Calcite spherulites were represented as spheres and with a mean diameter of 500 μm and a standard deviation of 50 μm, distributed into three percentages (43.2, 56.25, and 70.88 %). The dolomite crystals were positioned in the interstitial spaces previously occupied by Mg-clays and represented by cubes arranged regularly with little disturbance to optimize porosity and prevent crystal

overlapping. We have created 12 models considering the average spacing among the dolomite crystals of approximately 10, 14, 20, and 30 μm. Each dolomite model boasts a 50 μm side and 5 μm standard deviation. All spherulstone models were built with 1 μm resolution.

Additionally, we built models of shrubstones with three different volumes of calcite shrubs: 90.0, 80.10, and 70.26 %. The growth-framework porosity was filled with regularly-spaced cubes representing the matrix-replacive dolomite. The spacing between the dolomite crystals was around 15, 20, 30, 50, 70, 120, 160, and 175 μm, resulting in 21 models. We also created nine more models with heterogeneously arranged pore-filling dolomites, which were used to achieve porosity levels of 25, 15, 10, and 7.5 %. In the heterogeneous arrangement, the cubes are placed randomly and can overlap each other. The shrubs had a mean size of 750 μm, with a standard deviation of 75 μm, and the dolomites had a mean side of 50 μm and a standard deviation of 5 μm, just like in the spherulstone models. All shrubstones had a resolution equivalent to 2 μm. Figure 5-5 illustrates some examples of the 3D pore-scale models.

5.5.2   Simulations

The determination of Sor was performed in Geodict™ software (Geodict, 2024), using drainage and imbibition simulations through Quasi-Static Morphology (Hilpert and Miller, 2001), also known as Full-Morphology (FM) method. This method calculates the distribution of wetting and non-wetting phases at a specific capillary pressure. It operates on the assumption of a low capillary number, wherein the effects of gravitational and viscous forces are negligible, and a well-defined contact angle exists between the phases. In this way, the replacement of the non-wetting phase by the wetting phase is controlled by factors such as surface tension, contact angle, capillary pressure, and minimum pore access radius, which are interconnected by the Young-Laplace equation:

$$r = \frac{2\sigma cos\theta}{Pc} \qquad (5.1)$$

Where r is the pore radius, σ the interfacial tension, θ is the contact angle, and Pc is the capillary pressure. All simulations assumed a temperature of 80° C and surface tension of 0.03 N/m. The fluids used for brine and oil had the following properties: density of 1.14 kg/m³ and 0.7 kg/m³, dynamic viscosity of 3.41 x 10^{-4} kg/m s and 2.99 x 10^{-7} kg/m s, and kinematic viscosity of 2.8 x 10^{-6} m²/s and 2.99 x 10^{-7} m²/s, respectively. For water-wet conditions, the model was initially saturated with water and then drained by oil until irreducible water

saturation (Sw$_{irr}$) was reached, using a contact angle of 60°. Imbibition was then modeled starting from Sw$_{irr}$ until the oil saturation stabilization, computed as the Sor of the rock. In oil-wet conditions, the brine drained the oil-saturated material with a contact angle equivalent to 120° until the water could not remove the oil.
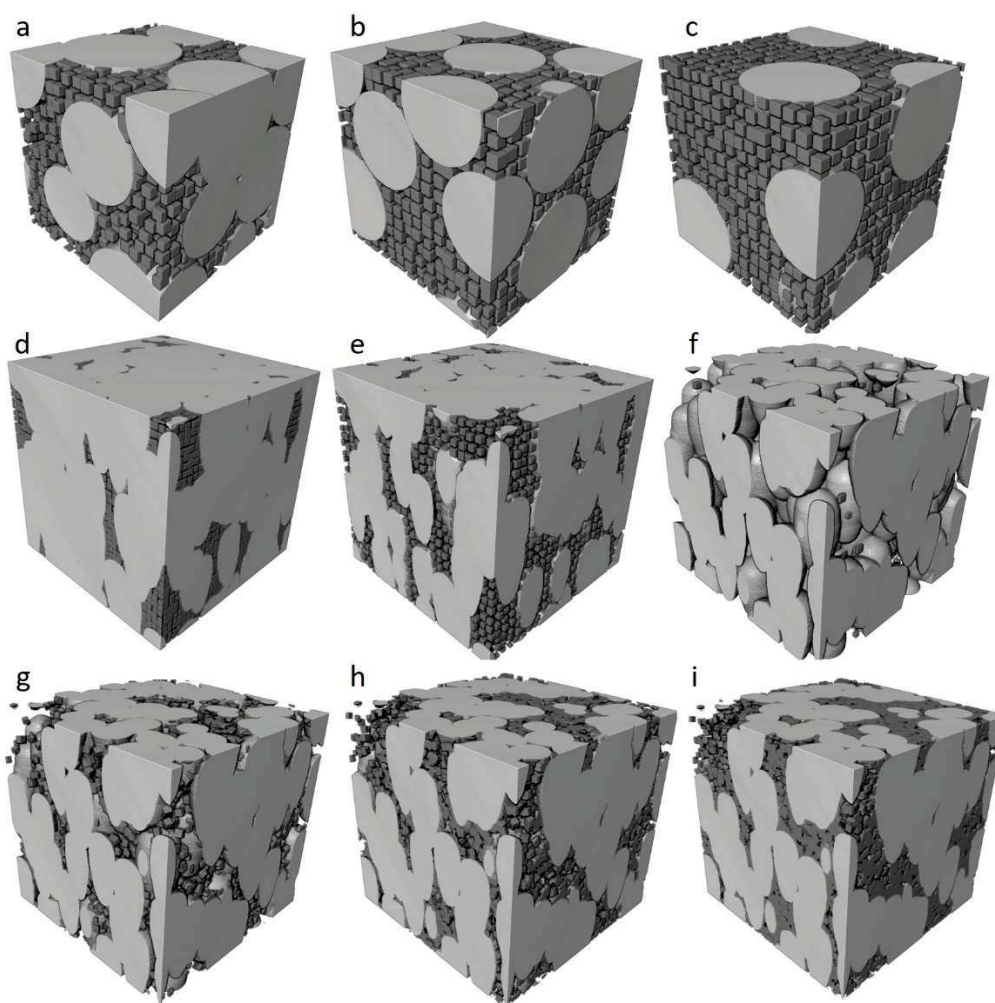
Figure 5-5 – Examples of models of spherulstones (a and b) and muddy spherulstone (c), shrubstones with different proportions of calcite shrubs and regularly-spaced dolomite crystals (d to f), and shrubstones with heterogeneous dolomite spacing (g to i). Models a to c have 1mm, and d to i has 2mm of side. Light gray are spherulites (a to c) and shrubs (d to i) of calcite, and dark gray are dolomites.

In addition to the waterflood simulations, tortuosity, surface area, and the distributions of pores and pore throats were estimated in the Geodict 2023™ software. The pore size was calculated according to the maximum sphere that can be placed in the pore space; in other words, each voxel included in the sphere received the value of its diameter. The pore throats, in turn, were estimated in the same way as in the porosimetry by mercury injection capillary pressure technique. If the pore is accessible from a small throat, then its voxels will receive the

diameter of the throat independently of pore size. Also, unconnected pores were not included for the throat distribution calculation. To calculate mineral surface area, the Crofton formula uses an integral over 1D rays that relate to the 3D surface area (Ohser and Mücklich, 2000). The surface area can be determined by analyzing the intersection points of rays in all directions with the structure. Finally, tortuosity considers the shortest path to be followed through the sample.

5.6   Results

The samples containing calcite spherulites and dolomite exhibit porosities ranging from 8.9-35.9 %, with a dolomite proportion of 10.2-40.4 %. The pore throat distributions had a P50 range of 9.1-34.1 µm, while P10 and P90 ranged from 4.3-16.6 µm and 13.4-43.6 µm, respectively. The pore size was slightly larger than the throats, with mean P10, P50, and P90 of 9.7 µm, 20.1 µm, and 29.9 µm, respectively. The average tortuosity was around 1.07, with a maximum ranging from 1.16-1.22. The surface area increased progressively with the addition of dolomite, ranging from around 15,000 m²/m³ to 38,000 m²/m³. The average Sor in water- and oil-wet conditions was 22.6 % (15.4-31.8 %) and 16.5 % (7.8-27.3 %), respectively.

The models made only with calcite shrubs had a mean P10, P50, and P90 pore throat distribution of 58.2 µm, 158.4 µm, and 317.5 µm, respectively. The pore size distribution's mean P10, P50, and P90 were 62.4 µm, 174.8 µm, and 329.1 µm. The tortuosity was proportional to the amount of calcite, with a mean of 1.4 and an average maximum of 1.8. The porosity of these models increased surface area, with measurements ranging from approximately 3,200-5,400 m²/m³. Finally, water-wet Sor was, on average, 28.3 %, while in the oil-wet condition, it was substantially lower, around 2.1 %.

The porosity of shrubstones made with regularly-spaced dolomites varied from 4.4-29.5 %, and the proportion of dolomite from 0.1-16.8 %. The pore throat distributions had a P50 between 13.3 µm and 169.4 µm, with P10 and P90 values ranging from 6.2 µm to 72.6 µm and 18.9 µm to 291.7 µm, respectively. The pore-to-throat were larger than the spherulstones and muddy-spherulstones, with mean P10, P50, and P90 of pore diameters of 28.6 µm, 66.6 µm, and 100.1 µm. The average tortuosity was roughly 1.43, and the maximum varied from 1.43-2.47. The surface area averaged approximately 8,700 m²/m³ (ranging from 3,282.96-19,436.85

m²/m³). The Sor in these samples was 27.9% and 11.1% for oil- and water-wet conditions, respectively.

Models made with calcite shrubs and heterogeneous-spaced dolomite had a mean P10, P50, and P90 of the distribution of pore throats from 6.0-32.8 µm, 17.6-67.7 µm, and 52-126.5 µm, respectively. The pore size distributions P10, P50, and P90 were from 8.5-33.9 µm, 25.0-79.7 µm, and 60.7-138.0 µm. Tortuosity ranged from 1.16-2.01, and the maximum ranged from 1.44-2.63 µm. Furthermore, the surface area ranged from around 3,250-12,500 m²/m³. Finally, the average Sor in water-wet conditions was approximately 33.7 %, while in oil-wet conditions, the value was around 10.8 %. For more information, please refer to Appendix F.
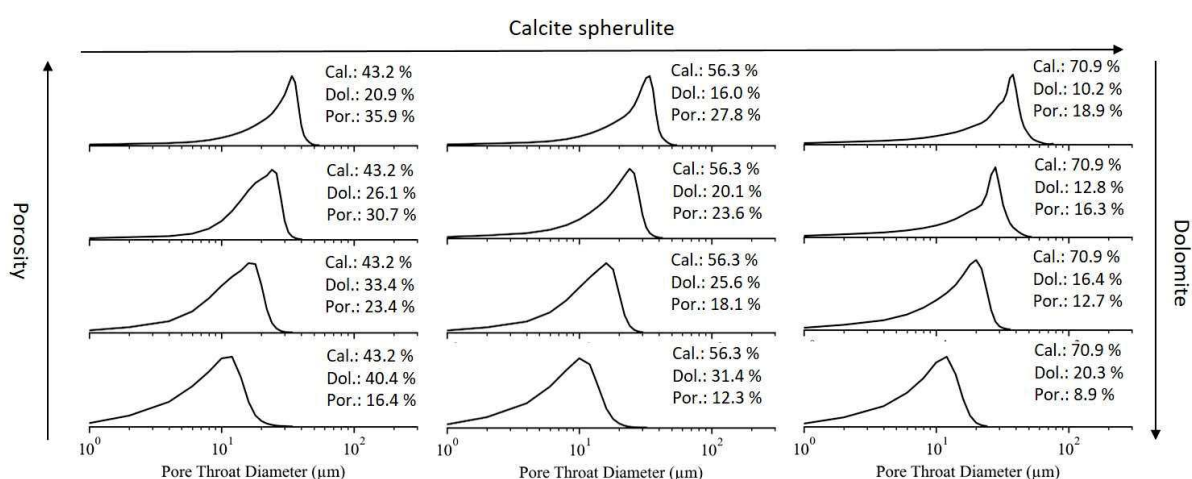
Figure 5-6 – Results of pore throat size distributions in models constituted by calcite spherulites and dolomite crystals. The figure correlates the increase in calcite and dolomite spherulites with porosity (as indicated by the arrows), and underscores their influence on the distribution of pore throats.

5.7 Discussion

Based on the analysis of pore throat distributions, the facies consisting of calcite spherulites and matrix-replacive dolomite show that the porous media are mostly dominated by intercrystalline pores generated by the dolomite framework (Figure 5-6). The volume of spherulites does not significantly impact the distribution of pore throats in the models. However, in models constituted by shrubs with small amounts of dolomite, the shrub fabric greatly impacts pore size distribution, resulting in a highly heterogeneous polymodal throat distribution (Figure 5-7). The increase in the volume of shrubs affects the heterogeneity of the pore systems, as models with larger shrub amounts tend to have broader pore-throat

distributions. As dolomite becomes more abundant, the pore systems become increasingly homogeneous, as observed in models with both regular and heterogeneous dolomite distribution, even though the heterogeneous dolomite distribution results in less homogeneous media (Figure 5-8). The predominance of intercrystalline porosity generates homogeneous pore-throat distributions, as observed in Brazilian Pre-salt dolostones (Herlinger *et al.*, 2023; Herlinger and Santos, 2018; Herlinger, Zambonato and De Ros, 2017). Furthermore, the increase in the amount of dolomite decreases the porosity and the pore throats, which contributes to the deterioration of the reservoir quality, as demonstrated in the seminal study of Wardlaw (1976).
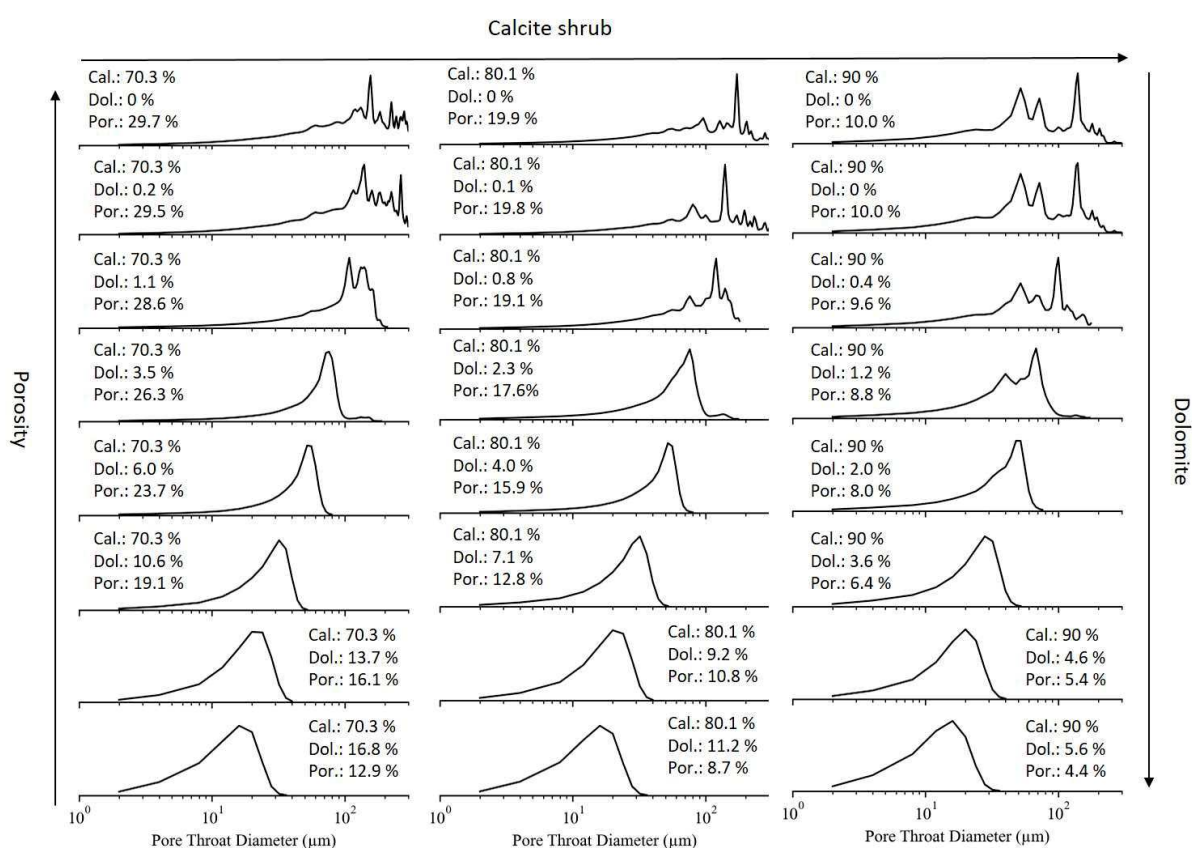
Figure 5-7 – Pore throat distributions of models built with calcite shrubs and regularly-spaced dolomite. The arrows indicate the relative variation in the quantity of spherulites, dolomite, and porosity, highlighting their impact on the pore-throat distributions.

When dolomite increases, pore throat size decreases (Figure 5-9a and b), negatively affecting the reservoir's quality. However, when pores are regularly arranged, the rate of decrease in the size of pores is greater than that of the throats (Figure 5-9c). This means that the increase of regularly-spaced dolomite can increase the throat-to-pore ratio, a crucial control on

the recovery or trapping of non-wetting phase by snap-off (Roof, 1970; Wardlaw, 1982; Wardlaw and McKellar, 1981). In other words, a high pore-to-throat ratio increases the trapping by snap-off. Conversely, irregularly arranged dolomites increase heterogeneity and the disparity between throat and pore sizes (Figure 5-9d). The impact of dolomite on tortuosity is generally minor, as the crystals are small and do not impede the flow significantly. In contrast, calcite, especially in the shrub habit, largely increases the flow path since the distribution of the large aggregates directly increases tortuosity (Figure 5-9e).
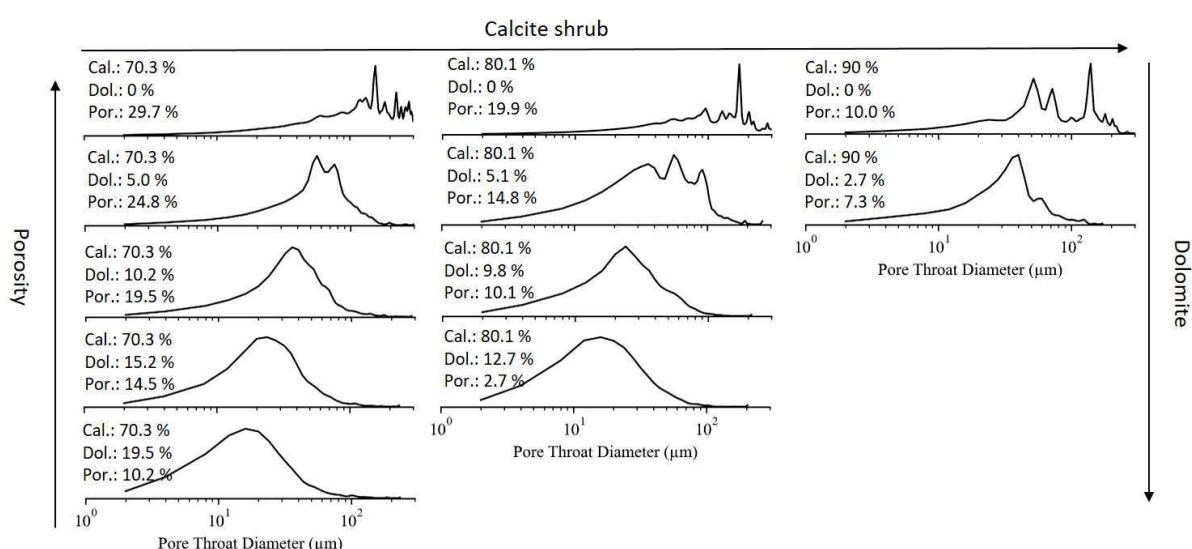
Figure 5-8 – Distributions of pore throats from models with calcite shrubs and heterogeneously-spaced dolomite. The arrows represent the relative changes in the amount of spherulites, dolomite, and porosity, emphasizing their effect on the pore-throat distributions.

The presence of dolomite, no matter whether regularly or heterogeneously distributed, has been observed to increase the surface area of the studied models. In models with regular dolomite, the rate of surface area increase remains consistent regardless of the facies or amount of calcite, highlighting the significant role of dolomite in enhancing the surface area (Figure 5-9f). However, models with heterogeneous dolomite exhibit more variability in surface area (Figure 5-9g), and a linear relationship is not apparent. At high dolomite volumes, the surface area tends to stabilize or even decrease, which may be attributed to the resolution of the models. Due to the resolution limitations, dolomites fill up the entire pore space, which should not be expected in natural media since dolomite probably would leave submicron pores and throats.
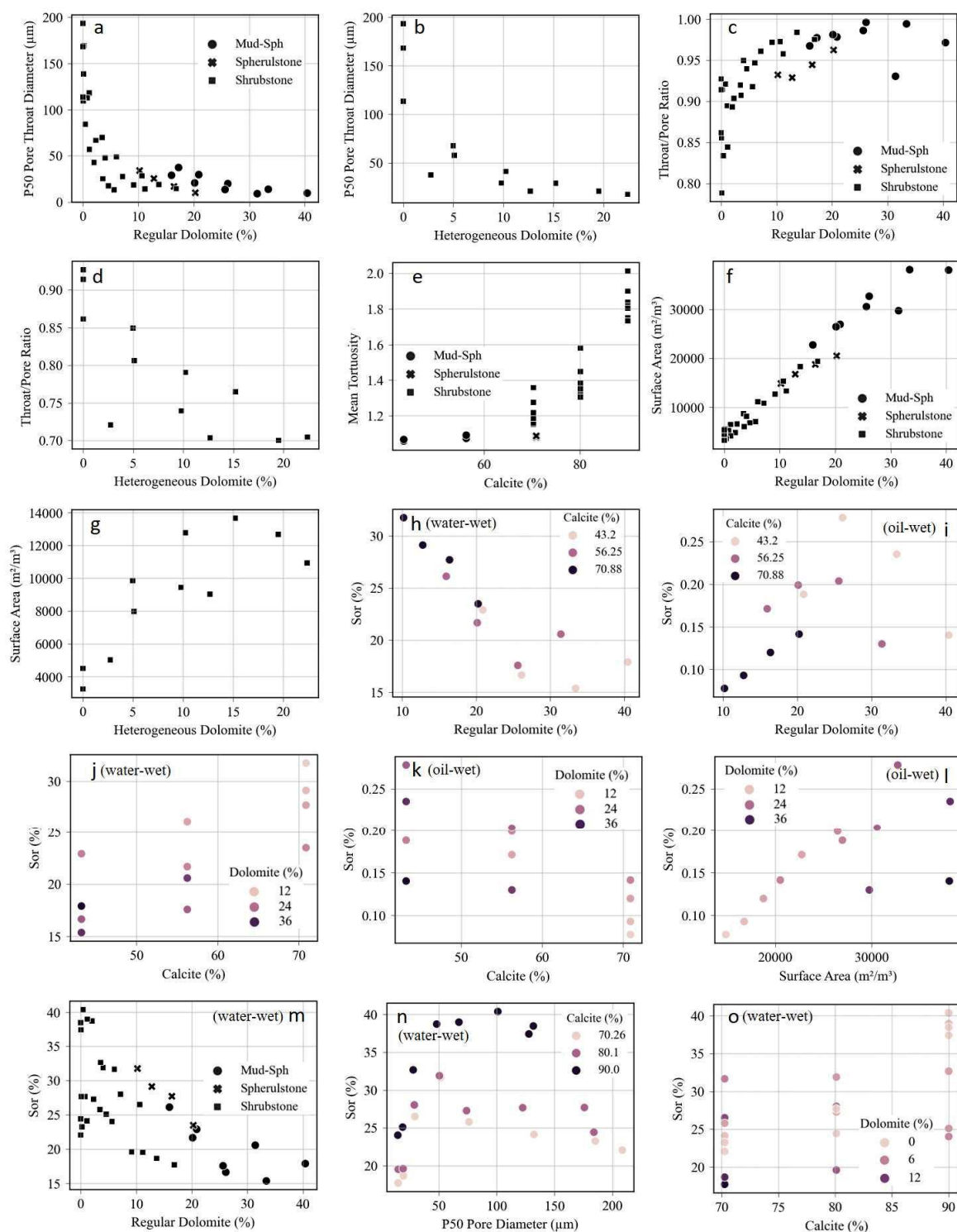
Figure 5-9 – Correlation between P50 pore throat diameter and regularly (a) and heterogeneously-distributed dolomite (b); pore-to-throat ratio vs. regular (c) and heterogeneous dolomite (d); mean tortuosity vs. calcite content (e); surface area vs. regular (f) and heterogeneous dolomite content (g); spherulstones and muddy-spherulstones Sor vs. regular dolomite amount at water- (h) and oil-wet (i) conditions; spherulstones and muddy-spherulstones Sor vs. calcite at water- (j) and oil-wet (k) conditions; Sor vs. surface area spherulstones and muddy-spherulstones at oil-wet conditions (l); Sor vs. regular dolomite at water-wet conditions; and finally, Sor vs shrubstones P50 pore diameter (n) and calcite (o) at water-wet conditions.

In the spherulstones and muddy spherulstones, the amount of dolomite clearly influences Sor under both water- and oil-wet conditions (Figure 5-9h and i). In water-wet conditions, Sor decreases significantly as dolomite increases, stabilizing at levels above 25 % of dolomite. This is because an increase in dolomite leads to a decrease in the pore-to-throat size ratio, thereby exerting a direct control over Sor in these rocks. Conversely, the trend is reversed in oil-wet conditions, although the relationship between dolomite and Sor is less definite. Spherulstone models with higher calcite content (70.88 %) show a marked increase in Sor with dolomite, while models with less calcite display parabolic behavior, with Sor increasing up to around 25% of calcite and declining thereafter.

Even though the calcite content correlates to Sor (Figure 5-9j and k), the amount of calcite spherulites does not seem to have a direct impact on oil trapping, as there is no strong correlation between Sor and tortuosity in these models, which should increase heterogeneity. On the other hand, calcite content does determine the volume of dolomite, with fewer spherulites allowing for more dolomite, which promotes homogeneity and facilitates oil recovery in water-wet simulations. Moreover, more dolomite leads to an increase in surface area that positively correlates with Sor up to a dolomite volume of approximately 25 % in oil-wet conditions (Figure 5-9l). Once the dolomite content reaches higher levels, the correlation no longer exists.

When shrubstones are in water-wet conditions, regularly-spaced dolomite tends to decrease Sor due to the homogenization and decrease in pore-to-throat size ratio, as seen in Figure 5-9c and m. In models with higher calcite content (around 90 %), Sor increases progressively with the increase of pores and throats sizes, until it stabilizes at values around 40 % Sor (Figure 5-9n). On the other hand, models with smaller amount of calcite have larger pores connected by large throats, resulting in lower Sor. In such models, calcite has a greater impact on Sor (Figure 5-9o), as it occurs in larger volumes of shrubs, progressively decrease the space between them, resulting in greater tortuosity and smaller pores and throats. Thus, larger calcite and smaller dolomite volumes may account for the higher Sor observed in shrubstones compared to other facies (Herlinger *et al.*, 2023).

In contrast to shrubstones with regular dolomite, models with heterogeneous dolomite produced conflicting results, as an increase in dolomite led to a higher pore-to-throat size ratio (Figure 5-9d), resulting in greater Sor. This differs from earlier studies (Herlinger *et al.*, 2023), which suggested that more dolomite leads to a more uniform system, and, thus, to lower Sor. Despite regularly-spaced dolomite arrangement seeming unnatural, it is a straightforward and

satisfactory method of depicting intercrystalline porosity resulting from clay dissolution. When the rock is oil-wet, there is a clear correlation between the size of the pores and throats and the Sor value. Rocks with higher amounts of dolomite tend to trap more oil (Figure 5-10). This trend is in contrast to the behavior observed in water-wet conditions.
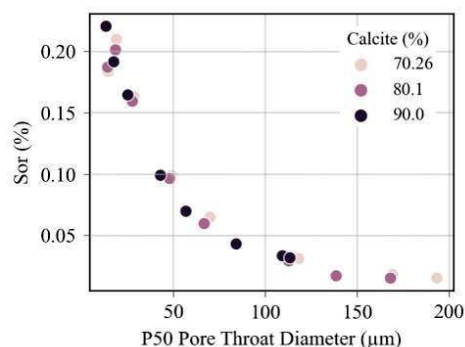
Figure 5-10 – Correlation between Sor and P50 pore throat diameter from shrubstones at oil-wet conditions.

In general, when it comes to water wettability, models with large and poorly-sorted pores tend to trap large oil droplets (Figure 5-11a). Conversely, regularly-spaced dolomite significantly alters the pore-to-throat condition, trapping oil in small isolated drops (Figure 5-11b). In oil-wet conditions, dolomite-free shrubstones have large throats, and oil is trapped in small amounts in constrictions and corners of the pore system (Figure 5-11c). Dolomite increases trapped oil under oil-wet conditions as bridges form between the crystals (Figure 5-11d). Heterogeneously-distributed dolomite results in more trapped oil in water-wet conditions, owing to greater pore system heterogeneity than with regularly-distributed dolomite. However, there are no significant differences in oil retention between the two dolomite modes under oil-wet conditions. To sum up, based on previous research concluding that the better reservoir facies have higher Sor, it is likely that most oil trapped in these rocks is related to snap-off under water- or mixed-wet conditions.

The results obtained indicate a clear link between deposition processes and diagenetic modification with hydrocarbon trapping in Pre-Salt reservoirs. Although clay-rich rocks often do not constitute reservoirs, areas with intense dissolution of Mg-clays can create conditions favorable for hydrocarbon storage. Therefore, the evolving diagenetic pattern, in addition to being crucial for hydrocarbon storage and flow, can influence the recovery factor of fields. In other words, it is observed that the presence of matrix-replacive dolomite may facilitate hydrocarbon sweep in facies where matrix dissolution occurred. However, these facies may

exhibit low permeabilities if dolomite precipitation was intense, which could impact well productivity. On the other hand, areas where the precipitation of shrubs was more intense tend to exhibit higher permeability, although they have a greater potential for oil trapping due to their higher pore complexity.
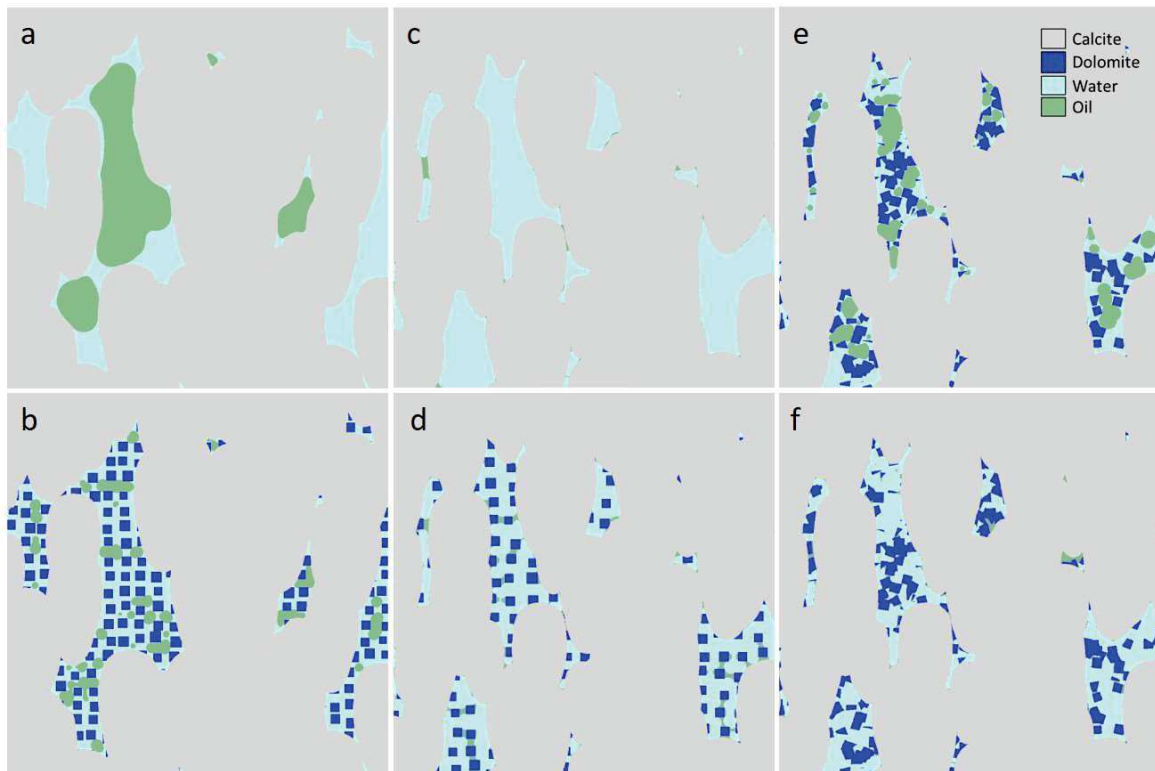
Figure 5-11 – Simulations demonstrating how dolomite amounts and distribution affect the saturation of oil and water in shrubstones under both water-wet and oil-wet conditions. Images a and b show the results of the water-wet simulation models free of dolomite (a) and with regularly-spaced dolomite (b). Models c and d depict oil-wet conditions. Finally, images e and f display heterogeneous-spaced dolomite in shrubstones under water- and oil-wet conditions.

5.8   Conclusions

After conducting pore-scale 3D modeling of *in-situ* facies from the Brazilian Pre-salt sag section, combining different proportions of calcite spherulites and fascicular shrubs, dolomite crystals and porosity, and characterizing the pore systems, we simulated imbibition and drainage processes under oil- and water-wet conditions. Our findings are as follows:

- The amount of dolomite significantly affects the pore systems of the models. An increase in dolomite content leads to a more uniform medium, a decrease in the pore-to-throat ratio, and an increase in surface area.

- The increase of calcite volume, especially in the form of shrubs, impacts the pore system heterogeneity and tortuosity. Furthermore, its increase can limit the possible amount of dolomite.

- The increase of dolomite in water-wet conditions decreases the residual oil saturation (Sor). However, in oil-wet simulations, increasing dolomite leads to an increase in oil entrapment.

- Based on previous research on the relationship between Sor, facies, and dolomite, it is probable that most of the oil trapped in the *in-situ* rocks is a result of snap-off under water- or mixed-wet conditions.

5.9   Acknowledgements

6. Article 5: HERLINGER, R.; KNACKSTEDT, M.; YOUNG, Y.; VIDAL, A. C. Coupling X-ray µCTs, BSE, and QEMSCAN Imaging to Unravel Details of Water Saturation and Oil Trapping in a Brazilian Pre-salt Carbonate Under Oil-wet Conditions. Tomography of Materials and Structures, submitted, 2025.

6.1 Abstract

We conducted drainage and imbibition cycles on a grainstone carbonate sample from the Barra Velha Formation of Brazil's Pre-salt integrating X-ray tomography, backscattered electron (BSE), and QEMSCAN to understand fluid saturation and oil trapping under oil-wet conditions at pore-scale. The integration of µCT imaging with BSE and QEMSCAN significantly enhances our understanding of fluid saturation within the pore system, particularly in regions where X-ray imaging alone encounters limitations. QEMSCAN imaging, beyond resolving microporosity, provides critical insights into the mineralogical factors influencing fluid distribution, offering a deeper perspective on the saturation controls. Following the drainage and aging cycles, oil effectively displaced nearly all brine within the interparticle macropores, relegating the brine to small, isolated droplets formed through snap-off processes. Additionally, a significant proportion of intraparticle micro and macroporosity was occupied by oil after drainage, with further oil saturation occurring during aging, demonstrating the rock's oil-wet affinity. Post-forced imbibition imaging revealed that nearly all the oil initially present in the interparticle macropores had been replaced by water, with only minor traces of oil remaining as thin films on mineral surfaces. Conversely, the intraparticle macro and micropores, which are typically less connected, retained most of the oil, highlighting the porous medium's tendency to trap fluids in poorly connected regions. Finally, our experiments did not reveal any substantial effect of mineralogical variations on fluid saturation during any phase of the cycles. This suggests that the observed oil-wet condition is independent of relative mineralogical variations, particularly given the sample's dominance of calcite and dolomite.

Keywords: Pre-salt, X-ray µCt, BSE, QEMSCAN, oil trapping

6.2 Introduction

Initially, it was believed that oil reservoirs were all water-wet. According to Anderson (1985) this belief was made because rocks were deposited in an aqueous environment. Thus, before oil migration, the mineral surfaces were all covered by connate water. This would prevent the oil from coming into contact with the mineral surfaces. However, Nutting (1934) observed that the Tensleep Sandstone had oil films that spontaneously formed again after removal by organic solvents. After this seminal study, several other reservoirs were described as oil-wet, especially carbonate reservoirs, as Treiber & Owens (1972) and Chilingar & Yen (1983) demonstrated. The latter authors compiled contact angle data for 161 carbonates and concluded that 80% of the rocks studied had a contact angle greater than 100 degrees, therefore classified as oil-wet.

Although classical contact angle measurement provides accurate information on the mineral surface's fluids affinity, it is measured on flat polished surfaces. In this way, the measurements do not take into account several factors that influence wettability and, consequently, the saturation of fluids in rocks, such as roughness (Chau *et al.*, 2009; Lam *et al.*, 2002; Morrow, 1975), which can favor water-wettability, or precipitation of crude oil organic heavy components, such as asphaltenes and bitumen, leading to oil-wettability (Alqam *et al.*, 2021; Kaminsky and Radke, 1997; Leontaritis and Mansoori, 1988). Moreover, the porous geometry and distribution of pore throats are of great importance, as the oil will struggle to replace water from small pores, thus the wettability inversion tends to be inhibited in microporosity. In addition to directly measuring contact angles, wettability is also commonly estimated indirectly by experiments that use drainage and imbibition cycles, relating the volume of displaced fluids to wettability (Amott, 1959; Donaldson, Thomas and Lorenz, 1969). Although useful and widely used, the Amot and USBM indices do not indicate where the oil and water fractions are, in other words, the configuration of fluids inside the porous media. Furthermore, these results are affected by porosity and permeability, since spontaneous imbibition processes tend to be more efficient in rocks with a well-connected porous medium (Isah *et al.*, 2023).

In the last two decades, with the advancement of X-ray µCT techniques, pore-scale imaging has made it possible to verify the configuration of fluids inside the porous media (Blunt, 2001; Wildenschild and Sheppard, 2013). As a result, there was a great increase in

knowledge regarding wettability, with the possibility of direct measurement of the contact angle (Andrew, Bijeljic and Blunt, 2014c; Singh, Branko and Blunt, 2016), the study of fluid saturation, and multiphase flow (Karpyn, Piri and Singh, 2010; Kumar, 2009; Wang *et al.*, 1984). These new observations together with increased computational capacity have driven the refinement of pore-scale flow simulation techniques (Blunt, 2017, 2001; Blunt, King and Scher, 1992; Valvatne and Blunt, 2004).

As aforementioned, reservoirs are initially filled with water. Therefore, it is assumed that they were originally water-wet (Bobek, Mattax and Denekas, 1958; Richardson, Perkins and Osoba, 1955). In this way, the collapse of water films and the adhesion of organic components on mineral surfaces can lead to oil affinity. According to Yao *et al.* (2021), the stability of the water film is related to the charges at the rock/water and water/oil interface, whose main control is pH. If both interface charges are similar, an electrostatic repulsion occurs between the interfaces, resulting in film stability. Otherwise, an attraction between the interfaces leads to the destabilization of the film. In carbonates, the net charge at the rock/water interface usually is positive, while the oil/water interface is negative for pH greater than 3, as studied by Hirasaki (1991). In this way, the water film is destabilized, and wettability inversion can occur by asphaltene interactions with the rock. Although asphaltene precipitation is commonly referred to as a wettability inverter, typically light and medium crude oils have a greater capacity for asphaltene precipitation when compared to heavy oils (Boer, de *et al.*, 1995; Leontaritis and Mansoori, 1988; Shikhov, Li and Arns, 2018).

Although mechanisms of oil entrapment in oil-wet rocks have been known and studied for many decades, their imaging is often challenging, as the oil is retained in discontinuous films or in microporous areas that are commonly below the resolutions typically obtained by μCT X-ray techniques and commonly are blurred by noise. On the other hand, secondary electron microscopy (SEM) images have submicrometer resolution with a very low noise level. Therefore, this work aims to understand the fluids saturation and oil entrapment in oil-wet conditions coupling X-ray μCT, SEM, and QEMSCAN images, relating them to petrographic features in particulate microporous carbonate from the Barra Velha Formation (BVF), Santos Basin, Brazil.

6.3   Geological Context

The Santos Basin is situated on the southeastern Brazilian coast between the Campos and Pelotas Basins, whose limits are the Cabo Frio High to the north and the Florianópolis High to the south (Figure 6-1). It has around 352,000 km^2 and is located practically all offshore. The Basin's sedimentation began with the rifting of the Gondwana supercontinent during the Early Cretaceous, which evolved into a passive margin during the formation and development of the Atlantic Ocean (Davison, 2007; Rabinowitz and LaBrecque, 1979; Szatmari, 2000; Turner *et al.*, 1994). The Basin's stratigraphy is divided into three Supersequences (Moreira *et al.*, 2007): Rift, Post-rift, and Drift (Figure 6-2).
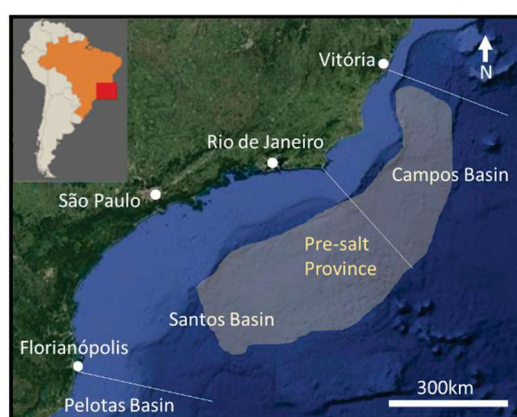
Figure 6-1 - Approximated localization of the Santos Basin and the Pre-salt Province. (Reproduced from Herlinger et al., (2020)).

The sample studied belongs to the BVF, whose reservoirs host the largest oil accumulations in the Brazilian Pre-salt. The BVF, deposited during the post-rift stage, covers the Itapema Formation stratigraphically located in the Rift Supersequence. The Itapema Formation is composed of thick bioclastic deposits known as Coquina (Carvalho Antunes, de, Guerrero and Jahnert, 2024; Chinelatto *et al.*, 2020b; Rocha, Favoreto and Borghi, 2021), whose analogs in the Campos Basin have had significant production since the 1980s (Baumgarten, 1985; Baumgarten *et al.*, 1988; Bruhn *et al.*, 2003; Horschutz and Scuta, 1992; Thompson, Stilwell and Hall, 2015). BVF is separated into Lower and Upper by the Intra-Alagoas unconformity. It is covered by the Ariri Formation formed by a thick package of evaporites deposited during the first marine incursions that mark the beginning of the drift phase of the Santos Basin (Moreira *et al.*, 2007).

My	Geochronology			Stratigraphy		Unconformities	Tectonic
	Epoch	Stage	Local Stage	Group	Formation		Stage
	Lower Cretaceous	Aptian	Alagoas	Guaratiba	Ariri	Salt Base	Drift
120					Barra Velha	Intra-Alagoas	Pos-Rift
125		Barremian	Jiquiá		Itapema	Pre-Alagoas	
			Buracica		Piçarras		Rift
130		Hauterivian	Aratu		Camboriú	Top Basalt	

Figure 6-2 - Stratigraphy of the continental deposits of the Santos Basin (Moreira et al., 2007).

The *in-situ* lacustrine carbonate deposits of the BVF were formed by the precipitation of calcite crusts with fascicular-optical texture that are referred to as stromatolites or shrubstones (Gomes *et al.*, 2020b; De Ros and Oliveira, 2023; Terra *et al.*, 2010), together with laminites formed by calcite and microcrystalline dolomite. Associated with carbonate precipitation are Mg-clays (Netto, Pozo, Manuel, *et al.*, 2022; Netto, Pozo, M., *et al.*, 2022; Silva, da *et al.*, 2021), whose preservation and dissolution relationships play an important role in the compartmentalization and generation of secondary porosity in these reservoirs and Campos Basin analogs (Herlinger *et al.*, 2020; Herlinger, Zambonato and De Ros, 2017; Tosca and Wright, 2015; Wright and Barnett, 2015, 2020). Finally, intraclastic rocks, such as the one we are using in this work, were formed from intraclastic particles predominantly originating from the fragmentation of *in-situ* rocks (such as calcite shrubs and spherulites, and laminites), Mg-clays ooids and peloids, and siliciclastic grains (Barnett *et al.*, 2021; Herlinger *et al.*, 2023; Rossoni *et al.*, 2024). These intraclastic rocks constitute important reservoirs in the main fields of the Santos Basin (Barnett *et al.*, 2021; Rodríguez-Berriguete *et al.*, 2022).

6.4 Materials and Methods

6.4.1 Materials

The sample utilized in this study was extracted from a core and subsequently subjected to cleaning using the Soxhlet extraction technique for the removal of crude oil residues (API, 1998). The porosity of the sample, determined through the helium pycnometer method, was found to be 21.2%, while its density was measured at 2.71 g/cm². The cylindrical plug, taken from the core, has a diameter of 7.79 mm and a height of 25.67 mm. Before saturating the sample, the plug underwent plasma cleaning process, as described in detail by Kumar (2009). This technique, notable for its operation at low temperatures and the absence of chemical solvents, efficiently removes organic impurities that adhere to the mineral surfaces. The plasma cleaning restores the sample's original wettability by eliminating any residual organic compounds. The apparatus employed consists of a vacuum chamber connected to a radiofrequency generator and a water vapor supply line. When the water vapor is ionized within the chamber, the organic contaminants break down and are expelled in the form of H_2O, CO_2, and CO (Kumar, 2009).

The sample comprises a well-sorted, massive intraclastic grainstone, with sub-rounded particles averaging a radius of approximately 0.4 mm. Interparticle porosity is predominant, though reduced by rhombohedral dolomite cementation and compaction. The particles are occasionally replaced by dolomite, quartz, and alkali feldspar. Other diagenetic phases appearing as traces include pyrite, barite, dawsonite, rutile, and strontianite. Intraparticle dissolutions are abundant, with dimensions ranging from hundreds of micrometers to microporosity. In this study, we are assuming that all unsolved porosity by X-ray μCT imaging is considered microporosity, in other words, below our image resolution (3.57 microns). According to mineral mapping conducted with QEMSCAN, the sample comprises 93.4% calcite, 3.9% dolomite, 1.2% quartz, and traces of the minerals mentioned above. Figure 6-3 illustrates the general aspect of the rock.

The fluids used in the experiments comprise 1.5M sodium iodide (NaI) brine solution and a synthetic crude oil mixture. Synthetic crude oil contains 5% bitumen, 30% conventional crude oil, 30% n-hexadecane ($C_{16}H_{34}$), and 35% toluene. The SARA analysis of the oil reveals the composition as follows: 42.17% saturates, 38.12% aromatics, 3.95% resins, and 1.23% asphaltenes.
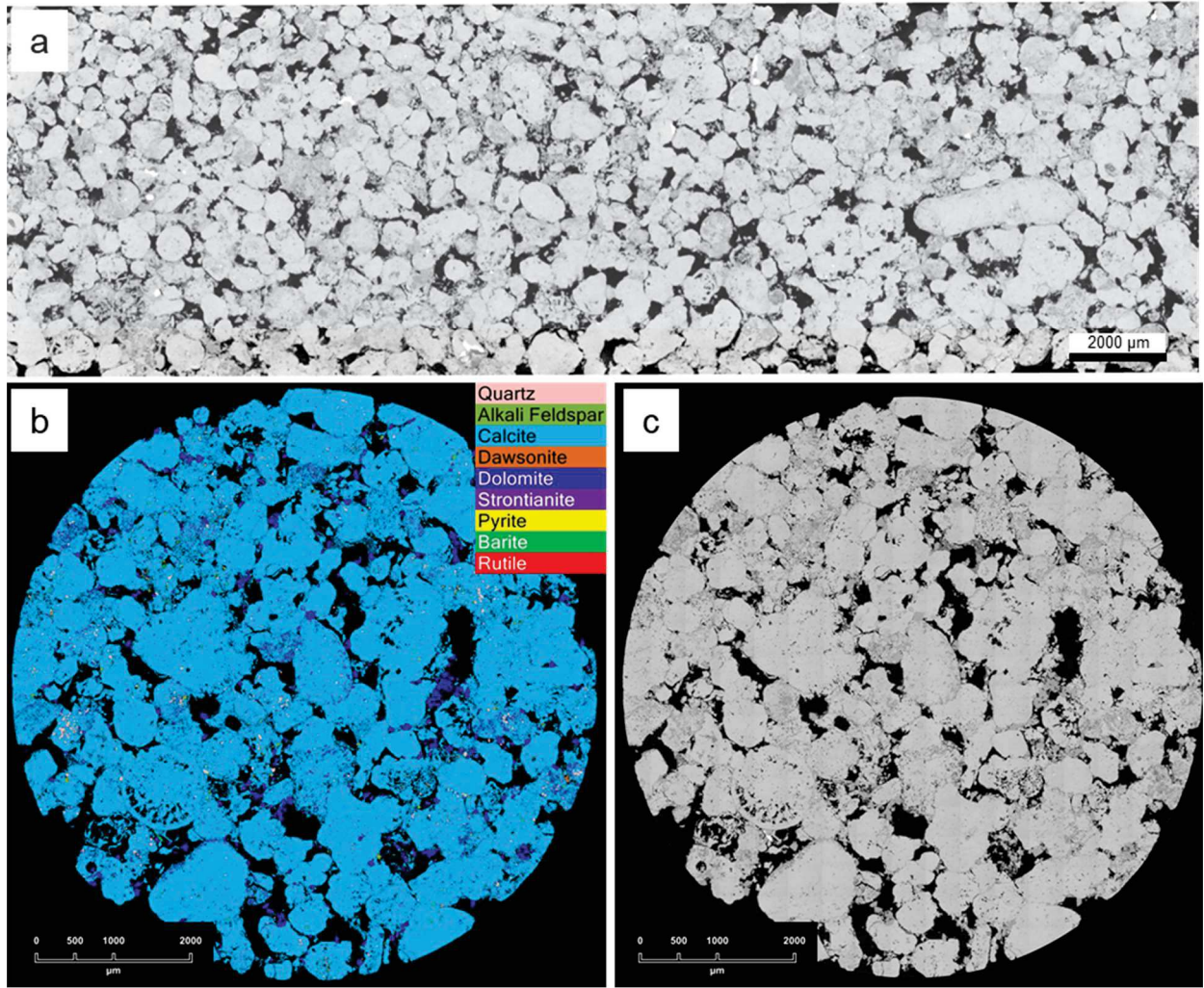
Figure 6-3 – X-ray µCT longitudinal slice (a), QEMSCAN (b), and BSE (c) images showing the aspect of the studied sample.

6.4.2 Methods

6.4.2.1 Experimental Procedure

The centrifuge method for fluid substitution and capillary pressure measurement was first introduced by Hassler and Brunner (1945) and later improved by Slobod *et al.* (1951). According to these authors, the capillary pressure (Pc) can be related to the rotation speed (ω), distance from the rotor center (r), and fluid density differences ($\Delta\rho$):

$$Pc = \frac{1}{2}\Delta\rho\omega(r_2^2 - r_1^2) \tag{6.1}$$

In a drainage/imbibition experiment, a saturated core plug is rotated at varying speeds while the displacing fluid replaces the saturating fluid. Fluid saturation is measured after equilibrium is reached, allowing the calculation of capillary pressure based on rotation speed. To reduce pressure variation along the core, the sample was flipped during rotation. Due to the small pore volume, the fluid volumes are hard to measure directly. In this way, saturation was determined using image processing. The stages of the experiment are referred to as drainage (water replaced by oil) and imbibition (oil replaced by water), consistent with laboratory wettability experiments (McPhee, Reed and Zubizarreta, 2015). The experimental procedure had the following steps:

1 - The sample was initially saturated with brine using a desiccator connected to a vacuum line to ensure thorough saturation. Subsequently, the sample was subjected to a pressing process to eliminate any entrapped air bubbles. This was achieved by applying a pressure of 560 bar for 48 hours.

2- Following the pressing process, the sample underwent its drainage phase by centrifuge. The sample was placed in a holder soaked in oil to perform the water replacement. The centrifugation was accomplished at a speed of 3000 RPM, which corresponds to a pressure of 11.52 psi.

3 - The next phase involved aging the sample in crude oil for a period of 16 days at a temperature of 60°C. During the aging process, the sample was X-ray imaged twice to monitor significant changes in saturation levels.

4 - Once equilibrium conditions were established, the sample was subjected to spontaneous imbibition. In this stage, the sample was immersed in brine for a period of 5 days at 60°C.

5 - Following this, the sample was submitted to forced imbibition in the centrifuge to replace the synthetic crude oil with brine. This process involved rotating the sample at two different speeds: 1000 RPM and 4000 RPM, corresponding to capillary pressures of 2.4 and 38.8 psi, respectively.

Throughout the experimental procedure, tomographic images were acquired at various stages to document the saturation changes in the sample. These stages included one image in the dry state, one image with the sample saturated with brine, one image after the first drainage, two images during the aging process (at 7 and 16 days), and one after spontaneous imbibition, and one image after each forced imbibition step.

6.4.2.2 Imaging

The images were acquired using a helical space-filling scanning trajectory, as detailed by Sheppard *et al.* (2014) and Kingstone *et al.* (2018). In each imaging session, the sample was hosted in a Polyether ether ketone (PEEK) tube and scanned for approximately 24 hours. The tube was filled with crude oil for imaging post-drainage and aging processes, and with brine during both spontaneous and forced imbibition phases. To reduce beam hardening effect, backscattering, and water radiolysis (Burns and Sims, 1981; Elnur and Alshibli, 2023), aluminum filters were utilized on the X-ray source to attenuate low-energy (soft) X-ray photons (Cullity and Stock, 2014; Naji *et al.*, 2016). Table 6-1 summarizes the acquisition parameters. Additionally, back-scattered electron (BSE) and QEMSCAN images were obtained from a polished section cut from the sample plug after the experimental procedures and subsequent cleaning by toluene for one week.

Table 6-1 - X-ray acquisition parameters.

	Dry and Saturated	Drainage, Aging, and Spontaneous and Forced Imbibition
Acquisition		
Mode	3040 x 3040 pixels	3040 x 3040 pixels
Exposure time (seconds)	0.4	0.4
Accumulations	12	12
Geometry		
Sample distance to source (mm)	9	9,1
Detector distance (mm)	350	350
Voxel size (μm)	3.574	3.614
Vision Field (X)	9.436	9.54096
Vision Field (Y)	9.436	9.54096
Vision Field (Z)	25.735	15.61248
Projections per revolution	3600	3600
X-ray		
Voltage (kV)	100	100
Current (micro ampere)	80	70
Aluminum Filter on Source (mm)	4	4
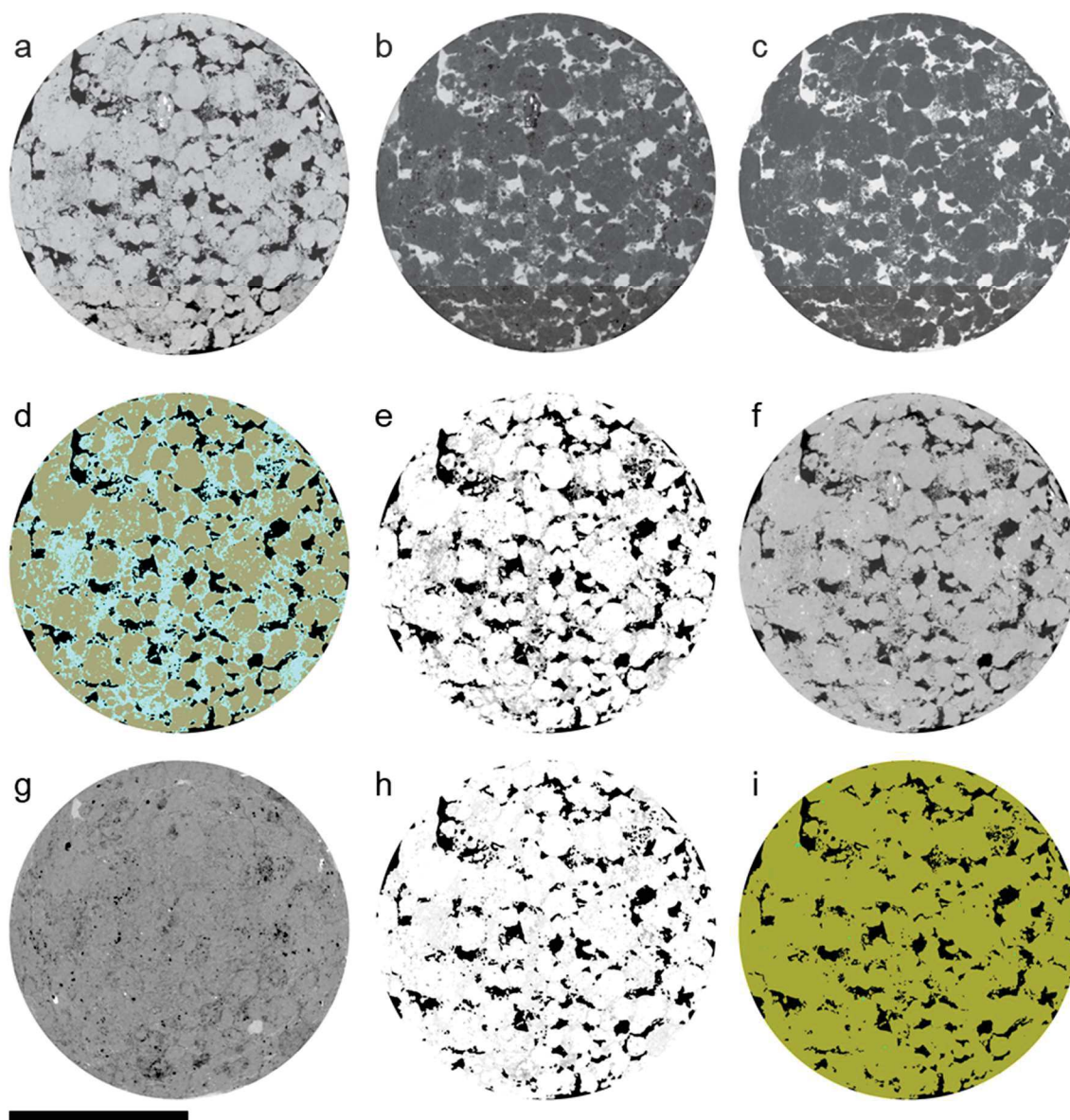
Figure 6-4 – Figure showing different steps of image processing (scale bar equals 4mm): dry (a) and registered brine saturated (b) images; c) difference between dry and saturated images, where lighter regions represent the influence of brine on X-ray attenuation; d) three-phase segmentation, including macropores (black), microporous (blue), and non-microporous minerals (olive); e) microporosity mapping, where darker values are higher values; f) registered drainage image; g) difference between dry and drainage images; h) water-filled microporosity mapping; and finally the segmented drainage image (i), showing that practically no water remained in macropores (oil in black and water in blue).

6.4.2.3 Image Processing

Following the reconstruction of the images, the µCTs were corrected to eliminate the beam-hardening effect. From a defined rotation axis (which should correspond to the experimental rotation axis) an average radial (distance from the rotation axis) intensity profile

was calculated. This profile is smoothed with a Gaussian function and then the µCT is normalized. Then, all the intensities are divided by this smoothed profile, therefore correcting the beam hardening artifact. Subsequently, all µCT, QEMSCAN, and BSE images were registered to the spatial coordinates of the dry image, by the methodologies described by Latham *et al.* (2008). Upon registration, the differential analysis between the dry image and the subsequent images was performed to evaluate subresolution porosity (Lin *et al.*, 2016), which in this study we relate as microporosity. This procedure effectively neutralizes attenuation discrepancies among minerals, thereby accentuating differences in saturation, including both visible pores and sub-resolution pore regions (Figure 6-4c).

Initially, three distinct phases were segmented using the differential images: macroporosity, microporous regions, and non-porous minerals (Figure 6-4d). The differential image was then utilized to quantify microporosity, specifically within the microporous regions. The other two regions were considered 0% microporous or macropore. It was posited that the smallest differences correspond to a microporosity of 0%, while the largest differences represent a porosity of 100% (Figure 6-4e). This approach facilitates the precise mapping of microporosity within the subsample.

Given that the attenuation intensity of crude oil is akin to that of air, it became feasible to assess the water-filled microporosity by analyzing the differential between the dry image and the images saturated with brine and crude oil obtained during the drainage and imbition phases (Figure 6-4f and g). Subsequently, the ratio between the microporosity map and the water-filled porosity map was used to determine the water saturation (Sw) within the microporosity for both drainage and imbibition images. Finally, Sw in the macroporosity was ascertained through segmentation using the converging active contours (CAC) method (Sheppard, Sok and Averdunk, 2004) (Figure 6-4i). With Sw values obtained for both macro and microporosity, the total Sw could be estimated. Finally, crude oil and brine were segmented directly on BSE and QEMSCAN pores, allowing an increase in resolution which gives a detailed configuration of fluids occupancy inside porous media (Figure 6-5).

6.5   Results and Discussion

6.5.1   Drainage and Aging

After centrifugation at 3000 RPM, equivalent to 11.52 psi, practically all the water from the macroporosity was drained. According to the segmentation of µCTs, the Sw in macroporosity was around 1.59%, located in droplets generated by water snap-off or in intraparticle macropores. On the other hand, the Sw in micropores was 26.24%, significantly higher than in the macropores, resulting in a total Sw equal to 8.10%. After aging in crude oil, a small decrease in macro and micro Sw was observed, 1.5 and 24.95% after 7 days, and 1.33 and 21.95% after 16 days, corresponding to a total Sw of 7.63 and 6.77%, respectively. This result indicated that the irreducible water was relegated to the micropores in both intraparticle and intracrystalline pores, even though most were filled with oil (Figure 6-6 and Figure 6-7).
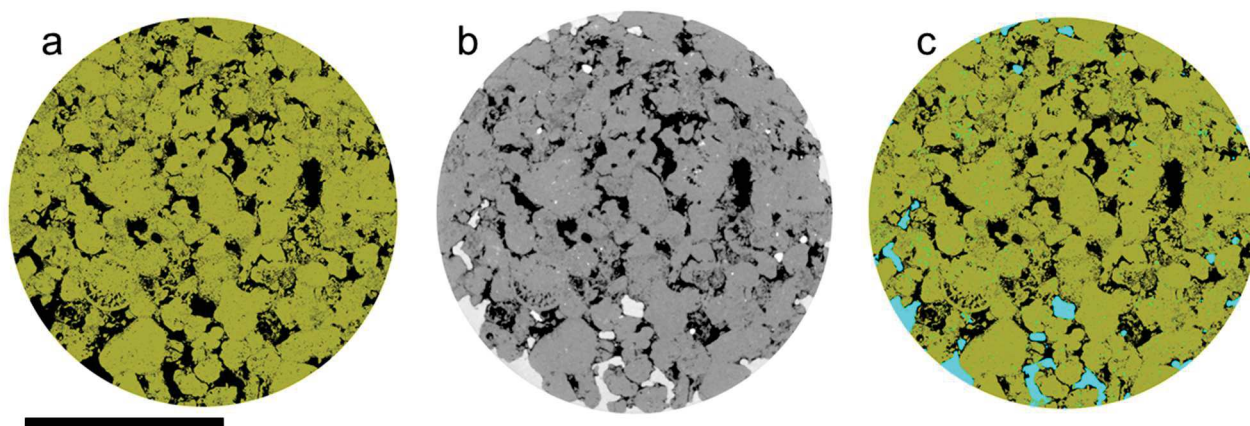
Figure 6-5 – Segmented BSE (a) and X-ray µCT (b) registration, and coupled two-phase oil/brine segmentation (c) (scale bar equals 4mm).

Water snap-off indicates affinity for oil, where most large pore surfaces were in contact with oil. No significant difference was observed in macro Sw during aging. This indicates that the water droplets were steadily trapped during drainage and were completely disconnected from the aqueous phase in the center of the pores.

After aging, part of the intraparticle pores becomes filled with oil (Figure 6-6). This indicates that even narrow throats can be reached by oil, resulting in brine drainage in the microporosity. This confirms the strong oil-wettability condition even in regions where the rock did not come into contact with oil during centrifuge drainage. The irreducible water is predominantly located in the micropores, hence the greater the macroporosity, which is mostly well-connected interparticle pores, the smaller the microporosity, and consequently, the lower the water saturation in the sample. Since macroporosity is directly related to total porosity (Figure 6-8a), we can correlate total porosity and Swi. In other words, the higher the total porosity, the lower the Swi (Figure 6-8b).
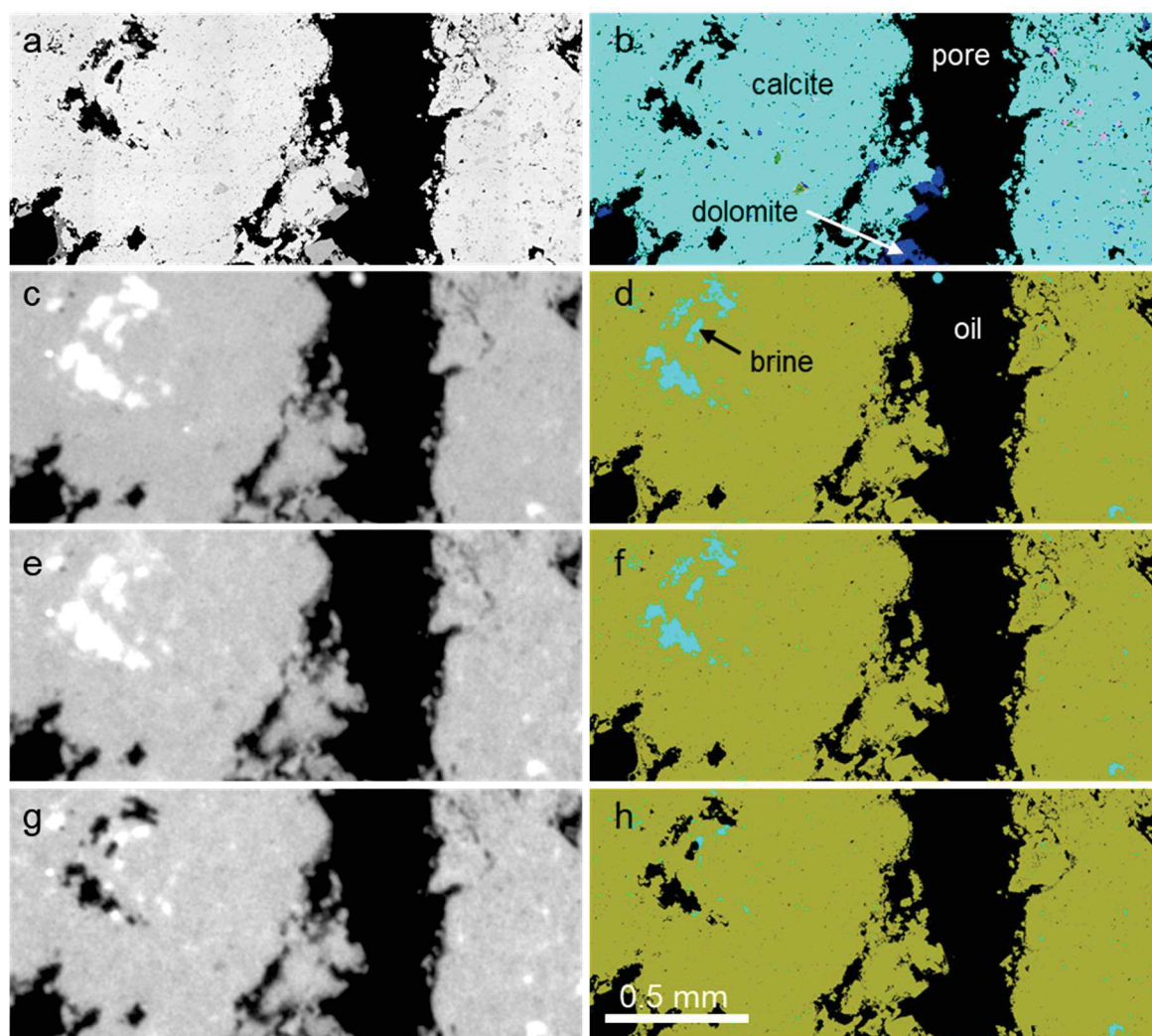
Figure 6-6 – Template showing details of the water replacement: a and b represent BSE and QEMSCAN images, while c, e, and g are X-ray μCTs after drainage and aging (7 and 16 days), and d, f, and h are the X-ray coupled BSE segmented images. The image sequence clearly shows the oil increase in intraparticle pores during aging.

The saturation profile across the sample does not show significant variation in Sw (Figure 6-7). Provided the maximum pressure is found at the face of the sample, a Sw gradient should be expected. Considering the sample was flipped during the test, an increase in Sw should be expected in the center of the sample, where the capillary pressure was lower. This indicates that the predominantly oil-wet behavior of the rock is more important in brine replacement by oil than the imposed capillary pressure to which the sample was subjected. This observation indicates that oil-wet reservoirs should have a thin or negligible transition water zone.
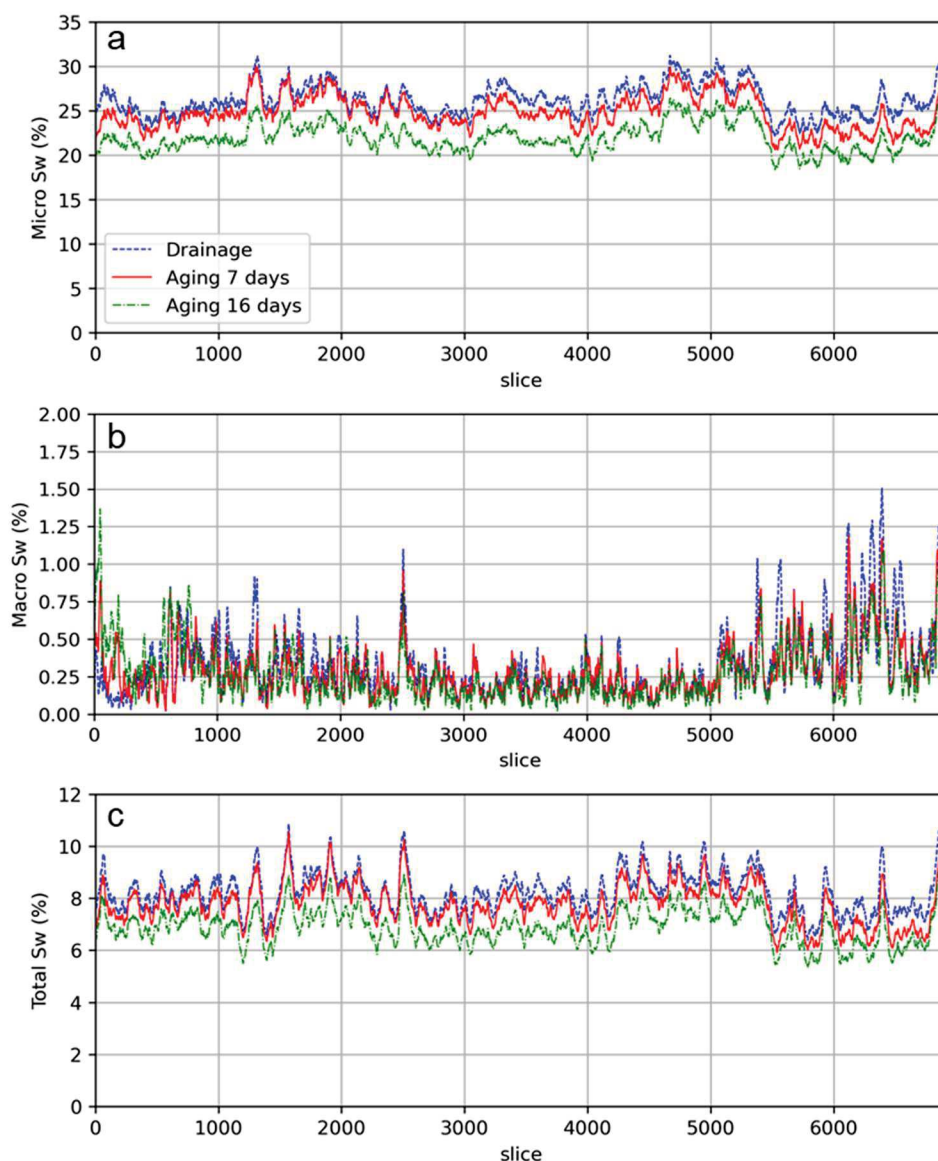
Figure 6-7 – Saturation profiles after drainage and aging, including micro (a), macro (b), and total Sw (c).

6.5.2   Spontaneous Imbibition

After spontaneous inhibition, the total Sw reached 21.45%, representing an increase of more than 10% compared to the Sw measured after drainage and aging processes. The macro Sw increased to 18.61%, while the micro Sw reached 28.05%. Although this process is referred to as spontaneous imbibition, we can see a typical oil drainage behavior (Figure 6-9). In the spontaneous imbibition stage, the sample was immersed (soaked) in brine within a test tube. Thus, despite being minimal, the pressure exerted by the brine column inside the test tube

(approximately 3 cm in height) is sufficient to displace some of the oil located within the macropores due to the wide pores and throats of this rock. Moreover, we can see that the water saturation is larger in the higher slices (Figure 6-10), which were at the bottom of the test tube during the spontaneous imbibition, asserting the impact of pressure on oil replacement, therefore assuring the oil-wet behavior speculated in the drainage step.
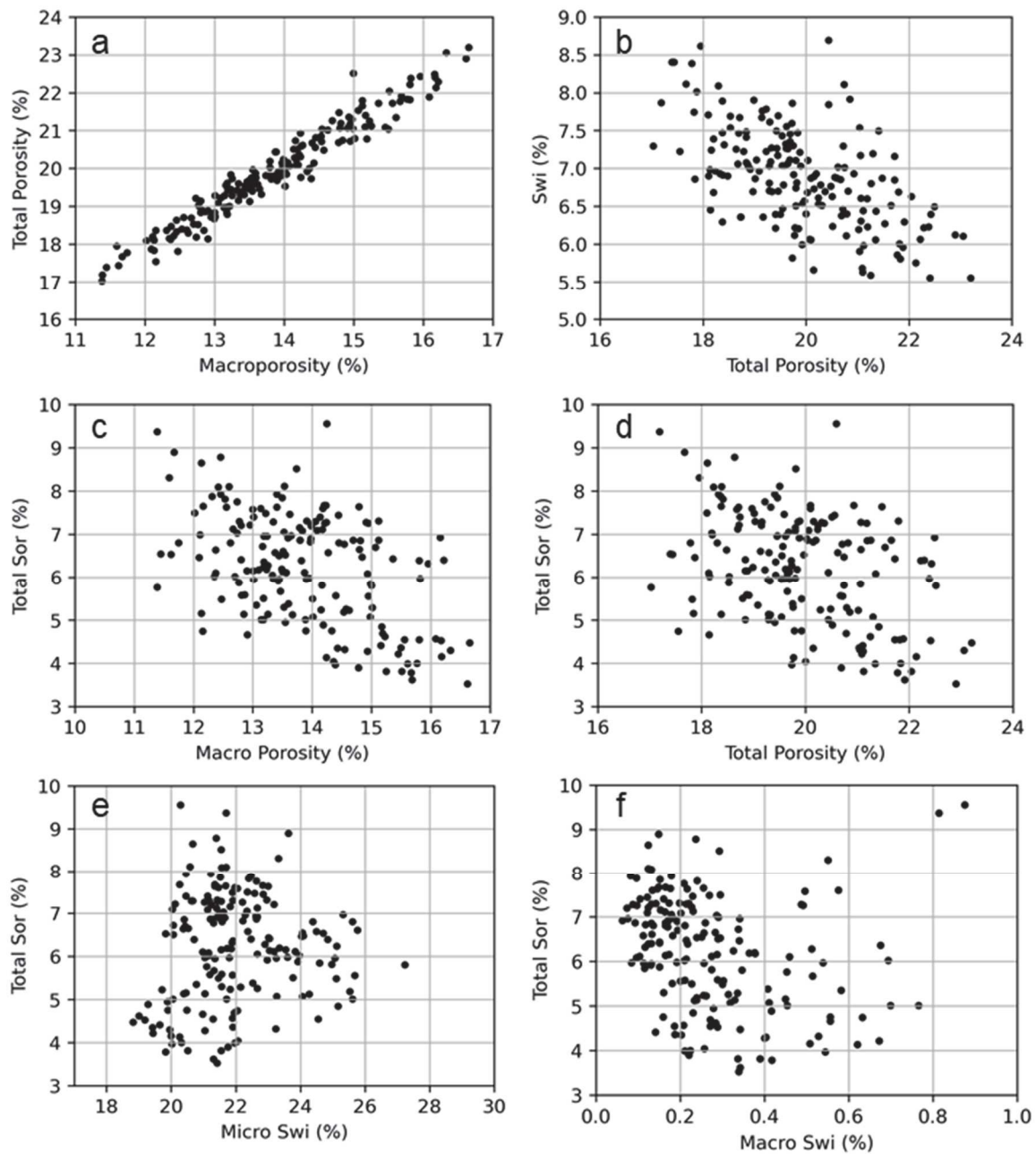
Figure 6-8 - Correlation between total and macroporosity (a), Swi and total porosity (b), and total Sor and macro porosity (c), total porosity (d), micro Swi (e), and macro Swi moving averages across the sample, calculated slice per slice.

Despite the modest increase of approximately 6% in the micro Sw (a relatively minor augmentation when juxtaposed with the macro Sw), no significant alterations were discerned in the coupled segmentation (Figure 6-9). Given that the Sw calculation is conducted utilizing μCT scans with a resolution of 3.6 microns, the interface between macropores and the mineral surface becomes blurred, which hinders the segmentation. Consequently, a considerable portion of this nebulous region is categorized as microporosity, thereby affecting the quantification of micro Sw. In essence, the observed decrease in micro Sw is, in reality, attributable to oil drainage within the macropores.
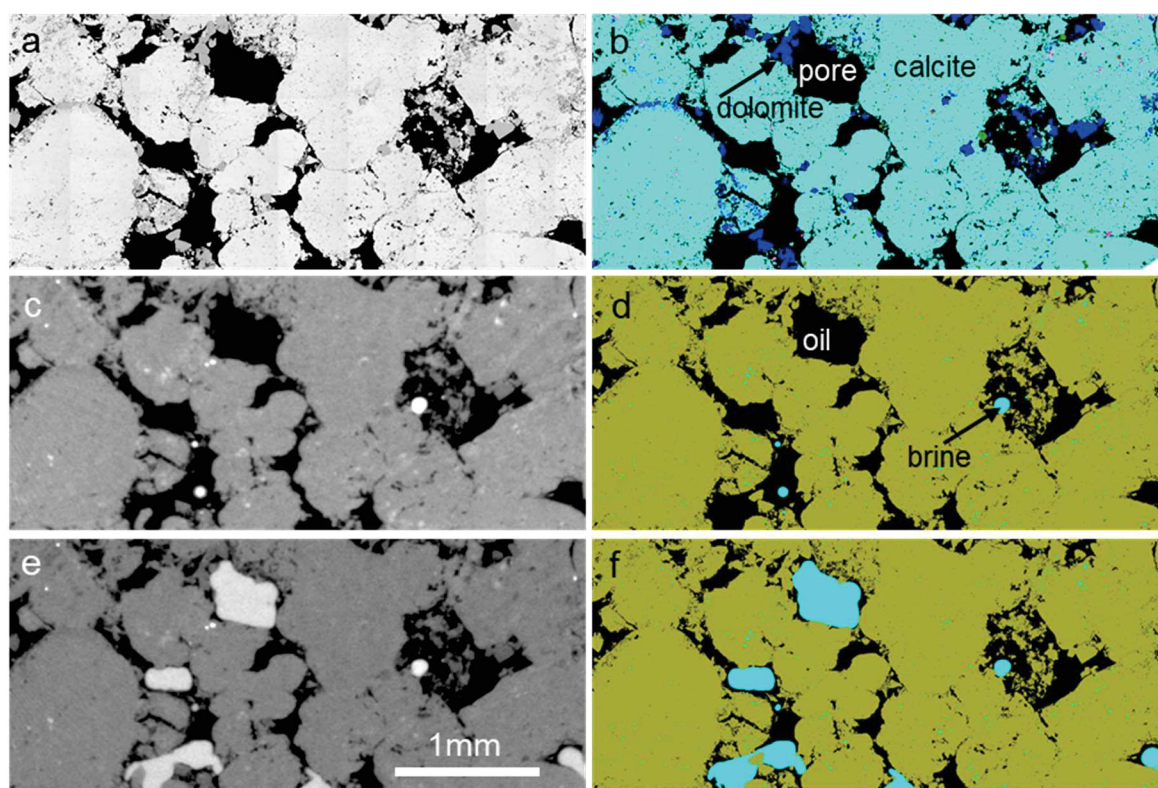
Figure 6-9 – Plot showing BSE (a), QEMSCAN (b), and X-ray μCTs before (aging after 16 days) (c) and after spontaneous imbition (e), and the segmented coupled BSE X-ray μCTs (d and f). In the aging images (c and d) we can see droplets of brine inside the pores trapped by snap-off. The last image pair (e and f) shows the replacement of oil by water in the center of the pores, while small intraparticle pores remain mostly unaltered.

The crude oil residing within the macroporosity was replaced by brine as the wetting phase, while only a minor fraction of the smaller pores, initially saturated with oil, was replaced by brine. This observation suggests that a small portion of the micropores exhibit water-wet characteristics. This underscores the fact that, despite the presence of a mixed wettability regime, the proportion of the rock wetted by oil in this sample is substantially greater than that

wetted by water. Consequently, given the oil affinity of the rock in this experiment, it can be classified as exhibiting an oil-wet regime.
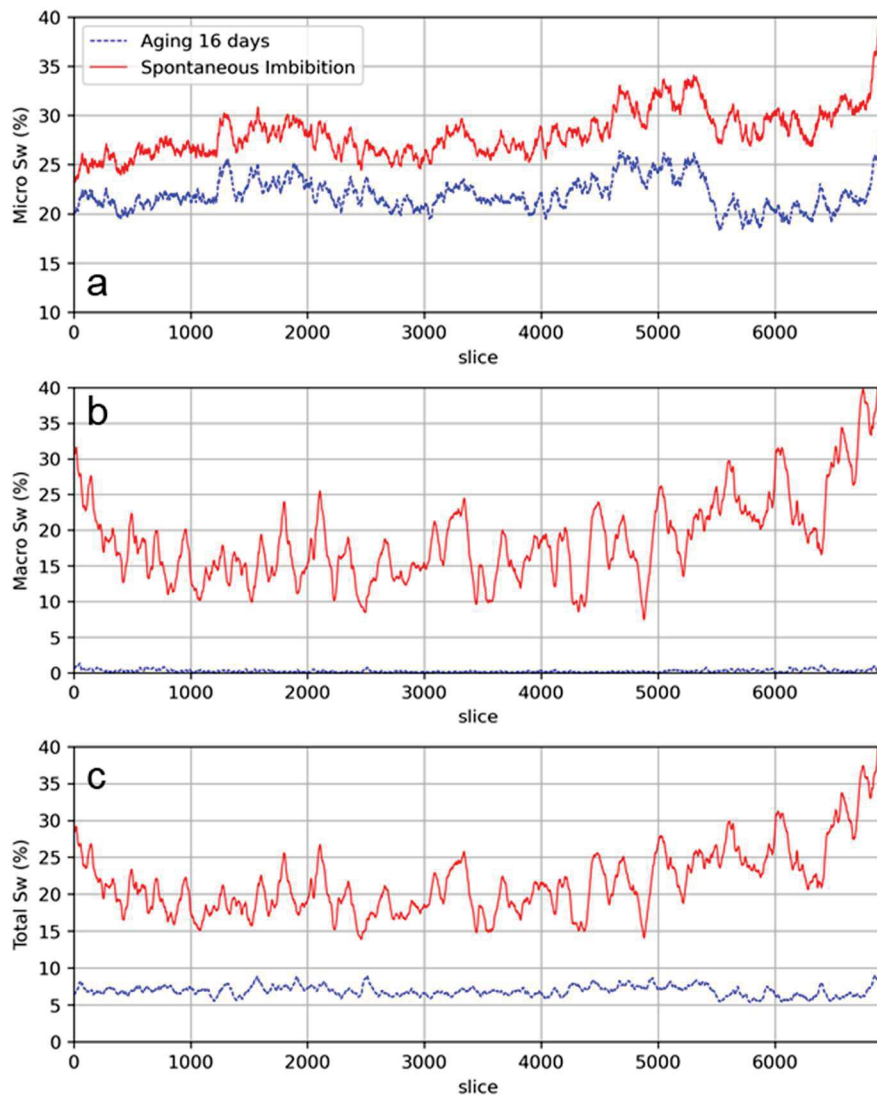
Figure 6-10 – Plots exhibiting the micro (a), macro (b), and total (c) Sw profiles before (aging after 16 days) and after spontaneous imbibition.

6.5.3 Forced Imbibition and Oil Trapping

Following the first forced imbibition step at an equivalent pressure of 2.4 psi, the macro Sw was 98.29%, while the micro and total Sw were 67.82% and 89.14%, respectively. The second step indicated micro Sw increasing to 80.53%, while macro Sw rose to 99.69%, resulting in a final Sw of 93.94%. The analysis of saturation profiles indicates that oil displacement in the macropores was highly efficient, with no clear saturation gradient observed due to capillary

pressure differences along the sample. This is likely because the pressure required for oil displacement in the macropores is quite low. Conversely, the saturation profile in the microporosity shows a distinct gradation, with higher Sw values at the center of the sample, indicating that the pressure necessary for oil removal in this region was not achieved. The saturation profiles are found in Figure 6-11.
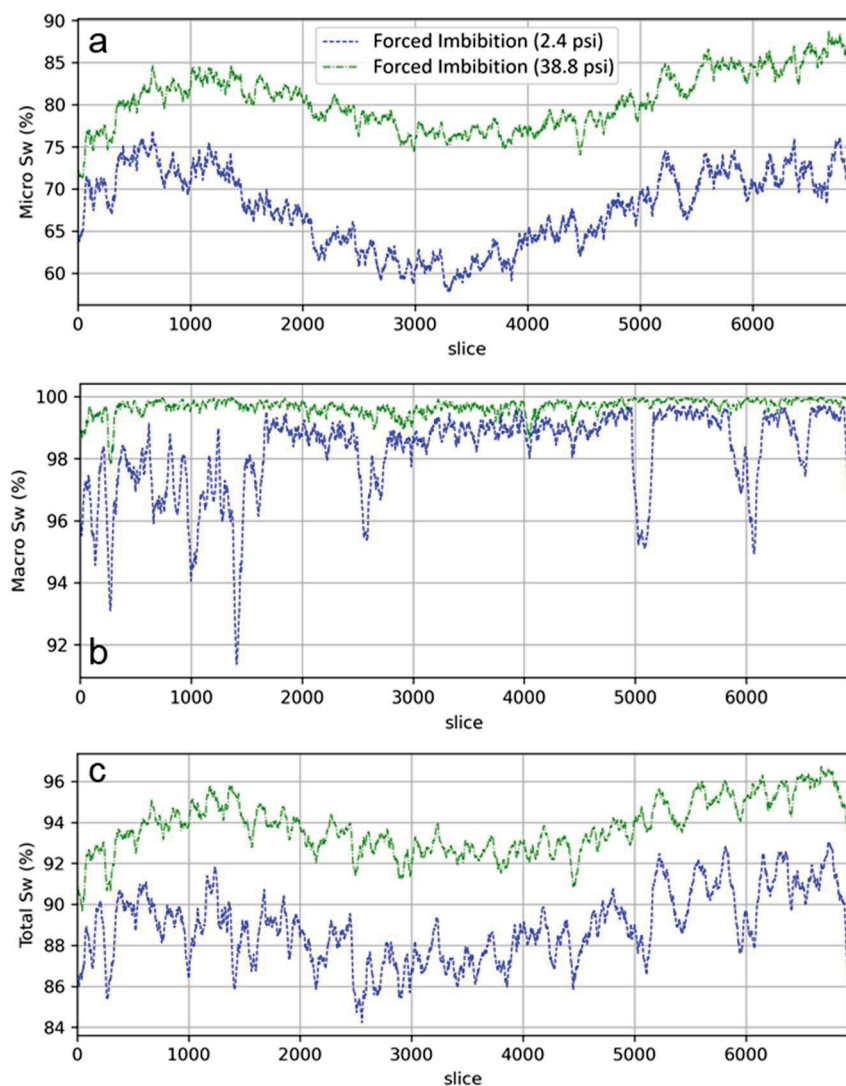
Figure 6-11 - Saturation profiles after the three steps of forced imbibition (micro (a), macro (b), and total Sw).

Although some residual oil is observed in the interparticle porosity, which constitutes the majority of the macroporosity, the quantity is quite small, confined to a few oil films and some more complex pore corners (Figure 6-12). Under oil-wet conditions, the residual oil is primarily controlled by capillary pressure; that is, the higher the pressure, the greater the amount of oil

displaced from the pores. Once the oil phase becomes disconnected, the oil can remain trapped. Given that the interparticle porous system of the grainstone specimen is well-connected, with large pores and throats, the oil is displaced with relatively low pressures, resulting in highly efficient oil displacement in the macropores.

Conversely, it is observed that most of the residual oil is located within intraparticle pores of varying dimensions, predominantly small pores. These pores are formed by irregular dissolutions resulting from the destabilization of particles composed of magnesian clays, fracture enlargements, and intracrystalline porosity due to the internal dissolution of dolomites, among others. Since these pores tend to be poorly connected, their pore throats are narrow, which hinders oil drainage.
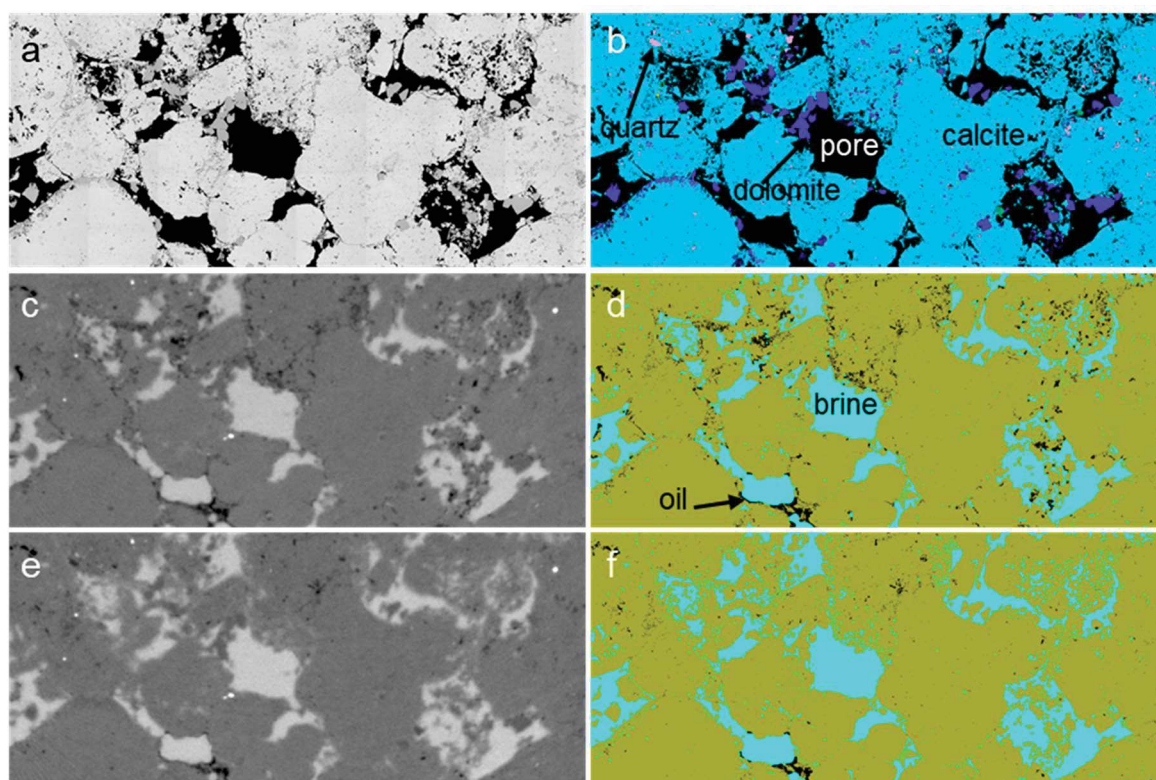
Figure 6-12 – Forced imbibition images: a and b are the BSE and QEMSCAN images, while c and d, and e and f are the pair X-ray μCT and the segmented coupled BSE X-ray μCT images of the two steps of forced imbibition at 2.7, and 21.8 psi. The images exhibit the oil trapped in small intraparticle pores and adhered as films to some mineral surfaces in interparticle pores.

S_{or} decreases with the increase in macro porosity (Figure 6-8c), even though the correlation is quite scattered. This impacts the relationship between S_{or} and total porosity (Figure 6-8d), given that macroporosity constitutes most of the rock's porosity. This occurs because the oil is trapped in the microporosity, and as porosity increases, the relative fraction

of particles reduces, where the microporosity is located. The initial oil saturations show different impacts on Sor: while micro Swi seems to not correlate with Sor (Figure 6-8e), macro Swi has a negative correlation (Figure 6-8f). Since both irreducible water and residual oil predominantly reside in the microporosity, an increase in both quantities should be expected in the presence of a high microporous volume, even though we cannot see a clear correlation. On the other hand, the greater the initial amount of oil in the macroporosity, the higher the Sor, as there is more oil to be trapped in the complex regions of the macropores.

6.6   Role of Mineralogy

The sample is predominantly composed of calcite (approximately 94%), with dolomite around 4% and quartz roughly 1%. As the particles are composed of calcite, most of the pore surface is constituted by this mineral (90.36%), followed by dolomite and quartz at 6.97% and 1.45%, respectively. Thus, the amount of surface coverage is proportional to the mineral content in the sample. However, since the particles are made of calcite, its specific surface area tends to be lower than other minerals. Conversely, dolomite primarily occurs as crystals approximately 50 microns in size, filling the interparticle porosity, and exhibits a higher specific surface area when compared to calcite. Finally, quartz appears mainly as crystals that replace the particles, often with dimensions less than 10 microns. Although located within the particles, quartz is frequently associated with intraparticle pores, which results in a higher specific surface area compared to the other minerals. Figure 6-13 illustrates the textural and mineralogical characteristics of the rock.

The amount of water adhered to calcite surfaces decreases from 16% to 13% during aging. In contrast, dolomite remained nearly unaltered around 9%, while quartz remained around 12%. The fact that dolomite preferentially occupies interparticle porosity, which primarily represents macroporosity, likely explains why its surfaces are more covered by oil, as the macro Sw was close to zero. On the other hand, intraparticle pores, typically micropores, are mainly coated by calcite and usually require higher pressures to be accessed due to their poor connectivity, which likely explains the higher amount of water adhered to calcite. Quartz, although mainly associated with intraparticle porosity, had a percentage of surfaces covered by water like dolomite, nearly 11%. Despite these variations, the differences between the minerals are small and do not imply a visible change in wettability after aging (Figure 6-14).
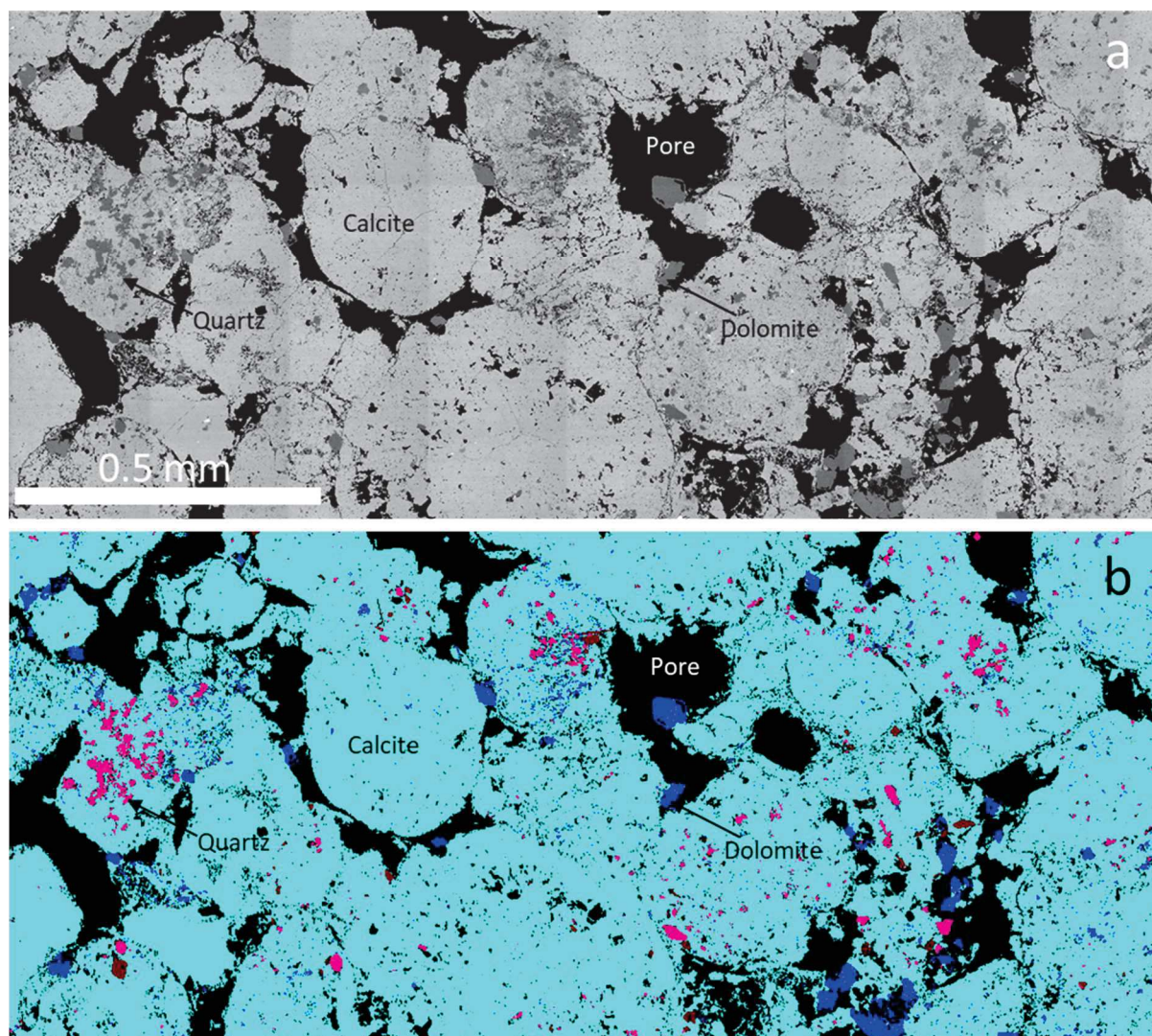
Figure 6-13 – BSE (a) and QEMSCAM (c) showing details of mineral localization. The particles are made of calcite, covering most of the pore surfaces including inter and intraparticle. Dolomite is located mostly inside interparticle macropores, while quartz replaces calcite, which means it has contact principally with intraparticle pores.
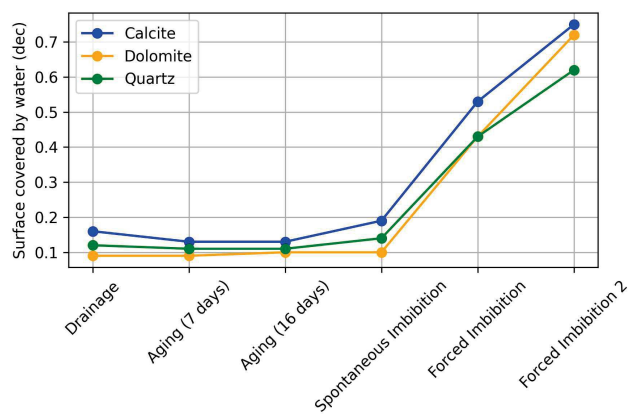
Figure 6-14 – Water surface coverage considering calcite, dolomite, and quartz during the experimental steps.

Following the spontaneous imbibition step, the percentage of surfaces covered by water increased by approximately 6% in calcite, while both dolomite and quartz experienced an increase of 1 and 3%. Although the differences among the minerals are undeniably significant, it is observed that the larger volumes of oil entered the macropores in a heterogeneous manner. Consequently, it is plausible that the sampling may have been affected, given that the distribution of dolomite and quartz is not homogeneous throughout the sample.

After the forced drainage steps, the number of surfaces wetted by water rose to 75 and 78%, considering calcite and dolomite. This indicates that the relative abundance between these minerals does not imply differences that could impact oil trapping. On the other hand, the amount of water adhered to the quartz after forced drainage was 62%. Since quartz tends to be water-wet, this result seems counterintuitive. A possible explanation for this behavior lies in the fact that quartz occurs within rock particles. Since most of the residual oil is hosted in intraparticle pores (Figure 6-15), the association of these pores with quartz possibly explains this result. In this way, there is probably a superimposition of porous geometry on the mineral composition regarding the oil trapping.

6.7   Conclusions

In this study, we performed drainage and imbibition cycles on a grainstone carbonate sample from the Barra Velha Formation of Brazil's Pre-salt utilizing X-ray imaging in conjunction with BSE and SEM techniques. From our investigation, we have drawn the following conclusions:

- Although the drainage and imbibition experiments conducted in a centrifuge yielded satisfactory results, they were not performed under reservoir conditions. Nevertheless, they represent a simple and cost-effective alternative that elucidates crucial aspects of multiphase configuration at the pore scale.
- The coupling of μCT with BSE and QEMSCAN imaging significantly enhances the understanding of fluid saturation in pores where X-ray techniques have limitations related to resolution. In addition to resolving micropores, QEMSCAN mapping elucidates the fluid saturation mineral controls.
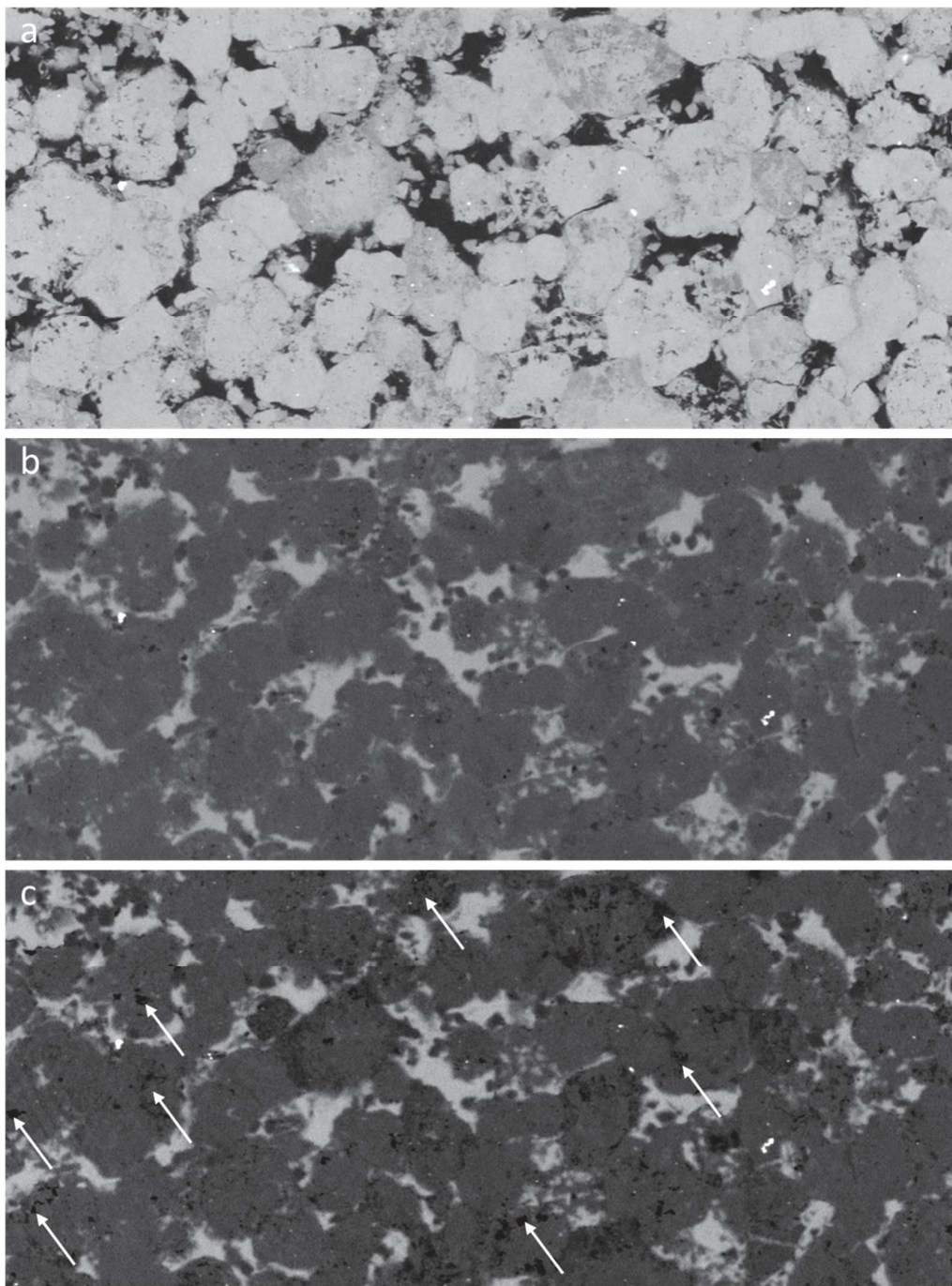
Figure 6-15 – X-ray μCTs including the dry sample (a), brine saturated sample (b), and image after forced imbibition cycle (c). The comparison of the b and c images reveals the localization of trapped oil inside intraparticle pores (white arrows). In image b all pores are filled with brine, therefore they show a high attenuation value (bright gray), while the same pores in image c present lower attenuation when filled with residual oil (dark gray).

- After drainage and aging cycles, oil replaced nearly all the brine in the interparticle macropores, relegating it to small, disconnected droplets caused by snap-off. Additionally, a significant portion of the intraparticle micro and

macroporosity was filled with oil after drainage, with a further increase during aging, highlighting the rock's affinity for oil.

- Post-forced imbibition imaging indicated that nearly all the oil content located in the interparticle macropores was replaced by water, with a small amount remaining as films covering the surfaces of the minerals. Conversely, most of the oil remained trapped in the intraparticle macro and micropores, regions where the porous medium tends to be poorly connected.

- Finally, no significant impact of mineralogical variations on fluid saturation was identified in any of the experimental cycles, indicating that the oil-wet condition is not affected by the relative variations of the minerals, which are predominantly calcite and dolomite.

6.8   Acknowledgments

7. Article 6: HERLINGER, R.; KNACKSTEDT, M.; YOUNG, Y.; VIDAL, A. C. Pore Scale Fluid Saturation and Oil Trapping in Heterogeneous Carbonates Under Mixed-Wet Conditions: Insights from Brazilian Pre-salt Reservoirs. SPE Journal, Submitted, 2025

7.1 Abstract

This study investigates fluid saturation and oil entrapment mechanisms at the pore scale in a highly complex carbonate sample from the Barra Velha Formation, Santos Basin, Brazil. For this purpose, we performed drainage and imbibition cycles followed by X-ray imaging to evaluate the impact of sedimentological features such as primary and secondary textures and minerals on fluid saturation. Under the applied conditions, the sample behaved mixed-wet in macropores and water-wet in micropores. Rock texture was a critical factor influencing fluid distribution during primary drainage and forced imbibition. Both irreducible water and residual oil were predominantly trapped in intracrystalline pores, where narrow pore throats limited connectivity and accessibility. During primary drainage, oil initially behaved as a non-wetting phase, transitioning to oil-wetting at higher pressures in macropores, while its entry into smaller pores remained restricted. Aging and spontaneous imbibition caused fluid redistribution, with water returning to tighter regions, especially in dolomite- and quartz-rich areas. Oil entrapment was primarily dictated by rock texture, with minor influence from mineral species on local entrapment. This behavior is likely due to the dominance of calcite, which displayed a higher affinity for oil during aging and spontaneous imbibition. Imaging of secondary drainage revealed complex wettability patterns: smaller pores retained their water-wet behavior, while macropores exhibited mixed conditions. Mineral precipitation, recrystallization, and dissolution contributed to surface roughness, promoting water-wet conditions in some, resulting in highly heterogeneous saturation patterns. These findings provide detailed insights into fluid behavior in complex carbonate systems, emphasizing the interplay between rock texture, wettability, and fluid distribution, with implications for carbonate reservoir characterization and enhanced oil recovery.

Keywords: Pre-salt, X-ray µCt, wettability, pore scale, oil trapping

7.2 Introduction

The understanding of fluid saturation at the pore scale has significantly increased in recent years, driven by advancements in computational resources and X-ray tomographic techniques (Wildenschild and Sheppard, 2013). X-ray imaging with micron-scale resolution has enabled direct visualization of fluid configurations within pores, thereby confirming many theories proposed in previous decades (Blunt, 2017; Blunt *et al.*, 2013). Moreover, this progress has improved simulation methods of pore-scale flow processes and machine-learning techniques to predict petrophysical properties (Alqahtani *et al.*, 2020; Bakke and Øren, 1997; Blunt, King and Scher, 1992; Hazlett, 1995; Keehm, 2004; Sudakov, Burnaev and Koroteev, 2019). This information is crucial for geological modeling and simulation, thus reducing uncertainties in reservoir management, which can increase hydrocarbon recovery.

The flow of fluids in porous media is governed by mineralogy, the involved fluids, flow velocity, and environmental conditions. The mineral composition is of great significance as it substantially impacts the wettability of the medium. Generally, carbonate reservoirs tend to have an affinity for oil, whereas siliciclastic ones are more favorable to water adhesion (Anderson, 1985, 1986, 1987). Even though this assumption is widely propagated; exceptions are related in the literature (Anderson, 1986). In addition to mineral composition, the nature of the involved fluids plays a crucial role in interfacial tension, thereby affecting wettability conditions (Alqam *et al.*, 2021; Blunt, 2017; Iyi *et al.*, 2021). The abundance of asphaltenes in crude oil is highly discussed as a common inverter of wettability, since this organic compound can precipitate on walls of minerals, favoring crude oil adherence (Iyi *et al.*, 2021; Kim, Boudh-Hir and Mansoori, 1990; Mohammed *et al.*, 2021). Lastly, temperature and pressure conditions have a significant impact on interfacial tension, thus influencing contact angles and, consequently, the fluid configuration (Hassan, Nielsen and Calhoun, 1953; Jennings, 1967; Toutouni *et al.*, 2021).

The flow of fluids in reservoirs tends to have low velocities, typically referred to as low capillary number flow (Bashiri and Kasiri, 2011; Guo, Song and Hilfer, 2020; Speight, 2017). In these cases, the capillary forces will be more important than viscous ones. Hence, fluid configuration during water flooding processes will be strongly governed by capillary pressure, primarily controlled by the abovementioned parameters. Hence, the capillary forces will have an important impact on relative permeability, a paramount petrophysical property, whose

uncertainty may have a massive economic implication in oil production projects, since it hugely impacts production prediction curves.

The term multi-phase flow refers to applications involving wetting and nonwetting fluid phases in porous media, including two-phase systems like oil-water and gas-water, and three-phase systems like gas-water-oil (Blunt, 2017; Wildenschild and Sheppard, 2013). After some multi-phase imaging in soil science in the 1980s, Wang *et al.*, (1984) published the first research in the petroleum engineering field where CT was used to map oil saturation distribution in a Berea sandstone core. Early studies in the 1980s used medical CT scanners, but these were limited in resolution, focusing on macro-scale phenomena rather than pore-scale details. Over time, advancements in lab-scale and synchrotron-based microtomography (μCT) significantly improved resolution, allowing for detailed pore-scale imaging of porous media and fluid distributions (Blunt, 2017; Sadeghnejad, Enzmann and Kersten, 2021a; Wildenschild and Sheppard, 2013).

The first true pore-scale images were produced in the 1990s (Clausnitzer and Hopmans, 2000; Jasti, Jesion and Feldkamp, 1993). Since then, μCT has become an essential tool in studying multi-phase flow in porous media, enabling high-resolution 3D imaging of pore structures and fluid interactions. Recent research continues to explore these applications, focusing on pore-scale resolution and processes in multi-phase systems.

The overwhelming majority of pore-scale investigations published focus on samples with low heterogeneity, typically composed of particles, such as Bentheimer and Berea sandstones (Bakke and Øren, 1997; Humphry *et al.*, 2014b; Peksa, Wolf and Zitha, 2015; Ryazanov, Dijke, Van and Sorbie, 2010; Valvatne and Blunt, 2004), and Ketton ooidal carbonate (Andrew, Bijeljic and Blunt, 2014b; Karlsons *et al.*, 2022; Wang *et al.*, 2024). Imaging these particulate samples, which have large pores and minimal interstitial cement, facilitates the examination of contact angles and interfaces, whose morphology often closely aligns with the resolutions achieved through X-ray tomography techniques. Conversely, this study aims to investigate fluid saturation and oil entrapment in a highly heterogeneous *in-situ* carbonate rock from the Barra Velha Formation, Brazilian Pre-salt, whose textures and mineralogy differ significantly from conventional carbonate reservoirs. Moreover, this theme is typically a petroleum engineering study area, hence here we intend to bring the discussion to the geologists' audience. To this end, drainage and imbibition cycles were conducted using a centrifuge, coupled with X-ray

tomography imaging, to understand the lithological control on fluid configuration and oil entrapment in these rocks.

7.3 Geological Setting

The Santos Basin, located on Brazil's southeastern margin, is bounded by the Cabo Frio High to the north and the Florianópolis platform to the south (Figure 7-1). It was formed during the early Cretaceous/Late Jurassic by tectonic extension, the event that preceded the separation of South America and Africa and led to the formation of the Atlantic Ocean (Blaich, Faleide and Tsikalas, 2011; Davison, 2007; Nürnberg and Müller, 1991). The basin's stratigraphy is divided into three super-sequences (Moreira *et al.*, 2007): Rift, Post-rift, and Drift (Figure 7-2).
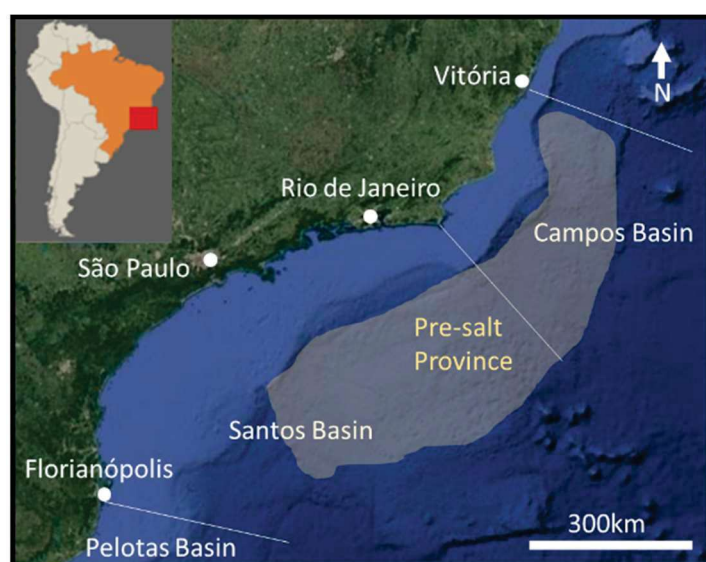
Figure 7-1- Approximated Santos Basin and Pre-salt Province geographical position. (Reproduced from Herlinger et al., (2020)).

The rift phase began with the deposition of Camboriú tholeiitic volcanic rocks over the Precambrian basement during the Lower Cretaceous (Mizusaki, Thomaz Filho and Cesero, 1998). This was followed by the Piçarras Formation in the Barremian, characterized by siliciclastic rocks, Mg-clay ooids, and peloids deposited in a highly alkaline environment (Leite, Silva and De Ros, 2020). The Itapema Formation, accumulated during the Jiquiá Local Stage, is notable for its bioclastic thick bivalve rocks ("coquinas") deposits (Chinelatto *et al.*, 2020b;

Rocha, Favoreto and Borghi, 2021). A regional stratigraphic marker at the top of these deposits generated by an uplift and consequent erosion marks deep changes in environmental conditions.

My	Geochronology			Stratigraphy		Unconformities	Tectonic Stage
	Epoch	Stage	Local Stage	Group	Formation		
	Lower Cretaceous	Aptian	Alagoas	Guaratiba	Ariri	Salt Base	Drift
120					Barra Velha	Intra-Alagoas	Pos-Rift
125		Barremian	Jiquiá		Itapema	Pre-Alagoas	
			Buracica		Piçarras		Rift
130			Aratu			Top Basalt	
	Hauterivian				Camboriú		

Figure 7-2 - Stratigraphy of the continental deposits of Santos Basin (Moreira et al., 2007).

The Barra Velha Formation unconformably covers the Rift Super-sequence and is divided into Lower and Upper sections by the Intra-Alagoas unconformity. This Formation was accumulated in an alkaline lacustrine environment and includes calcite shrub crusts, Mg-clay with calcite spherulites, laminated carbonates, dolomite, and intraclastic rocks (Barnett *et al.*, 2021; Gomes *et al.*, 2020b; Herlinger *et al.*, 2023; Netto, Pozo, Manuel, *et al.*, 2022; Rodríguez-Berriguete *et al.*, 2022; Wright and Barnett, 2015, 2020).

Calcite crusts, also known as shrubstones or stromatolites, are composed of fibrous calcite aggregates ("shrubs") with distinctive fascicular-optic extinction (Kendall, 1977), which grows vertically and merge horizontally, resulting in crusts of varying dimensions (Herlinger, Zambonato and De Ros, 2017; Lima and De Ros, 2019; Rodríguez-Berriguete *et al.*, 2022; Wright and Barnett, 2015). These minerals are closely associated with Mg-clay deposition, which occurs as laminations, peloids, ooids, and coatings (Herlinger *et al.*, 2020; Netto, Pozo, M., *et al.*, 2022; Silva, da *et al.*, 2021). The Mg-clays are highly reactive, often dissolving and generating secondary porosity (Tosca and Wright, 2015; Wright and Tosca, 2016). Frequently they were replaced by dolomite crystals and other minerals. Finally, calcite spherulites, which

are fibro-radial aggregates, often replace Mg-clays laminations during early diagenesis, in a similar way to what happens in the Campos basin Pre-salt reservoirs (Carvalho *et al.*, 2022; Herlinger, Zambonato and De Ros, 2017; Lima and De Ros, 2019).

7.4 Materials and Methods

7.4.1 Materials

The sample utilized in this study was plugged from a 1.5" horizontal plug, and cleaned according to Soxhlet methodology for crude oil extraction (API, 1998). The plug exhibits a helium porosity of 15.10 % and a permeability of 65.8 mD. The sub-plug extracted from the main plug has a radius of 6 mm and a height of 36 mm. After the sampling, the sub-plug underwent plasma cleaning according to the method described by Kumar (2009). This is a low-temperature and free-of-solvents procedure that can remove organic compounds impurities adhered to mineral surfaces, therefore restoring the original wettability condition. The apparatus consists of a vacuum chamber linked to a radiofrequency generator and a water vapor line. Once the vapor gets ionized, the organic contaminants are removed as H_2O, CO_2, and CO (Kumar, 2009).

The sample comprises calcite spherulites with an average diameter of approximately 1 mm (Figure 7-3), Mg-clay matrix replacive dolomite at the base (Figure 7-4a), and fine to silt-sized quartz and alkali feldspar clasts. Calcite shrubs up to about 10 mm in height overlie this material, with the intershrub porosity heterogeneously filled mainly by dolomite (Figure 7-4). Finally, the shrubs are irregularly overlain by another muddy cycle, featuring spherulites and matrix replacive dolomite. In addition to the well-connected porosity between dolomite crystals and intershrub spaces (Figure 7-4c), the rock exhibits abundant intracrystalline dissolution porosity with various morphologies: microporosity marking the growth of the shrubs, related to dissolution or recrystallization processes, dissolutions associated with peloid inclusions within the shrubs, dissolved dolomite cores, as well as channels associated fractures enlargement (Figure 7-4). The mineralogy predominantly comprises calcite, with subordinate amounts of dolomite, quartz, and alkali feldspar. Additionally, smaller quantities of dawsonite, pyrite, goyazite, rutile, kaolinite, barite, fluorite, anhydrite, siderite, strontianite, zircon, apatite, and ilmenite were mapped by QEMSCAN (Table 7-1, Figure 7-5).

The fluids employed in the experiments consist of a 1.5M NaI brine solution and a synthetic crude oil mixture composed of 5% bitumen, 30% crude oil, 30% $C_{16}H_{34}$, and 35% toluene. The SARA (saturates, aromatics, resins, and asphaltenes) analysis and stability indicators of the oil constituents are presented in Table 7-2.

Table 7-1 – QEMSCAN mineral quantification.

Mineral	Composition	Section 1 Area (%)	Section 2 Area (%)
Calcite	$CaCO_3$	85.09	86.53
Dolomite	$CaMg(CO_3)_2$	8.92	9.40
Quartz	SiO_2	2.40	2.32
Alkali Feldspar	$(K,Na)AlSi_3O_8$	1.10	1.05
Dawsonite	$NaAlCO_3(OH)_2$	0.40	0.35
Pyrite	FeS_2	0.11	0.20
Goyazite	$SrAl_3(PO_4)(PO_3OH)(OH)_6$	0.08	0.09
Rutile	TiO_2	0.01	0.02
Kaolinite	$Al_2Si_2O_5(OH)_4$	0.02	0.01
Barite	$BaCO_3$	<0.01	<0.01
Fluorite	CaF_2	<0.01	<0.01
Anhydrite	$CaSO_4$	<0.01	<0.01
Siderite	$FeCO_3$	<0.01	<0.01
Strontianite	$SrCO_3$	<0.01	<0.01
Zircon	$ZrSiO_4$	<0.01	<0.01
Apatite	$Ca_2(PO_4)_3F$	<0.01	<0.01
Ilmenite	$FeTiO_3$	<0.01	<0.01
Unclassified		1.84	<0.01
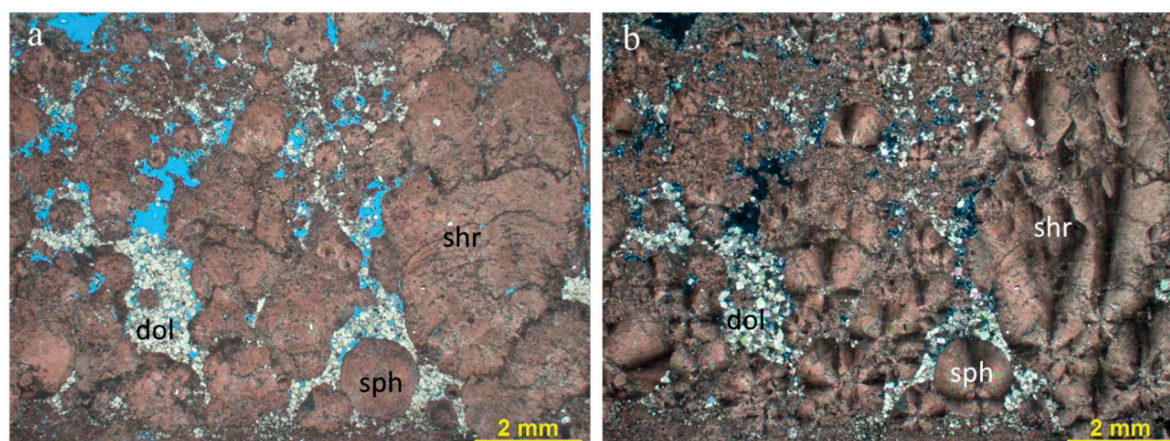
Figure 7-3 – Photomicrography showing the main aspect of the sample. The sample is mainly composed of calcite spherulites (sph) and shrubs (shr), and matrix replacive dolomite (dol). The macroporosity is mainly formed by intershrub and intercrystalline porosity, while a large volume of micropores occurs inside crystals of shrubs, spherulites, and dolomite.
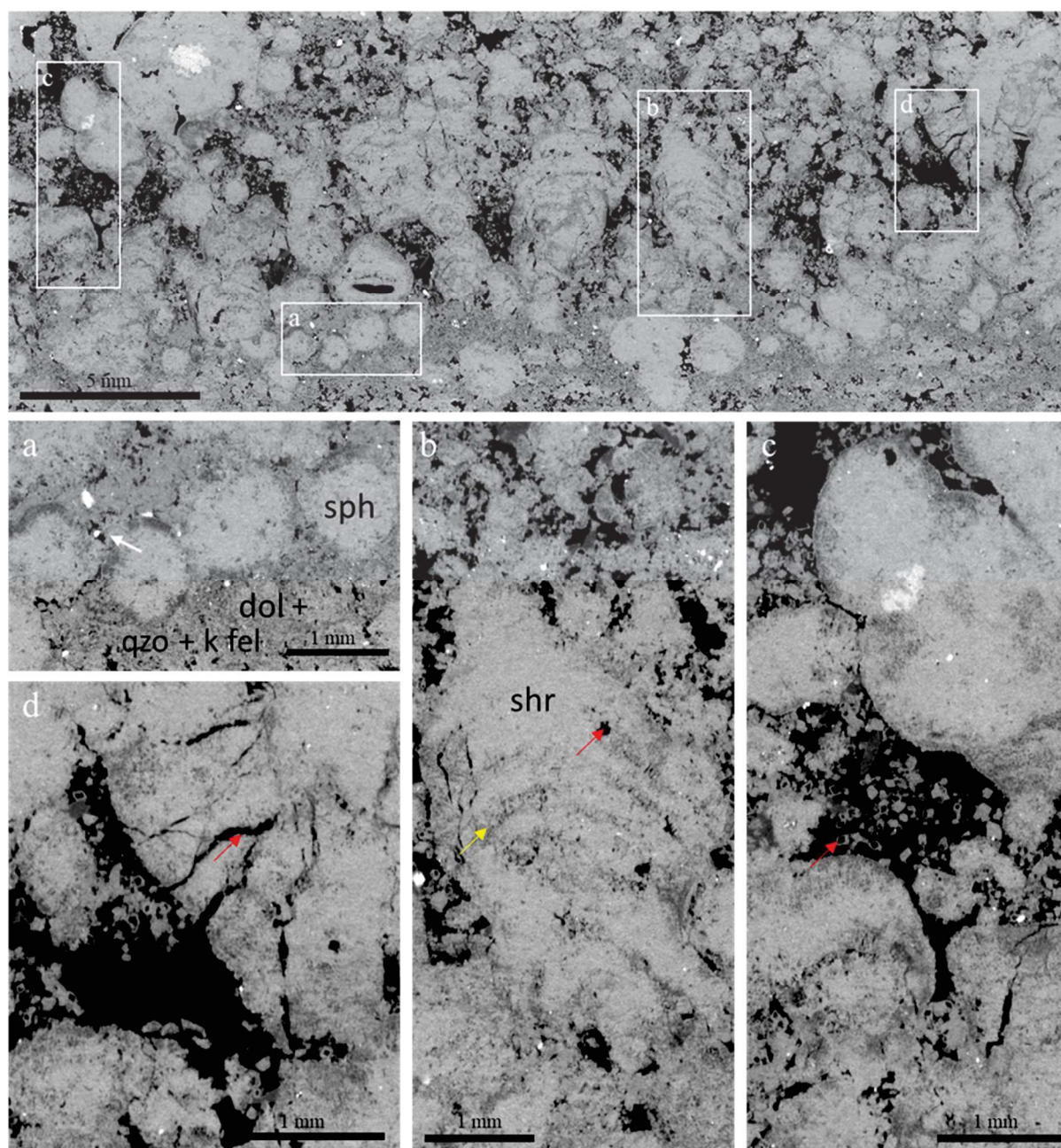
Figure 7-4 – X-ray μCT central slice of studied sample illustrating components and textural aspects of the rock: a) calcite spherulites (sph) and matrix replacive dolomite (dol) associated with quartz (qzo) and alkali feldspar (k fel); b) calcite shrub (shr) with abundant microporosity (yellow arrow) and rounded intracrystalline pores formed by clay peloids dissolution (red arrow); c) intershrub porosity filled by partially dissolved dolomite (red arrow); d) channel porosity resulting from fracture enlargement (red arrow).
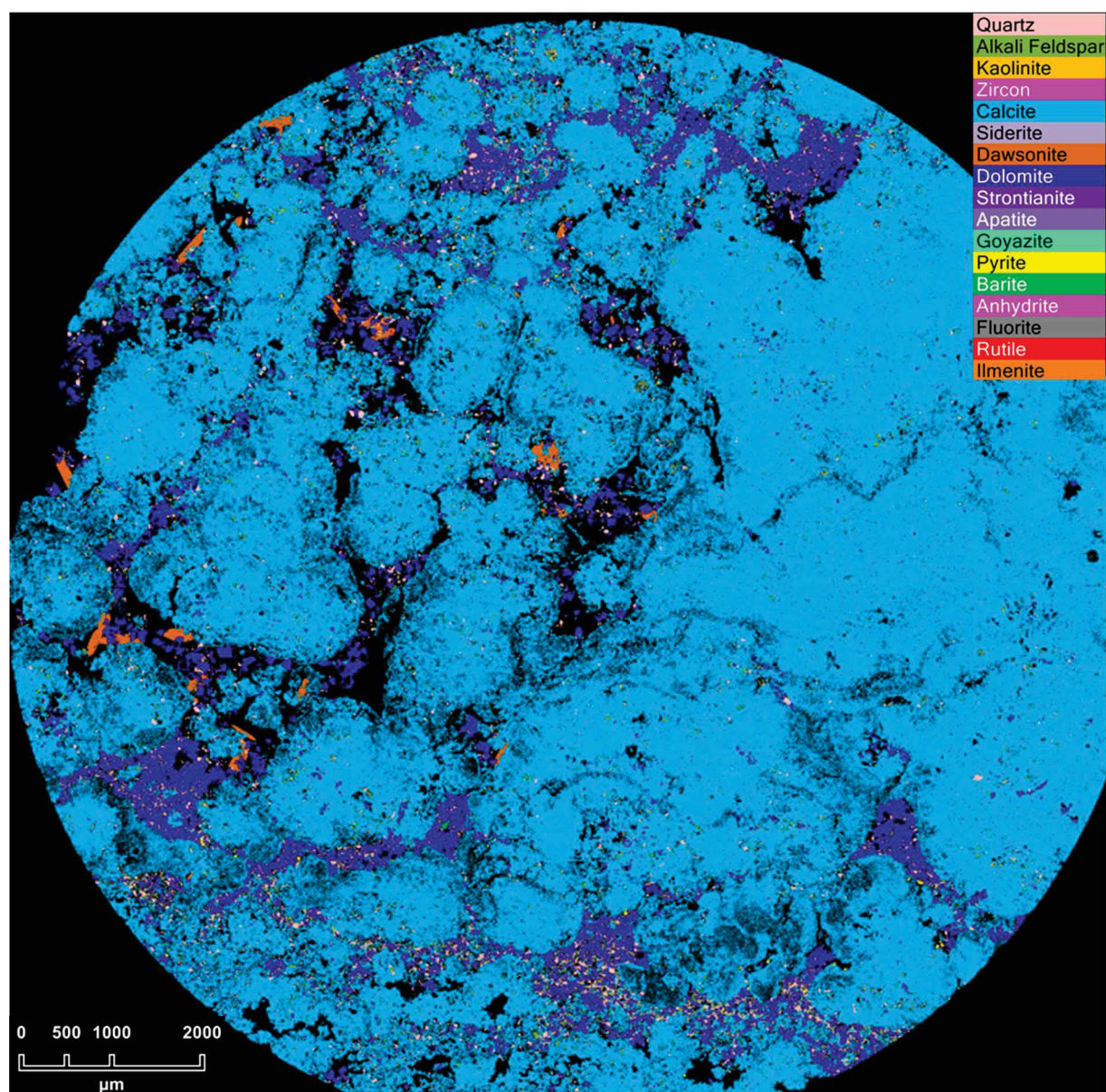
Figure 7-5 – QEMSCAN mineral mapping.

Table 7-2 – Composition of the organic components of the synthetic crude oil mixture and their stability indicators.

	Saturates	Aromatics	Resins	Asphaltenes	Volatiles + LOC[a]	Asphaltenes to resins	CII[b] index
	wt%	wt%	wt%	wt%	wt%		
Crude oil	38.4	5.6	6.2	1.49	48.3	0.24	-
Bitumen	12.9	28.8	41.7	15.72	0.9	0.38	0.41
Synthetic oil	42.17	38.12	3.95	1.23	14.54	0.31	1.03

[a] LOC – loss on column (mainly dissolved gas and light-end paraffin).
[b] CII (Colloidal Instability Index) = (Saturates + Asphaltenes) [wt%]/ (Resins + Aromatics) [wt%].

7.4.2   Methods

7.4.2.1   Drainage and Imbibition

The centrifuge method for fluid substitution and capillary pressure measurement was initially proposed by Hassler & Brunner (1945) and later refined by Slobod *et al.* (1951). In a drainage/imbibition experiment, a saturated core plug is placed in a specific holder and subjected to rotation at different velocities. The displacing fluid is placed into the holder to replace the fluid saturating the sample. Once fluid saturation reaches equilibrium inside the core, the volume of produced fluid is measured, enabling the calculation of fluid saturation at the capillary pressure corresponding to the rotation speed, as described by Hassler & Brunner (1945):

$$Pc = \frac{1}{2}\Delta\rho\omega(r_2^2 - r_1^2) \tag{7.1}$$

where *r* represents the distance from the centrifuge axis, ω the rotational speed, and $\Delta\rho$ is the density difference between the fluid phases. Since capillary pressure varies with distance from the center of rotation, there is a corresponding variation in capillary pressure along the length of the sample, as illustrated in Figure 7-6. To minimize this pressure variation and ensure more homogeneous fluid saturation, the sample was flipped during the rotational process at each speed step. In each drainage and imbibition step, the sample was spun for at least 21 hours, with a minimum of 4 hours of rotation on each side. Given the small pore volume of the sample, the volumes of oil or water produced are quite small, making direct measurement rather imprecise. Therefore, saturation was determined through image processing, which will be detailed below. Although the replacement of the wetting phase by the non-wetting phase is typically defined as drainage, and the displacement of the non-wetting phase by the wetting phase is defined as imbibition, here we are referring to the stages as usually used in laboratory wettability and relative permeability experiments (McPhee, Reed and Zubizarreta, 2015). Hence, replacing water with oil was referred to as drainage, and replacing oil with water was referred to as imbibition to simplify the identification of experimental stages.
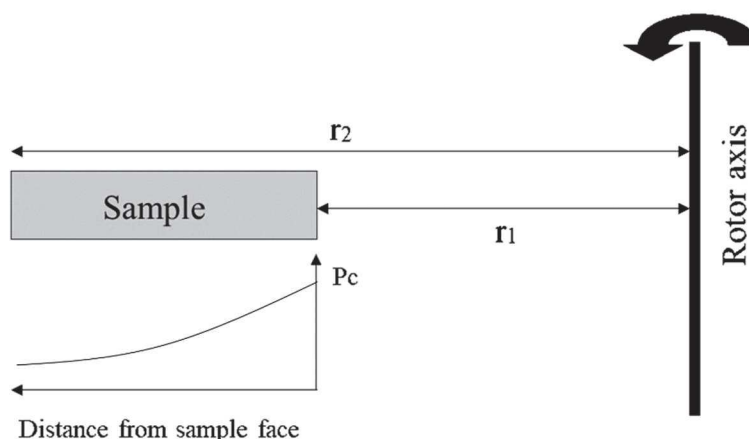
Figure 7-6 – Cartoon showing the relationship between rotor distance and decrease of capillary pressure across the sample.

7.4.2.2 Experimental Procedure

The sample was initially imaged via X-ray tomography in its dry state and subsequently saturated with brine using a desiccator connected to a vacuum line. The sample was then placed under a press to ensure the removal of air bubbles at a pressure of 560 bar for 48 hours. Following this, the sample underwent brine drainage (primary drainage) by centrifugation. It was placed in a holder soaked in oil to facilitate water removal. Two centrifugation steps were performed at speeds of 400 and 1000 RPM, corresponding to pressures of 0.25 and 1.56 psi, respectively. The sample was imaged after each step. The sample was then aged in crude oil at 60°C for 7 days and scanned again to verify any significant changes in fluid configuration. Once equilibrium conditions were achieved, the sample underwent spontaneous imbibition. In this stage, the sample was immersed in brine for 13 days at 60°C. Afterward, the sample was subjected to forced imbibition in the centrifuge for crude oil replacement by water. It was rotated at three speeds: 500, 1000, and 4000 RPM, corresponding to pressures of 0.38, 3.03, and 48.52 psi, respectively. Finally, the sample was soaked in crude oil for the second drainage stage at 60°C, which lasted 27 days. Tomographic images were acquired after each experimental stage, including 1 in the dry state, 1 with the sample saturated with brine, 2 during the primary drainage, 1 after aging, 1 after spontaneous imbibition, 3 during forced imbibition, and finally, 2 during the second drainage.

7.4.2.3 X-ray Image Acquisition

The images were acquired following the helical space-filling scanning trajectory (Kingston *et al.*, 2018; Sheppard *et al.*, 2014). Each image acquisition took approximately 24 hours, with the sub-plug hosted in a Polyether ether ketone (PEEK) tube, soaked in either crude oil or brine, depending on the experimental stage (drainage or imbibition). Aluminum filters were applied at both the source and detector to attenuate low-energy (soft) X-ray photons and prevent backscattering and water radiolysis (Burns and Sims, 1981; Cullity and Stock, 2014; Elnur and Alshibli, 2023; Naji *et al.*, 2016). Table 7-3 summarizes the key acquisition parameter. In addition to the tomographic images, back-scattered electrons (BSE) and QEMSCAN images were acquired from two polished sections cut from the sub-plug after the experimental procedure and sample cleaning.

Table 7-3 – Main X-ray acquisition parameters.

Sample state	Dry	Primary Drainage and Aging	Spontaneous and Forced Imbibition, and Second Drainage
Acquisition			
Mode (pixels)	3040 x 3040	3040 x 3040	3040 x 3040
Exposure time (seconds)	0.4	0.4	0.4
Accumulations	12	12	12
Geometry			
Sample distance to source (mm)	14.3	15.3	15.3
Detector distance (mm)	400	400	400
Voxel size (µm)	4.96925	5.31675	5.31675
Vision Field (X)	13.51636	14.46156	14.46156
Vision Field (Y)	13.51636	14.46156	14.46156
Vision Field (Z)	29.8155	28.71045	28.71045
Projections per revolution	3600	3600	3600
X-ray			
Voltage (kV)	100	100	100
Current (micro ampere)	80	80	60
Aluminum Filter			
Detector (mm)	4	4	4
Source (mm)	1	1	2

7.4.2.4 Image Processing

After image reconstruction, they were initially processed to remove the beam hardening effect by applying a radial normalization. All acquired images, including X-ray µCT, QEMSCAN, and BSE were registered according to the dry sample (Latham, Varslot and Sheppard, 2008; Latham, Varslot and Seppard, 2008). Once registered (Figure 7-7b), the difference between the dry image and the other images was calculated (Figure 7-7c). This procedure eliminates attenuation differences between minerals, highlighting differences in saturation, including visible pores and regions with pores below the image resolution.

The difference image between the dry and saturated images was used to segment porosity and microporosity (Lin *et al.*, 2016). Initially, three phases were separated using the difference between dry and saturated images, including macropores, microporous (under-resolution porosity), and non-porous minerals (Figure 7d). Then, the difference image was used to calculate microporosity, which is applied only in the microporous region. The smallest differences correspond to microporosity 0, while the largest differences are porosity 100%. This way, it is possible to map the microporosity of the subsample (Figure 7-7e).

As the attenuation of crude oil tends to be close to that of air, it is possible to evaluate the water-filled microporosity using the difference between the dry and the image-saturated with brine and crude oil (Figure 7-7g and i). Then, from the ratio between the microporosity map and the porosity map filled with water, the water saturation (Sw) in the microporosity is obtained in drainage and imbibition images (Figure 7-7j). Finally, Sw in the macroporosity was obtained by segmentation by the converging active contours (CAC) method (Sheppard, Sok and Averdunk, 2004) (Figure 7-7h). Once we have the Sw in both the macro and microporosity, the total Sw can be estimated. The figure 7-7 shows the image processing steps and saturation calculation procedure.

7.5   Results

After the drainage cycles, the total water saturation (Sw) in the sample reached values of 71.52% and 34.37%, under capillary pressures of 0.25 and 1.56 psi, respectively. Micro Sw was measured at 90.61% and 48.02%, while macro Sw recorded values of 27.03% and 2.56%. During the aging process, total Sw exhibited a variation below 0.3%. After spontaneous

imbibition, total Sw increased by approximately 4% to 38.97%, while macro and micro Sw rose to 8.1% and 52.21%, respectively. Forced imbibition cycles raised total Sw to 71.72%, 79.50%, and 85.17% after the three steps, suggesting a residual oil saturation (Sor) of about 15%. Macro and micro Sw values were observed at 88.97%, 95.74%, and 97.25%, and 64.31%, 72.54%, and 79.98%, respectively. Finally, in the second drainage phase, total Sw levels were 55.25% and 48.13% after 11 and 27 days, with macro Sw at 36.46% and 27.75% and micro Sw at 63.30% and 56.87%. Figure 7-8 presents the relationship between saturation and capillary pressure (Pc) during the drainage and imbibition stages, as well as the saturation trend over time in the second drainage. Figure 7-9 and Figure 7-10 further illustrate the saturation profile throughout the sample, and Figure 7-11 exhibits the 3d segmented images showing the oil and water occupancy in macropores.

The percentage of surfaces in contact with water exhibits distinct evolutionary trends across the primary minerals constituting the sample, as illustrated in Figure 7-12. Calcite, alkali feldspar, and kaolinite display a similar evolution, with a relatively modest rate of increase from the aging stage to the end of forced drainage. This behavior contrasts with that of quartz, and particularly dolomite, whose water contact increases are more pronounced than those of the previously mentioned minerals. Dawsonite, however, shows markedly different values, with significantly lower water contact percentages compared to the other minerals.

7.6   Discussion

7.6.1   Impact of Textures on Primary Drainage

The sample under study exhibits high textural complexity, generally determined by the primary texture of the rock (Figure 7-4). Its laminated character introduces significant petrophysical contrasts, with regions dominated by muddy sediment originally composed of a mixture of Mg-clay and siliciclastic sediment. Although initially rich in Mg-clays, the muddy region is mainly composed of dolomite and spherulites, diagenetic components nucleated within the muddy sediment before clay destabilization (Herlinger, Zambonato and De Ros, 2017; Tosca and Wright, 2015). As a result, while this region of the rock contains well-connected pores between dolomite crystals and spherulites, the pores tend to be small and typically are below the resolution threshold used, thus being predominantly classified as

microporosity, which results in low permeability. Conversely, the shrub-rich regions contain large, well-connected pores, resulting in a greater pore volume and higher porosity. While intershrub pores are partially occupied by dolomite (Figure 7-3 andFigure 7-13), the volume is minor and does not significantly impede fluid flow.

Figure 7-7 – Fluxogram showing the main steps of image processing: a) dry image with higher attenuations represented by lighter colors; b) registered brine saturated image: brine has higher attenuation than minerals; c) attenuation difference between a and b images; d) three phase segmentation, exhibiting porosity (black), non-microporous (ocher), and microporous minerals (olive); e) porosity map: white represents 0% and black 100% of porosity; f) registered image with two fluids: higher attenuations with brine and lower representing crude oil; g) attenuation difference between a and f images; h) macropore segmentation with oil (black) and water (blue); i) water-filled microporosity map; and j) microporosity Sw map.

Figure 7-8 – Plots illustrating the relationship between Sw and Pc during primary drainage and forced imbibition phases, as well as Sw versus time during the second drainage phase.

Following the first drainage cycle step, oil effectively infiltrates the intershrub pores (Figure 7-13), whose throats possess substantial dimensions. Upon completion of the second drainage step, the entire intershrub pore volume becomes fully saturated with oil, representing the majority of the macroporosity (Figure 7-13). Consequently, the macro Sw approaches a value close to zero (Figure 7-8). The dolomite within these intershrub pores is sparse and does not hinder the replacement of water by oil. In contrast, the intercrystalline pores of the muddy region have smaller throats that are inaccessible under the imposed capillary pressure (3.03 psi). Furthermore, the rock contains a substantial amount of intracrystalline pores, especially within the shrubs observed in the BSE image (Figure 7-13b); however, the resolution of X-ray µCTs cannot adequately resolve it. These pores, resulting from dissolution and recrystallization processes, are poorly connected and inaccessible to oil under the current pressure conditions, leading to high micro Sw content (Figure 7-8 and Figure 7-13).
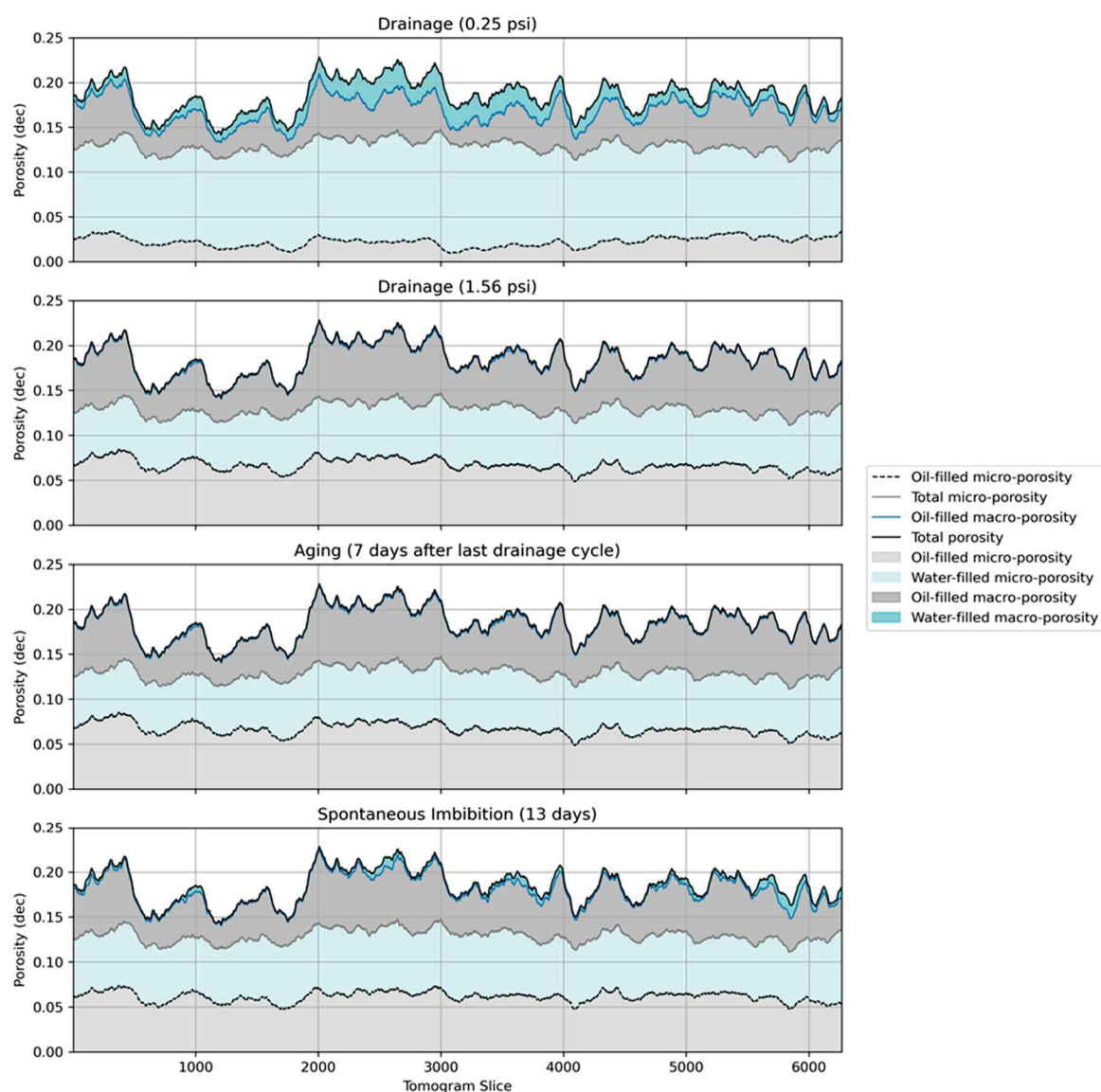
Figure 7-9 – Saturation profile throughout the sample during drainage, aging, and spontaneous imbibition phases.

After the first drainage step, water behaves as the wetting phase, indicating that oil displaces it through applied pressure without significant wettability inversion. This can be very clearly seen in the segmented image (Figure 7-13d and f), where the oil advances through the center of the larger pores. Thus, the rock retains its original wettability characteristics, confirming the effectiveness of plasma cleaning. At this stage, fluid saturation is strongly controlled by the texture governing pore throat geometry, while mineralogy appears to exert minimal impact, although crystal location and morphology may influence fluid flow dynamics. Following the second drainage step, water was trapped in some large pores by snap-off,

denoting that during the drainage cycle, the wettability was inverted inside the macroporosity at least in part of the pores.
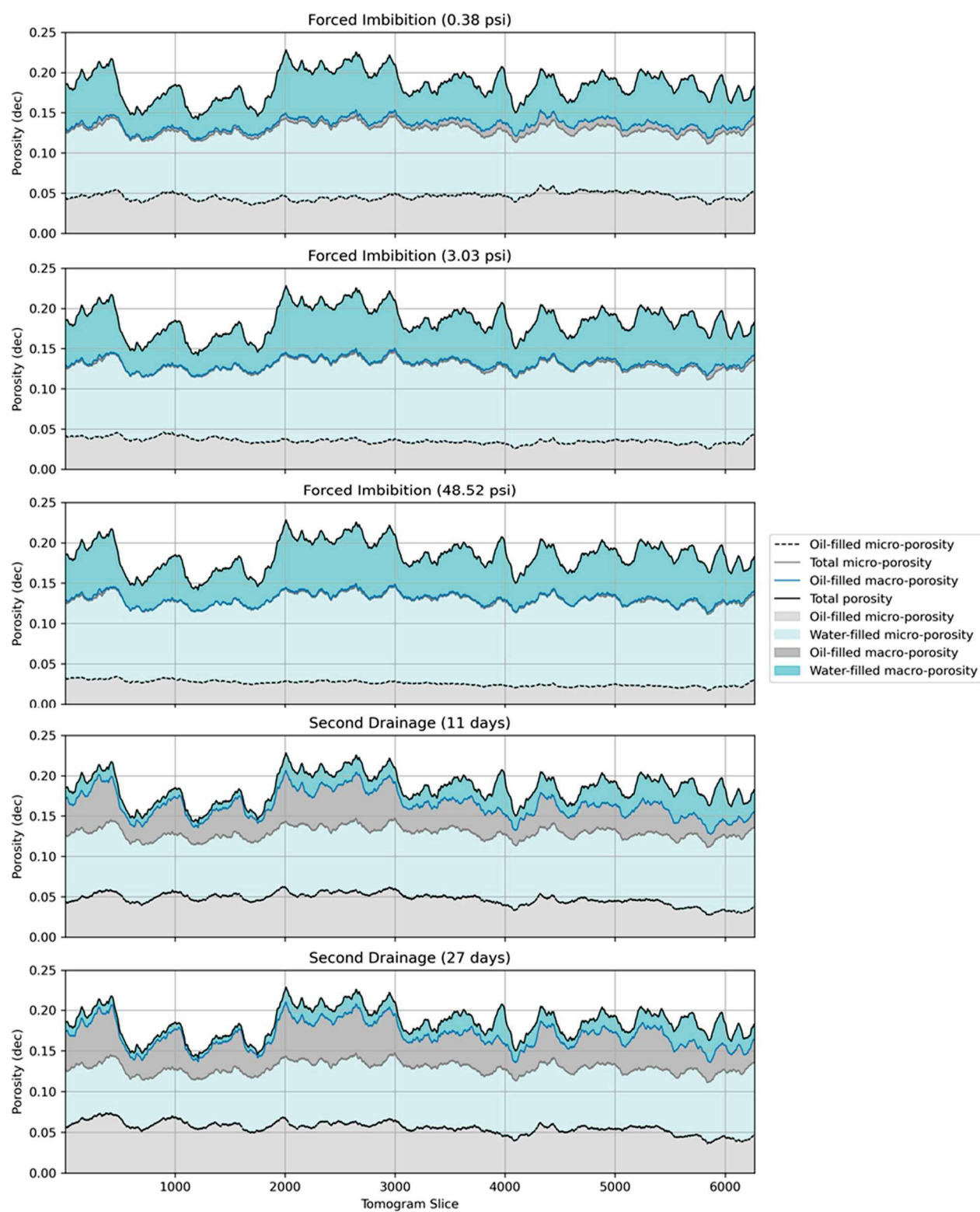
Figure 7-10 – Saturation profile along the sample during the forced imbibition and secondary drainage steps.
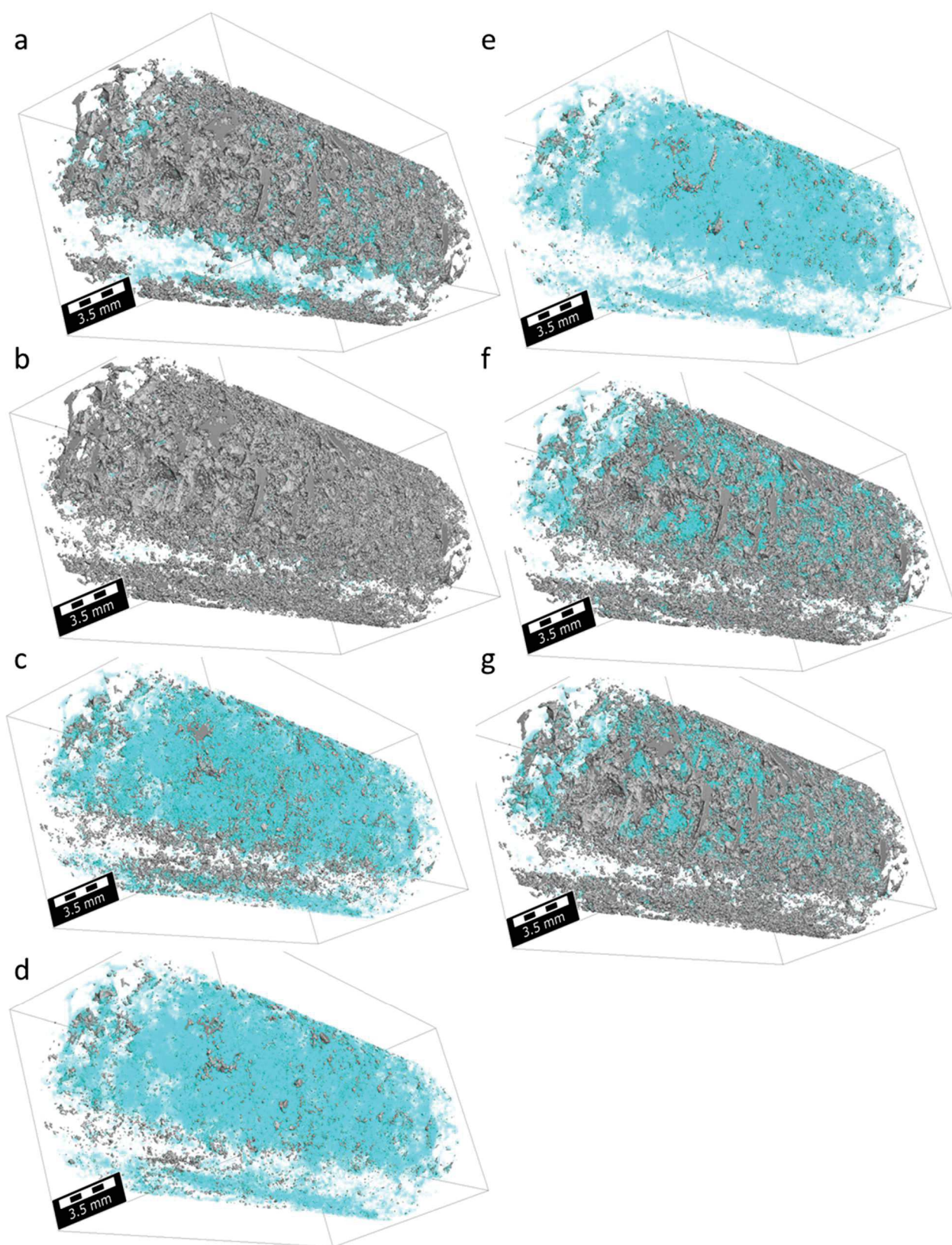
Figure 7-11 – Segmented 3D images in water (blue) and oil (gray). Images a to b correspond to the primary drainage cycle, c to e forced imbibition, and f to g second drainage.
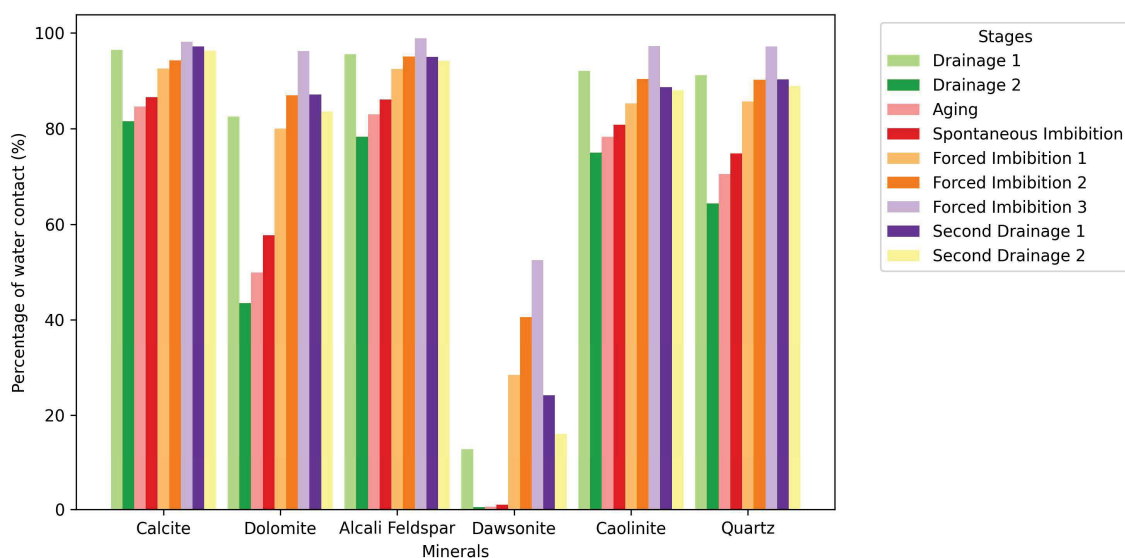
Figure 7-12 – Bar chart showing the percentage of mineral surfaces in contact with water during each experimental stage.

7.6.2 Implications of Mineralogy on Wettability During Aging and Spontaneous Imbibition

As previously discussed, in addition to the commonly observed textural complexity in marine carbonates, the sample exhibits a broad compositional diversity. This intricacy contrasts with marine carbonates, whose mineralogy predominantly comprises calcite and dolomite. The mineralogy typically found in non-marine carbonates results from deposition in a continental environment, where the compositional availability greatly influences geochemistry in the depositional setting (Armenteros, 2010; Gierlowski-Kordesch, 2009; Tanner, 2010), unlike marine carbonates which tend to have a homogenized composition. Besides depositional geochemistry, reservoirs in the Barra Velha Formation and analogous formations have experienced significant input from hydrothermal fluids that altered the primary textures and mineralogy (Herlinger, Zambonato and De Ros, 2017; Lima *et al.*, 2020; Lima and De Ros, 2019). Despite being quite varied, the mineralogy is dominated by calcite and dolomite, with smaller amounts of quartz, dawsonite, alkali feldspar, and other minerals. Given that the prevalent mineralogy is carbonate, it is expected that the wettability tends toward oil, as observed in most carbonate reservoirs mentioned in the literature (Chilingar and Yen, 1983; Treiber and Owens, 1972).

After the drainage cycles, oil entry in small pores is limited (Figure 7-13). Conversely, a tendency for oil entry into these pores could be explained by oil-wet wettability. However, such behavior is not observed, indicating that the rock behaves as water-wet in smaller pores, as no

oil enters these pores during aging. Most microporosity is located inside calcite shrubs, although it is also noted that in tighter regions between dolomite crystals and quartz or alkali feldspar clasts, oil does not enter during aging either. Thus, it seems that mineralogy, although controlling pore morphology, does not influence wettability inversion in micropores due to mineral species variation.
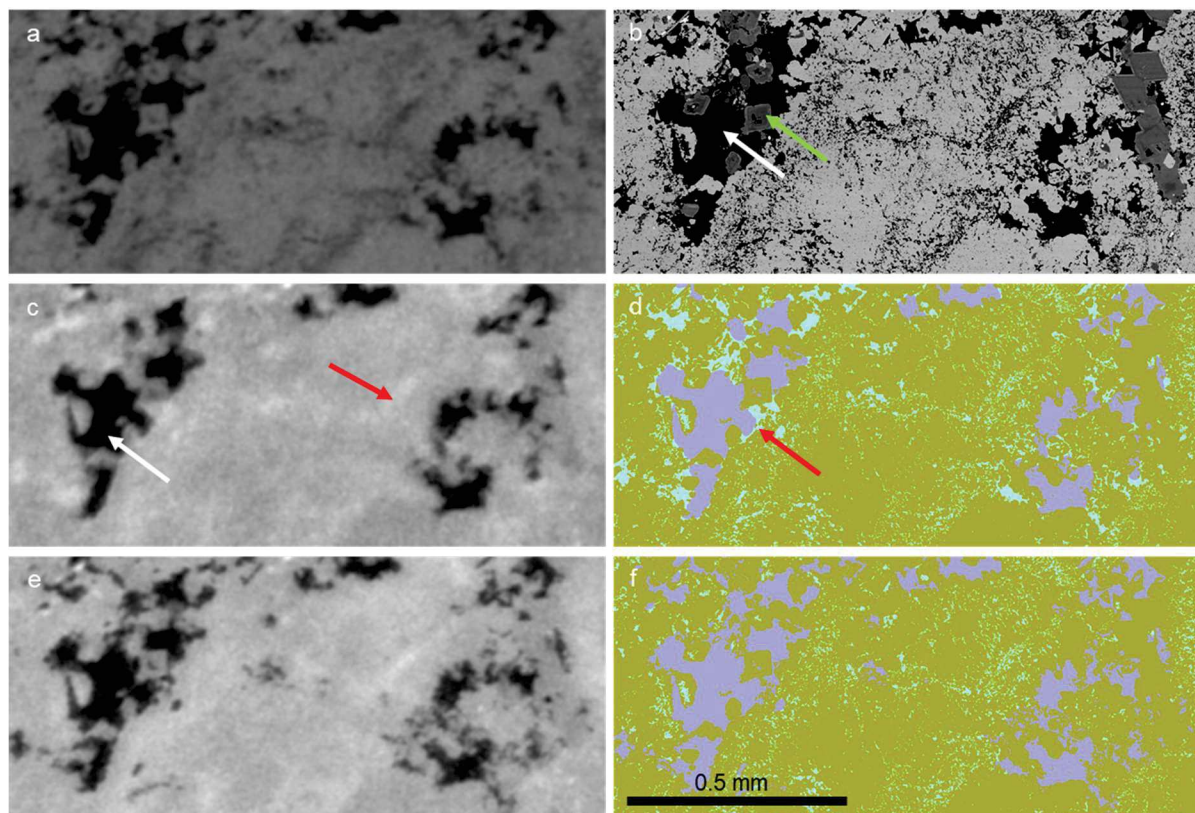
Figure 7-13 – Template illustrating the dry sample X-ray μCT (a), BSE image (b), μCTs following the first (0.25 psi) and second (1.56 psi) drainage steps (c and e), and a segmented composition using μCT and BSE images, which reveals porosity that cannot be resolved by the resolution employed in the X-ray imaging, and therefore were quantified as microporosity. The BSE image (b) depicts the intershrub pores (white arrow) partially filled with dolomites (green arrow) and abundant microporosity. The μCTs (c and d) exhibit the oil with lower attenuation (white arrow) and the macro- and microporous brine-filled regions with higher attenuation (red arrow). The segmented coupled X-ray μCT/BSE images (d and f) illustrate the oil (purple) occupying the larger and brine (cyan) the smaller pores, wherein the advancement of the oil through the center of the pore (red arrow) can be observed, exhibiting a morphology typical of water-wet conditions after the first drainage step (d), and culminating in the total occupation of the pore.

On the other hand, there is a general increase in the amount of water in contact with the minerals after aging (Figure 7-12), indicating that water trapped by snap-off during drainage may have been reconfigured, partially wetting the minerals. Although the number of surfaces in contact with water has increased across all minerals, the rate of increase varies by mineral. While calcite shows an increase of around 4% and alkali feldspar 7%, quartz increases by about

10%, and dolomite around 15%. This behavior indicates that mineralogy locally controls wettability, showing a greater favorability of dolomite and quartz to water compared to other minerals, a fact that can be directly observed in the images (Figure 7-14). So, although mineralogy is not impactful in the first drainage, it is observed that, during the resting stages, fluid reconfiguration occurs depending on the mineral location in the macropores.
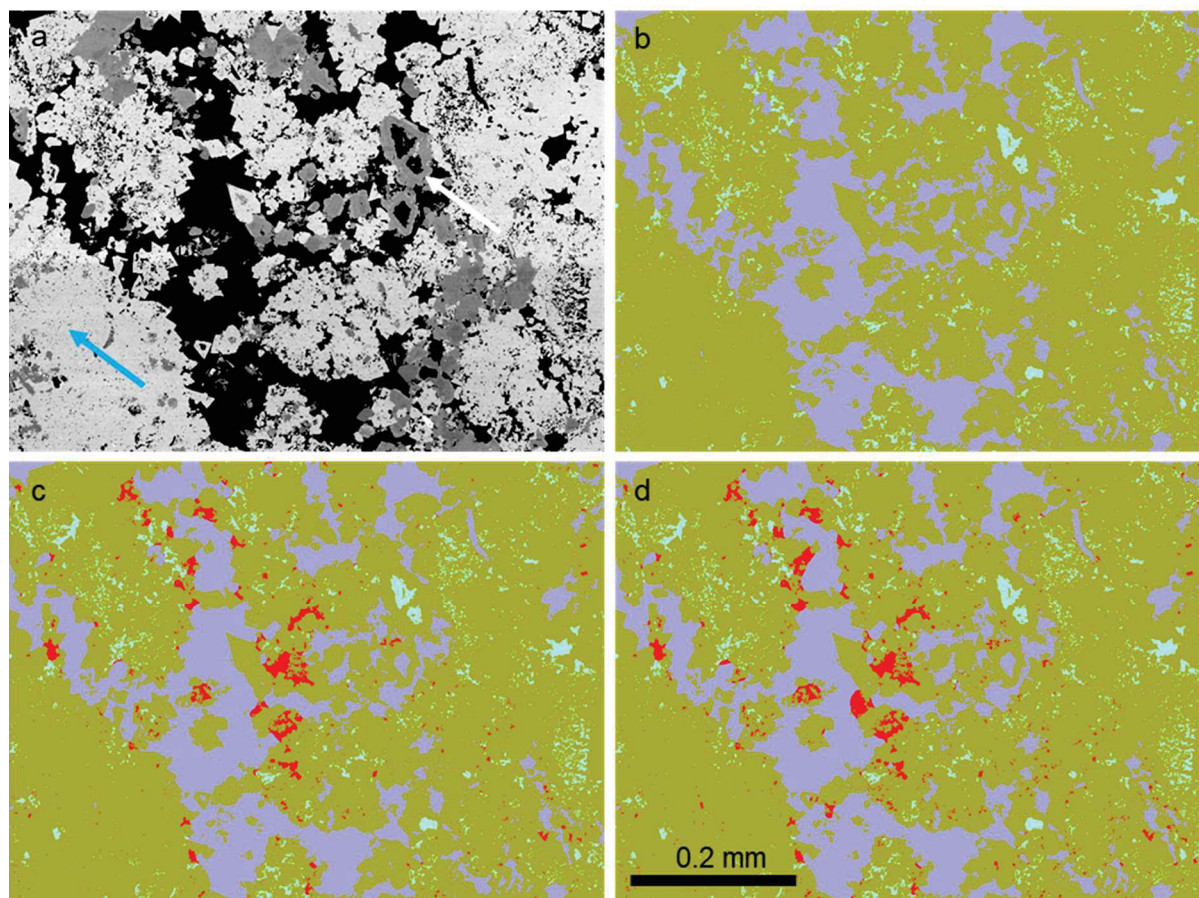
Figure 7-14 – Template illustrating the increase in water clusters (highlighted in red) during the aging and spontaneous imbibition stages. The BSE image (a) reveals the highly heterogeneous porous framework dominated by calcite (indicated by the blue arrow) and dolomite (white arrow) minerals. Figure b presents a combined segmented BSE/μCT image showing water (cyan) and oil (purple) after the drainage phase. Figures (c) and (d) display the water increase after aging and spontaneous imbibition, respectively.

After spontaneous imbibition, there is a greater increase in water-covered surfaces, with rates of 2.36, 15.63, 3.73, and 6.10% for calcite, dolomite, alkali feldspar, and quartz, respectively. This result confirms the changes generated during aging, indicating local variations in wettability caused by mineral variations. Furthermore, it is possible to identify that the mineral's location and its relationship with the surrounding mineralogy may affect these results, as minerals like dawsonite, for example, are located filling large pores where almost all

brine was displaced by oil during drainage. Hence, there are practically no surfaces in contact with water. Although other minerals may influence wettability, they do not occur in significant quantities and thus have a minimal global impact on the overall fluid saturation. Finally, it is paramount to emphasize that resolution may significantly influence the quantification of surfaces covered by water or oil, as fluid films are often thinner than the resolutions typically employed.

7.6.3   Oil Trapping

Given the observed mixed wettability behavior, it is anticipated that oil is entrapped both by adherence to minerals and by snap-off mechanisms. However, water wettability predominantly occurs in microporosity, whereas oil wettability prevails in macroporosity. As the oleic phase remains connected, oil drainage is observed, signifying that oil displacement by water occurs through the drainage of the wetting phase, essentially the inverse of the oil-to-water displacement process in the initial experimental stage. This indicates that oil is continuously drained through smaller throats with increased capillary pressure, a phenomenon evident in the images (Figure 7-15). Since the pores and throats among the shrubs are considerably large, a substantial amount of oil is drained at low pressures. Oil snap-off trapping is not observed, indicating that the entrapment primarily occurs under oil-wet conditions in macropores. Since the smaller pores appear to be water-wet, oil snap-off may occur within these pores; however, due to resolution limitations, this process cannot be adequately observed.

Similar to the first drainage, in forced imbibition, oil drainage is strongly conditioned by the imposed capillary pressure as discussed previously. Although the predominant mineralogy globally controls the overall wettability of the sample, no local variations are observed that could imply different oil entrapment patterns. During the steps of forced imbibition, discontinuous entrapment related to complex regions of the porous medium is observed (Figure 7-15). In the first step, a large amount of oil is trapped between dolomite crystals, both those filling the intershrub porosity and those replacing magnesian clays in muddy regions of the sample. As pressure increases, part of this oil is removed, leaving most of the residual oil in intracrystalline pores, mainly within the calcite shrubs, where the connection is more complex, resulting in isolated clusters of trapped oil.

Although mineralogy influences wettability, as discussed above, there is no clear preference for the adherence of residual oil to specific mineral surfaces. The evolution of

contacts between minerals and oil during the forced imbibition cycle is more related to the mineral's location within the porous framework. This means minerals in areas with greater accessibility, such as larger intershrub pores and throats, tend to experience more efficient oil removal. Consequently, minerals that tend to fill macropores (*e.g.*, dolomite and dawsonite) located among the shrubs will exhibit a greater reduction in oil-mineral contact rates during forced imbibition than those that replace shrubs. This is because intracrystalline pores are less accessible and tend to retain more oil. Hence, while capillary pressure is predominant in the process, mineralogy significantly influences texture construction rather than controlling the adhesion forces that impact wettability variations observed during aging and spontaneous imbibition cycles.
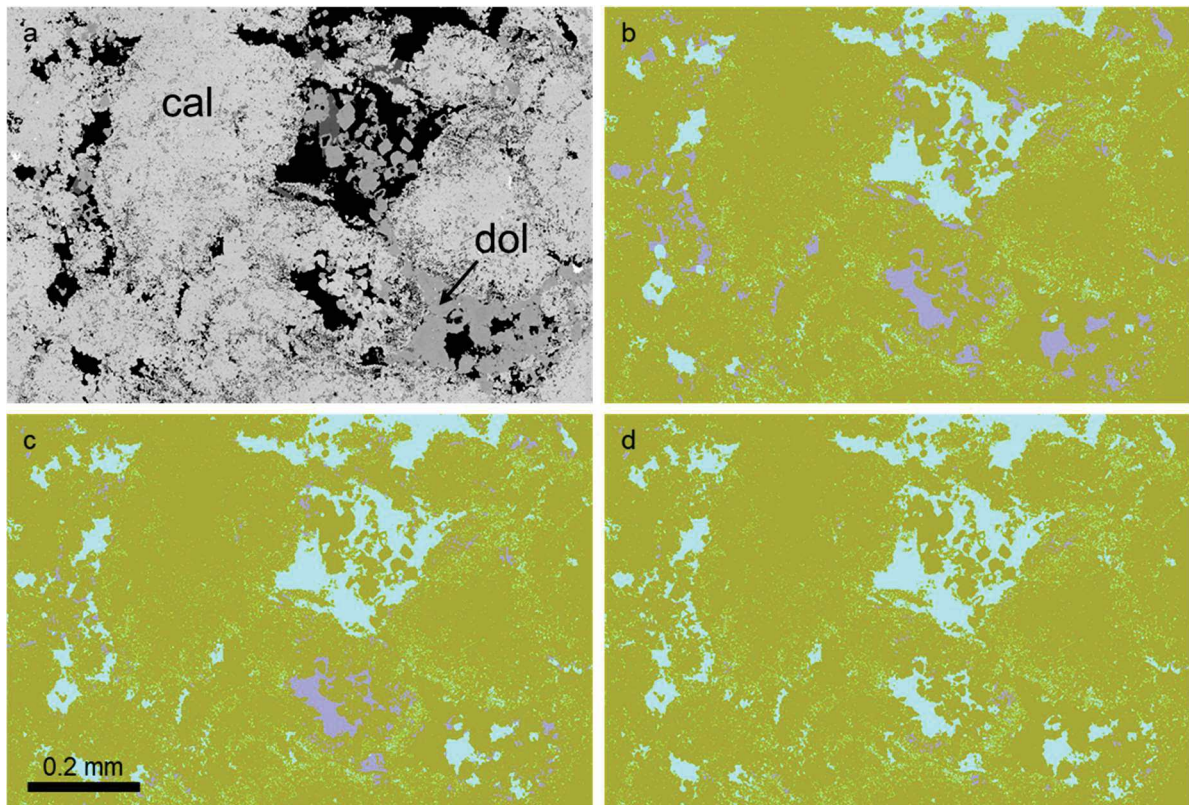
Figure 7-15 – Trapping after forced imbibition cycle: (a) BSE image and segmented coupled BSE/μCT images after steps 1 (a), 2 (b), and (c) which corresponds to capillary pressure of 0.38, 3.03, and 48.52 psi.

7.6.4   Second Drainage Cycle

The secondary drainage imaging allowed for a very clear observation of the spontaneous displacement of water by oil within the porous medium. Although it is a common laboratory procedure for calculating wettability indices like Amott and USBM (Amott, 1959; Donaldson,

Thomas and Lorenz, 1969) along with the other drainage and imbibition cycles, this experimental stage is typically not imaged. Despite being underestimated, this stage reveals important details about the displacement process of the non-wetting phase in a rock that has undergone wettability inversion, detailing the degree of wettability reversibility.

As macroporosity predominantly exhibits an affinity for oil as previously discussed, the entry of this phase occurs through the attraction of mineral surfaces. Oil saturation begins with films of this phase that grow until the macropore is completely filled (Figure 7-16). This process proved quite efficient in the sample, ultimately removing more than 70% of the oil present in the macropores (Figure 7-8), confirming the predominance of oil wettability in these pores. Sometimes, the filling is incomplete, with water trapped in the form of bubbles by snap-off, commonly observed throughout the images.
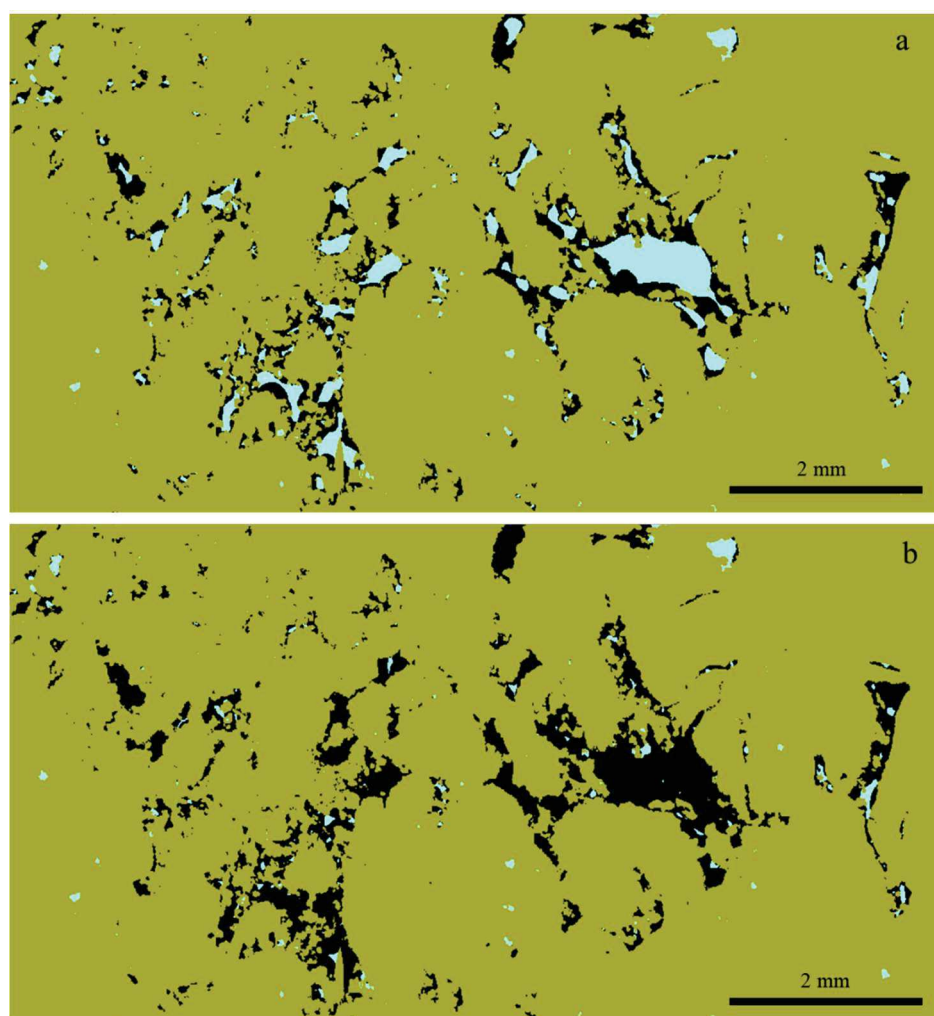
Figure 7-16 – Segmented X-ray µCT showing water replacement by oil spontaneously after 11 (a) and 27 (b) days.

Conversely, microporosity exhibits an opposing behavior, characterized by a limited entry of oil (Figure 7-17). Quantification through X-ray μCT indicated an increase of slightly over 20% in micro Sw (Figure 7-8). Although this value seems high, it is crucial to emphasize that the quantified microporosity in this study refers to the unresolved porosity of X-ray tomography. Consequently, a significant portion of these values represents the unsolved edges of macropores, resulting in an overestimation of microporosity. Figure 7-17c shows that part of the small pores was flooded with oil during drainage and it was mostly removed after forced imbibition Figure 7-17e. After the second drainage Figure 7-17g, the oil replaced the water in macropores, but part of the small pores where the oil entered during primary drainage remained with water. Thus, it is stressed that there was no wettability inversion in these pores in significative amounts, confirming the water-wet nature of the smaller pores.

Even though there is a predominant preference for oil adherence, part of the macroporosity is water-wet, confirming that macropores, while preferentially oil-wet, exhibit mixed wettability, as previously discussed. This characteristic results in a rather complex pattern of oil-to-water displacement (Figure 7-18), whose resolution sometimes can hinder the interpretation. As oil grows in the pores from mineral surfaces and eventually fills the entire pore, the region filled with oil exerts enough pressure to displace water from the water-wet pores. Consequently, oil enters the center of the pore in water-wet regions, indicating a simultaneous drainage and imbibition process. This phenomenon often creates an intriguing pattern, where one surface of the pore is oil-wet, while the opposite surface can be water-wet, which results in deformed oil/water surfaces. Moreover, at least part of the wettability differences is linked to rock texture, as the roughness generated by textural complexity (*e.g.* calcite recrystallization, dolomite precipitation, or dissolution) creates water-filled spaces, leading to localized water-wettability differences as studied by various authors (Mehmani *et al.*, 2019; Morrow, 1975; Wolansky and Marmur, 1998). This pattern is not evident during the first drainage, likely because the applied pressure allows oil to enter small indentations, confirming the impact of capillary pressure on wettability.

Once again, the relationship between wettability and mineralogy is complex, with the mineral's location complicating the analysis. Qualitative observations from the images show that many dolomite surfaces are covered by water in pores inundated with oil, indicating that this mineral may have a greater affinity for water concerning calcite, although quantitative results are ambiguous due to the mineral's location. On the other hand, other abundant minerals

such as quartz and alkali feldspar are located in tighter regions of the porous medium where microporosity predominates. Consequently, oil does not enter these pores, complicating the interpretation of the role of these minerals on wettability, even though previous experimental stages suggest that quartz has a greater affinity for water compared to calcite and alkali feldspar.
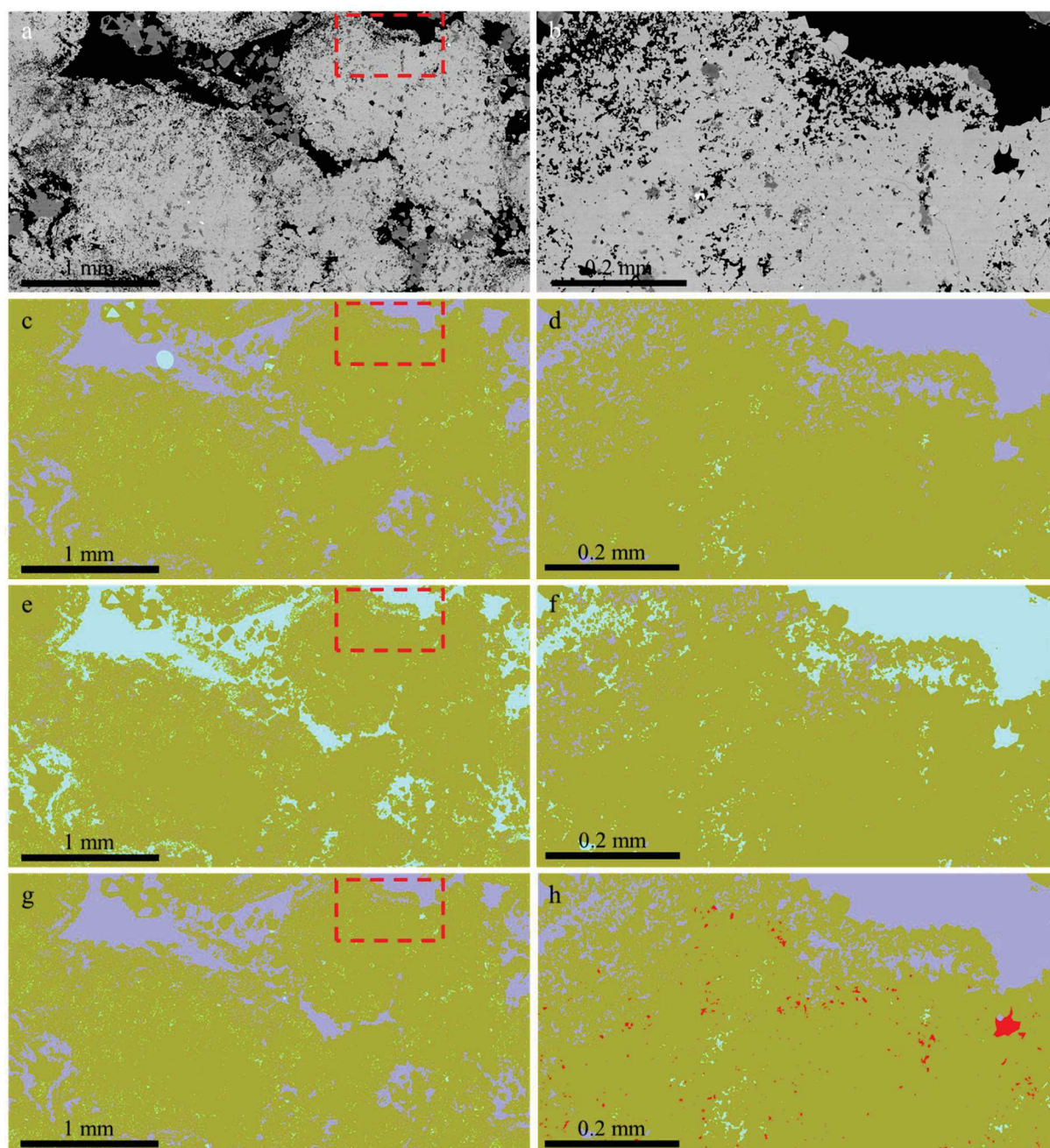
Figure 7-17 – BSE (a) and segmented X-ray µCT/BSE images illustrate the evolution of fluid saturation during first drainage (c), forced imbibition (e), and second drainage (g). Figures b, d, f, and h provide close-up views of the dashed areas in figures a, c, e, and g, respectively. In figure h, the red-highlighted regions show the saturation differences between the primary and second drainage: in these pores, water was displaced during the primary drainage but remained present after the second drainage.
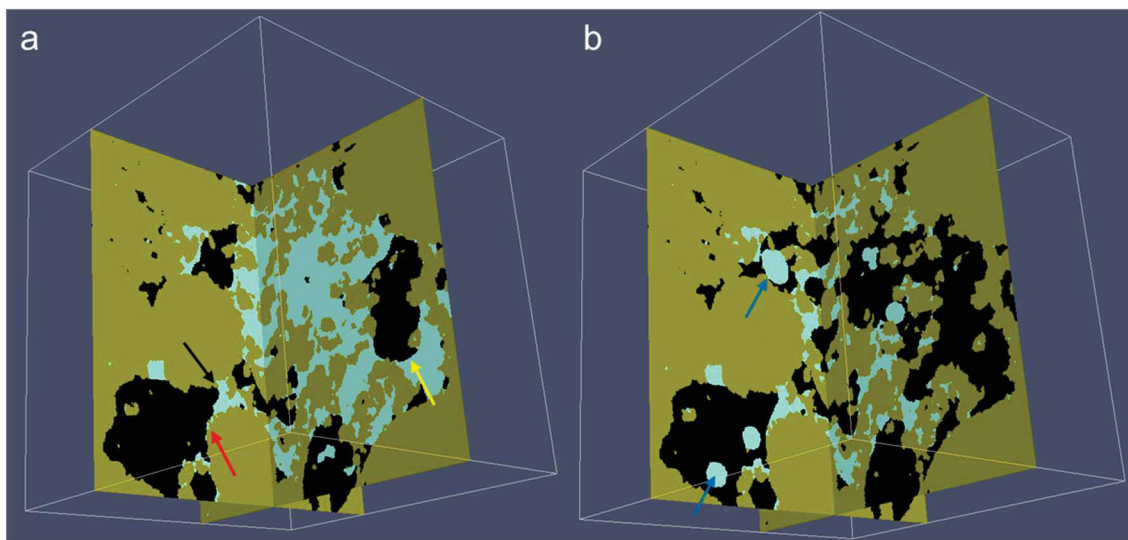
Figure 7-18 – 3D segmented images showing the evolution of saturation during the second drainage exhibiting highly complex pattern: a) After 11 days, the advancement of oil (black) can be observed as both a wetting phase (red arrow) and a non-wetting phase (black arrow) in the same pore, as well as the occupation of the pore by oil with a typical non-wetting pattern (yellow arrow); b) After 27 days, oil progresses in filling the pores, with the formation of water snap-off (blue arrows), confirming the mixed wettability condition.

7.7   Conclusions

In this study, we conducted drainage and imbibition cycles, followed by X-ray imaging at the pore scale, on a carbonate sample from the Barra Velha Formation in the Santos Basin, Brazil. The aim was to investigate fluid saturation and oil entrapment mechanisms at the pore scale. The main conclusions derived from the analyses are as follows:

- During the experiment, the sample exhibited mixed wettability in macropores, whereas micropores predominantly displayed water-wet behavior.
- The texture of the carbonate matrix played a critical role during the primary drainage and forced imbibition cycles, influencing the distribution of initial water saturation and residual oil. Irreducible water and residual oil were primarily trapped in intracrystalline pores, where the complexity of narrow pore throats limited connectivity and accessibility.
- During the primary drainage cycle, oil first acted as the non-wetting phase and tended to wet the rock only under higher pressure conditions, particularly in macroporosity. In smaller pores, oil invasion was significantly restricted due to the geometric constraints of the pore throats.

- Through aging and spontaneous imbibition, fluids underwent reconfiguration, with water tending to migrate back into narrower regions, especially in areas associated with dolomite and quartz denoting the importance of these minerals on wettability.

- Oil entrapment was primarily governed by the rock texture, with no clear influence from mineralogy. This behavior appears to be related to the predominant presence of calcite, which exhibited a higher affinity for oil compared to other minerals during aging and spontaneous imbibition stages.

- Imaging after secondary drainage revealed important aspects of water-oil replacement behavior following wettability inversion. No significant wettability inversion was observed in smaller pores, while macropores were predominantly oil-wet, even though we can see locally a mixed-wet behavior generated by mineral variations and textural framework patterns.

These findings provide detailed insights into fluid saturation and trapping mechanisms in complex carbonate systems, with significant implications for characterizing carbonate reservoirs and enhancing oil recovery strategies.

7.8   Acknowledgments

8. Article 7: HERLINGER, R.; KNACKSTEDT, M.; YOUNG, Y.; VIDAL, A. C. Integrating X-ray µCT and Pore-Scale Simulation for Relative Permeability Prediction. Geoenergy and Engineering Science, submitted, 2025.

8.1 Abstract

This study presents a methodology that integrates multiphase imaging with pore-scale simulations to derive relative permeability curves. Drainage cycles were performed using a centrifuge to displace brine with mineral oil until the sample reached the initial saturation condition for the experiment. Subsequently, the sample underwent spontaneous imbibition to replace the oil with brine. X-ray imaging was conducted after both the drainage and imbibition cycles to obtain saturation data for the sample. Post-drainage images were subdivided into sub-samples to construct a capillary pressure curve. Hence, saturation was measured directly for each sub-sample, and pressure was estimated based on the distance from the centrifuge rotor. The relative permeability curve was derived through simulations conducted on segmented oil and water phases under various saturation conditions after spontaneous imbibition. The results obtained under water-wet conditions demonstrated agreement with experimentally derived relative permeability curves under analogous conditions. This methodology can be adapted and applied to predict these properties under reservoir conditions, providing valuable insights into the dynamics of multiphase flow. Unlike SCAL experiments, which do not allow for direct visualization of the porous medium, this approach enables the identification and analysis of operational challenges that might otherwise remain undetected or poorly understood.

Keywords: relative permeability, X-ray µCT, digital rock physics

8.2 Introduction

Relative permeability traces back to the early days of the petroleum industry when there was a critical need to replicate waterflooding processes in laboratory settings to predict the behavior of fluids in the reservoir (Fettke and Copeland, 1931; Hassler, Rice and Leeman,

1936). This approach enabled the forecasting of reservoir productivity over its operational lifespan. Over the decades, relative permeability curves have become a benchmark in the petroleum industry, integrating into simulation models to predict fluid production (Behrenbruch *et al.*, 2018; Moodie *et al.*, 2021). Consequently, this laboratory data holds significant importance as it can influence the economic viability of a project, underscoring the critical need for its reliability (Moghadasi *et al.*, 2015).

Although they have been used for nearly a century, their results remain uncertain. These ambiguities may arise from a wide range of factors, including sampling, where the core must be intact, in other words, free from both natural fractures and those induced during sampling, as well as undamaged by the invasion of drilling fluids. Furthermore, the samples must be homogeneous (Mansour, Al *et al.*, 2024) and representative in terms of rock typing (Kamath *et al.*, 2005). Additionally, uncertainties tied to testing conditions, such as the methodology employed (steady-state or non-steady-state), can yield significantly different outcomes (Honarpour and Mahmood, 1988). Experiment parameters, including pressure, temperature, and capillary number, can also profoundly influence the results (Kamath *et al.*, 2005). Capillary end effects may further disrupt measurements, sometimes drastically (Huang and Honarpour, 1998). Issues like sample damage during testing, such as fines migration, can induce pressure drops, complicating the accurate determination of the curve's endpoint values (Zeinijahromi *et al.*, 2016). Thus, the sole reliable approach is to observe fluid configurations at the pore scale directly through X-ray microtomography (μCT) to comprehend relative permeability results. Accordingly, we present a methodology for deriving relative permeability curves by integrating multiphase X-ray μCT with pore-scale simulations.

8.3   Materials and Methods

The subsample was extracted from a 1.5" core plug with helium porosity 23.4% and permeability 101mD obtained from a reservoir of the Barra Velha Formation, Brazilian Pre-Salt. The sub-sample was plugged with a diameter of 3 mm and a length of 8.9 mm. The fluids utilized in the experiments consisted of a 0.75 M NaI brine solution and mineral oil (CAS 8042-47-5). The rock specimen is a well-sorted, massive grainstone composed of carbonate particles approximately 100 μm in size composed predominantly of calcite.

The sub-sample was saturated with brine under vacuum, followed by pressing at 560 bar for 48 hours to eliminate air bubbles. Drainage was then performed by centrifuging the sample at 500, 1000, 2000, and 4000 RPM (0.13, 0.5, 2.02, and 8.1 psi) to displace the brine with oil for 21 hours. The sample was flipped during the process to ensure more homogeneous saturating through the sample. Then the sample underwent spontaneous imbibition soaked in water for 17 days. Throughout the experiment, tomographic imaging documented saturation changes at the dry state (Figure 8-1), brine saturated, post-drainage, and after-imbibition stages. The images were acquired using a helical scanning trajectory (Sheppard *et al.*, 2014) with the sample placed in a 4 mm NMR glass tube and scanned for approximately 24 hours. The tube was filled with mineral oil for imaging after drainage and brine after spontaneous imbibition. The μCTs were acquired with a 1-second exposure time, 12 averages, a voltage of 100 kV, 60 μA, and a resolution of 1.5 μm.
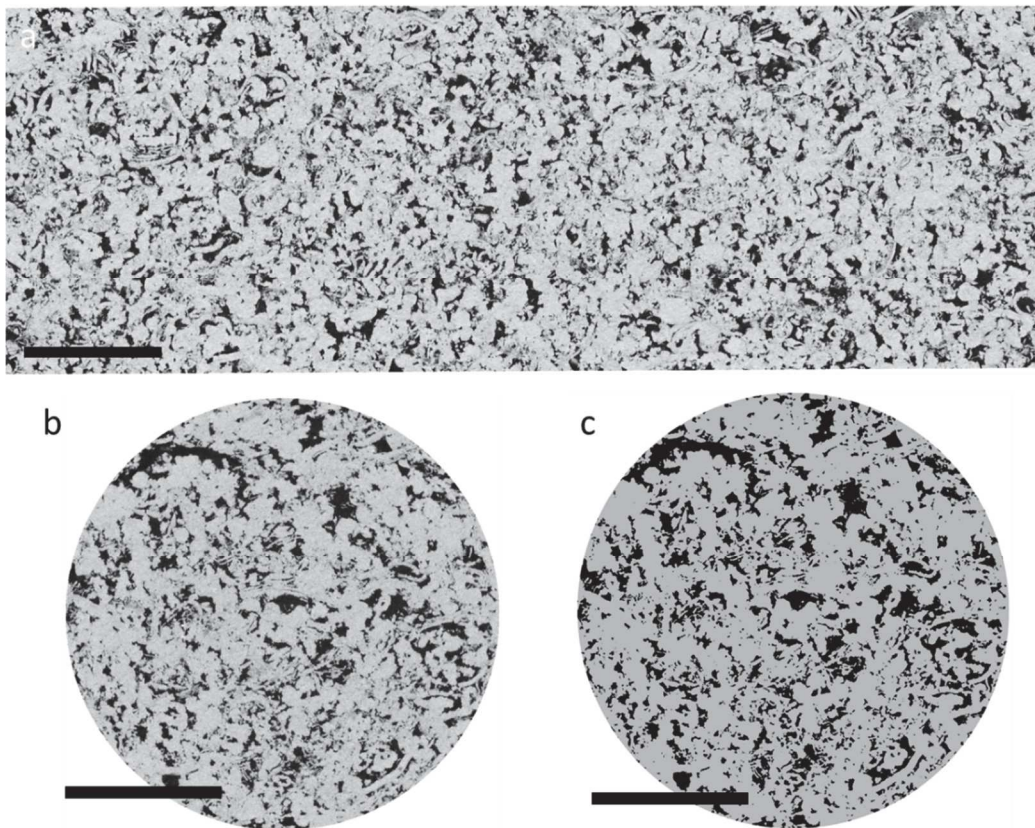
Figure 8-1 – Longitudinal (a) and orthogonal slices (b) of the μCT, along with the segmented image (c), illustrating the homogeneous nature of the sample (scale bar = 1 mm).

After image reconstruction, the μCTs were corrected for beam-hardening effects using a smoothed radial intensity profile, followed by normalization. The differential images technique

was employed to estimate microporosity volume (Lin *et al.*, 2016). Pore/solid and brine/oil segmentations were determined using the converging active contours (CAC) method (Sheppard, Sok and Averdunk, 2004), from which porosities and fluid saturations were calculated. The capillary pressures reached during centrifugation were estimated using the equation below:

$$Pc = \frac{1}{2}\Delta\rho\omega(r_2^2 - r_1^2)$$
(8.1)

where Pc is the capillary pressure, ω is the rotation speed, r is the distance from the rotor center, and $\Delta\rho$ represents the density differences between the fluids. Absolute permeability, as well as oil and water permeabilities, were directly simulated using the Stokes-Brinkman method implemented in the Geodict software, utilizing the left identity right (LIR) solver (Linden, Wiegmann and Hagen, 2015). The method proposed by Brinkman (1947) is described by the following equations:

$$\nabla p = -\mu K^{-1}\vec{v} + \nabla . \mu^*(\nabla\vec{v} + \vec{v}^T)$$
(8.2)

$$\nabla . \vec{v} = 0 (8.3)$$
(8.3)

where p represents the fluid pressure, $\vec{v}$ is the fluid velocity, K is the permeability tensor, μ is the fluid viscosity, and μ^* is the effective fluid viscosity. The sample image was subdivided into 36 regions, each comprising 500^3 voxels, to compute the saturation versus capillary pressure, enabling the extraction of a high-resolution capillary pressure curve. Subsequently, the relative permeability was determined based on 20 regions of the sample, also defined by 500^3 voxels. In the final drainage cycle, relative permeabilities were calculated concerning the initial saturation condition (Swi). In addition to the 500^3 voxel models, two models with 1000^3 and 1250^3 voxels were simulated. Finally, permeabilities corresponding to varying saturation states were derived from the μCT dataset obtained following the spontaneous imbibition process, and the relative permeability model was adjusted according to the Brooks-Corey modified power-law model (Lake *et al.*, 2014):

$$k_{ro} = k_{ro,\ max}\left(\frac{S_o - S_{or}}{1 - S_{or} - S_{wi}}\right)^{n_o}$$
(8.4)

$$k_{rw} = k_{rw,\ max}\left(\frac{S_w - S_{wi}}{1 - S_{or} - S_{wi}}\right)^{n_w}$$
(8.5)

where k_{ro} and k_{rw} represent the relative permeabilities of oil and water, respectively, S_o, S_{or}, S_w, and S_{wi} denote the oil, residual oil, water, and initial water saturations, respectively, and n_o and n_w are the fitting exponents for oil and water.

8.4 Results and Discussion

The total porosity of the sub-plug, as determined via µCT, was 23.54%, closely aligning with the helium experimentally derived value. The porosities of the 500³ voxel models exhibited a range between 22.01% and 25.02%, while the absolute permeabilities spanned from 172.9 to 663.1 mD. For the larger models, with resolutions of 1000³ and 1250³ voxels, porosities were measured at 23.24% and 23.34%, respectively, with corresponding permeabilities of 263.7 and 292.4 mD. Notably, porosities remained consistent across the investigated scales. Permeabilities, however, demonstrated greater variability due to the influence of minor internal heterogeneities, which can substantially reduce permeability in larger investigation volumes.

The representative elementary volume (REV) analysis indicated that porosity variations become negligible for volumes exceeding 450³ voxels, suggesting that the utilized volume is larger than the REV (Figure 8-2a). Drainage results showed that, at a pressure of 0.13 psi, oil did not enter the sample. With subsequent pressures, the sample's saturation increased until stabilizing at approximately 17% (Figure 8-2b). k_{ro} under initial saturation conditions revealed a maximum value of approximately 0.82. Other adjusting parameters using the Brooks-Corey model included S_{or} of 30%, n_o of 1.80, n_w 1.87, and k_{rw} of 0.14. For the simulated relative permeability values in the volume of size 1000³, k_{ro} and k_{rw} were 0.33 and 0.04, respectively, for a water saturation S_w of 0.38. Meanwhile, for the 1250³ sized-volume, the S_w values were 0.25 and 0.06, respectively, considering a S_w of 0.44 (Figure 8-3).
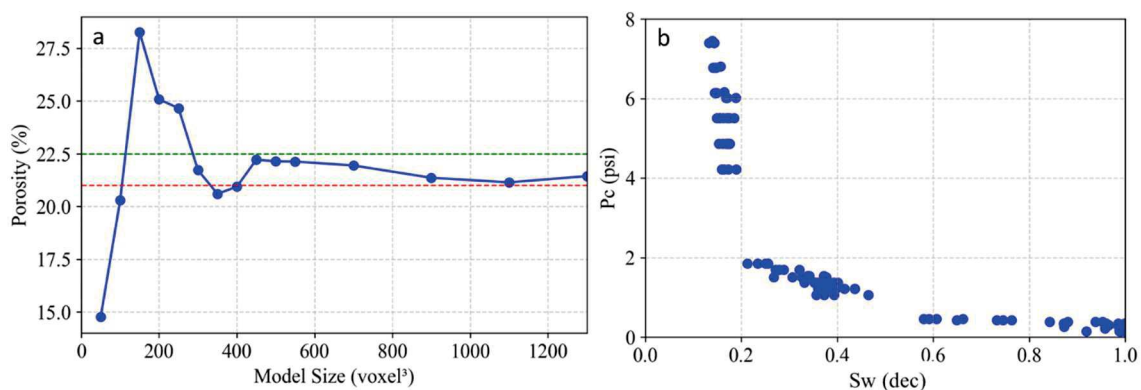
Figure 8-2 - (a) Analysis of porosity variation as a function of the model size for the determination of the REV; (b) Results of saturation calculations as a function of capillary pressure variation across the sample.
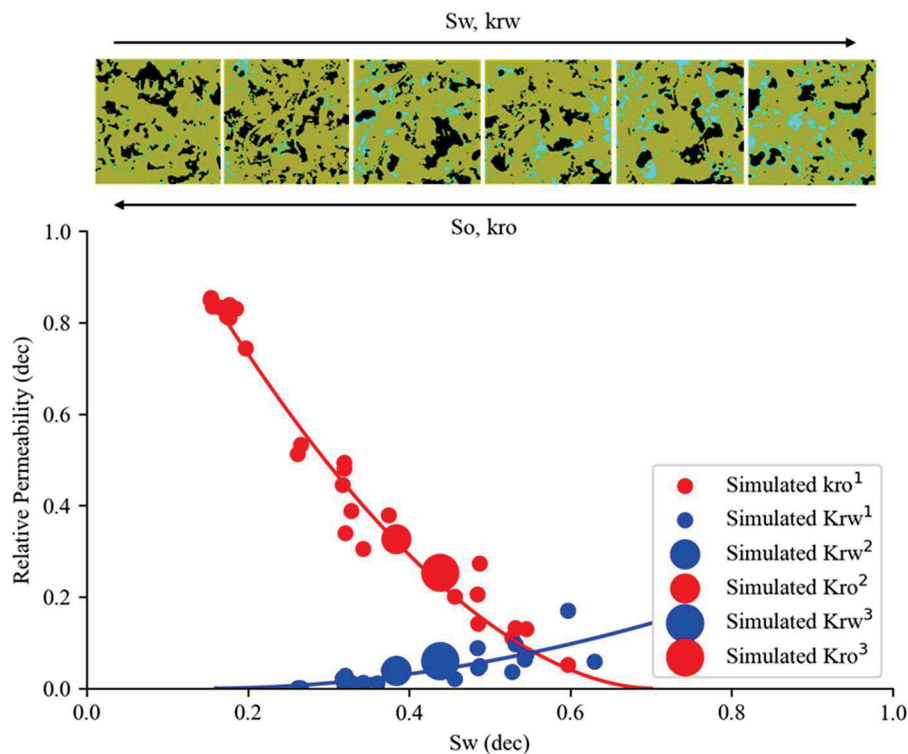
Figure 8-3 – Relative permeability curves for water and oil resulting from direct simulation on the segmented oil and water phases ([1]500^3, [2]1000^3, and [3]1250^3 sized models). The schematic above the curves illustrates the variation in fluid saturation across the simulated models (solid, brine, and oil in ocher, cyan, and black).

The capillary pressure curve derived from the saturations of the sub-samples exhibits a homogeneous profile, indicating the absence of significant saturation variations attributable to lithological heterogeneities that might induce alterations in porosity, pore sizes, or their associated throats, and, consequently, in permeability. Furthermore, a pronounced transition zone, typically expected in more heterogeneous systems, is not observed, as we could expect due to sample homogeneity. In a broader context, it is evident that pressure variations along the sample can be substantial, driving differences in saturation. Accordingly, given that the sample face oriented toward the rotor center during testing experiences maximum pressure, while the opposite face is subjected to minimum pressure, it becomes feasible to construct a capillary pressure curve using a single centrifuge drainage cycle. This approach would significantly expedite the process of acquiring capillary pressure curves.

The relative permeability curves demonstrated results consistent with experimental laboratory data of other fields obtained under water-wet conditions (Figure 8-4), even though they were derived during a spontaneous imbibition process. This observation suggests that oil trapping mechanisms and fluid distribution may be similar during spontaneous and forced imbibition. However, under oil-wet or mixed-wet scenarios, the pressure would be required to

displace oil, rendering the determination of relative permeabilities through a simple spontaneous imbibition process infeasible. Alternatively, a rapid core flooding process could be implemented to achieve partial oil replacement under laboratory or reservoir conditions or even under centrifugation, enabling the calculation of relative permeabilities.
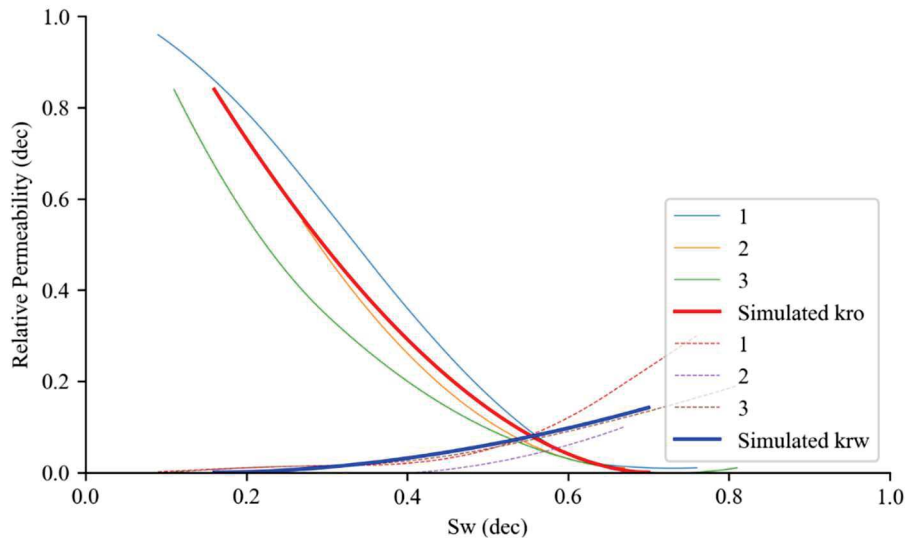
Figure 8-4– Comparison between the simulated curve and relative permeability curves obtained under water-wet conditions: 1 (Verre et al., 2007), 2 (Lin and Huang, 1990), and 3 (Khosravi, Simjoo and Chahardowli, 2024). Continuous and dashed lines represents k_{ro} and k_{rw}, respectively.

While the method shows potential for coupling laboratory results with simulations to better understand plug-scale phenomena, the selection of the sample is critical. Permeability is significantly influenced by lithological heterogeneities due to its tensorial nature, and local variations in lithology can heavily impact results. Additionally, capillary pressure curves are sensitive to pore throat variations. Smaller samples, with fewer pores, are expected to have less variability of throats, resulting in thinner transition zones, and may also be affected by border effects at low pressures. Hence, the proposed method is subject to scale limitations, a challenge extensively discussed in the literature related to digital rock physics (Blunt, 2017; Karimpouli *et al.*, 2018; Malik and Sharma, 2020; Sadeghnejad, Enzmann and Kersten, 2021b).

8.5   Conclusions

In this study, we present a straightforward methodology that integrates multiphase imaging with pore scale simulation to estimate relative permeability and directly measure

saturation for the construction of capillary pressure curves. The results obtained under water-wet conditions demonstrated strong agreement with relative permeability curves derived experimentally under similar conditions. This approach can be adapted and employed to predict these properties under reservoir conditions, providing insights into multiphase flow dynamics. Unlike SCAL experiments, which do not allow for direct observation of the porous medium, this method offers a means to identify and understand operational issues that might otherwise remain undetected or poorly understood.

9. Conclusions

This study integrates multiple methodologies across various observation scales, ranging from pore to well, to investigate the residual oil in reservoirs of the Barra Velha Formation within the Santos Basin, Brazil. The interpretation of the results allowed us to propose the following conclusions:

The textural characteristics of the rocks in the Barra Velha Formation represent an important control on oil retention in reservoirs. Rocks with more complex textures, characterized by greater morphological and dimensional pore diversity, tend to exhibit higher residual oil saturation (Sor), according to analyses combining relative permeability data with petrography and X-ray µCT imaging. Thus, a correlation between sedimentary facies and oil retention tendencies can be drawn: *in-situ* rocks showed a higher tendency for oil retention due to their textural complexity, while laminated reservoirs dominated by intercrystalline porosity demonstrated greater sweeping efficiency. Reworked rocks showed better oil recovery when composed of fine particles, such as fine grainstones, whereas rudstones tended to exhibit higher Sor.

X-ray µCT analysis following relative permeability tests under reservoir conditions indicated mixed wettability, both intra- and inter-sample. This result suggests that Sor also can vary independently of texture, even though when we compare rocks with the same wet conditions, the differences should be controlled by rock textures. In oil-wet rocks, Sor tends to be lower, as oil is trapped in corners and more complex regions, which represent a smaller relative volume of the porous system. Conversely, oil trapped under water-wet conditions tends to remain in the pore centers, occupying larger volumes. Thus, relative permeability data analysis indicates that most of the trapped oil is likely located at pore centers due to snap-off mechanisms in rocks where wettability may be mixed or water-wet, although a minor part of the experiments suggests oil-wet conditions.

Sor analysis based on well log data indicated trends consistent with those from rock data, where Sor increases in rocks with complex porous systems, as opposed to more homogeneous rocks. This alignment between laboratory and well log data validates the upscaling of these results, in addition to indicating that conventional formation evaluation techniques, combined with machine learning, can be employed to propagate Sor data across other wells.

Pore-scale modeling of Pre-salt rocks proved to be an alternative for simulating at pore-scale in a controlled environment. By systematically varying sedimentary and diagenetic textures, it was possible to assess the sensitivity of these variations on petrophysical properties. It was observed that dolomite content in the rocks homogenizes the porous medium, favoring oil drainage under water-wet conditions. On the other hand, increased surface area promotes oil retention under oil-wet conditions.

High-resolution imaging under laboratory conditions during drainage and imbibition cycles in a centrifuge enabled detailed identification of saturation evolution under oil-wet and mixed-wettability conditions. In general, primary drainage was observed to be influenced by wettability when oil-wet conditions were stronger; otherwise, it was controlled by texture. Additionally, texture and mineralogy significantly affected pore-scale wettability, where pores smaller than 5 micrometers were generally water-wet. The analysis indicated that dolomite and quartz could locally affect wettability, although calcite predominance appeared to support a macro-scale wettability trend in the sample. Finally, it was highlighted that oil remained trapped after forced imbibition cycles primarily in pores within calcite shrubs where accessibility complexity was significant.

These findings highlight the intricate interplay between texture, mineralogy, and wettability in controlling residual oil distribution, providing valuable insights for reservoir characterization and enhanced oil recovery strategies.

References

ADEBAYO, A. R.; BARRI, A. A.; KAMAL, M. S. Effect of flow direction on relative permeability curves in water/gas reservoir system: Implications in geological CO2 sequestration. **Geofluids**, v. 2017, p. 1–10, 2017.

AHMED, T. **Reservoir Engineering Handbook**. Fourth Edition ed. [s.l.] Elsevier, 2010.

ALHAMMADI, A. M.; ALRATROUT, A.; SINGH, K.; BIJELJIC, B.; BLUNT, M. J. In situ characterization of mixed-wettability in a reservoir rock at subsurface conditions. **Scientific Reports**, v. 7, n. 1, p. 10753, 7 dez. 2017.

AL-HOUSANI, H.; WAZEER, F. EL; ALI, A. E.; AL-SAHN, H.; XU, S. Using residual oil saturation (Sor) to reduce uncertainty in reservoir modeling - A case study. **Society of Petroleum Engineers - Abu Dhabi International Petroleum Exhibition and Conference 2012, ADIPEC 2012 - Sustainable Energy Growth: People, Responsibility, and Innovation**, v. 3, p. 1830–1844, 2012.

ALQAHTANI, N.; ALZUBAIDI, F.; ARMSTRONG, R. T.; SWIETOJANSKI, P.; MOSTAGHIMI, P. Machine learning for predicting properties of porous media from 2d X-ray images. **Journal of Petroleum Science and Engineering**, v. 184, n. March 2019, p. 106514, 2020.

ALQAM, M. H.; ABU-KHAMSIN, S. A.; SULTAN, A. S.; AL-AFNAN, S. F.; ALAWANI, N. A. An investigation of factors influencing carbonate rock wettability. **Energy Reports**, v. 7, p. 1125–1132, 1 nov. 2021.

AL-SHALABI, E. W.; GHOSH, B. Effect of Pore-Scale Heterogeneity and Capillary-Viscous Fingering on Commingled Waterflood Oil Recovery in Stratified Porous Media. **Journal of Petroleum Engineering**, v. 2016, p. 1–14, 25 maio 2016.

AMANULLAH, M.; ALLEN, T. **Extended Aramco Method- Its technico-Economic Significance in Non-damaging Drill-in Fluid Design.** SPE/IADC Middle East Drilling Technology and Exhibition. **Anais**...Byrne and Patey, 2013

AMOTT, E. Observations Relating to the Wettability of Porous Rock. **Transactions of the AIME**, v. 216, n. 01, p. 156–162, 1 dez. 1959.

ANDERSON, W. G. Wettability Literature Survey - Part 1: Rock-Oil-Brine Interactions and the Effects of Core Handling on Wettability. **Society of Petroleum Engineers of AIME, (Paper) SPE**, n. October, p. 1125–1144, 1985.

___. Wettability Literature Survey - Part 2: Wettability Measurement. **Journal of Petroleum Technology**, v. 38, n. 12, p. 1246–1262, 1986.

___. Wettability Literature Survey - Part 6: The Effects of Wettability on Waterflooding. **Journal of Petroleum Technology**, n. December, p. 1605–1622, 1987.

ANDRÄ, H. *et al.* Digital rock physics benchmarks-part II: Computing effective properties. **Computers and Geosciences**, v. 50, p. 33–43, jan. 2013.

ANDREW, M.; BIJELJIC, B.; BLUNT, M. J. Pore-scale contact angle measurements at reservoir conditions using X-ray microtomography. **Advances in Water Resources**, v. 68, p. 24–31, 2014.

ANTO, R.; BHUI, U. K. Surfactant flooding for enhanced oil recovery – Insights on oil solubilization through optical spectroscopic approach. **Journal of Petroleum Science and Engineering**, v. 208, 1 jan. 2022.

API. **Recommended Practices for Core Analysis, Recommended Practice 40**. Second Edition ed. [s.l.] American Petroleum Institute, 1998.

ARCHIE, G. E. The Electrical Resistivity Log as an Aid in Determining Some Reservoir Characteristics. **Transactions of the AIME**, v. 146, n. 01, p. 54–62, 1 dez. 1942.

ARGANDA-CARRERAS, I.; KAYNIG, V.; RUEDEN, C.; ELICEIRI, K. W.; SCHINDELIN, J.; CARDONA, A.; SEBASTIAN SEUNG, H. Trainable Weka Segmentation: a machine learning tool for microscopy pixel classification. **Bioinformatics**, v. 33, n. 15, p. 2424–2426, 1 ago. 2017.

ARMELENTI, G.; GOLDBERG, K.; KUCHLE, J.; ROS, L. F. DE. Deposition, diagenesis and reservoir potential of non-carbonate sedimentary rocks from the Rift Section of Campos Basin, Brazil. **Petroleum Geoscience**, v. 22, n. 3, p. 223–239, 2016.

ARMENTEROS, I. **Carbonates in Continental Settings: Geochemistry, Diagenesis and Applications**. [s.l.] Elsevier, 2010. v. 62

ARSHADI, M.; GESHO, M.; QIN, T.; GOUAL, L.; PIRI, M. Impact of mineralogy and wettability on pore-scale displacement of NAPLs in heterogeneous porous media. **Journal of Contaminant Hydrology**, v. 230, p. 103599, 2020.

AUSTIN, J. A. J.; UCHUPI, E. Continental-oceanic crustal transition off southwest Africa. **AAPG Bulletin**, v. 66, n. 9, p. 1328–1347, 1982.

BAKKE, S.; ØREN, P.-E. 3-D Pore-Scale Modelling of Sandstones and Flow Simulations in the Pore Networks. **SPE Journal**, v. 2, n. 2, p. 136–149, 1997.

BALLAH, J.; CHAMEROIS, M.; DURAND-VIDAL, S.; MALIKOVA, N.; LEVITZ, P.; MICHOT, L. J. Effect of chemical and geometrical parameters influencing the wettability of smectite clay films. **Colloids and Surfaces A: Physicochemical and Engineering Aspects**, v. 511, p. 255–263, dez. 2016.

BARNETT, A. J.; OBERMAIER, M.; AMTHOR, J.; SHARAFODIN, M.; BOLTON, M.; CLARKE, D.; CAMARA, R. Origin and Significance of Thick Carbonate Grainstone Packages in Nonmarine Successions: A Case Study from the Barra Velha Formation, Santos Basin, Brazil. *Em*: **The Supergiant Lower Cretaceous Pre-Salt Petroleum Systems of the Santos Basin, Brazil**. [s.l.] AAPG, 2021. v. 124p. 155–174.

BASHIRI, A.; KASIRI, N. Properly use effect of capillary number on residual oil saturation. **Society of Petroleum Engineers Nigeria Annual International Conference and Exhibition 2011**, p. 649–651, 2011.

BASSO, M.; BELILA, A. M. P.; CHINELATTO, G. F.; SOUZA, J. P. DA P.; VIDAL, A. C. Sedimentology and petrophysical analysis of pre-salt lacustrine carbonate reservoir from the

Santos Basin, southeast Brazil. **International Journal of Earth Sciences**, v. 110, n. 7, p. 2573–2595, 1 out. 2021.

BAUMGARTEN, C. S. Evolução estrutural de Pampo, Badejo e Linguado durante a deposição da Formação Lagoa Feia. **Boletim Técnico da Petrobras**, v. 28, n. 2, p. 91–101, 1985.

BAUMGARTEN, C. S.; DUTRA, A. J. C.; SCUTA, M. S.; FIGUEIREDO, M. V. L.; SERQUEIRA, M. F. P. B. Coquinas da formação Lagoa Feia, Bacia de Campos: evolução da geologia de desenvolvimento. **Boletim de Geociências da Petrobras**, v. 2, n. 1, p. 27–36, 1988.

BEHRENBRUCH, P.; HOANG, T. G.; HUU, M. T. DO; BUI, K. D.; KENNAIRD, T. **The Importance of Optimal Choice of Relative Permeability Relationships in Reservoir Simulation.** SPE Asia Pacific Oil and Gas Conference and Exhibition. **Anais**...SPE, 23 out. 2018

BENNER, F. C.; BARTEL, F. The effect of Polar Impurities Upon Capillary and Surface Phenomena In Petroleum Production. *Em*: **Drilling and Production Practice**. [s.l.] API, 1941. p. 341–348.

BERRY, M. V. The molecular mechanism of surface tension. **Physics Education**, v. 6, n. 2, p. 001, 1 mar. 1971.

BEUCHER, S. The Watershed Transformation Applied to Image Segmentation. **Scanning Microscopy-Supplement-**, v. 6, p. 299–314, 1992.

BLAICH, O. A.; FALEIDE, J. I.; TSIKALAS, F. Crustal breakup and continent-ocean transition at South Atlantic conjugate margins. **Journal of Geophysical Research: Solid Earth**, v. 116, n. 1, p. 1–38, 2011.

BLUNT, M. Physically-based network modeling of multiphase flow in intermediate-wet porous media. **Journal of Petroleum Science and Engineering**, v. 20, n. 3–4, p. 117–125, 1998.

___. **Multiphase Flow in Permeable Media: A Pore-Scale Perspective**. Cambridge: Cambridge University Press, 2017.

___. Flow in porous media — pore-network models and multiphase flow. **Current Opinion in Colloid & Interface Science**, v. 6, n. 3, p. 197–207, jun. 2001.

BLUNT, M. J.; BIJELJIC, B.; DONG, H.; GHARBI, O.; IGLAUER, S.; MOSTAGHIMI, P.; PALUSZNY, A.; PENTLAND, C. Pore-scale imaging and modelling. **Advances in Water Resources**, v. 51, p. 197–216, jan. 2013.

BLUNT, M.; KING, M. J.; SCHER, H. Simulation and theory of two-phase flow in porous media. **Physical Review A**, v. 46, n. 12, p. 7680–7699, 1 dez. 1992.

BOBEK, J. E.; MATTAX, C. C.; DENEKAS, M. O. Reservoir Rock Wettability - Its Significance and Evaluation. **Transactions of the AIME**, v. 213, n. 01, p. 155–160, 1 dez. 1958.

BOER, R. B. DE; LEERLOOYER, K.; EIGNER, M. R. P.; BERGEN, A. R. D. VAN. Screening of Crude Oils for Asphalt Precipitation: Theory, Practice, and the Selection of Inhibitors. **SPE Production & Facilities**, v. 10, n. 01, p. 55–61, 1 fev. 1995.

BRITO, J. P. S.; SANTOS, R. V.; GONÇALVES, G. O.; BARBOSA, P. F.; SOUZA CRUZ, C. E.; USHIROBIRA, C. A.; SOUZA, V. S.; RICHTER, F.; ABREU, C. J. U-Pb dating of Barra Velha carbonates reveals the influence of Santos Basin sedimentary and tectonothermal history on pre-salt carbonate ages. Marine and Petroleum Geology, v. 168, p. 107035, out. 2024.

BROOKS, R. A.; CHIRO, G. DI. Beam hardening in X-ray reconstructive tomography. **Physics in Medicine and Biology**, v. 21, n. 3, p. 390–398, 1 maio 1976.

BRUHN, C. H. L.; GOMES, J. A. T.; UCCHESE JR, C. DEL; JOHANN, P. **Campos Basin: Reservoir characterization and management – Historical overview and future challenges.** Proceedings of the Offshore Technology Conference. **Anais**...Houston, Texas: 2003

BRYANT, S.; CADE, C.; MELLOR, D. Permeability Prediction from Geologic Models. **AAPG Bulletin**, v. 77, n. 8, p. 1338–1350, 1993.

BURNS, W. G.; SIMS, H. E. Effect of radiation type in water radiolysis. **Journal of the Chemical Society, Faraday Transactions 1: Physical Chemistry in Condensed Phases**, v. 77, n. 11, p. 2803, 1981.

CAINELLI, C.; MOHRIAK, W. U. Some remarks on the evolution of sedimentary basins along the Eastern Brazilian continental margin. **Episodes**, v. 22, n. 3, p. 206–216, 1999.

CALVERT, T. J.; WELLS, L. E. **Electromagnetic Propagation ... A New Dimension In Logging.** SPE California Regional Meeting. **Anais**...SPE, 13 abr. 1977

CARMO, M. DO. **Differential Geometry of Curves and Surfaces**. [s.l.] Dover Publications, 2016.

CARRAMAL, N. G.; OLIVEIRA, D. M.; CACELA, A. S. M.; CUGLIERI, M. A. A.; ROCHA, N. P.; VIANA, S. M.; TOLEDO, S. L. V.; PEDRINHA, S.; ROS, L. F. DE. Paleoenvironmental insights from the deposition and diagenesis of Aptian pre-salt magnesium silicates from the Lula Field, Santos Basin, Brazil. **Journal of Sedimentary Research**, v. 92, n. 1, p. 12–31, 31 jan. 2022.

CARVALHO, A. M. A.; HAMON, Y.; GOMES DE SOUZA JR, O.; GOULART CARRAMAL, N.; COLLARD, N. Facies and diagenesis distribution in an Aptian pre-salt carbonate reservoir of the Santos Basin, offshore Brazil: A comprehensive quantitative approach. **Marine and Petroleum Geology**, v. 141, p. 105708, 1 jul. 2022.

CARVALHO, A. S. G. C.; ROS, L. F. DE. Diagenesis of Aptian sandstones and conglomerates of the Campos Basin. **Journal of Petroleum Science and Engineering**, v. 125, p. 189–200, jan. 2015.

CARVALHO ANTUNES, R. DE; GUERRERO, J. C.; JAHNERT, R. J. Coquina depositional model, Buzios Field, Brazil. **Marine and Petroleum Geology**, v. 160, p. 106607, fev. 2024.

CHANDLER, R.; KOPLIK, J.; LERMAN, K.; WILLEMSEN, J. F. Capillary displacement and percolation in porous media. **Journal of Fluid Mechanics**, v. 119, p. 249–267, 20 jun. 1982a.

CHANG, M. M.; MAEREFAT, N. L.; TOMUTSA, L.; HONARPOUR, M. M. Evaluation and Comparison of Residual Oil Saturation Determination Techniques. **SPE Formation Evaluation**, v. 3, n. 1, p. 251–262, 1988a.

CHATZIS, I.; MORROW, N. R.; LIM, H. T. Magnitude and Detailed Structure of Residual Oil Saturation. **Society of Petroleum Engineers Journal**, v. 23, n. 2, p. 311–326, 1983.

CHAU, T. T.; BRUCKARD, W. J.; KOH, P. T. L.; NGUYEN, A. V. **A review of factors that affect contact angle and implications for flotation practice. Advances in Colloid and Interface Science**, 30 set. 2009.

CHAYES, F. A simple point counter for thin-section analysis. **American Mineralogist**, v. 34, n. 1–2, p. 1–11, 1949.

CHEN, T.; GUESTRIN, C. XGBoost: A scalable tree boosting system. **Proceedings of the ACM SIGKDD International Conference on Knowledge Discovery and Data Mining**, v. 13–17, p. 785–794, 2016.

CHILINGAR, G. V.; YEN, T. F. Some Notes on Wettability and Relative Permeabilities of Carbonate Reservoir Rocks, II. **Energy Sources**, v. 7, n. 1, p. 67–75, 23 jan. 1983.

CHINELATTO, G. F.; BELILA, A. M. P.; BASSO, M.; SOUZA, J. P. P.; VIDAL, A. C. A taphofacies interpretation of shell concentrations and their relationship with petrophysics: A case study of Barremian-Aptian coquinas in the Itapema Formation, Santos Basin-Brazil. **Marine and Petroleum Geology**, v. 116, n. November 2019, p. 104317, 2020.

CIEPLAK, M.; ROBBINS, M. O. Dynamical Transition in Quasistatic Fluid Invasion in Porous Media. **Physical Review Letters**, v. 60, n. 20, p. 2042–2045, 16 maio 1988.

___. Influence of contact angle on quasistatic fluid invasion of porous media. **Physical Review B**, v. 41, n. 16, p. 11508–11521, 1 jun. 1990.

CLAUSNITZER, V.; HOPMANS, J. W. Pore-scale measurements of solute breakthrough using microfocus X-ray computed tomography. **Water Resources Research**, v. 36, n. 8, p. 2067–2079, 2000.

CLEMSON, J.; CARTWRIGHT, J.; BOOTH, J. Structural segmentation and the influence of basement structure on the Namibian passive margin. **Journal of the Geological Society**, v. 154, p. 477–482, 1997.

COATES, G. R.; XIAO, L.; PRAMMER, M. G. **NMR Logging Principles and Applications**. Houston: Halliburton Energy Services, 1999.

COSKUN, S. B.; WARDLAW, N. C.; HAVERSLEW, B. Effects of composition, texture and diagenesis on porosity, permeability and oil recovery in a sandstone reservoir. **Journal of Petroleum Science and Engineering**, v. 8, n. 4, p. 279–292, 1993.

CROFTON, M. W. On the Theory of Local Probability, Applied to Straight Lines Drawn at Random in a Plane; The Methods Used Being Also Extended to the Proof of Certain New Theorems in the Integral Calculus. **Philosophical Transactions of the Royal Society of London**, v. 158, p. 181–199, 1868.

CUDDY, S. The benefits and dangers of using artificial intelligence in petrophysics. **Artificial Intelligence in Geosciences**, v. 2, n. April, p. 1–10, 2021.

CULLITY, B. D.; STOCK, S. R. **Elements of X-Ray Diffraction**. 3rd. ed. [s.l.] Pearson Education Limited, 2014.

DAVISON, I. Tectonics and hydrocarbon distribution along the Brazilian South Atlantic margin. *Em*: CAMERON, R.; BATE, R.; CLURE, V. (Eds.). **The Oil and Gas Habitats of the South Atlantic**. London: Geological Society of London, 1999. v. 153p. 133–151.

___. Geologic evolution of conjugate volcanic passive margins: Influence on the petroleum systems of the South Atlantic. *Em*: AC, R.; RWH, B.; RH, G. (Eds.). **Deformation of the Continental Crust: The Legacy of Mike Coward**. London: Geological Society of London, 2007. p. 345–359.

DIAS, J. L. Tectônica, estratigrafia e sedimentação no Andar Aptiano da margem leste brasileira. **Boletim de Geociências da Petrobras da Petrobras**, v. 13, n. 1, p. 7–25, 2005.

DIAS, M. M.; WILKINSON, D. Percolation with trapping. **Journal of Physics A: Mathematical and General**, v. 19, n. 15, p. 3131–3146, out. 1986.

DICKSON, J. A. D. A modified staining technique for carbonates in thin section. **Nature**, v. 205, n. 4971, p. 587, 1965.

DONADILLE, J.-M.; FAIVRE, O.; LEECH, R. **Fundamentals of dielectric dispersion logging**. Houston: Schlumberger, 2016.

DONALDSON, E. C. Introduction. *Em*: DONALDSON, E. C.; CHILINGARIAN, G. V.; YEN, T. F. (Eds.). **Developments in Petroleum Science - Enhanced Oil Recovery, II Processes and Operations**. Amsterdam: Elsevier B.V., 1989. p. 1–11.

DONALDSON, E. C.; THOMAS, R. D.; LORENZ, P. B. Wettability Determination and Its Effect on Recovery Efficiency. **Society of Petroleum Engineers Journal**, v. 9, n. 01, p. 13–20, 1 mar. 1969.

EHRENBERG, S. N. Assessing the Relative Importance of Compaction Processes and Cementation to Reduction of Porosity in Sandstones: Discussion; Compaction and Porosity Evolution of Pliocene Sandstones, Ventura Basin, California: Discussion. **AAPG Bulletin**, v. 73, p. 1274–1276, 1989.

EHRENBERG, S. N.; EBERLI, G. P.; KERAMATI, M.; MOALLEMI, S. A. Porosity-permeability relationships in interlayered limestone-dolostone reservoirs. **AAPG Bulletin**, v. 90, n. 1, p. 91–114, jan. 2006.

ELKATATNY, S.; JAFAROV, T.; AL-MAJED, A.; MAHMOUD, M. Formation Damage Avoidance by Reducing Invasion with Sodium Silicate-Modified Water-Based Drilling Fluid. **Energies**, v. 12, n. 8, p. 1485, 19 abr. 2019.

ELNUR, M.; ALSHIBLI, K. A. Influence of X-Ray beam exposure on the development of gas bubbles during triaxial testing of sand using 3D synchrotron micro-computed tomography. **Tomography of Materials and Structures**, v. 3, p. 100016, set. 2023.

FARAMARZI-PALANGAR, M.; MIRZAEI-PAIAMAN, A.; GHOREISHI, S. A.; GHANBARIAN, B. Wettability of carbonate reservoir rocks: A comparative analysis. **Applied Sciences (Switzerland)**, v. 12, n. 1, 1 jan. 2022.

FERRARI, J. V.; SILVEIRA, B. M. DE O.; ARISMENDI-FLOREZ, J. J.; FAGUNDES, T. B.; SILVA, M. A. DA T.; SKINNER, R.; ULSEN, C.; CARNEIRO, C. DE C. Influence of carbonate reservoir mineral heterogeneities on contact angle measurements. **Journal of Petroleum Science and Engineering**, v. 199, 1 abr. 2021.

FETTKE, C. R.; COPELAND, W. A. Permeability Studies of Pennsylvania Oil Sands. **Transactions of the AIME**, v. 92, n. 01, p. 329–339, 1 dez. 1931.

FIX, E.; HODGES, J. L. Discriminatory Analysis. Nonparametric Discrimination: Consistency Properties. **International Statistical Review / Revue Internationale de Statistique**, v. 57, n. 3, p. 238, dez. 1989.

FLANNERY, B. P.; DECKMAN, H. W.; ROBERGE, W. G.; D'AMICO, K. L. Three-Dimensional X-ray Microtomography. **Science**, v. 237, p. 1439–1444, 1987.

FOLK, R. L.; WARD, W. C. Brazos River bar [Texas]; a study in the significance of grain size parameters. **Journal of Sedimentary Research**, v. 27, n. 1, p. 3–26, 1 mar. 1957.

FREUND, Y.; SCHAPIRE, R. E. A decision-theoretic generalization of on-line learning and an application to boosting. **Journal of Computer and System Sciences**, v. 55, p. 119–139, 1997.

FRIEDMAN, J. H. Greedy function approximation: A gradient boosting machine. **Annals of Statistics**, v. 29, n. 5, p. 1189–1232, 2001.

GAO, B.; WU, J.; CHEN, S.; KWAK, H.; FUNK, J. New method for predicting capillary pressure curves from NMR data in carbonate rocks. **SPWLA 52nd Annual Logging Symposium**, p. 1–11, 2011.

GHARBI, O.; BLUNT, M. J. The impact of wettability and connectivity on relative permeability in carbonates: A pore network modeling analysis. **Water Resources Research**, v. 48, n. 12, p. 1–14, 2012.

GIERLOWSKI-KORDESCH, E. H. Lacustrine Carbonates. *Em*: ALONSO-ZARZA, A. M.; TANNER, L. H. (Eds.). **Carbonates in Continental Settings**. Developments in Sedimentology. Amsterdan: Elsevier B.V., 2009. v. 61p. 1–101.

GODEAU, N.; GIRARD, J.-P.; GUIHOU, A.; HAMELIN, B.; DESCHAMPS, P. **U-Pb and Th-Pb dating of diagenetic/hydrothermal phases in the pre-salt series, Angola offshore: implication for the paleo-thermal history during South Atlantic rifting.** Goldschmidt 2021. **Anais**...France: European Association of Geochemistry, 2021.

GOMES, J. P.; BUNEVICH, R. B.; TEDESCHI, L. R.; TUCKER, M. E.; WHITAKER, F. F. Facies classification and patterns of lacustrine carbonate deposition of the Barra Velha Formation, Santos Basin, Brazilian Pre-salt. **Marine and Petroleum Geology**, v. 113, n. December 2019, p. 104176, 2020.

GRABAU, A. W. On the classification of sedimentary rocks. **American Geologist**, v. 33, p. 228–247, 1904.

GUO, H.; DOU, M.; HANQING, W.; WANG, F.; YUANYUAN, G.; YU, Z.; YANSHENG, W.; LI, Y. Proper Use of Capillary Number in Chemical Flooding. **Journal of Chemistry**, v. 2017, p. 1–11, 2017.

GUO, H.; SONG, K.; HILFER, R. **A critical review of capillary number and its application in enhanced oil recovery.** SPE Symposium on Improved Oil Recovery. **Anais**...Tulsa: 2020

GUYON, I.; WESTON, J.; BARNHILL, S. Gene Selection for Cancer Classification using Support Vector Machines. **Machine Learning**, v. 46, p. 389–422, 2002.

GUZZO, J. V. P.; ROCHA, Y. S.; MENEZES, T. R.; PESTILHO, A. L. S.; BINOTTO, R.; MATOS, T. F.; SILVA, Y. M. P.; TONIETO, S. N.; CARVALHO, B. R. B. M. **Hydrothermal petroleums and solid reservoir bitumens: recognition of an atypical petroleum system in the Brazilian Pre-salt deposits (Santos Basin).** XV Latin American Congress on Organic Geochemistry. **Anais**...2018.

HASSAN, M. E.; NIELSEN, R. F.; CALHOUN, J. C. Effect of Pressure and Temperature on Oil-Water Interfacial Tensions for a Series of Hydrocarbons. **Journal of Petroleum Technology**, v. 5, n. 12, p. 299–306, 1 dez. 1953.

HASSLER, G. L.; BRUNNER, E. Measurement of Capillary Pressures in Small Core Samples. **Transactions of the AIME**, v. 160, n. 01, p. 114–123, 1 dez. 1945.

HASSLER, G. L.; RICE, R. R.; LEEMAN, E. H. Investigations on the Recovery of Oil from Sandstones by Gas Drive. **Transactions of the AIME**, v. 118, n. 01, p. 116–137, 1 dez. 1936.

HAZLETT, R. D. Simulation of capillary-dominated displacements in microtomographic images of reservoir rocks. **Transport in Porous Media**, v. 20, n. 1–2, p. 21–35, ago. 1995.

HERLINGER JR, R.; NASCIMENTO FREITAS, G. DO; ANJOS, C. D. W. DOS; ROS, L. F. DE. **Petrological and petrophysical implications of magnesian clays in Brazilian pre-salt deposits.** SPWLA 61st Annual Logging Symposium. **Anais**...Online: Society of Petrophysicists and Well Log Analysts (SPWLA), 2020

HERLINGER, R.; NASCIMENTO FREITAS, G. DO; ANJOS, C. D. W. DOS; ROS, L. F. DE. **Petrological and petrophysical implications of magnesian clays in Brazilian Pre-Salt deposits.** SPWLA 61st Annual Logging Symposium. **Anais**...Society of Petrophysicists and Well-Log Analysts (SPWLA), 2020

HERLINGER, R.; ROS, L. F. DE; SURMAS, R.; VIDAL, A. Residual oil saturation investigation in Barra Velha Formation reservoirs from the Santos Basin, Offshore Brazil: A sedimentological approach. **Sedimentary Geology**, v. 448, 15 abr. 2023.

HERLINGER, R.; SANTOS, B. C. C. DOS. **THE IMPACT OF PORE TYPE ON NMR T2 AND MICP IN BIOCLASTIC CARBONATE RESERVOIRS.** SPWLA 59th Annual Logging Symposium. **Anais**...2018

HERLINGER, R.; VIDAL, A. C. X-ray μCt extracted pore attributes to predict and understand Sor using ensemble learning techniques in the Barra Velha Pre-salt carbonates, Santos Basin, Offshore Brazil. **Journal of Petroleum Science and Engineering**, v. 212, p. 110282, 1 maio 2022.

HERLINGER, R.; ZAMBONATO, E. E.; ROS, L. F. DE. Influence of Diagenesis on the Quality of Lower Cretaceous Pre-salt Lacustrine Carbonate Reservoirs from Northern Campos Basin, Offshore Brazil. **Journal of Sedimentary Research**, v. 87 (12), n. November, p. 1285–1313, 2017.

HILPERT, M.; MILLER, C. T. Pore-morphology-based simulation of drainage in totally wetting porous media. **Advances in Water Resources**, v. 24, n. 3–4, p. 243–255, fev. 2001.

HIRASAKI, G. J. Wettability: fundamentals and surface forces. **SPE Formation Evaluation**, v. 6, n. 2, p. 217–226, 1991.

HO, T. K. Random decision forests. **Proceedings of the International Conference on Document Analysis and Recognition, ICDAR**, v. 1, p. 278–282, 1995.

HOEILAND, S.; BARTH, T.; BLOKHUS, A. M.; SKAUGE, A. The effect of crude oil acid fractions on wettability as studied by interfacial tension and contact angles. **Journal of Petroleum Science and Engineering**, v. 30, n. 2, p. 91–103, 2001.

HONARPOUR, M. M.; SAAD, N. **Influence of Small-Scale Rock Laminations on Core Plug Oil/Water Relative Permeability and Capillary Pressure.** University of Tulsa Centennial Petroleum Engineering Symposium. **Anais**...Society of Petroleum Engineers, 4 abr. 1994.

HONARPOUR, M.; MAHMOOD, S. M. Relative-Permeability Measurements: An Overview. **Journal of Petroleum Technology**, v. 40, n. 08, p. 963–966, 1 ago. 1988.

HORSCHUTZ, P.; SCUTA, M. Fácies-perfis e mapeamento de qualidade do reservatório de coquinas da Formação Lagoa Feia do Campo de Pampo. **Boletim de Geociências da Petrobras**, v. 6, n. 1/2, p. 45–58, 1992.

HOSA, A.; WOOD, R. Order of diagenetic events controls evolution of porosity and permeability in carbonates. **Sedimentology**, v. 67, n. 6, p. 3042–3054, 1 out. 2020.

HOSA, A.; WOOD, R. A.; CORBETT, P. W. M.; SCHIFFER DE SOUZA, R.; ROEMERS, E. Modelling the impact of depositional and diagenetic processes on reservoir properties of the crystal-shrub limestones in the 'Pre-Salt' Barra Velha Formation, Santos Basin, Brazil. **Marine and Petroleum Geology**, v. 112, p. 104100, 1 fev. 2020.

HOUSEKNECHT, D. H. Assessing the Relative Importance of Compaction Processes and Cementation to Reduction of Porosity in Sandstones. **AAPG Bulletin**, v. 71, n. 6, p. 633–642, 1987.

HUANG, D. D.; HONARPOUR, M. M. Capillary end effects in coreflood calculations. **Journal of Petroleum Science and Engineering**, v. 19, n. 1–2, p. 103–117, jan. 1998.

HUANG, Z.; CHEN, Z. Comparison of different machine learning algorithms for predicting the SAGD production performance. **Journal of Petroleum Science and Engineering**, v. 202, n. February, p. 108559, 2021.

HUMPHRY, K. J.; SUIJKERBUIJK, B. M. J. M.; LINDE, H. A. VAN DER; PIETERSE, S. G. J.; MASALMEH, S. K. Impact of Wettability on Residual Oil Saturation and Capillary Desaturation Curves. **Petrophysics**, v. 55, n. 4, p. 313–318, 2014a.

HUTCHISON, C. S. **Laboratory Handbook of Petrographic Techniques**. New York: John Wiley & Sons, 1974.

IGLAUER, S.; FERNØ, M. A.; SHEARING, P.; BLUNT, M. J. Comparison of residual oil cluster size distribution, morphology and saturation in oil-wet and water-wet sandstone. **Journal of Colloid and Interface Science**, v. 375, n. 1, p. 187–192, 2012.

ISAH, A.; ARIF, M.; MAHMOUD, M.; KAMAL, M. S. Influence of rock permeability and surface conditioning on carbonate wettability: A link between contact angle and Amott-index. **Geoenergy Science and Engineering**, v. 227, 1 ago. 2023.

IVERSON, W. P.; DUNN, T. L.; AJDARI, I. **Relative Permeability Anisotropy Measurements in Tensleep Sandstones.** SPE/DOE Improved Oil Recovery Symposium. **Anais**...Society of Petroleum Engineers, 4 abr. 1996.

IYI, D.; BALOGUN, Y.; OYENEYIN, B.; FAISAL, N. Numerical modelling of the effect of wettability, interfacial tension and temperature on oil recovery at pore-scale level. **Journal of Petroleum Science and Engineering**, v. 201, p. 108453, jun. 2021.

JASTI, J. K.; JESION, G.; FELDKAMP, L. Microscopic Imaging of Porous Media With X-Ray Computer Tomography. **SPE Formation Evaluation**, v. 8, n. 03, p. 189–193, 1 set. 1993.

JENNINGS, H. Y. The effect of temperature and pressure on the interfacial tension of benzene-water and normal decane-water. **Journal of Colloid and Interface Science**, v. 24, n. 3, p. 323–329, jul. 1967.

JERAULD, G. R. General Three-Phase Relative Permeability Model for Prudhoe Bay. **SPE Reservoir Engineering**, v. 12, n. 4, p. 255–263, 1997.

JIA, K.; ZENG, J.; WANG, X.; LI, B.; GAO, X.; WANG, K. Wettability of Tight Sandstone Reservoir and Its Impacts on the Oil Migration and Accumulation: A Case Study of Shahejie Formation in Dongying Depression, Bohai Bay Basin. **Energies**, v. 15, n. 12, 1 jun. 2022.

KAHN, J. S. **Analysis and Distribution of Packing Properties in Sand-Sized Sediments: 2. The Distribution of the Packing Measurements and an Example of Packing AnalysisSource: The Journal of Geology**. [s.l: s.n.].

KAMATH, J.; NAKAGAWA, F.; SCHEMBRE, J.; FATE, T.; DEZABALA, E.; AYYALASOMAYAJULA, P. **Core based perspective on uncertainty in relative permeability.** International Symposium of the Society of Core Analysts. **Anais**...2005

KAMINSKY, R.; RADKE, C. J. Asphaltenes, Water Films, and Wettability Reversal. **SPE Journal**, v. 2, n. 04, p. 485–493, 1 dez. 1997.

KARIMPOULI, S.; KHOSHLESAN, S.; SAENGER, E. H.; KOOCHI, H. H. Application of alternative digital rock physics methods in a real case study: a challenge between clean and cemented samples. **Geophysical Prospecting**, v. 66, n. 4, p. 767–783, maio 2018.

KARLSONS, K.; KORT, D. W. DE; ALPAK, F. O.; DIETDERICH, J.; FREEMAN, J. J.; APPEL, M.; MANTLE, M. D.; SEDERMAN, A. J.; GLADDEN, L. F. Integrating Pore-Scale Flow MRI and X-ray μCT for Validation of Numerical Flow Simulations in Porous Sedimentary Rocks. **Transport in Porous Media**, v. 143, n. 2, p. 373–396, 1 jun. 2022.

KARNER, G.; DRISCOLL, N. Tectonic and stratigraphic development of the West African and eastern Brazilian margins: insights from quantitative basin modelling. *Em*: CAMERON, N.; BATE, R.; CLURE, V. (Eds.). **The Oil and Gas Habitats of the South Atlantic**. Special Publication 153. Geological ed. London: Geological Society of London, 1999. p. 11–40.

KARPYN, Z. T.; PIRI, M.; SINGH, G. Experimental investigation of trapped oil clusters in a water-wet bead pack using X-ray microtomography. **Water Resources Research**, v. 46, n. 4, p. 1–25, 2010.

KEEHM, Y. Permeability prediction from thin sections: 3D reconstruction and Lattice-Boltzmann flow simulation. **Geophysical Research Letters**, v. 31, n. 4, 28 fev. 2004.

KENDALL, A. Fascicular-optic calcite: a replacement of bundled acicular carbonate cements. **Journal of Sedimentary Petrology**, v. 47, n. 3, p. 1056–1062, 1977.

KHOSRAVI, R.; SIMJOO, M.; CHAHARDOWLI, M. Low salinity water flooding: estimating relative permeability and capillary pressure using coupling of particle swarm optimization and machine learning technique. **Scientific Reports**, v. 14, n. 1, p. 13213, 8 jun. 2024.

KIM, S. T.; BOUDH-HIR, M.-E.; MANSOORI, G. A. **The Role of Asphaltene in Wettability Reversal**. **Anais**...SPE, 23 set. 1990

KINGSTON, A. M.; MYERS, G. R.; LATHAM, S. J.; RECUR, B.; LI, H.; SHEPPARD, A. P. Space-Filling X-Ray Source Trajectories for Efficient Scanning in Large-Angle Cone-Beam Computed Tomography. **IEEE Transactions on Computational Imaging**, v. 4, n. 3, p. 447–458, 28 maio 2018.

KUMAR, M. **Multiphase Flow in Reservoir Cores using Digital Core Analysis**. Canberra: The Australian National University, dez. 2009.

LAKE, L.; JOHNS, R. T.; ROSSEN, W. R.; POPE, G. A. **Fundamentals of Enhanced Oil Recovery**. [s.l.] Society of Petroleum Engineers, 2014.

LAM, C. N. C.; WU, R.; LI, D.; HAIR, M. L.; NEUMANN, A. W. Study of the advancing and receding contact angles: liquid sorption as a cause of contact angle hysteresis. **Advances in Colloid and Interface Science**, v. 96, n. 1–3, p. 169–191, fev. 2002.

LAND, C. VAN DER; WOOD, R.; WU, K.; DIJKE, M. I. J. VAN; JIANG, Z.; CORBETT, P. W. M.; COUPLES, G. Modelling the permeability evolution of carbonate rocks. **Marine and Petroleum Geology**, v. 48, p. 1–7, dez. 2013.

LARSON, R. G.; SCRIVEN, L. E.; DAVIS, H. T. Percolation theory of residual phases in porous media. **Nature**, v. 268, n. 5619, p. 409–413, 1977.

LATHAM, S. J.; VARSLOT, T. K.; SHEPPARD, A. P. **Automated registration for augmenting micro-CT 3D images. Austral. Mathematical Soc**. [s.l: s.n.]. Disponível em: <http://anziamj.austms.org.au/ojs/index.php/ANZIAMJ/article/view/>.

LATHAM, S.; VARSLOT, T.; SEPPARD, A. **Image Registration: Enhancing and Calibrating X-ray Micro-CT Imaging.** International Symposium of the Society of Core Analysts. **Anais**...Abu Dhabi: 2008.

LEITE, C.; SILVA, C.; ROS, L. DE. Depositional and diagenetic processes in the pre-salt rift section of a Santos Basin area, SE Brazil. **Journal of Sedimentary Research**, v. 90, n. 6, p. 584–608, 2020.

LENORMAND, R.; ZARCONE, C. **Role of Roughness and Edges During Imbibition in Square Capillaries.** Annual Technical Conference and Exhibition of the Society of Petroleum Engineers. **Anais**...Houston: 1984

LENORMAND, R.; ZARCONE, C.; SARR, A. Mechanisms of the displacement of one fluid by another in a network of capillary ducts. **Journal of Fluid Mechanics**, v. 135, n. October 1983, p. 337–353, 1983.

LEONTARITIS, K. J.; MANSOORI, G. A. **Asphaltene Deposition: A Survey of Field Experiences and Research Approaches. Journal of Petroleum Science and Engineering**. [s.l: s.n.].

LEVERETT, M. C. Capillary Behavior in Porous Solids. **Transactions of the AIME**, v. 142, n. 01, p. 152–169, 1 dez. 1941.

LI, Y.; CHEN, S.; LU, J.; WANG, G.; ZOU, X.; XIAO, Z.; SU, K.; HE, Q.; LUO, X. The logging recognition of solid bitumen and its effect on physical properties, AC, resistivity and NMR parameters. **Marine and Petroleum Geology**, v. 112, 1 fev. 2020.

LIMA, B. E. M.; ROS, L. F. DE. Deposition, diagenetic and hydrothermal processes in the Aptian Pre-Salt lacustrine carbonate reservoirs of the northern Campos Basin, offshore Brazil. **Sedimentary Geology**, v. 383, p. 55–81, 2019.

LIMA, B. E. M.; TEDESCHI, L. R.; PESTILHO, A. L. S.; SANTOS, R. V.; VAZQUEZ, J. C.; GUZZO, J. V. P.; ROS, L. F. DE. Deep-burial hydrothermal alteration of the Pre-Salt carbonate reservoirs from northern Campos Basin, offshore Brazil: Evidence from petrography, fluid inclusions, Sr, C and O isotopes. **Marine and Petroleum Geology**, v. 113, p. 104143, mar. 2020.

LIN, E. C.; HUANG, E. T. S. The Effect of Rock Wettability on Water Blocking During Miscible Displacement. **SPE Reservoir Engineering**, v. 5, n. 02, p. 205–212, 1 maio 1990.

LIN, Q.; AL-KHULAIFI, Y.; BLUNT, M. J.; BIJELJIC, B. Quantification of sub-resolution porosity in carbonate rocks by applying high-salinity contrast brine using X-ray microtomography differential imaging. **Advances in Water Resources**, v. 96, p. 306–322, 1 out. 2016.

LINDEN, S.; WIEGMANN, A.; HAGEN, H. The LIR space partitioning system applied to the Stokes equations. **Graphical Models**, v. 82, p. 58–66, nov. 2015.

LING, K.; HE, J. A new correlation to calculate oil-water interfacial tension. **Society of Petroleum Engineers - Kuwait International Petroleum Conference and Exhibition 2012, KIPCE 2012: People and Innovative Technologies to Unleash Challenging Hydrocarbon Resources**, v. 1, n. December, p. 522–530, 2012.

LIU, J.; ZHOU, H.; PUJOL, M.; SELBY, D.; LI, J.; TIAN, H. The bitumen formation and Re-Os characteristics of a CO2-rich pre-salt gas reservoir of the Kwanza Basin, offshore Angola. **Marine and Petroleum Geology**, v. 143, p. 105786, set. 2022.

LIU, Z.; WICKRAMASINGHE, S. R.; QIAN, X. Ion-specificity in protein binding and recovery for the responsive hydrophobic poly(vinylcaprolactam) ligand. **RSC Advances**, v. 7, n. 58, p. 36351–36360, 2017.

LLOYD, S. Least squares quantization in PCM. **IEEE Transactions on Information Theory**, v. 28, n. 2, p. 129–137, mar. 1982.

LUCIA, F. J. Origin and petrophysics of dolostone pore space. **Geological Society, London, Special Publications**, v. 235, n. 1, p. 141–155, 2004.

LUO, P.; MACHEL, H. G. Pore size and pore throat types in a heterogeneous dolostone reservoir, Devonian Grosmont Formation, Western Canada Sedimentary Basin. **American Association of Petroleum Geologists Bulletin**, v. 79, n. 11, p. 1698–1720, 1995.

MACHEL, H. Concepts and models of dolomitization: a critical reappraisal. *Em*: BRAITHWAITE, C.; RIZZI, G.; DARKE, G. (Eds.). **The Geometry and Petrogenesis of Dolomite Hydrocarbon Reservoirs**. London: The Geological Society of London, 2004. p. 7–63.

MALIK, S.; SHARMA, R. Scaling Issues in Estimation of Pore Space Using Digital Rock Physics. *Em*: **Petro-physics and Rock Physics of Carbonate Reservoirs**. Singapore: Springer Singapore, 2020. p. 177–187.

MANSOORI, S. K. AL; ITSEKIRI, E.; IGLAUER, S.; PENTLAND, C. H.; BIJELJIC, B.; BLUNT, M. J. Measurements of non-wetting phase trapping applied to carbon dioxide storage. **International Journal of Greenhouse Gas Control**, v. 4, n. 2, p. 283–288, 2010.

MANSOUR, O. AL; SAUD, M. A. AL; AYIRALA, S.; CINAR, Y. **An Investigation of Core Plug Heterogeneity Effect on Estimated Relative Permeability.** GOTECH. **Anais**...Dubai: SPE, 7 maio 2024

MASALMEH, S. K. Determination of waterflooding residual oil saturation for mixed to oil-wet carbonate reservoir and its impact on EOR. **Society of Petroleum Engineers - SPE Reservoir Characterisation and Simulation Conference and Exhibition, RCSC 2013: New Approaches in Characterisation and Modelling of Complex Reservoirs**, v. 1, p. 442–455, 2013.

MASSARWEH, O.; ABUSHAIKHA, A. S. **The use of surfactants in enhanced oil recovery: A review of recent advances. Energy Reports.** Elsevier Ltd, 1 nov. 2020.

MCPHEE, C.; REED, J.; ZUBIZARRETA, I. **Core Analysis: A Best Practice Guide**. 1st. ed. Amsterdam: Elsevier B.V., 2015.

MEADOR, R. A.; COX, P. T. **Dielectric Independent Constant Estimation of Water Volume.** 50th Annual Fall Meeting of the Society of Petroleum Engineers of AIME. **Anais**...Dallas: 1975

MEHMANI, A.; KELLY, S.; TORRES-VERDÍN, C.; BALHOFF, M. Residual oil saturation following gas injection in sandstones: Microfluidic quantification of the impact of pore-scale surface roughness. **Fuel**, v. 251, p. 147–161, 2019.

MEHMANI, A.; VERMA, R.; PRODANOVIĆ, M. **Pore-scale modeling of carbonates. Marine and Petroleum Geology.** Elsevier Ltd, , 1 abr. 2020.

MEISLING, K. E.; COBBOLD, P. R.; MOUNT, V. S. Segmentation of an obliquely rifted margin, Campos and Santos basins, southeastern Brazil. **AAPG Bulletin**, v. 85, n. 11, p. 1925–1944, 2001.

MIZUSAKI, A. M. P.; PETRINI, R.; BELLIENI, G.; COMIN-CHIARAMONTI, P.; DIAS, J. L.; MIN, A. DE; PICCIRILLO, E. M. Basalt magmatism along the passive continental margin of SE Brazil (Campos basin). **Contribution to Mineralogy and Petrology**, v. 111, p. 143–160, 1992.

MIZUSAKI, A. M. P.; THOMAZ FILHO, A.; CESERO, P. Ages of the magmatism and the opening of the South Atlantic Ocean. **Pesquisas em Geociências**, v. 25, n. 2, p. 47–57, 1998.

MOGHADASI, L.; GUADAGNINI, A.; INZOLI, F.; BARTOSEK, M. Interpretation of two-phase relative permeability curves through multiple formulations and Model Quality criteria. **Journal of Petroleum Science and Engineering**, v. 135, p. 738–749, 1 nov. 2015.

MOHAMED, S. S. E. D.; KALAM, M. Z.; DERNAIKA, M.; BRAHMAKULAM, J. V. **Remaining Oil Saturation Study in a Giant Oil Field: Integration of Reservoir Core Scale and Field Scale Measurements.** SPE Middle East Oil and Gas Show and Conference, MEOS, Proceedings. **Anais**...Manama: 2011

MOHAMMED, I.; MAHMOUD, M.; EL-HUSSEINY, A.; SHEHRI, D. AL; AL-GARADI, K.; KAMAL, M. S.; ALADE, O. S. Impact of Asphaltene Precipitation and Deposition on Wettability and Permeability. **ACS Omega**, v. 6, n. 31, p. 20091–20102, 10 ago. 2021.

MOHANTY, K. K.; DAVIS, H. T.; SCRIVEN, L. E. Physics of Oil Entrapment in Water-Wet Rock. **SPE Reservoir Engineering (Society of Petroleum Engineers)**, v. 2, n. 1, p. 113–128, 1987.

MOHRIAK, W.; NEMCOK, M.; ENCISO, G. South Atlantic divergent margin evolution: rift-border uplift and salt tectonics in the basins of SE Brazil. *Em*: PANKHURST, R. J.; TROUW, R. A. J.; BRITO NEVES, B. B.; WIT, M. J. DE (Eds.). **West Gondwana: Pre-Cenozoic Correlations Across the South Atlantic Region**. Special Publications, 294. London: Geological Society of London, 2008. p. 365–398.

MOODIE, N.; AMPOMAH, W.; JIA, W.; MCPHERSON, B. Relative permeability: A critical parameter in numerical simulations of multiphase flow in porous media. **Energies**, v. 14, n. 9, 1 maio 2021.

MOREIRA, J. L. P.; MADEIRA, C.; GIL, J.; MACHADO, M. Bacia de Santos. **Boletim de Geociências da Petrobras**, v. 15, n. 2, p. 531–549, 2007.

MORROW, N. R. Effects of Surface Roughness on Contact Angle With Special Reference To Petroleum Recovery. **Journal of Canadian Petroleum Technology**, v. 14, n. 4, p. 42–53, 1975.

MOUNTJOY, E. W.; MARQUEZ, X. M. Predicting reservoir properties in dolomites: Upper Devonian Leduc Buildups, Deep Alberta Basin. *Em*: KUPECZ, J.; GLUYAS, J.; BLOCK, S. (Eds.). **Reservoir quality prediction in sandstones and carbonates**. AAPG Memoir 69. Tulsa: [s.n.]. v. 69p. 267–306.

MUÑOZ, E. R.; WINTER, A.; TREVISAN, O. V. **Wettability Alteration in Limestone and Dolomite with Brines and CO2.** Proceedings of the 34th International Conference on Ocean, Offshore and Artic Engineering. **Anais**...ASME International, 31 maio 2015

MURPHY, R. P.; OWENS, W. W. The Use of Special Coring and Logging Procedures for Defining Reservoir Residual Oil Saturations. **Journal of Petroleum Technology**, v. 25, p. 841–850, 1973.

NADEAU, P. H. The physical dimensions of fundamental clay particles. **Clay Minerals**, v. 20, n. 4, p. 499–514, dez. 1985.

NAJI, A. T.; JAAFAR, M. S.; ALI, E. A.; AL-ANI, S. K. J. X-ray Attenuation and Reduction of Backscattered Radiation. **Applied Physics Research**, v. 8, n. 4, p. 92–102, 29 jul. 2016.

NETTO, P. R. A.; POZO, MANUEL; SILVA, M. D. DA; GOMES, M. E. B.; MEXIAS, A.; RAMNANI, C. W.; PARIZEK-SILVA, Y.; BORGHI, L.; RIOS-NETTO, A. DE M. Paleoenvironmental Implications of Authigenic Magnesian Clay Formation Sequences in the Barra Velha Formation (Santos Basin, Brazil). **Minerals**, v. 12, n. 2, 1 fev. 2022.

NETTO, P. R. A.; POZO, M.; SILVA, M. D. DA; MEXIAS, A. S.; GOMES, M. E. B.; BORGHI, L.; RIOS-NETTO, A. M. Authigenic Mg-clay assemblages in the Barra Velha Formation (Upper Cretaceous) from Santos Basin (Brazil): The role of syngenetic and diagenetic process. **Applied Clay Science**, v. 216, 1 jan. 2022.

NÜRNBERG, D.; MÜLLER, R. D. The tectonic evolution of the South Atlantic from Late Jurassic to present. **Tectonophysics**, v. 191, n. 1–2, p. 27–53, 1991.

NUTTING, P. G. Some Physical and Chemical Properties of Reservoir Rocks Bearing on the Accumulation and Discharge of Oil. *Em*: W.E. WRATHER; F.H. LAHEE (Eds.). **Problems of Petroleum Geology**. Tulsa: AAPG, 1934. p. 825–832.

OHSER, J.; MÜCKLICH. **Statistical Analysis of Microstructures in Materials Science**. 1st Edition ed. [s.l.] Wiley and Sons, 2000.

OLIVEIRA, L. A. B.; CARNEIRO, C. DE C. Synthetic geochemical well logs generation using ensemble machine learning techniques for the Brazilian pre-salt reservoirs. **Journal of Petroleum Science and Engineering**, v. 196, 1 jan. 2021.

ØREN, P. ˚ A.-E.; BAKKE, S. **Process Based Reconstruction of Sandstones and Prediction of Transport PropertiesTransport in Porous Media**. [s.l: s.n.].

PANDEY, A.; KESARWANI, H.; SAXENA, A.; AZIN, R.; SHARMA, S. Effect of heterogeneity and injection rates on the recovery of oil from conventional sand packs: A simulation approach. **Petroleum Research**, v. 8, n. 1, p. 96–102, 1 mar. 2023.

PATHAK, P.; FITZ, D. E.; BABCOCK, K. P.; WACHTMAN, R. J. Residual oil saturation determination for EOR projects in means field, a mature west Texas carbonate field. **SPE Reservoir Evaluation and Engineering**, v. 15, n. 5, p. 541–553, 2012.

PEKSA, A. E.; WOLF, K. H. A. A.; ZITHA, P. L. J. **Bentheimer sandstone revisited for experimental purposes. Marine and Petroleum Geology.** Elsevier Ltd, , 1 nov. 2015.

PENNEY, R. K.; CALCRAFT, A. P.; PIETSCH, A. P. Quantitative EPT interpretation in Australian reservoirs. **SPE - Asia Pacific Oil & Gas Conference**, p. 151–157, 1996.

PERKINS, F. M. An Investigation of the Role of Capillary Forces in Laboratory Water Floods. **Journal of Petroleum Technology**, v. 9, n. 11, p. 49–51, 1957.

PHAM, T. R.; AL-SHAHRI, A. M. **Assessment of residual oil saturation in a large carbonate reservoir.** SPE Middle East Oil Show. **Anais**...2001

PIRRONE, M.; BONA, N.; GALLI, M. T.; PAMPURI, F.; FAIVRE, O.; HAN, M.; HIZEM, M.; MOSSE, L. An innovative dielectric dispersion measurement for better evaluation of thin layered reservoirs applied in a South Italy well. **Offshore Mediterranean Conference and Exhibition 2011, OMC 2011**, p. 1–12, 2011.

PLAS, L. VAN DER; TOBI, A. C. A Chart for Judging the Reliability of Point Counting Results. **American Journal of Science**, v. 263, p. 87–90, 1965.

PRODANOVIĆ, M.; BRYANT, S. L.; DAVIS, J. S. Numerical Simulation of Diagenetic Alteration and Its Effect on Residual Gas in Tight Gas Sandstones. **Transport in Porous Media**, v. 96, n. 1, p. 39–62, 19 jan. 2013.

PSARRAS, G. C. **Fundamentals of dielectric theories**. [s.l.] Elsevier Inc., 2018.

RABINOWITZ, P. D.; LABRECQUE, J. The Mesozoic South Atlantic Ocean and evolution of its continental margins. **Journal of Geophysical Research**, v. 84, n. B11, p. 5973–6002, 1979.

RATHMELL, J. J.; BRAUN, P. H.; PERKINS, T. K. Reservoir Waterflood Residual Oil Saturation from Laboratory Tests. **Journal of Petroleum Technology**, v. 25, n. 02, p. 175–185, 1 fev. 1973.

REHIM, H.; MIZUSAKI, A. M. P.; CARVALHO, M. D.; MONTEIRO, M. **Talco e estevensita na Formação Lagoa Feia da Bacia de Campos – Possíveis implicações no ambiente deposicional.** XXXIV Congresso Brasileiro de Geologia. **Anais**...1986.

RICHARDSON, J. G.; PERKINS, F. M.; OSOBA, J. S. Differences in Behavior of Fresh and Aged East Texas Woodbine Cores. **Transactions of the AIME**, v. 204, n. 01, p. 86–91, 1 dez. 1955.

ROCHA, L.; FAVORETO, J.; BORGHI, L. Coquinas from Itapema formation, Mero field (Pre-salt of Santos basin): Microfacies analysis and depositional paleoenvironment. **Anuario do Instituto de Geociencias**, v. 44, 2021.

ROCHELLE-BATES, N.; WOOD, R.; SCHRÖDER, S.; ROBERTS, N. M. W. In situ U–Pb geochronology of Pre-Salt carbonates reveals links between diagenesis and regional tectonics. **Terra Nova**, v. 34, n. 4, p. 271–277, 1 ago. 2022.

RODRÍGUEZ-BERRIGUETE, Á.; DAL' BO, P. F.; VALLE, B.; BORGHI, L. When distinction matters: Carbonate shrubs from the Aptian Barra Velha Formation of Brazilian's Pre-salt. **Sedimentary Geology**, v. 440, 1 out. 2022.

ROOF, F. G. Snap-Off of Oil Droplets in Water- Wet Pores. **Society of Petroleum Engineers Journal**, v. 10, n. 1, p. 85–90, 1970.

ROS, L. F. DE; OLIVEIRA, D. M. An operational classification system for the South Atlantic pre-salt rocks. **Journal of Sedimentary Research**, 31 out. 2023.

ROSENDAHL, B.; MOHRIAK, W.; NEMCOK, M.; ODEGARD, M.; TURNER, J.; DICKSON, W. **West African and Brazilian conjugate margins: Crustal types, architecture, and plate configurations.** 4th HGS/PESGB International Conference on African E&P. **Anais**...Houston: 2005

ROSSONI, R. B.; PORCHER, C. C.; KOESTER, E.; SOBIESIAK, J. S.; SILVA, L. A. C. DA; MEXIAS, A. S.; GOMES, M. E. B.; RAMNANI, C. W.; ROS, L. F. DE. The role of compaction in the diagenetic evolution of Pre-Salt Aptian deposits of Santos Basin, Brazil. **Sedimentary Geology**, v. 466, p. 106650, jun. 2024.

RYAZANOV, A. V.; DIJKE, M. I. J. VAN; SORBIE, K. S. Pore-network prediction of residual oil saturation based on oil layer drainage in mixed-wet systems. **Proceedings - SPE Symposium on Improved Oil Recovery**, v. 2, n. 2001, p. 1217–1232, 2010.

RYAZANOV, A. V.; SORBIE, K. S.; DIJKE, M. I. J. VAN. Structure of residual oil as a function of wettability using pore-network modeling. **Advances in Water Resources**, v. 63, p. 11–21, 2014.

SABATO-CERALDI, T.; GREEN, D. Evolution of the South Atlantic lacustrine deposits in response to Early Cretaceous rifting, subsidence and lake hydrology. **Geological Society, London, Special Publications**, v. 438, n. 1, p. 77–98, 21 jan. 2017.

SADEGHNEJAD, S.; ENZMANN, F.; KERSTEN, M. Digital rock physics, chemistry, and biology: challenges and prospects of pore-scale modelling approach. **Applied Geochemistry**, v. 131, p. 105028, ago. 2021a.

SAFAEI-FAROUJI, M.; KADKHODAIE, A. Application of ensemble machine learning methods for kerogen type estimation from petrophysical well logs. **Journal of Petroleum Science and Engineering**, v. 208, n. PB, p. 109455, 2022.

SAKTHIVEL, S. Wettability Alteration of Carbonate Reservoirs Using Imidazolium-Based Ionic Liquids. **ACS Omega**, v. 6, n. 45, p. 30315–30326, 16 nov. 2021.

SALATHIEL, R. A. Oil Recovery by Surface Film Drainage in Mixed-Wettability Rocks. **Journal of Petroleum Technology**, v. 25, n. 10, p. 1216–1224, 1 out. 1973.

SALLER, A.; RUSHTON, S.; BUAMBUA, L.; INMAN, K.; MCNEIL, R.; DICKSON, J. A. D. T. Presalt stratigraphy and depositional systems in the Kwanza Basin, offshore Angola. v. 7, n. 7, p. 1135–1164, 2016.

SCHINDELIN, J. *et al.* Fiji: an open-source platform for biological-image analysis. **Nature Methods**, v. 9, n. 7, p. 676–682, 28 jul. 2012.

SCHLEIFER, N.; KESSE, E.; LAWRENCE, G. **Avoiding routine core analysis plug damage by proper evaluation of core gamma-ray, core description and wellsite core sampling.** International Symposium of the Society of Core Analysts. **Anais**...2018

SELEZNEV, N. V.; HABASHY, T. M.; BOYD, A. J.; HIZEM, M. **Formation properties derived from a multi-frequency dielectric measurement.** 47th Annual Logging Symposium. **Anais**...Veracruz: 2006

SERRA, O.; ABBOTT, H. T. Contribution of Logging Data to Sedimentology and Stratigraphy. **Society of Petroleum Engineers of Journal**, February, p. 117–131, 1982.

SHEPPARD, A. *et al.* Techniques in helical scanning, dynamic imaging and image segmentation for improved quantitative analysis with X-ray micro-CT. **Nuclear Instruments and Methods in Physics Research Section B: Beam Interactions with Materials and Atoms**, v. 324, p. 49–56, abr. 2014.

SHEPPARD, A. P.; SOK, R. M.; AVERDUNK, H. Techniques for image enhancement and segmentation of tomographic images of porous materials. **Physica A: Statistical Mechanics and its Applications**, v. 339, n. 1–2, p. 145–151, ago. 2004.

SHIKHOV, I.; LI, R.; ARNS, C. H. Relaxation and relaxation exchange NMR to characterise asphaltene adsorption and wettability dynamics in siliceous systems. **Fuel**, v. 220, p. 692–705, 15 maio 2018.

SHOKIR, E. M. E. M.; ALSUGHAYER, A. A.; AL-ATEEQ, A. Permeability estimation from well log responses. **Journal of Canadian Petroleum Technology**, v. 45, n. 11, p. 41–46, 2005.

SILVA, M. D. DA *et al.* Mineralogical study of levels with magnesian clay minerals in the Santos Basin, Aptian pre-salt Brazil. **Minerals**, v. 11, n. 9, 1 set. 2021.

SINGH, K.; BRANKO, B.; BLUNT, M. Imaging of oil layers, curvature and contact angle in a mixed-wet and a water-wet carbonate rock. **Water Resources Research**, v. 52, p. 1716–1728, set. 2016.

SINGH, K.; MENKE, H.; ANDREW, M.; LIN, Q.; RAU, C.; BLUNT, M. J.; BIJELJIC, B. Dynamics of snap-off and pore-filling events during two-phase fluid flow in permeable media. **Scientific Reports**, v. 7, n. 1, p. 1–13, 2017.

SKELT, C.; HARRISON, B. **An Integrated Approach To Saturation Height Analysis.** SPWLA 36th Annual Logging Symposium. **Anais**...Paris: 1995

SLOBOD, R. L.; CHAMBERS, A.; PREHN, W. L. Use of Centrifuge for Determining Connate Water, Residual Oil, and Capillary Pressure Curves of Small Core Samples. **Journal of Petroleum Technology**, v. 3, n. 04, p. 127–134, 1 abr. 1951.

SLOWINSKI, E. J.; GATES, E. E.; WARING, C. E. The Effect of Pressure on the Surface Tensions of Liquids. **The Journal of Physical Chemistry**, v. 61, n. 6, p. 808–810, 1 jun. 1957.

SPEIGHT, J. G. Capillary Number. **Rules of Thumb for Petroleum Engineers**, p. 107–107, 2017.

SPERRY, J. M.; PEIRCE, J. J. Ion Exchange and Surface Charge on Montmorillonite Clay. **Water Environment Research**, v. 71, n. 13, p. 316–322, 1999.

SPITERI, E. J.; JUANES, R.; BLUNT, M. J.; ORR, F. M. A new model of trapping and relative permeability hysteresis for all wettability characteristics. **SPE Journal**, v. 13, n. 3, p. 277–288, 2008.

STEGEMEIER, G. L. MECHANISMS OF ENTRAPMENT AND MOBILIZATION OF OIL IN POROUS MEDIA. *Em*: **Improved Oil Recovery by Surfactant and Polymer Flooding**. New York: Elsevier, 1977. p. 55–91.

SUDAKOV, O.; BURNAEV, E.; KOROTEEV, D. Driving digital rock towards machine learning: Predicting permeability with gradient boosting and deep neural networks. **Computers and Geosciences**, v. 127, n. February 2018, p. 91–98, 2019.

SZATMARI, P. Habitat of petroleum along the South Atlantic margins. *Em*: MELLO, M.; KATZ, B. (Eds.). **Petroleum Systems of South Atlantic Margins**. AAPG Memoir 73. Tulsa: AAPG, 2000. p. 69–75.

TAIWO, O. A.; MAMUDU, A.; DAGOGO-JACK, C.; JOSHUA, D.; OLAFUYI, O. **Grain size effects on residual oil saturation.** Society of Petroleum Engineers - SPE Nigeria Annual International Conference and Exhibition. **Anais**...2016

TANNER, L. H. **CARBONATES IN CONTINENTAL SETTINGS: FACIES, ENVIRONMENTS AND PROCESS**. Amsterdan: Elsevier B.V., 2010.

TEKLU, T. W.; BROWN, J. S.; KAZEMI, H.; GRAVES, R. M.; ALSUMAITI, A. M. **A Critical Literature Review of Laboratory and Field Scale Determination of Residual Oil Saturation**. **Anais**...SPE, 23 mar. 2013

TEMBELY, M.; ALSUMAITI, A. M.; ALAMERI, W. S. Machine and deep learning for estimating the permeability of complex carbonate rock from X-ray micro-computed tomography. **Energy Reports**, v. 7, p. 1460–1472, 2021.

TERRA, G. J. S. *et al.* Carbonate rock classification applied to Brazilian sedimentary basins. **Boletim de Geociências da Petrobras**, v. 18, n. 1, p. 9–29, 2010.

THOMPSON, D. L.; STILWELL, J. D.; HALL, M. Lacustrine carbonate reservoirs from Early Cretaceous rift lakes of Western Gondwana: Pre-Salt coquinas of Brazil and West Africa. **Gondwana Research**, v. 28, p. 26–51, 2015.

TORSKAYA, T.; SHABRO, V.; TORRES-VERDÍN, C.; SALAZAR-TIO, R.; REVIL, A. Grain Shape Effects on Permeability, Formation Factor, and Capillary Pressure from Pore-Scale Modeling. **Transport in Porous Media**, v. 102, n. 1, p. 71–90, 1 mar. 2014.

TOSCA, N. J.; MASTERSON, A. L. Chemical controls on incipient Mg-silicate crystallization at 25°C: Implications for early and late diagenesis. **Clay Minerals**, v. 49, n. 2, p. 165–194, 1 maio 2014.

TOSCA, N. J.; WRIGHT, V. P. **The formation and diagenesis of Mg-clay minerals in lacustrine carbonate reservoirs.** AAPG Annual Convention and Exhibition. **Anais**...Houston: 2014

TOSCA, N. J.; WRIGHT, V. P. Diagenetic pathways linked to labile Mg-clays in lacustrine carbonate reservoirs: a model for the origin of secondary porosity in the Cretaceous pre-salt Barra Velha Formation, offshore Brazil. **Geological Society, London, Special Publications**, v. 435, p. 33–46, 2015.

TOUTOUNI, R.; TAN, S. P.; PLANCHER, H.; PIRI, M. Effects of Temperature and Pressure on Interfacial Tensions of Fluid Mixtures. I. CO_2 / n -Pentane Binary. **Journal of Chemical & Engineering Data**, v. 66, n. 5, p. 1977–1983, 13 maio 2021.

TREIBER, L. E.; OWENS, W. W. A Laboratory Evaluation of the Wettability of Fifty Oil-Producing Reservoirs. **Society of Petroleum Engineers Journal**, v. 12, n. 06, p. 531–540, 1 dez. 1972.

TURNER, S.; REGELOUS, M.; KELLEY, S.; HAWKESWORTH, C.; MANTOVANI, M. Magmatism and continental break-up in the South Atlantic: high precision 40Ar-39Ar geochronology. **Earth and Planetary Science Letters**, v. 121, n. 3–4, p. 333–348, fev. 1994.

VALENTI, N. P.; VALENTI, R. M.; KOEDERITZ, L. F. A Unified Theory on Residual Oil Saturation and Irreducible Water Saturation. **Proceedings - SPE Annual Technical Conference and Exhibition**, p. 1887–1904, 2002.

VALVATNE, P. H.; BLUNT, M. J. Predictive pore-scale modeling of two-phase flow in mixed wet media. **Water Resources Research**, v. 40, n. 7, p. 1–21, 2004.

VERRE, F.; BLUNT, M.; MORRISON, A.; MCGARVA, T. **Applicability of Water Shutoff Treatment for Horizontal Wells in Heavy-Oil Reservoirs**. **Anais**...SPE, 11 jun. 2007

WANG, S. Y.; AYRAL, S.; CASTELLANA, F. S.; GRYTE, C. C. Reconstruction of oil saturation distribution histories during immiscible liquid-liquid displacement by computer-assisted tomography. **AIChE Journal**, v. 30, n. 4, p. 642–646, 17 jul. 1984.

WANG, T.; WANG, Y. DA; SUN, C.; MCCLURE, J. E.; MOSTAGHIMI, P.; ARMSTRONG, R. T. Surface wetting characterization in pore-scale multiphase flow simulations: A Ketton carbonate case study. **Geoenergy Science and Engineering**, v. 240, 1 set. 2024.

WARDLAW, N. C. Pore geometry of carbonate rocks as revealed by pore casts and capillary pressure. **The AAPG Bulletin**, v. 60, n. 2, p. 245–257, 1976.

WARDLAW, N. C. The effects of geometry, wettability, viscosity and interfacial tension on trapping in single pore-throat pairs. **Journal of Canadian Petroleum Technology**, v. May-June, p. 21–27, 1982.

WARDLAW, N. C.; MCKELLAR, M. Mercury porosimetry and the interpretation of pore geometry in sedimentary rocks and artificial models. **Powder Technology**, v. 29, n. 1, p. 127–143, maio 1981.

WARREN, J. Dolomite: occurrence, evolution and economically important associations. **Earth-Science Reviews**, v. 52, n. 1–3, p. 1–81, nov. 2000.

WEN, J.; SHI, K.; SUN, Q.; SUN, Z.; GU, H. Measurement for Surface Tension of Aqueous Inorganic Salt. **Frontiers in Energy Research**, v. 6, 12 mar. 2018.

WEN, Y.; BRYAN, J.; KANTZAS, A. **Estimation of Diffusion Coefficients in Bitumen Solvent Mixtures as Derived From Low Field NMR Spectra.** Canadian International Petroleum Conference. **Anais**...Petroleum Society of Canada, 5 abr. 2003

WILDENSCHILD, D.; SHEPPARD, A. P. X-ray imaging and analysis techniques for quantifying pore-scale structure and processes in subsurface porous medium systems. **Advances in Water Resources**, v. 51, p. 217–246, jan. 2013.

WINTER, W. R.; JAHNERT, R. J.; FRANÇA, A. B. Bacia de Campos. **Boletim de Geociências da Petrobras**, v. 15, n. 2, p. 511–529, 2007.

WOLANSKY, G.; MARMUR, A. The actual contact angle on a heterogeneous rough surface in three dimensions. **Langmuir**, v. 14, n. 18, p. 5292–5297, 1998.

WOLF, F. G.; SIEBERT, D. N.; SURMAS, R. Influence of the wettability on the residual fluid saturation for homogeneous and heterogeneous porous systems. **Physics of Fluids**, v. 32, n. 5, 2020.

WOLFF, M.; AL-JALAHMA, A. M.; HOOK, P. F. Log determination of residual oil saturation in the Mauddud zone, Bahrain field. **Proceedings of the Middle East Oil Show**, v. 2, p. 431–444, 1993.

WONG, P. M.; SHIBLI, S. A. R. Use of interpolation neural networks for permeability estimation from well logs. **Log Analyst**, v. 39, n. 6, p. 18–25, 1998.

WRIGHT, P.; TOSCA, N. A Geochemical Model for the Formation of the Pre-Salt Reservoirs, Santos Basin, Brazil: Implications for Understanding Reservoir Distribution. v. 51304, p. 29–30, 2016.

WRIGHT, V. P. The mantle, CO2 and the giant Aptian chemogenic lacustrine carbonate factory of the South Atlantic: Some carbonates are made, not born. **Sedimentology**, v. 69, n. 1, p. 47–73, 1 jan. 2022.

WRIGHT, V. P.; BARNETT, A. J. An abiotic model for the development of textures in some South Atlantic early Cretaceous lacustrine carbonates. *Em*: GROTZINGER, J. P.; JAMES, N. (Eds.). **Microbial Carbonates in Space and Time: Implications for Global Exploration and Production**. Special Publications 418. London: The Geological Society of London, 2015. p. 209–219.

WRIGHT, V. P.; BARNETT, A. J. The textural evolution and ghost matrices of the Cretaceous Barra Velha Formation carbonates from the Santos Basin, offshore Brazil. **Facies**, v. 66, n. 1, p. 7, 7 jan. 2020.

YANG, Z.; HIRASAKI, G. J. NMR measurement of bitumen at different temperatures. **Journal of Magnetic Resonance**, v. 192, n. 2, p. 280–293, jun. 2008.

YAO, Y.; WEI, M.; KANG, W. **A review of wettability alteration using surfactants in carbonate reservoirs. Advances in Colloid and Interface Science,** Elsevier B.V., 1 ago. 2021.

YUAN, H. H. **The influence of pore coordination on petrophysical parameters,** SPE Annual Technical Conference and Exhibition. **Anais**...San Antonio: 1981

ZEINIJAHROMI, A.; FARAJZADEH, R.; (HANS) BRUINING, J.; BEDRIKOVETSKY, P. Effect of fines migration on oil–water relative permeability during two-phase flow in porous media. **Fuel**, v. 176, p. 222–236, jul. 2016.

ZHU, J.; ROSSET, S.; ZOU, H.; HASTIE, T. Multi-class AdaBoost. **Statistics and Its Interface**, v. 2, n. 3, p. 349–360, 2009.

APPENDIX A - Statistics of Attributes Extracted from X-ray Microtomography - Article 1.

Sample	Area3d Log_Std	Area3d _Avg	Area3d _Avg_w	Area3d _Log_Avg	Area3d_Log_ Avg_w
	nm²	nm²	nm²	nm²	nm²
W02-S01	1.04E+00	1.02E+11	5.06E+13	2.33E+01	3.03E+01
W02-S03	1.22E+00	7.06E+10	2.01E+12	2.37E+01	2.71E+01
W02-S04	8.82E-01	2.72E+10	1.53E+11	2.35E+01	2.49E+01
W02-S05	7.47E-01	1.97E+10	1.47E+11	2.33E+01	2.45E+01
W03-S01	1.67E+00	6.32E+11	5.02E+13	2.42E+01	3.10E+01
W03-S02	1.37E+00	1.14E+11	1.74E+12	2.43E+01	2.72E+01
W03-S03	1.33E+00	1.07E+11	3.94E+12	2.42E+01	2.76E+01
W03-S06	1.02E+00	3.93E+10	1.05E+12	2.35E+01	2.61E+01
W03-S09	1.27E+00	1.10E+11	4.27E+13	2.39E+01	2.93E+01
W03-S10	1.33E+00	1.11E+11	2.26E+12	2.43E+01	2.73E+01
W06-S02	1.36E+00	1.65E+11	1.06E+14	2.44E+01	2.96E+01
W06-S03	1.36E+00	1.53E+11	6.34E+13	2.44E+01	2.87E+01
W07-S01	1.48E+00	3.87E+11	1.57E+14	2.42E+01	3.19E+01
W07-S02	1.71E+00	9.42E+11	8.18E+13	2.43E+01	3.16E+01
W07-S04	1.95E+00	1.28E+12	7.15E+13	2.44E+01	3.14E+01
W08-S01	1.39E+00	1.15E+11	7.63E+11	2.45E+01	2.66E+01
W08-S03	1.23E+00	5.20E+11	1.98E+14	2.40E+01	3.23E+01
W08-S04	1.48E+00	1.33E+11	1.15E+12	2.45E+01	2.71E+01
W09-S01	1.56E+00	2.44E+11	1.55E+13	2.46E+01	2.87E+01
W09-S02	1.71E+00	6.94E+11	4.84E+13	2.45E+01	3.08E+01
W09-S03	1.42E+00	1.41E+11	2.67E+12	2.45E+01	2.73E+01
W09-S04	1.44E+00	2.41E+11	3.89E+13	2.43E+01	2.99E+01
W09-S05	1.53E+00	6.43E+11	1.04E+14	2.41E+01	3.16E+01
W10-S06	1.19E+00	2.21E+11	1.03E+14	2.36E+01	3.14E+01
W10-S07	1.06E+00	5.33E+10	5.00E+12	2.34E+01	2.77E+01
W11-S03	1.29E+00	8.35E+10	5.31E+12	2.39E+01	2.77E+01
W11-S04	1.17E+00	1.14E+11	8.03E+13	2.36E+01	3.00E+01
W14-S01	1.29E+00	1.62E+11	4.46E+13	2.37E+01	3.01E+01
W14-S02	1.03E+00	1.06E+11	1.49E+14	2.34E+01	3.10E+01
W14-S04	1.20E+00	3.19E+11	1.14E+14	2.35E+01	3.17E+01
W14-S05	1.29E+00	2.95E+11	1.10E+14	2.37E+01	3.15E+01
W14-S06	1.30E+00	1.35E+11	4.58E+13	2.38E+01	2.98E+01
W14-S07	1.12E+00	9.59E+10	6.15E+13	2.36E+01	2.97E+01
W14-S09	1.29E+00	7.94E+10	2.56E+12	2.38E+01	2.73E+01
W14-S10	1.11E+00	1.68E+11	1.08E+14	2.35E+01	3.14E+01
W14-S12	1.20E+00	1.26E+11	4.39E+13	2.36E+01	3.01E+01
W15-S02	1.11E+00	1.43E+11	9.64E+13	2.35E+01	3.12E+01
W15-S03	1.12E+00	5.82E+10	3.64E+12	2.36E+01	2.75E+01
W15-S05	1.10E+00	6.78E+10	1.28E+13	2.36E+01	2.84E+01
W15-S06	1.19E+00	2.12E+11	5.49E+13	2.35E+01	3.09E+01
W15-S07	1.17E+00	2.97E+11	7.68E+13	2.35E+01	3.15E+01
W15-S08	1.15E+00	2.64E+11	1.14E+14	2.35E+01	3.17E+01

Sample	Area3d Log_Std	Area3d _Avg	Area3d _Avg_w	Area3d _Log_Avg	Area3d_Log_ Avg_w
	nm²	nm²	nm²	nm²	nm²
W15-S09	1.13E+00	1.57E+11	5.59E+13	2.35E+01	3.08E+01
W15-S12	1.31E+00	2.93E+11	8.62E+13	2.36E+01	3.12E+01
W15-S14	1.11E+00	5.39E+10	3.18E+12	2.37E+01	2.67E+01
W16-S01	1.02E+00	3.89E+10	2.42E+12	2.35E+01	2.62E+01
W16-S03	1.13E+00	8.34E+10	2.48E+13	2.35E+01	2.91E+01
W16-S05	1.04E+00	2.00E+11	1.27E+14	2.34E+01	3.18E+01
W16-S06	1.02E+00	1.83E+11	1.08E+14	2.34E+01	3.17E+01
W17-S01	1.26E+00	3.66E+11	2.19E+14	2.39E+01	3.22E+01
W17-S03	1.35E+00	2.41E+11	6.92E+13	2.41E+01	3.06E+01
W17-S04	1.40E+00	3.59E+11	7.47E+13	2.42E+01	3.11E+01
W17-S05	1.21E+00	2.37E+11	1.93E+14	2.36E+01	3.17E+01
W18-S01	1.36E+00	2.22E+11	5.93E+13	2.39E+01	3.05E+01
W18-S02	1.16E+00	1.08E+11	6.44E+13	2.36E+01	3.00E+01
W18-S03	1.29E+00	3.19E+11	9.61E+13	2.37E+01	3.15E+01
W18-S04	1.15E+00	1.75E+11	1.23E+14	2.36E+01	3.12E+01
W18-S05	9.73E-01	3.76E+10	3.14E+12	2.35E+01	2.65E+01
W18-S06	1.25E+00	2.69E+11	6.38E+13	2.36E+01	3.11E+01
W19-S01	1.64E+00	4.52E+11	3.19E+14	2.48E+01	3.08E+01
W19-S02	1.15E+00	2.44E+11	4.73E+14	2.35E+01	3.26E+01
W19-S03	8.96E-01	2.93E+10	4.07E+12	2.34E+01	2.60E+01
W19-S04	1.04E+00	4.57E+10	5.50E+12	2.35E+01	2.69E+01
W19-S05	1.14E+00	1.17E+11	4.14E+14	2.36E+01	3.09E+01
W19-S06	1.09E+00	4.47E+10	6.28E+11	2.36E+01	2.61E+01
W20-S01	1.01E+00	3.92E+10	9.20E+12	2.36E+01	2.63E+01
W20-S02	1.02E+00	2.00E+11	4.03E+14	2.34E+01	3.21E+01
W20-S03	1.15E+00	7.95E+10	1.89E+13	2.37E+01	2.86E+01
W20-S04	9.80E-01	3.45E+10	4.46E+11	2.35E+01	2.57E+01
W20-S05	1.22E+00	2.06E+11	6.00E+13	2.36E+01	3.08E+01
W20-S06	8.45E-01	2.43E+10	1.61E+11	2.34E+01	2.49E+01
W21-S01	1.12E+00	2.20E+11	9.97E+13	2.35E+01	3.16E+01
W21-S02	1.14E+00	9.62E+10	4.57E+13	2.36E+01	2.96E+01
W21-S03	1.19E+00	2.50E+11	1.07E+14	2.36E+01	3.16E+01
W21-S04	1.21E+00	2.65E+11	1.56E+14	2.37E+01	3.18E+01
W21-S05	1.16E+00	2.34E+11	1.48E+14	2.36E+01	3.18E+01
W21-S06	1.30E+00	3.80E+11	1.01E+14	2.37E+01	3.17E+01
W21-S07	1.25E+00	1.29E+11	6.64E+13	2.37E+01	2.99E+01
W21-S08	1.14E+00	2.72E+11	1.44E+14	2.36E+01	3.19E+01
W22-S01	8.64E-01	2.20E+11	7.58E+13	2.31E+01	3.16E+01
W22-S02	1.21E+00	2.06E+11	1.74E+14	2.36E+01	3.16E+01
W22-S04	1.52E+00	3.51E+11	4.21E+13	2.39E+01	3.06E+01
W22-S05	1.02E+00	3.95E+11	4.38E+14	2.34E+01	3.32E+01
W24-S01	1.30E+00	1.06E+11	5.73E+13	2.39E+01	2.87E+01

Sample	Area3d Log_Std	Area3d _Avg	Area3d _Avg_w	Area3d _Log_Avg	Area3d_Log_ Avg_w
	nm²	nm²	nm²	nm²	nm²
W24-S02	1.25E+00	1.24E+11	9.10E+13	2.38E+01	3.00E+01
W24-S03	1.15E+00	1.27E+11	1.05E+14	2.36E+01	3.06E+01
W24-S04	1.04E+00	1.23E+11	8.92E+13	2.35E+01	3.10E+01
W24-S05	1.15E+00	2.24E+11	8.52E+13	2.36E+01	3.14E+01
W25-S01	9.00E-01	4.11E+10	4.94E+13	2.33E+01	2.85E+01
W25-S02	1.34E+00	1.76E+11	9.79E+13	2.38E+01	3.05E+01
W25-S03	1.24E+00	1.32E+11	5.19E+13	2.36E+01	3.00E+01
W25-S04	1.16E+00	1.91E+11	1.64E+14	2.35E+01	3.16E+01
W26-S02	1.21E+00	1.25E+11	4.93E+13	2.36E+01	2.99E+01
W27-S01	1.09E+00	1.68E+11	6.25E+13	2.34E+01	3.10E+01
W27-S03	1.04E+00	3.67E+10	2.34E+11	2.36E+01	2.55E+01
W27-S04	1.11E+00	5.74E+10	1.30E+13	2.36E+01	2.81E+01
W27-S05	9.09E-01	2.77E+10	4.34E+11	2.34E+01	2.53E+01
W27-S06	1.01E+00	3.53E+10	2.93E+11	2.36E+01	2.55E+01
W28-S02	1.28E+00	1.14E+11	6.65E+12	2.35E+01	2.88E+01
W28-S04	1.33E+00	2.95E+11	7.43E+13	2.42E+01	3.09E+01
W28-S05	8.57E-01	2.79E+10	5.91E+12	2.33E+01	2.64E+01
W29-S01	1.06E+00	6.21E+10	2.06E+13	2.35E+01	2.89E+01
W29-S02	8.40E-01	4.15E+10	4.71E+13	2.32E+01	2.91E+01
W30-S01	7.31E-01	1.95E+10	4.07E+11	2.33E+01	2.48E+01
W30-S03	9.17E-01	1.25E+11	2.38E+14	2.34E+01	3.20E+01
W30-S04	1.56E+00	2.84E+11	4.43E+13	2.42E+01	3.01E+01
W30-S05	1.22E+00	1.32E+11	3.96E+13	2.36E+01	2.99E+01
W30-S07	1.21E+00	1.15E+11	6.19E+13	2.36E+01	2.98E+01
W30-S08	1.09E+00	8.46E+10	1.17E+14	2.36E+01	3.00E+01
W31-S01	1.11E+00	1.57E+11	6.48E+13	2.35E+01	3.09E+01
W31-S03	1.48E+00	4.36E+11	1.01E+14	2.38E+01	3.14E+01

Sample	Area3d_ Max	Area3d_ Log_ Median	Area3d_ Max	Area3d_ Median	Area 3d_Std	Crofton Perimeter Log_Std
	nm²	nm²	nm²	nm²	nm²	nm
W02-S01	2.32E+14	2.49E+01	3.31E+01	6.35E+10	2.09E+12	1.01E+00
W02-S03	1.63E+13	2.50E+01	3.04E+01	7.40E+10	3.26E+11	1.19E+00
W02-S04	4.94E+12	2.46E+01	2.92E+01	5.01E+10	5.17E+10	8.40E-01
W02-S05	7.45E+12	2.45E+01	2.96E+01	4.55E+10	4.08E+10	7.10E-01
W03-S01	1.96E+14	2.53E+01	3.29E+01	9.58E+10	5.14E+12	1.61E+00
W03-S02	2.33E+13	2.52E+01	3.08E+01	8.93E+10	3.46E+11	1.29E+00
W03-S03	4.74E+13	2.51E+01	3.15E+01	7.86E+10	5.15E+11	1.25E+00
W03-S06	5.52E+13	2.48E+01	3.16E+01	5.90E+10	1.65E+11	9.80E-01
W03-S09	2.96E+14	2.50E+01	3.33E+01	7.25E+10	1.65E+12	1.20E+00
W03-S10	3.31E+13	2.52E+01	3.11E+01	8.42E+10	3.84E+11	1.28E+00
W06-S02	1.17E+15	2.52E+01	3.47E+01	8.57E+10	3.50E+12	1.28E+00

Sample	Area3d_Max	Area3d_Log_Median	Area3d_Max	Area3d_Median	Area 3d_Std	Crofton Perimeter Log_Std
	nm²	nm²	nm²	nm²	nm²	nm
W06-S03	1.25E+15	2.52E+01	3.48E+01	8.70E+10	2.60E+12	1.28E+00
W07-S01	5.94E+14	2.52E+01	3.40E+01	8.71E+10	5.95E+12	1.38E+00
W07-S02	3.42E+14	2.53E+01	3.35E+01	9.87E+10	8.06E+12	1.64E+00
W07-S04	4.97E+14	2.57E+01	3.38E+01	1.42E+11	9.02E+12	1.87E+00
W08-S01	4.86E+13	2.54E+01	3.15E+01	1.11E+11	2.28E+11	1.27E+00
W08-S03	9.18E+14	2.52E+01	3.45E+01	8.92E+10	9.85E+12	1.19E+00
W08-S04	1.23E+13	2.55E+01	3.01E+01	1.18E+11	3.08E+11	1.37E+00
W09-S01	3.34E+14	2.55E+01	3.34E+01	1.13E+11	1.66E+12	1.49E+00
W09-S02	2.45E+14	2.54E+01	3.31E+01	1.08E+11	5.48E+12	1.65E+00
W09-S03	6.60E+13	2.53E+01	3.18E+01	1.01E+11	4.32E+11	1.35E+00
W09-S04	2.26E+14	2.52E+01	3.31E+01	8.54E+10	2.71E+12	1.37E+00
W09-S05	8.70E+14	2.51E+01	3.44E+01	8.33E+10	7.67E+12	1.47E+00
W10-S06	4.35E+14	2.49E+01	3.37E+01	6.64E+10	4.38E+12	1.15E+00
W10-S07	7.13E+13	2.49E+01	3.19E+01	6.82E+10	4.29E+11	1.03E+00
W11-S03	6.38E+13	2.51E+01	3.18E+01	8.01E+10	4.77E+11	1.26E+00
W11-S04	4.92E+14	2.49E+01	3.38E+01	6.69E+10	2.73E+12	1.14E+00
W14-S01	3.36E+14	2.50E+01	3.34E+01	7.40E+10	2.40E+12	1.25E+00
W14-S02	1.14E+15	2.48E+01	3.47E+01	6.05E+10	3.61E+12	9.98E-01
W14-S04	4.98E+14	2.49E+01	3.38E+01	6.71E+10	5.72E+12	1.16E+00
W14-S05	3.48E+14	2.50E+01	3.35E+01	7.16E+10	5.32E+12	1.25E+00
W14-S06	3.79E+14	2.50E+01	3.36E+01	7.52E+10	2.02E+12	1.26E+00
W14-S07	9.23E+14	2.48E+01	3.45E+01	6.05E+10	2.18E+12	1.09E+00
W14-S09	7.76E+13	2.52E+01	3.20E+01	8.39E+10	3.65E+11	1.25E+00
W14-S10	4.25E+14	2.49E+01	3.37E+01	6.22E+10	3.79E+12	1.08E+00
W14-S12	2.39E+14	2.49E+01	3.31E+01	6.85E+10	1.99E+12	1.16E+00
W15-S02	3.35E+14	2.49E+01	3.34E+01	6.28E+10	3.27E+12	1.07E+00
W15-S03	3.69E+13	2.49E+01	3.12E+01	6.52E+10	3.59E+11	1.08E+00
W15-S05	8.87E+13	2.48E+01	3.21E+01	6.09E+10	7.58E+11	1.06E+00
W15-S06	4.44E+14	2.49E+01	3.37E+01	6.70E+10	3.21E+12	1.15E+00
W15-S07	3.15E+14	2.49E+01	3.34E+01	6.37E+10	4.49E+12	1.13E+00
W15-S08	5.63E+14	2.49E+01	3.40E+01	6.50E+10	5.20E+12	1.11E+00
W15-S09	2.48E+14	2.49E+01	3.31E+01	6.22E+10	2.68E+12	1.09E+00
W15-S12	6.38E+14	2.51E+01	3.41E+01	7.87E+10	4.82E+12	1.27E+00
W15-S14	1.31E+14	2.49E+01	3.25E+01	6.23E+10	3.35E+11	1.08E+00
W16-S01	9.04E+13	2.48E+01	3.21E+01	6.05E+10	2.09E+11	9.86E-01
W16-S03	1.86E+14	2.50E+01	3.29E+01	6.98E+10	1.22E+12	1.10E+00
W16-S05	4.88E+14	2.48E+01	3.38E+01	6.13E+10	4.64E+12	1.02E+00
W16-S06	4.21E+14	2.48E+01	3.37E+01	5.67E+10	4.10E+12	9.85E-01
W17-S01	1.03E+15	2.49E+01	3.46E+01	6.78E+10	8.43E+12	1.19E+00
W17-S03	7.36E+14	2.50E+01	3.42E+01	7.48E+10	3.70E+12	1.29E+00
W17-S04	2.65E+14	2.51E+01	3.32E+01	7.81E+10	4.72E+12	1.34E+00

Sample	Area3d_ Max	Area3d_ Log_ Median	Area3d_ Max	Area3d_ Median	Area 3d_Std	Crofton Perimeter Log_Std
	nm²	nm²	nm²	nm²	nm²	nm
W17-S05	7.65E+14	2.50E+01	3.43E+01	7.19E+10	6.63E+12	1.17E+00
W18-S01	3.02E+14	2.51E+01	3.33E+01	7.62E+10	3.33E+12	1.32E+00
W18-S02	2.97E+14	2.49E+01	3.33E+01	6.83E+10	2.27E+12	1.14E+00
W18-S03	5.59E+14	2.50E+01	3.40E+01	7.19E+10	5.29E+12	1.26E+00
W18-S04	7.91E+14	2.49E+01	3.43E+01	6.32E+10	4.30E+12	1.12E+00
W18-S05	6.59E+13	2.47E+01	3.18E+01	5.53E+10	2.62E+11	9.43E-01
W18-S06	3.60E+14	2.50E+01	3.35E+01	6.90E+10	3.81E+12	1.22E+00
W19-S01	2.03E+15	2.56E+01	3.52E+01	1.32E+11	1.14E+13	1.57E+00
W19-S02	2.05E+15	2.50E+01	3.53E+01	7.17E+10	1.05E+13	1.11E+00
W19-S03	1.11E+14	2.47E+01	3.23E+01	5.29E+10	2.16E+11	8.64E-01
W19-S04	2.92E+14	2.48E+01	3.33E+01	5.91E+10	4.00E+11	1.00E+00
W19-S05	3.11E+15	2.49E+01	3.57E+01	6.74E+10	6.47E+12	1.10E+00
W19-S06	1.66E+13	2.49E+01	3.04E+01	6.52E+10	1.46E+11	1.04E+00
W20-S01	2.73E+14	2.48E+01	3.32E+01	5.72E+10	3.87E+11	9.72E-01
W20-S02	6.53E+15	2.48E+01	3.64E+01	5.86E+10	8.70E+12	9.84E-01
W20-S03	2.37E+14	2.49E+01	3.31E+01	6.37E+10	1.01E+12	1.12E+00
W20-S04	1.10E+13	2.47E+01	3.00E+01	5.58E+10	9.56E+10	9.47E-01
W20-S05	4.56E+14	2.49E+01	3.38E+01	6.66E+10	3.31E+12	1.18E+00
W20-S06	2.07E+12	2.46E+01	2.84E+01	5.05E+10	4.62E+10	8.16E-01
W21-S01	4.32E+14	2.48E+01	3.37E+01	6.10E+10	4.31E+12	1.08E+00
W21-S02	3.89E+14	2.49E+01	3.36E+01	6.37E+10	1.86E+12	1.11E+00
W21-S03	4.08E+14	2.49E+01	3.36E+01	6.48E+10	4.74E+12	1.16E+00
W21-S04	8.37E+14	2.49E+01	3.44E+01	6.71E+10	6.07E+12	1.18E+00
W21-S05	5.38E+14	2.49E+01	3.39E+01	6.51E+10	5.48E+12	1.13E+00
W21-S06	4.19E+14	2.50E+01	3.37E+01	7.17E+10	5.83E+12	1.26E+00
W21-S07	4.80E+14	2.50E+01	3.38E+01	7.39E+10	2.57E+12	1.21E+00
W21-S08	7.72E+14	2.49E+01	3.43E+01	6.27E+10	5.96E+12	1.11E+00
W22-S01	4.19E+14	2.47E+01	3.37E+01	5.10E+10	3.95E+12	8.43E-01
W22-S02	7.52E+14	2.50E+01	3.43E+01	7.36E+10	5.66E+12	1.17E+00
W22-S04	1.76E+14	2.52E+01	3.28E+01	9.00E+10	3.60E+12	1.49E+00
W22-S05	1.67E+15	2.49E+01	3.51E+01	6.24E+10	1.29E+13	9.87E-01
W24-S01	1.09E+15	2.51E+01	3.46E+01	7.60E+10	1.89E+12	1.26E+00
W24-S02	7.90E+14	2.50E+01	3.43E+01	7.21E+10	2.91E+12	1.21E+00
W24-S03	4.45E+14	2.49E+01	3.37E+01	6.60E+10	3.33E+12	1.12E+00
W24-S04	4.48E+14	2.48E+01	3.37E+01	5.85E+10	2.99E+12	1.01E+00
W24-S05	5.30E+14	2.49E+01	3.39E+01	6.23E+10	4.04E+12	1.12E+00
W25-S01	2.92E+14	2.47E+01	3.33E+01	5.49E+10	1.14E+12	8.90E-01
W25-S02	4.53E+14	2.51E+01	3.37E+01	8.20E+10	3.67E+12	1.31E+00
W25-S03	2.72E+14	2.50E+01	3.32E+01	7.48E+10	2.28E+12	1.21E+00
W25-S04	6.82E+14	2.50E+01	3.42E+01	6.98E+10	5.25E+12	1.13E+00
W26-S02	3.60E+14	2.50E+01	3.35E+01	6.86E+10	2.19E+12	1.17E+00

Sample	Area3d_Max	Area3d_Log_Median	Area3d_Max	Area3d_Median	Area 3d_Std	Crofton Perimeter Log_Std
	nm²	nm²	nm²	nm²	nm²	nm
W27-S01	3.17E+14	2.49E+01	3.34E+01	6.64E+10	2.92E+12	1.07E+00
W27-S03	5.30E+12	2.49E+01	2.93E+01	6.43E+10	7.01E+10	1.02E+00
W27-S04	8.43E+13	2.49E+01	3.21E+01	6.84E+10	5.79E+11	1.10E+00
W27-S05	3.70E+13	2.47E+01	3.12E+01	5.45E+10	7.60E+10	8.72E-01
W27-S06	9.57E+12	2.48E+01	2.99E+01	6.00E+10	7.92E+10	9.67E-01
W28-S02	3.92E+13	2.51E+01	3.13E+01	8.06E+10	7.22E+11	1.25E+00
W28-S04	4.25E+14	2.50E+01	3.37E+01	7.39E+10	4.12E+12	1.27E+00
W28-S05	1.07E+14	2.48E+01	3.23E+01	5.63E+10	2.85E+11	8.35E-01
W29-S01	2.02E+14	2.49E+01	3.29E+01	6.37E+10	8.25E+11	1.03E+00
W29-S02	5.57E+14	2.47E+01	3.40E+01	5.48E+10	1.12E+12	8.15E-01
W30-S01	2.21E+13	2.45E+01	3.07E+01	4.49E+10	6.49E+10	6.98E-01
W30-S03	9.09E+14	2.47E+01	3.44E+01	5.34E+10	4.97E+12	9.02E-01
W30-S04	3.81E+14	2.53E+01	3.36E+01	9.71E+10	3.05E+12	1.52E+00
W30-S05	3.77E+14	2.50E+01	3.36E+01	7.12E+10	2.07E+12	1.19E+00
W30-S07	5.67E+14	2.50E+01	3.40E+01	7.49E+10	2.41E+12	1.18E+00
W30-S08	8.22E+14	2.49E+01	3.43E+01	6.28E+10	2.71E+12	1.06E+00
W31-S01	2.47E+14	2.48E+01	3.31E+01	5.95E+10	2.88E+12	1.08E+00
W31-S03	7.68E+14	2.52E+01	3.43E+01	8.62E+10	5.62E+12	1.45E+00

Sample	Crofton Perimeter _Avg	Crofton Perimeter _Avg_w	Crofton Perimeter _Log_Avg	Crofton Perimeter _Log_Avg_w	Crofton Perimeter _Log_Max	Crofton Perimeter _Log_ Median
	nm	nm	nm	nm	nm	nm
W02-S01	1.67E+06	8.20E+08	1.24E+01	1.93E+01	2.20E+01	1.39E+01
W02-S03	1.15E+06	3.21E+07	1.27E+01	1.61E+01	1.94E+01	1.40E+01
W02-S04	4.43E+05	2.44E+06	1.25E+01	1.39E+01	1.82E+01	1.36E+01
W02-S05	3.27E+05	2.35E+06	1.23E+01	1.35E+01	1.85E+01	1.35E+01
W03-S01	9.64E+06	7.72E+08	1.32E+01	1.99E+01	2.18E+01	1.41E+01
W03-S02	1.66E+06	2.61E+07	1.33E+01	1.61E+01	1.97E+01	1.40E+01
W03-S03	1.59E+06	6.07E+07	1.31E+01	1.65E+01	2.04E+01	1.39E+01
W03-S06	6.40E+05	1.67E+07	1.26E+01	1.51E+01	2.06E+01	1.38E+01
W03-S09	1.69E+06	6.77E+08	1.29E+01	1.82E+01	2.23E+01	1.39E+01
W03-S10	1.67E+06	3.51E+07	1.33E+01	1.62E+01	2.01E+01	1.40E+01
W06-S02	2.36E+06	1.55E+09	1.32E+01	1.85E+01	2.36E+01	1.40E+01
W06-S03	2.18E+06	9.18E+08	1.33E+01	1.75E+01	2.36E+01	1.40E+01
W07-S01	5.65E+06	2.38E+09	1.31E+01	2.08E+01	2.29E+01	1.40E+01
W07-S02	1.40E+07	1.23E+09	1.32E+01	2.04E+01	2.23E+01	1.41E+01
W07-S04	1.85E+07	1.04E+09	1.33E+01	2.03E+01	2.27E+01	1.45E+01
W08-S01	1.51E+06	9.88E+06	1.34E+01	1.54E+01	2.02E+01	1.42E+01
W08-S03	7.14E+06	2.71E+09	1.28E+01	2.11E+01	2.33E+01	1.40E+01
W08-S04	1.79E+06	1.58E+07	1.34E+01	1.59E+01	1.90E+01	1.42E+01

Sample	Crofton Perimeter _Avg	Crofton Perimeter _Avg_w	Crofton Perimeter _Log_Avg	Crofton Perimeter _Log_Avg_w	Crofton Perimeter _Log_Max	Crofton Perimeter _Log_ Median
	nm	nm	nm	nm	nm	nm
W09-S01	3.53E+06	2.28E+08	1.35E+01	1.75E+01	2.23E+01	1.43E+01
W09-S02	1.02E+07	7.10E+08	1.34E+01	1.97E+01	2.20E+01	1.42E+01
W09-S03	2.01E+06	3.94E+07	1.34E+01	1.62E+01	2.07E+01	1.42E+01
W09-S04	3.57E+06	5.80E+08	1.32E+01	1.88E+01	2.19E+01	1.40E+01
W09-S05	9.62E+06	1.56E+09	1.31E+01	2.05E+01	2.33E+01	1.40E+01
W10-S06	3.52E+06	1.64E+09	1.26E+01	2.04E+01	2.27E+01	1.39E+01
W10-S07	8.82E+05	8.13E+07	1.24E+01	1.66E+01	2.09E+01	1.39E+01
W11-S03	1.37E+06	8.67E+07	1.29E+01	1.66E+01	2.08E+01	1.41E+01
W11-S04	1.85E+06	1.30E+09	1.26E+01	1.90E+01	2.28E+01	1.39E+01
W14-S01	2.62E+06	7.15E+08	1.28E+01	1.91E+01	2.24E+01	1.40E+01
W14-S02	1.72E+06	2.40E+09	1.25E+01	2.00E+01	2.36E+01	1.38E+01
W14-S04	5.09E+06	1.81E+09	1.26E+01	2.07E+01	2.28E+01	1.39E+01
W14-S05	4.75E+06	1.77E+09	1.28E+01	2.05E+01	2.24E+01	1.40E+01
W14-S06	2.19E+06	7.33E+08	1.28E+01	1.87E+01	2.25E+01	1.40E+01
W14-S07	1.56E+06	9.98E+08	1.26E+01	1.87E+01	2.34E+01	1.38E+01
W14-S09	1.28E+06	4.07E+07	1.28E+01	1.63E+01	2.09E+01	1.41E+01
W14-S10	2.73E+06	1.74E+09	1.26E+01	2.04E+01	2.27E+01	1.38E+01
W14-S12	2.03E+06	7.02E+08	1.26E+01	1.91E+01	2.21E+01	1.39E+01
W15-S02	2.27E+06	1.53E+09	1.25E+01	2.02E+01	2.24E+01	1.38E+01
W15-S03	9.41E+05	5.79E+07	1.26E+01	1.65E+01	2.02E+01	1.39E+01
W15-S05	1.08E+06	2.02E+08	1.26E+01	1.73E+01	2.11E+01	1.38E+01
W15-S06	3.36E+06	8.65E+08	1.25E+01	1.98E+01	2.27E+01	1.39E+01
W15-S07	4.69E+06	1.21E+09	1.25E+01	2.04E+01	2.23E+01	1.38E+01
W15-S08	4.16E+06	1.80E+09	1.26E+01	2.06E+01	2.29E+01	1.39E+01
W15-S09	2.49E+06	8.82E+08	1.26E+01	1.98E+01	2.21E+01	1.38E+01
W15-S12	4.58E+06	1.34E+09	1.27E+01	2.01E+01	2.30E+01	1.40E+01
W15-S14	8.86E+05	5.17E+07	1.27E+01	1.57E+01	2.15E+01	1.38E+01
W16-S01	6.38E+05	3.94E+07	1.26E+01	1.52E+01	2.11E+01	1.38E+01
W16-S03	1.34E+06	3.93E+08	1.25E+01	1.81E+01	2.18E+01	1.39E+01
W16-S05	3.23E+06	2.05E+09	1.24E+01	2.07E+01	2.28E+01	1.38E+01
W16-S06	2.91E+06	1.72E+09	1.24E+01	2.06E+01	2.26E+01	1.37E+01
W17-S01	5.51E+06	3.30E+09	1.29E+01	2.11E+01	2.35E+01	1.38E+01
W17-S03	3.66E+06	1.05E+09	1.31E+01	1.96E+01	2.31E+01	1.39E+01
W17-S04	5.42E+06	1.13E+09	1.31E+01	2.00E+01	2.21E+01	1.40E+01
W17-S05	3.74E+06	3.03E+09	1.26E+01	2.06E+01	2.32E+01	1.40E+01
W18-S01	3.57E+06	9.45E+08	1.29E+01	1.95E+01	2.23E+01	1.40E+01
W18-S02	1.84E+06	1.09E+09	1.26E+01	1.91E+01	2.23E+01	1.40E+01
W18-S03	5.08E+06	1.53E+09	1.27E+01	2.04E+01	2.29E+01	1.40E+01
W18-S04	2.84E+06	1.98E+09	1.26E+01	2.02E+01	2.33E+01	1.38E+01
W18-S05	6.24E+05	5.14E+07	1.25E+01	1.55E+01	2.08E+01	1.37E+01
W18-S06	4.32E+06	1.02E+09	1.26E+01	2.01E+01	2.25E+01	1.40E+01

Sample	Crofton Perimeter _Avg	Crofton Perimeter _Avg_w	Crofton Perimeter _Log_Avg	Crofton Perimeter _Log_Avg_w	Crofton Perimeter _Log_Max	Crofton Perimeter _Log_ Median
	nm	nm	nm	nm	nm	nm
W19-S01	6.56E+06	4.65E+09	1.37E+01	1.97E+01	2.41E+01	1.44E+01
W19-S02	3.87E+06	7.47E+09	1.26E+01	2.16E+01	2.42E+01	1.40E+01
W19-S03	4.85E+05	6.31E+07	1.24E+01	1.49E+01	2.12E+01	1.37E+01
W19-S04	7.44E+05	8.80E+07	1.26E+01	1.58E+01	2.23E+01	1.38E+01
W19-S05	1.86E+06	6.50E+09	1.26E+01	1.99E+01	2.46E+01	1.39E+01
W19-S06	7.22E+05	9.95E+06	1.26E+01	1.50E+01	1.94E+01	1.39E+01
W20-S01	6.41E+05	1.47E+08	1.26E+01	1.53E+01	2.22E+01	1.37E+01
W20-S02	3.22E+06	6.46E+09	1.24E+01	2.11E+01	2.54E+01	1.38E+01
W20-S03	1.30E+06	3.04E+08	1.27E+01	1.75E+01	2.21E+01	1.39E+01
W20-S04	5.71E+05	7.21E+06	1.26E+01	1.47E+01	1.90E+01	1.37E+01
W20-S05	3.30E+06	9.57E+08	1.26E+01	1.98E+01	2.27E+01	1.39E+01
W20-S06	4.08E+05	2.68E+06	1.24E+01	1.39E+01	1.73E+01	1.36E+01
W21-S01	3.55E+06	1.60E+09	1.25E+01	2.05E+01	2.27E+01	1.38E+01
W21-S02	1.56E+06	7.36E+08	1.26E+01	1.86E+01	2.26E+01	1.39E+01
W21-S03	4.02E+06	1.72E+09	1.26E+01	2.06E+01	2.26E+01	1.39E+01
W21-S04	4.26E+06	2.50E+09	1.27E+01	2.07E+01	2.33E+01	1.39E+01
W21-S05	3.79E+06	2.39E+09	1.26E+01	2.07E+01	2.29E+01	1.39E+01
W21-S06	5.97E+06	1.59E+09	1.27E+01	2.06E+01	2.26E+01	1.40E+01
W21-S07	2.06E+06	1.05E+09	1.27E+01	1.89E+01	2.28E+01	1.40E+01
W21-S08	4.36E+06	2.30E+09	1.26E+01	2.08E+01	2.32E+01	1.38E+01
W22-S01	3.52E+06	1.20E+09	1.22E+01	2.05E+01	2.26E+01	1.37E+01
W22-S02	3.28E+06	2.76E+09	1.26E+01	2.05E+01	2.32E+01	1.40E+01
W22-S04	5.72E+06	6.83E+08	1.30E+01	1.95E+01	2.18E+01	1.42E+01
W22-S05	6.22E+06	6.88E+09	1.24E+01	2.21E+01	2.40E+01	1.38E+01
W24-S01	1.69E+06	9.25E+08	1.29E+01	1.77E+01	2.36E+01	1.40E+01
W24-S02	2.00E+06	1.46E+09	1.28E+01	1.90E+01	2.33E+01	1.40E+01
W24-S03	2.06E+06	1.69E+09	1.27E+01	1.96E+01	2.27E+01	1.39E+01
W24-S04	1.97E+06	1.42E+09	1.25E+01	2.00E+01	2.27E+01	1.38E+01
W24-S05	3.57E+06	1.35E+09	1.26E+01	2.04E+01	2.28E+01	1.38E+01
W25-S01	7.15E+05	8.40E+08	1.24E+01	1.75E+01	2.23E+01	1.38E+01
W25-S02	2.91E+06	1.62E+09	1.28E+01	1.95E+01	2.27E+01	1.41E+01
W25-S03	2.14E+06	8.33E+08	1.27E+01	1.89E+01	2.22E+01	1.40E+01
W25-S04	3.09E+06	2.65E+09	1.25E+01	2.05E+01	2.31E+01	1.40E+01
W26-S02	2.02E+06	7.87E+08	1.27E+01	1.89E+01	2.25E+01	1.39E+01
W27-S01	2.71E+06	1.00E+09	1.24E+01	2.00E+01	2.24E+01	1.39E+01
W27-S03	6.16E+05	3.89E+06	1.26E+01	1.45E+01	1.83E+01	1.39E+01
W27-S04	9.82E+05	2.20E+08	1.26E+01	1.71E+01	2.11E+01	1.40E+01
W27-S05	4.57E+05	6.84E+06	1.25E+01	1.42E+01	2.02E+01	1.37E+01
W27-S06	5.74E+05	4.66E+06	1.26E+01	1.45E+01	1.88E+01	1.38E+01
W28-S02	1.89E+06	1.10E+08	1.26E+01	1.78E+01	2.03E+01	1.41E+01
W28-S04	4.41E+06	1.12E+09	1.31E+01	1.98E+01	2.26E+01	1.39E+01

Sample	Crofton Perimeter _Avg	Crofton Perimeter _Avg_w	Crofton Perimeter _Log_Avg	Crofton Perimeter _Log_Avg_w	Crofton Perimeter _Log_Max	Crofton Perimeter _Log_ Median
	nm	nm	nm	nm	nm	nm
W28-S05	4.71E+05	9.56E+07	1.23E+01	1.54E+01	2.12E+01	1.38E+01
W29-S01	1.01E+06	3.28E+08	1.25E+01	1.79E+01	2.19E+01	1.39E+01
W29-S02	6.86E+05	7.60E+08	1.23E+01	1.81E+01	2.29E+01	1.37E+01
W30-S01	3.27E+05	6.73E+06	1.23E+01	1.38E+01	1.97E+01	1.35E+01
W30-S03	2.09E+06	3.98E+09	1.24E+01	2.10E+01	2.34E+01	1.37E+01
W30-S04	4.60E+06	7.15E+08	1.32E+01	1.90E+01	2.25E+01	1.43E+01
W30-S05	2.14E+06	6.35E+08	1.26E+01	1.89E+01	2.25E+01	1.40E+01
W30-S07	1.86E+06	9.94E+08	1.26E+01	1.87E+01	2.29E+01	1.40E+01
W30-S08	1.37E+06	1.87E+09	1.26E+01	1.89E+01	2.33E+01	1.38E+01
W31-S01	2.56E+06	1.05E+09	1.25E+01	1.99E+01	2.21E+01	1.38E+01
W31-S03	7.03E+06	1.62E+09	1.29E+01	2.04E+01	2.32E+01	1.42E+01

Sample	Crofton Perimeter _Max	Crofton Perimeter _Median	Crofton Perimeter _Std	Elongation _Avg	Elongation _Avg_w	Elongation _Median
	nm	nm	nm	adim	adim	adim
W02-S01	3.76E+09	1.05E+06	3.39E+07	3.97E-01	4.26E-01	3.68E-01
W02-S03	2.59E+08	1.20E+06	5.21E+06	3.70E-01	3.58E-01	3.37E-01
W02-S04	7.92E+07	8.09E+05	8.21E+05	3.80E-01	3.72E-01	3.45E-01
W02-S05	1.13E+08	7.26E+05	6.52E+05	3.94E-01	3.85E-01	3.63E-01
W03-S01	2.94E+09	1.37E+06	7.89E+07	4.11E-01	4.26E-01	3.81E-01
W03-S02	3.57E+08	1.24E+06	5.19E+06	4.68E-01	4.14E-01	4.51E-01
W03-S03	7.32E+08	1.09E+06	7.93E+06	4.48E-01	3.84E-01	4.22E-01
W03-S06	8.70E+08	9.55E+05	2.63E+06	4.04E-01	3.90E-01	3.73E-01
W03-S09	4.74E+09	1.05E+06	2.61E+07	4.35E-01	4.05E-01	4.02E-01
W03-S10	5.17E+08	1.21E+06	5.94E+06	4.46E-01	3.96E-01	4.19E-01
W06-S02	1.69E+10	1.17E+06	5.08E+07	4.34E-01	4.09E-01	3.99E-01
W06-S03	1.81E+10	1.20E+06	3.75E+07	4.33E-01	3.89E-01	4.00E-01
W07-S01	8.66E+09	1.16E+06	8.93E+07	4.25E-01	4.63E-01	3.89E-01
W07-S02	5.08E+09	1.36E+06	1.21E+08	4.57E-01	4.35E-01	4.36E-01
W07-S04	7.10E+09	1.94E+06	1.31E+08	4.38E-01	4.26E-01	4.12E-01
W08-S01	5.67E+08	1.41E+06	2.96E+06	4.80E-01	4.06E-01	4.68E-01
W08-S03	1.26E+10	1.25E+06	1.35E+08	4.11E-01	4.51E-01	3.82E-01
W08-S04	1.73E+08	1.52E+06	4.22E+06	4.92E-01	4.25E-01	4.80E-01
W09-S01	4.98E+09	1.58E+06	2.44E+07	4.18E-01	3.73E-01	3.84E-01
W09-S02	3.63E+09	1.51E+06	8.04E+07	4.13E-01	4.02E-01	3.78E-01
W09-S03	1.01E+09	1.41E+06	6.30E+06	4.26E-01	3.74E-01	3.93E-01
W09-S04	3.34E+09	1.24E+06	4.04E+07	4.24E-01	4.11E-01	3.90E-01
W09-S05	1.32E+10	1.21E+06	1.15E+08	3.96E-01	4.22E-01	3.62E-01
W10-S06	6.93E+09	1.08E+06	6.95E+07	3.76E-01	4.07E-01	3.45E-01
W10-S07	1.17E+09	1.13E+06	6.99E+06	3.90E-01	3.75E-01	3.60E-01

Sample	Crofton Perimeter _Max	Crofton Perimeter _Median	Crofton Perimeter _Std	Elongation _Avg	Elongation _Avg_w	Elongation _Median
	nm	nm	nm	adim	adim	adim
W11-S03	1.05E+09	1.31E+06	7.79E+06	4.14E-01	3.91E-01	3.86E-01
W11-S04	7.95E+09	1.09E+06	4.43E+07	3.79E-01	3.65E-01	3.47E-01
W14-S01	5.38E+09	1.21E+06	3.84E+07	3.80E-01	3.93E-01	3.48E-01
W14-S02	1.83E+10	9.83E+05	5.82E+07	3.96E-01	4.12E-01	3.67E-01
W14-S04	7.91E+09	1.09E+06	9.11E+07	3.89E-01	4.47E-01	3.58E-01
W14-S05	5.52E+09	1.17E+06	8.56E+07	3.77E-01	4.30E-01	3.43E-01
W14-S06	6.05E+09	1.22E+06	3.23E+07	3.85E-01	3.88E-01	3.53E-01
W14-S07	1.50E+10	9.83E+05	3.54E+07	3.90E-01	3.90E-01	3.60E-01
W14-S09	1.23E+09	1.35E+06	5.80E+06	3.82E-01	3.65E-01	3.50E-01
W14-S10	6.98E+09	1.02E+06	6.13E+07	3.77E-01	4.34E-01	3.45E-01
W14-S12	3.95E+09	1.12E+06	3.18E+07	3.86E-01	3.92E-01	3.54E-01
W15-S02	5.29E+09	1.01E+06	5.18E+07	3.84E-01	3.98E-01	3.53E-01
W15-S03	5.76E+08	1.05E+06	5.71E+06	3.95E-01	3.74E-01	3.65E-01
W15-S05	1.43E+09	9.83E+05	1.20E+07	3.94E-01	3.78E-01	3.63E-01
W15-S06	7.14E+09	1.08E+06	5.06E+07	3.87E-01	4.21E-01	3.57E-01
W15-S07	4.94E+09	1.02E+06	7.06E+07	3.87E-01	4.42E-01	3.55E-01
W15-S08	8.78E+09	1.05E+06	8.17E+07	3.93E-01	4.47E-01	3.62E-01
W15-S09	3.91E+09	1.01E+06	4.23E+07	3.87E-01	4.08E-01	3.55E-01
W15-S12	9.87E+09	1.25E+06	7.49E+07	3.83E-01	4.22E-01	3.51E-01
W15-S14	2.13E+09	1.02E+06	5.45E+06	4.10E-01	3.93E-01	3.79E-01
W16-S01	1.50E+09	9.83E+05	3.40E+06	3.94E-01	3.88E-01	3.64E-01
W16-S03	2.98E+09	1.13E+06	1.94E+07	3.96E-01	3.96E-01	3.65E-01
W16-S05	7.89E+09	1.01E+06	7.49E+07	3.82E-01	4.22E-01	3.50E-01
W16-S06	6.75E+09	9.27E+05	6.50E+07	3.86E-01	4.49E-01	3.55E-01
W17-S01	1.54E+10	9.83E+05	1.27E+08	4.10E-01	4.39E-01	3.75E-01
W17-S03	1.11E+10	1.11E+06	5.64E+07	4.20E-01	4.21E-01	3.87E-01
W17-S04	3.92E+09	1.14E+06	7.16E+07	4.14E-01	4.13E-01	3.80E-01
W17-S05	1.20E+10	1.14E+06	1.04E+08	3.91E-01	4.20E-01	3.62E-01
W18-S01	4.80E+09	1.24E+06	5.30E+07	3.90E-01	4.14E-01	3.60E-01
W18-S02	5.05E+09	1.16E+06	3.83E+07	3.74E-01	3.83E-01	3.41E-01
W18-S03	8.95E+09	1.17E+06	8.43E+07	3.71E-01	4.23E-01	3.39E-01
W18-S04	1.28E+10	1.03E+06	6.93E+07	3.85E-01	3.76E-01	3.54E-01
W18-S05	1.09E+09	9.16E+05	4.29E+06	3.98E-01	3.75E-01	3.68E-01
W18-S06	5.72E+09	1.14E+06	6.10E+07	3.70E-01	4.16E-01	3.38E-01
W19-S01	2.95E+10	1.88E+06	1.66E+08	4.00E-01	3.88E-01	3.68E-01
W19-S02	3.23E+10	1.14E+06	1.65E+08	3.94E-01	4.87E-01	3.63E-01
W19-S03	1.68E+09	8.60E+05	3.38E+06	3.99E-01	3.60E-01	3.69E-01
W19-S04	4.67E+09	9.55E+05	6.40E+06	3.90E-01	3.75E-01	3.59E-01
W19-S05	4.87E+10	1.08E+06	1.02E+08	3.87E-01	4.15E-01	3.56E-01
W19-S06	2.66E+08	1.05E+06	2.32E+06	3.80E-01	3.66E-01	3.48E-01
W20-S01	4.43E+09	9.27E+05	6.21E+06	4.05E-01	3.87E-01	3.75E-01

Sample	Crofton Perimeter _Max	Crofton Perimeter _Median	Crofton Perimeter _Std	Elongation _Avg	Elongation _Avg_w	Elongation _Median
	nm	nm	nm	adim	adim	adim
W20-S02	1.05E+11	9.55E+05	1.39E+08	4.03E-01	4.63E-01	3.74E-01
W20-S03	3.79E+09	1.05E+06	1.62E+07	3.95E-01	3.69E-01	3.66E-01
W20-S04	1.76E+08	9.16E+05	1.55E+06	4.11E-01	3.87E-01	3.81E-01
W20-S05	7.26E+09	1.09E+06	5.29E+07	3.93E-01	4.18E-01	3.64E-01
W20-S06	3.41E+07	8.32E+05	7.66E+05	4.27E-01	4.12E-01	3.92E-01
W21-S01	6.93E+09	1.01E+06	6.93E+07	3.95E-01	4.40E-01	3.65E-01
W21-S02	6.35E+09	1.04E+06	3.00E+07	4.02E-01	4.03E-01	3.72E-01
W21-S03	6.49E+09	1.05E+06	7.60E+07	3.84E-01	4.17E-01	3.52E-01
W21-S04	1.34E+10	1.09E+06	9.72E+07	3.91E-01	4.47E-01	3.61E-01
W21-S05	8.67E+09	1.06E+06	8.84E+07	3.85E-01	4.31E-01	3.54E-01
W21-S06	6.61E+09	1.14E+06	9.16E+07	3.63E-01	4.25E-01	3.31E-01
W21-S07	7.62E+09	1.18E+06	4.06E+07	3.92E-01	4.10E-01	3.62E-01
W21-S08	1.23E+10	1.02E+06	9.55E+07	4.02E-01	4.57E-01	3.73E-01
W22-S01	6.59E+09	8.48E+05	6.28E+07	3.94E-01	4.31E-01	3.65E-01
W22-S02	1.19E+10	1.18E+06	8.95E+07	3.95E-01	4.72E-01	3.66E-01
W22-S04	2.82E+09	1.49E+06	5.84E+07	3.61E-01	3.79E-01	3.30E-01
W22-S05	2.63E+10	1.01E+06	2.03E+08	4.04E-01	5.26E-01	3.74E-01
W24-S01	1.78E+10	1.24E+06	3.05E+07	4.05E-01	4.05E-01	3.77E-01
W24-S02	1.27E+10	1.17E+06	4.68E+07	3.96E-01	4.18E-01	3.66E-01
W24-S03	7.13E+09	1.08E+06	5.37E+07	4.03E-01	4.44E-01	3.72E-01
W24-S04	7.20E+09	9.43E+05	4.75E+07	3.92E-01	4.39E-01	3.62E-01
W24-S05	8.31E+09	1.01E+06	6.40E+07	3.91E-01	4.36E-01	3.61E-01
W25-S01	4.98E+09	9.55E+05	1.93E+07	3.69E-01	3.55E-01	3.37E-01
W25-S02	7.57E+09	1.36E+06	6.07E+07	3.91E-01	3.92E-01	3.63E-01
W25-S03	4.38E+09	1.22E+06	3.66E+07	3.94E-01	3.84E-01	3.64E-01
W25-S04	1.12E+10	1.14E+06	8.48E+07	3.77E-01	4.36E-01	3.44E-01
W26-S02	5.70E+09	1.12E+06	3.50E+07	3.87E-01	3.83E-01	3.56E-01
W27-S01	5.12E+09	1.10E+06	4.68E+07	3.87E-01	4.39E-01	3.56E-01
W27-S03	9.08E+07	1.08E+06	1.17E+06	4.33E-01	4.32E-01	4.07E-01
W27-S04	1.43E+09	1.14E+06	9.86E+06	3.93E-01	3.54E-01	3.64E-01
W27-S05	5.65E+08	8.88E+05	1.20E+06	4.07E-01	3.87E-01	3.76E-01
W27-S06	1.52E+08	9.66E+05	1.25E+06	3.91E-01	3.68E-01	3.60E-01
W28-S02	6.57E+08	1.33E+06	1.19E+07	4.02E-01	4.21E-01	3.74E-01
W28-S04	6.28E+09	1.05E+06	6.18E+07	4.14E-01	4.02E-01	3.75E-01
W28-S05	1.69E+09	9.55E+05	4.62E+06	3.99E-01	4.05E-01	3.69E-01
W29-S01	3.25E+09	1.05E+06	1.32E+07	3.97E-01	3.75E-01	3.67E-01
W29-S02	8.95E+09	9.16E+05	1.81E+07	3.93E-01	4.09E-01	3.64E-01
W30-S01	3.68E+08	7.26E+05	1.07E+06	3.96E-01	3.86E-01	3.66E-01
W30-S03	1.52E+10	9.16E+05	8.29E+07	3.65E-01	4.06E-01	3.34E-01
W30-S04	6.15E+09	1.59E+06	4.92E+07	3.85E-01	3.92E-01	3.55E-01
W30-S05	6.03E+09	1.17E+06	3.33E+07	3.77E-01	3.92E-01	3.45E-01

Sample	Crofton Perimeter _Max	Crofton Perimeter _Median	Crofton Perimeter _Std	Elongation _Avg	Elongation _Avg_w	Elongation _Median
	nm	nm	nm	adim	adim	adim
W30-S07	9.13E+09	1.22E+06	3.87E+07	3.68E-01	3.95E-01	3.36E-01
W30-S08	1.31E+10	1.02E+06	4.33E+07	3.90E-01	4.19E-01	3.60E-01
W31-S01	4.02E+09	9.83E+05	4.69E+07	3.91E-01	4.02E-01	3.60E-01
W31-S03	1.23E+10	1.41E+06	9.04E+07	3.68E-01	4.30E-01	3.37E-01

Sample	Elongation _Std	EqDiameter Log_Std	Eq Diameter _Avg	Eq Diameter _Avg_w	Eq Diameter _Log_Avg	EqDiameter _Log_Avg_w
	adim	nm	nm	nm	nm	nm
W02-S01	1.98E-01	4.00E-01	8.78E+04	1.40E+06	1.13E+01	1.39E+01
W02-S03	1.96E-01	4.71E-01	1.04E+05	4.06E+05	1.14E+01	1.27E+01
W02-S04	2.00E-01	3.35E-01	8.80E+04	1.59E+05	1.13E+01	1.19E+01
W02-S05	2.01E-01	2.83E-01	8.00E+04	1.41E+05	1.12E+01	1.17E+01
W03-S01	2.11E-01	6.75E-01	1.57E+05	1.98E+06	1.16E+01	1.44E+01
W03-S02	2.15E-01	5.56E-01	1.39E+05	4.52E+05	1.17E+01	1.28E+01
W03-S03	2.17E-01	5.32E-01	1.28E+05	5.50E+05	1.16E+01	1.30E+01
W03-S06	2.01E-01	3.94E-01	9.26E+04	2.89E+05	1.13E+01	1.23E+01
W03-S09	2.13E-01	5.01E-01	1.14E+05	1.23E+06	1.15E+01	1.36E+01
W03-S10	2.14E-01	5.42E-01	1.37E+05	4.86E+05	1.17E+01	1.29E+01
W06-S02	2.17E-01	5.46E-01	1.38E+05	1.62E+06	1.17E+01	1.38E+01
W06-S03	2.17E-01	5.44E-01	1.41E+05	1.01E+06	1.17E+01	1.34E+01
W07-S01	2.22E-01	5.91E-01	1.42E+05	3.68E+06	1.16E+01	1.49E+01
W07-S02	2.21E-01	6.95E-01	1.67E+05	2.43E+06	1.16E+01	1.46E+01
W07-S04	2.18E-01	7.93E-01	1.90E+05	2.19E+06	1.17E+01	1.45E+01
W08-S01	2.21E-01	5.67E-01	1.49E+05	3.34E+05	1.17E+01	1.26E+01
W08-S03	2.03E-01	4.80E-01	1.23E+05	2.70E+06	1.15E+01	1.47E+01
W08-S04	2.18E-01	6.07E-01	1.51E+05	4.17E+05	1.17E+01	1.28E+01
W09-S01	2.13E-01	6.28E-01	1.63E+05	8.33E+05	1.18E+01	1.34E+01
W09-S02	2.14E-01	6.89E-01	1.72E+05	1.68E+06	1.17E+01	1.42E+01
W09-S03	2.13E-01	5.75E-01	1.50E+05	4.77E+05	1.17E+01	1.29E+01
W09-S04	2.11E-01	5.77E-01	1.40E+05	1.35E+06	1.16E+01	1.39E+01
W09-S05	2.09E-01	6.09E-01	1.42E+05	2.29E+06	1.16E+01	1.45E+01
W10-S06	2.01E-01	4.60E-01	1.01E+05	2.12E+06	1.14E+01	1.44E+01
W10-S07	1.96E-01	4.10E-01	8.98E+04	5.61E+05	1.13E+01	1.29E+01
W11-S03	2.00E-01	5.15E-01	1.14E+05	6.10E+05	1.15E+01	1.30E+01
W11-S04	1.98E-01	4.52E-01	9.87E+04	1.41E+06	1.14E+01	1.38E+01
W14-S01	1.98E-01	5.01E-01	1.08E+05	1.39E+06	1.14E+01	1.39E+01
W14-S02	1.99E-01	3.99E-01	9.06E+04	2.02E+06	1.13E+01	1.42E+01
W14-S04	1.98E-01	4.65E-01	1.00E+05	2.22E+06	1.13E+01	1.45E+01
W14-S05	1.99E-01	4.99E-01	1.09E+05	2.09E+06	1.14E+01	1.44E+01
W14-S06	2.01E-01	5.08E-01	1.10E+05	1.38E+06	1.14E+01	1.38E+01
W14-S07	2.00E-01	4.33E-01	9.82E+04	1.33E+06	1.14E+01	1.37E+01

Sample	Elongation _Std	EqDiameter Log_Std	Eq Diameter _Avg	Eq Diameter _Avg_w	Eq Diameter _Log_Avg	EqD iameter _Log_Avg_w
	adim	nm	nm	nm	nm	nm
W14-S09	2.00E-01	5.06E-01	1.09E+05	4.64E+05	1.14E+01	1.28E+01
W14-S10	1.98E-01	4.28E-01	9.57E+04	2.21E+06	1.13E+01	1.44E+01
W14-S12	1.99E-01	4.67E-01	1.02E+05	1.45E+06	1.14E+01	1.39E+01
W15-S02	1.98E-01	4.28E-01	9.53E+04	2.17E+06	1.13E+01	1.44E+01
W15-S03	1.99E-01	4.36E-01	9.64E+04	5.49E+05	1.14E+01	1.29E+01
W15-S05	2.00E-01	4.26E-01	9.68E+04	7.86E+05	1.14E+01	1.32E+01
W15-S06	1.99E-01	4.63E-01	9.89E+04	1.65E+06	1.13E+01	1.42E+01
W15-S07	1.99E-01	4.57E-01	9.94E+04	2.12E+06	1.13E+01	1.45E+01
W15-S08	1.99E-01	4.47E-01	9.83E+04	2.15E+06	1.13E+01	1.44E+01
W15-S09	2.00E-01	4.38E-01	9.73E+04	1.76E+06	1.13E+01	1.42E+01
W15-S12	1.98E-01	5.11E-01	1.07E+05	1.82E+06	1.14E+01	1.42E+01
W15-S14	2.04E-01	4.33E-01	1.00E+05	3.83E+05	1.14E+01	1.26E+01
W16-S01	1.99E-01	3.97E-01	9.29E+04	3.36E+05	1.13E+01	1.24E+01
W16-S03	2.01E-01	4.40E-01	9.51E+04	1.02E+06	1.13E+01	1.35E+01
W16-S05	1.97E-01	4.02E-01	9.01E+04	2.41E+06	1.13E+01	1.45E+01
W16-S06	2.00E-01	3.92E-01	9.05E+04	2.28E+06	1.13E+01	1.45E+01
W17-S01	2.07E-01	4.94E-01	1.17E+05	2.73E+06	1.15E+01	1.46E+01
W17-S03	2.08E-01	5.36E-01	1.28E+05	1.75E+06	1.16E+01	1.41E+01
W17-S04	2.08E-01	5.58E-01	1.35E+05	1.95E+06	1.16E+01	1.43E+01
W17-S05	1.99E-01	4.72E-01	1.01E+05	2.23E+06	1.14E+01	1.44E+01
W18-S01	2.01E-01	5.33E-01	1.17E+05	1.57E+06	1.15E+01	1.40E+01
W18-S02	1.98E-01	4.48E-01	9.80E+04	1.45E+06	1.14E+01	1.38E+01
W18-S03	1.98E-01	5.06E-01	1.09E+05	2.14E+06	1.14E+01	1.44E+01
W18-S04	2.00E-01	4.44E-01	9.83E+04	1.99E+06	1.14E+01	1.43E+01
W18-S05	2.01E-01	3.76E-01	9.04E+04	3.77E+05	1.13E+01	1.25E+01
W18-S06	1.97E-01	4.84E-01	1.03E+05	1.89E+06	1.13E+01	1.43E+01
W19-S01	2.12E-01	6.56E-01	1.75E+05	2.07E+06	1.18E+01	1.41E+01
W19-S02	1.99E-01	4.47E-01	9.66E+04	3.01E+06	1.13E+01	1.47E+01
W19-S03	2.03E-01	3.45E-01	8.57E+04	3.39E+05	1.13E+01	1.23E+01
W19-S04	2.00E-01	4.01E-01	9.30E+04	4.26E+05	1.13E+01	1.26E+01
W19-S05	1.99E-01	4.43E-01	9.68E+04	2.21E+06	1.13E+01	1.41E+01
W19-S06	1.96E-01	4.14E-01	9.50E+04	2.58E+05	1.14E+01	1.23E+01
W20-S01	2.02E-01	3.90E-01	9.39E+04	4.17E+05	1.14E+01	1.24E+01
W20-S02	2.00E-01	3.93E-01	9.00E+04	2.57E+06	1.13E+01	1.45E+01
W20-S03	2.00E-01	4.48E-01	1.01E+05	8.49E+05	1.14E+01	1.33E+01
W20-S04	2.03E-01	3.82E-01	9.20E+04	2.39E+05	1.13E+01	1.22E+01
W20-S05	2.00E-01	4.75E-01	1.03E+05	1.65E+06	1.14E+01	1.41E+01
W20-S06	2.04E-01	3.29E-01	8.51E+04	1.71E+05	1.13E+01	1.19E+01
W21-S01	2.01E-01	4.34E-01	9.66E+04	2.26E+06	1.13E+01	1.45E+01
W21-S02	2.00E-01	4.44E-01	9.84E+04	1.23E+06	1.14E+01	1.37E+01
W21-S03	1.99E-01	4.62E-01	1.02E+05	2.28E+06	1.14E+01	1.45E+01

Sample	Elongation _Std	EqDiameter Log_Std	Eq Diameter _Avg	Eq Diameter _Avg_w	Eq Diameter _Log_Avg	EqD iameter _Log_Avg_w
	adim	nm	nm	nm	nm	nm
W21-S04	2.01E-01	4.72E-01	1.04E+05	2.35E+06	1.14E+01	1.45E+01
W21-S05	1.99E-01	4.51E-01	9.95E+04	2.39E+06	1.14E+01	1.45E+01
W21-S06	2.01E-01	5.12E-01	1.11E+05	2.36E+06	1.14E+01	1.46E+01
W21-S07	2.01E-01	4.88E-01	1.05E+05	1.39E+06	1.14E+01	1.38E+01
W21-S08	2.02E-01	4.45E-01	9.94E+04	2.31E+06	1.14E+01	1.45E+01
W22-S01	1.99E-01	3.35E-01	8.19E+04	2.13E+06	1.12E+01	1.45E+01
W22-S02	2.00E-01	4.68E-01	1.01E+05	2.16E+06	1.14E+01	1.43E+01
W22-S04	2.01E-01	5.98E-01	1.28E+05	1.52E+06	1.15E+01	1.41E+01
W22-S05	2.00E-01	3.96E-01	9.00E+04	3.19E+06	1.13E+01	1.49E+01
W24-S01	2.03E-01	5.14E-01	1.15E+05	1.05E+06	1.15E+01	1.34E+01
W24-S02	2.01E-01	4.89E-01	1.08E+05	1.54E+06	1.14E+01	1.38E+01
W24-S03	2.01E-01	4.50E-01	9.99E+04	1.73E+06	1.14E+01	1.40E+01
W24-S04	2.01E-01	4.04E-01	9.22E+04	1.90E+06	1.13E+01	1.42E+01
W24-S05	2.01E-01	4.50E-01	1.00E+05	2.15E+06	1.14E+01	1.44E+01
W25-S01	1.98E-01	3.42E-01	8.35E+04	1.02E+06	1.13E+01	1.32E+01
W25-S02	1.98E-01	5.27E-01	1.13E+05	1.73E+06	1.15E+01	1.40E+01
W25-S03	1.97E-01	4.85E-01	1.03E+05	1.38E+06	1.14E+01	1.38E+01
W25-S04	1.98E-01	4.48E-01	9.65E+04	2.29E+06	1.13E+01	1.44E+01
W26-S02	1.99E-01	4.69E-01	1.02E+05	1.35E+06	1.14E+01	1.38E+01
W27-S01	1.96E-01	4.26E-01	9.21E+04	1.92E+06	1.13E+01	1.43E+01
W27-S03	2.00E-01	4.11E-01	9.58E+04	2.13E+05	1.14E+01	1.21E+01
W27-S04	2.00E-01	4.36E-01	9.59E+04	8.44E+05	1.13E+01	1.32E+01
W27-S05	2.01E-01	3.51E-01	8.67E+04	2.02E+05	1.13E+01	1.20E+01
W27-S06	2.00E-01	3.91E-01	9.36E+04	2.12E+05	1.14E+01	1.21E+01
W28-S02	1.96E-01	5.09E-01	1.03E+05	8.72E+05	1.13E+01	1.35E+01
W28-S04	2.09E-01	5.28E-01	1.32E+05	1.90E+06	1.16E+01	1.42E+01
W28-S05	1.96E-01	3.30E-01	8.12E+04	4.19E+05	1.12E+01	1.25E+01
W29-S01	1.98E-01	4.13E-01	9.17E+04	1.08E+06	1.13E+01	1.35E+01
W29-S02	1.97E-01	3.22E-01	7.98E+04	1.20E+06	1.12E+01	1.35E+01
W30-S01	2.01E-01	2.77E-01	7.90E+04	1.72E+05	1.12E+01	1.18E+01
W30-S03	1.98E-01	3.48E-01	8.53E+04	2.62E+06	1.13E+01	1.45E+01
W30-S04	2.00E-01	6.20E-01	1.40E+05	1.42E+06	1.16E+01	1.39E+01
W30-S05	1.98E-01	4.73E-01	1.01E+05	1.26E+06	1.14E+01	1.38E+01
W30-S07	1.97E-01	4.67E-01	9.96E+04	1.29E+06	1.14E+01	1.37E+01
W30-S08	1.99E-01	4.22E-01	9.53E+04	1.56E+06	1.13E+01	1.37E+01
W31-S01	2.00E-01	4.30E-01	9.54E+04	1.77E+06	1.13E+01	1.42E+01
W31-S03	2.00E-01	5.87E-01	1.25E+05	2.37E+06	1.15E+01	1.45E+01

Sample	Eq Diameter _Log_Max	EqDiameter _Log_Median	Eq Diameter _Max	Eq Diameter _Median	Eq Diameter _Std	Flatness _Avg
	nm	nm	nm	nm	nm	adim
W02-S01	1.49E+01	1.19E+01	2.84E+06	1.42E+05	8.00E+04	4.49E-01
W02-S03	1.39E+01	1.19E+01	1.11E+06	1.50E+05	7.25E+04	4.25E-01
W02-S04	1.35E+01	1.18E+01	7.06E+05	1.29E+05	3.64E+04	4.42E-01
W02-S05	1.36E+01	1.17E+01	7.77E+05	1.24E+05	2.89E+04	4.40E-01
W03-S01	1.51E+01	1.20E+01	3.58E+06	1.68E+05	2.33E+05	4.22E-01
W03-S02	1.42E+01	1.20E+01	1.52E+06	1.66E+05	9.66E+04	4.12E-01
W03-S03	1.45E+01	1.20E+01	1.90E+06	1.56E+05	9.30E+04	4.04E-01
W03-S06	1.43E+01	1.18E+01	1.66E+06	1.38E+05	5.18E+04	4.65E-01
W03-S09	1.52E+01	1.19E+01	3.95E+06	1.50E+05	9.04E+04	4.28E-01
W03-S10	1.44E+01	1.20E+01	1.80E+06	1.63E+05	9.53E+04	4.40E-01
W06-S02	1.55E+01	1.20E+01	5.23E+06	1.63E+05	1.08E+05	3.80E-01
W06-S03	1.55E+01	1.20E+01	5.25E+06	1.63E+05	1.03E+05	3.97E-01
W07-S01	1.58E+01	1.20E+01	7.03E+06	1.63E+05	1.92E+05	3.26E-01
W07-S02	1.53E+01	1.21E+01	4.58E+06	1.71E+05	2.79E+05	4.06E-01
W07-S04	1.54E+01	1.22E+01	4.67E+06	2.01E+05	3.17E+05	3.72E-01
W08-S01	1.44E+01	1.21E+01	1.87E+06	1.81E+05	9.11E+04	3.39E-01
W08-S03	1.54E+01	1.20E+01	4.80E+06	1.69E+05	1.61E+05	4.63E-01
W08-S04	1.40E+01	1.21E+01	1.19E+06	1.86E+05	1.06E+05	3.60E-01
W09-S01	1.51E+01	1.21E+01	3.61E+06	1.81E+05	1.35E+05	4.20E-01
W09-S02	1.50E+01	1.21E+01	3.29E+06	1.79E+05	2.21E+05	4.08E-01
W09-S03	1.48E+01	1.21E+01	2.65E+06	1.74E+05	1.03E+05	4.11E-01
W09-S04	1.49E+01	1.20E+01	3.06E+06	1.63E+05	1.34E+05	4.30E-01
W09-S05	1.55E+01	1.20E+01	5.34E+06	1.60E+05	2.09E+05	3.98E-01
W10-S06	1.52E+01	1.19E+01	4.14E+06	1.42E+05	1.17E+05	3.81E-01
W10-S07	1.45E+01	1.19E+01	1.95E+06	1.46E+05	6.56E+04	4.42E-01
W11-S03	1.47E+01	1.20E+01	2.41E+06	1.56E+05	8.64E+04	4.84E-01
W11-S04	1.51E+01	1.19E+01	3.59E+06	1.42E+05	8.55E+04	4.20E-01
W14-S01	1.51E+01	1.19E+01	3.75E+06	1.50E+05	1.07E+05	4.22E-01
W14-S02	1.54E+01	1.18E+01	4.92E+06	1.38E+05	7.81E+04	4.43E-01
W14-S04	1.53E+01	1.19E+01	4.29E+06	1.42E+05	1.36E+05	4.25E-01
W14-S05	1.51E+01	1.19E+01	3.71E+06	1.46E+05	1.30E+05	4.19E-01
W14-S06	1.53E+01	1.19E+01	4.52E+06	1.50E+05	1.02E+05	4.32E-01
W14-S07	1.53E+01	1.18E+01	4.46E+06	1.38E+05	8.09E+04	4.37E-01
W14-S09	1.46E+01	1.20E+01	2.15E+06	1.56E+05	8.21E+04	4.36E-01
W14-S10	1.53E+01	1.18E+01	4.29E+06	1.38E+05	1.01E+05	4.03E-01
W14-S12	1.51E+01	1.19E+01	3.66E+06	1.46E+05	9.63E+04	4.22E-01
W15-S02	1.52E+01	1.18E+01	4.15E+06	1.38E+05	9.82E+04	4.06E-01
W15-S03	1.45E+01	1.19E+01	1.92E+06	1.42E+05	7.01E+04	4.34E-01
W15-S05	1.47E+01	1.18E+01	2.31E+06	1.38E+05	7.06E+04	4.44E-01
W15-S06	1.51E+01	1.19E+01	3.78E+06	1.42E+05	1.20E+05	4.27E-01
W15-S07	1.52E+01	1.19E+01	4.02E+06	1.42E+05	1.44E+05	4.12E-01

Sample	Eq Diameter _Log_Max	EqDiameter _Log_Median	Eq Diameter _Max	Eq Diameter _Median	Eq Diameter _Std	Flatness _Avg
	nm	nm	nm	nm	nm	adim
W15-S08	1.53E+01	1.19E+01	4.61E+06	1.42E+05	1.22E+05	4.31E-01
W15-S09	1.51E+01	1.18E+01	3.51E+06	1.38E+05	1.05E+05	4.30E-01
W15-S12	1.52E+01	1.19E+01	4.04E+06	1.53E+05	1.31E+05	4.21E-01
W15-S14	1.47E+01	1.19E+01	2.33E+06	1.42E+05	6.20E+04	4.66E-01
W16-S01	1.47E+01	1.18E+01	2.42E+06	1.38E+05	5.23E+04	4.49E-01
W16-S03	1.49E+01	1.19E+01	2.87E+06	1.46E+05	7.99E+04	4.28E-01
W16-S05	1.53E+01	1.18E+01	4.27E+06	1.38E+05	1.11E+05	4.00E-01
W16-S06	1.53E+01	1.18E+01	4.20E+06	1.34E+05	1.04E+05	3.97E-01
W17-S01	1.55E+01	1.19E+01	5.25E+06	1.46E+05	1.37E+05	4.15E-01
W17-S03	1.53E+01	1.19E+01	4.27E+06	1.53E+05	1.30E+05	4.38E-01
W17-S04	1.51E+01	1.20E+01	3.55E+06	1.56E+05	1.54E+05	4.40E-01
W17-S05	1.52E+01	1.19E+01	4.10E+06	1.50E+05	1.09E+05	4.44E-01
W18-S01	1.50E+01	1.19E+01	3.21E+06	1.53E+05	1.23E+05	4.39E-01
W18-S02	1.50E+01	1.19E+01	3.29E+06	1.46E+05	8.52E+04	3.86E-01
W18-S03	1.53E+01	1.19E+01	4.26E+06	1.50E+05	1.45E+05	4.17E-01
W18-S04	1.53E+01	1.19E+01	4.25E+06	1.42E+05	9.95E+04	4.30E-01
W18-S05	1.44E+01	1.18E+01	1.83E+06	1.34E+05	5.01E+04	4.41E-01
W18-S06	1.51E+01	1.19E+01	3.79E+06	1.46E+05	1.38E+05	4.10E-01
W19-S01	1.56E+01	1.22E+01	5.86E+06	1.95E+05	1.54E+05	4.29E-01
W19-S02	1.55E+01	1.19E+01	5.64E+06	1.50E+05	9.60E+04	4.55E-01
W19-S03	1.48E+01	1.18E+01	2.65E+06	1.29E+05	4.25E+04	4.47E-01
W19-S04	1.49E+01	1.18E+01	2.97E+06	1.38E+05	5.71E+04	4.46E-01
W19-S05	1.57E+01	1.19E+01	6.40E+06	1.46E+05	7.89E+04	4.48E-01
W19-S06	1.38E+01	1.19E+01	1.01E+06	1.42E+05	5.43E+04	4.47E-01
W20-S01	1.51E+01	1.18E+01	3.63E+06	1.34E+05	5.00E+04	4.67E-01
W20-S02	1.60E+01	1.18E+01	8.85E+06	1.38E+05	9.68E+04	4.54E-01
W20-S03	1.49E+01	1.19E+01	2.89E+06	1.42E+05	7.66E+04	4.42E-01
W20-S04	1.39E+01	1.18E+01	1.06E+06	1.34E+05	4.78E+04	4.65E-01
W20-S05	1.51E+01	1.19E+01	3.77E+06	1.42E+05	1.16E+05	4.41E-01
W20-S06	1.34E+01	1.18E+01	6.42E+05	1.29E+05	3.67E+04	4.71E-01
W21-S01	1.53E+01	1.18E+01	4.50E+06	1.38E+05	1.20E+05	4.41E-01
W21-S02	1.50E+01	1.19E+01	3.38E+06	1.42E+05	8.20E+04	4.48E-01
W21-S03	1.52E+01	1.19E+01	4.19E+06	1.42E+05	1.27E+05	4.23E-01
W21-S04	1.54E+01	1.19E+01	4.81E+06	1.46E+05	1.20E+05	4.41E-01
W21-S05	1.53E+01	1.19E+01	4.60E+06	1.42E+05	1.16E+05	4.18E-01
W21-S06	1.53E+01	1.19E+01	4.36E+06	1.50E+05	1.61E+05	4.17E-01
W21-S07	1.52E+01	1.19E+01	3.80E+06	1.50E+05	9.44E+04	4.33E-01
W21-S08	1.54E+01	1.19E+01	4.79E+06	1.42E+05	1.19E+05	4.54E-01
W22-S01	1.53E+01	1.18E+01	4.22E+06	1.29E+05	1.24E+05	4.21E-01
W22-S02	1.53E+01	1.19E+01	4.34E+06	1.50E+05	9.97E+04	4.60E-01
W22-S04	1.48E+01	1.20E+01	2.78E+06	1.63E+05	1.60E+05	4.08E-01

Sample	Eq Diameter _Log_Max	EqDiameter _Log_Median	Eq Diameter _Max	Eq Diameter _Median	Eq Diameter _Std	Flatness _Avg
	nm	nm	nm	nm	nm	adim
W22-S05	1.55E+01	1.19E+01	5.49E+06	1.42E+05	1.12E+05	4.52E-01
W24-S01	1.55E+01	1.19E+01	5.58E+06	1.53E+05	9.17E+04	4.61E-01
W24-S02	1.53E+01	1.19E+01	4.55E+06	1.50E+05	9.19E+04	4.54E-01
W24-S03	1.51E+01	1.19E+01	3.54E+06	1.42E+05	8.61E+04	4.59E-01
W24-S04	1.51E+01	1.18E+01	3.77E+06	1.38E+05	8.74E+04	4.39E-01
W24-S05	1.52E+01	1.19E+01	4.11E+06	1.42E+05	1.23E+05	4.42E-01
W25-S01	1.49E+01	1.18E+01	3.04E+06	1.34E+05	4.97E+04	3.58E-01
W25-S02	1.51E+01	1.20E+01	3.78E+06	1.56E+05	1.10E+05	4.31E-01
W25-S03	1.50E+01	1.19E+01	3.21E+06	1.50E+05	9.76E+04	4.31E-01
W25-S04	1.53E+01	1.19E+01	4.49E+06	1.46E+05	1.05E+05	4.28E-01
W26-S02	1.51E+01	1.19E+01	3.45E+06	1.46E+05	9.41E+04	4.35E-01
W27-S01	1.52E+01	1.19E+01	3.81E+06	1.42E+05	1.14E+05	4.27E-01
W27-S03	1.37E+01	1.19E+01	9.26E+05	1.42E+05	5.06E+04	4.63E-01
W27-S04	1.49E+01	1.19E+01	2.81E+06	1.46E+05	6.92E+04	4.08E-01
W27-S05	1.45E+01	1.18E+01	1.89E+06	1.34E+05	4.07E+04	4.61E-01
W27-S06	1.37E+01	1.18E+01	9.22E+05	1.38E+05	4.76E+04	4.48E-01
W28-S02	1.46E+01	1.19E+01	2.12E+06	1.53E+05	1.11E+05	4.32E-01
W28-S04	1.53E+01	1.19E+01	4.33E+06	1.50E+05	1.42E+05	3.94E-01
W28-S05	1.47E+01	1.18E+01	2.36E+06	1.34E+05	4.35E+04	4.30E-01
W29-S01	1.50E+01	1.19E+01	3.27E+06	1.42E+05	7.14E+04	4.47E-01
W29-S02	1.52E+01	1.18E+01	3.84E+06	1.34E+05	5.25E+04	4.29E-01
W30-S01	1.40E+01	1.17E+01	1.22E+06	1.24E+05	2.94E+04	4.35E-01
W30-S03	1.55E+01	1.18E+01	5.42E+06	1.29E+05	7.59E+04	3.56E-01
W30-S04	1.52E+01	1.20E+01	3.85E+06	1.68E+05	1.49E+05	4.43E-01
W30-S05	1.50E+01	1.19E+01	3.30E+06	1.46E+05	9.58E+04	4.27E-01
W30-S07	1.51E+01	1.19E+01	3.65E+06	1.50E+05	8.81E+04	3.94E-01
W30-S08	1.53E+01	1.19E+01	4.32E+06	1.42E+05	7.12E+04	4.41E-01
W31-S01	1.50E+01	1.18E+01	3.33E+06	1.38E+05	1.02E+05	4.33E-01
W31-S03	1.56E+01	1.20E+01	5.95E+06	1.60E+05	1.88E+05	4.00E-01

Sample	Flatness _Avg_w	Flatness _Median	Flatness _Std	Orientation 2Phi_Avg	Orientation 2Phi_Avg_w	Orientation 2Phi_Median
	adim	adim	adim	graus	graus	graus
W02-S01	5.29E-01	4.47E-01	2.04E-01	5.60E+01	5.75E+01	5.64E+01
W02-S03	4.53E-01	4.19E-01	2.04E-01	5.50E+01	5.69E+01	5.66E+01
W02-S04	4.57E-01	4.46E-01	2.08E-01	5.01E+01	5.03E+01	4.96E+01
W02-S05	4.55E-01	4.47E-01	2.10E-01	5.25E+01	5.39E+01	5.38E+01
W03-S01	4.91E-01	4.23E-01	2.27E-01	3.89E+01	5.58E+01	3.60E+01
W03-S02	4.81E-01	4.18E-01	2.40E-01	3.20E+01	4.70E+01	2.75E+01
W03-S03	4.53E-01	4.11E-01	2.44E-01	3.24E+01	5.43E+01	2.78E+01
W03-S06	4.85E-01	4.61E-01	2.05E-01	5.32E+01	5.40E+01	5.46E+01
W03-S09	3.78E-01	4.36E-01	2.37E-01	3.45E+01	6.67E+01	3.14E+01

Sample	Flatness _Avg_w	Flatness _Median	Flatness _Std	Orientation 2Phi_Avg	Orientation 2Phi_Avg_w	Orientation 2Phi_Median
	adim	adim	adim	graus	graus	graus
W03-S10	4.67E-01	4.44E-01	2.30E-01	3.75E+01	5.41E+01	3.38E+01
W06-S02	4.75E-01	3.81E-01	2.36E-01	3.01E+01	5.26E+01	2.54E+01
W06-S03	4.49E-01	3.98E-01	2.32E-01	3.05E+01	4.56E+01	2.60E+01
W07-S01	4.74E-01	3.14E-01	2.35E-01	2.89E+01	5.38E+01	2.40E+01
W07-S02	4.93E-01	4.10E-01	2.42E-01	3.21E+01	5.58E+01	2.70E+01
W07-S04	4.76E-01	3.63E-01	2.35E-01	3.45E+01	5.32E+01	2.89E+01
W08-S01	4.07E-01	3.28E-01	2.31E-01	2.20E+01	2.95E+01	1.70E+01
W08-S03	5.31E-01	4.62E-01	2.13E-01	5.53E+01	5.71E+01	5.75E+01
W08-S04	4.52E-01	3.52E-01	2.39E-01	2.52E+01	3.67E+01	1.93E+01
W09-S01	4.46E-01	4.20E-01	2.29E-01	3.53E+01	5.05E+01	3.11E+01
W09-S02	4.73E-01	4.09E-01	2.33E-01	3.56E+01	4.95E+01	3.15E+01
W09-S03	4.50E-01	4.12E-01	2.29E-01	3.32E+01	4.36E+01	2.91E+01
W09-S04	4.84E-01	4.35E-01	2.29E-01	3.76E+01	5.17E+01	3.40E+01
W09-S05	4.29E-01	3.99E-01	2.30E-01	3.87E+01	5.05E+01	3.55E+01
W10-S06	4.54E-01	3.73E-01	2.23E-01	5.56E+01	5.50E+01	5.75E+01
W10-S07	4.64E-01	4.37E-01	2.04E-01	5.84E+01	5.97E+01	6.13E+01
W11-S03	4.61E-01	4.79E-01	2.01E-01	5.91E+01	6.33E+01	6.22E+01
W11-S04	4.14E-01	4.13E-01	2.09E-01	5.68E+01	6.39E+01	5.94E+01
W14-S01	4.70E-01	4.15E-01	2.13E-01	5.65E+01	5.56E+01	5.86E+01
W14-S02	4.37E-01	4.41E-01	2.08E-01	5.62E+01	5.87E+01	5.82E+01
W14-S04	5.21E-01	4.21E-01	2.13E-01	5.46E+01	5.59E+01	5.68E+01
W14-S05	5.02E-01	4.13E-01	2.09E-01	5.66E+01	5.45E+01	5.86E+01
W14-S06	4.46E-01	4.27E-01	2.11E-01	5.72E+01	5.70E+01	5.97E+01
W14-S07	4.54E-01	4.35E-01	2.11E-01	5.75E+01	5.87E+01	6.00E+01
W14-S09	4.47E-01	4.29E-01	2.08E-01	5.43E+01	5.47E+01	5.61E+01
W14-S10	4.93E-01	3.96E-01	2.17E-01	5.70E+01	5.64E+01	5.96E+01
W14-S12	4.52E-01	4.18E-01	2.13E-01	5.54E+01	5.86E+01	5.74E+01
W15-S02	4.70E-01	4.03E-01	2.17E-01	5.33E+01	5.24E+01	5.50E+01
W15-S03	4.55E-01	4.31E-01	2.10E-01	5.40E+01	5.53E+01	5.57E+01
W15-S05	4.66E-01	4.42E-01	2.09E-01	5.21E+01	5.19E+01	5.31E+01
W15-S06	4.97E-01	4.25E-01	2.13E-01	5.36E+01	5.46E+01	5.52E+01
W15-S07	5.27E-01	4.11E-01	2.20E-01	5.19E+01	5.44E+01	5.30E+01
W15-S08	5.48E-01	4.30E-01	2.13E-01	5.24E+01	5.49E+01	5.35E+01
W15-S09	4.97E-01	4.30E-01	2.23E-01	5.39E+01	5.49E+01	5.56E+01
W15-S12	4.99E-01	4.16E-01	2.14E-01	5.08E+01	4.93E+01	5.14E+01
W15-S14	4.76E-01	4.63E-01	2.07E-01	5.73E+01	5.96E+01	6.00E+01
W16-S01	4.63E-01	4.46E-01	2.06E-01	5.50E+01	5.67E+01	5.70E+01
W16-S03	4.60E-01	4.24E-01	2.11E-01	5.37E+01	5.75E+01	5.55E+01
W16-S05	4.84E-01	3.94E-01	2.17E-01	5.70E+01	5.07E+01	5.96E+01
W16-S06	4.93E-01	3.94E-01	2.23E-01	5.48E+01	5.39E+01	5.68E+01
W17-S01	4.93E-01	4.24E-01	2.32E-01	3.80E+01	5.42E+01	3.48E+01
W17-S03	4.95E-01	4.43E-01	2.28E-01	4.01E+01	5.71E+01	3.73E+01

Sample	Flatness _Avg_w	Flatness _Median	Flatness _Std	Orientation 2Phi_Avg	Orientation 2Phi_Avg_w	Orientation 2Phi_Median
	adim	adim	adim	graus	graus	graus
W17-S04	4.50E-01	4.43E-01	2.30E-01	4.07E+01	5.76E+01	3.80E+01
W17-S05	5.27E-01	4.41E-01	2.07E-01	5.13E+01	5.03E+01	5.16E+01
W18-S01	4.90E-01	4.34E-01	2.10E-01	5.63E+01	5.98E+01	5.88E+01
W18-S02	3.76E-01	3.76E-01	2.18E-01	6.72E+01	7.32E+01	7.21E+01
W18-S03	4.98E-01	4.11E-01	2.11E-01	5.63E+01	5.55E+01	5.89E+01
W18-S04	5.00E-01	4.25E-01	2.13E-01	5.64E+01	5.84E+01	5.89E+01
W18-S05	4.51E-01	4.40E-01	2.11E-01	5.79E+01	5.93E+01	6.07E+01
W18-S06	4.92E-01	4.03E-01	2.15E-01	5.72E+01	5.86E+01	6.04E+01
W19-S01	4.83E-01	4.26E-01	2.20E-01	3.61E+01	4.77E+01	3.20E+01
W19-S02	5.72E-01	4.51E-01	2.05E-01	5.33E+01	5.52E+01	5.47E+01
W19-S03	4.07E-01	4.48E-01	2.11E-01	5.72E+01	5.90E+01	6.00E+01
W19-S04	4.57E-01	4.44E-01	2.05E-01	5.46E+01	5.42E+01	5.61E+01
W19-S05	4.98E-01	4.44E-01	2.07E-01	5.16E+01	5.27E+01	5.23E+01
W19-S06	4.54E-01	4.43E-01	2.03E-01	4.98E+01	4.77E+01	4.95E+01
W20-S01	4.69E-01	4.64E-01	2.05E-01	5.42E+01	5.30E+01	5.57E+01
W20-S02	5.16E-01	4.53E-01	2.09E-01	5.63E+01	5.53E+01	5.85E+01
W20-S03	4.56E-01	4.39E-01	2.09E-01	5.78E+01	6.05E+01	6.04E+01
W20-S04	4.83E-01	4.64E-01	2.07E-01	5.75E+01	5.95E+01	6.00E+01
W20-S05	4.96E-01	4.38E-01	2.09E-01	5.58E+01	5.64E+01	5.80E+01
W20-S06	4.80E-01	4.69E-01	2.07E-01	5.93E+01	6.29E+01	6.28E+01
W21-S01	5.14E-01	4.39E-01	2.09E-01	5.71E+01	5.90E+01	5.96E+01
W21-S02	4.77E-01	4.45E-01	2.08E-01	5.55E+01	5.71E+01	5.74E+01
W21-S03	5.05E-01	4.19E-01	2.11E-01	5.55E+01	5.57E+01	5.76E+01
W21-S04	4.99E-01	4.39E-01	2.10E-01	5.68E+01	6.52E+01	5.92E+01
W21-S05	4.89E-01	4.13E-01	2.14E-01	5.74E+01	6.27E+01	6.00E+01
W21-S06	4.88E-01	4.12E-01	2.15E-01	5.38E+01	5.74E+01	5.56E+01
W21-S07	4.81E-01	4.28E-01	2.11E-01	5.51E+01	5.76E+01	5.70E+01
W21-S08	5.41E-01	4.51E-01	2.09E-01	5.62E+01	5.46E+01	5.82E+01
W22-S01	5.03E-01	4.22E-01	2.18E-01	5.87E+01	5.57E+01	6.18E+01
W22-S02	5.36E-01	4.55E-01	2.04E-01	5.34E+01	5.69E+01	5.48E+01
W22-S04	4.47E-01	4.00E-01	2.14E-01	6.12E+01	6.27E+01	6.53E+01
W22-S05	5.65E-01	4.51E-01	2.10E-01	5.37E+01	5.51E+01	5.52E+01
W24-S01	4.75E-01	4.58E-01	2.11E-01	5.56E+01	5.07E+01	5.82E+01
W24-S02	4.90E-01	4.49E-01	2.09E-01	5.69E+01	5.93E+01	5.94E+01
W24-S03	5.24E-01	4.56E-01	2.05E-01	5.69E+01	6.13E+01	5.93E+01
W24-S04	4.95E-01	4.38E-01	2.10E-01	5.41E+01	5.41E+01	5.61E+01
W24-S05	5.17E-01	4.41E-01	2.11E-01	5.47E+01	5.64E+01	5.65E+01
W25-S01	1.71E-01	3.40E-01	2.14E-01	7.10E+01	8.09E+01	7.62E+01
W25-S02	3.79E-01	4.26E-01	2.06E-01	6.25E+01	7.13E+01	6.69E+01
W25-S03	4.63E-01	4.25E-01	2.07E-01	5.68E+01	5.72E+01	5.95E+01
W25-S04	4.67E-01	4.21E-01	2.10E-01	5.71E+01	5.79E+01	5.99E+01
W26-S02	4.36E-01	4.30E-01	2.10E-01	5.56E+01	5.78E+01	5.78E+01

Sample	Flatness _Avg_w	Flatness Median	Flatness Std	Orientation 2Phi_Avg	Orientation 2Phi_Avg_w	Orientation 2Phi_Median
	adim	adim	adim	graus	graus	graus
W27-S01	5.03E-01	4.24E-01	2.07E-01	5.79E+01	5.39E+01	6.08E+01
W27-S03	4.82E-01	4.58E-01	2.07E-01	6.20E+01	6.38E+01	6.60E+01
W27-S04	2.76E-01	3.98E-01	2.09E-01	6.67E+01	7.73E+01	7.17E+01
W27-S05	4.82E-01	4.59E-01	2.06E-01	5.37E+01	5.31E+01	5.51E+01
W27-S06	4.63E-01	4.46E-01	2.08E-01	5.29E+01	5.27E+01	5.41E+01
W28-S02	3.95E-01	4.25E-01	2.07E-01	5.91E+01	6.89E+01	6.28E+01
W28-S04	4.79E-01	4.00E-01	2.37E-01	3.72E+01	6.12E+01	3.40E+01
W28-S05	4.52E-01	4.26E-01	2.09E-01	6.04E+01	6.02E+01	6.37E+01
W29-S01	4.60E-01	4.43E-01	2.06E-01	5.74E+01	5.57E+01	6.00E+01
W29-S02	4.60E-01	4.27E-01	2.10E-01	5.77E+01	5.45E+01	6.01E+01
W30-S01	4.50E-01	4.40E-01	2.12E-01	5.42E+01	5.67E+01	5.57E+01
W30-S03	5.11E-01	3.47E-01	2.28E-01	6.60E+01	5.91E+01	7.00E+01
W30-S04	4.64E-01	4.35E-01	2.08E-01	5.94E+01	6.04E+01	6.27E+01
W30-S05	4.74E-01	4.22E-01	2.10E-01	5.76E+01	5.89E+01	6.03E+01
W30-S07	4.72E-01	3.83E-01	2.16E-01	5.64E+01	5.88E+01	5.92E+01
W30-S08	4.75E-01	4.38E-01	2.07E-01	5.45E+01	5.65E+01	5.62E+01
W31-S01	4.54E-01	4.32E-01	2.09E-01	5.84E+01	6.27E+01	6.14E+01
W31-S03	5.10E-01	3.90E-01	2.18E-01	5.81E+01	6.26E+01	6.11E+01

Sample	Orientation 2Phi_Std	Orientation 2Theta_Avg	Orientation 2Theta_Avg_w	Orientation 2Theta_Median	Orientation 2Theta_Std	Orientation Phi_Avg
	graus	graus	graus	graus	graus	graus
W02-S01	2.15E+01	3.27E+00	-2.63E+00	4.60E-01	1.05E+02	5.81E+01
W02-S03	2.33E+01	5.44E+00	1.80E+00	-2.70E-02	1.05E+02	5.91E+01
W02-S04	2.39E+01	-2.98E+00	-3.31E+00	1.39E-01	1.00E+02	6.32E+01
W02-S05	2.38E+01	-8.30E+00	-8.38E+00	-5.85E+00	1.02E+02	6.07E+01
W03-S01	2.48E+01	1.06E+01	7.44E+00	1.17E+01	1.02E+02	6.80E+01
W03-S02	2.41E+01	4.50E+00	4.32E+00	6.45E+00	1.04E+02	7.05E+01
W03-S03	2.49E+01	1.63E+00	-2.46E+00	9.22E+00	9.96E+01	7.10E+01
W03-S06	2.33E+01	4.12E+00	2.25E+00	4.47E+00	1.01E+02	6.04E+01
W03-S09	2.50E+01	1.82E+00	-5.01E+00	3.57E-01	1.03E+02	7.01E+01
W03-S10	2.52E+01	-5.62E-01	-1.12E+01	4.04E+00	1.03E+02	6.79E+01
W06-S02	2.36E+01	1.55E+01	1.26E-01	3.22E+01	1.03E+02	7.19E+01
W06-S03	2.32E+01	3.99E+00	1.93E+00	3.70E+00	1.04E+02	7.19E+01
W07-S01	2.36E+01	2.17E+01	2.46E+01	4.50E+01	1.05E+02	7.28E+01
W07-S02	2.47E+01	5.75E+00	7.52E+00	8.15E+00	1.04E+02	7.07E+01
W07-S04	2.54E+01	3.78E+00	1.08E+01	-3.40E+00	9.79E+01	6.98E+01
W08-S01	1.96E+01	-2.19E+00	-9.02E+00	-4.54E-03	1.03E+02	7.63E+01
W08-S03	2.34E+01	4.39E+00	1.08E+01	1.64E+00	1.04E+02	5.84E+01
W08-S04	2.17E+01	9.51E+00	9.65E+00	1.44E+01	1.03E+02	7.44E+01
W09-S01	2.42E+01	2.08E+00	7.59E-03	4.72E+00	1.06E+02	6.93E+01
W09-S02	2.47E+01	1.47E+00	-3.06E+00	2.32E+00	1.03E+02	6.89E+01

Sample	Orientation 2Phi_Std	Orientation 2Theta_Avg	Orientation 2Theta_ Avg_w	Orientation 2Theta _Median	Orientation 2Theta_Std	Orientation Phi_Avg
	graus	graus	graus	graus	graus	graus
W09-S03	2.35E+01	4.58E+00	4.58E+00	6.12E+00	9.85E+01	7.03E+01
W09-S04	2.47E+01	1.56E+00	-4.26E+00	3.19E+00	1.04E+02	6.81E+01
W09-S05	2.52E+01	2.01E-01	-7.68E+00	2.51E+00	1.03E+02	6.81E+01
W10-S06	2.36E+01	7.44E+00	3.20E+01	7.29E+00	1.08E+02	5.82E+01
W10-S07	2.20E+01	1.16E+00	-1.32E+00	2.46E-03	1.03E+02	5.64E+01
W11-S03	2.17E+01	9.00E-01	1.06E+01	1.41E+00	1.05E+02	5.60E+01
W11-S04	2.27E+01	4.65E+00	9.56E+00	6.17E+00	1.03E+02	5.81E+01
W14-S01	2.27E+01	1.27E-01	-2.21E+01	0.00E+00	1.03E+02	5.83E+01
W14-S02	2.26E+01	6.91E+00	5.46E+01	9.57E+00	1.05E+02	5.84E+01
W14-S04	2.36E+01	-1.84E-01	-7.79E+00	0.00E+00	1.03E+02	5.94E+01
W14-S05	2.26E+01	2.47E+00	2.35E+01	0.00E+00	1.03E+02	5.77E+01
W14-S06	2.25E+01	-7.65E-01	-5.80E+00	0.00E+00	1.03E+02	5.72E+01
W14-S07	2.25E+01	3.56E+00	2.04E+01	1.21E+00	1.03E+02	5.75E+01
W14-S09	2.31E+01	8.47E-01	-3.08E+00	7.57E-01	1.05E+02	5.96E+01
W14-S10	2.30E+01	4.38E-01	9.27E+00	1.21E-01	1.04E+02	5.76E+01
W14-S12	2.31E+01	1.01E+01	1.90E+01	1.32E+01	1.03E+02	5.91E+01
W15-S02	2.39E+01	4.51E+00	1.40E+01	4.38E-01	1.02E+02	6.04E+01
W15-S03	2.34E+01	4.14E+00	6.77E+00	1.02E+01	1.03E+02	5.97E+01
W15-S05	2.36E+01	3.36E+00	6.18E+00	0.00E+00	1.07E+02	6.12E+01
W15-S06	2.37E+01	-1.26E+00	-3.54E+00	0.00E+00	1.06E+02	5.95E+01
W15-S07	2.43E+01	4.49E+00	-5.35E-01	3.36E+00	1.05E+02	6.12E+01
W15-S08	2.39E+01	8.51E-01	-2.24E+00	1.46E+00	1.03E+02	6.12E+01
W15-S09	2.38E+01	4.47E+00	1.25E+01	3.63E+00	1.01E+02	6.01E+01
W15-S12	2.43E+01	-2.78E+00	-1.05E+01	-1.30E+00	9.94E+01	6.17E+01
W15-S14	2.25E+01	4.33E+00	1.02E+01	8.49E-01	1.03E+02	5.70E+01
W16-S01	2.31E+01	-6.97E-01	-8.87E+00	-2.22E+00	1.03E+02	5.95E+01
W16-S03	2.35E+01	-3.59E-01	-2.49E+00	-8.46E-01	1.07E+02	5.98E+01
W16-S05	2.32E+01	-5.88E+00	-1.97E+01	-8.48E+00	1.01E+02	5.79E+01
W16-S06	2.36E+01	5.92E+00	1.37E+01	5.81E+00	9.78E+01	5.92E+01
W17-S01	2.51E+01	4.91E+00	-1.26E+00	4.12E+00	1.03E+02	6.85E+01
W17-S03	2.51E+01	2.53E+00	8.79E-02	1.98E+00	1.04E+02	6.70E+01
W17-S04	2.51E+01	-3.55E+00	-9.90E+00	-4.70E+00	1.03E+02	6.67E+01
W17-S05	2.36E+01	-1.37E+00	1.09E+01	0.00E+00	1.03E+02	6.13E+01
W18-S01	2.30E+01	5.87E-02	-2.88E+00	-7.82E-01	1.03E+02	5.81E+01
W18-S02	2.00E+01	-2.40E+01	-5.03E+01	-4.82E-01	1.07E+02	5.00E+01
W18-S03	2.32E+01	6.64E-02	7.55E+00	-6.47E-01	1.04E+02	5.84E+01
W18-S04	2.30E+01	-2.66E-01	-1.27E+01	1.51E-01	1.04E+02	5.78E+01
W18-S05	2.25E+01	6.47E+00	2.04E+01	5.92E+00	1.04E+02	5.69E+01
W18-S06	2.34E+01	-1.18E+00	-3.28E+00	-1.98E-01	1.03E+02	5.72E+01
W19-S01	2.39E+01	-4.76E+00	-9.38E+00	-6.80E+00	1.05E+02	6.94E+01
W19-S02	2.34E+01	-5.57E+00	-7.99E+00	-2.53E+00	1.05E+02	6.04E+01

Sample	Orientation 2Phi_Std	Orientation 2Theta_Avg	Orientation 2Theta_ Avg_w	Orientation 2Theta _Median	Orientation 2Theta_Std	Orientation Phi_Avg
	graus	graus	graus	graus	graus	graus
W19-S03	2.30E+01	1.34E+01	2.89E+01	9.63E+00	1.03E+02	5.71E+01
W19-S04	2.29E+01	3.49E+00	-3.18E+00	0.00E+00	1.04E+02	5.89E+01
W19-S05	2.37E+01	-4.91E+00	-5.71E+00	-1.13E+00	1.02E+02	6.16E+01
W19-S06	2.38E+01	4.41E+00	3.38E+00	-3.84E+00	1.03E+02	6.37E+01
W20-S01	2.28E+01	2.60E+00	-3.36E+00	1.74E+01	1.05E+02	5.96E+01
W20-S02	2.27E+01	2.25E+00	8.02E+00	3.01E+00	1.03E+02	5.80E+01
W20-S03	2.24E+01	1.23E+00	-6.80E+00	2.37E+00	1.03E+02	5.69E+01
W20-S04	2.24E+01	-5.95E-01	-1.48E+00	2.90E-01	1.03E+02	5.64E+01
W20-S05	2.30E+01	2.52E+00	-9.07E-01	2.39E+00	1.02E+02	5.83E+01
W20-S06	2.20E+01	-2.91E+00	-5.36E+00	0.00E+00	1.05E+02	5.58E+01
W21-S01	2.24E+01	-1.76E-01	-1.69E+00	-4.91E-01	1.03E+02	5.75E+01
W21-S02	2.29E+01	-8.74E-01	-3.60E+00	0.00E+00	1.04E+02	5.87E+01
W21-S03	2.33E+01	-4.60E-01	-4.55E+00	-2.69E-01	1.03E+02	5.89E+01
W21-S04	2.27E+01	1.15E+00	1.28E+01	1.21E-02	1.03E+02	5.75E+01
W21-S05	2.29E+01	2.96E-01	-3.80E+00	0.00E+00	1.04E+02	5.75E+01
W21-S06	2.37E+01	-3.48E-01	2.25E+01	8.89E-04	1.03E+02	5.98E+01
W21-S07	2.30E+01	6.12E+00	1.25E+01	2.03E+01	1.00E+02	5.86E+01
W21-S08	2.26E+01	3.61E+00	2.62E+00	1.15E+01	1.07E+02	5.77E+01
W22-S01	2.27E+01	1.58E+00	9.31E+00	2.36E-01	1.04E+02	5.65E+01
W22-S02	2.33E+01	-2.55E+00	-1.66E+00	1.75E-02	1.03E+02	6.06E+01
W22-S04	2.17E+01	-5.13E-01	1.69E-01	2.24E-01	1.04E+02	5.44E+01
W22-S05	2.36E+01	9.70E-02	1.58E+01	0.00E+00	1.04E+02	6.03E+01
W24-S01	2.32E+01	-1.22E+00	1.02E+00	0.00E+00	1.04E+02	5.90E+01
W24-S02	2.26E+01	1.95E+00	6.74E+00	0.00E+00	1.05E+02	5.73E+01
W24-S03	2.26E+01	1.40E+00	-3.84E+00	1.97E-01	1.03E+02	5.78E+01
W24-S04	2.35E+01	2.46E+00	-6.70E+00	3.11E+00	1.05E+02	6.03E+01
W24-S05	2.33E+01	5.38E+00	1.58E+01	1.33E+01	1.05E+02	5.99E+01
W25-S01	1.78E+01	-2.98E+01	-4.58E+01	-2.68E+01	9.96E+01	4.66E+01
W25-S02	2.11E+01	1.73E+01	3.53E+01	4.54E+01	9.88E+01	5.44E+01
W25-S03	2.27E+01	-1.00E+01	-4.04E+00	-1.26E+01	1.06E+02	5.79E+01
W25-S04	2.27E+01	1.62E+00	-4.56E+00	1.06E+00	1.05E+02	5.81E+01
W26-S02	2.30E+01	4.47E+00	4.54E+00	3.60E+00	1.05E+02	5.87E+01
W27-S01	2.24E+01	-7.94E-01	-7.15E-01	8.96E-02	1.03E+02	5.72E+01
W27-S03	2.11E+01	7.35E+00	1.19E+01	1.17E+00	1.14E+02	5.36E+01
W27-S04	2.00E+01	1.53E+01	1.31E+01	-1.88E+00	9.79E+01	5.17E+01
W27-S05	2.32E+01	-1.13E+00	-6.98E-01	3.59E+00	1.02E+02	6.10E+01
W27-S06	2.36E+01	6.35E+00	5.81E+00	5.56E-02	1.03E+02	6.13E+01
W28-S02	2.25E+01	1.40E+00	7.27E-02	1.65E+01	1.02E+02	5.65E+01
W28-S04	2.57E+01	2.75E+00	-1.22E+01	6.48E+00	1.04E+02	6.78E+01
W28-S05	2.15E+01	8.16E-01	2.99E+00	2.65E-01	1.03E+02	5.49E+01
W29-S01	2.22E+01	-2.83E+00	-4.96E+00	-1.20E-02	1.03E+02	5.75E+01

Sample	Orientation 2Phi_Std	Orientation 2Theta_Avg	Orientation 2Theta_Avg_w	Orientation 2Theta_Median	Orientation 2Theta_Std	Orientation Phi_Avg
	graus	graus	graus	graus	graus	graus
W29-S02	2.24E+01	1.86E+00	5.32E+00	3.39E+00	1.02E+02	5.72E+01
W30-S01	2.33E+01	2.33E-01	4.86E+00	3.49E-01	1.03E+02	5.98E+01
W30-S03	2.07E+01	-3.47E+00	-1.01E+01	0.00E+00	1.11E+02	5.21E+01
W30-S04	2.19E+01	2.17E+00	1.18E+01	2.41E+00	1.03E+02	5.62E+01
W30-S05	2.26E+01	1.59E+00	3.30E+00	1.84E-01	1.04E+02	5.70E+01
W30-S07	2.36E+01	4.39E+00	-8.85E+00	3.34E+00	1.02E+02	5.78E+01
W30-S08	2.31E+01	9.66E-01	1.14E+01	2.94E-01	1.04E+02	5.93E+01
W31-S01	2.24E+01	3.24E+00	8.43E+00	0.00E+00	1.04E+02	5.66E+01
W31-S03	2.30E+01	1.92E+00	3.38E+00	2.86E+00	1.04E+02	5.80E+01

Sample	Orientation Phi_Avg_w	Orientation Phi_Median	Orientation Phi_Std	Orientation Theta_Avg	Orientation Theta_Avg_w	Orientation Theta_Median
	graus	graus	graus	graus	graus	graus
W02-S01	5.93E+01	5.95E+01	2.12E+01	-3.45E-01	7.27E+00	1.16E-01
W02-S03	5.68E+01	6.18E+01	2.17E+01	-2.77E+00	2.30E+00	1.80E+00
W02-S04	6.31E+01	6.65E+01	2.00E+01	5.93E+00	6.01E+00	2.37E-01
W02-S05	5.92E+01	6.23E+01	2.11E+01	6.24E+00	6.12E-01	9.30E+00
W03-S01	5.95E+01	7.15E+01	1.86E+01	-7.53E+00	-8.74E+00	-1.47E+00
W03-S02	6.22E+01	7.47E+01	1.80E+01	2.78E+00	1.18E+00	0.00E+00
W03-S03	5.95E+01	7.54E+01	1.80E+01	9.28E+00	8.17E+00	4.39E+00
W03-S06	5.94E+01	6.30E+01	2.11E+01	-1.33E+00	6.11E-01	-6.92E-01
W03-S09	5.32E+01	7.39E+01	1.83E+01	-3.98E-01	-1.53E+01	7.84E+00
W03-S10	6.00E+01	7.16E+01	1.90E+01	5.77E+00	9.29E+00	2.69E-01
W06-S02	5.98E+01	7.62E+01	1.74E+01	-4.62E+00	-1.08E+01	-1.75E+00
W06-S03	6.43E+01	7.58E+01	1.68E+01	1.51E+00	-2.00E+00	1.02E-01
W07-S01	5.87E+01	7.69E+01	1.69E+01	-8.82E+00	-1.26E+01	-1.76E+01
W07-S02	5.92E+01	7.53E+01	1.83E+01	-3.24E-01	-1.46E+01	0.00E+00
W07-S04	6.04E+01	7.44E+01	1.84E+01	-1.18E+00	-1.00E+01	7.69E+00
W08-S01	7.21E+01	7.99E+01	1.38E+01	9.82E+00	1.03E+01	6.14E+00
W08-S03	5.80E+01	6.11E+01	2.19E+01	-8.87E-01	-4.51E+00	0.00E+00
W08-S04	6.83E+01	7.86E+01	1.56E+01	1.82E-02	-3.29E+00	0.00E+00
W09-S01	6.19E+01	7.34E+01	1.80E+01	1.75E+00	-9.70E-01	0.00E+00
W09-S02	6.32E+01	7.29E+01	1.85E+01	2.44E+00	2.39E+00	8.48E-01
W09-S03	6.54E+01	7.41E+01	1.74E+01	-2.53E-02	-2.09E+00	0.00E+00
W09-S04	5.99E+01	7.19E+01	1.87E+01	1.75E+00	-4.77E-01	3.74E-01
W09-S05	6.36E+01	7.21E+01	1.91E+01	3.90E+00	1.29E+01	8.86E-01
W10-S06	5.90E+01	6.04E+01	2.21E+01	-4.80E+00	-1.91E+01	-8.81E+00
W10-S07	5.49E+01	5.86E+01	2.22E+01	1.07E+00	6.20E+00	7.34E-01
W11-S03	5.28E+01	5.81E+01	2.21E+01	-6.84E-01	-1.63E+01	0.00E+00
W11-S04	5.43E+01	6.04E+01	2.19E+01	-3.60E+00	-1.89E+01	-2.44E+00
W14-S01	5.87E+01	6.08E+01	2.17E+01	4.21E+00	1.01E+01	5.46E+00

Sample	Orientation Phi_Avg_w	Orientation Phi_Median	Orientation Phi_Std	Orientation Theta_Avg	Orientation Theta_Avg_w	Orientation Theta_Median
	graus	graus	graus	graus	graus	graus
W14-S02	5.60E+01	6.05E+01	2.15E+01	-4.77E+00	-3.19E+01	-3.36E+00
W14-S04	5.95E+01	6.20E+01	2.16E+01	1.55E+00	7.29E+00	3.28E-01
W14-S05	5.50E+01	6.00E+01	2.19E+01	-2.84E-01	-8.19E+00	0.00E+00
W14-S06	5.70E+01	5.96E+01	2.21E+01	1.64E+00	8.48E+00	7.98E-01
W14-S07	5.71E+01	5.98E+01	2.20E+01	-6.10E-01	-1.68E+01	1.47E-01
W14-S09	5.92E+01	6.26E+01	2.13E+01	5.81E-01	2.54E+00	1.67E-01
W14-S10	5.91E+01	6.01E+01	2.21E+01	1.95E+00	-1.10E+01	5.58E-01
W14-S12	5.69E+01	6.17E+01	2.16E+01	-4.08E+00	-9.70E+00	-8.83E+00
W15-S02	6.06E+01	6.34E+01	2.15E+01	-9.67E-02	3.20E+00	1.15E+00
W15-S03	5.83E+01	6.24E+01	2.14E+01	-1.94E+00	-7.00E+00	-3.88E+00
W15-S05	6.12E+01	6.43E+01	2.09E+01	-3.94E-01	-3.88E+00	1.33E+00
W15-S06	5.96E+01	6.23E+01	2.16E+01	1.08E+00	-4.35E+00	1.83E+00
W15-S07	5.83E+01	6.45E+01	2.13E+01	-2.31E-01	-1.05E+00	0.00E+00
W15-S08	5.94E+01	6.44E+01	2.11E+01	1.04E+00	3.61E+00	1.12E-01
W15-S09	5.99E+01	6.30E+01	2.15E+01	-2.38E+00	-1.28E+01	0.00E+00
W15-S12	6.40E+01	6.55E+01	2.11E+01	2.60E+00	8.59E+00	1.94E+00
W15-S14	5.55E+01	5.92E+01	2.22E+01	-3.38E+00	-1.11E+01	9.55E-10
W16-S01	5.77E+01	6.19E+01	2.15E+01	2.10E+00	4.50E+00	3.12E+00
W16-S03	5.66E+01	6.25E+01	2.15E+01	2.82E-01	-3.01E-01	3.18E+00
W16-S05	6.31E+01	6.03E+01	2.22E+01	3.20E+00	7.23E+00	5.87E+00
W16-S06	5.91E+01	6.15E+01	2.19E+01	-6.28E-01	-8.87E+00	0.00E+00
W17-S01	6.04E+01	7.22E+01	1.86E+01	-1.37E+00	1.14E+01	8.11E-02
W17-S03	5.67E+01	7.10E+01	1.93E+01	6.50E-01	7.78E-01	7.06E-02
W17-S04	5.57E+01	7.06E+01	1.94E+01	6.05E+00	6.42E+00	6.24E+00
W17-S05	6.05E+01	6.43E+01	2.09E+01	1.99E+00	8.22E+00	1.35E+00
W18-S01	5.67E+01	6.06E+01	2.18E+01	-3.04E-01	-7.16E+00	9.79E-01
W18-S02	4.92E+01	5.06E+01	2.42E+01	1.10E+01	2.41E+01	-1.99E-01
W18-S03	5.90E+01	6.12E+01	2.21E+01	-6.97E-01	-4.75E-01	2.82E-01
W18-S04	5.65E+01	6.02E+01	2.21E+01	1.89E+00	3.58E-01	5.84E-01
W18-S05	5.62E+01	5.91E+01	2.21E+01	-4.09E+00	-1.59E+01	-1.01E+00
W18-S06	5.50E+01	6.00E+01	2.25E+01	1.30E+00	-5.63E+00	3.59E+00
W19-S01	6.35E+01	7.34E+01	1.77E+01	6.04E+00	9.06E+00	4.75E+00
W19-S02	6.07E+01	6.36E+01	2.13E+01	4.46E+00	9.77E-01	2.73E+00
W19-S03	5.37E+01	5.93E+01	2.23E+01	-9.28E+00	-2.73E+01	-7.89E+00
W19-S04	5.86E+01	6.10E+01	2.14E+01	1.05E-01	3.89E+00	8.35E-01
W19-S05	6.38E+01	6.49E+01	2.08E+01	4.90E+00	1.05E+01	2.32E+00
W19-S06	6.51E+01	6.78E+01	2.01E+01	-3.12E+00	-4.29E+00	5.02E+00
W20-S01	5.98E+01	6.18E+01	2.10E+01	-1.47E+00	-1.39E+00	-8.77E+00
W20-S02	5.93E+01	6.00E+01	2.18E+01	-1.04E+00	2.55E+00	-4.02E-01
W20-S03	5.42E+01	5.90E+01	2.21E+01	7.58E-01	8.27E+00	-1.04E+00
W20-S04	5.50E+01	5.85E+01	2.22E+01	1.75E+00	1.38E+00	5.76E-01

Sample	Orientation Phi_Avg_w	Orientation Phi_Median	Orientation Phi_Std	Orientation Theta_Avg	Orientation Theta_Avg_w	Orientation Theta_Median
	graus	graus	graus	graus	graus	graus
W20-S05	5.73E+01	6.06E+01	2.19E+01	6.80E-01	4.16E+00	0.00E+00
W20-S06	5.44E+01	5.74E+01	2.23E+01	1.09E+00	9.26E-01	8.81E-08
W21-S01	5.58E+01	5.97E+01	2.18E+01	1.58E+00	1.15E+00	2.59E+00
W21-S02	5.71E+01	6.11E+01	2.16E+01	1.76E+00	-4.44E-01	2.03E+00
W21-S03	5.82E+01	6.14E+01	2.18E+01	2.21E+00	-5.02E+00	1.11E+00
W21-S04	5.30E+01	5.99E+01	2.21E+01	7.10E-01	5.18E+00	5.43E-01
W21-S05	5.51E+01	6.00E+01	2.22E+01	1.15E+00	-1.20E+00	2.59E-01
W21-S06	5.79E+01	6.26E+01	2.15E+01	3.05E+00	-7.90E+00	1.84E+00
W21-S07	5.77E+01	6.11E+01	2.17E+01	-4.44E+00	-1.00E+01	-7.40E+00
W21-S08	6.08E+01	6.00E+01	2.18E+01	-1.46E+00	6.20E+00	-3.94E+00
W22-S01	5.83E+01	5.90E+01	2.26E+01	1.51E+00	-4.13E+00	9.44E-01
W22-S02	5.97E+01	6.37E+01	2.11E+01	2.96E+00	1.65E+01	1.83E-01
W22-S04	5.27E+01	5.60E+01	2.29E+01	1.20E+00	-6.95E+00	2.62E-01
W22-S05	6.04E+01	6.32E+01	2.14E+01	1.49E+00	-7.99E+00	8.60E-01
W24-S01	6.34E+01	6.20E+01	2.16E+01	2.28E+00	-1.39E+00	1.51E+00
W24-S02	5.66E+01	5.97E+01	2.20E+01	-6.07E-01	-2.84E+00	2.79E-01
W24-S03	5.52E+01	5.99E+01	2.19E+01	5.59E-02	6.17E+00	5.71E-02
W24-S04	6.06E+01	6.29E+01	2.12E+01	-1.09E+00	6.96E+00	-1.23E-01
W24-S05	5.86E+01	6.25E+01	2.14E+01	-4.58E+00	-2.29E+01	-1.54E+01
W25-S01	4.50E+01	4.55E+01	2.44E+01	2.59E+01	2.72E+01	2.56E+00
W25-S02	4.63E+01	5.61E+01	2.31E+01	-1.40E+01	-3.94E+01	-1.01E+01
W25-S03	6.00E+01	6.04E+01	2.19E+01	7.35E+00	6.06E-01	6.76E+00
W25-S04	5.63E+01	6.07E+01	2.20E+01	5.88E-01	-8.78E+00	1.40E-02
W26-S02	5.74E+01	6.13E+01	2.17E+01	-1.44E+00	1.02E+00	-4.06E-01
W27-S01	6.00E+01	5.94E+01	2.22E+01	1.68E+00	8.97E+00	8.96E-02
W27-S03	5.25E+01	5.52E+01	2.30E+01	-1.84E+00	-3.16E+00	1.50E+00
W27-S04	5.25E+01	5.30E+01	2.38E+01	-2.08E+01	-3.32E+01	1.11E+00
W27-S05	6.07E+01	6.40E+01	2.10E+01	2.52E+00	4.36E-01	-3.64E-01
W27-S06	6.08E+01	6.47E+01	2.10E+01	-3.69E+00	-3.10E+00	3.93E-01
W28-S02	5.37E+01	5.91E+01	2.27E+01	1.37E+00	8.94E+00	-8.13E+00
W28-S04	5.59E+01	7.16E+01	1.95E+01	4.09E+00	3.72E+00	0.00E+00
W28-S05	5.53E+01	5.69E+01	2.26E+01	6.36E-01	-1.81E+00	2.25E-01
W29-S01	5.88E+01	5.98E+01	2.19E+01	1.17E+00	-1.76E+00	1.87E-01
W29-S02	5.85E+01	5.95E+01	2.21E+01	-1.29E+00	-1.38E-01	-3.48E-01
W30-S01	5.81E+01	6.15E+01	2.12E+01	1.13E+00	-4.60E-01	0.00E+00
W30-S03	5.67E+01	5.33E+01	2.37E+01	1.50E+00	-3.04E+00	-1.64E-01
W30-S04	5.61E+01	5.86E+01	2.23E+01	9.10E-01	-1.07E+01	0.00E+00
W30-S05	5.54E+01	5.93E+01	2.22E+01	-4.37E-01	-8.22E+00	6.69E-01
W30-S07	5.66E+01	6.05E+01	2.25E+01	-1.25E+00	6.85E+00	0.00E+00
W30-S08	6.03E+01	6.16E+01	2.14E+01	-3.69E-02	-6.34E+00	1.10E-01
W31-S01	5.21E+01	5.87E+01	2.23E+01	-8.18E-01	-8.10E+00	1.02E+00

Sample	Orientation Phi_Avg_w	Orientation Phi_Median	Orientation Phi_Std	Orientation Theta_Avg	Orientation Theta_Avg_w	Orientation Theta_Median
	graus	graus	graus	graus	graus	graus
W31-S03	5.15E+01	6.09E+01	2.22E+01	3.35E-01	-1.61E+00	0.00E+00

Sample	Orientation Theta_Std	Perimeter Log_Std	Perimeter _Avg	Perimeter _Avg_w	Perimeter _Log_Avg	Perimeter _Log_Avg_w
	graus	n pixel	n pixel	n pixel	n pixel	n pixel
W02-S01	1.02E+02	1.19E+00	2.87E+01	1.59E+04	6.78E-01	8.33E+00
W02-S03	1.03E+02	1.40E+00	1.62E+01	5.55E+02	1.12E+00	4.95E+00
W02-S04	1.07E+02	1.00E+00	4.77E+00	3.31E+01	8.58E-01	2.46E+00
W02-S05	1.04E+02	8.49E-01	3.27E+00	3.40E+01	6.23E-01	2.02E+00
W03-S01	1.03E+02	1.93E+00	2.16E+02	1.82E+04	1.73E+00	9.27E+00
W03-S02	1.02E+02	1.62E+00	2.98E+01	5.65E+02	1.87E+00	5.18E+00
W03-S03	1.03E+02	1.56E+00	2.81E+01	1.31E+03	1.66E+00	5.59E+00
W03-S06	1.05E+02	1.18E+00	8.20E+00	2.91E+02	9.16E-01	3.87E+00
W03-S09	1.03E+02	1.48E+00	3.04E+01	1.54E+04	1.35E+00	7.32E+00
W03-S10	1.02E+02	1.58E+00	2.96E+01	7.68E+02	1.86E+00	5.31E+00
W06-S02	1.02E+02	1.59E+00	4.53E+01	3.47E+04	1.86E+00	7.69E+00
W06-S03	1.01E+02	1.59E+00	4.05E+01	2.01E+04	1.94E+00	6.67E+00
W07-S01	9.77E+01	1.70E+00	1.25E+02	5.80E+04	1.73E+00	1.02E+01
W07-S02	1.01E+02	1.97E+00	3.23E+02	2.95E+04	1.79E+00	9.79E+00
W07-S04	1.06E+02	2.24E+00	4.29E+02	2.48E+04	1.89E+00	9.61E+00
W08-S01	1.02E+02	1.63E+00	2.75E+01	2.09E+02	2.08E+00	4.51E+00
W08-S03	1.03E+02	1.42E+00	1.22E+02	4.84E+04	1.08E+00	1.01E+01
W08-S04	1.02E+02	1.74E+00	3.38E+01	3.44E+02	2.02E+00	5.03E+00
W09-S01	1.01E+02	1.82E+00	6.84E+01	4.96E+03	2.19E+00	6.72E+00
W09-S02	1.03E+02	1.98E+00	2.20E+02	1.60E+04	2.05E+00	8.97E+00
W09-S03	1.06E+02	1.67E+00	3.64E+01	8.83E+02	2.08E+00	5.29E+00
W09-S04	1.02E+02	1.68E+00	7.12E+01	1.28E+04	1.79E+00	8.03E+00
W09-S05	1.04E+02	1.76E+00	2.12E+02	3.62E+04	1.61E+00	9.78E+00
W10-S06	1.01E+02	1.36E+00	6.82E+01	3.50E+04	9.73E-01	9.57E+00
W10-S07	1.05E+02	1.22E+00	1.29E+01	1.54E+03	7.57E-01	5.59E+00
W11-S03	1.03E+02	1.52E+00	2.22E+01	1.89E+03	1.33E+00	5.68E+00
W11-S04	1.04E+02	1.34E+00	3.10E+01	2.53E+04	9.66E-01	8.01E+00
W14-S01	1.02E+02	1.48E+00	4.72E+01	1.47E+04	1.13E+00	8.23E+00
W14-S02	1.02E+02	1.19E+00	3.03E+01	4.86E+04	7.96E-01	9.12E+00
W14-S04	1.04E+02	1.37E+00	1.03E+02	3.87E+04	8.92E-01	9.90E+00
W14-S05	1.04E+02	1.48E+00	9.26E+01	3.72E+04	1.13E+00	9.66E+00
W14-S06	1.03E+02	1.50E+00	3.86E+01	1.55E+04	1.20E+00	7.88E+00
W14-S07	1.04E+02	1.29E+00	2.61E+01	1.99E+04	9.91E-01	7.78E+00
W14-S09	1.03E+02	1.50E+00	1.98E+01	8.01E+02	1.19E+00	5.26E+00
W14-S10	1.03E+02	1.27E+00	5.22E+01	3.79E+04	8.86E-01	9.61E+00
W14-S12	1.04E+02	1.38E+00	3.65E+01	1.49E+04	1.01E+00	8.22E+00
W15-S02	1.04E+02	1.27E+00	4.35E+01	3.38E+04	8.75E-01	9.39E+00

Sample	Orientation Theta_Std	Perimeter Log_Std	Perimeter Avg	Perimeter Avg_w	Perimeter Log_Avg	Perimeter Log_Avg_w
	graus	n pixel	n pixel	n pixel	n pixel	n pixel
W15-S03	1.04E+02	1.29E+00	1.43E+01	1.17E+03	9.41E-01	5.49E+00
W15-S05	1.01E+02	1.27E+00	1.69E+01	4.09E+03	9.75E-01	6.33E+00
W15-S06	1.02E+02	1.36E+00	6.46E+01	1.80E+04	8.67E-01	8.98E+00
W15-S07	1.03E+02	1.34E+00	9.66E+01	2.65E+04	8.46E-01	9.65E+00
W15-S08	1.04E+02	1.32E+00	8.14E+01	3.76E+04	8.95E-01	9.79E+00
W15-S09	1.05E+02	1.29E+00	4.75E+01	1.89E+04	9.05E-01	8.98E+00
W15-S12	1.07E+02	1.50E+00	8.76E+01	2.71E+04	1.02E+00	9.29E+00
W15-S14	1.04E+02	1.29E+00	1.21E+01	9.54E+02	1.10E+00	4.55E+00
W16-S01	1.03E+02	1.18E+00	8.28E+00	8.02E+02	9.23E-01	4.02E+00
W16-S03	1.02E+02	1.30E+00	2.23E+01	7.93E+03	8.67E-01	7.12E+00
W16-S05	1.05E+02	1.19E+00	6.48E+01	4.54E+04	7.05E-01	9.96E+00
W16-S06	1.06E+02	1.16E+00	5.69E+01	3.69E+04	7.56E-01	9.84E+00
W17-S01	1.03E+02	1.46E+00	1.17E+02	7.49E+04	1.37E+00	1.03E+01
W17-S03	1.02E+02	1.57E+00	7.31E+01	2.33E+04	1.59E+00	8.78E+00
W17-S04	1.03E+02	1.63E+00	1.13E+02	2.55E+04	1.69E+00	9.26E+00
W17-S05	1.04E+02	1.40E+00	6.94E+01	5.94E+04	9.73E-01	9.76E+00
W18-S01	1.04E+02	1.57E+00	6.74E+01	1.98E+04	1.31E+00	8.63E+00
W18-S02	9.76E+01	1.33E+00	3.09E+01	2.20E+04	9.51E-01	8.13E+00
W18-S03	1.03E+02	1.49E+00	1.02E+02	3.28E+04	1.08E+00	9.64E+00
W18-S04	1.04E+02	1.32E+00	5.23E+01	4.06E+04	9.46E-01	9.35E+00
W18-S05	1.03E+02	1.12E+00	7.99E+00	9.66E+02	8.66E-01	4.25E+00
W18-S06	1.05E+02	1.42E+00	8.70E+01	2.25E+04	9.19E-01	9.33E+00
W19-S01	1.02E+02	1.90E+00	1.30E+02	9.70E+04	2.35E+00	8.84E+00
W19-S02	1.02E+02	1.33E+00	6.97E+01	1.41E+05	9.02E-01	1.07E+01
W19-S03	1.02E+02	1.03E+00	5.79E+00	1.31E+03	7.52E-01	3.67E+00
W19-S04	1.02E+02	1.20E+00	1.01E+01	1.64E+03	9.06E-01	4.68E+00
W19-S05	1.04E+02	1.32E+00	3.08E+01	1.20E+05	9.34E-01	8.88E+00
W19-S06	1.03E+02	1.24E+00	8.95E+00	1.49E+02	9.69E-01	3.76E+00
W20-S01	1.02E+02	1.17E+00	8.11E+00	2.96E+03	9.70E-01	4.09E+00
W20-S02	1.04E+02	1.17E+00	6.06E+01	1.29E+05	7.54E-01	1.02E+01
W20-S03	1.04E+02	1.33E+00	2.06E+01	6.22E+03	1.06E+00	6.55E+00
W20-S04	1.04E+02	1.14E+00	7.06E+00	1.26E+02	9.21E-01	3.43E+00
W20-S05	1.04E+02	1.40E+00	6.24E+01	1.96E+04	9.98E-01	8.93E+00
W20-S06	1.02E+02	9.84E-01	4.53E+00	4.29E+01	7.56E-01	2.58E+00
W21-S01	1.04E+02	1.28E+00	7.12E+01	3.53E+04	8.63E-01	9.77E+00
W21-S02	1.03E+02	1.32E+00	2.62E+01	1.46E+04	9.77E-01	7.62E+00
W21-S03	1.04E+02	1.36E+00	8.17E+01	3.83E+04	9.64E-01	9.81E+00
W21-S04	1.04E+02	1.40E+00	8.36E+01	5.29E+04	1.05E+00	9.94E+00
W21-S05	1.03E+02	1.33E+00	7.41E+01	5.07E+04	9.45E-01	9.95E+00
W21-S06	1.04E+02	1.50E+00	1.26E+02	3.56E+04	1.09E+00	9.91E+00
W21-S07	1.05E+02	1.44E+00	3.59E+01	2.14E+04	1.10E+00	7.96E+00
W21-S08	9.98E+01	1.32E+00	8.50E+01	4.78E+04	9.52E-01	1.00E+01

Sample	Orientation Theta_Std	Perimeter Log_Std	Perimeter _Avg	Perimeter _Avg_w	Perimeter Log_Avg	Perimeter Log_Avg_w
	graus	n pixel	n pixel	n pixel	n pixel	n pixel
W22-S01	1.03E+02	9.76E-01	7.38E+01	2.65E+04	4.42E-01	9.77E+00
W22-S02	1.04E+02	1.39E+00	5.86E+01	5.33E+04	9.86E-01	9.63E+00
W22-S04	1.03E+02	1.75E+00	1.11E+02	1.42E+04	1.38E+00	8.71E+00
W22-S05	1.03E+02	1.18E+00	1.17E+02	1.34E+05	7.38E-01	1.12E+01
W24-S01	1.03E+02	1.51E+00	2.85E+01	2.02E+04	1.35E+00	6.78E+00
W24-S02	1.03E+02	1.45E+00	3.50E+01	3.03E+04	1.18E+00	8.09E+00
W24-S03	1.04E+02	1.34E+00	3.58E+01	3.33E+04	1.02E+00	8.68E+00
W24-S04	1.02E+02	1.20E+00	3.61E+01	2.97E+04	8.25E-01	9.12E+00
W24-S05	1.01E+02	1.33E+00	7.16E+01	2.95E+04	9.45E-01	9.61E+00
W25-S01	9.95E+01	1.02E+00	9.66E+00	1.62E+04	6.58E-01	6.39E+00
W25-S02	1.07E+02	1.56E+00	5.31E+01	3.39E+04	1.24E+00	8.62E+00
W25-S03	1.01E+02	1.43E+00	3.81E+01	1.74E+04	1.02E+00	8.05E+00
W25-S04	1.02E+02	1.33E+00	5.90E+01	5.62E+04	8.67E-01	9.73E+00
W26-S02	1.02E+02	1.39E+00	3.57E+01	1.63E+04	1.02E+00	8.02E+00
W27-S01	1.04E+02	1.25E+00	5.35E+01	2.19E+04	7.09E-01	9.21E+00
W27-S03	9.55E+01	1.23E+00	7.70E+00	6.55E+01	1.01E+00	3.27E+00
W27-S04	1.05E+02	1.30E+00	1.49E+01	5.00E+03	9.33E-01	6.16E+00
W27-S05	1.05E+02	1.05E+00	5.26E+00	1.28E+02	7.84E-01	2.93E+00
W27-S06	1.03E+02	1.17E+00	7.03E+00	7.75E+01	9.64E-01	3.21E+00
W28-S02	1.05E+02	1.48E+00	3.48E+01	2.42E+03	9.07E-01	6.98E+00
W28-S04	1.02E+02	1.54E+00	9.06E+01	2.54E+04	1.67E+00	9.06E+00
W28-S05	1.05E+02	9.84E-01	5.79E+00	1.89E+03	5.91E-01	4.23E+00
W29-S01	1.04E+02	1.23E+00	1.61E+01	7.00E+03	8.16E-01	6.97E+00
W29-S02	1.04E+02	9.58E-01	1.03E+01	1.54E+04	5.31E-01	7.13E+00
W30-S01	1.03E+02	8.31E-01	3.32E+00	1.12E+02	5.88E-01	2.30E+00
W30-S03	9.84E+01	1.04E+00	3.84E+01	8.25E+04	6.89E-01	1.02E+01
W30-S04	1.04E+02	1.81E+00	8.92E+01	1.58E+04	1.67E+00	8.22E+00
W30-S05	1.03E+02	1.40E+00	3.69E+01	1.25E+04	9.92E-01	7.93E+00
W30-S07	1.05E+02	1.39E+00	3.08E+01	1.90E+04	9.62E-01	7.76E+00
W30-S08	1.04E+02	1.26E+00	2.20E+01	3.71E+04	9.33E-01	7.95E+00
W31-S01	1.03E+02	1.27E+00	4.82E+01	2.23E+04	8.57E-01	9.05E+00
W31-S03	1.03E+02	1.71E+00	1.49E+02	3.73E+04	1.24E+00	9.66E+00

Sample	Perimeter _Log_ Max	Perimeter _Log_ Median	Perimeter _Max	Perimeter _Median	Perimeter _Std	Shape _VA3d _Avg
	n pixel	n pixel	n pixel	n pixel	n pixel	n pixel
W02-S01	1.12E+01	2.48E+00	7.31E+04	1.20E+01	6.58E+02	2.99E+00
W02-S03	8.46E+00	2.64E+00	4.73E+03	1.40E+01	9.02E+01	2.04E+00
W02-S04	7.19E+00	2.20E+00	1.32E+03	9.00E+00	1.15E+01	1.20E+00
W02-S05	7.48E+00	2.08E+00	1.77E+03	8.00E+00	9.72E+00	1.09E+00
W03-S01	1.11E+01	3.00E+00	6.95E+04	2.00E+01	1.86E+03	2.68E+00
W03-S02	8.99E+00	2.94E+00	8.03E+03	1.90E+01	1.12E+02	1.43E+00

Sample	Perimeter _Log_ Max	Perimeter _Log_ Median	Perimeter _Max	Perimeter _Median	Perimeter _Std	Shape _VA3d _Avg
	n pixel	n pixel	n pixel	n pixel	n pixel	n pixel
W03-S03	9.63E+00	2.77E+00	1.53E+04	1.60E+01	1.70E+02	1.52E+00
W03-S06	9.68E+00	2.40E+00	1.60E+04	1.10E+01	4.59E+01	1.42E+00
W03-S09	1.16E+01	2.64E+00	1.13E+05	1.40E+01	5.87E+02	1.70E+00
W03-S10	9.34E+00	2.83E+00	1.14E+04	1.70E+01	1.30E+02	1.40E+00
W06-S02	1.28E+01	2.83E+00	3.73E+05	1.70E+01	1.13E+03	1.74E+00
W06-S03	1.29E+01	2.89E+00	3.92E+05	1.80E+01	8.18E+02	1.71E+00
W07-S01	1.23E+01	2.83E+00	2.11E+05	1.70E+01	2.16E+03	2.14E+00
W07-S02	1.17E+01	3.04E+00	1.24E+05	2.10E+01	2.88E+03	2.96E+00
W07-S04	1.20E+01	3.47E+00	1.70E+05	3.20E+01	3.12E+03	4.12E+00
W08-S01	9.47E+00	3.14E+00	1.30E+04	2.30E+01	6.35E+01	1.45E+00
W08-S03	1.23E+01	2.56E+00	2.18E+05	1.30E+01	2.40E+03	4.19E+00
W08-S04	8.27E+00	3.22E+00	3.91E+03	2.50E+01	9.23E+01	1.50E+00
W09-S01	1.16E+01	3.22E+00	1.11E+05	2.50E+01	5.30E+02	2.15E+00
W09-S02	1.13E+01	3.14E+00	8.21E+04	2.30E+01	1.81E+03	3.37E+00
W09-S03	1.01E+01	3.04E+00	2.48E+04	2.10E+01	1.38E+02	1.65E+00
W09-S04	1.12E+01	2.89E+00	7.32E+04	1.80E+01	8.94E+02	2.05E+00
W09-S05	1.26E+01	2.83E+00	3.06E+05	1.70E+01	2.66E+03	3.33E+00
W10-S06	1.19E+01	2.48E+00	1.52E+05	1.20E+01	1.48E+03	2.98E+00
W10-S07	1.00E+01	2.56E+00	2.23E+04	1.30E+01	1.32E+02	1.95E+00
W11-S03	1.00E+01	2.77E+00	2.29E+04	1.60E+01	1.67E+02	1.49E+00
W11-S04	1.19E+01	2.48E+00	1.52E+05	1.20E+01	8.57E+02	2.59E+00
W14-S01	1.17E+01	2.64E+00	1.19E+05	1.40E+01	7.88E+02	2.60E+00
W14-S02	1.28E+01	2.40E+00	3.57E+05	1.10E+01	1.17E+03	2.38E+00
W14-S04	1.20E+01	2.48E+00	1.67E+05	1.20E+01	1.94E+03	4.04E+00
W14-S05	1.17E+01	2.56E+00	1.20E+05	1.30E+01	1.80E+03	3.50E+00
W14-S06	1.18E+01	2.64E+00	1.35E+05	1.40E+01	6.75E+02	2.18E+00
W14-S07	1.26E+01	2.40E+00	2.95E+05	1.10E+01	7.00E+02	2.09E+00
W14-S09	1.02E+01	2.77E+00	2.57E+04	1.60E+01	1.13E+02	1.83E+00
W14-S10	1.19E+01	2.40E+00	1.50E+05	1.10E+01	1.32E+03	2.68E+00
W14-S12	1.14E+01	2.56E+00	8.66E+04	1.30E+01	6.72E+02	2.22E+00
W15-S02	1.17E+01	2.40E+00	1.21E+05	1.10E+01	1.14E+03	2.33E+00
W15-S03	9.45E+00	2.48E+00	1.27E+04	1.20E+01	1.14E+02	1.62E+00
W15-S05	1.03E+01	2.40E+00	3.02E+04	1.10E+01	2.41E+02	1.76E+00
W15-S06	1.19E+01	2.48E+00	1.52E+05	1.20E+01	1.05E+03	3.33E+00
W15-S07	1.16E+01	2.48E+00	1.10E+05	1.20E+01	1.54E+03	3.29E+00
W15-S08	1.22E+01	2.48E+00	1.96E+05	1.20E+01	1.70E+03	3.68E+00
W15-S09	1.13E+01	2.40E+00	8.15E+04	1.10E+01	9.00E+02	2.37E+00
W15-S12	1.22E+01	2.71E+00	1.99E+05	1.50E+01	1.51E+03	4.31E+00
W15-S14	1.06E+01	2.48E+00	4.16E+04	1.20E+01	1.00E+02	1.56E+00
W16-S01	1.04E+01	2.40E+00	3.27E+04	1.10E+01	6.80E+01	1.35E+00
W16-S03	1.10E+01	2.56E+00	6.19E+04	1.30E+01	3.91E+02	2.17E+00

Sample	Perimeter _Log_ Max	Perimeter _Log_ Median	Perimeter _Max	Perimeter _Median	Perimeter _Std	Shape _VA3d _Avg
	n pixel	n pixel	n pixel	n pixel	n pixel	n pixel
W16-S05	1.21E+01	2.40E+00	1.72E+05	1.10E+01	1.65E+03	3.32E+00
W16-S06	1.19E+01	2.30E+00	1.49E+05	1.00E+01	1.39E+03	2.86E+00
W17-S01	1.28E+01	2.56E+00	3.51E+05	1.30E+01	2.88E+03	2.89E+00
W17-S03	1.24E+01	2.71E+00	2.34E+05	1.50E+01	1.24E+03	2.12E+00
W17-S04	1.14E+01	2.77E+00	8.74E+04	1.60E+01	1.60E+03	2.43E+00
W17-S05	1.23E+01	2.64E+00	2.30E+05	1.40E+01	2.03E+03	4.08E+00
W18-S01	1.15E+01	2.71E+00	9.87E+04	1.50E+01	1.11E+03	2.64E+00
W18-S02	1.15E+01	2.56E+00	1.04E+05	1.30E+01	7.74E+02	2.36E+00
W18-S03	1.22E+01	2.64E+00	1.93E+05	1.40E+01	1.80E+03	3.22E+00
W18-S04	1.24E+01	2.48E+00	2.52E+05	1.20E+01	1.41E+03	3.09E+00
W18-S05	9.93E+00	2.30E+00	2.06E+04	1.00E+01	8.02E+01	1.38E+00
W18-S06	1.17E+01	2.56E+00	1.26E+05	1.30E+01	1.34E+03	3.47E+00
W19-S01	1.33E+01	3.40E+00	6.17E+05	3.00E+01	3.45E+03	3.44E+00
W19-S02	1.33E+01	2.64E+00	6.10E+05	1.40E+01	3.12E+03	5.00E+00
W19-S03	1.05E+01	2.20E+00	3.67E+04	9.00E+00	6.85E+01	1.28E+00
W19-S04	1.14E+01	2.40E+00	8.80E+04	1.10E+01	1.19E+02	1.57E+00
W19-S05	1.37E+01	2.56E+00	8.97E+05	1.30E+01	1.88E+03	2.92E+00
W19-S06	8.32E+00	2.48E+00	4.09E+03	1.20E+01	3.51E+01	1.75E+00
W20-S01	1.13E+01	2.30E+00	7.87E+04	1.00E+01	1.21E+02	1.34E+00
W20-S02	1.45E+01	2.40E+00	2.08E+06	1.10E+01	2.78E+03	3.82E+00
W20-S03	1.12E+01	2.48E+00	7.61E+04	1.20E+01	3.30E+02	1.85E+00
W20-S04	8.17E+00	2.30E+00	3.54E+03	1.00E+01	2.73E+01	1.22E+00
W20-S05	1.19E+01	2.48E+00	1.50E+05	1.20E+01	1.08E+03	3.01E+00
W20-S06	6.57E+00	2.20E+00	7.13E+02	9.00E+00	1.26E+01	1.04E+00
W21-S01	1.20E+01	2.40E+00	1.59E+05	1.10E+01	1.51E+03	2.79E+00
W21-S02	1.17E+01	2.48E+00	1.23E+05	1.20E+01	5.93E+02	2.10E+00
W21-S03	1.19E+01	2.48E+00	1.50E+05	1.20E+01	1.69E+03	2.86E+00
W21-S04	1.26E+01	2.56E+00	2.90E+05	1.30E+01	2.05E+03	3.18E+00
W21-S05	1.21E+01	2.48E+00	1.86E+05	1.20E+01	1.87E+03	3.05E+00
W21-S06	1.19E+01	2.64E+00	1.51E+05	1.40E+01	2.04E+03	2.96E+00
W21-S07	1.20E+01	2.64E+00	1.58E+05	1.40E+01	8.25E+02	2.36E+00
W21-S08	1.25E+01	2.48E+00	2.65E+05	1.20E+01	1.98E+03	3.51E+00
W22-S01	1.19E+01	2.20E+00	1.47E+05	9.00E+00	1.38E+03	4.30E+00
W22-S02	1.24E+01	2.64E+00	2.38E+05	1.40E+01	1.73E+03	3.87E+00
W22-S04	1.10E+01	2.89E+00	5.85E+04	1.80E+01	1.22E+03	3.37E+00
W22-S05	1.32E+01	2.48E+00	5.20E+05	1.20E+01	3.94E+03	8.47E+00
W24-S01	1.29E+01	2.71E+00	3.99E+05	1.50E+01	6.62E+02	1.73E+00
W24-S02	1.25E+01	2.64E+00	2.66E+05	1.40E+01	9.67E+02	2.05E+00
W24-S03	1.18E+01	2.48E+00	1.39E+05	1.20E+01	1.06E+03	2.43E+00
W24-S04	1.19E+01	2.40E+00	1.46E+05	1.10E+01	9.88E+02	2.33E+00
W24-S05	1.21E+01	2.48E+00	1.76E+05	1.20E+01	1.39E+03	2.51E+00

Sample	Perimeter _Log_ Max	Perimeter _Log_ Median	Perimeter _Max	Perimeter _Median	Perimeter _Std	Shape _VA3d _Avg
	n pixel	n pixel	n pixel	n pixel	n pixel	n pixel
W25-S01	1.15E+01	2.30E+00	9.65E+04	1.00E+01	3.71E+02	1.85E+00
W25-S02	1.20E+01	2.77E+00	1.56E+05	1.60E+01	1.27E+03	2.44E+00
W25-S03	1.14E+01	2.64E+00	9.28E+04	1.40E+01	7.61E+02	2.57E+00
W25-S04	1.24E+01	2.56E+00	2.47E+05	1.30E+01	1.79E+03	3.28E+00
W26-S02	1.17E+01	2.56E+00	1.19E+05	1.30E+01	7.22E+02	2.37E+00
W27-S01	1.16E+01	2.48E+00	1.13E+05	1.20E+01	1.02E+03	2.73E+00
W27-S03	7.62E+00	2.48E+00	2.03E+03	1.20E+01	2.00E+01	1.16E+00
W27-S04	1.05E+01	2.56E+00	3.53E+04	1.30E+01	2.19E+02	1.59E+00
W27-S05	9.48E+00	2.30E+00	1.31E+04	1.00E+01	2.15E+01	1.18E+00
W27-S06	7.94E+00	2.40E+00	2.81E+03	1.10E+01	2.12E+01	1.25E+00
W28-S02	9.63E+00	2.71E+00	1.53E+04	1.50E+01	2.59E+02	2.18E+00
W28-S04	1.19E+01	2.64E+00	1.46E+05	1.40E+01	1.39E+03	2.37E+00
W28-S05	1.04E+01	2.30E+00	3.39E+04	1.00E+01	9.04E+01	1.45E+00
W29-S01	1.11E+01	2.48E+00	6.79E+04	1.20E+01	2.77E+02	1.74E+00
W29-S02	1.20E+01	2.30E+00	1.68E+05	1.00E+01	3.62E+02	1.87E+00
W30-S01	8.77E+00	2.08E+00	6.43E+03	8.00E+00	1.79E+01	1.11E+00
W30-S03	1.27E+01	2.20E+00	3.27E+05	9.00E+00	1.71E+03	2.93E+00
W30-S04	1.18E+01	3.00E+00	1.36E+05	2.00E+01	1.09E+03	2.53E+00
W30-S05	1.17E+01	2.56E+00	1.15E+05	1.30E+01	6.52E+02	2.68E+00
W30-S07	1.20E+01	2.64E+00	1.68E+05	1.40E+01	7.35E+02	2.79E+00
W30-S08	1.25E+01	2.40E+00	2.59E+05	1.10E+01	8.55E+02	2.16E+00
W31-S01	1.13E+01	2.40E+00	8.22E+04	1.10E+01	9.86E+02	2.68E+00
W31-S03	1.26E+01	2.83E+00	2.91E+05	1.70E+01	2.07E+03	3.01E+00

Sample	Shape_ VA3d_ Avg_w	Shape_ VA3d_ Median	Shape_V A3d_Std	Volume Log_Std	Volume _Avg	Volume _Avg_w
	adim	adim	adim	n voxel	n voxel	n voxel
W02-S01	1.79E+02	1.06E+00	1.74E+01	1.52E+00	1.73E+06	9.82E+08
W02-S03	1.26E+01	1.19E+00	3.28E+00	1.72E+00	3.12E+05	1.15E+07
W02-S04	2.47E+00	9.30E-01	9.35E-01	9.95E-01	3.90E+04	2.71E+05
W02-S05	2.42E+00	8.69E-01	8.02E-01	1.32E+00	8.81E+05	9.88E+06
W03-S01	3.98E+01	1.18E+00	6.85E+00	2.21E+00	7.72E+06	7.52E+08
W03-S02	4.53E+00	1.10E+00	1.15E+00	1.96E+00	2.13E+06	6.35E+07
W03-S03	9.96E+00	1.07E+00	1.90E+00	1.88E+00	1.60E+06	1.08E+08
W03-S06	7.25E+00	9.88E-01	1.82E+00	1.56E+00	3.51E+06	1.64E+08
W03-S09	6.70E+01	1.05E+00	5.12E+00	1.80E+00	3.98E+06	2.50E+09
W03-S10	5.21E+00	1.07E+00	1.21E+00	1.89E+00	1.91E+06	6.18E+07
W06-S02	1.90E+02	1.12E+00	9.73E+00	1.91E+00	6.33E+06	6.03E+09
W06-S03	1.49E+02	1.11E+00	8.32E+00	1.92E+00	8.94E+06	7.44E+09
W07-S01	2.99E+01	1.18E+00	6.35E+00	2.03E+00	1.37E+07	8.46E+09
W07-S02	5.19E+01	1.14E+00	9.44E+00	2.27E+00	4.12E+07	4.96E+09

Sample	Shape_ VA3d_ Avg_w	Shape_ VA3d_ Median	Shape_V A3d_Std	Volume Log_Std	Volume _Avg	Volume _Avg_w
	adim	adim	adim	n voxel	n voxel	n voxel
W07-S04	6.11E+01	1.36E+00	1.22E+01	2.56E+00	2.59E+07	1.48E+09
W08-S01	2.97E+00	1.21E+00	8.99E-01	2.00E+00	7.05E+06	8.14E+07
W08-S03	3.61E+02	1.02E+00	3.36E+01	1.71E+00	3.67E+07	1.54E+10
W08-S04	3.34E+00	1.23E+00	9.92E-01	2.08E+00	2.81E+06	3.99E+07
W09-S01	3.59E+01	1.24E+00	5.13E+00	2.12E+00	1.21E+07	9.45E+08
W09-S02	7.82E+01	1.24E+00	1.23E+01	2.23E+00	2.15E+07	1.73E+09
W09-S03	5.72E+00	1.18E+00	1.58E+00	1.98E+00	5.47E+06	2.60E+08
W09-S04	7.25E+01	1.11E+00	7.33E+00	1.99E+00	4.57E+06	6.24E+08
W09-S05	1.21E+02	1.15E+00	1.50E+01	2.09E+00	1.10E+07	1.47E+09
W10-S06	1.81E+02	1.09E+00	1.65E+01	1.67E+00	1.20E+07	6.50E+09
W10-S07	2.03E+01	1.13E+00	3.82E+00	1.55E+00	6.36E+06	8.52E+08
W11-S03	8.60E+00	1.11E+00	1.53E+00	1.79E+00	2.39E+06	2.69E+08
W11-S04	2.87E+02	1.10E+00	1.92E+01	1.66E+00	6.27E+06	5.49E+09
W14-S01	1.08E+02	1.15E+00	1.12E+01	1.79E+00	1.27E+07	4.88E+09
W14-S02	3.99E+02	1.02E+00	2.25E+01	1.56E+00	2.55E+07	3.64E+10
W14-S04	2.16E+02	1.10E+00	2.41E+01	1.69E+00	2.28E+07	9.32E+09
W14-S05	2.39E+02	1.13E+00	2.21E+01	1.75E+00	2.98E+06	1.18E+09
W14-S06	7.67E+01	1.14E+00	7.79E+00	1.80E+00	1.06E+07	6.85E+09
W14-S07	1.94E+02	1.02E+00	1.40E+01	1.63E+00	8.22E+06	6.81E+09
W14-S09	9.16E+00	1.22E+00	2.24E+00	1.79E+00	4.89E+06	2.22E+08
W14-S10	1.71E+02	1.06E+00	1.50E+01	1.60E+00	1.85E+07	1.70E+10
W14-S12	7.97E+01	1.10E+00	7.76E+00	1.69E+00	1.03E+07	5.82E+09
W15-S02	1.33E+02	1.06E+00	1.12E+01	1.60E+00	1.00E+07	1.01E+10
W15-S03	1.03E+01	1.06E+00	2.08E+00	1.64E+00	3.03E+06	3.13E+08
W15-S05	3.90E+01	1.02E+00	4.54E+00	1.61E+00	4.52E+06	1.04E+09
W15-S06	1.22E+02	1.09E+00	1.57E+01	1.68E+00	1.82E+07	5.13E+09
W15-S07	9.95E+01	1.07E+00	1.42E+01	1.67E+00	2.96E+07	8.92E+09
W15-S08	2.46E+02	1.06E+00	2.41E+01	1.65E+00	3.02E+07	1.44E+10
W15-S09	9.25E+01	1.03E+00	1.01E+01	1.62E+00	2.05E+07	9.90E+09
W15-S12	2.45E+02	1.20E+00	2.70E+01	1.80E+00	1.94E+07	6.05E+09
W15-S14	1.62E+01	1.00E+00	2.89E+00	1.63E+00	6.09E+06	6.69E+08
W16-S01	7.85E+00	1.02E+00	1.41E+00	1.53E+00	2.19E+06	1.07E+08
W16-S03	6.92E+01	1.14E+00	7.19E+00	1.64E+00	6.45E+06	2.79E+09
W16-S05	1.86E+02	1.07E+00	1.94E+01	1.52E+00	9.48E+06	6.73E+09
W16-S06	1.68E+02	9.98E-01	1.62E+01	1.51E+00	2.05E+07	1.61E+10
W17-S01	3.79E+02	1.03E+00	2.48E+01	1.76E+00	9.84E+06	6.89E+09
W17-S03	1.21E+02	1.06E+00	1.12E+01	1.87E+00	1.29E+07	4.63E+09
W17-S04	1.11E+02	1.06E+00	1.12E+01	1.93E+00	1.06E+07	2.64E+09
W17-S05	6.91E+02	1.11E+00	4.77E+01	1.67E+00	3.70E+06	3.03E+09
W18-S01	1.37E+02	1.12E+00	1.33E+01	1.87E+00	8.46E+06	2.79E+09
W18-S02	1.64E+02	1.12E+00	1.17E+01	1.64E+00	2.61E+06	2.06E+09

Sample	Shape_ VA3d_ Avg_w	Shape_ VA3d_ Median	Shape_V A3d_Std	Volume Log_Std	Volume _Avg	Volume _Avg_w
	adim	adim	adim	n voxel	n voxel	n voxel
W18-S03	1.62E+02	1.13E+00	1.94E+01	1.77E+00	1.30E+07	4.40E+09
W18-S04	3.32E+02	1.06E+00	2.44E+01	1.65E+00	1.05E+07	8.60E+09
W18-S05	1.48E+01	9.61E-01	2.25E+00	1.49E+00	1.27E+06	1.93E+08
W18-S06	9.54E+01	1.15E+00	1.30E+01	1.75E+00	1.07E+07	3.17E+09
W19-S01	1.05E+03	1.34E+00	4.79E+01	2.16E+00	1.60E+07	9.61E+09
W19-S02	1.99E+03	1.11E+00	9.02E+01	1.62E+00	2.14E+07	3.99E+10
W19-S03	1.21E+01	9.35E-01	1.63E+00	1.42E+00	1.76E+06	2.10E+08
W19-S04	2.60E+01	1.01E+00	3.44E+00	1.56E+00	5.19E+06	1.27E+09
W19-S05	1.91E+03	1.09E+00	5.85E+01	1.63E+00	1.74E+07	5.86E+10
W19-S06	6.81E+00	1.10E+00	2.35E+00	1.59E+00	8.71E+06	1.69E+08
W20-S01	2.63E+01	9.62E-01	2.80E+00	1.54E+00	6.66E+06	1.51E+09
W20-S02	1.16E+03	9.88E-01	5.75E+01	1.50E+00	3.77E+07	9.25E+10
W20-S03	5.60E+01	1.04E+00	5.67E+00	1.65E+00	2.63E+06	8.85E+08
W20-S04	3.12E+00	9.45E-01	9.11E-01	1.52E+00	1.75E+06	3.59E+07
W20-S05	1.49E+02	1.07E+00	1.67E+01	1.72E+00	1.68E+07	5.74E+09
W20-S06	1.70E+00	8.83E-01	5.11E-01	1.38E+00	9.02E+04	9.41E+05
W21-S01	1.39E+02	1.02E+00	1.54E+01	1.60E+00	3.18E+07	1.96E+10
W21-S02	1.42E+02	1.04E+00	1.14E+01	1.65E+00	1.04E+07	6.43E+09
W21-S03	1.45E+02	1.07E+00	1.40E+01	1.69E+00	1.64E+07	8.59E+09
W21-S04	3.26E+02	1.06E+00	2.51E+01	1.71E+00	2.80E+07	1.98E+10
W21-S05	2.66E+02	1.07E+00	2.11E+01	1.67E+00	2.03E+07	1.43E+10
W21-S06	1.15E+02	1.12E+00	1.34E+01	1.81E+00	1.35E+07	3.74E+09
W21-S07	1.81E+02	1.13E+00	1.31E+01	1.76E+00	1.50E+07	1.12E+10
W21-S08	3.26E+02	1.01E+00	2.77E+01	1.62E+00	4.04E+07	2.35E+10
W22-S01	9.98E+01	9.53E-01	1.78E+01	1.38E+00	2.92E+07	1.06E+10
W22-S02	6.35E+02	1.11E+00	4.06E+01	1.68E+00	2.62E+07	2.53E+10
W22-S04	8.52E+01	1.27E+00	1.26E+01	1.99E+00	6.09E+06	8.72E+08
W22-S05	1.63E+03	1.02E+00	1.11E+02	1.50E+00	3.17E+07	3.80E+10
W24-S01	1.01E+02	1.09E+00	6.28E+00	1.82E+00	1.32E+07	1.17E+10
W24-S02	2.23E+02	1.09E+00	1.28E+01	1.75E+00	1.48E+07	1.39E+10
W24-S03	3.42E+02	1.05E+00	2.08E+01	1.65E+00	6.23E+06	6.16E+09
W24-S04	1.84E+02	9.98E-01	1.40E+01	1.55E+00	1.49E+07	1.47E+10
W24-S05	1.14E+02	1.02E+00	1.21E+01	1.65E+00	1.88E+07	8.66E+09
W25-S01	1.95E+02	1.01E+00	1.00E+01	1.40E+00	1.18E+06	1.20E+09
W25-S02	2.11E+02	1.18E+00	1.44E+01	1.84E+00	2.14E+06	1.48E+09
W25-S03	1.28E+02	1.17E+00	1.19E+01	1.75E+00	4.43E+06	1.65E+09
W25-S04	3.75E+02	1.14E+00	2.72E+01	1.63E+00	9.90E+06	1.09E+10
W26-S02	1.27E+02	1.10E+00	1.10E+01	1.70E+00	5.64E+06	2.83E+09
W27-S01	7.50E+01	1.12E+00	9.34E+00	1.58E+00	5.29E+06	2.17E+09
W27-S03	1.81E+00	1.01E+00	5.63E-01	1.56E+00	1.20E+06	1.17E+07
W27-S04	1.75E+01	1.10E+00	2.28E+00	1.62E+00	1.72E+06	8.78E+08

Sample	Shape_ VA3d_ Avg_w	Shape_ VA3d_ Median	Shape_V A3d_Std	Volume Log_Std	Volume _Avg	Volume _Avg_w
	adim	adim	adim	n voxel	n voxel	n voxel
W27-S05	2.91E+00	9.53E-01	8.64E-01	1.45E+00	3.50E+06	6.13E+07
W27-S06	2.55E+00	1.01E+00	8.22E-01	1.55E+00	1.83E+06	2.56E+07
W28-S02	9.78E+00	1.23E+00	2.80E+00	1.78E+00	2.73E+06	2.41E+08
W28-S04	1.02E+02	1.09E+00	1.02E+01	1.84E+00	1.18E+07	3.71E+09
W28-S05	2.09E+01	1.02E+00	2.42E+00	1.40E+00	1.34E+06	7.17E+08
W29-S01	2.88E+01	1.05E+00	3.52E+00	1.54E+00	5.78E+06	4.17E+09
W29-S02	1.25E+02	9.95E-01	8.61E+00	1.37E+00	6.31E+06	7.52E+09
W30-S01	4.36E+00	8.63E-01	1.04E+00	1.30E+00	2.54E+06	9.65E+07
W30-S03	5.57E+02	9.96E-01	3.02E+01	1.43E+00	7.98E+06	1.83E+10
W30-S04	6.85E+01	1.24E+00	7.66E+00	2.08E+00	6.18E+06	9.70E+08
W30-S05	1.24E+02	1.14E+00	1.27E+01	1.72E+00	1.12E+07	3.56E+09
W30-S07	2.28E+02	1.21E+00	1.82E+01	1.70E+00	7.27E+06	4.02E+09
W30-S08	3.99E+02	1.05E+00	1.83E+01	1.59E+00	6.25E+06	1.23E+10
W31-S01	1.23E+02	1.02E+00	1.24E+01	1.61E+00	1.08E+07	5.73E+09
W31-S03	6.25E+01	1.25E+00	8.26E+00	2.02E+00	1.20E+07	2.70E+09

Sample	Volume _Log _Avg	Volume _Log_ Avg_w	Volume _Log_ Max	Volume _Log_ Median	Volume _Max	Volume _Median
	n voxel	n voxel	n voxel	n voxel	n voxel	n voxel
W02-S01	1.14E+01	1.91E+01	2.23E+01	1.33E+01	4.90E+09	6.18E+05
W02-S03	1.06E+01	1.45E+01	1.86E+01	1.23E+01	1.20E+08	2.30E+05
W02-S04	9.88E+00	1.15E+01	1.62E+01	1.12E+01	1.14E+07	7.28E+04
W02-S05	1.28E+01	1.42E+01	2.05E+01	1.46E+01	8.00E+08	2.15E+06
W03-S01	1.13E+01	1.94E+01	2.25E+01	1.27E+01	5.93E+09	3.19E+05
W03-S02	1.25E+01	1.61E+01	2.11E+01	1.37E+01	1.43E+09	8.56E+05
W03-S03	1.21E+01	1.63E+01	2.12E+01	1.33E+01	1.56E+09	6.17E+05
W03-S06	1.35E+01	1.66E+01	2.32E+01	1.52E+01	1.24E+10	3.95E+06
W03-S09	1.26E+01	1.89E+01	2.40E+01	1.41E+01	2.56E+10	1.34E+06
W03-S10	1.25E+01	1.61E+01	2.07E+01	1.36E+01	9.81E+08	8.04E+05
W06-S02	1.32E+01	1.92E+01	2.47E+01	1.43E+01	5.50E+10	1.67E+06
W06-S03	1.37E+01	1.87E+01	2.58E+01	1.48E+01	1.65E+11	2.61E+06
W07-S01	1.20E+01	2.15E+01	2.44E+01	1.33E+01	3.96E+10	5.92E+05
W07-S02	1.23E+01	2.13E+01	2.41E+01	1.36E+01	2.83E+10	8.08E+05
W07-S04	1.21E+01	2.01E+01	2.32E+01	1.38E+01	1.15E+10	1.03E+06
W08-S01	1.40E+01	1.67E+01	2.30E+01	1.52E+01	9.72E+09	3.99E+06
W08-S03	1.31E+01	2.23E+01	2.54E+01	1.47E+01	1.04E+11	2.54E+06
W08-S04	1.28E+01	1.61E+01	2.04E+01	1.41E+01	7.24E+08	1.28E+06
W09-S01	1.38E+01	1.85E+01	2.36E+01	1.49E+01	1.86E+10	2.92E+06
W09-S02	1.27E+01	2.01E+01	2.34E+01	1.39E+01	1.43E+10	1.05E+06
W09-S03	1.35E+01	1.69E+01	2.34E+01	1.46E+01	1.43E+10	2.26E+06
W09-S04	1.24E+01	1.86E+01	2.24E+01	1.36E+01	5.09E+09	8.30E+05

Sample	Volume _Log _Avg	Volume _Log_ Avg_w	Volume _Log_ Max	Volume _Log_ Median	Volume _Max	Volume _Median
	n voxel	n voxel	n voxel	n voxel	n voxel	n voxel
W09-S05	1.18E+01	1.99E+01	2.32E+01	1.32E+01	1.19E+10	5.46E+05
W10-S06	1.23E+01	2.12E+01	2.42E+01	1.41E+01	3.35E+10	1.30E+06
W10-S07	1.35E+01	1.83E+01	2.38E+01	1.54E+01	2.21E+10	5.11E+06
W11-S03	1.25E+01	1.69E+01	2.27E+01	1.40E+01	7.06E+09	1.24E+06
W11-S04	1.27E+01	1.98E+01	2.44E+01	1.45E+01	4.07E+10	2.00E+06
W14-S01	1.30E+01	2.04E+01	2.48E+01	1.47E+01	5.91E+10	2.32E+06
W14-S02	1.38E+01	2.22E+01	2.64E+01	1.57E+01	3.06E+11	6.48E+06
W14-S04	1.25E+01	2.17E+01	2.48E+01	1.44E+01	5.83E+10	1.76E+06
W14-S05	1.11E+01	1.92E+01	2.26E+01	1.27E+01	6.61E+09	3.42E+05
W14-S06	1.30E+01	2.01E+01	2.53E+01	1.47E+01	9.26E+10	2.42E+06
W14-S07	1.31E+01	2.01E+01	2.50E+01	1.48E+01	7.55E+10	2.73E+06
W14-S09	1.33E+01	1.73E+01	2.27E+01	1.50E+01	7.50E+09	3.41E+06
W14-S10	1.28E+01	2.22E+01	2.55E+01	1.46E+01	1.19E+11	2.11E+06
W14-S12	1.29E+01	2.05E+01	2.48E+01	1.46E+01	5.97E+10	2.17E+06
W15-S02	1.23E+01	2.16E+01	2.45E+01	1.41E+01	4.51E+10	1.28E+06
W15-S03	1.27E+01	1.74E+01	2.24E+01	1.45E+01	5.53E+09	1.99E+06
W15-S05	1.31E+01	1.84E+01	2.37E+01	1.48E+01	1.97E+10	2.60E+06
W15-S06	1.28E+01	2.11E+01	2.45E+01	1.47E+01	4.29E+10	2.31E+06
W15-S07	1.27E+01	2.18E+01	2.50E+01	1.45E+01	7.32E+10	1.96E+06
W15-S08	1.30E+01	2.21E+01	2.54E+01	1.48E+01	1.08E+11	2.79E+06
W15-S09	1.31E+01	2.16E+01	2.52E+01	1.49E+01	8.85E+10	2.89E+06
W15-S12	1.28E+01	2.11E+01	2.45E+01	1.46E+01	4.23E+10	2.20E+06
W15-S14	1.39E+01	1.74E+01	2.43E+01	1.54E+01	3.70E+10	5.10E+06
W16-S01	1.31E+01	1.61E+01	2.18E+01	1.48E+01	3.07E+09	2.78E+06
W16-S03	1.29E+01	1.94E+01	2.40E+01	1.48E+01	2.60E+10	2.68E+06
W16-S05	1.20E+01	2.15E+01	2.45E+01	1.39E+01	4.38E+10	1.07E+06
W16-S06	1.28E+01	2.21E+01	2.55E+01	1.46E+01	1.24E+11	2.22E+06
W17-S01	1.20E+01	2.11E+01	2.45E+01	1.34E+01	4.50E+10	6.85E+05
W17-S03	1.30E+01	2.04E+01	2.45E+01	1.43E+01	4.53E+10	1.66E+06
W17-S04	1.24E+01	2.03E+01	2.35E+01	1.37E+01	1.57E+10	8.48E+05
W17-S05	1.15E+01	1.96E+01	2.36E+01	1.33E+01	1.71E+10	5.75E+05
W18-S01	1.24E+01	2.00E+01	2.37E+01	1.40E+01	1.96E+10	1.21E+06
W18-S02	1.19E+01	1.89E+01	2.35E+01	1.37E+01	1.59E+10	9.07E+05
W18-S03	1.21E+01	2.11E+01	2.41E+01	1.39E+01	2.84E+10	1.04E+06
W18-S04	1.26E+01	2.11E+01	2.50E+01	1.44E+01	7.00E+10	1.74E+06
W18-S05	1.25E+01	1.59E+01	2.23E+01	1.42E+01	5.01E+09	1.45E+06
W18-S06	1.18E+01	2.07E+01	2.38E+01	1.37E+01	2.24E+10	8.81E+05
W19-S01	1.36E+01	2.01E+01	2.53E+01	1.47E+01	9.88E+10	2.42E+06
W19-S02	1.32E+01	2.26E+01	2.61E+01	1.51E+01	2.21E+11	3.48E+06
W19-S03	1.31E+01	1.58E+01	2.29E+01	1.48E+01	9.23E+09	2.71E+06
W19-S04	1.37E+01	1.75E+01	2.51E+01	1.54E+01	8.14E+10	4.86E+06

Sample	Volume _Log _Avg	Volume _Log_ Avg_w	Volume _Log_ Max	Volume _Log_ Median	Volume _Max	Volume _Median
	n voxel	n voxel	n voxel	n voxel	n voxel	n voxel
W19-S05	1.38E+01	2.16E+01	2.68E+01	1.56E+01	4.17E+11	6.17E+06
W19-S06	1.44E+01	1.73E+01	2.26E+01	1.61E+01	6.22E+09	1.00E+07
W20-S01	1.42E+01	1.72E+01	2.54E+01	1.59E+01	1.06E+11	7.73E+06
W20-S02	1.35E+01	2.31E+01	2.81E+01	1.53E+01	1.53E+12	4.48E+06
W20-S03	1.25E+01	1.79E+01	2.36E+01	1.41E+01	1.71E+10	1.33E+06
W20-S04	1.30E+01	1.55E+01	2.07E+01	1.46E+01	9.77E+08	2.30E+06
W20-S05	1.29E+01	2.09E+01	2.45E+01	1.47E+01	4.35E+10	2.39E+06
W20-S06	1.04E+01	1.21E+01	1.70E+01	1.21E+01	2.32E+07	1.77E+05
W21-S01	1.30E+01	2.24E+01	2.55E+01	1.48E+01	1.22E+11	2.61E+06
W21-S02	1.34E+01	2.01E+01	2.51E+01	1.51E+01	7.79E+10	3.57E+06
W21-S03	1.23E+01	2.16E+01	2.49E+01	1.41E+01	6.51E+10	1.27E+06
W21-S04	1.30E+01	2.23E+01	2.57E+01	1.46E+01	1.41E+11	2.27E+06
W21-S05	1.28E+01	2.18E+01	2.51E+01	1.46E+01	8.17E+10	2.22E+06
W21-S06	1.20E+01	2.08E+01	2.36E+01	1.37E+01	1.85E+10	8.81E+05
W21-S07	1.34E+01	2.06E+01	2.53E+01	1.52E+01	9.78E+10	3.92E+06
W21-S08	1.34E+01	2.26E+01	2.58E+01	1.51E+01	1.54E+11	3.52E+06
W22-S01	1.27E+01	2.20E+01	2.56E+01	1.47E+01	1.28E+11	2.43E+06
W22-S02	1.35E+01	2.21E+01	2.60E+01	1.54E+01	1.94E+11	4.65E+06
W22-S04	1.16E+01	1.92E+01	2.24E+01	1.32E+01	5.38E+09	5.60E+05
W22-S05	1.28E+01	2.31E+01	2.62E+01	1.47E+01	2.50E+11	2.44E+06
W24-S01	1.38E+01	1.96E+01	2.61E+01	1.53E+01	2.17E+11	4.27E+06
W24-S02	1.36E+01	2.07E+01	2.53E+01	1.52E+01	9.97E+10	4.00E+06
W24-S03	1.26E+01	2.03E+01	2.43E+01	1.43E+01	3.48E+10	1.59E+06
W24-S04	1.31E+01	2.18E+01	2.51E+01	1.49E+01	8.30E+10	2.82E+06
W24-S05	1.26E+01	2.16E+01	2.48E+01	1.43E+01	5.65E+10	1.65E+06
W25-S01	1.22E+01	1.76E+01	2.31E+01	1.41E+01	1.09E+10	1.30E+06
W25-S02	1.14E+01	1.86E+01	2.32E+01	1.31E+01	1.18E+10	4.92E+05
W25-S03	1.23E+01	1.91E+01	2.35E+01	1.41E+01	1.66E+10	1.31E+06
W25-S04	1.22E+01	2.12E+01	2.49E+01	1.41E+01	6.83E+10	1.29E+06
W26-S02	1.24E+01	1.96E+01	2.37E+01	1.42E+01	1.90E+10	1.43E+06
W27-S01	1.15E+01	2.00E+01	2.32E+01	1.35E+01	1.14E+10	7.11E+05
W27-S03	1.26E+01	1.49E+01	2.01E+01	1.43E+01	5.61E+08	1.61E+06
W27-S04	1.21E+01	1.74E+01	2.28E+01	1.39E+01	7.95E+09	1.07E+06
W27-S05	1.38E+01	1.60E+01	2.22E+01	1.56E+01	4.57E+09	5.91E+06
W27-S06	1.30E+01	1.54E+01	2.11E+01	1.47E+01	1.51E+09	2.45E+06
W28-S02	1.16E+01	1.79E+01	2.19E+01	1.36E+01	3.17E+09	8.12E+05
W28-S04	1.28E+01	2.03E+01	2.47E+01	1.39E+01	5.21E+10	1.13E+06
W28-S05	1.25E+01	1.63E+01	2.35E+01	1.45E+01	1.62E+10	1.99E+06
W29-S01	1.31E+01	1.95E+01	2.46E+01	1.48E+01	5.05E+10	2.81E+06
W29-S02	1.35E+01	1.99E+01	2.51E+01	1.55E+01	7.70E+10	5.29E+06
W30-S01	1.38E+01	1.55E+01	2.29E+01	1.56E+01	8.97E+09	6.09E+06

Sample	Volume _Log _Avg	Volume _Log_ Avg_w	Volume _Log_ Max	Volume _Log_ Median	Volume _Max	Volume _Median
	n voxel	n voxel	n voxel	n voxel	n voxel	n voxel
W30-S03	1.25E+01	2.18E+01	2.58E+01	1.43E+01	1.60E+11	1.67E+06
W30-S04	1.24E+01	1.89E+01	2.26E+01	1.38E+01	6.51E+09	9.99E+05
W30-S05	1.32E+01	2.00E+01	2.44E+01	1.50E+01	3.78E+10	3.20E+06
W30-S07	1.29E+01	1.97E+01	2.46E+01	1.48E+01	4.77E+10	2.68E+06
W30-S08	1.31E+01	2.01E+01	2.55E+01	1.48E+01	1.14E+11	2.73E+06
W31-S01	1.25E+01	2.09E+01	2.43E+01	1.43E+01	3.62E+10	1.61E+06
W31-S03	1.17E+01	2.04E+01	2.37E+01	1.35E+01	1.99E+10	7.14E+05

Sample	Volume _Std	VoxelFace Area Log_Std	VoxelFace Area _Avg	VoxelFace Area_ Avg_w	VoxelFace Area_Log_Avg	VoxelFace Area_Log Avg_w
	n voxel	n voxel	n voxel	n voxel	n voxel	n voxel
W02-S01	4.45E+07	9.76E-01	1.73E+11	8.51E+13	2.40E+01	3.08E+01
W02-S03	2.12E+06	1.15E+00	1.15E+11	3.19E+12	2.43E+01	2.76E+01
W02-S04	9.43E+04	8.08E-01	4.64E+10	2.50E+11	2.41E+01	2.54E+01
W02-S05	3.19E+06	6.76E-01	3.43E+10	2.40E+11	2.39E+01	2.51E+01
W03-S01	8.88E+07	1.56E+00	9.68E+11	8.00E+13	2.42E+01	8.79E+04
W03-S02	1.36E+07	1.29E+00	1.83E+11	2.80E+12	2.49E+01	2.77E+01
W03-S03	1.50E+07	1.25E+00	1.74E+11	6.42E+12	2.47E+01	2.81E+01
W03-S06	2.80E+07	9.44E-01	6.59E+10	1.71E+12	2.41E+01	2.66E+01
W03-S09	1.04E+08	1.19E+00	1.82E+11	7.16E+13	2.45E+01	2.98E+01
W03-S10	1.20E+07	1.26E+00	1.78E+11	3.64E+12	2.49E+01	2.78E+01
W06-S02	2.17E+08	1.28E+00	2.59E+11	1.65E+14	2.49E+01	3.01E+01
W06-S03	3.16E+08	1.28E+00	2.40E+11	9.97E+13	2.49E+01	2.91E+01
W07-S01	3.64E+08	1.39E+00	5.99E+11	2.40E+14	2.48E+01	3.24E+01
W07-S02	5.12E+08	1.63E+00	1.47E+12	1.28E+14	2.48E+01	3.20E+01
W07-S04	2.23E+08	1.86E+00	1.97E+12	1.10E+14	2.49E+01	3.18E+01
W08-S01	2.77E+07	1.30E+00	1.78E+11	1.16E+12	2.51E+01	2.71E+01
W08-S03	8.73E+08	1.15E+00	8.27E+11	3.13E+14	2.46E+01	3.27E+01
W08-S04	1.19E+07	1.38E+00	2.06E+11	1.77E+12	2.50E+01	2.75E+01
W09-S01	1.19E+08	1.48E+00	3.81E+11	2.41E+13	2.52E+01	2.91E+01
W09-S02	2.18E+08	1.63E+00	1.07E+12	7.46E+13	2.51E+01	3.13E+01
W09-S03	4.18E+07	1.34E+00	2.21E+11	4.18E+12	2.51E+01	2.78E+01
W09-S04	5.78E+07	1.36E+00	3.78E+11	6.08E+13	2.48E+01	3.04E+01
W09-S05	1.54E+08	1.45E+00	1.01E+12	1.64E+14	2.47E+01	3.20E+01
W10-S06	3.19E+08	1.11E+00	3.54E+11	1.64E+14	2.42E+01	3.19E+01
W10-S07	8.47E+07	9.93E-01	8.93E+10	8.16E+12	2.40E+01	2.82E+01
W11-S03	2.86E+07	1.21E+00	1.35E+11	8.40E+12	2.45E+01	2.81E+01
W11-S04	2.06E+08	1.10E+00	1.86E+11	1.31E+14	2.42E+01	3.05E+01
W14-S01	2.90E+08	1.21E+00	2.61E+11	7.09E+13	2.43E+01	3.06E+01
W14-S02	1.06E+09	9.60E-01	1.74E+11	2.43E+14	2.41E+01	3.15E+01
W14-S04	5.31E+08	1.13E+00	5.11E+11	1.81E+14	2.41E+01	3.22E+01

Sample	Volume _Std	VoxelFace Area Log_Std	VoxelFace Area _Avg	VoxelFace Area_ Avg_w	VoxelFace Area_Log_Avg	VoxelFace Area_Log _Avg_w
	n voxel	n voxel	n voxel	n voxel	n voxel	n voxel
W14-S05	7.48E+07	1.21E+00	4.74E+11	1.76E+14	2.43E+01	3.20E+01
W14-S06	3.08E+08	1.22E+00	2.18E+11	7.25E+13	2.44E+01	3.03E+01
W14-S07	2.55E+08	1.05E+00	1.57E+11	9.98E+13	2.42E+01	3.02E+01
W14-S09	3.59E+07	1.21E+00	1.29E+11	4.10E+12	2.44E+01	2.78E+01
W14-S10	6.28E+08	1.04E+00	2.76E+11	1.77E+14	2.41E+01	3.19E+01
W14-S12	2.80E+08	1.12E+00	2.04E+11	7.01E+13	2.42E+01	3.06E+01
W15-S02	3.48E+08	1.04E+00	2.32E+11	1.56E+14	2.41E+01	3.17E+01
W15-S03	3.48E+07	1.04E+00	9.59E+10	5.84E+12	2.42E+01	2.80E+01
W15-S05	7.71E+07	1.03E+00	1.12E+11	2.08E+13	2.42E+01	2.89E+01
W15-S06	3.57E+08	1.12E+00	3.40E+11	8.74E+13	2.41E+01	3.13E+01
W15-S07	5.93E+08	1.10E+00	4.76E+11	1.22E+14	2.41E+01	3.19E+01
W15-S08	7.50E+08	1.08E+00	4.23E+11	1.82E+14	2.41E+01	3.21E+01
W15-S09	5.29E+08	1.06E+00	2.54E+11	8.98E+13	2.41E+01	3.13E+01
W15-S12	3.96E+08	1.24E+00	4.66E+11	1.36E+14	2.42E+01	3.17E+01
W15-S14	7.42E+07	1.04E+00	8.91E+10	5.16E+12	2.43E+01	2.72E+01
W16-S01	1.53E+07	9.47E-01	6.51E+10	3.91E+12	2.42E+01	2.67E+01
W16-S03	1.50E+08	1.06E+00	1.37E+11	4.00E+13	2.41E+01	2.96E+01
W16-S05	2.84E+08	9.80E-01	3.27E+11	2.06E+14	2.40E+01	3.22E+01
W16-S06	6.84E+08	9.50E-01	2.97E+11	1.75E+14	2.40E+01	3.22E+01
W17-S01	3.03E+08	1.18E+00	5.82E+11	3.47E+14	2.45E+01	3.26E+01
W17-S03	2.84E+08	1.27E+00	3.85E+11	1.10E+14	2.47E+01	3.11E+01
W17-S04	1.92E+08	1.32E+00	5.63E+11	1.17E+14	2.47E+01	3.16E+01
W17-S05	1.30E+08	1.14E+00	3.81E+11	3.08E+14	2.42E+01	3.22E+01
W18-S01	1.76E+08	1.28E+00	3.54E+11	9.39E+13	2.45E+01	3.10E+01
W18-S02	8.45E+07	1.08E+00	1.75E+11	1.03E+14	2.42E+01	3.05E+01
W18-S03	2.72E+08	1.22E+00	5.06E+11	1.52E+14	2.43E+01	3.19E+01
W18-S04	3.44E+08	1.08E+00	2.85E+11	1.99E+14	2.42E+01	3.17E+01
W18-S05	1.75E+07	8.99E-01	6.31E+10	5.13E+12	2.41E+01	2.70E+01
W18-S06	2.10E+08	1.18E+00	4.32E+11	1.02E+14	2.42E+01	3.16E+01
W19-S01	4.31E+08	1.56E+00	7.02E+11	4.94E+14	2.53E+01	3.12E+01
W19-S02	1.08E+09	1.07E+00	3.92E+11	7.55E+14	2.41E+01	3.31E+01
W19-S03	2.29E+07	8.23E-01	4.96E+10	6.41E+12	2.40E+01	2.65E+01
W19-S04	9.83E+07	9.67E-01	7.62E+10	8.97E+12	2.41E+01	2.74E+01
W19-S05	1.14E+09	1.07E+00	1.91E+11	6.66E+14	2.42E+01	3.14E+01
W19-S06	4.43E+07	1.02E+00	7.55E+10	1.04E+12	2.42E+01	2.66E+01
W20-S01	1.07E+08	9.33E-01	6.56E+10	1.50E+13	2.42E+01	2.68E+01
W20-S02	2.10E+09	9.45E-01	3.25E+11	6.52E+14	2.40E+01	3.26E+01
W20-S03	5.50E+07	1.08E+00	1.30E+11	3.06E+13	2.43E+01	2.90E+01
W20-S04	8.89E+06	9.02E-01	5.78E+10	7.14E+11	2.41E+01	2.62E+01
W20-S05	3.64E+08	1.14E+00	3.30E+11	9.53E+13	2.42E+01	3.13E+01
W20-S06	3.13E+05	1.29E+00	3.43E+10	2.30E+11	2.33E+01	3.01E+01

Sample	Volume _Std	VoxelFace Area Log_Std	VoxelFace Area _Avg	VoxelFace Area_ Avg_w	VoxelFace Area_Log_Avg	VoxelFace Area_Log _Avg_w
	n voxel	n voxel	n voxel	n voxel	n voxel	n voxel
W21-S01	9.17E+08	1.04E+00	3.53E+11	1.59E+14	2.41E+01	3.20E+01
W21-S02	2.97E+08	1.07E+00	1.58E+11	7.42E+13	2.42E+01	3.01E+01
W21-S03	4.39E+08	1.12E+00	4.04E+11	1.72E+14	2.42E+01	3.21E+01
W21-S04	8.33E+08	1.13E+00	4.24E+11	2.49E+14	2.43E+01	3.23E+01
W21-S05	6.41E+08	1.09E+00	3.76E+11	2.36E+14	2.42E+01	3.22E+01
W21-S06	2.72E+08	1.22E+00	5.96E+11	1.58E+14	2.43E+01	3.21E+01
W21-S07	4.62E+08	1.17E+00	2.08E+11	1.05E+14	2.43E+01	3.04E+01
W21-S08	1.13E+09	1.07E+00	4.37E+11	2.30E+14	2.42E+01	3.23E+01
W22-S01	6.72E+08	8.10E-01	3.53E+11	1.20E+14	2.38E+01	3.20E+01
W22-S02	9.44E+08	1.13E+00	3.32E+11	2.79E+14	2.42E+01	3.21E+01
W22-S04	8.42E+07	1.44E+00	5.50E+11	6.56E+13	2.45E+01	3.10E+01
W22-S05	1.30E+09	9.51E-01	6.30E+11	6.96E+14	2.40E+01	3.36E+01
W24-S01	3.88E+08	1.21E+00	1.70E+11	9.47E+13	2.45E+01	2.92E+01
W24-S02	5.04E+08	1.17E+00	2.01E+11	1.48E+14	2.44E+01	3.05E+01
W24-S03	2.24E+08	1.08E+00	2.08E+11	1.71E+14	2.42E+01	3.11E+01
W24-S04	5.20E+08	9.73E-01	2.02E+11	1.45E+14	2.41E+01	3.15E+01
W24-S05	4.70E+08	1.08E+00	3.61E+11	1.36E+14	2.42E+01	3.19E+01
W25-S01	3.32E+07	8.33E-01	6.94E+10	8.05E+13	2.39E+01	2.90E+01
W25-S02	6.59E+07	1.26E+00	2.81E+11	1.56E+14	2.44E+01	3.10E+01
W25-S03	9.79E+07	1.17E+00	2.16E+11	8.42E+13	2.42E+01	3.05E+01
W25-S04	3.81E+08	1.09E+00	3.09E+11	2.65E+14	2.41E+01	3.21E+01
W26-S02	1.42E+08	1.13E+00	2.02E+11	7.84E+13	2.42E+01	3.04E+01
W27-S01	1.24E+08	1.03E+00	2.72E+11	1.00E+14	2.40E+01	3.15E+01
W27-S03	4.13E+06	9.60E-01	6.10E+10	3.72E+11	2.42E+01	2.60E+01
W27-S04	4.61E+07	1.04E+00	9.43E+10	2.04E+13	2.42E+01	2.86E+01
W27-S05	1.69E+07	8.34E-01	4.72E+10	7.02E+11	2.40E+01	2.58E+01
W27-S06	7.94E+06	9.29E-01	5.90E+10	4.69E+11	2.42E+01	2.60E+01
W28-S02	2.94E+07	1.21E+00	1.86E+11	1.06E+13	2.42E+01	2.93E+01
W28-S04	2.49E+08	1.26E+00	4.69E+11	1.18E+14	2.47E+01	3.14E+01
W28-S05	3.52E+07	7.92E-01	4.80E+10	9.77E+12	2.39E+01	2.70E+01
W29-S01	1.79E+08	9.91E-01	1.02E+11	3.29E+13	2.41E+01	2.94E+01
W29-S02	2.35E+08	7.78E-01	7.06E+10	7.81E+13	2.38E+01	2.97E+01
W30-S01	1.77E+07	6.63E-01	3.42E+10	6.72E+11	2.39E+01	2.53E+01
W30-S03	4.44E+08	8.49E-01	2.09E+11	3.96E+14	2.40E+01	3.26E+01
W30-S04	8.23E+07	1.47E+00	4.47E+11	6.93E+13	2.48E+01	3.05E+01
W30-S05	2.27E+08	1.15E+00	2.14E+11	6.33E+13	2.42E+01	3.04E+01
W30-S07	1.85E+08	1.14E+00	1.87E+11	9.95E+13	2.42E+01	3.02E+01
W30-S08	3.21E+08	1.02E+00	1.39E+11	1.89E+14	2.42E+01	3.05E+01
W31-S01	2.90E+08	1.04E+00	2.56E+11	1.05E+14	2.41E+01	3.14E+01
W31-S03	2.07E+08	1.40E+00	6.86E+11	1.58E+14	2.44E+01	3.19E+01

Sample	VoxelFace Area_Log _Max	VoxelFace Area_Log _Median	VoxelFace Area_Max	VoxelFace Area_Median
	n voxel	n voxel	n voxel	n voxel
W02-S01	3.36E+01	2.54E+01	3.90E+14	1.05E+11
W02-S03	3.09E+01	2.55E+01	2.57E+13	1.20E+11
W02-S04	2.97E+01	2.52E+01	8.05E+12	8.50E+10
W02-S05	3.01E+01	2.50E+01	1.22E+13	7.50E+10
W03-S01	3.34E+01	2.56E+01	3.11E+14	1.30E+11
W03-S02	3.13E+01	2.57E+01	3.82E+13	1.40E+11
W03-S03	3.20E+01	2.56E+01	7.81E+13	1.25E+11
W03-S06	3.21E+01	2.53E+01	8.93E+13	9.50E+10
W03-S09	3.38E+01	2.55E+01	4.99E+14	1.20E+11
W03-S10	3.16E+01	2.56E+01	5.34E+13	1.35E+11
W06-S02	3.51E+01	2.56E+01	1.83E+15	1.35E+11
W06-S03	3.52E+01	2.56E+01	1.98E+15	1.35E+11
W07-S01	3.44E+01	2.56E+01	9.08E+14	1.35E+11
W07-S02	3.39E+01	2.58E+01	5.40E+14	1.55E+11
W07-S04	3.43E+01	2.61E+01	7.65E+14	2.20E+11
W08-S01	3.19E+01	2.59E+01	7.29E+13	1.70E+11
W08-S03	3.49E+01	2.57E+01	1.46E+15	1.47E+11
W08-S04	3.06E+01	2.59E+01	1.90E+13	1.85E+11
W09-S01	3.39E+01	2.59E+01	5.23E+14	1.75E+11
W09-S02	3.36E+01	2.59E+01	3.77E+14	1.70E+11
W09-S03	3.23E+01	2.58E+01	1.05E+14	1.60E+11
W09-S04	3.35E+01	2.56E+01	3.55E+14	1.35E+11
W09-S05	3.49E+01	2.56E+01	1.39E+15	1.35E+11
W10-S06	3.42E+01	2.54E+01	6.87E+14	1.10E+11
W10-S07	3.24E+01	2.55E+01	1.18E+14	1.15E+11
W11-S03	3.23E+01	2.56E+01	1.02E+14	1.30E+11
W11-S04	3.43E+01	2.54E+01	8.01E+14	1.10E+11
W14-S01	3.39E+01	2.55E+01	5.33E+14	1.20E+11
W14-S02	3.52E+01	2.53E+01	1.88E+15	1.00E+11
W14-S04	3.43E+01	2.54E+01	7.99E+14	1.10E+11
W14-S05	3.40E+01	2.55E+01	5.58E+14	1.15E+11
W14-S06	3.40E+01	2.55E+01	6.00E+14	1.20E+11
W14-S07	3.50E+01	2.53E+01	1.51E+15	1.00E+11
W14-S09	3.25E+01	2.56E+01	1.24E+14	1.35E+11
W14-S10	3.42E+01	2.53E+01	7.03E+14	1.00E+11
W14-S12	3.36E+01	2.54E+01	3.76E+14	1.10E+11
W15-S02	3.39E+01	2.54E+01	5.42E+14	1.05E+11
W15-S03	3.17E+01	2.54E+01	5.88E+13	1.05E+11
W15-S05	3.26E+01	2.53E+01	1.45E+14	1.00E+11
W15-S06	3.42E+01	2.54E+01	7.29E+14	1.10E+11
W15-S07	3.38E+01	2.54E+01	5.00E+14	1.05E+11

Sample	VoxelFace Area_Log_Max	VoxelFace Area_Log_Median	VoxelFace Area_Max	VoxelFace Area_Median
W15-S08	3.44E+01	2.54E+01	8.91E+14	1.05E+11
W15-S09	3.36E+01	2.53E+01	3.98E+14	1.00E+11
W15-S12	3.45E+01	2.56E+01	1.01E+15	1.30E+11
W15-S14	3.30E+01	2.53E+01	2.14E+14	1.00E+11
W16-S01	3.26E+01	2.53E+01	1.46E+14	1.00E+11
W16-S03	3.33E+01	2.55E+01	3.03E+14	1.15E+11
W16-S05	3.43E+01	2.53E+01	8.00E+14	1.00E+11
W16-S06	3.41E+01	2.53E+01	6.78E+14	9.50E+10
W17-S01	3.50E+01	2.54E+01	1.63E+15	1.10E+11
W17-S03	3.47E+01	2.55E+01	1.17E+15	1.20E+11
W17-S04	3.36E+01	2.56E+01	4.11E+14	1.25E+11
W17-S05	3.47E+01	2.55E+01	1.22E+15	1.20E+11
W18-S01	3.38E+01	2.56E+01	4.79E+14	1.25E+11
W18-S02	3.38E+01	2.54E+01	4.74E+14	1.10E+11
W18-S03	3.44E+01	2.55E+01	8.82E+14	1.15E+11
W18-S04	3.48E+01	2.54E+01	1.28E+15	1.05E+11
W18-S05	3.23E+01	2.52E+01	1.09E+14	9.00E+10
W18-S06	3.40E+01	2.55E+01	5.71E+14	1.15E+11
W19-S01	3.57E+01	2.60E+01	3.14E+15	2.05E+11
W19-S02	3.57E+01	2.55E+01	3.26E+15	1.15E+11
W19-S03	3.28E+01	2.52E+01	1.74E+14	8.50E+10
W19-S04	3.38E+01	2.53E+01	4.76E+14	9.50E+10
W19-S05	3.61E+01	2.54E+01	4.99E+15	1.10E+11
W19-S06	3.09E+01	2.54E+01	2.76E+13	1.10E+11
W20-S01	3.37E+01	2.53E+01	4.45E+14	9.50E+10
W20-S02	3.69E+01	2.53E+01	1.06E+16	9.50E+10
W20-S03	3.36E+01	2.54E+01	3.84E+14	1.05E+11
W20-S04	3.05E+01	2.52E+01	1.77E+13	9.00E+10
W20-S05	3.42E+01	2.54E+01	7.21E+14	1.10E+11
W20-S06	2.88E+01	2.50E+01	3.35E+12	7.00E+10
W21-S01	3.42E+01	2.53E+01	6.91E+14	1.00E+11
W21-S02	3.41E+01	2.54E+01	6.33E+14	1.05E+11
W21-S03	3.41E+01	2.54E+01	6.63E+14	1.05E+11
W21-S04	3.48E+01	2.54E+01	1.33E+15	1.10E+11
W21-S05	3.44E+01	2.54E+01	8.51E+14	1.05E+11
W21-S06	3.41E+01	2.55E+01	6.59E+14	1.15E+11
W21-S07	3.43E+01	2.55E+01	7.59E+14	1.20E+11
W21-S08	3.47E+01	2.53E+01	1.23E+15	1.00E+11
W22-S01	3.41E+01	2.52E+01	6.67E+14	8.50E+10
W22-S02	3.47E+01	2.55E+01	1.20E+15	1.20E+11
W22-S04	3.32E+01	2.57E+01	2.75E+14	1.45E+11
W22-S05	3.55E+01	2.53E+01	2.67E+15	1.00E+11

Sample	VoxelFace Area_Log _Max	VoxelFace Area_Log _Median	VoxelFace Area_Max	VoxelFace Area_Median
W24-S01	3.51E+01	2.56E+01	1.84E+15	1.25E+11
W24-S02	3.48E+01	2.55E+01	1.29E+15	1.15E+11
W24-S03	3.42E+01	2.54E+01	7.25E+14	1.10E+11
W24-S04	3.42E+01	2.53E+01	7.45E+14	9.50E+10
W24-S05	3.44E+01	2.53E+01	8.56E+14	1.00E+11
W25-S01	3.38E+01	2.52E+01	4.76E+14	9.00E+10
W25-S02	3.42E+01	2.56E+01	7.22E+14	1.30E+11
W25-S03	3.37E+01	2.55E+01	4.43E+14	1.20E+11
W25-S04	3.46E+01	2.55E+01	1.11E+15	1.15E+11
W26-S02	3.40E+01	2.54E+01	5.71E+14	1.10E+11
W27-S01	3.39E+01	2.54E+01	5.05E+14	1.10E+11
W27-S03	2.98E+01	2.54E+01	8.56E+12	1.05E+11
W27-S04	3.25E+01	2.54E+01	1.31E+14	1.10E+11
W27-S05	3.17E+01	2.52E+01	5.95E+13	9.00E+10
W27-S06	3.04E+01	2.53E+01	1.53E+13	1.00E+11
W28-S02	3.18E+01	2.56E+01	6.31E+13	1.35E+11
W28-S04	3.41E+01	2.55E+01	6.74E+14	1.20E+11
W28-S05	3.28E+01	2.53E+01	1.77E+14	9.50E+10
W29-S01	3.34E+01	2.54E+01	3.24E+14	1.05E+11
W29-S02	3.45E+01	2.52E+01	9.20E+14	9.00E+10
W30-S01	3.12E+01	2.50E+01	3.68E+13	7.50E+10
W30-S03	3.50E+01	2.52E+01	1.51E+15	9.00E+10
W30-S04	3.40E+01	2.58E+01	5.96E+14	1.55E+11
W30-S05	3.40E+01	2.55E+01	6.01E+14	1.15E+11
W30-S07	3.44E+01	2.56E+01	9.14E+14	1.25E+11
W30-S08	3.48E+01	2.54E+01	1.33E+15	1.05E+11
W31-S01	3.36E+01	2.53E+01	4.03E+14	1.00E+11
W31-S03	3.47E+01	2.57E+01	1.23E+15	1.40E+11

Sample	VoxelFaceArea_Std	Sor	k	phi	Swi	rho
		%	mD	%	%	g/cm³
W02-S01	3.52E+12	26.80	109.00	19.40	18.90	2.73
W02-S03	5.18E+11	20.10	247.00	22.30	15.60	2.71
W02-S04	8.37E+10	15.40	18.50	18.60	21.20	2.73
W02-S05	6.63E+10	17.20	21.70	20.00	15.50	2.72
W03-S01	8.20E+12	31.60	99.30	16.20	18.50	2.69
W03-S02	5.57E+11	20.70	5.93	16.70	22.00	2.72
W03-S03	8.39E+11	27.50	23.40	16.20	27.79	2.75
W03-S06	2.68E+11	21.10	6.20	18.80	24.00	2.71
W03-S09	2.76E+12	22.14	62.40	19.10	17.71	2.71
W03-S10	6.15E+11	16.10	4.52	13.50	23.30	2.73
W06-S02	5.46E+12	25.10	19.10	17.00	19.30	2.74

Sample	VoxelFaceArea_Std	Sor	k	phi	Swi	rho
		%	mD	%	%	g/cm³
W06-S03	4.08E+12	22.90	63.70	18.70	18.90	2.75
W07-S01	9.09E+12	39.50	1.84	10.30	17.20	2.68
W07-S02	1.26E+13	44.00	12.70	14.00	18.40	2.71
W07-S04	1.39E+13	44.80	173.00	14.00	22.50	2.72
W08-S01	3.47E+11	26.70	20.10	16.40	25.30	2.72
W08-S03	1.56E+13	41.90	522.00	15.80	18.00	2.70
W08-S04	4.72E+11	24.70	6.26	13.40	23.40	2.74
W09-S01	2.58E+12	41.20	530.00	24.60	24.30	2.72
W09-S02	8.45E+12	57.20	2293.00	25.70	12.80	2.73
W09-S03	6.73E+11	31.30	62.70	18.00	22.00	2.72
W09-S04	4.24E+12	44.20	22.20	19.70	22.30	2.75
W09-S05	1.21E+13	55.80	951.00	16.60	16.20	2.70
W10-S06	6.98E+12	33.80	178.00	12.80	28.70	2.73
W10-S07	7.02E+11	18.70	25.40	15.40	30.40	2.73
W11-S03	7.54E+11	30.20	65.30	11.10	34.00	2.69
W11-S04	4.44E+12	21.60	40.70	8.60	31.40	2.70
W14-S01	3.81E+12	21.70	86.20	12.50	28.20	2.71
W14-S02	5.91E+12	33.00	98.50	19.20	32.60	2.73
W14-S04	9.14E+12	32.00	1866.00	18.80	18.10	2.71
W14-S05	8.52E+12	31.50	512.00	11.80	25.80	2.70
W14-S06	3.20E+12	28.70	40.50	12.20	23.70	2.72
W14-S07	3.54E+12	21.90	158.00	13.60	29.40	2.73
W14-S09	5.83E+11	16.90	24.00	14.60	36.30	2.73
W14-S10	6.23E+12	20.30	327.00	11.60	20.70	2.74
W14-S12	3.18E+12	26.20	104.00	15.30	33.60	2.71
W15-S02	5.29E+12	23.50	640.00	17.80	24.50	2.74
W15-S03	5.75E+11	19.70	17.40	16.40	26.70	2.74
W15-S05	1.23E+12	25.00	77.00	21.30	22.00	2.67
W15-S06	5.11E+12	45.80	389.00	18.20	21.50	2.73
W15-S07	7.15E+12	34.50	7893.00	23.70	20.50	2.68
W15-S08	8.29E+12	39.00	380.00	24.60	9.80	2.68
W15-S09	4.31E+12	54.00	590.00	20.70	9.30	2.68
W15-S12	7.60E+12	38.20	4714.00	23.00	10.10	2.69
W15-S14	5.44E+11	24.60	5.83	17.30	17.60	2.68
W16-S01	3.38E+11	14.28	51.00	19.57	18.44	2.73
W16-S03	1.97E+12	33.49	96.20	19.20	20.37	2.73
W16-S05	7.56E+12	29.84	861.00	17.72	13.89	2.71
W16-S06	6.64E+12	34.13	265.00	17.94	19.30	2.72
W17-S01	1.34E+13	29.00	103.33	17.90	17.90	2.69
W17-S03	5.90E+12	30.80	25.60	15.60	25.70	2.73
W17-S04	7.39E+12	30.00	915.14	13.60	19.40	2.69
W17-S05	1.06E+13	31.50	131.97	14.90	18.10	2.68
W18-S01	5.27E+12	32.30	85.70	16.30	23.90	2.72

Sample	VoxelFaceArea_Std	Sor	k	phi	Swi	rho
		%	mD	%	%	g/cm³
W18-S02	3.64E+12	25.40	4.02	14.00	30.00	2.76
W18-S03	8.36E+12	23.20	1157.00	14.50	29.80	2.74
W18-S04	6.95E+12	23.60	34.60	9.70	39.50	2.73
W18-S05	4.28E+11	17.40	1.94	9.30	31.30	2.77
W18-S06	6.09E+12	23.90	135.00	6.80	32.80	2.74
W19-S01	1.76E+13	31.50	251.00	19.60	15.10	2.72
W19-S02	1.67E+13	15.00	568.00	22.10	12.10	2.75
W19-S03	3.41E+11	22.00	48.70	21.40	25.70	2.79
W19-S04	6.52E+11	21.30	25.50	20.00	24.70	2.72
W19-S05	1.04E+13	18.60	427.00	22.60	13.20	2.71
W19-S06	2.41E+11	12.10	69.80	22.60	20.90	2.72
W20-S01	6.32E+11	15.70	3.52	14.10	21.80	2.73
W20-S02	1.41E+13	25.50	50.20	16.60	20.60	2.71
W20-S03	1.63E+12	20.20	3.06	14.30	26.40	2.72
W20-S04	1.53E+11	17.00	3.15	13.60	25.80	2.73
W20-S05	5.27E+12	37.20	193.00	20.90	15.30	2.71
W20-S06	7.06E+10	18.30	12.50	19.50	19.90	2.73
W21-S01	6.88E+12	20.40	143.00	12.70	27.30	2.68
W21-S02	3.02E+12	23.20	9.89	17.60	23.00	2.73
W21-S03	7.63E+12	40.90	848.00	17.10	20.20	2.70
W21-S04	9.68E+12	41.80	440.00	18.80	16.40	2.69
W21-S05	8.72E+12	41.30	1853.00	19.50	20.60	2.69
W21-S06	9.11E+12	37.80	2709.00	15.60	16.60	2.69
W21-S07	4.07E+12	32.70	89.30	13.80	21.70	2.68
W21-S08	9.54E+12	29.40	387.00	18.50	22.90	2.70
W22-S01	6.28E+12	42.20	2126.00	12.50	20.00	2.67
W22-S02	9.05E+12	23.50	254.00	15.60	23.30	2.68
W22-S04	5.61E+12	35.00	408.00	20.00	24.50	2.71
W22-S05	2.05E+13	24.10	1109.00	18.70	23.30	2.70
W24-S01	3.12E+12	24.40	7.89	14.40	32.00	2.70
W24-S02	4.74E+12	24.20	14.40	16.10	24.20	2.74
W24-S03	5.43E+12	19.40	6.69	16.30	27.90	2.72
W24-S04	4.86E+12	27.20	14.00	16.50	24.80	2.71
W24-S05	6.47E+12	26.90	150.00	18.10	29.20	2.67
W25-S01	1.85E+12	18.30	3.50	9.00	36.80	2.73
W25-S02	5.83E+12	20.30	84.10	8.90	25.50	2.76
W25-S03	3.70E+12	19.70	90.90	12.50	26.20	2.71
W25-S04	8.49E+12	19.50	379.00	12.00	27.50	2.74
W26-S02	3.48E+12	22.64	53.00	9.10	32.02	2.73
W27-S01	4.68E+12	19.60	1389.00	15.40	29.30	2.67
W27-S03	1.11E+11	13.70	1.85	14.56	21.20	2.77
W27-S04	9.13E+11	11.70	4.32	14.70	30.70	2.71
W27-S05	1.23E+11	16.90	26.20	14.22	32.10	2.70

Sample	VoxelFaceArea_Std	Sor	k	phi	Swi	rho
		%	mD	%	%	g/cm³
W27-S06	1.26E+11	24.70	322.00	16.30	28.40	2.70
W28-S02	1.15E+12	20.27	1.63	10.60	28.33	2.72
W28-S04	6.52E+12	38.86	145.00	15.90	17.54	2.70
W28-S05	4.71E+11	13.32	1.48	15.20	23.59	2.72
W29-S01	1.32E+12	19.60	14.70	12.90	23.60	2.72
W29-S02	1.85E+12	14.80	8.47	13.60	29.40	2.72
W30-S01	1.07E+11	15.40	455.00	32.50	30.70	2.80
W30-S03	8.26E+12	30.00	259.00	12.70	29.40	2.74
W30-S04	4.77E+12	26.30	18.40	12.60	29.50	2.72
W30-S05	3.32E+12	25.60	204.00	17.60	23.50	2.70
W30-S07	3.87E+12	13.70	459.00	16.70	26.90	2.72
W30-S08	4.38E+12	28.00	43.60	15.30	27.20	2.73
W31-S01	4.67E+12	31.20	360.00	13.00	21.40	2.71
W31-S03	8.84E+12	29.20	237.00	10.00	22.10	2.70

APPENDIX B – Petrographic Descriptions – *In-situ* rocks- Article 2.

	Constituent (%)	W01-S04	W01-S02	W01-S01	W02-S05	W19-S03	W21-S08	W21-S07	W21-S06	W21-S05	W13-S02	W24-S04	W14-S10
Primary	**Ostracod**	0.0	0.0	0.0	0.0	0.0	0.0	0.0	0.0	0.0	0.0	0.3	0.0
Syngenetic	**Mg-clay**	0.0	0.0	0.0	0.0	0.0	0.0	2.3	0.3	0.0	0.0	1.0	0.0
	Calcite shrub	53.7	81.0	77.3	0.0	0.0	40.3	50.0	70.0	68.3	70.3	23.0	47.0
Diagenetic	**Calcite spherulite**	7.3	1.0	0.7	57.3	9.3	20.3	24.0	13.7	5.0	1.0	22.3	3.0
	Silica replacing calcite shrubs	11.0	1.7	1.0	0.0	0.0	1.3	1.0	0.0	0.0	1.0	0.3	1.7
	Silica replacing spherulites	0.0	0.0	0.0	0.0	0.0	1.0	0.7	0.0	0.0	0.7	2.0	0.0
	Silica replacing Mg-clays + filling matrix dissolution porosity	0.0	0.3	2.0	0.0	0.0	1.0	0.0	0.0	0.0	0.0	1.0	3.0
	Silica growth-framework pores filling	0.3	0.3	0.0	0.0	0.0	0.0	0.0	0.3	0.0	1.3	0.0	0.0
	Dolomite replacing calcite shrubs	10.0	1.0	7.0	0.0	0.0	3.7	1.3	0.3	8.0	3.7	3.0	19.3
	Dolomite replacing calcite spherulites	1.3	0.0	0.0	1.0	0.0	1.3	0.7	0.0	0.0	0.0	15.0	1.0
	Dolomite replacing Mg-clays + filling matrix dissolution porosity	0.0	1.3	4.3	21.3	76.0	11.3	5.0	1.3	5.0	0.0	12.7	19.3
	Dolomite growth-framework pores filling	7.0	0.3	0.3	0.0	0.0	0.0	0.0	1.3	0.0	11.3	0.0	0.0
	Dolomite replacing undifferentiated primary constituent	0.0	0.0	0.0	0.0	0.0	0.0	0.0	0.0	0.0	0.0	4.7	0.0
	Calcite replacing Mg-clays + filling matrix dissolution porosity	0.0	0.0	0.0	0.0	0.0	0.0	0.3	0.0	0.0	0.0	0.0	0.0
	Calcite growth-framework pores filling	5.3	0.0	0.3	0.0	0.0	0.0	0.0	0.0	0.0	0.0	0.0	0.0
	Other diagenetic constituents	0.0	3.3	0.0	0.7	1.0	0.0	0.3	0.0	0.3	0.0	0.3	0.0
Porosity	**Matrix dissolution porosity**	0.0	4.7	4.0	18.0	13.3	9.7	6.7	0.3	5.0	0.0	6.0	4.3
	Intra-aggregate porosity	0.0	0.3	0.0	1.7	0.3	7.7	3.0	1.3	3.0	0.0	4.7	0.0
	Growth-framework porosity	4.0	4.7	3.0	0.0	0.0	2.3	3.7	11.0	3.7	10.7	0.0	1.3
	Other porosity (Vugs, fractures, channels, molds, and breccia)	0.0	0.0	0.0	0.0	0.0	0.0	1.0	0.0	1.7	0.0	3.7	0.0

	Constituent (%)	W14-S07	W14-S12	W14-S05	W14-S04	W14-S03	W14-S02	W14-S01	W15-S14	W15-S06	W15-S05	W15-S01	W03-S09
Primary	**Ostracod**	0.0	0.0	0.0	0.0	0.0	0.0	0.0	0.0	0.0	0.0	0.0	0.0
Syngenetic	**Mg-clay**	0.0	0.0	0.0	0.0	0.0	0.0	0.0	8.0	0.0	0.0	0.0	3.0
	Calcite shrub	46.0	53.7	60.0	68.7	69.3	47.0	3.0	0.0	45.7	4.0	31.3	0.3
Diagenetic	**Calcite spherulite**	13.3	13.3	10.0	8.0	8.3	12.0	75.0	62.3	26.7	43.0	24.3	64.3
	Silica replacing calcite shrubs	0.7	1.0	4.7	1.7	4.0	0.0	0.0	0.0	1.0	0.0	5.3	0.0
	Silica replacing spherulites	0.3	0.0	0.7	0.0	0.0	0.0	0.7	0.0	0.0	11.0	1.0	0.0
	Silica replacing Mg-clays + filling matrix dissolution porosity	0.0	0.0	3.0	0.3	3.3	0.0	0.0	2.3	0.0	1.3	0.3	0.3
	Silica growth-framework pores filling	0.0	0.0	0.0	0.3	0.0	0.0	0.0	0.0	0.0	0.0	0.0	0.0
	Dolomite replacing calcite shrubs	2.3	4.0	1.3	2.3	0.0	6.3	0.0	0.0	4.3	0.0	0.3	0.0
	Dolomite replacing calcite spherulites	0.7	1.0	0.3	0.7	0.3	5.7	3.3	2.7	1.7	0.3	1.3	5.0
	Dolomite replacing Mg-clays + filling matrix dissolution porosity	25.0	19.0	10.7	3.7	3.0	14.0	9.0	12.3	6.0	32.3	15.3	15.7
	Dolomite growth-framework pores filling	0.0	0.0	0.7	1.7	0.0	2.3	0.0	0.0	1.7	0.0	0.0	0.0
	Dolomite replacing undifferentiated primary constituent	0.0	0.0	0.0	0.0	0.0	0.0	0.0	0.0	0.0	0.0	0.0	0.0
	Calcite replacing Mg-clays + filling matrix dissolution porosity	0.0	0.0	0.0	0.0	5.3	0.0	0.0	0.0	0.0	0.0	0.0	0.0
	Calcite growth-framework pores filling	0.0	0.0	0.0	0.0	0.0	0.0	0.0	0.0	0.0	0.0	0.0	0.0
	Other diagenetic constituents	0.0	0.0	0.0	0.0	0.0	0.0	0.0	0.3	0.0	0.0	0.0	0.0
Porosity	**Matrix dissolution porosity**	6.3	5.7	6.0	4.0	3.3	5.7	8.0	2.0	4.7	4.3	11.7	9.7
	Intra-aggregate porosity	4.3	1.7	1.3	3.0	2.3	6.3	1.0	10.0	3.7	3.7	3.7	1.3
	Growth-framework porosity	0.3	0.0	1.3	4.3	0.7	0.7	0.0	0.0	3.7	0.0	0.0	0.0
	Other porosity (Vugs, fractures, channels, molds, and breccia)	0.7	0.7	0.0	1.3	0.0	0.0	0.0	0.0	1.0	0.0	5.3	0.3

	Constituent (%)	W03-S08	W03-S07	W03-S02	W03-S01	W06-S02	W07-S02	W08-S04	W09-S05	W16-S06	W16-S05	W10-S03	W10-S02
Primary	**Ostracod**	0.0	0.0	0.0	0.0	0.0	0.0	0.0	0.0	0.0	0.0	0.0	0.0
Syngenetic	**Mg-clay**	0.0	0.0	1.0	0.0	0.0	0.0	0.0	0.0	0.0	0.0	0.0	0.0
	Calcite shrub	45.3	0.0	2.0	56.4	1.3	68.0	0.0	26.3	76.7	53.7	62.7	59.7
Diagenetic	**Calcite spherulite**	20.0	64.0	57.7	24.0	52.7	0.0	49.3	15.3	0.0	6.3	8.3	15.0
	Silica replacing calcite shrubs	0.0	0.0	0.0	0.0	0.0	1.0	0.0	0.0	1.7	2.0	2.7	0.3
	Silica replacing spherulites	0.0	0.0	0.7	0.0	0.0	0.0	0.0	0.0	0.0	0.3	0.3	0.0
	Silica replacing Mg-clays + filling matrix dissolution porosity	0.0	0.0	0.0	0.3	0.0	0.0	0.0	6.0	0.0	0.0	10.7	0.0
	Silica growth-framework pores filling	0.0	0.0	0.0	0.0	0.0	11.0	0.0	0.0	0.0	0.0	0.0	0.0
	Dolomite replacing calcite shrubs	0.0	0.0	0.0	1.7	0.0	3.3	0.0	0.3	1.7	4.3	0.3	0.0
	Dolomite replacing calcite spherulites	0.0	0.0	0.7	0.0	3.3	0.0	7.0	22.0	0.0	1.7	0.0	0.0
	Dolomite replacing Mg-clays + filling matrix dissolution porosity	12.7	15.7	28.0	3.8	31.7	0.0	35.3	18.0	5.3	16.0	6.0	12.3
	Dolomite growth-framework pores filling	0.0	0.0	0.0	0.0	0.0	0.0	0.0	1.0	0.3	0.3	0.0	0.7
	Dolomite replacing undifferentiated primary constituent	0.0	0.0	0.0	0.0	0.0	0.0	0.0	0.0	0.0	0.0	0.0	0.0
	Calcite replacing Mg-clays + filling matrix dissolution porosity	0.0	0.0	0.0	0.3	0.0	0.0	0.0	0.0	0.0	0.0	0.0	0.0
	Calcite growth-framework pores filling	0.7	0.0	0.0	1.0	0.0	0.0	0.0	0.0	0.0	0.0	0.0	0.0
	Other diagenetic constituents	0.0	2.0	0.7	0.7	0.7	10.0	0.3	0.0	0.0	0.0	0.0	0.3
Porosity	**Matrix dissolution porosity**	15.7	9.7	5.3	8.6	10.3	0.0	6.3	7.7	3.3	11.0	9.0	7.3
	Intra-aggregate porosity	4.3	8.7	4.0	0.7	0.0	0.0	1.7	1.0	4.0	2.3	0.0	0.7
	Growth-framework porosity	1.3	0.0	0.0	2.1	0.0	6.7	0.0	2.3	4.7	0.3	0.0	3.3
	Other porosity (Vugs, fractures, channels, molds, and breccia)	0.0	0.0	0.0	0.3	0.0	0.0	0.0	0.0	2.3	1.7	0.0	0.3

APPENDIX C - Petrographic Descriptions – Intraclastic rocks- Article 2.

	Constituents (%)	W01-S03	W02-S04	W19-S06	W19-S05	W19-S02	W19-S01	W22-S05	W22-S04
Primary	**Calcite intraclasts**	77.7	61.7	25.7	20.0	4.3	9.0	83.0	70.3
	Mg-clay ooids	0.0	0.0	0.0	53.0	53.0	57.7	1.3	0.0
	Mg-clay peloids	0.0	3.3	44.0	0.0	0.0	0.0	0.0	0.0
	Mg-clay matrix	0.0	0.0	0.0	0.0	0.0	0.0	0.0	0.0
	Calcite intraclasts	0.0	0.0	14.0	0.0	0.0	0.0	0.0	0.0
Diagenetic	**Intraparticle calcite**	0.3	2.7	44.0	0.3	0.0	0.0	0.0	0.0
	Interparticle calcite	0.0	1.3	0.7	1.3	0.0	0.7	0.0	0.0
	Intraparticle dolomite	2.0	14.3	0.0	1.0	22.0	14.7	0.0	4.7
	Interparticle dolomite	2.7	6.0	0.0	0.3	2.3	2.3	0.3	12.3
	Pore linning dolomite	0.7	0.0	0.0	0.0	0.0	0.0	0.0	6.0
	Pore filling dolomite	2.0	6.0	0.0	0.3	2.3	2.3	0.3	6.3
	Matrix replacive dolomite	0.0	0.0	0.0	0.0	0.0	0.0	0.0	0.0
	Intraparticle silica	1.3	0.0	0.3	1.7	0.3	0.3	0.0	0.3
	Interparticle silica	0.0	0.0	0.0	0.0	0.3	0.0	0.0	0.0
	Others (clay minerals, bitumen, pyrite, undifferenced)	0.0	0.0	0.0	0.0	0.0	0.0	0.0	0.0
Porosity	**Interparticle**	12.3	9.7	13.3	7.3	15.7	11.7	13.7	10.3
	Intraparticle	1.7	4.3	2.0	8.7	1.7	3.7	1.7	2.0
	Others (vug, channel, mold)	2.0	0.0	0.0	0.3	0.3	0.0	0.0	0.0
	Total	16.0	14.0	15.3	16.3	17.7	15.3	15.3	12.3
	Packing	45	52	54	52	65	60	57	29

	Constituents (%)	W22-S01	W13-S01	W24-S03	W24-S02	W27-S06	W27-S05	W27-S04	W27-S03
Primary	Calcite intraclasts	6.7	78.0	31.0	36.3	74.7	66.7	28.7	0.0
	Mg-clay ooids	75.7	0.0	0.0	0.0	0.0	0.0	0.0	0.0
	Mg-clay peloids	0.0	0.0	0.0	0.0	0.0	0.0	54.3	54.7
	Mg-clay matrix	0.0	0.0	0.0	0.0	0.0	0.0	1.3	0.0
	Calcite intraclasts	0.0	0.0	0.0	0.0	0.0	0.0	0.0	0.0
Diagenetic	Intraparticle calcite	0.0	0.0	0.0	0.0	0.0	0.0	42.3	36.3
	Interparticle calcite	0.0	0.0	0.0	0.0	1.0	0.0	0.0	7.7
	Intraparticle dolomite	4.7	5.3	37.0	30.3	2.3	4.3	7.3	17.7
	Interparticle dolomite	0.7	1.3	21.7	23.7	4.7	13.3	7.7	23.0
	Pore linning dolomite	0.0	0.0	9.7	12.0	4.0	13.0	2.7	4.0
	Pore filling dolomite	0.7	1.3	12.0	11.7	0.7	0.3	5.0	19.0
	Matrix replacive dolomite	0.0	0.0	0.0	0.0	0.0	0.0	0.0	0.0
	Intraparticle silica	0.3	1.0	1.0	0.7	2.0	1.3	7.0	0.7
	Interparticle silica	1.3	0.0	0.0	0.0	0.0	0.0	0.0	0.0
	Others (clay minerals, bitumen, pyrite, undifferenced)	0.0	0.0	0.0	0.0	0.0	0.0	0.0	0.0
Porosity	Interparticle	10.7	10.0	5.0	5.3	12.0	10.3	3.3	2.7
	Intraparticle	0.0	4.3	4.3	3.3	3.3	4.0	3.3	10.7
	Others (vug, channel, mold)	0.0	0.0	0.0	0.3	0.0	0.0	0.3	1.3
	Total	10.7	14.3	9.3	9.0	15.3	14.3	7.0	14.7
	Packing	70	56	21	39	28	0	27	33

	Constituents (%)	W14-S09	W14-S06	W15-S13	W15-S12	W15-S04	W15-S03	W15-S02	W06-S03
Primary	**Calcite intraclasts**	65.0	67.0	70.7	77.0	75.3	75.0	60.0	53.0
	Mg-clay ooids	0.0	0.0	0.0	0.0	0.0	0.0	0.0	0.0
	Mg-clay peloids	0.0	0.0	0.0	0.0	0.0	0.3	0.0	0.0
	Mg-clay matrix	0.0	2.0	0.3	0.0	0.0	0.0	0.0	0.0
	Calcite intraclasts	0.0	0.0	0.0	0.0	0.0	0.0	0.0	0.0
Diagenetic	**Intraparticle calcite**	0.0	0.0	0.0	0.0	0.0	0.0	0.0	0.0
	Interparticle calcite	0.0	0.0	1.0	2.7	0.0	0.0	0.0	1.0
	Intraparticle dolomite	5.3	6.0	4.7	0.0	3.0	1.3	12.3	11.7
	Interparticle dolomite	15.3	13.0	10.0	0.0	2.3	13.7	12.3	23.3
	Pore linning dolomite	11.3	4.3	0.0	0.0	0.0	0.0	8.3	0.0
	Pore filling dolomite	4.0	8.7	10.0	0.0	2.3	13.7	4.0	23.3
	Matrix replacive dolomite	0.0	1.3	0.0	0.0	0.0	0.0	0.0	0.0
	Intraparticle silica	0.3	0.3	0.3	0.0	2.7	0.3	2.7	0.0
	Interparticle silica	1.0	0.0	0.3	0.0	0.0	0.0	0.3	0.0
	Others (clay minerals, bitumen, pyrite, undifferenced)	0.0	0.3	0.7	0.0	2.0	0.3	0.0	0.0
Porosity	**Interparticle**	8.3	6.7	12.0	17.0	11.7	6.7	9.7	6.3
	Intraparticle	4.7	5.3	0.3	3.3	3.0	2.7	2.7	4.0
	Others (vug, channel, mold)	0.0	0.0	0.0	0.0	0.0	0.0	0.0	0.7
	Total	13.0	12.3	13.0	20.3	16.7	9.7	12.3	11.0
	Packing	34	14	3	32	60	55	45	37

	Constituents (%)	W08-S03	W08-S02	W08-S01	W09-S03	W09-S02	W09-S01	W16-S03	W16-S02
Primary	**Calcite intraclasts**	73.0	52.0	69.7	66.0	56.0	27.3	55.7	65.0
	Mg-clay ooids	0.0	0.0	0.0	0.0	0.0	27.3	0.0	0.0
	Mg-clay peloids	1.3	16.7	0.0	0.0	0.0	0.0	0.0	0.0
	Mg-clay matrix	0.0	7.0	0.0	0.0	0.0	0.0	4.3	0.0
	Calcite intraclasts	0.0	0.0	0.3	0.0	0.0	0.0	0.0	0.0
Diagenetic	**Intraparticle calcite**	1.3	16.3	0.0	0.0	0.0	0.0	0.0	0.0
	Interparticle calcite	1.7	3.3	2.7	0.3	0.0	4.0	0.0	0.0
	Intraparticle dolomite	4.0	1.0	16.7	2.3	5.3	5.7	8.0	9.3
	Interparticle dolomite	6.0	11.0	8.0	17.7	16.7	17.3	16.0	9.7
	Pore linning dolomite	0.0	0.0	1.7	1.7	12.3	0.0	0.0	2.7
	Pore filling dolomite	6.0	11.0	6.3	16.0	4.3	17.3	16.0	7.0
	Matrix replacive dolomite	0.0	7.0	0.0	0.0	0.0	0.0	4.3	0.0
	Intraparticle silica	1.7	0.3	0.3	0.0	0.0	0.0	1.0	2.3
	Interparticle silica	0.3	0.0	0.0	0.0	0.0	0.0	0.0	0.0
	Others (clay minerals, bitumen, pyrite, undifferenced)	0.0	0.0	0.0	0.3	0.0	0.0	0.0	0.0
Porosity	**Interparticle**	7.3	5.0	8.0	11.0	15.0	12.0	11.0	4.7
	Intraparticle	2.0	4.0	2.7	2.3	6.0	6.3	3.7	9.0
	Others (vug, channel, mold)	2.7	0.0	0.0	0.0	1.0	0.0	0.3	0.0
	Total	12.0	9.0	10.7	13.7	22.0	18.3	15.0	13.7
	Packing	46	60	49	42	31	34	21	36

	Constituents (%)	W16-S01	W10-S08	W10-S04	W10-S01
Primary	Calcite intraclasts	53.7	68.0	60.7	75.3
	Mg-clay ooids	0.0	0.0	0.0	0.0
	Mg-clay peloids	0.0	0.0	0.0	0.0
	Mg-clay matrix	0.0	0.0	17.3	0.0
	Calcite intraclasts	0.0	0.0	0.3	0.0
Diagenetic	Intraparticle calcite	0.0	0.0	0.0	0.0
	Interparticle calcite	1.7	0.3	0.3	0.0
	Intraparticle dolomite	17.7	8.3	15.3	7.7
	Interparticle dolomite	11.0	1.0	0.0	7.7
	Pore linning dolomite	0.0	0.0	0.0	0.0
	Pore filling dolomite	11.0	1.0	0.0	7.7
	Matrix replacive dolomite	0.0	0.0	3.0	0.0
	Intraparticle silica	0.0	5.7	3.0	1.3
	Interparticle silica	0.0	3.0	7.7	1.0
	Others (clay minerals, bitumen, pyrite, undifferenced)	0.0	0.3	0.7	0.0
Porosity	Interparticle	10.0	7.0	8.7	4.3
	Intraparticle	6.0	6.3	0.3	2.7
	Others (vug, channel, mold)	0.0	0.0	0.3	0.0
	Total	16.0	13.7	10.0	7.0
	Packing	30	54	83	60

APPENDIX D - Compilation of *In-Situ* Rock Statistics Derived from Petrography and Laboratory Data (Pore Size, RCAL, and SCAL) - Article 2.

Sample	Sor	Phi	k	Swi	Average Pore Area	Modal Radius	P50 Radius	P10 Radius	P90 Radius	Eq Pore Radius	FAC
	%	%	mD	%	mm²	µm	µm	µm	µm	mm	
W17-S01	29	17.9	88.2	17.9	0.0043					0.037	Muddy Spherulstone
W32-S01	36.6	11.9	5.9	34.2	0.0090					0.054	
W10-S02	37.9	13	852	29.2	0.0312	9.69	5.33	32.71	0.46	0.100	Muddy Shrubstone
W10-S03	34.5	13.8	788	20	0.0312	43.70	15.37	65.42	0.13	0.100	Muddy Shrubstone
W10-S09	39.3	20	499.2	25.8	0.0004	9.69	4.44	32.71	0.49	0.011	Shrub-spherulstone
W01-S01	38.8	9.3	587	20.1	0.0034	88.13	12.19	125.45	0.08	0.033	Shrubstone
W01-S02	42	9.6	2519	19.7	0.0487	125.45	12.93	133.29	0.09	0.125	Shrubstone
W01-S04	41.6	6.7	284	21.5	0.0275	62.00	5.06	118.48	0.06	0.094	Shrubstone
W02-S05	17.2	20	21.7	15.5	0.0003	2.41	1.46	2.76	0.33	0.009	Muddy Spherulstone
W03-S01	31.6	16.2	99.3	18.5	0.0046	3.95	1.32	8.20	0.12	0.038	Shrub-spherulstone
W03-S02	20.7	16.7	5.93	22	0.0002					0.007	Muddy Spherulstone
W03-S07	20	13.5	11.4	26.9	0.0005					0.012	Spherulstone
W03-S08	46.5	20.3	143	18.1	0.0017	0.98	1.98	43.88	0.22	0.023	Muddy Shrubstone
W03-S09	22.14	19.1	62.4	17.71	0.0008					0.016	Spherulstone
W11-S01	47.7	12	335	21.9	0.0012	16.33	4.25	24.57	0.37	0.020	Shrub-spherulstone
W11-S04	21.6	8.6	40.7	31.4	0.0010	10.25	5.05	12.93	0.55	0.018	Shrubstone
W18-S02	25.4	14	4.02	30	0.0012	1.01	0.59	1.45	0.07	0.020	Muddy Spherulstone
W18-S03	23.2	14.5	1157	29.8	0.0131	53.05	18.35	83.96	0.59	0.064	Shrub-spherulstone
W18-S04	23.6	9.7	34.6	39.5	0.0082	10.22	2.30	26.14	0.05	0.051	Shrubstone
W18-S06	23.9	6.8	135	32.8	0.0069	37.15	5.70	46.98	0.08	0.047	Muddy Spherulstone
W30-S02	7.8	11.6	836	30.9	0.0092					0.054	

Sample	Sor	Phi	k	Swi	Average Pore Area	Modal Radius	P50 Radius	P10 Radius	P90 Radius	Eq Pore Radius	FAC
	%	%	mD	%	mm²	µm	µm	µm	µm	mm	
W30-S04	26.3	12.6	18.4	29.5	0.0182					0.076	Spherulstone
W30-S06	33.6	16.5	87.8	39.9	0.0028					0.030	Spherulstone
W31-S01	31.2	13	360	21.4	0.0103					0.057	Muddy Shrubstone
W31-S04	46.6	9.7	30.1	18.8	0.0113	0.41	0.32	0.59	0.08	0.060	Shrubstone
W25-S01	18.3	9	3.5	36.8	0.0009	0.41	0.41	1.86	0.07	0.017	Mg-Clay Mudstone
W25-S03	19.7	12.5	90.9	26.2	0.0024	7.18	1.46	11.49	0.10	0.028	Muddy Spherulstone
W25-S04	19.5	12	379	27.5	0.0161	46.77	20.63	65.82	0.07	0.072	Spherulstone
W26-S01	16.25	9.9	52	24.87	0.0085	14.49	11.47	29.21	0.67	0.052	Shrub-spherulstone
W26-S02	22.64	9.1	53	32.02		7.19	6.40	16.28	0.52		Shrubstone
W16-S05	29.84	17.72	861	13.89	0.0051					0.040	Muddy Shrubstone
W16-S06	34.13	17.94	265	19.3	0.0067	26.14	9.09	53.05	0.66	0.046	Shrubstone
W29-S02	14.8	13.6	8.47	29.4	0.0078					0.050	Muddy Spherulstone
W14-S01	21.7	12.5	86.2	28.2	0.0050					0.040	Spherulstone
W14-S02	33	19.2	98.5	32.6	0.0127					0.064	Muddy Shrubstone
W14-S03	23.9	13.1	677	22.3	0.0045	23.23	9.72	78.41	0.09	0.038	Shrubstone
W14-S04	32	18.8	1866	18.1	0.0231	54.68	29.79	99.66	0.83	0.086	Shrubstone
W14-S05	31.5	11.8	512	25.8	0.0145	38.22	23.23	48.91	0.11	0.068	Shrubstone
W14-S07	21.9	13.6	158	29.4	0.0156					0.070	Muddy Shrubstone
W14-S10	20.3	11.6	327	20.7	0.0044					0.037	Shrubstone
W14-S12	26.2	15.3	104	33.6	0.0081					0.051	Muddy Shrubstone
W19-S03	22	21.4	48.7	25.7	0.0002					0.008	Mg-Clay Mudstone
W15-S01	38.1	20.4	1395	17.5	0.0214					0.083	Shrub-spherulstone

Sample	Sor	Phi	k	Swi	Average Pore Area	Modal Radius	P50 Radius	P10 Radius	P90 Radius	Eq Pore Radius	FAC
	%	%	mD	%	mm²	µm	µm	µm	µm	mm	
W15-S07	34.5	23.7	7893	20.5	0.0175					0.075	Shrub-spherulstone
W15-S09	54	20.7	590	9.3	0.0077					0.050	Muddy Shrubstone
W22-S06	38.2	20.8	1273	17.9	0.0147					0.068	Shrubstone
W15-S05	25	21.3	77	22	0.0021	1.86	2.38	9.08	0.85	0.026	Muddy Spherulstone
W15-S06	45.8	18.2	389	21.5	0.0196	2.09	1.44	4.50	0.14	0.079	Shrub-spherulstone
W20-S03	20.2	14.3	6.03	26.4	0.0001	1.00	0.66	2.61	0.06	0.006	Spherulstone
W20-S04	17	13.6	3.15	25.8	0.0051	1.64	0.66	1.85	0.11	0.040	Mg-Clay Mudstone
W21-S03	40.9	17.1	848	20.2		29.21	8.08	41.49	1.13		Shrub-spherulstone
W21-S04	41.8	18.8	440	16.4	0.0160	0.83	1.61	14.47	0.26	0.071	Shrub-spherulstone
W21-S05	41.3	19.5	1853	20.6	0.0197	16.28	5.68	46.36	0.23	0.079	Shrubstone
W21-S06	37.8	15.6	2709	16.6	0.0191	0.83	4.57	103.53	0.29	0.078	Shrubstone
W15-S14	24.6	17.3	5.83	17.6	0.0004					0.011	Spherulstone
W21-S07	32.7	13.8	89.3	21.7	0.0061	8.08	2.70	41.33	0.18	0.044	Shrub-spherulstone
W21-S08	29.4	18.5	387	22.9	0.0059	32.71	6.40	46.36	0.46	0.043	Shrub-spherulstone
W06-S02	25.1	17	19.1	19.3	0.0007					0.015	Muddy Spherulstone
W24-S04	27.2	16.5	14	24.8	0.0191					0.078	Shrub-spherulstone
W07-S05	48.2	16.5	79.4	13.1	0.0268					0.092	Shrubstone
W07-S02	44	14	12.7	18.4	0.0148					0.069	Shrubstone
W07-S04	44.8	14	173	22.5	0.0038					0.035	Shrubstone
W08-S04	24.7	13.4	6.26	23.4	0.0007	4.58	3.10	6.40	1.45	0.015	Muddy Spherulstone
W09-S04	44.2	19.7	22.2	22.3	0.0172					0.074	Shrub-spherulstone
W09-S05	55.8	16.6	951	16.2	0.0050	1.00	18.29	82.03	0.53	0.040	Muddy Spherulstone

APPENDIX E - Compilation of Intraclastic Rock Statistics Derived from Petrography and Laboratory Data (Pore Size, RCAL, and SCAL) - Article 2.

Sample	Sor	k	Phi	Swi	Particle size	Sorting	Average Pore Area	Equivalent Pore Radius	Modal Radius	P50 Radius	P10 Radius	P90 Radius	FAC
	%	mD	%	%	mm	adim	mm	mm	μm	μm	μm	μm	
W01-S03	37.9	1762	12	22.1	1.0209	0.4563	0.0106	0.0581	34.73	9.64	36.77	0.15	Rudstone
W02-S04	15.4	18.5	18.6	21.2	0.1330	0.0521	0.0003	0.0096	1.98	1.00	2.57	0.23	Grainstone
W02-S02	20.5	53	17.5	20.2	0.9624	0.4580	0.0026	0.0286	10.20	1.62	12.89	0.20	Grainstone
W02-S01	26.8	109	19.4	18.9	0.7247	0.5070	0.0018	0.0242	12.89	3.53	14.49	0.32	Grainstone
W02-S03	20.1	247	22.3	15.6	0.3398	0.1604	0.0026	0.0288	12.89	6.40	20.55	0.41	Grainstone
W03-S06	21.1	6.2	18.8	24	0.2395	0.1390	0.0003	0.0099					Grainstone
W03-S05	22	10.3	21.3	24.2	0.1041	0.0421	0.0002	0.0072	3.95	1.32	8.20	0.12	Grainstone
W03-S03	27.5	23.4	16.2	27.79	0.0720	0.0222	0.0006	0.0134					Grainstone
W33-S06	31.1	42.9	15.5	19.6	1.0178	0.4518	0.0077	0.0496	8.58	4.50	14.53	0.26	Rudstone
W33-S01	50.6	156	18.4	18.7	1.0001	0.4688	0.0117	0.0609	3.62	2.13	17.31	0.06	Rudstone
W33-S07	20.6	244	16.1	41	0.8692	0.5644	0.0163	0.0719					Grainstone
W33-S02	20.2	1488	15.8	17.4	0.7030	0.3237			31.00	20.63	43.88	0.55	Grainstone
W33-S09	14.9	4.57	15	23.6	0.2587	0.1568	0.0005	0.0127	2.51	1.40	3.16	0.13	Grainstone
W33-S03	24.1	20.9	17.4	20.7	0.2143	0.0732			3.78	1.58	4.50	0.18	Grainstone
W33-S08	15.2	48.7	24.6	29.6	0.1205	0.0428	0.0004	0.0118	2.01	1.12	3.78	0.11	Grainstone
W06-S03	22.9	63.7	18.7	18.9	0.5698	0.2622	0.0003	0.0090					Grainstone
W08-S02	35.1	6.31	15	18	0.3307	0.1345	0.0003	0.0105	1.01	1.14	3.04	0.26	Grainstone
W08-S01	26.7	20.1	16.4	25.3	0.3058	0.1115	0.0010	0.0177					Grainstone
W08-S03	41.9	522	15.8	18	0.9073	0.4169	0.0036	0.0340					Grainstone
W09-S01	41.2	530	24.6	24.3	0.6460	0.3272	0.0058	0.0431					Grainstone
W09-S02	57.2	2293	25.7	12.8	1.0474	0.5375	0.0070	0.0472					Grainstone
W09-S03	31.3	62.7	18	22	0.7315	0.2687	0.0037	0.0342	1.01	1.43	9.08	0.37	Grainstone

Sample	Sor	k	Phi	Swi	Particle size	Sorting	Average Pore Area	Equivalent Pore Radius	Modal Radius	P50 Radius	P10 Radius	P90 Radius	FAC
	%	mD	%	%	mm	adim	mm	mm	μm	μm	μm	μm	
W10-S04	46.8	330	9.7	15.1	1.2161	0.5599	0.0020	0.0250	20.63	15.37	36.64	0.94	Rudstone
W10-S08	43.5	737.9	21.1	20.3	0.9238	0.3956	0.0065	0.0456	9.69	4.44	32.71	0.49	Rudstone
W10-S01	29.1	35.2	13.7	32.5	0.8874	0.6534			9.69	3.23	9.69	0.46	Rudstone
W11-S02	38.4	694	15.7	22.9	0.7087	0.2715	0.0078	0.0500	19.46	8.60	23.18	0.44	Grainstone
W11-S03	30.2	65.3	11.1	34	0.3016	0.1228	0.0055	0.0420	3.43	3.24	8.60	0.31	Grainstone
W13-S01	27.4	851	18.4	20.8	1.2195	0.5289	0.0278	0.0940					Rudstone
W14-S09	16.9	24	14.6	36.3	0.6588	0.3624	0.0036	0.0337	7.57	3.39	11.00	0.64	Rudstone
W14-S06	28.7	40.5	12.2	23.7	0.7283	0.3966	0.0082	0.0512					Grainstone
W15-S02	23.5	640	17.8	24.5	0.7893	0.3360	0.0046	0.0383					Grainstone
W15-S13	21	708	17.3	16.9	0.7186	0.3740	0.0231	0.0857					Grainstone
W15-S03	19.7	17.4	16.4	26.7	0.6746	0.3624	0.0023	0.0270					Grainstone
W15-S04	33	499	19.4	14.9	0.4961	0.1851	0.0039	0.0352	20.51	11.45	23.13	0.84	Grainstone
W15-S12	38.2	4714	23	10.1	0.7175	0.2561	0.0076	0.0491					Grainstone
W15-S01	38.1	1395	20.4	17.5	1.2318	0.5480	0.0314	0.1000					Rudstone
W15-S08	39	380	24.6	9.8	0.6516	0.4122	0.0100	0.0564					Grainstone
W15-S05	25	77	21.3	22	0.4977	0.1691	0.0078	0.0499					Grainstone
W16-S01	14.28	51	19.57	18.44	0.3987	0.2238	0.0007	0.0147	5.69	2.69	6.40	0.52	Grainstone
W16-S03	33.49	96.2	19.2	20.37	0.6010	0.2709	0.0013	0.0206	1.01	1.86	10.23	0.29	Grainstone
W16-S02	12.08	11.2	13.8	26.26	0.6186	0.2617	0.0039	0.0351	3.04	2.42	9.10	0.75	Grainstone
W16-S04	22.74	785	17.39	17.94	0.3660	0.2183	0.0023	0.0271	12.91	6.38	23.23	0.75	Grainstone
W17-S02	9.1	4.47	11.6	29.4	0.3122	0.0966							Grainstone
W19-S02	15	568	22.1	12.1	0.4506	0.1830	0.0061	0.0440	26.20	8.08	26.20	0.47	Grainstone

Sample	Sor	k	Phi	Swi	Particle size	Sorting	Average Pore Area	Equivalent Pore Radius	Modal Radius	P50 Radius	P10 Radius	P90 Radius	FAC
	%	mD	%	%	mm	adim	mm	mm	μm	μm	μm	μm	
W19-S01	31.5	251	19.6	15.1	0.6310	0.2222	0.0064	0.0452					Grainstone
W19-S05	18.6	427	22.6	13.2	0.7998	0.4015	0.0031	0.0313					Grainstone
W19-S06	12.1	69.8	22.6	20.9	0.2478	0.0872	0.0006	0.0135	5.68	3.95	6.40	0.33	Grainstone
W20-S05	37.2	193	20.9	15.3	0.9540	0.4023	0.0003	0.0098	1.66	1.66	12.94	0.18	Grainstone
W20-S02	25.5	50.2	16.6	20.6	0.8503	0.4535	0.0085	0.0520	5.70	2.11	9.08	0.23	Grainstone
W20-S01	15.7	3.52	14.1	21.8	0.5972	0.2176	0.0007	0.0146	1.01	1.01	3.02	0.20	Grainstone
W20-S06	18.3	12.5	19.5	19.9	0.2210	0.0860	0.0035	0.0332	1.88	0.85	2.11	0.14	Grainstone
W21-S08	29.4	387	18.5	22.9					32.71	6.40	46.36	0.46	Grainstone
W22-S01	42.2	2126	12.5	20	1.0588	0.4893	0.0395	0.1121					Rudstone
W22-S04	35	408	20	24.5	0.7094	0.3315	0.0071	0.0474					Grainstone
W22-S05	24.1	1109	18.7	23.3	0.6506	0.2411	0.0072	0.0478					Grainstone
W22-S02	23.5	254	15.6	23.3	0.5233	0.2455	0.0043	0.0369					Grainstone
W24-S03	19.4	6.693	16.3	27.9	0.4590	0.1719	0.0015	0.0219					Grainstone
W24-S02	24.2	14.4	16.1	24.2	0.4553	0.1735	0.0033	0.0326					Grainstone
W24-S01	24.4	7.89	14.4	32									Rudstone
W27-S03	13.7	1.85	14.56	21.2	0.2099	0.0705	0.0002	0.0087					Grainstone
W27-S04	11.7	4.32	14.7	30.7	0.1773	0.1109	0.0004	0.0114					Grainstone
W27-S05	16.9	26.2	14.22	32.1	0.1669	0.0623	0.0016	0.0223					Grainstone
W27-S06	24.7	322	16.3	28.4	0.2999	0.1138	0.0036	0.0337					Grainstone
W28-S01	47.7	15.4	13.5	16.94	0.8381	0.3435	0.0102	0.0570	0.67	0.67	2.08	0.18	Rudstone
W28-S02	20.27	1.63	10.6	28.33	0.5582	0.2133	0.0052	0.0406					Grainstone
W28-S05	13.32	1.48	15.2	23.59	0.2843	0.1400	0.0017	0.0230					Grainstone

Sample	Sor	k	Phi	Swi	Particle size	Sorting	Average Pore Area	Equivalent Pore Radius	Modal Radius	P50 Radius	P10 Radius	P90 Radius	FAC
	%	mD	%	%	mm	adim	mm	mm	μm	μm	μm	μm	
W30-S01	15.4	455	32.5	30.7	0.0546	0.0177	0.0005	0.0124					Grainstone

APPENDIX F - Compilation of results from the simulations - Article 4.

Model	Facies	Porosity (%)	Calcite (%)	Dolomite (%)	Water-wet Sor (%)	Oil-wet Sor (%)	Pore Throat Diameter (µm)			Pore Diameter (µm)			Max tortuosity (µm)	Mean tortuosity (µm)	Surface Area (m²/m³)
							P10	P50	P90	P10	P50	P90			
Sph_Dol_60_20	Mud-Spherulstone	35.9	43.2	20.9	22.9	18.8	15.8	29.7	36.5	15.8	30.4	42.5	1.22	1.05	26970.2
Sph_Dol_60_15	Mud-Spherulstone	30.7	43.2	26.1	16.6	27.8	11.3	20.0	25.9	11.3	20.1	28.9	1.22	1.05	32712.8
Sph_Dol_60_10	Mud-Spherulstone	23.4	43.2	33.4	15.4	23.5	6.8	13.9	19.0	6.8	14.0	21.6	1.22	1.06	38147.8
Sph_Dol_60_6	Mud-Spherulstone	16.4	43.2	40.4	17.9	14.0	4.3	9.7	13.9	4.3	10.0	17.2	1.22	1.07	38062.2
Sph_Dol_40_20	Mud-Spherulstone	27.8	56.3	16.0	26.1	17.1	15.0	29.0	35.7	15.0	30.0	42.0	1.16	1.07	22754.7
Sph_Dol_40_15	Mud-Spherulstone	23.6	56.3	20.1	21.7	19.9	10.6	20.8	27.0	10.6	21.2	31.1	1.16	1.07	26473.5
Sph_Dol_40_10	Mud-Spherulstone	18.1	56.3	25.6	17.6	20.4	6.7	13.6	18.0	6.7	13.8	21.4	1.16	1.07	30575.9
Sph_Dol_40_6	Mud-Spherulstone	12.3	56.3	31.4	20.6	13.0	4.3	9.1	13.4	4.3	9.8	17.0	1.22	1.09	29761.7
Sph_Dol_30_20	Spherulstone	18.9	70.9	10.2	31.8	7.8	16.6	34.1	43.6	16.7	36.6	53.4	1.19	1.07	14871.9
Sph_Dol_30_15	Spherulstone	16.3	70.9	12.8	29.1	9.3	12.2	25.4	33.0	12.2	27.4	39.8	1.20	1.08	16775.4
Sph_Dol_30_10	Spherulstone	12.7	70.9	16.4	27.7	12.0	7.9	16.9	22.6	8.0	17.9	27.2	1.21	1.09	18777
Sph_Dol_30_6	Spherulstone	8.9	70.9	20.3	23.5	14.1	4.5	10.1	13.8	4.5	10.5	16.6	1.20	1.09	20522.5
Shrub_Dol_Reg_30_10	Shrubstone	12.9	70.3	16.8	17.7	18.4	6.9	14.5	19.4	6.9	14.8	22.8	1.47	1.17	19436.85
Shrub_Dol_Reg_30_15	Shrubstone	16.1	70.3	13.7	18.7	21.0	9.8	19.0	25.3	9.8	19.3	28.5	1.44	1.17	18316.05
Shrub_Dol_Reg_30_20	Shrubstone	19.1	70.3	10.6	26.5	16.3	14.8	28.5	35.2	14.8	29.3	39.7	1.45	1.16	15351.2

Model	Facies	Porosity (%)	Calcite (%)	Dolomite (%)	Water-wet Sor (%)	Oil-wet Sor (%)	Pore Throat Diameter (µm)			Pore Diameter (µm)			Max tortuosity (µm)	Mean tortuosity (µm)	Surface Area (m²/m³)
Shrub_Dol_Reg_30_35	Shrubstone	23.7	70.3	6.0	31.7	9.9	26.9	48.8	58.6	27.1	51.6	67.3	1.45	1.16	11170.05
Shrub_Dol_Reg_30_50	Shrubstone	26.3	70.3	3.5	25.8	6.5	39.1	69.9	90.0	39.7	76.0	102.2	1.43	1.16	8686.05
Shrub_Dol_Reg_30_100	Shrubstone	28.6	70.3	1.1	24.1	3.1	58.9	118.2	158.8	60.9	132.2	176.3	1.43	1.15	6493.85
Shrub_Dol_Reg_30_200	Shrubstone	29.5	70.3	0.2	23.3	1.8	72.6	169.4	291.7	74.5	185.2	313.4	1.43	1.15	5581.75
Shrub_Dol_Reg_20_10	Shrubstone	8.7	80.1	11.2	19.5	18.7	6.8	14.2	19.4	6.8	14.9	22.8	1.72	1.38	13342.6
Shrub_Dol_Reg_20_15	Shrubstone	10.8	80.1	9.2	19.6	20.1	9.5	18.5	24.2	9.6	19.1	28.0	1.69	1.34	12721.25
Shrub_Dol_Reg_20_20	Shrubstone	12.8	80.1	7.1	28.0	15.9	14.1	27.7	34.6	14.2	28.8	39.6	1.69	1.34	10838.8
Shrub_Dol_Reg_20_35	Shrubstone	15.9	80.1	4.0	31.9	9.6	25.0	47.9	57.0	25.4	50.5	66.8	1.67	1.32	8176.15
Shrub_Dol_Reg_20_50	Shrubstone	17.6	80.1	2.3	27.3	6.0	34.5	66.8	90.4	35.8	73.9	100.8	1.66	1.32	6582.75
Shrub_Dol_Reg_20_100	Shrubstone	19.1	80.1	0.8	27.7	2.9	48.7	112.8	151.0	50.7	122.5	173.9	1.65	1.31	5233.1
Shrub_Dol_Reg_20_200	Shrubstone	19.8	80.1	0.1	27.7	1.7	56.0	138.6	274.0	60.2	175.8	293.4	1.69	1.34	4608.66
Shrub_Dol_Reg_10_10	Shrubstone	4.4	90.0	5.6	24.0	22.1	6.2	13.3	18.9	6.4	14.5	22.5	2.47	1.90	7099.6
Shrub_Dol_Reg_10_15	Shrubstone	5.4	90.0	4.6	25.1	19.2	8.9	17.5	23.4	9.2	18.7	27.9	2.42	1.84	6852.7
Shrub_Dol_Reg_10_20	Shrubstone	6.4	90.0	3.6	32.7	16.4	12.4	25.2	32.3	13.1	27.8	39.2	2.40	1.82	6051.45
Shrub_Dol_Reg_10_35	Shrubstone	8.0	90.0	2.0	38.7	9.9	20.7	43.0	52.0	22.4	48.1	65.2	2.34	1.80	4857.375
Shrub_Dol_Reg_10_50	Shrubstone	8.8	90.0	1.2	39.0	7.0	26.1	56.8	79.9	29.8	67.3	94.7	2.32	1.74	4169.16
Shrub_Dol_Reg_10_100	Shrubstone	9.6	90.0	0.4	40.4	4.3	35.9	84.2	133.8	38.5	101.0	157.7	2.33	1.75	3582.265
Shrub_Dol_Reg_10_200	Shrubstone	10.0	90.0	0.1	37.4	3.3	38.8	109.3	184.8	44.4	127.8	218.6	2.30	1.73	3282.96
Shrub_30	Shrubstone	29.7	70.3	0.0	22.1	1.5	76.9	193.4	418.3	79.1	208.6	418.3	1.43	1.15	5390.95
Shrub_20	Shrubstone	19.9	80.1	0.0	24.4	1.5	58.1	168.2	345.5	62.8	184.0	349.1	1.65	1.30	4501.905
Shrub_10	Shrubstone	10.0	90.0	0.0	38.5	3.2	39.6	113.5	188.7	45.4	131.7	219.8	2.30	1.73	3248.65
Shrub_Dol_Het_30_25	Shrubstone	24.8	70.3	5.0	27.7	3.7	32.8	67.7	126.5	33.9	79.7	138.0	1.44	1.16	9851.25
Shrub_Dol_Het_30_20	Shrubstone	19.5	70.3	10.2	31.6	4.8	19.6	41.1	87.5	20.5	52.0	98.2	1.48	1.18	12774.95
Shrub_Dol_Het_30_15	Shrubstone	14.5	70.3	15.2	35.4	7.5	12.2	29.0	69.4	14.1	37.9	78.3	1.53	1.22	13668.5
Shrub_Dol_Het_30_10	Shrubstone	10.2	70.3	19.5	33.9	17.7	7.7	20.8	59.9	10.4	29.6	66.1	1.58	1.28	12666.75

Model	Facies	Porosity (%)	Calcite (%)	Dolomite (%)	Water-wet Sor (%)	Oil-wet Sor (%)	Pore Throat Diameter (µm)			Pore Diameter (µm)			Max tortuosity (µm)	Mean tortuosity (µm)	Surface Area (m²/m³)
Shrub_Dol_Het_30_075	Shrubstone	7.3	70.3	22.4	31.1	26.1	6.0	17.6	56.5	8.5	25.0	60.7	2.01	1.36	10924.85
Shrub_Dol_Het_20_15	Shrubstone	14.8	80.1	5.1	32.3	4.6	20.8	57.7	107.4	23.8	71.6	135.2	1.70	1.35	7970.95
Shrub_Dol_Het_20_10	Shrubstone	10.1	80.1	9.8	35.1	9.1	11.7	29.3	65.0	14.2	39.6	77.0	1.75	1.45	9439.85
Shrub_Dol_Het_20_075	Shrubstone	7.2	80.1	12.7	37.6	15.2	8.0	20.9	52.0	10.4	29.7	61.4	2.09	1.58	9023.95
Shrub_Dol_Het_10_075	Shrubstone	7.3	90.0	2.7	38.4	8.0	17.5	37.7	80.5	20.2	52.3	94.7	2.63	2.01	3248.65

APPENDIX G – Raw and processed µCT slices - Article 5.

Dry Sample

Raw image (x central slice)
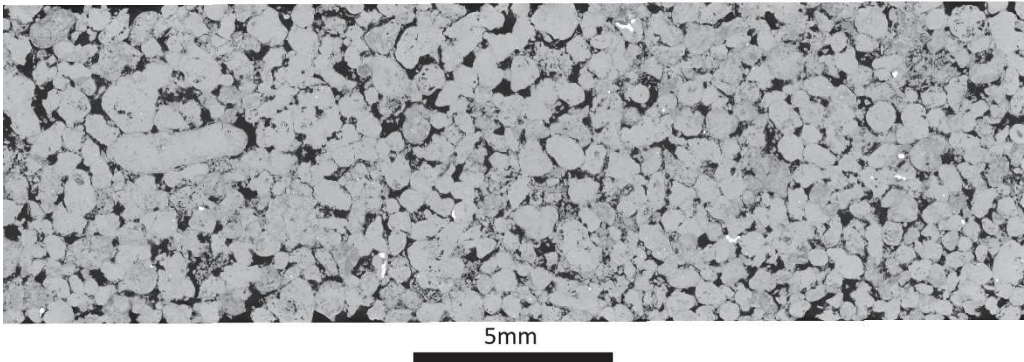
5mm

Raw image (z central slice)

4mm

Three phases segmented image (macropore (black), nonporous solid (ocher), and microporous solid (cyan)).

4mm

Porosity map (black 100% porous and white 0% porous).

4mm

Total porosity (%):	23.54
Macroporosity (%):	21.61
Microporosity (%):	1.93

Brine Saturated Sample

Raw image (x central slice)

5mm

Raw image (z central slice)

4mm
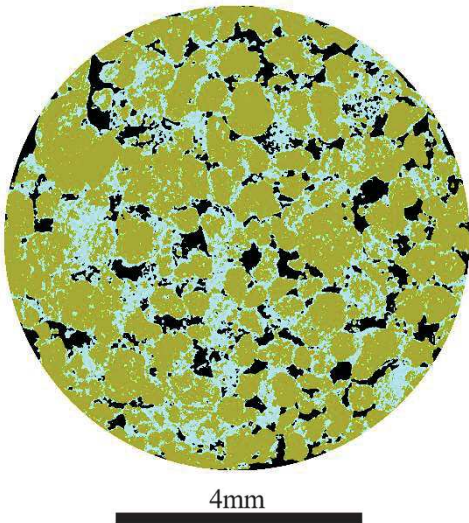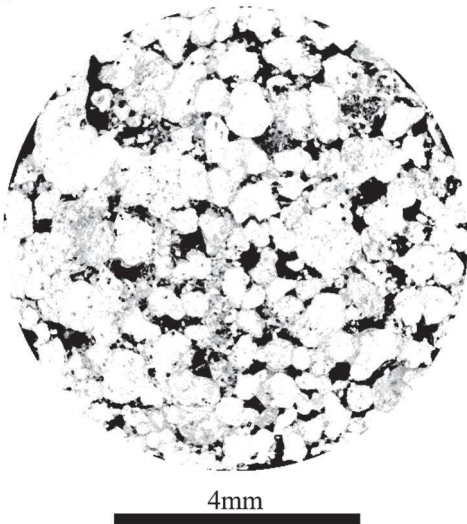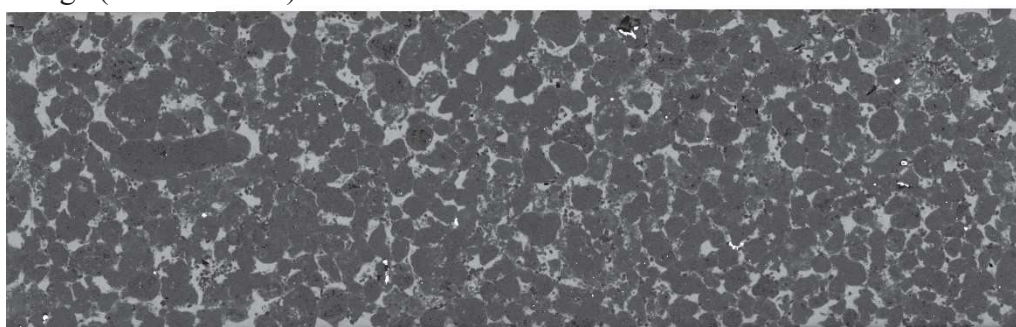
Drainage (11.52 psi)

Raw image (x central slice)
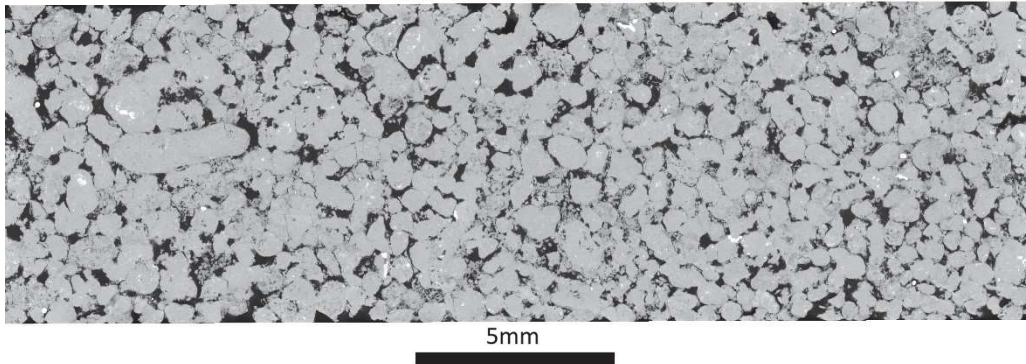
5mm

Raw image (z central slice)

Three phases segmented image (oil (black), solid (ocher), and brine (cyan)).

4mm

4mm

Brine-filled microporosity map (black 100% brine and white 0% brine).

4mm
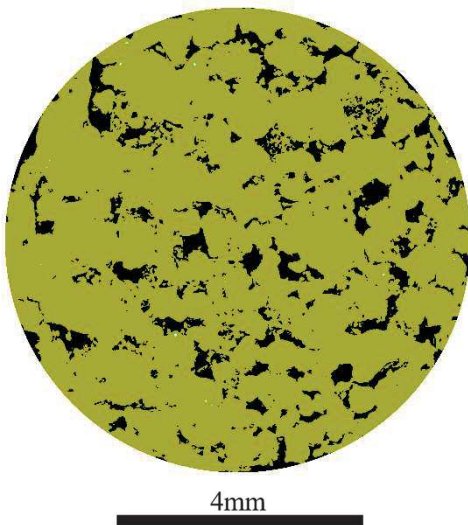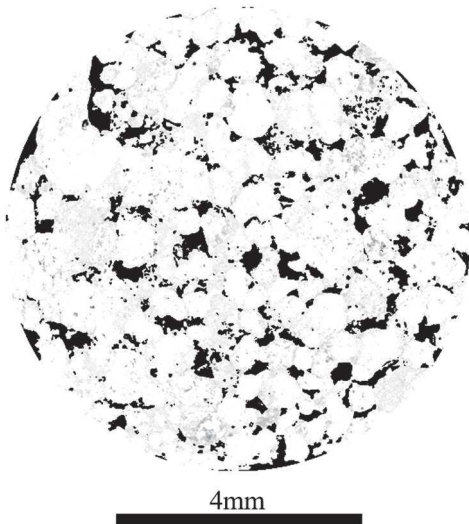
Total Sw (%):	8.10
Macro Sw (%):	0.33
Micro Sw (%):	26.24

Aging (7 days)

Raw image (x central slice)
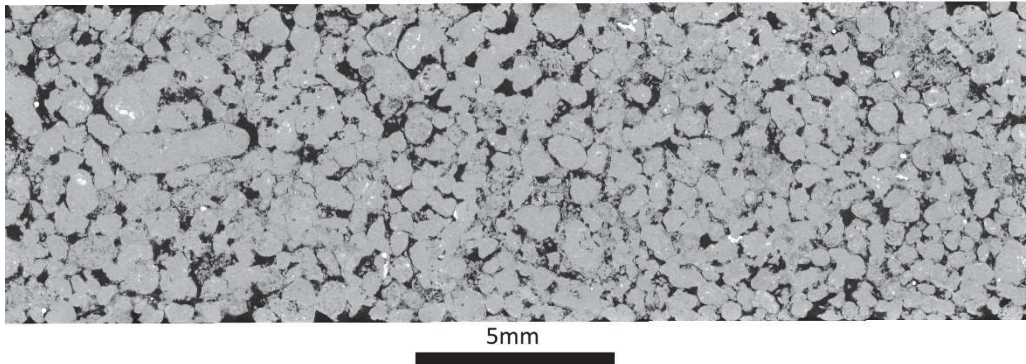
5mm

Raw image (z central slice)

4mm

Three phases segmented image (oil (black), solid (ocher), and brine (cyan)).

4mm

Brine-filled microporosity map (black 100% brine and white 0% brine).

4mm
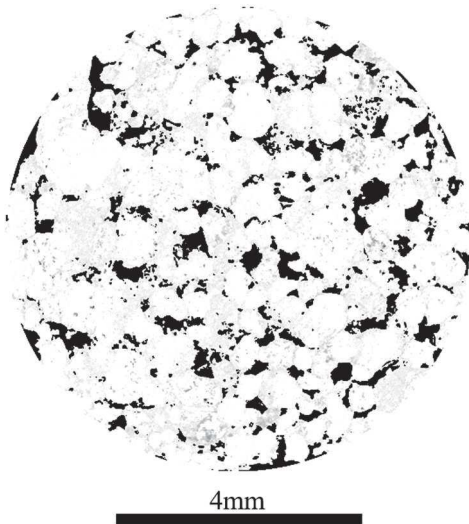
Total Sw (%):	7.63
Macro Sw (%):	0.29
Micro Sw (%):	24.75

Aging (16 days)

Raw image (x central slice)
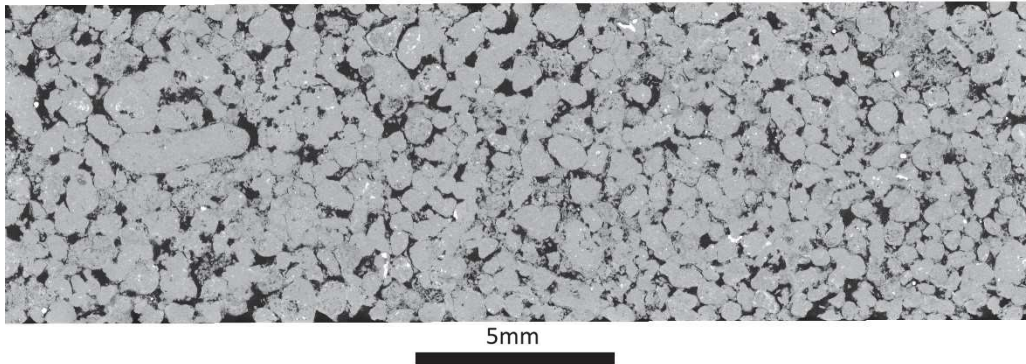
5mm

Raw image (z central slice)

4mm

Three phases segmented image (oil (black), solid (ocher), and brine (cyan)).

4mm

Brine-filled microporosity map (black 100% brine and white 0% brine).

4mm
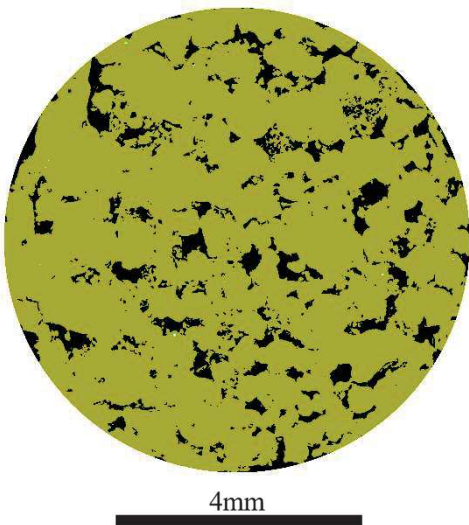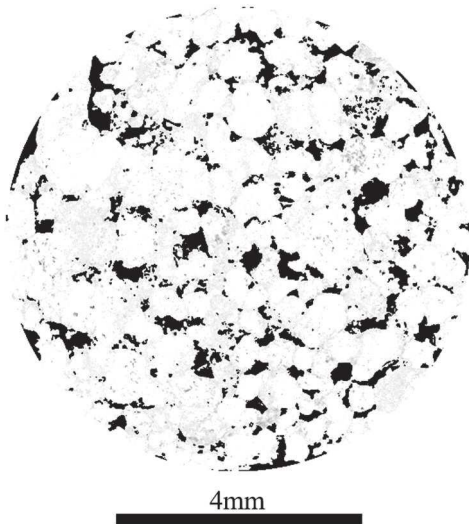
Total Sw (%):	6.77
Macro Sw (%):	0.27
Micro Sw (%):	21.95

Spontaneous Imbibition (5 days)

Raw image (x central slice)
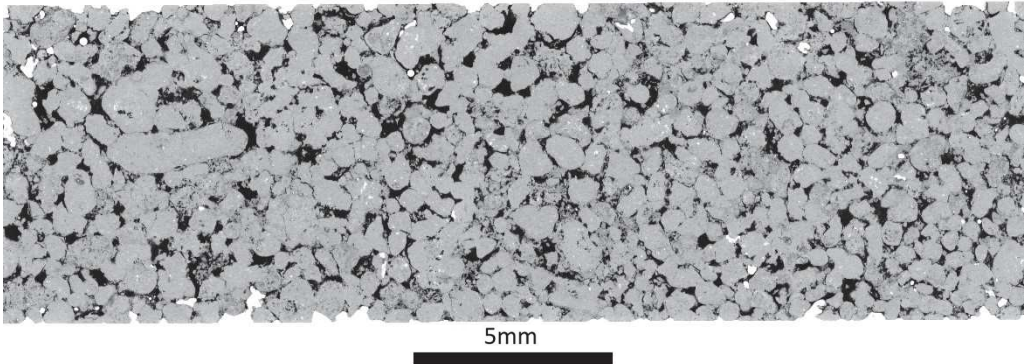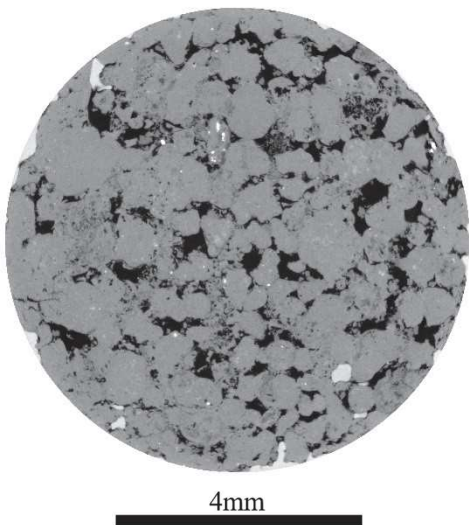
5mm

Raw image (z central slice)

Three phases segmented image (oil (black), solid (ocher), and brine (cyan)).

4mm

4mm

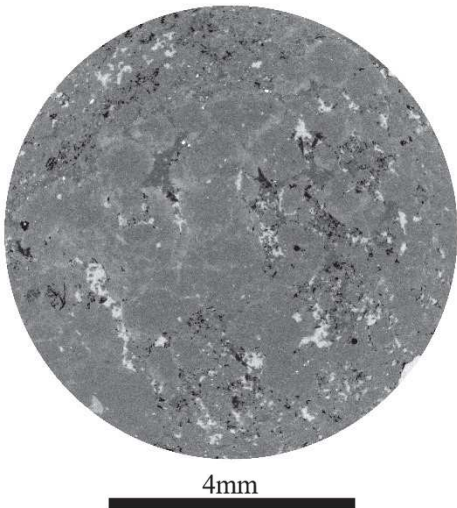Brine-filled microporosity map (black 100% brine and white 0% brine).

4mm
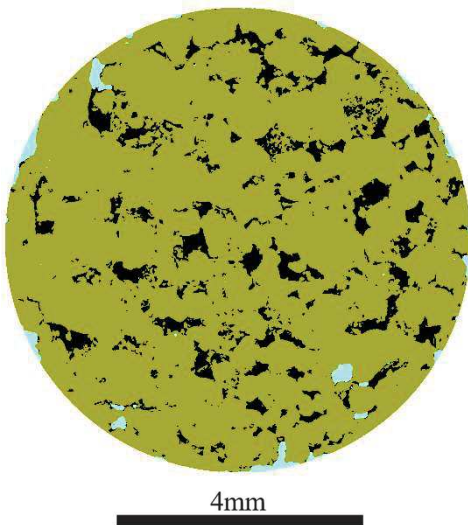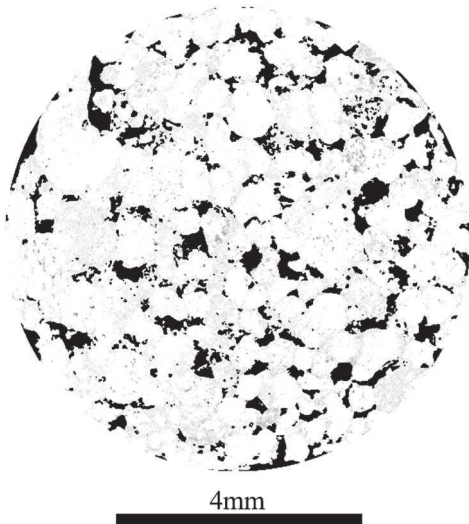
Total Sw (%):	21.45
Macro Sw (%):	18.61
Micro Sw (%):	28.05

Forced Imbibition (2.4 psi)

Raw image (x central slice)
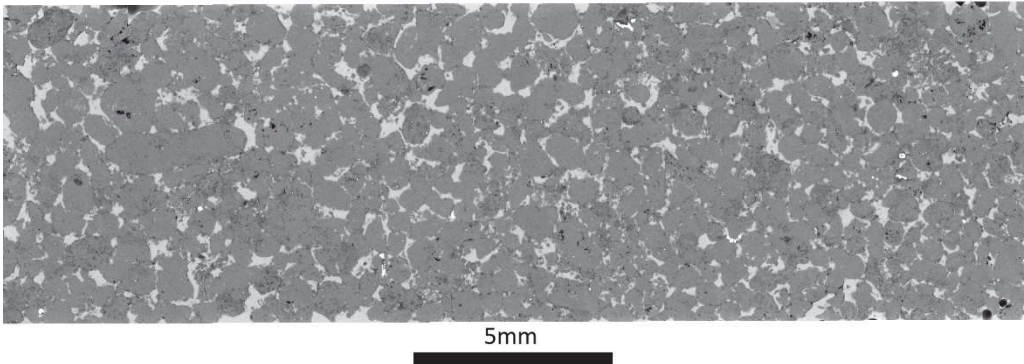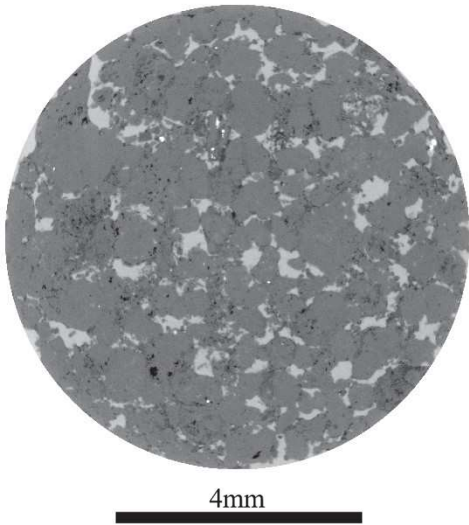
5mm

Raw image (z central slice)

4mm

Three phases segmented image (oil (black), solid (ocher), and brine (cyan)).

4mm

Brine-filled microporosity map (black 100% brine and white 0% brine).

4mm
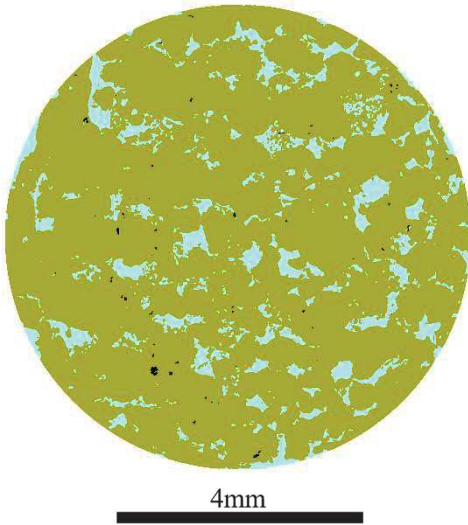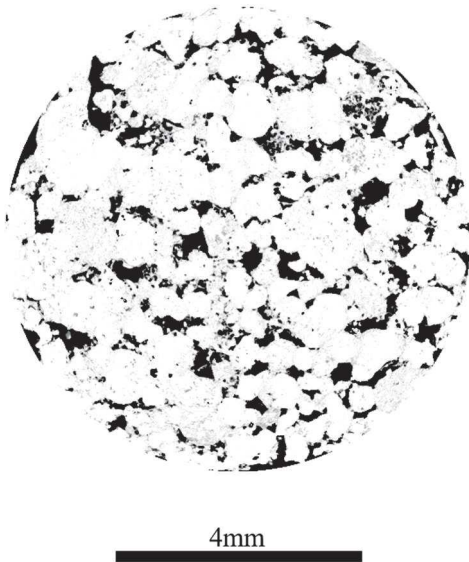
Total Sw (%):	89.14
Macro Sw (%):	98.29
Micro Sw (%):	67.82

Forced Imbibition (38.8 psi)

Raw image (x central slice)
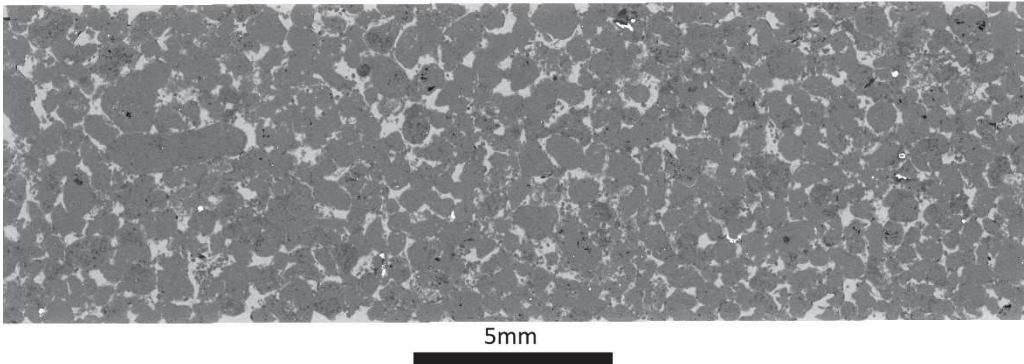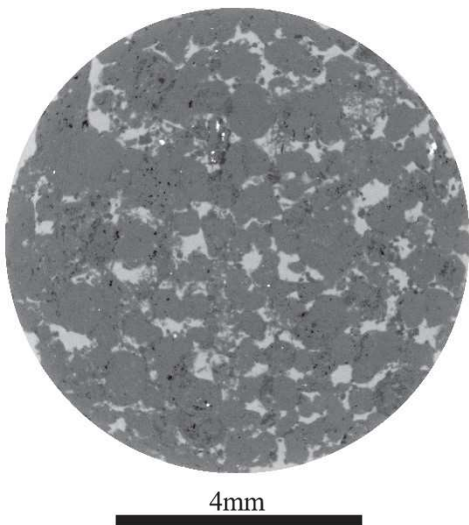
5mm

Raw image (z central slice)

4mm

Three phases segmented image (oil (black), solid (ocher), and brine (cyan)).

4mm

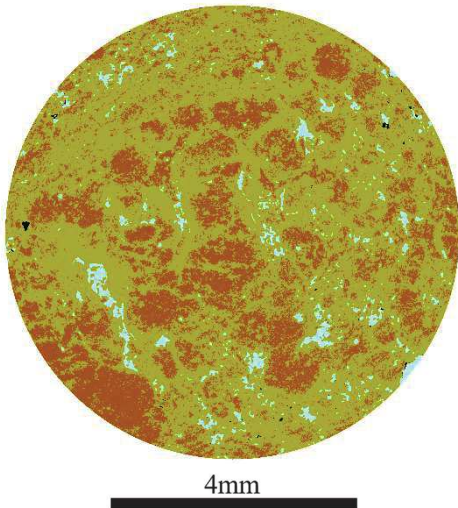Brine-filled microporosity map (black 100% brine and white 0% brine).

4mm
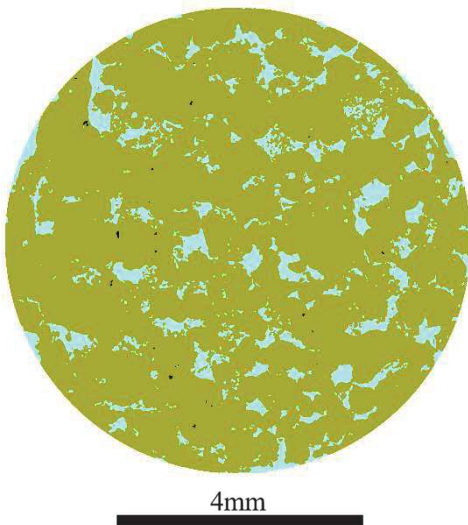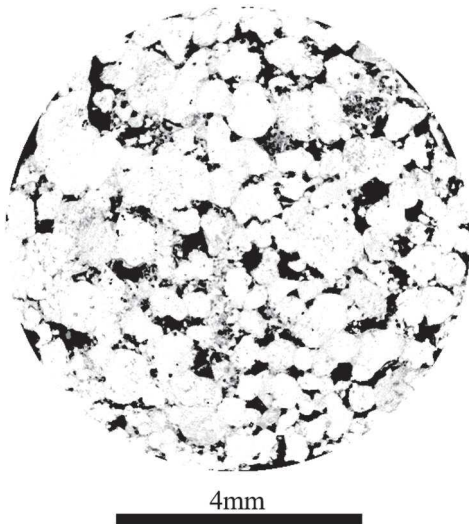
Total Sw (%):	93.94
Macro Sw (%):	99.69
Micro Sw (%):	80.53

APPENDIX H – Raw and processed μCT slices - Article 6.

Dry Sample

Raw image (x central slice)
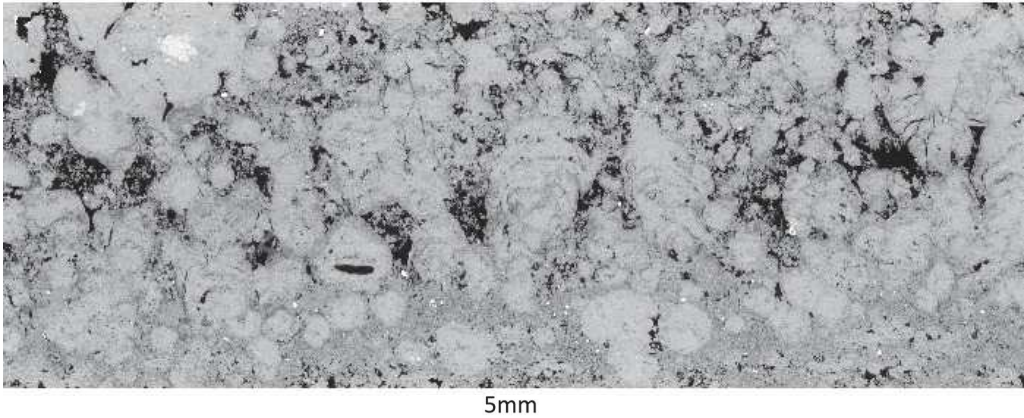
5mm

Raw image (z central slice).

4mm

Three phases segmented image (macropore (black), nonporous solid (ocher), and microporous solid (cyan)).

4mm

Porosity map (black 100% porous and white 0% porous).

4mm
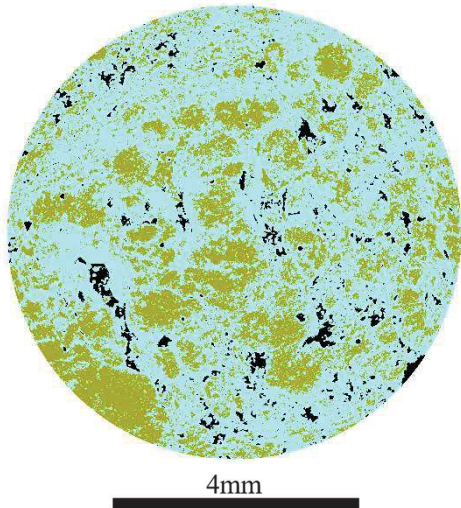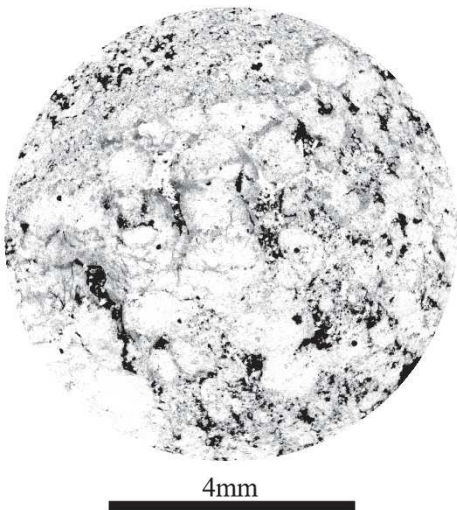
Total porosity (%):	18.42
Macroporosity (%):	5.53
Microporosity (%):	12.89

Brine Saturated Sample

Raw image (x central slice).
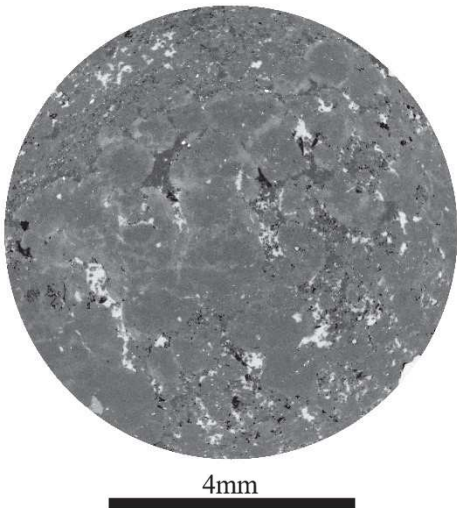

5mm
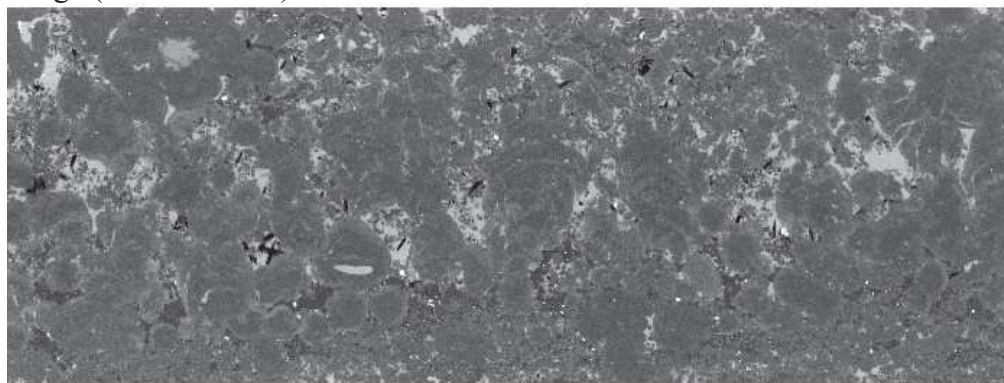
Raw image (z central slice).

4mm

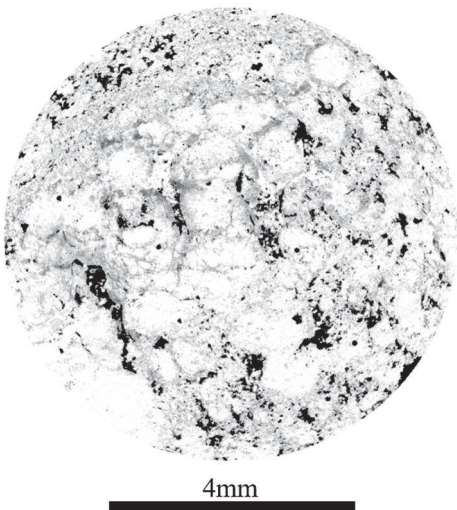# Primary Drainage (0.25 psi)

Raw image (x central slice).
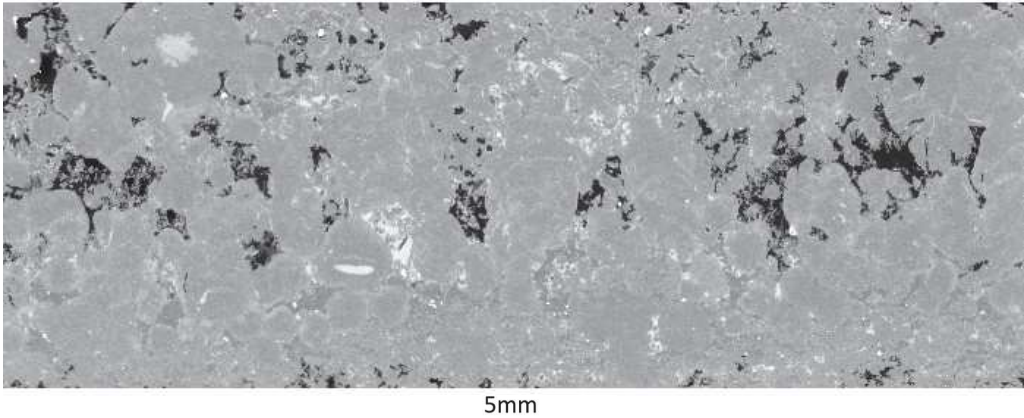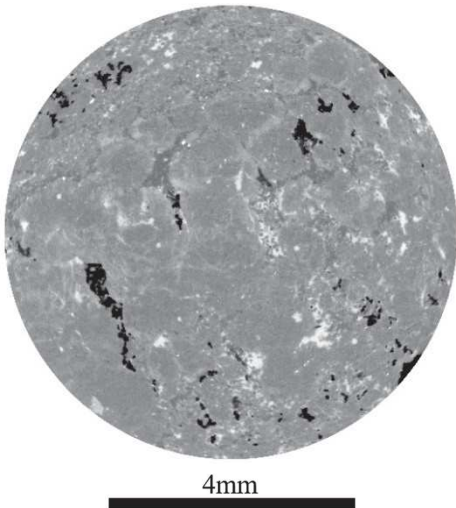
5mm

Raw image (z central slice).

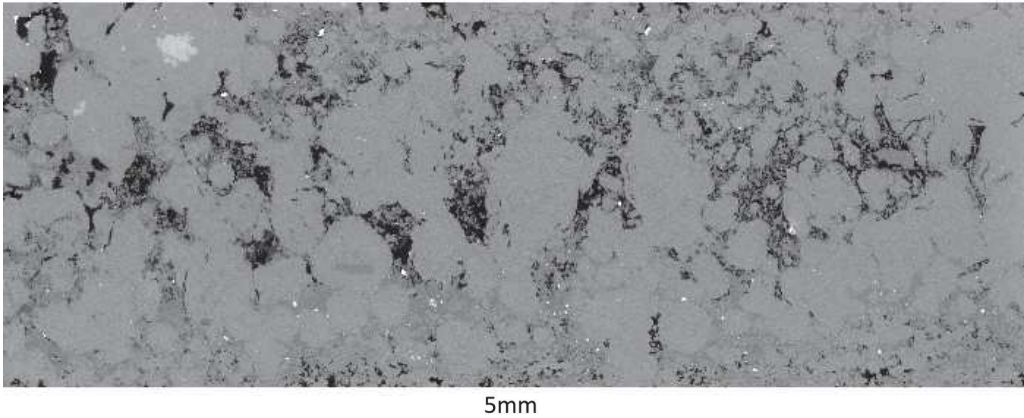For phases segmented image (oil (black), solid nonporous (ocher), solid porous (beige), and brine (cyan)).

4mm

4mm

Brine-filled microporosity map (black 100% brine and white 0% brine).

4mm
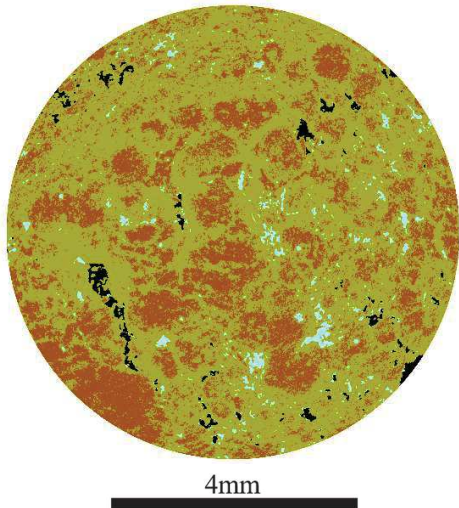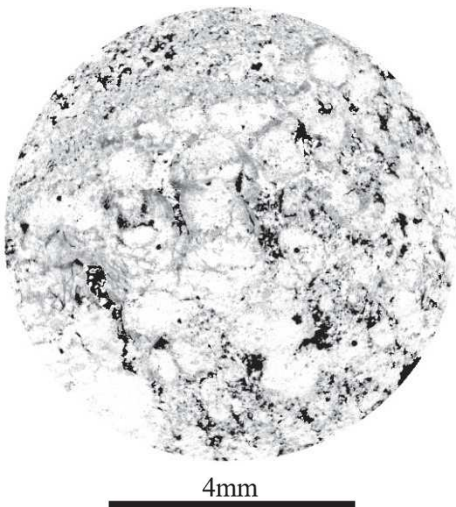
|	
Total Sw (%):	71.52
Macro Sw (%):	27.03
Micro Sw (%):	90.51

Primary Drainage (1.56 psi)

Raw image (x central slice).
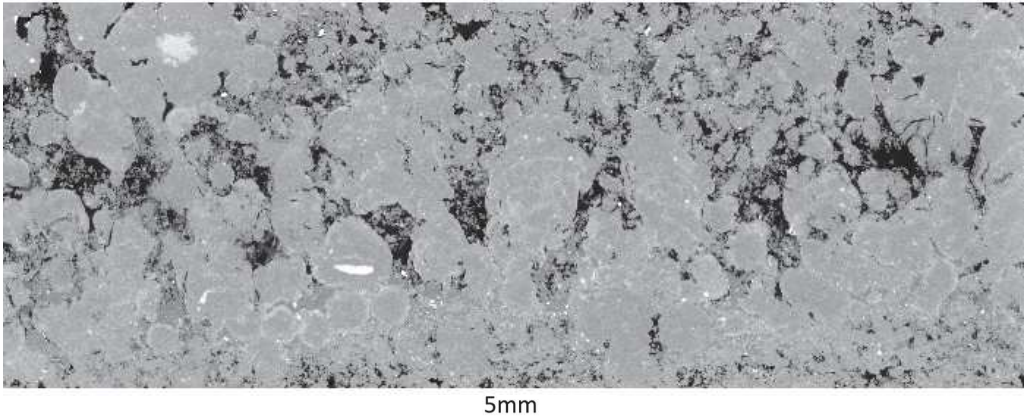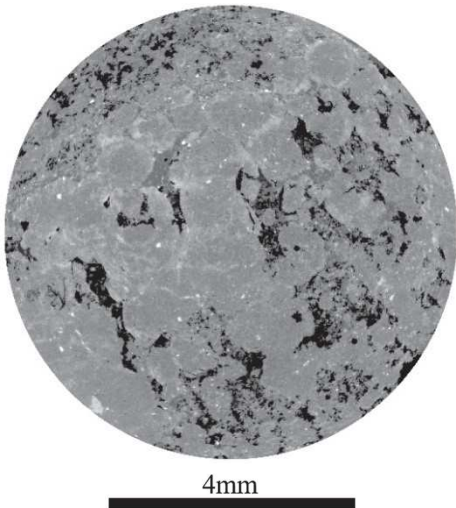
5mm

Raw image (z central slice).

4mm

For phases segmented image (oil (black), solid nonporous (ocher), solid porous (beige), and brine (cyan)).

4mm

Brine-filled microporosity map (black 100% brine and white 0% brine).

4mm
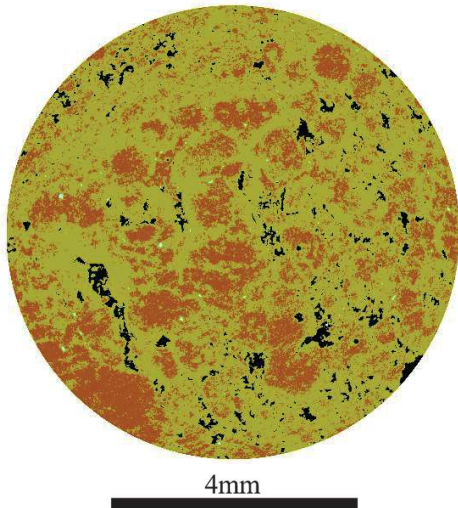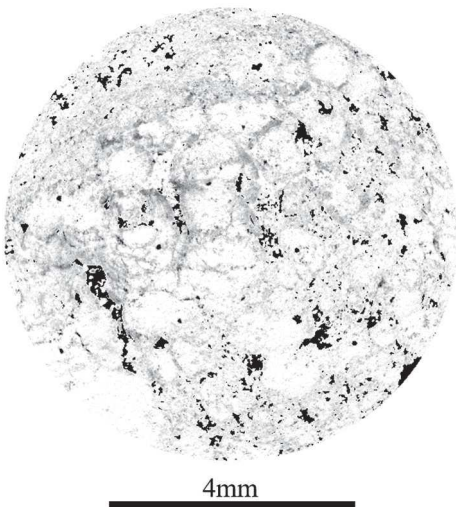
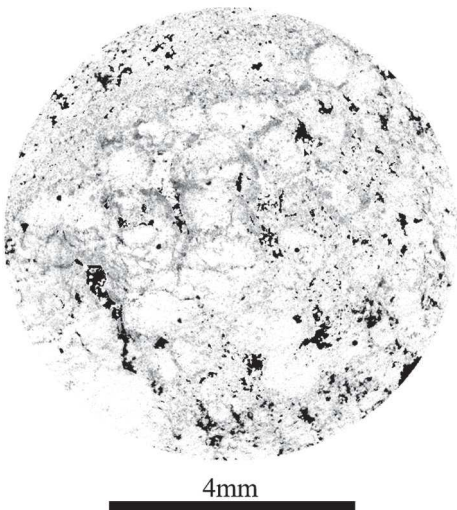|	
Total Sw (%):	34.37
Macro Sw (%):	2.56
Micro Sw (%):	48.02

Aging (7 days)

Raw image (x central slice).
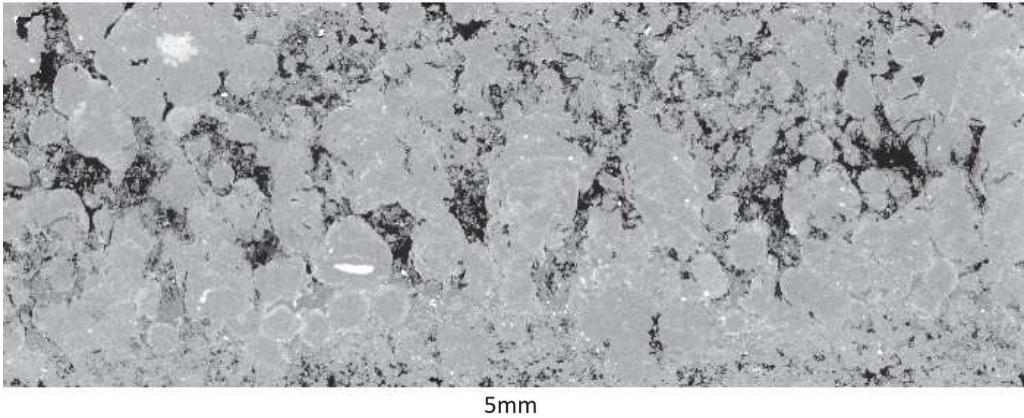
5mm

Raw image (z central slice).

For phases segmented image (oil (black), solid nonporous (ocher), solid porous (beige), and brine (cyan)).

4mm

4mm

Brine-filled microporosity map (black 100% brine and white 0% brine).

4mm
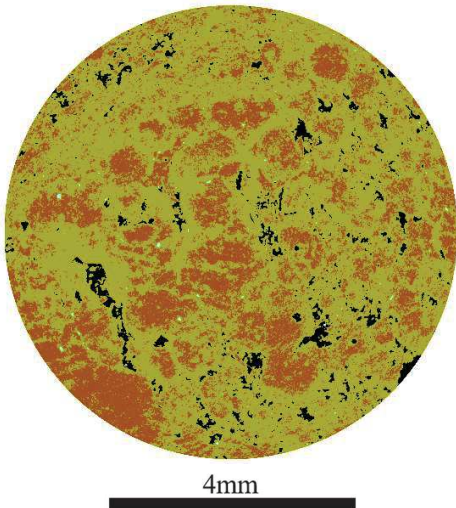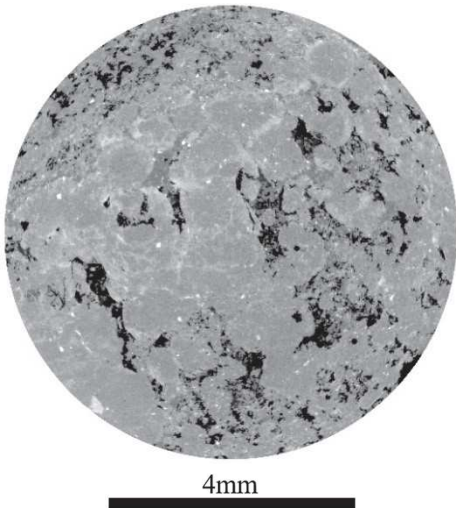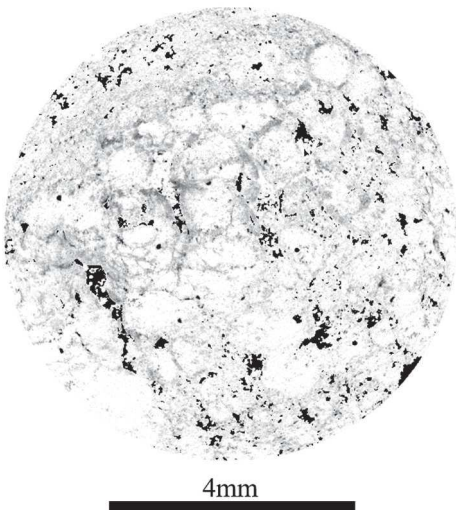
Total Sw (%):	34.51
Macro Sw (%):	2.83
Micro Sw (%):	48.10

Spontaneous Imbibition (13 days)

Raw image (x central slice).
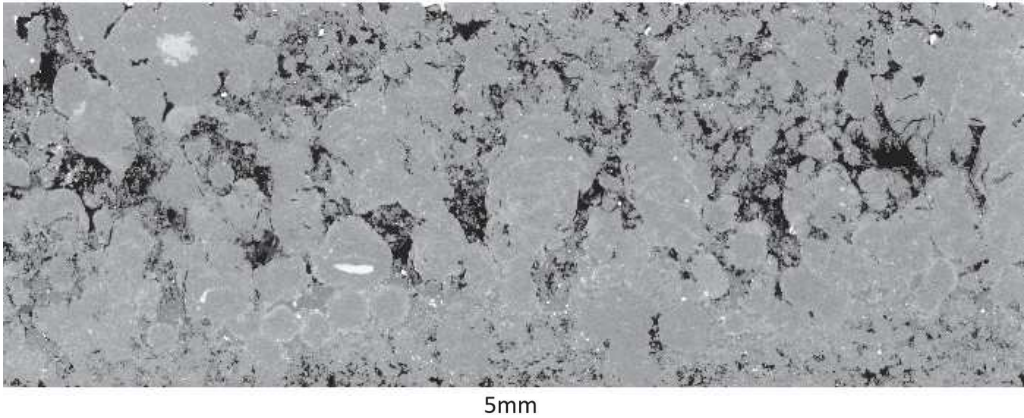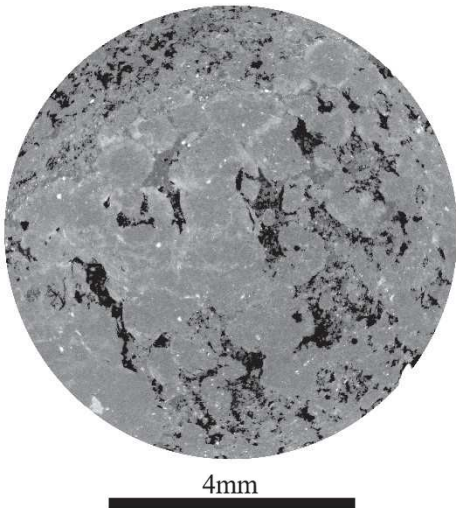
5mm

Raw image (z central slice).

4mm

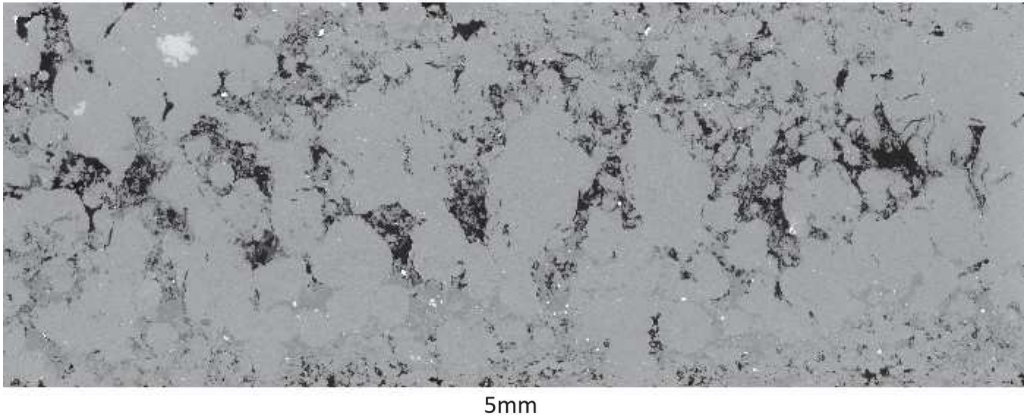For phases segmented image (oil (black), solid nonporous (ocher), solid porous (beige), and brine (cyan)).

4mm

Brine-filled microporosity map (black 100% brine and white 0% brine).

4mm
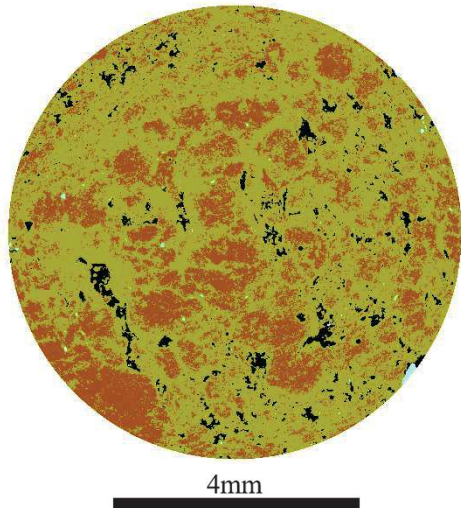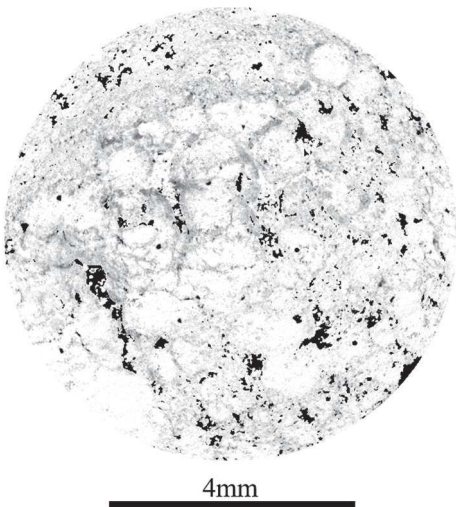
|	
Total Sw (%):	38.97
Macro Sw (%):	8.10
Micro Sw (%):	52.21

# Forced Imbibition (0.38 psi)

Raw image (x central slice).
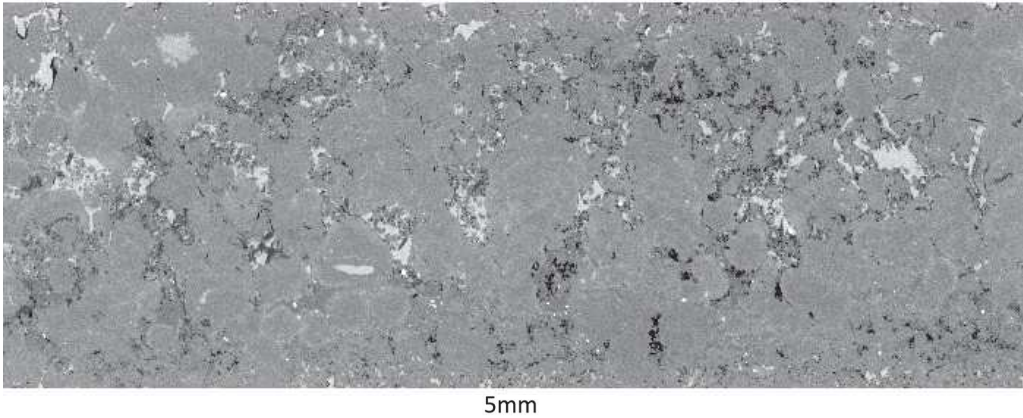
5mm

Raw image (z central slice).

For phases segmented image (oil (black), solid nonporous (ocher), solid porous (beige), and brine (cyan)).

4mm

4mm

Brine-filled microporosity map (black 100% brine and white 0% brine).

4mm
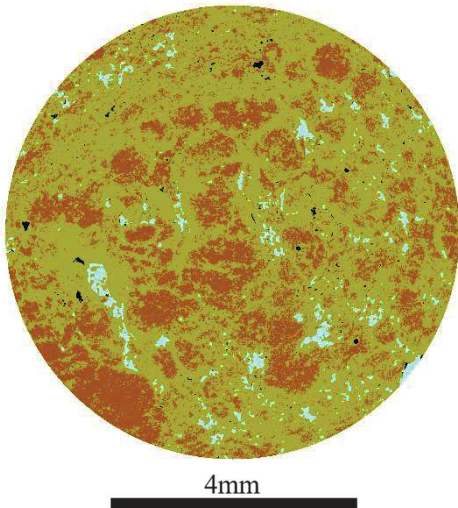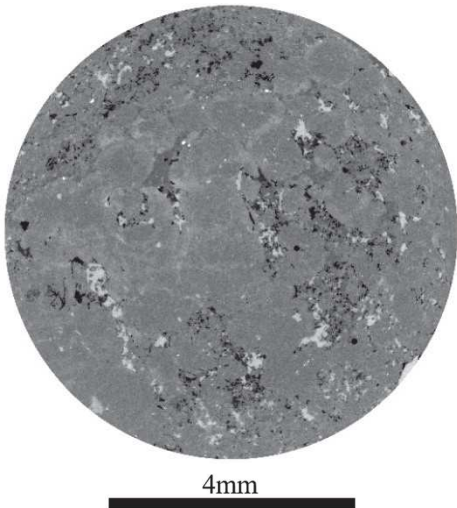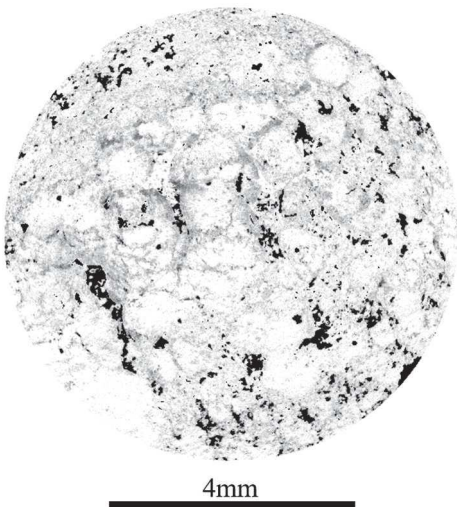
Total Sw (%):	71.72
Macro Sw (%):	88.97
Micro Sw (%):	64.31

Forced Imbibition (3.03 psi)

Raw image (x central slice).
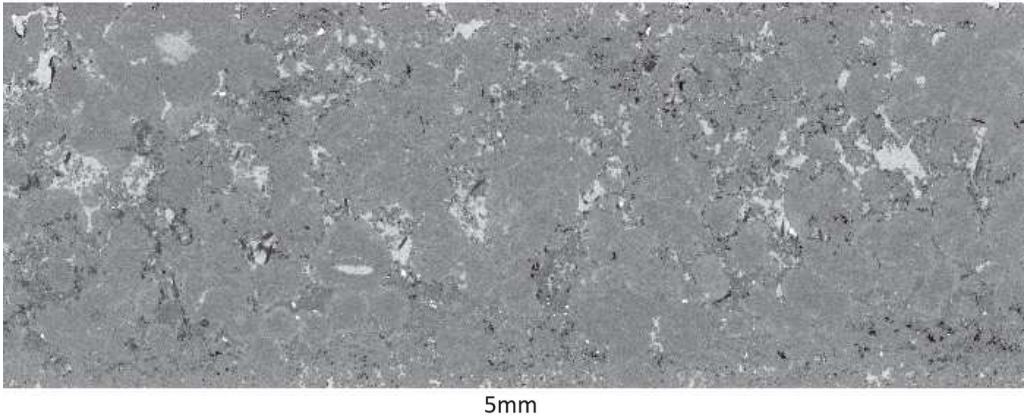
5mm

Raw image (z central slice).

For phases segmented image (oil (black), solid nonporous (ocher), solid porous (beige), and brine (cyan)).

4mm

4mm

Brine-filled microporosity map (black 100% brine and white 0% brine).

4mm
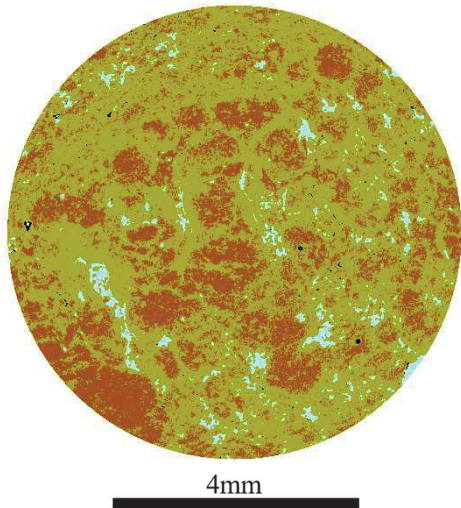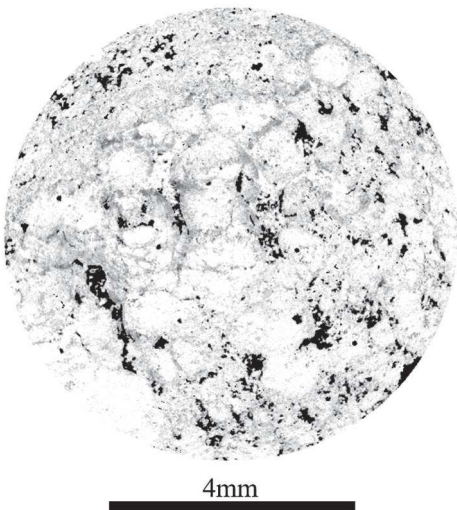
Total Sw (%):	79.50
Macro Sw (%):	95.74
Micro Sw (%):	72.54

Forced Imbibition (48.52 psi)

Raw image (x central slice).
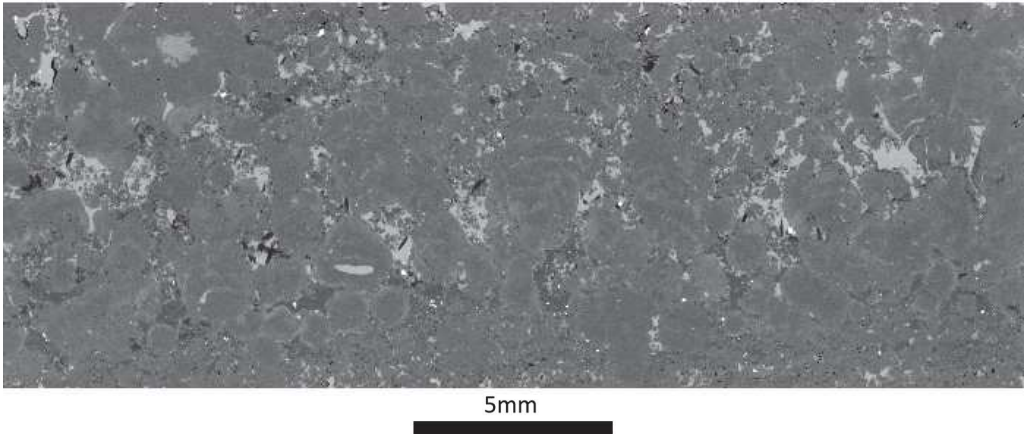
5mm

Raw image (z central slice).

For phases segmented image (oil (black), solid nonporous (ocher), solid porous (beige), and brine (cyan)).

4mm

4mm

Brine-filled microporosity map (black 100% brine and white 0% brine).

4mm

Total Sw (%):	85.17
Macro Sw (%):	97.25
Micro Sw (%):	79.98

Second Drainage (11 days)

Raw image (x central slice).

5mm

Raw image (z central slice).

4mm

For phases segmented image (oil (black), solid nonporous (ocher), solid porous (beige), and brine (cyan)).

4mm

Brine-filled microporosity map (black 100% brine and white 0% brine).

4mm
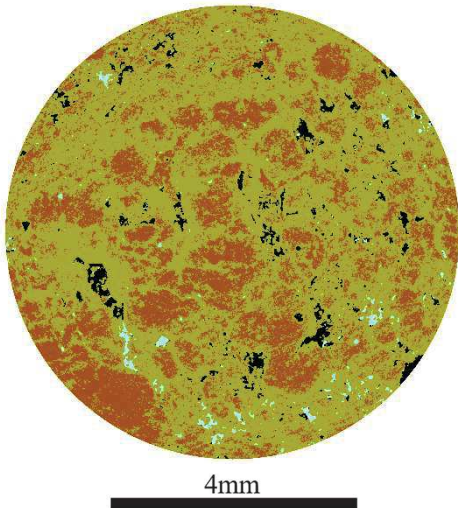
Total Sw (%):	36.46
Macro Sw (%):	63.30
Micro Sw (%):	55.25

Second Drainage (27 days)

Raw image (x central slice).

5mm

Raw image (z central slice).

For phases segmented image (oil (black), solid nonporous (ocher), solid porous (beige), and brine (cyan)).


4mm

4mm

Brine-filled microporosity map (black 100% brine and white 0% brine).

4mm
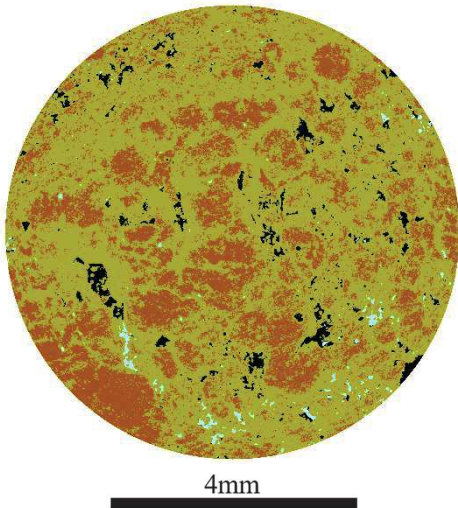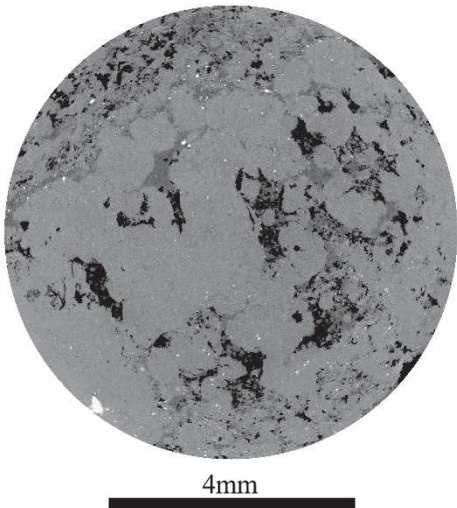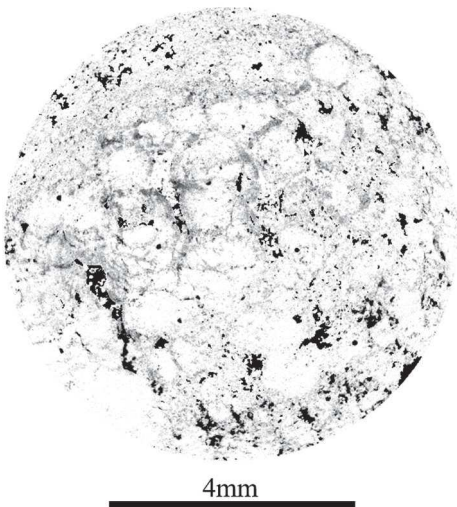
Total Sw (%):	27.75
Macro Sw (%):	56.87
Micro Sw (%):	48.13

APPENDIX I – Raw and processed µCT slices – Short communication.

Dry Sample

Raw image (x central slice)
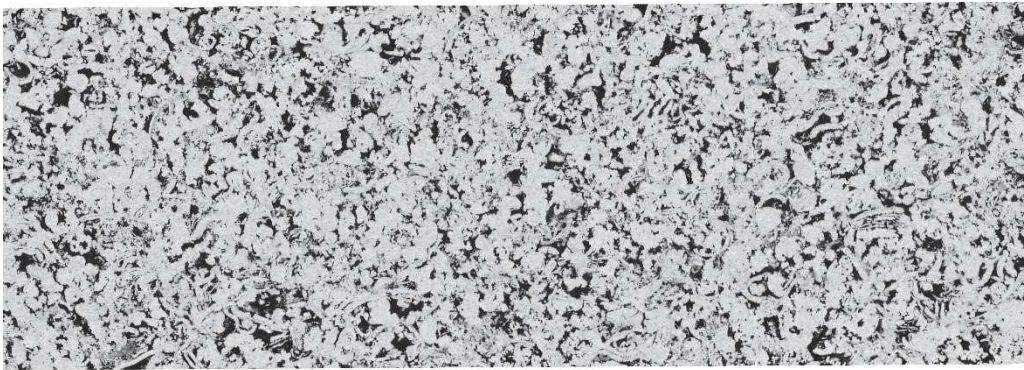
2 mm

Raw image (z central slice).

Three phases segmented image (macropore (black), nonporous solid (ocher), and microporous solid (cyan)).

2 mm
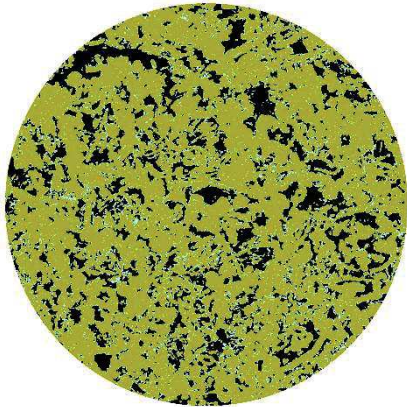
2 mm

Porosity map (black 100% porous and white 0% porous).
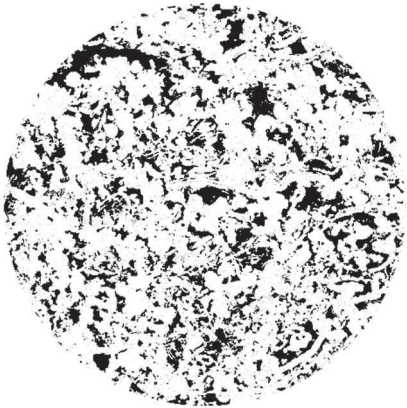
2 mm

Total porosity (%):	23.54
Macroporosity (%):	21.61
Microporosity (%):	1.93

Brine Saturated Sample

Raw image (x central slice).

2 mm
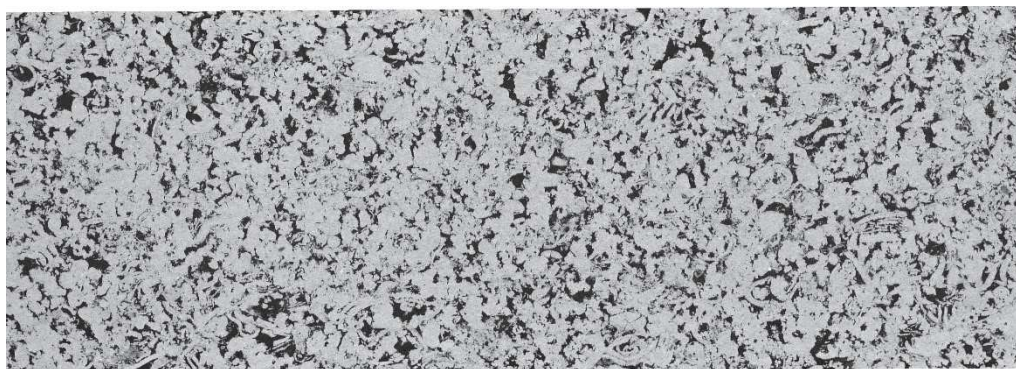
Raw image (z central slice).

2 mm

Primary Drainage (2.02 psi)

Raw image (x central slice).

2 mm

Raw image (z central slice).

Three phases segmented image (oil (black), solid (ocher), and brine (cyan)).

2 mm

2 mm

Macro Sw (%):   29.79
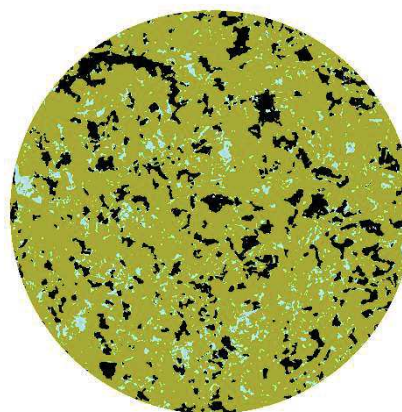
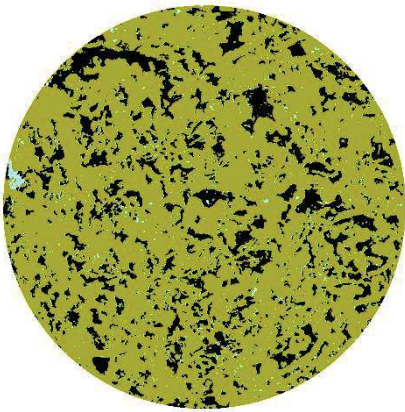# Primary Drainage (8.09 psi)

Raw image (x central slice).
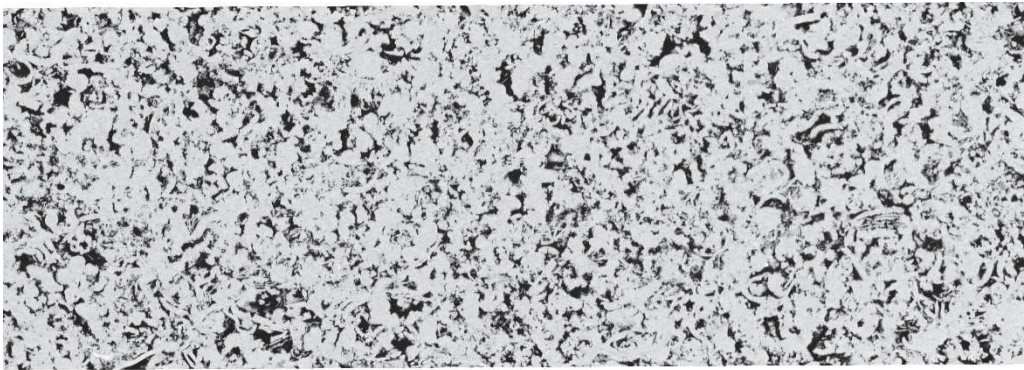
2 mm

Raw image (z central slice).

Three phases segmented image (oil (black), solid (ocher), and brine (cyan)).

2 mm

2 mm

Macro Sw (%):   9.19

Spontaneous Imbibition (17 days)

Raw image (x central slice).
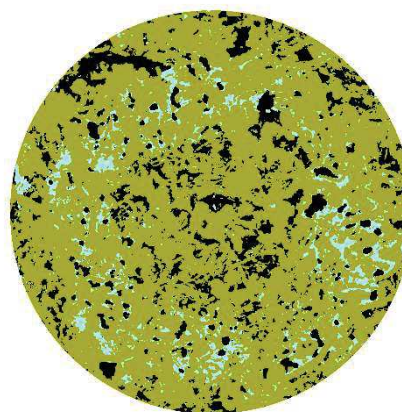

2 mm

Raw image (z central slice).   Three phases segmented image (oil (black), solid (ocher), and brine (cyan)).

2 mm   2 mm

Macro Sw (%):   78.39

APPENDIX J – Elsevier publishing permission – Articles 1, 2, and 3.

Elsevier Policies

Copyright

Licensing and copyright option   Comparing reuse rights   Publishing Agreements   CC BY-NC-ND/ CC BY-NC licenses

Authors' licensing and copyright options when publishing research articles with Elsevier

In order for Elsevier to publish and disseminate research articles, we need authors to grant us certain publishing rights, which are determined by the author's choice of publishing model and, in the case of open access articles, the author's choice of end user license.

Irrespective of the model under which an article is published, Elsevier is committed to protecting and defending authors' works and their reputation. We take allegations of infringement, plagiarism, ethical disputes, and fraud very seriously.

Elsevier offers two publishing routes for authors to choose from, which have different implications for authors and others:

1. Pay-to-publish, also known as open access, which usually requires a fee from the author, or their institution or funder, to publish. When publishing open access with Elsevier, the author retains their copyright in the article and grants Elsevier a license to publish it. Authors have a choice of end user license:

- If the author selects a Creative Commons Attribution (CC BY) license, end users are bound by this license. Each author can re-use their article themselves and *also* grant others (additional to Elsevier) a license to re-use their article for any purpose without permission from, or payment to, Elsevier.
- If the author selects a Creative Commons Attribution-NonCommercial-NoDerivatives (CC BY-NC-ND) license or a Creative Commons Attribution-NonCommercial (CC BY-NC) license, end users are bound by the license. Each author retains the right to re-use the article for their own commercial and non-commercial purposes, including creating derivative works, without permission from, or payment to, Elsevier.

2. Pay-to-read, where articles are free to publish, but usually require a subscription or payment to read. When publishing subscription the author typically transfers copyright to the publisher. However, each author retains the right to re-use the article for certain personal and scholarly purposes, including the creation of some derivative works, without permission from, or payment to, Elsevier.

In all cases, any rights the author grants to Elsevier apply only to the published article. Elsevier does not require, nor ever request, rights to the underlying research itself. Authors (and institutions or employers) will continue to retain patent, trademark and other intellectual property rights relating to the research, as well as the right to use their research data freely and without restriction.

Comparing reuse rights

The below tables compare rights for authors and others under the publishing agreements for open access articles (OA) with CC BY, CC BY-NC and CC BY-NC-ND licenses and subscription articles.

Authors' rights in the article

	OA with CC BY	OA with CC BY-NC	OA with CC BY-NC-ND	Subscription
Receive proper attribution and credit for their published work	Yes	Yes	Yes	Yes
Re-use their article in their own new works, without permission from Elsevier or payment to Elsevier, including by: • making copies of the article (or part of the article) to promote companies or products they own, whether or not such promotion is commercial; • including the article in a thesis or dissertation; • extending the article to a book, including the article in a subsequent compilation of their own work, or re-using portions, excerpts, and their own figures, tables and images from the article in their own new works (which in each case may be published with Elsevier or with a third party commercial or non-commercial publisher, at the author's discretion)	Yes	Yes	Yes •	Yes[1]

Notes:

• [1] The list is exhaustive in the case of articles published under the subscription model; additional uses/ sharing beyond those listed would require permissions to be requested from Elsevier.

APPENDIX L – Lyell publishing Permission – Article 4.

Lyell Collection

Geological Society Publications

Anywhere | Search Lyell Collection 🔍 🛒 👤 Log In | Register

Republishing material from Geological Society publications

Extensive quotation (more than c. 100 words) and reproduction of previously published illustrations (even if redrawn) require permission from the rights holder (the Geological Society in this case). In the UK, material remains in copyright until 70 years after the death of the author.

Material that can be used without permission:

- Authors may reuse their own material without permission subject to the exceptions listed below. They may include the whole article in a PhD or other thesis provided that it will not be published, and that the original source is fully acknowledged in the standard form (see below for examples). If the thesis is to be included in the institution's electronic repository or other online host, authors must use their own finally accepted version, not the typeset PDF (unless it is Gold OA). Authors may not republish their whole article, or a substantial part of it, without permission. Such permission will be granted only in exceptional circumstances.
- Anyone may use up to three items (text extracts of 100 words or less, figures or tables) from Geological Society-published material without permission or charge provided that a proper acknowledgement of source is made (see below for examples).
- There are no free items if formal permission is required from the Geological Society (e.g. a letter of authorization or completion of a form); please use the Copyright Clearance Center (see details below).
- The abstracts of articles can be reproduced without permission or fees provided that a full reference and a link to the article abstract page are included.
- The Geological Society is not usually the rights holder for cover photographs; permission must be sought from the owner/photographer.
- If your article forms part of a multi-author book, the publisher must ensure the total number of items from Geological Society publications does not exceed three (this does not apply to journal issues).